ANALYSIS OF FLOW EVOLUTION IN THE CYLINDERS OF MOTORED RECIPROCATING ENGINES

by

Bizhan Ahmadi-Befrui

BSc(Eng), MSc(Eng), DIC

Thesis submitted for the degree of

Doctor of Philosophy

of the

University of London

May 1985

Mechanical Engineering Department,
Imperial College of Science & Technology.

ABSTRACT

The thesis is concerned with the assessment of a multi-dimensional mathematical prediction method for the in-cylinder flow processes, and the utilisation of the same for the detailed analysis of the mean flow and turbulence evolution in motored reciprocating engines.

The mathematical model comprises the differential conservation equations of mass, momentum and stagnation enthalpy for Favre (density-weighted) ensemble-averaged quantities and incorporates the two equation k-ε model of turbulence. The equations are discretised according to the 'finite-volume' method and are solved numerically on a computational grid that expands and contracts with the piston and the valve motions.

The mathematical method is assessed through simulation of flow in a four-stroke, disc-chamber, central-valve motored model engine and comparison of the predictions with the measurements of the mean velocity and turbulence intensity for the operating conditions of 200 rpm and compression ratios 3.5 and 6.7. The investigations involve assessment of the accuracy of predictions based on two different treatments of the flow boundary conditions at valve and that for three variants of the k-ε turbulence model, developed for the strongly compressible engine flows, namely, those of Watkins [1977], Morel & Mansour [1982] and El Tahry [1983]. It is found that (i) the effect of inlet flow boundary conditions diminish to an insignificant level near TDC compression, and (ii) the turbulence models produce closely similar predictions of the mean flow and turbulence intensity. In general, good qualitative and moderate quantitative agreement with measurements are obtained.

The predicted structure and evolution of the in-cylinder mean flow and turbulence - as characterised by the intensity, length and dissipation time scales and turbulent viscosity - are analysed in depth. The characteristics of the turbulence evolution is further analysed with the aid of the volume-integral balances of the turbulence model transport equations. In general, it was found that (i) the intake jet turbulence is in quasi-equilibrium and a quasi-steady state, (ii) over the cylinder-volume, turbulence is in quasi-equilibrium during most of induction, (iii) the intake-generated mean flow and turbulence intensity decay during compression, and turbulence relaxes into a structure predominantly controlled by the engine geometry at TDC compression, and (iv) turbulence generation by the intake-generated flow and that by distortion (compression) contribute towards turbulence sustainment during compression.

The influence of the turbulence model variants on the predictions of

the turbulence parameters are examined in order to identify the version(s) that produces physically plausible and consistent variations of these parameters during the engine cycle. It is concluded that on this basis the Watkins [1977] version is not suitable for engine applications, but the Morel & Mansour [1982] and El Tahry [1983] models are both suitable, with the former one marginally preferable.

The influence of compression ratio, engine speed and the inlet valve lift on the in-cylinder mean flow and turbulence characteristics is studied in detail. The predictions pertain to the axisymmetric model engine and are presented for compression ratios 3.5, 6.7 and 10.5; engine speeds 200, 500 and 1000 rpm; and two valves with (maximum lift/valve diameter) of 0.24 and 0.14. In all cases, the flow evolution is subjected to the kind of detailed analysis outlined above. In general, the predictions are in good agreement with experimental trends.

ACKNOWLEDGEMENTS

I would like to express my deep gratitude to my supervisor, Dr A.D. Gosman, for his guidance, constructive criticism and advice, and continuous support throughout the course of this research.

I am thankful to Dr A.P. Watkins and Dr R.J.R. Johns for many helpful discussions on the subtle aspects of the computational fluid mechanics.

I am grateful to Professor P. Bradshaw, Dr P.W. Bearman and Dr W.P. Jones for their valuable discussions on the turbulence structure and its modelling.

I have benefitted from my association with all my colleagues, in particular Dr C. Arcoumanis, Dr A.F. Bicen, Mr A. Jahanbakhsh and Mr C. Vafidis; their assistance and numerous fruitful discussions are deeply appreciated.

I am grateful to my parents and my wife Christina for their continuous support and encouragement.

I thank Mrs E.A. Hall for her excellent and speedy typing of the thesis.

I would like to thank the staff of the Imperial College Computer Centre, in particular Mr A.G. Spirling, for their assistance. My thanks also go to Miss E.M. Archer, Mrs N. Scott-Knight and Mr G. Tindall for their unstinted help.

The financial support provided by the United Kingdom Atomic Energy Authority for this work is gratefully acknowledged.

To my parents and teachers,
who taught me in the humanities and sciences,
and to my wife Christina.

CONTENTS

		Page
Title Page		1
Abstract		2
Acknowledgements		4
Dedication		5
Contents		6
Nomenclature		10
CHAPTER 1:	INTRODUCTION	14
1.1	Background	14
1.2	The Problem and Objectives	15
1.3	The Present Contribution	16
1.4	The Thesis Outline	17
CHAPTER 2:	SURVEY OF PREVIOUS RESEARCH	19
2.1	Introduction	19
2.2	Experimental Studies	19
2.2.1	Statistical characterisation of the flow	19
2.2.2	The important turbulence-characterising parameters	25
2.2.2.1	Spatial covariance and length scales	26
2.2.2.2	Autocorrelation coefficient and time scales	29
2.2.2.3	The spectral density function, $E(\omega)$	32
2.2.3	Measurement techniques	32
2.2.3.1	Hot-wire anemometry	32
2.2.3.2	Laser-Doppler anemometry	34
2.2.4	Review of the measurements	36
2.2.5	Characteristics of the in-cylinder flow processes	37
2.2.5.1	Induction process	37
2.2.5.1.1	Characteristics of flow through a valve	37
2.2.5.1.2	The in-cylinder pressure variation	41
2.2.5.1.3	Mean flow structure in the cylinder	42

Page

2.2.5.1.4 Turbulence characteristics 45
2.2.5.2 Compression process 48
2.2.5.2.1 Mean flow structure in the cylinder 48
2.2.5.2.2 Turbulence characteristics 50
2.2.5.3 Expansion stroke 52
2.3 Theoretical Studies 52
2.3.1 Multi-dimensional predictions of the flow 52
2.3.2 Turbulence modelling aspect 58
2.4 Closure 59

CHAPTER 3: THE MATHEMATICAL MODEL 62
3.1 Introduction 62
3.2 The Instantaneous Equations 62
3.3 The Statistical Approach 64
3.3.1 The ensemble-averaged equations 64
3.4 Turbulence Modelling 66
3.4.1 The nature of turbulence 67
3.4.2 Choice of a turbulence model 69
3.4.2.1 Mean flow or eddy viscosity type closures 69
3.4.2.2 Reynolds stress closures 71
3.4.2.3 Multiple time-scale closure 73
3.4.2.4 Large eddy simulation 73
3.4.2.5 Choice of model 74
3.4.3 The k-ε model of turbulence 74
3.4.3.1 The k-transport equation 74
3.4.3.2 The ε-transport equation 76
3.4.3.3 The scalar quantities 84
3.4.4 Shortcomings of model for complex compressible flow applications 85
3.5 General Transport Equation 88
3.6 Boundary Conditions 89
3.6.1 Wall boundary conditions 89
3.6.2 Symmetry axis 92
3.6.3 Planes of inlet and exhaust apertures 92
3.7 Closure 95

		Page
CHAPTER 4:	THE NUMERICAL SOLUTION METHOD	97
4.1	Introduction	97
4.2	Transformation to Moving Coordinate Frame	97
4.2.1	The transformation relations	97
4.2.2	Transformed general transport equation	100
4.3	The Method of Discretisation	100
4.3.1	Derivation of the general difference equation	101
4.3.2	Treatment of momentum equations	106
4.3.3	The differencing schemes	108
4.3.4	Differencing of the source terms	111
4.4	Pressure Calculation	113
4.5	Implementation of the Boundary Conditions	119
4.5.1	Wall boundary conditions	119
4.5.2	Axis of symmetry	121
4.5.3	Planes of inlet and exhaust apertures	121
4.6	Solution Procedure	122
CHAPTER 5:	ASSESSMENT OF THE CALCULATION METHOD AND THE TURBULENCE MODELS	125
5.1	Introduction	125
5.2	Details of the Test Cases	126
5.3	Effects of the Grid Density and Time-Step Size	127
5.3.1	Grid density	127
5.3.2	Time-step	128
5.4	The Influence of Inlet Conditions	129
5.5	Predictions and Comparison with Experimental Data	131
5.5.1	Test case I (Ahmadi-Befrui, et al. [1982])	131
5.5.1.1	The predicted flow evolution	131
5.5.1.2	The integral balances of the k-ε transport equations	141
5.5.1.3	Comparison with experimental data	143
5.5.2	Test case II (Arcoumanis, et al. [1981a])	149
5.5.2.1	The predicted flow evolution	149
5.5.2.2	The integral balances of the k-ε transport equations	155
5.5.2.3	Comparison with experimental data	156
5.6	Assessment of the Turbulence Models	158
5.7	Closure	160

		Page
CHAPTER 6:	STUDY OF TURBULENT ENGINE FLOWS	164
6.1	Introduction	164
6.2	The Influence of Variations in Compression Ratio	164
	6.2.1 Mean flow and turbulence parameters	164
	6.2.2 Turbulence energy balance	169
6.3	The Influence of Valve Lift	171
	6.3.1 Mean flow and turbulence parameters	171
	6.3.2 Turbulence energy balance	174
6.4	The Influence of Engine Speed	175
	6.4.1 Mean flow and turbulence parameters	175
	6.4.2 Turbulence energy balance	180
6.5	Closure	181
CHAPTER 7:	CONCLUSIONS	184
7.1	Main Findings and Achievements	184
7.2	Suggestions for Future Work	186
References		188
APPENDIX A:	DIFFERENTIAL EQUATIONS FOR ENSEMBLE-AVERAGED QUANTITIES AND CYCLE-TO-CYCLE VARIATIONS	208
APPENDIX B:	INTRODUCTION OF DENSITY-WEIGHTED AVERAGING AND DERIVATION OF THE GOVERNING DIFFERENTIAL EQUATIONS FOR DWEA PROPERTIES	211
APPENDIX C:	TRANSPORT EQUATIONS FOR THE REYNOLDS STRESSES AND THE TURBULENCE KINETIC ENERGY	215
Tables		219
Figures		246

NOMENCLATURE

Roman Characters

A	:	coefficient of finite difference equation (subscripted P, W, E, N, S), area
a	:	cell-face area (subscripted w, e, n, s, etc.)
A_L	:	valve exit area
A_M	:	valve minimum area
B	:	cylinder diameter (bore)
BDC	:	bottom dead centre
C_μ, $C_{\varepsilon 1} - C_{\varepsilon 4}$	:	coefficients of the turbulence model
C_D	:	valve discharge coefficient
CA	:	crank angle
CR	:	compression ratio
D	:	valve diameter, velocity divergence ($\equiv$ div. $\underline{U}$)
d	:	valve stem diameter
DWEA	:	density-weighted ensemble-averaging
E	:	constant of the turbulence model, cylinder-volume-integral of dissipation rate ε
EA	:	ensemble-averaging
e	:	internal energy
$E(\omega)$	:	spectral density function
f	:	frequency, spatial weighting factor
G_S, G_N, G_C	:	cylinder-volume-integrals of turbulence generation terms
h_s	:	stagnation enthalpy
K	:	cylinder-volume-integral of turbulence energy k
k	:	turbulence kinetic energy
L	:	turbulence integral length scale, valve lift
L_{cr}	:	connecting rod length
L_t	:	turbulence integral time scale
L_{max}	:	maximum valve lift
ℓ	:	length scale of turbulence energy containing eddies (dissipation length scale)
ℓ_m	:	Prandtl mixing length
Ma	:	Mach number
$\dot{m}$	:	mass flow rate through the valve
P	:	pressure, total turbulence energy production
P_{cyl}	:	cylinder mean pressure
Pe	:	Peclet number
$\dot{q}$	:	heat flux

R : gas constant

$R_{ij}(r)$: spatial correlation

$R(\tau)$: autocorrelation coefficient

$R_\theta(\phi)$: autocorrelation coefficient for a non-stationary flow

r : radial coordinate

Re : Reynolds number

S : engine speed

S_{ij} : strain field of the $\tilde{u}_i$ velocity field

S_t : engine stroke

S_ϕ : source term in the partial differential and finite difference equations

S_I, S_E : implicit and explicit contributions to S_ϕ

T : temperature

T/E : hybrid of time/ensemble-averaging

t : time, valve seat thickness (in equation (2.36))

T_{cycle} : cycle period (period of one revolution of crank shaft)

T_{cyl} : cylinder mean temperature

u : instantaneous velocity

$\overline{u}$: mean (time- or ensemble-averaged) velocity

$\tilde{u}$: density-weighted ensemble-averaged velocity

$\hat{u}$: axial velocity relative to grid

u_c : centreline velocity of round and plane jets

u_τ : friction velocity

u_{in} : inlet velocity (normal to the valve exit plane)

u' : turbulence intensity, turbulence fluctuations about $\overline{u}$ (in Chapter 3)

u'' : turbulence fluctuations about $\tilde{u}$

V : volume, radial velocity

v : turbulence velocity scale (in Chapter 3)

$\overline{V}_p$: mean piston speed

y : normal distance from the wall

y^+ : dimensionless distance from the wall

z : axial coordinate

Z_{sep} : width of the reverse flow region at valve

Greek Characters

α : spatial difference coefficient

β : temporal difference coefficient

Γ : turbulent diffusivity

γ : ratio of specific heats

Δ	:	increment
δ_{ij}	:	Kroneker delta
ε	:	turbulence energy dissipation rate
η	:	Kolmogorov micro length scale
η_v	:	volumetric efficiency
θ	:	crank angle, circumferential coordinate
κ	:	wave number, von Kármán constant
λ	:	turbulence micro (Taylor) length scale
λ_t	:	turbulence micro time scale
μ	:	molecular viscosity
μ_T	:	turbulent viscosity
μ_{eff}	:	effective viscosity ($\equiv \mu + \mu_T$)
ν	:	kinematic viscosity
ξ	:	non-dimensional axial coordinate
ρ	:	density
σ_T	:	turbulent Prandtl/Schmidt number
τ_d	:	dissipation (or decay) time scale
τ_{ij}	:	stress tensor
τ_w	:	wall shear stress
ϕ	:	a dependent variable
ψ	:	valve seat angle
ω	:	frequency, engine angular velocity

Subscripts

cyl	:	cylinder
d	:	downstream
E	:	ensemble-averaged
G	:	grid
i, j, k, l	:	Cartesian tensor notation
o	:	stagnation condition
p	:	piston
T	:	time-averaged, turbulent
t	:	temporal
u	:	upstream
v	:	valve
w	:	wall
X, x	:	longitudinal (direction x), spatial
Y, y	:	lateral (direction y)

Superscripts

n	:	new time level
o	:	old time level
$-$	:	time- or ensemble-averaged
$'$	:	turbulence intensity, fluctuating component about time/ ensemble mean, correction quantity
$\sim$	:	density-weighted ensemble-mean
$''$	:	fluctuating component about density-weighted ensemble mean
$*$	:	prevailing variable field
$+$	:	dimensionless (in the 'wall functions')

CHAPTER 1
INTRODUCTION

1.1 BACKGROUND

In the past 10 to 15 years, there has been a growing recognition by the automotive industry of the limitations of the cut-and-try empirical method of engine development in keeping pace with the increasing demands on performance, fuel economy and reduced pollutant emissions. In this connection, it has become apparent that a more complete understanding of the characteristics of the flow evolution in engines and its interaction with the combustion process is needed. This realisation has lead the automotive industry to direct its research activity more towards a fundamental understanding of the in-cylinder flow processes.

The fact that the turbulent flow field in an engine plays a paramount rôle in determining its combustion characteristics was discovered early in the history of reciprocating engines through the pioneering works of Clerk [1912], Ricardo [1922] and Alcock [1934]. Their qualitative findings - which have been confirmed and extended by the more recent quantitative experiments of, for example, Cole & Swords [1980] and Groff & Matekunas [1980] - have been effectively exploited by the engine designers to improve performance, fuel economy, emissions and the lean operating limit, through modification of the chamber and induction configurations (see, for example, Lancaster, et al. [1976], Brandl, et al. [1979]). However, the nature of the dependence of the in-cylinder flow on the engine geometry and operating conditions, the characteristics of its evolution during the engine cycle and the details of its influence on and interaction with the combustion processes (i.e. ignition, formation and propagation of a turbulent flame) are largely unknown.

The past decade has witnessed, as a consequence of the situation just described: a substantial increase in the detailed mathematical analysis of the in-cylinder flow processes; a growth in the recognition of the capabilities of the mathematical models; the development of more versatile, accurate and efficient numerical solution methods; and the availability of increasing computer power. As a result, it can now be stated with confidence that mathematical models offer an expedient and cost-effective means for:

(i) the development of a more complete knowledge of the in-cylinder flow processes; and

(ii) the identification of key controlling variables and their

effects, that can provide guidelines to less costly experimental test programmes.

The mathematical modelling activity may be categorised between attempts to predict the burn-rate and the exhaust emissions as a function of engine operating variables through 'phenomenological' models (see, for example, Blumberg, et al. [1979]) and efforts directed towards the detailed prediction of the in-cylinder flow processes through 'multi-dimensional' methods (see, for example, Watkins [1977], Ramos & Sirignano [1980a], El Tahry [1982], Gosman, et al. [1984]). The 'phenomenological' or 'zero-dimensional' models are structured from the first law of thermodynamics and chemical-kinetic considerations, in which the only real independent variable is time: thus, they do not provide detailed, geometry-dependent information on the flow field and the spatial distributions of such variables as temperature, species concentration, etc. These models are also limited in their design applications by their reliance on engine-dependent empirical or semi-empirical input flame propagation information (see, for example, Hires, et al. [1978], Tabaczynski, et al. [1980]).

The multi-dimensional method is more fundamental in that the partial differential conservation equations that govern the flow, heat transfer and combustion process are invoked and numerically solved over the entire combustion chamber: thus, it provides detailed information about the spatial and temporal development of the key characterising variables. However, in the case of turbulent flows in engines, the method requires additional equations representing mathematical models of the small, numerically-unresolvable features of important processes occurring within the flow, notably the turbulent transport of momentum, heat and chemical species. The accuracy of these models is thus of utmost importance in the engine circumstances, due to their significant rôle in the flow evolution, fuel/air mixing and combustion processes. The turbulence model is particularly important, for the mixing and combustion models rely on the key information, regarding the turbulence characteristics, it provides (see, for example, Andrews, et al. [1975], Ahmadi-Befrui [1980], Gosman & Harvey [1982], Brandstatter & Johns [1983]).

1.2 THE PROBLEM AND OBJECTIVES

As noted above, it is evident that the prediction capability of multi-dimensional methods is heavily reliant on turbulence models. However, considerable uncertainty exists about the turbulence modelling of

the non-stationary, strongly compressible engine flows. The approach adopted to date by researchers in this field is to assume that the turbulence models developed for stationary, non-compressible flows can be employed - with minor modifications to allow for the effect of compressibility - for engine applications. In this respect, several variants of the well-known k-ε turbulence model (Launder & Spalding [1972]) have been developed - with the differences in all instances due to the compressibility treatment - and employed in multi-dimensional calculation methods. However, hitherto the suitability and relative accuracy of these models have not been adequately assessed.

The present thesis addresses this problem by applying three selected k-ε variants to the complete simulation of the flow in model motored engines and assessing their suitability and accuracy through (i) detailed analysis of the predictions of the important turbulence parameters and comparison with their known behaviour in similar flows, and (ii) comparison with the experimental data obtained in the forementioned engines by previous investigators. The predictions and measurements presented in this study pertain to an axi-symmetric, central-valve, disc-chamber engine; however, the conclusions are believed to be valid for more complex engine configurations.

1.3 THE PRESENT CONTRIBUTION

The specific contributions of the work presented in this thesis are:

(i) Prediction and detailed analysis of the mean flow and turbulence evolution in motored reciprocating engines.

(ii) Assessment of three compressible flow variants of the k-ε turbulence model and establishment of the most suitable of these for application to engine flows, through comparison with two sets of data and analysis of the predicted turbulence parameters.

(iii) Provision of evidence and analysis of the influence of variations in the design and operating conditions - viz. the inlet valve lift, compression ratio and engine speed - on the in-cylinder flow.

(iv) Assessment of the influence of the flow boundary conditions at the inlet valve on the in-cylinder behaviour, through detailed comparison with data.

1.4 THE THESIS OUTLINE

Chapter 2 presents a review of previous theoretical and experimental studies of flows in engines. The difficulties in statistical characterisation of the non-stationary turbulent engine flows are explained and the techniques adopted for this by engine researchers are discussed. The important turbulence parameters are presented and their significance is explained. The capabilities and limitations of hot-wire anemometry and laser-Doppler anemometry techniques in the engine context are discussed. The experimental studies are then reviewed and their findings are used to assemble an overall picture of the in-cylinder flow evolution and to deduce the general trends of its dependence on the design and operating conditions. The remainder of Chapter 2 is devoted to a review of previous multi-dimensional calculations of the in-cylinder flow. The studies that have involved comparison of predictions with data are examined in detail and their capabilities and shortcomings are outlined. Finally, the studies concerning comparison of the variants of the k-ε turbulence model for engine applications are reviewed.

Chapter 3 is concerned with assembly of the differential equations that govern the in-cylinder turbulent flow. The need for a statistical approach is explained; the averaging procedures that can be applied to the non-stationary compressible engine flows are examined, and the most suitable one is selected. The differential equations for the statistically averaged flow properties are then derived. The choice of a turbulence model is discussed and the k-ε model is selected. The arguments concerning the modelling and the most suitable formulation of the k- and ε-transport equations for the strongly compressible, confined engine flows are presented, and the three variants examined in this study are discussed. The remainder of Chapter 3 is concerned with the flow conditions at the boundaries of the combustion chamber. The flow through the inlet valve is given especial attention and a new treatment, that takes the flow separation in the valve passage into effect, is proposed.

Chapter 4 is concerned with the discretisation of the differential equations. The transformation of the equations into a flexible coordinates frame that moves according to the piston and the valve motions is presented. The discretisation method is then outlined and the temporal and spatial differencing schemes employed are detailed. The procedure for pressure calculation is then explained. Finally, the implementation of the boundary conditions and the treatment of the inlet/exhaust valve flow are outlined.

Chapter 5 presents a detailed analysis of the predicted evolution of

the flow in a central-valve, disc-chamber model engine and assessment of the mathematical model through comparison of the predictions - for all three k-ε model variants - with two sets of data. The latter pertain to the operating speed of 200 rpm and compression ratios of 3.5 and 6.7. The numerical accuracy of the calculations is tested and the influence of the treatment of the inlet flow boundary condition on the predictions is evaluated. The predicted evolution of the in-cylinder flow - involving the mean velocity field and distributions of the key turbulence parameters, i.e. intensity, length-scale, dissipation time-scale and viscosity - is then analysed in depth, and the characteristics of the turbulence evolution are further examined with the aid of the cylinder-volume-integral balances of the components of the k- and ε-transport equations. The predictions of the turbulence model variants are then compared with the experimental data and their relative accuracy is assessed. The turbulence models are then further evaluated via analysis of the predictions of the key turbulence parameters they produce.

In Chapter 6, a parametric study of the influence of variations in the inlet-valve lift, compression ratio and engine speed on the in-cylinder mean flow, key turbulence parameters and components of the turbulence energy transport equation is presented and discussed. The predictions are compared with the available data and experimental trends in order to assess the capabilities of the mathematical model.

Finally, Chapter 7 provides a summary of the main findings and achievements of this dissertation and makes suggestions for possible further research.

CHAPTER 2
SURVEY OF PREVIOUS RESEARCH

2.1 INTRODUCTION

This chapter is concerned with a survey of the previous experimental and theoretical studies of the flow* in engines. Particular attention is paid to the experimental data and an effort is made to present a collective view of the characteristics of the in-cylinder mean flow and turbulence evolution.

Section 2.2 is devoted to the review of the experimental studies. Subsection 2.2.1 explains the difficulties associated with statistical characterisation of the non-stationary turbulent flows in engines and discusses the techniques that have been adopted by different engine researchers. In subsection 2.2.2, the important turbulence parameters are defined and their physical significance is explained. In subsection 2.2.3, the capabilities and limitations of hot-wire anemometry and laser-Doppler anemometry techniques - widely employed for quantitative description of the in-cylinder air motion - are discussed in the context of their engine application. In subsection 2.2.4, a review of the experiments and their main findings is presented. The data from these and other sources are used to assemble in subsection 2.2.5 an overall picture of the in-cylinder mean flow and turbulence evolution (in motored engines) and their response to changes in the design and operating parameters such as valve geometry and engine speed.

Section 2.3 presents a review of the multi-dimensional numerical studies pertaining to the prediction of mean flow and turbulence in engines.

Finally, the overall conclusions of the survey are presented in Section 2.4.

2.2 EXPERIMENTAL STUDIES

2.2.1 Statistical Characterisation of the Flow

The flow in the combustion chamber of a reciprocating engine is non-stationary (i.e. non-steady) and turbulent, as shown by a typical experimental record of the instantaneous velocity in Figure 2.1. A statistical approach is thus required in order to (i) condense the data, usually containing records of several engine cycles, into a manageable form, (ii) determine the 'regular' or 'mean' features of the flow, and

---

* In the present study, the term 'flow' represents both the mean flow and the turbulence component.

(iii) characterise the irregular random motions commonly called 'turbulence'*. The procedure most suitable for this purpose is, however, at present a matter of confusion and controversy.

The conventional statistical approach for 'stationary' (i.e. steady) turbulent flows, devised by Reynolds [1895], is to decompose the instantaneous velocity $U(t)$ into its time-average $\overline{U}_T$ and fluctuating component $u_T(t)$ (see, for example, Bradshaw [1971]) as

$$U(t) = \overline{U}_T + u_T(t) \tag{2.1}$$

where $\overline{U}_T$ is defined as

$$\overline{U}_T = \lim_{T\to\infty} \left[\frac{1}{T} \int_{t_o}^{t_o+T} U(t)\, dt\right] \tag{2.2}$$

and is held to characterise the 'mean' motion. The fluctuating component is expressed in terms of the mean-square-root (rms) value of $u(t)$, defined as

$$u'_T = \lim_{T\to\infty} \left[\frac{1}{T} \int_{t_o}^{t_o+T} (U(t) - \overline{U}_T)^2\, dt\right]^{\frac{1}{2}} \tag{2.3}$$

and termed the 'absolute intensity' or 'intensity' of turbulence.

The non-stationary character of the in-cylinder flow disallows application of this procedure, since neither the 'mean' motion nor turbulence will be appropriately characterised (see Figure 2.1). However, for reasons that will be discussed later, this process, for certain stages in the engine cycle and limited averaging time interval Δt, is sometimes applied to engine flows.

The statistical procedure most commonly employed for non-stationary flows, such as those in engines, is ensemble-averaging (Bradshaw [1971]), in which the statistical mean is obtained from an ensemble of data over a number of realisations. According to this scheme, the instantaneous velocity at crank angle θ in the ith engine cycle $U(\theta,i)$ is decomposed as:

$$U(\theta,i) = \overline{U}_E(\theta) + u_E(\theta,i) \tag{2.4}$$

where the ensemble-average velocity $\overline{U}_E(\theta)$ is defined as:

---

* The general features of 'turbulence' are discussed extensively in Chapter 3 in connection with turbulence modelling.

$$\overline{U}_E(\theta) = \lim_{N\to\infty} \left[\frac{1}{N} \sum_{i=1}^{N} U(\theta,i)\right] \qquad (2.5)$$

in which N is the number of realisations (i.e. cycles). The turbulence intensity is defined as:

$$u'_E(\theta) = \lim_{N\to\infty} \frac{1}{N} \left[\sum_{i=1}^{N} (U(\theta,i) - U_E(\theta))^2\right]^{\frac{1}{2}} \qquad (2.6)$$

The ensemble-average scheme provides a more appropriate characterisation of the in-cylinder flow (see Figure 2.2). However, it has the drawback that the very nature of the process suppresses information about individual cycles. This information is of importance in connection with engine combustion efficiency and its cycle-to-cycle variations (e.g. Cole & Swords [1980]). Furthermore, the cycle-to-cycle variations of the flow - such as shown in the experiments of Semenov [1963], Lancaster [1976], Rask [1981], Liou & Santavicca [1983] and Vafidis [1984] - are incorrectly assimilated into $u'_E(\theta)$, resulting in over-estimation of the 'true' turbulence intensity (see Figure 2.2), as shown, for example, by Lancaster [1976], Rask [1981] and Liou & Santavicca [1983].

A variety of schemes have been devised by engine researchers to separate the cycle-to-cycle variations from the 'true' turbulence. One such scheme that employs a hybrid of time/ensemble averaging, involves evaluation of the time-average mean velocity and turbulence intensity over a finite crank angle interval $\Delta\theta$ ($\Delta\theta$ = 10° to 45° crank angle; see Table 2.1) and subsequent ensemble-averaging over a sufficient number of cycles. The turbulence intensity levels so produced are shown to differ from those obtained through standard ensemble-averaging (Lancaster [1976]). The deficiencies of this scheme are (i) the variations in the 'mean' velocity during $\Delta\theta$ will be lumped into turbulence, producing spuriously large values of intensity (see Figure 2.3), and (ii) the choice of the averaging interval is arbitrary and must influence the results (for example, in the limit $\Delta t \to 0$, $\overline{U}_T \to U(\theta)$ and $u'_T \to 0$).

A more elaborate procedure of the hybrid nature was devised by Lancaster [1976], in which he attempted to eliminate the non-stationary component of the instantaneous velocity by subtracting the ensemble-average velocity from the instantaneous velocity record prior to time-averaging. For this purpose, he decomposed the instantaneous velocity at crank angle θ for the ith engine cycle record $U(\theta,i)$ as:

$$U(\theta,i) = \overline{U}_E(\theta) + \overline{U}_T(i) + u(\theta,i) \qquad (2.7)$$

where $\overline{U}_E(\theta)$ is the ensemble-average mean velocity, $\overline{U}_T(i)$ is the time-average mean velocity for the ith record after $\overline{U}_E(\theta)$ has been subtracted from the instantaneous velocity $U(\theta,i)$ at each crank angle θ, and $u(\theta,i)$ is the 'true' turbulence component (see Figure 2.4). The method assumes that the in-cylinder (instantaneous) velocity record is composed of a stationary turbulent flow superimposed on a time varying mean velocity. However, since the assumption of stationarity is not valid for long time-averaging intervals, $\overline{U}_T(i)$ and $u'_T(i)$ are evaluated over a relatively short time interval Δt (Lancaster [1976] used an interval $\Delta\theta = 45°$ CA). The drawback of this approach, apart from a considerable amount of data processing, is that choice of the averaging interval Δt is arbitrary and influences the results. This procedure produced turbulence intensity levels that differed from those obtained through standard ensemble-averaging and the normal hybrid time/ensemble averaging processes.

Another time/ensemble averaging approach, adopted by Semenov [1963] and Dent & Salama [1975a], is to pass the instantaneous velocity record through a high-pass frequency filter to remove the low-frequency components associated with the mean flow periodicity: the rest is then processed to obtain information about turbulence. Dent & Salama [1975a] argue that this procedure effectively renders a measurement record of turbulence that is stationary and thus amenable to time-averaging. However, the need for data accumulation over several engine cycles, prior to its processing, renders the method incapable of resolving individual cycles. Furthermore, the choice of the cut-off frequency of the high-pass filter is subjective, and in view of the fact that for major phases of the engine cycle turbulence energy is contained in the low-frequency components (see Table 2.4), the filtering process may remove part of the turbulence. Neither study provides information about the sensitivity of the results to the choice of the filter cut-off frequency or the length of the time interval Δt over which the data were analysed.

A new scheme that, in principle, is capable of cycle-to-cycle data analysis has been devised by Rask [1981]. The scheme involves fitting the instantaneous velocity data with a continuous smooth curve that represents the mean velocity variations: turbulence is defined as the deviations of the data from the fitted curve. The approach may be regarded as equivalent to low-pass filtering of the instantaneous velocity

measurements, with larger degrees of smoothing corresponding to lower cut-off filter frequencies. Therefore, the results depend on the choice regarding the degree of smoothing.

The procedure employed by Rask [1971] operates by splitting the instantaneous velocity measurement for a single engine cycle (for a cycle-to-cycle analysis) or a number of cycles (for a 'smooth' ensemble analysis) into 1° crank angle 'windows' or intervals, each containing one velocity datum (which is the arithmetic average of the measurements within the window). The cubic-spline method is then employed to fit a smooth curve to the data in an iterative fashion, using the standard deviations of the data from the fitted curve as a weighting parameter that controls the smoothness. The turbulence intensity is determined in each window from the difference between the measured velocities and the fitted mean-velocity curve. The procedure thus may be regarded as operationalisation of the filtering concept for finite crank angle intervals with a pre-assumption regarding the form of variation of the mean flow. Rask [1981] argues that the curve-fitting procedure is consistent with the notion that turbulence may be regarded as equivalent to a random error in the measurement of the mean velocity and hence is not arbitrary (in particular with regard to the amount of smoothing). However, treatment of turbulence as random measurement error is incorrect, for the fact that turbulent motions are spatially and temporally correlated (as will be discussed in Section 2.2.2).

Application of this procedure to laser-Doppler velocity measurements in a motored engine showed (Rask [1981]):

(i) Cycle-to-cycle variations occur predominantly in the higher frequencies.

(ii) A strong correlation exists between the level of the cycle-to-cycle variations and the mean velocity field: a strong, well-directed mean flow produces smaller cycle-to-cycle variations.

(iii) The level of cycle-to-cycle variations is large compared with the 'true' turbulence intensity during compression.

The first and second findings raise considerable doubt about the capability of the procedure in separating the turbulence from the mean velocity variations. The specific objections are:

(i) The measurements of, for example, Semenov [1963], Liou & Santavicca [1983] and Vafidis [1984] show that cycle-to-cycle variations are associated with the low frequency fluctuations in velocity.

(ii) The measurements of Daneshyar & Fuller [1981] show relatively large (25% to 35%) cyclic variations in the level of turbulence intensity (obtained from time-averaging over $\Delta\theta$ = 30° CA before TDC).

(iii) In the above, the level of cyclic variations in turbulence intensity correlates with the strength of the mean flow field in a manner similar to that Rask [1981] associates with the cycle-to-cycle variations (of the mean flow).

Therefore, it can be argued that a considerable fraction of what is evaluated by Rask [1981] as mean flow variations is indeed low-frequency turbulence of time-scales larger than the data processing time interval (note that the cubic-spline method uses 4 velocity data for curve-fitting, thus $\Delta\theta \simeq 4°$ CA).

Recently, Liou & Santavicca [1982,1983] (hereafter referred to as LS) have devised a new scheme for cycle-to-cycle data processing. This scheme may also be regarded as equivalent to low-pass filtering of the instantaneous velocity, in which the Fourier transformation method is used to obtain the appropriate cut-off frequency of the 'filter'. The procedure operates as follows: the instantaneous velocity data is split into 1° crank angle 'windows' or intervals, each containing one (average) velocity datum. This velocity data set is then Fourier transformed in order to obtain its fequency spectrum. A cut-off frequency is selected by reference to the shape of the frequency spectrum and all frequency components above it are set to zero (i.e. filtered). The inverse Fourier transform of the remaining frequency spectrum is then obtained and defined as the mean velocity variations.

LS [1982,1983] applied this procedure to the laser-Doppler velocity measurements in a motored ported-engine. The results (for the interval ±30° CA around TDC), however, revealed that an obvious cut-off frequency for separation of the 'mean' velocity variations and the turbulence cannot be deduced from the frequency spectrum of the instantaneous velocity (Figure 2.5(a)). Therefore, the cut-off frequency was selected on the basis of the shape of the frequency spectrum of the ensemble-averaged velocity (Figure 2.5(b)) (and was found to depend on the mean flow field and engine speed). This analysis suggested that:

(i) A well-directed strong mean flow (i.e. incorporating swirl) reduces the cycle-to-cycle variations of the mean velocity.

(ii) In the absence of a strong mean flow, the cycle-to-cycle variations are large, i.e. 100% to 200% of the ensemble-mean velocity.

(iii) The 'true' turbulence intensity is over-estimated by the ensemble-averaging process by nearly 50% to 100%, due to inclusion of the cycle-to-cycle variations.

(iv) The cyclic variations in the turbulence intensity levels produced by the LS method is small, i.e. about 10%.

The main concern over this procedure stems from the apparent overlap of the frequency spectrums of the mean velocity variations and the turbulence (Figure 2.5(a)). The objection is that all the low-frequency components of the turbulence, that lie below the cut-off frequency, are treated as mean velocity variations. These components contain a major fraction of the turbulence kinetic energy near the TDC compression (see Table 2.4) and hence their inclusion into the mean velocity variations results in a large level of cycle-to-cycle variations and under-estimation of the 'true' turbulence intensity. Therefore, it can be argued that the results are not conclusive: for example, the larger magnitude of the cycle-to-cycle variations obtained for flows without swirl can be due to the higher cut-off frequencies used (300 Hz to 900 Hz for flows without swirl compared with 200 Hz to 500 Hz for flows with swirl).

It must be concluded that the picture is one of uncertainty about the most suitable procedure for characterisation of the flow in engines. The ensemble-average method is general and unambiguous, but may be suppressing important information. On the other hand, other methods involve subjective data analysis and therefore their generality and definitiveness is questionable. In this respect, choice of the time-averaging interval, the cut-off frequency and the amount of smoothing must be expected to have considerable bearing on the results. Therefore, it is important that in reviewing the experimental data, due attention is paid to the limitations and influence of the method of analysis.

2.2.2 The Important Turbulence-Characterising Parameters

The full complexities of the turbulent flow field in engines cannot be completely described in terms of only the mean velocity and turbulence intensity: other parameters are also required in order to characterise the turbulence (see Bradshaw [1971], Hinze [1975] and

Tennekes & Lumley [1980]). The identification and quantitative determination of these parameters is essential to the understanding of the flow, and is of importance in relation to characteristics of the combustion process in engines (for example, see Brandl, et al. [1979], Groff & Matekunas [1980], Smith [1982]).

In the context of engine processes, some of the relevant parameters are described by Dent & Salama [1975a], Tabaczynski [1979] and Reynolds [1980]. The following is a summary of the definitions of the important turbulence parameters and their physical significance.

In passing, it needs mentioning that measurement of these parameters in engine flows is based on the assumption that turbulence is stationary (over the averaging time interval) and hence its statistical properties are time invariant. This assumption may not be valid for certain phases of the engine cycle and over large averaging intervals.

2.2.2.1 Spatial covariance and length scales

(i) The covariance and correlation coefficient: The time-mean product of the fluctuating velocities at two different points in space is called a 'covariance' or 'correlation', for example

$$\overline{u_i(\underline{X})\ u_j(\underline{X}+\underline{r})} = \frac{1}{T}\int_{t_o}^{t_o+T} u_i(\underline{X},t)\ u_j(\underline{X}+\underline{r},t)\ dt \qquad (2.8)$$

where $\underline{X}$ and $\underline{r}$ are vectors. The corresponding 'correlation coefficient' is defined as

$$R_{ij}(\underline{r}) = \frac{\overline{u_i(\underline{X})\ u_j(\underline{X}+\underline{r})}}{\overline{u_i'(\underline{X})\ u_j'(\underline{X}+\underline{r})}} \qquad (2.9)$$

Very roughly, $R_{ij}(\underline{r})$ is a measure of the contribution to $\overline{u_i(\underline{X})\ u_j(\underline{X}+\underline{r})}$ from eddies of size larger than $\underline{r}$ (since eddies smaller than this cannot produce a correlation between velocities at points $\underline{r}$ apart).

In practice, the correlation coefficient is measured for individual velocity components ($u_1 = u$, $u_2 = v$, $u_3 = w$) and the components of $\underline{r}$ in the x, y and z directions, for example

$$R_{12}(x) = \frac{\overline{u(\underline{X})\ v(\underline{X}+x)}}{\overline{u'(\underline{X})\ v'(\underline{X}+x)}} \qquad (2.10)$$

(ii) Integral length scale, L: Integrals of any $R_{ij}(x,y,z)$ over any component x,y,z of the separation distance $\underline{r}$ define 'integral length scales'; for example

$$L_X = \int_0^\infty R_{11}(x)\, dx = \int_0^\infty \frac{\overline{u(\underline{X})\, u(\underline{X}+x)}}{u'(\underline{X})\, u'(\underline{X}+x)}\, dx \tag{2.11}$$

defines the 'longitudinal' (direction-x) integral length scale. L is an important parameter of the turbulence structure: it is a measure of the average spatial extent or coherence of the fluctuations (Reynolds [1974]). It is also a measure of the typical size of the energy-containing eddies (Hinze [1975]).

The more frequently measured length scales are L_X and L_Y, commonly defined as (Hinze [1975])

$$\begin{aligned} L_X &= \int_0^\infty R_X\, dx = \int_0^\infty \frac{\overline{u(\underline{X})\, u(\underline{X}+x)}}{u'(\underline{X})^2}\, dx \\ L_Y &= \int_0^\infty R_Y\, dy = \int_0^\infty \frac{\overline{u(\underline{X})\, u(\underline{X}+y)}}{u'(\underline{X})^2}\, dy \end{aligned} \tag{2.12}$$

For isotropic turbulence, $L_Y = \frac{1}{2} L_X$ (Hinze [1975]).

(iii) Length scale of energy-containing eddies, ℓ: In the context of the turbulence model used in the present study, a length scale, that is a measure of the average size of the energy-containing eddies, is defined as

$$\ell = C_\mu^{3/4} \frac{k^{3/2}}{\varepsilon} \tag{2.13}$$

where $C_\mu = 0.09$ (Launder & Spalding [1972]), k ($\equiv (\overline{u^2} + \overline{v^2} + \overline{w^2})/2$) is the turbulence kinetic energy, and ε* is its dissipation rate. Generally, ℓ is of the same order as L_X (Hinze [1975], p. 224).

(iv) Micro length scale: This length scale is defined in terms of the curvature of the correlation coefficient at origin, as, for example

$$\lambda_X^2 = \frac{-2}{(\partial^2 R_X/\partial x^2)_{x=0}} \tag{2.14}$$

which, as depicted in Figure 2.6, gives the distance of the intercept with the x-axis of a parabola fit of R_X at origin. Relation (2.14) can be recast into the following form (Reynolds [1974])

---

* For high Reynolds number flows, $\varepsilon = \nu \overline{(\partial u_i/\partial x_j)^2}$ (see Chapter 3 on turbulence modelling).

$$\lambda_x^2 = \frac{2u'^2}{(\partial u/\partial x)^2_{x=0}} \tag{2.15}$$

Hence, it is a measure of the local spatial change of u. Hinze [1975] suggests that since this change is caused by the smallest eddies present in the turbulent field, λ may be regarded as a measure of the average dimension of the smallest eddies.

λ is also referred to as 'dissipation length scale'. This is because for isotropic turbulence, it can be shown that* (Hinze [1975])

$$\varepsilon = 15\nu \overline{\left(\frac{\partial u}{\partial x}\right)^2} = 15\nu \frac{u'^2}{\lambda_y^2} \tag{2.16}$$

where ν is the kinematic viscosity. Thus, λ may be regarded as a measure of the average size of the eddies mainly responsible for the dissipation of turbulence energy (Hinze [1975]). However, it must be emphasised that the 'true' dissipation scales, known as the Kolmogorov microscale η, are considerably smaller than λ. Indeed, for isotropic turbulence (Hinze [1975])

$$\frac{\lambda_y}{\eta} = 15^{\frac{1}{4}} Re_\lambda^{\frac{1}{2}} \tag{2.17}$$

where $Re_\lambda = u' \lambda_y/\nu$ is the turbulent Reynolds number. Therefore, λ is intermediate between the large scales of order L and the smallest scales of order η that are responsible for viscous dissipation of the turbulence energy.

The microscale λ features in correlations for smoke formation in diesel engines (Brandl, et al. [1979], Dent [1980]) and in theories for the ignition and flame propagation processes in spark-ignition engines (Hires, et al. [1978], Tabaczynski, et al. [1980]). Dent [1980] considers λ as the length parameter associated with fine-scale turbulent mixing rate, but Hires, et al. [1978] and Tabaczynski, et al. [1980] interpret it as the measure of spacing between the eddies of order η. The latter interpretation follows from the theory of Tennekes [1968], according to which the dissipation is concentrated in randomly distributed vortex tubes with a diameter of the order Kolmogorov microscale η and spaced on the order of the microscale λ. A different model has been proposed by Corrsin [1962] according to which the dissipation is

---

* In turbulence work, commonly the 'Taylor microscale', $\lambda_y = \lambda_x/\sqrt{2}$ (only in isotropic turbulence) is used.

concentrated in randomly distributed thin sheets or slabs of a characteristic thickness η, separated by regions of order integral scale L. However, the experimental results of Kuo & Corrsin [1971] and others (cited from Hinze [1975], p. 243) are in disagreement with both models.

(iv) Kolmogorov microscale, η: As noted above, this scale is the measure of the smallest eddies in a turbulent field, in which the viscous dissipation of the turbulence kinetic energy into heat occurs. It is defined, on the dimensional grounds (Batchelor [1960]), as:

$$\eta = \left(\frac{\nu^3}{\varepsilon}\right)^{\frac{1}{4}} \tag{2.18}$$

The Kolmogorov scale is of interest in connection with the molecular mixing and combustion processes (Chomiak [1979]) since it represents the region of maximum molecular interactions. There is evidence of wrinkled regions of high reaction rate in Schlieren photographs of premixed flames in engines (e.g. Namazian, et al. [1980], Smith [1982]) that may be interpreted as regions of concentrated Kolmogorov eddies.

2.2.2.2 Autocorrelation coefficient and time scales

(i) Autocorrelation coefficient: Corresponding to the spatial correlation, the temporal correlation is defined as

$$\overline{u_i(\underline{X},t)\ u_j(\underline{X},t+\tau)} = \frac{1}{T}\int_{t_o}^{t_o+T} u_i(\underline{X},t)\ u_j(\underline{X},t+\tau)\ dt \tag{2.19}$$

where τ is the time delay between the two signals. It is common that the correlation is made for components in the same direction (i.e. $i = j$): the autocorrelation coefficient $R(\tau)$ for this situation is given by

$$R(\tau) = \frac{\overline{u_i(\underline{X},t)\ u_i(\underline{X},t+\tau)}}{u_i'^2} \tag{2.20}$$

In practice, this can be obtained from single-point velocity measurements by correlating a tape recorded signal with a replica delayed by a fixed interval.

Witze [1976a,1977] has defined an autocorrelation coefficient, for the non-stationary condition of in-cylinder flow, according to an ensemble-averaging procedure as

$$R_\theta(\phi) = \frac{\frac{1}{N}\sum_{i=1}^{N} u(\theta,i)\ u(\theta-\phi,i)}{u'(\theta)\ u'(\theta-\phi)} \tag{2.21}$$

where $u(\theta,i)$ is the fluctuating component of the ith velocity record (from the ensemble-average velocity) at crank angle θ and ϕ is a delay crank angle interval.

(ii) Integral time-scale, L_t: The integral time-scale is defined, for relation (2.20), as

$$L_t = \int_0^\infty R(\tau)\, d\tau \tag{2.22}$$

and for relation (2.21) as

$$L_{t,\theta} = \frac{1}{S} \int_{-\infty}^{0} R_\theta(\phi)\, d\phi \tag{2.23}$$

where S is the engine speed. The integration is from $-\infty$ to zero, since it is considered that the integration from zero to $+\infty$ involves events in the future: for stationary flows, both integrations produce unique results.

The integral time-scale is a measure of the average persistence of the turbulent motions at a point. Taylor's hypothesis states that the disturbances with different wavelengths (length scales) all travel at the speed of the mean flow $\overline{u}_T$ (Reynolds [1974]); therefore, L_t (= $L/\overline{u}_T$) is a measure of the typical frequency of the energy-containing eddies. In the absence of a mean flow, Taylor's hypothesis is not valid and L_t may be regarded as a measure of the life-time of larger eddies.

(iii) Micro time-scale, λ_t: The micro time-scale is defined analogous to the micro length scale as

$$\lambda_t^2 = \frac{-2}{[\partial^2 R(\tau)/\partial\tau^2]_{\tau=0}} \tag{2.24}$$

which can be recast into the following relation (Reynolds [1974])

$$\lambda_t^2 = \frac{2u'^2}{(\partial u/\partial t)^2_{\tau=0}} \tag{2.25}$$

λ_t is a measure of the most rapid changes of the fluctuations and hence relates to the highest frequencies occurring in the turbulence field (Hinze [1975], p. 61).

(iv) Decay or dissipation time-scale, τ_d: A time-scale for decay of turbulence energy can be defined through consideration of the decay of isotropic turbulence (Reynolds [1974], p. 79) as

$$\tau_d = -\frac{\overline{u^2}}{d\overline{u^2}/dt} = \frac{\lambda_y^2}{10\nu} \tag{2.26}$$

The 'dissipation time-scale' τ_d may be defined within the context of the model of turbulence used in the present study (see Chapter 3) as

$$\tau_d = \frac{k}{\varepsilon} \tag{2.27}$$

It can be shown (with the aid of relation (2.16)) that for isotropic turbulence, the two relations are identical.

It should be mentioned that τ_d does not represent the overall time for the decay of turbulence, since λ_y increases as the decay proceeds (Batchelor [1960]). Rather, it represents a time over which, in the absence of any turbulence production by the mean flow, a significant change in turbulence energy occurs.

(v) Relations between spatial and temporal scales:

Taylor's hypothesis gives simple relations between certain spatial and temporal scales. These, for a stationary homogeneous turbulent field with the mean velocity $\overline{U}$, are

$$\begin{aligned} L &= \overline{U}\, L_\tau \\ \lambda &= \overline{U}\, \lambda_\tau \end{aligned} \tag{2.28}$$

and are strictly valid only for conditions where $u'/\overline{U} \ll 1$ ($u'/\overline{U} = 0.01$ to 0.02 is recommended by Hinze [1975], p. 47). These conditions seldom prevail in engine circumstances: hence, although these relations are frequently employed by experimentalists to simplify their tasks (time-scales being considerably easier to measure than length scales), the results must be interpreted with great caution. For instance, Tabaczynski [1979] notes that in the absence of a mean flow (a condition prevailing at TDC of compression in most petrol engines), an expression of the form

$$L = C\, u'\, L_\tau \tag{2.29}$$

where C is a constant of order unity, is more appropriate.

2.2.2.3 The spectral density function, $E(\omega)$

The spectral density function, or energy spectrum, gives the distribution of the kinetic energy of turbulence with respect to frequency $\omega = 2\pi f$ or equivalently wave number $\kappa = 2\pi f/\overline{U}$ (Reynolds [1974], Hinze [1975]). In general, it is obtained for the streamwise component of turbulence 'u', so that

$$u'^2 = \int_0^\infty E(\omega)\, d\omega \tag{2.30}$$

using the Fourier transform pair that relate the autocorrelation and the frequency spectrum (Reynolds [1974], Hinze [1975]), viz.

$$\begin{aligned} R(\tau) &= \int_0^\infty \phi(\omega) \cos \omega\tau \, d\omega \\ \phi(\omega) &= \frac{2}{\pi} \int_0^\infty R(\tau) \cos \omega\tau \, d\tau \end{aligned} \tag{2.31}$$

where

$$\phi(\omega) = \frac{1}{u'^2} E(\omega) \tag{2.32}$$

However, it is also possible to obtain $E(\omega)$ through direct Fourier transformation of the measurement signal (Liou & Santavicca [1982]) or by using a consistent range of band-pass filters (James & Lucas [1975]). (For more information, see Reynolds [1974] and Daneshyar & Fuller [1981].)

The energy spectrum provides detailed information about the frequency range and energy distribution of the turbulent motions (see Figure 2.7) and the isotropy of the small scales (see Hinze [1975]). Therefore, it can greatly assist the understanding of the turbulence evolution in engines (see Figure 2.7) and the manner in which it is influenced by variations in the engine design and operating conditions (see, for example, Semenov [1963], James & Lucas [1975]).

2.2.3 Measurement Techniques

An exposition of the techniques employed for the study of the air motion in engines is given by Arcoumanis [1983]. The two techniques most widely used to measure the in-cylinder flow are hot-wire anemometry (HWA) and laser-Doppler anemometry (LDA). The intention here is not to provide details of their principles and application, but to examine their capabilities and shortcomings - and hence the accuracy of the measurements - in the context of engine flows.

2.2.3.1 Hot-wire anemometry

The principle of HWA is the relationship between the

convective heat loss from the surface of a thin, heated wire and the velocity of the gas flow past it. In constant temperature anemometry, the wire is maintained at a constant temperature via a feedback control system that adjusts the electrical current and the anemometer output is the variations in the voltage. This output is a non-linear function of the component of velocity perpendicular to the wire, the temperature difference between the wire and the gas and the gas properties (density, viscosity, thermal conductivity). The magnitude of the velocity is determined by a calibration relationship that includes corrections for the gas temperature and pressure variations that occur during parts of the engine cycle (for details of the techniques that are commonly used for including the influence of time-varying gas temperature, see Witze [1979, 1980]).

The suitability of the HWA for engine applications was carefully assessed by Witze [1979,1980] and his principal conclusions were as follows. On the positive side, HWA provides a continuous signal, good frequency response and high signal-to-noise ratio that are especially advantageous for the measurement of the time correlations and turbulence scales. On the negative side, the hot-wire probe is delicate, flow-perturbing and cannot withstand combustion. The additional disadvantages are:

(i) Calibration: individual probes require calibration over the whole range of velocities and temperatures encountered in engines - an impractical task in view of frequent probe breakage.

(ii) Gas temperature variations: there are serious drawbacks with regard to the accuracy of the measured mean velocity and turbulence intensity, when the available semi-empirical correlations are used to correct the anemometer output for deviations from the calibration conditions that are usually ambient.

(iii) Directional insensitivity: the HWA is limited in its ability to determine flow direction or to isolate individual velocity components. Therefore, for HWA to give an accurate indication of velocity, *a priori* knowledge of the mean flow direction is necessary.

(iv) Limited turbulence intensity: the linearisation approximation that is used in the hot-wire theory to separate turbulence from the mean velocity is valid for $u'/\overline{U} \lesssim 20\%$. Above this limit - that is often

exceeded in engine flows - error can be expected (Witze [1977,1979]).

This assessment suggests that in-cylinder data obtained by HWA may be subject to considerable uncertainties, particularly in the region of flow recirculation and during the compression and expansion phases of the engine cycle. Indeed, the experiments of Witze [1979,1980], performed using HWA and LDA techniques, showed serious errors in the HWA measured mean velocity and turbulence intensity during major parts of the compression and expansion strokes. Witze [1979,1980] implies that similar errors may exist in the published HWA data of other engine researchers, although he argues that the integral and micro time-scales determined by this technique are less prone to errors than other quantities. Whatever the validity of this argument, the length scale data obtained from relation (2.27) are subject to uncertainties about its applicability and errors in the measurement of the mean velocity.

In view of the large body of data on in-cylinder air motion obtained by this technique (see Table 2.1), the best course appears to be to draw on this information, but with complete awareness of its possible limitations.

2.2.3.2 Laser-Doppler anemometry

This optical technique has been extensively used in engines over the past few years (see Table 2.1). The principle of operation is that two coherent beams, that are generated by passing a single laser through a beam splitter, are passed through a focusing lens and made to intersect at the location of interest in the flow. An interference fringe pattern is formed in the intersection or 'measuring volume'. Particles, most often deliberately introduced into the flow, scatter light as they cross the fringes. Collection of the scattered light by use of additional lenses and measurement of its frequency with the aid of a photomultiplier allows direct determination of the particle velocity perpendicular to the fringes. The flow direction is also determined by introducing a frequency shift between the two incident beams.

In a critical comparison of the HWA and LDA techniques in the engine context, Witze [1979,1980] concluded that LDA offers considerable advantages over HWA because it is

(i) absolute and linear, and thus requires no calibration, irrespective of the conditions of the flow under

investigation;

(ii) direction sensitive and thus capable of resolving the velocity components and their associated turbulent fluctuations;

(iii) accurate for all levels of turbulence intensity;

(iv) non-intrusive;

(v) can be applied to combusting flows.

The principal drawbacks are:

(i) Intermittent signal due to the random arrival of light-scattering particles at the measurement volume.

(ii) The need for optical access that imposes severe restrictions on the extent to which the flow field in the production engines can be investigated.

(iii) Low signal-to-noise ratio.

The intermittency of the signal is of significance in respect of LDA data acquisition in engines. The low sampling rate necessitates use of a sampling window, centred around the crank angle of interest, over which the LDA signal(s) is either sample-selected (Arcoumanis [1983]) or time-averaged (Witze [1978]). This precludes determination of the turbulence scales and introduces uncertainties in the ensemble-averaged data (that will be discussed later). However, Rask [1981], Liou & Santavicca [1983] and Vafidis [1984] have shown that this problem can be overcome - at least during parts of the engine cycle - by using high seeding to obtain a near-continuous signal. Liou & Santavicca [1983] were also able to determine the autocorrelation coefficient and turbulence integral scales.

The sources of uncertainty in LDA measurements are velocity gradient (or Doppler) and crank angle broadenings. The former is due to the lateral (with respect to the direction of the measured component) gradients of velocity within the measurement volume. The magnitude of this error is proportional to the size of the measurement volume and the magnitude of the velocity gradient: maximum values of order 5% to 10% in the mean and 5% to 15% in the rms fluctuating velocities are estimated (Vlachos [1977], Arcoumanis [1983]). Crank angle broadening is due to the variation of velocity in time during the sampling interval. A theoretical analysis by Morse [1977] shows that the effect of crank angle broadening on the ensemble-mean and rms velocities is

proportional to the rate of data sampling, the acceleration ($\partial\overline{U}/\partial\theta$) and the square of the sampling interval. Experimental studies by Rask [1981] and Arcoumanis, et al. [1982b] suggest that a sampling window of 5° CA is a good choice in respect of both the data acquisition rate and the level of error; larger windows result in large over-estimation of the rms fluctuations during the phases of rapid velocity variations.

2.2.4 Review of the Measurements

Interest in in-cylinder flow dates from early this century (c.f. Clerk [1912], Ricardo [1922]) and has resulted in an extensive literature on experimental studies of various aspects of flow in engines (such as the flow evolution, influence of the induction system, swirl and squish interaction, etc.). In spite of this, the flow characteristics are not well understood and only a few, if any, general scaling laws have been identified. This is in part due to the non-stationary, three-dimensional and complex character of the flow and in part due to the limited capabilities of the measurement techniques. However, the recent need for a more comprehensive knowledge of the in-cylinder flows, aided by the development of measurement facilities, has lead to more systematic investigations (e.g. Bicen [1983], Arcoumanis [1983]).

A number of reviews of the experimental and theoretical studies of flows in engines are present in the literature, for example those by Tabaczynski [1979], Johns [1980], Arcoumanis [1983] and Gosman [1984]. Of these, Johns [1980] focuses attention on the swirl and swirl/squish interaction and Tabaczynski [1979] concentrates on the in-cylinder turbulence evolution and influence on the combustion characteristics of the spark-ignition engines. The review of Gosman [1984] is most comprehensive and deals with the characteristics of the in-cylinder flow processes and their dependence on the engine design and operating parameters.

In the present study, a review of the experimental studies, together with a summary of their main findings, is presented in Table 2.1. Attention is then focused on experiments that are specifically concerned with the investigation of the characteristics of the flow evolution in engines: the data on mean velocity and turbulence parameters u', L_t, λ_t, L_χ, λ_χ and energy spectrum $E(f)$ during the induction and compression phases of the engine cycle, and their dependence on the operating conditions (namely, engine speed, compression ratio and volumetric efficiency) are presented in Tables 2.2 to 2.6.

2.2.5 Characteristics of the In-Cylinder Flow Processes

This subsection presents a review of the current state of knowledge, drawn from the experimental studies, about the characteristics of the in-cylinder flow processes. In this context, two aspects are of particular interest, namely (i) the evolutionary character of the mean flow and turbulence, and (ii) the influence of induction and operating parameters on the flow at TDC compression. The attention is thus focused on the disc-chamber configuration since, in other configurations (such as bowl-in-piston), generation of 'squish' strongly influences the evolution of the induction generated mean flow and turbulence during the compression stroke. (For a review of the flow structure in 'squish' generating configurations, see Gosman [1984].)

2.2.5.1 Induction process

2.2.5.1.1 Characteristics of flow through a valve:

It has long been recognised that the design of the induction system plays an important rôle in determining the engine breathing capacity (volumetric efficiency) and in shaping the in-cylinder flow structure. These are evidenced by two groups of experimental studies concerned with (i) the induction system design and its effect on the structure of the in-cylinder air motion (e.g. Tindal & Williams [1977], Brandl, et al. [1979]), and (ii) the influence of valve geometric and operating characteristics on the engine volumetric efficiency (e.g. Kastner, et al. [1963-64], Vafidis & Whitelaw [1984]).

(i) Design aspects of the induction system:

The induction system consists of the inlet port and the valve assembly, including various means for imparting swirl or giving directional effects to the flow as it enters the cylinder (see, for example, Gosman [1984]). There are various types of swirl-producing inlet ports, all conforming to two basic categories, depending on whether the swirl is produced upstream or downstream of the inlet valve. Pre-valve swirl is produced by helical-type ports (Monaghan & Pettifer [1981]) or by guide-vanes located in the port upstream of the valve (Arcoumanis, et al. [1983]). Post-valve swirl is produced by directional ports (Wigley & Hawkins [1978], Hirotomi, et al. [1981]) and by masked (shrouded) valves (Arnold, et al. [1972], Wakisaka, et al. [1979]).

The in-cylinder flow structure is shown to strongly depend on the design of the induction system, i.e. whether it is directional or helical type (Tindal & Williams [1977]); the (directional)

position of the directional ports with respect to the cylinder wall (Hirotomi, et al. [1981]); and the orientation of the valve-mask (Arnold, et al. [1972], Wakisaka, et al. [1979]). Furthermore, it is shown that the in-cylinder flow structure is also influenced by the intake valve lift (Tindal & Williams [1977], Hirotomi, et al. [1981]).

In general, choice of the induction system is governed by cut-and-try experiments in order to produce an efficient combustion over a wide range of operating conditions (Brandl, et al. [1979], Hirotomi, et al. [1981]). In this respect, the importance of the induction port design, and to some extent the lack of understanding of its operation, is manifested by the variety of the port configurations that are employed in the production engines.

(ii) Mass flow through the inlet valve: The dependence of the engine volumetric efficiency (η_v) - and hence power output - on the mass flow characteristics of the induction system and, in particular, the inlet valve is well recognised. A large number of experiments have been carried out to investigate the influence of geometric and flow parameters on the valve discharge coefficient C_D, defined as

$$C_D = \frac{\dot{m}_v}{\dot{m}_i} \tag{2.33}$$

where $\dot{m}_v$ and $\dot{m}_i$ are, respectively, the measured mass flow rate through the valve and that of an ideal nozzle of the same flow area under identical pressure drop. $\dot{m}_i$ is calculated from the following relation for an isentropic, compressible, subsonic flow through a nozzle (e.g. Bicen [1983]):

$$\dot{m}_i = A \left[2 P_o \rho_o \frac{\gamma}{\gamma - 1} \left(\frac{P}{P_o}\right)^{2/\gamma} \left[1 - \left(\frac{P}{P_o}\right)^{\gamma - 1/\gamma} \right] \right]^{\frac{1}{2}} \tag{2.34}$$

in which P_o and ρ_o are the stagnation upstream pressure and density, A is a representative flow cross-section area, and P is the downstream static pressure. In calculating the ideal mass flow rate $\dot{m}_i$ - and hence C_D - for a valve, two important flow areas are generally considered. These are the valve exit area A_L, defined as

$$A_L = \pi D L \tag{2.35}$$

where D and L are, respectively, the valve diameter and lift, and the valve minimum area A_M given by the following relations for the whole valve lift

range (see Figure 2.8) (Kastner, et al. [1963-64], Bicen [1983]):

Mode I

For $0 < L \leqslant 2t/\sin 2\psi$

$$A_M = \pi L \cos\psi \left[D - 2t + \left(\frac{L}{2}\right) \sin 2\psi\right] \tag{2.36a}$$

Mode II

For $2t/\sin 2\psi < L \leqslant t \tan\psi + \sqrt{\left[\frac{(D-2t)^2 - d^2}{4(D-t)}\right]^2 - t^2}$

$$A_M = \pi (D-t) \sqrt{(L - t\tan\psi)^2 + t^2} \tag{2.36b}$$

Mode III

For $L > t \tan\psi + \sqrt{\left[\frac{(D-2t)^2 - d^2}{4(D-t)}\right]^2 - t^2}$

$$A_M = \frac{\pi}{4}\left[(D-2t)^2 - d^2\right] \tag{2.36c}$$

where mode III represents the condition where the minimum flow area occurs in the inlet port.

In the majority of cases, C_D has been measured under steady flow conditions, by imposing constant pressure difference between the inlet port and the valve exit and measuring the mass flow rate as a function of the dimensionless valve lift (L/D) for a range of lifts and a range of pressure drops corresponding to engine operating conditions. However, the measurements of Bicen [1983] and Vafidis & Whitelaw [1984] (hereafter referred to as VW for brevity) provide evidence that C_D under steady and unsteady flow (pressure difference induced by piston motion) conditions do not differ appreciably, although the effect of dynamic valve operation is, in general, to reduce C_D (Kastner, et al. [1963-64], Fukutani & Watanabe [1982]). VW [1984] also showed that the off-centre location of the valve, and hence proximity to cylinder wall, in production engines does not affect C_D obtained in idealised test conditions.

The measured variations of C_D against valve lift, for several pressure drops, are given in Figure 2.9. These variations correspond to the changes in the flow pattern at valve exit that will be discussed later. The effect of increase in pressure drop

across the valve is to increase C_D without altering its characteristic variations with lift (see Figure 2.9) (Kastner, et al. [1963-64], VW [1984]). The measurements of VW [1984] show that C_D is not independent of the flow Reynolds number (see Figure 2.10) and therefore this assumption generally made in calculation methods is not valid.

The most effective way to improve C_D is found to be the rounding-off of the sharp corners at the valve head and seat (Kastner, et al. [1963-64], VW [1984]). The experiments show that this delays flow separation at valve (e.g. VW [1984]) and can result in an increase of up to 20% to 30% in C_D. It is also shown that C_D can be improved through modification of the inlet port design immediately upstream of the valve (Kastner, et al. [1963-64], Wallace [1967-68]). The influence of seat angle ψ on C_D has been investigated by Tanaka [1929] and Annand [1969]: the performance of the 30° and 45° seat angle valves was found to be superior to that with a 60° seat angle.

(iii) Flow characteristics at valve exit: The influence of valve lift on the flow at valve exit plane has been investigated by Kastner, et al. [1963-64], Annand [1969], Bicen [1983] and VW [1984]. In general, four distinct flow modes corresponding to discontinuities in C_D~L variations have been identified (see Figure 2.11). At small lifts, flow is attached to the walls of the valve passage (régime I, Figure 2.11) and C_D increases with L due to reduction in the viscous effects due to the walls (Figure 2.9). Increasing valve lift causes flow separation at the valve head (régime II, Figure 2.11) and results in rapid reduction of C_D. The size of the separation bubble, after a rapid initial growth, apparently becomes independent of the valve lift (Bicen [1983]); hence, thereafter, C_D increases with L due to the increase in the flow area (Figure 2.9). At some larger lift, flow also separates from the seat (régime III, Figure 2.11), resulting in a reduction of C_D (Figure 2.9). At high lifts, flow reattaches on the valve head (régime IV, Figure 2.11) and C_D tends to recover (Kastner, et al. [1963-64]). The experiments have also shown that the flow transition from one régime to another can be delayed by rounding-off of the valve head and seat sharp corners.

The only experimental data on velocity distribution at the valve exit plane are the LDA measurements of Bicen [1983], Bicen, et al. [1984] and VW [1984]. These show changes in the velocity profile and angle of entry of the intake jet with increase in the valve lift and flow separation (Figure 2.12): for small L, the

velocity distribution and angle of entry are that of a plug flow and valve seat angle, respectively, deviating considerably from these conditions at larger lifts. Therefore, the assumptions of plug flow distribution and flow entry at valve seat angle (independent of L) made in almost all multi-dimensional predictions of the in-cylinder flow are not correct for large valve lifts.

Other findings of these studies can be summarised as:

(i) The flow angle of entry at valve exit is influenced by the cylinder confinement and wall proximity in the case of an off-centre valve.

(ii) The velocity distribution and angle of entry at valve exit under unsteady conditions are the same as found in steady flow tests.

(iii) The flow field downstream of the valve differs appreciably under steady and unsteady conditions, with the residual effects from the exhaust process and the transient intake jet influencing the development of post-valve flow structure.

(iv) The turbulence intensity at the plane of valve exit is almost negligible compared with the levels generated in the shear layers of the post-valve induction jet.

2.2.5.1.2 The in-cylinder pressure variation: In the early stages of the induction, the in-cylinder mean pressure P_{cyl} falls rapidly below the port pressure. This is because the valve opening is small and, in spite of high C_D, the rate of air flow is not sufficient to counterbalance the pressure drop due to rapid increase in cylinder volume following the piston acceleration. The maximum level of pressure drop and its timing depend on the inlet valve/port design and both increase with increase in engine speed (Figure 2.13). Thereafter, P_{cyl} recovers as a result of increase in the mass flow rate, due to the large pressure difference and greater valve lift, and the reduction in piston speed (and hence volume change) after mid-induction. The rate of pressure recovery is also influenced by the valve/port design (Kastner, et al. [1963-64]) and strongly depends on the engine speed (Figure 2.13).

The magnitude and variation, with crank angle, of the intake jet velocity thus depend on the variations of the in-cylinder pressure (and hence the mass flow rate) and the valve lift characteristics and, as a consequence of the pressure behaviour, they are both influenced by the engine speed. The single-point in-cylinder measurements of the intake jet velocity, in general, indicate a rapid linear increase of velocity up to $\theta \simeq 60°$ CA; a phase of slowly varying velocity for $\theta \simeq 60°$ to 120° CA; and an almost rapid fall thereafter until bottom dead centre (BDC) of induction.

2.2.5.1.3 Mean flow structure in the cylinder: The complex design of the induction system and the cylinder head in production engines produces a three-dimensional and highly complex flow structure inside the cylinder (see Figure 2.14) that strongly depends on the port/valve design and changes considerably during the induction (Hirotomi, et al. [1981]). The only configuration that produces a two-dimensional swirl-free flow field in the cylinder is that of an axisymmetric central valve engine; a small displacement of the valve axis with respect to the cylinder axis produces three-dimensionality and swirl formation (Morse, et al. [1980b], Hirotomi, et al. [1981]).

An extensive work on axisymmetric engine configuration has been carried out at Imperial College (see, for example, Morse, et al. [1980a], Bicen [1983] and Arcoumanis [1983]). Two kinds of motored 'engine' were used: one with a permanently open central valve, and the other with a cam-driven (similar) valve operating in the manner of a four-stroke cycle. These engines were operated at low speeds (200 rpm and 325 rpm to 675 rpm) and compression ratios 3.5 to 6.7. However, they produced information which, on current evidence, is quite representative of real engine behaviour and can provide a basis for understanding the more general features of the in-cylinder flows.

(a) Axisymmetric configuration: The flow field during the early stages of induction is dominated by the transient annular intake jet that separates at the cylinder head and valve, forming strong recirculation patterns near the cylinder head/wall corner and behind the valve (see Figure 5.16(a))*. The intake jet penetrates through the vortex

---

* These predicted velocity fields are in good agreement with the measurements of Ahmadi-Befrui, et al. [1982], as will be shown in Chapter 5, and qualitatively similar to other measurements in this engine configuration (e.g. Arcoumanis, et al. [1982a], Bicen [1983]).

system, without major deflection or distortion, and impinges on the piston or cylinder wall, depending on the valve seat angle and piston position (Arcoumanis, et al. [1982a]).

The main feature of the development of the flow thereafter is the displacement and growth of the main vortex (behind the valve) due to piston displacement (initially causing its displacement and then its stretching) and entrainment of the intake mass flow (Arcoumanis, et al. [1982a]). This causes the deflection and impingement of the intake jet on the cylinder wall which restricts the growth of the cylinder head/wall vortex (Figure 5.16(a)). This may also cause formation of a weak secondary vortex behind the valve which disintegrates later in the induction (Arcoumanis, et al. [1982a]).

At some stage during the latter half of induction, flow separates from the cylinder wall, forming a third vortex near the piston (Arcoumanis, et al. [1982a]) (see Figure 5.16(a)). Near the end of induction, the mean flow decays rapidly due to the fall-off of the intake jet velocity and the effect of turbulent stresses. However, the vortex structure persists, under its inertia, to the end of induction (Bicen [1983], Arcoumanis [1983]).

The effect of variations in engine design and operating parameters on the flow will now be examined.

(i) Effect of swirl: In this configuration, swirl may be generated by the aid of pre-valve guide vanes imparting a rotational component onto the incoming air, as for example in the studies of Morse, et al. [1980a], Morse & Whitelaw [1981], Arcoumanis [1983] and Vafidis [1984]. The measurements show that the in-cylinder swirl distribution is irregular (axially stratified); depends on the vane angle (and hence the strength of the swirl component); and in any case is far from the (often assumed) solid body rotation (Vafidis [1984]). The swirl also affects the flow in the axial plane, as evidenced by the measurements of Morse, et al. [1980a] and Bicen [1983], causing enlargement of the main vortex, formation of small recirculation patterns behind the valve, and suppression of the third vortex near the piston/cylinder wall corner. The effect is related to the negative pressure gradient necessary to counterbalance the centrifugal forces set up by the rotating fluid.

(ii) Effect of valve seat angle and maximum lift: The effects of changes in the valve seat angle and maximum lift have been explored by Ekchian & Hoult [1979] and Arcoumanis, et al. [1982a,

1982c]. These studies show that for valve seat angle $\psi = 30°$, an alternative structure (to that described) occurs, in which the intake jet does not separate from the (valve) seat, thus adhering to the cylinder head and suppressing the cylinder head/wall corner vortex (see Figure 2.17). Furthermore, according to Ekchian & Hoult [1979], this occurs only at small valve lifts, although in some circumstances the intake jet becomes bistable, i.e. at times it separates from the cylinder head, while sometimes it remains attached. These studies suggest that for larger seat angles ($\psi = 45°$ to $60°$), the general flow pattern remains essentially as described before, over the entire range of lifts.

The effect of reduction in the maximum valve lift, from the experiment of Arcoumanis, et al. [1982c], is to increase the intake jet velocity, which produces a stronger in-cylinder mean flow and, in particular, a larger main vortex.

(iii) Effect of clearance gap and stroke: The measurements of Bicen & Vlachos [1980] and Arcoumanis, et al. [1982a] in a non-compressing engine show that reduction in the clearance gap (corresponding to increase in compression ratio from 3.5 to 6.7) results in impingement of the intake jet on the piston early during induction, but later (before mid-induction) the flow pattern is similar to that described before, except for the stronger main vortex (due to the prolonged jet impingement on the piston) and formation of a secondary weak vortex behind the valve. However, in this case, the decay of the mean flow near the end of induction is faster than for the larger gap case, thus the strength of the vortex structure at the end of induction is nearly the same.

The effect of increase in stroke (Ekchian & Hoult [1979], Bicen & Vlachos [1980]) is to increase the strength of the initial vortex structure and produce faster decay near the end of induction; the basic flow structure is not changed.

(iv) Effect of engine speed: The measurements of Morse, et al. [1979] in a non-compressing (open valve) engine, for a speed range 100 rpm to 350 rpm, and the flow visualisation study of Ekchian & Hoult [1979] in a water-model engine, for the range 500 rpm to 2500 rpm, show no significant changes in the flow structure and almost linear scaling of the flow (mean) velocity with engine speed. However, it should be noted that in the particular circumstances of these studies, the non-linear characteristics of the inlet jet velocity with variations of

the pressure drop across the valve, as discussed by Gosman [1984], is absent. Thus, the linear scaling may not hold for higher engine speeds (see Table 2.3).

(b) Non-axisymmetric configuration: A small displacement of the inlet valve axis with respect to the cylinder axis produces three-dimensionality and swirl formation (Morse, et al. [1980b], Hirotomi, et al. [1981]). The measurements of Morse, et al. [1980b] show that in these circumstances, a vortex-pair structure is formed in the diametrical plane whose strength and size varies (is stratified) along the cylinder axis and changes during induction. However, as this and other studies (e.g. Arcoumanis [1983]) show, the flow structure in the axial plane is similar to that for the central valve configuration, except for circumferential variations due to the off-centre positioning of the valve.

The measurements of Arcoumanis [1983] show that imparting swirl to the incoming flow in these circumstances influences the flow structure in the diametrical plane, but the characteristic structure in the axial plane is almost unaffected. The flow visualisation study of Hirotomi, et al. [1981] of various directional (practical) port designs show that, although the vortex-pair structure is the most common pattern at small valve lifts, for larger lifts the flow structure in the diametrical plane is strongly influenced by the port design.

(i) The effect of operating parameters: The effect of engine operating parameters, namely, speed (S), compression ratio (CR) and volumetric efficiency (η_v) (by varying the port pressure) on the mean velocity, found by different investigators, is presented in Table 2.3. The effect of increase in engine speed is to increase the mean velocity $\overline{U}$: Semenov [1963], Lancaster [1976] and Witze [1977] show an approximately linear scaling (see Figure 2.15), while the experiments of Rask [1979] (of swirl component) and Gerber [1982] show no trends. The increase in η_v increases $\overline{U}$, although the measurements of Semenov [1963] show that the effect is mainly during the later part of induction (i.e. after $\theta \simeq 60°$ CA). The effect of CR on $\overline{U}$ is insignificant.

2.2.5.1.4 Turbulence characteristics: During induction, turbulence is generated in the shear layers of the induction jet and other regions of large mean flow strain (such as regions of impingement on the cylinder wall and piston), as evidence by the close correspondence between the distribution and level of the turbulence

intensity (u') and that of the mean velocity gradients shown in measurements (e.g. Semenov [1963], Morse, et al. [1979], Bicen [1983], Arcoumanis [1983]). This turbulence is convected and diffused throughout the cylinder. The measurements of Vafidis & Whitelaw [1984], noted earlier, indicate that the amount of turbulence convected into the cylinder by the intake jet is almost negligible compared with that generated within the cylinder.

The turbulence during this phase is, expectedly, largely influenced by the characteristics of the intake jet and is strongly non-homogeneous and, to a lesser extent, anisotropic (although Arcoumanis, et al. [1982b] show a large degree of isotropy outside the path of the induction jet). The relative level of u' is large: Witze's [1977] measurements show $u'/\overline{U} \simeq 0.5$ and Arcoumanis, et al. [1982b,1982c] data give the ratio of $\simeq 0.35$ to 0.5 for the axial and radial components and $\simeq 0.5$ to 1.0 for the tangential component. Furthermore, turbulence energy is contained mainly within the higher frequency components (f = 1000 Hz to 3500 Hz) (Table 2.2).

Near the end of induction ($\theta \simeq 120°$ to 180° CA), turbulence decays due to the rapid fall-off of the intake jet velocity, that removes the major source of turbulence energy production, and decay of the mean flow, and tends toward homogeneity and isotropy (Bicen [1983], Arcoumanis [1983]). The single-point measurements (generally taken at locations within the path of the intake jet) show a rapid reduction of u', which follows that of $\overline{U}$, during this phase. This has been incorrectly interpreted by many engine researchers as rapid decay of the <u>in-cylinder</u> turbulence. However, the detailed in-cylinder measurements of Bicen [1983] and Arcoumanis [1983] show that turbulence outside the region of intake jet decays at appreciably slower rates. This, which is also evidenced by the rapid tendency of turbulence towards homogeneity, indicates that the turbulence parameters τ_d and λ_x (and likely L_x, etc.) are appreciably different within and without the intake jet region and the data presented in Table 2.2 cannot be taken as representing the <u>in-cylinder</u> turbulence (particularly that which carries into compression). Also, it indicates that the conclusions of Tabaczynski [1979], based on single-point data for the induction and compression strokes (Figures 2.7 and 2.16) that the rapid decay near the end of induction causes major structural changes in the in-cylinder turbulence, may not be correct (the decay process indeed modifies the turbulence structure, as discussed by Batchelor [1960]; however, analysis of the effects must be based on measurements outside the region of intake jet, e.g. near the

cylinder axis).

The effects of engine operating parameters on the turbulence are as follows.

(i) Effect of swirl: Swirl increases the in-cylinder turbulence level by producing a more complex flow field and additional velocity gradients (Morse, et al. [1980a], Arcoumanis [1983]). However, the measurements of Arcoumanis, et al. [1982c] in the axisymmetric model engine shows that near the end of induction, the turbulence decays to the levels similar (slightly below) that for the no-swirl case. This has been attributed to the tendency of the swirl to organise into a solid-body rotation near the end of induction, which on one hand diminishes the velocity gradients associated with the swirl, and on the other has a streamline-curvature stabilising effect on turbulence (Townsend [1980]).

(ii) Effect of maximum valve lift: The effect of reduction in the valve lift is to increase the intake jet velocity and produce stronger vortex structure, resulting in higher levels of turbulence intensity (Arcoumanis, et al. [1982c]). However, the decay of the mean velocity and turbulence near the end of the induction diminishes the differences and leads to similar levels of u' (Arcoumanis, et al. [1982c]).

(iii) Effect of clearance gap: The measurements of Bicen & Vlachos [1980] show that the effect of reduction in the clearance gap is to produce higher levels of u', due to larger turbulence generation by the prolonged impingement of the intake jet on the piston and stronger vortex structure, during the former part of induction (θ = 0 to 90°). The decay of turbulence (and the mean flow) near the end of induction is faster in this case, resulting in similar levels of u' at BDC. The measurements of Lancaster show that $\overline{U}$ and u' (within the intake jet path) are not affected by changes in the clearance gap (i.e. the compression ratio).

(iv) Effect of engine speed: The measurements of Morse, et al. [1979] for the speed range S = 100 rpm to 350 rpm show an almost linear increase of u', throughout the cylinder, with speed. However, the data of Witze [1977] for S = 500 rpm to 2500 rpm show that the variation of $u' \sim S$ is only very approximately linear (see Figure 2.15); several other studies show a similar trend (Table 2.3).

The data presented in Table 2.3 show that

the integral time-scale L_t decreases linearly with engine speed and the integral length-scale L_x is nearly independent of speed.

(v) Effect of volumetric efficiency: The effect of increase in η_v, by increasing the port pressure, is to increase the turbulence intensity, as evidenced by the data of Table 2.3.

2.2.5.2 Compression process

2.2.5.2.1 Mean flow structure in the cylinder: Attention here is restricted to the disc (flat cylinder head and piston) configuration relevant to the present study. An extensive review of the flow in engine configurations with recesses in the piston and the cylinder head is given by Gosman [1984].

The measurements in the axisymmetric engine configuration show that during early phase of compression, the highly-structured induction-generated vortex system breaks up (in the axial plane) under the influence of the pressure field induced by piston motion (Bicen [1983], Arcoumanis [1983]). The remains of the intake-generated vortices steadily diminish and disappear in the axial plane, except that the main vortex may persist, depending on its size and strength at the end of induction, until mid-compression (for example, in the case of a 30° valve seat angle (Arcoumanis, et al. [1982c])). Thereafter, the lingering residue structure disappears in the axial plane and the flow becomes almost one-dimensional.

The measurements of Arcoumanis [1983] and Bicen [1983] in the axisymmetric engine configuration show that swirl, generated during induction via pre-valve guide vanes, does not change the described pattern of the flow development in the axial plane. However, the three-dimensional flow structures produced by off-centre valve positioning do appear to persist longer (Arcoumanis [1983]).

Swirl, if present, tends to organise into a nearly axially-uniform single vortex, often with an off-centre axis of rotation, early during compression (Hirotomi, et al. [1981], Vafidis [1984]). This vortex retains most of its angular momentum ($\simeq$ 70%) during the compression. The swirl velocity distribution away from the walls is shown in many cases to resemble solid body rotation (e.g. Morse & Whitelaw [1981], Arcoumanis, et al. [1982c]); however, the measurements of Vafidis [1984] show that it strongly depends on the induction history.

The effects of changes in the engine design and operating conditions on the flow near the end of compression

are as follows.

(i) Effect of valve seat angle and maximum lift: The measurements of Arcoumanis, et al. [1982c] in an axisymmetric engine show that changes in the intake valve (maximum) lift has no significant effect on the flow in the axial plane, after mid-compression ($\theta = 270°$). However, it influences the swirl velocity profile in the diametrical plane which tends toward a solid-body rotation for smaller maximum valve lifts.

These measurements also show that changing the inlet valve seat angle from 30° to 60° has no significant effect on the flow, both in the axial and diametrical (swirl velocity profile) planes, near the end of induction ($\theta = 324°$ CA).

However, as mentioned earlier, the measurements of Arcoumanis [1983] show that the off-centre positioning of the intake valve tends to prolong the persistence of the induction generated structure in the axial plane, during the compression. Therefore, in this arrangement, the induction history may persist and be, to some degree, reflected at top dead centre (TDC) of compression.

(ii) Effect of compression ratio (CR): The measurements of Arcoumanis, et al. [1981a] show that in an axisymmetric engine, an increase in CR tends to produce a faster break-up and decay of the induction generated vortex system in the axial plane, during early compression. Thus, it does not affect the flow near the end of compression. However, in cases with induction-generated swirl (Arcoumanis, et al. [1982b]), an increase in compression ratio tends to prolong the persistence of the intake-generated main vortex in the axial plane but has no effect on the swirl velocity profile in the diametrical plane, near the end of compression ($\theta = 324°$ CA). The differences may be expected to disappear by TDC, as is the case in production engines (e.g. Semenov [1963], Lancaster [1976]) (Table 2.6).

(iii) Effect of volumetric efficiency, η_v: As shown in Table 2.6, no particular trend can be identified for the variations of $\overline{U} \sim \eta_v$.

(iv) Effect of engine speed: The measurements presented in Table 2.6 show $\overline{U}$ at TDC increases with engine speed. Of these, Witze [1977], Wakisaka, et al. [1979] and Coghe & Ghezzi [1981] have

found a linear $\overline{U}\sim S$ variation; Semenov [1963] found $\overline{U}\sim S^{2\cdot1}$; while the measurements of Lancaster [1976], Gerber [1982] and Liou & Santavicca [1983] did not show a consistent trend of variation of $\overline{U}\sim S$ (i.e. $\overline{U}$ normalised by the mean piston speed $\overline{V}_p$ varied inconsistently).

2.2.5.2.2 Turbulence characteristics: The (rapid) decay of turbulence intensity u', observed near the end of induction, continues into the compression stroke until inlet valve closure ($\theta \simeq 220°$ to $240°$ CA) (see, for example, Bicen [1983] and Arcoumanis [1983]). Thereafter, u' remains nearly constant until shortly before TDC ($\theta = 330°$ to $340°$) and then tends to decrease markedly as TDC is approached (e.g. Lancaster [1976], Rask [1979], Arcoumanis, et al. [1982c]). These data (obtained in both the production and model engines) show a nearly constant level of $u'/\overline{V}_p \simeq 0.7$ to 0.5 during the major part of the compression. However, some measurements show a continuous decay (e.g. Dent & Salama [1975b], James & Lucas [1975], Witze [1979]); although in some cases involving engines with shrouded intake valves, u' increases during the compression (see Table 2.5). The latter behaviour is in contrast with the measurements of Arcoumanis, et al. [1982c] and Vafidis [1984], in which the effect of swirl (whether or not with a solid-body rotation distribution) was found to be to reduce the u' level during compression.

During compression, turbulence tends towards homogeneity and isotropy (Lancaster [1976], Arcoumanis, et al. [1982c]). Indeed, the latter data show that turbulence is isotropic throughout compression and almost homogeneous after $\theta = 270°$ CA. The frequency spectrum data (see Table 2.4) show that the turbulence energy is mainly contained in the low frequency components ($f \leqslant 700$ Hz to 1000 Hz, depending on the engine speed).

The measured values of the turbulence parameters L_t, L_x, λ_t and λ_x and the variation during the compression stroke are presented in Tables 2.4 and 2.5, respectively. The magnitude and variation of these parameters depend on the induction characteristics and operating conditions (Figure 2.16) (e.g. Lancaster [1976], Wakisaka, et al. [1979] and Brandl, et al. [1979]) and also, as discussed earlier, on the method of data processing (e.g. see Liou & Santavicca [1983]). The typical values and the more frequently observed trends are:

(a) $L_t \simeq 0.4$ msec to 2.0 msec ($S \simeq 1500$ rpm) and increases during compression.

(b) $L_x \simeq$ 3 mm to 10 mm ($S \simeq$ 1500 rpm), except in the case of Dent & Salama's [1975a] data for Heron (squish) chamber ($L_x \simeq$ 0.4 mm to 0.6 mm at S = 1000 rpm). It is found that $L_x \simeq (2.5 - 5.0)\lambda_x$. There is no consistent trend of variation during compression.

(c) $\lambda_t \simeq$ 0.1 msec to 0.2 msec, showing small influence of engine design and operating conditions in agreement with Dent & Salama [1975a]. λ_t is either constant (Wakisaka, et al. [1979]) or tends to increase during compression (Dent & Salama [1975b], Lancaster [1976]) (Figure 2.16).

(d) $\lambda_x \simeq$ 0.5 mm to 2.0 mm (S = 1500 rpm) and tends to increase during the former part of compression and decrease near TDC.

The effects of changes in the engine operating parameters on the turbulence will now be discussed.

(i) Effect of valve seat angle and maximum lift: The measurements of Arcoumanis, et al. [1982c] show that changes in the valve seat angle (ψ = 30° and 60°) and maximum valve lift (L_{max}/D = 0.12, 0.21 and 0.27) have no significant effect on u' near the end of compression (θ = 270° to 360° CA) (except for the smallest valve lift which produces slightly larger levels of u'). However, the data of Wakisaka, et al. [1979] and Brandl, et al. [1979] for production engines show that u' and the parameters L_t, L_x and λ_x at TDC are appreciably affected by the design of the port/valve assembly.

(ii) Effect of compression ratio: The measurements of Arcoumanis, et al. [1981a, 1982b] for CR = 3.5 and 6.7 show that the effect of CR on u' near the end of compression (θ = 324° to 360°) is negligible. The same effect (for u' at TDC) has been found in production engines by Semenov [1963] and Lancaster [1976]. However, the frequency spectrum data of Semenov [1963] showed that an increase in CR changes the u' spectral distribution by reducing the energy of the low-frequency (large scale) fluctuations and increasing that of the high-frequency components (in a manner that the total energy remains unchanged). As shown in Table 2.6, λ_t is not affected and there is no trend for the variation of $\lambda_x \sim CR$.

(iii) Effect of volumetric efficiency, η_v: The data presented in Table 2.6 show that, in general, u', L_t and L_x at TDC increase with increasing η_v; λ_t is independent of η_v and there is no

consistent trend of the variation of λ_x.

(iv) Effect of engine speed, S: The data of Table 2.6 show that in most experiments, a (nearly) linear variation of the TDC turbulence intensity with engine speed has been found. The exceptions are Semenov [1963], who found the relationship to be $u' \sim S^{1.5}$, and Gerber [1982] whose data for the interval θ = 180° to 315° CA shows no clear trend in the variations of u' with speed. The frequency spectrum data of Semenov [1963], James & Lucas [1975] and Daneshyar & Fuller [1981] show that the increase in u' is produced by an increase in the energy of all the frequency components.

Table 2.2 shows that, in general, L_t decreases with increase in speed; λ_t is constant (Dent & Salama [1975a]) or otherwise decreases and there is no clear trend of the variations of L_x and λ_x.

2.2.5.3 Expansion stroke

The onset of combustion significantly influences the mean flow and turbulence during the late compression and early expansion strokes (Wigley, et al. [1981], Witze, et al. [1983b]). For this reason, limited measurements have been performed during expansion in motored engines.

The measurements of Arcoumanis, et al. [1981a] in a disc chamber show that early during expansion, the mean flow in the axial plane is one-dimensional in the direction of the piston motion. Swirl, if present, persists and only loses angular momentum due to wall shear stresses. The turbulence remains homogeneous and decays rapidly. The data of Liou & Santavicca [1983] show that $L_t \simeq$ 0.2 msec to 0.3 msec and $L_x \simeq$ 4 mm to 6 mm (S = 2400 rpm) both increasing during early expansion.

2.3 THEORETICAL STUDIES

2.3.1 Multi-Dimensional Predictions of the Flow

This section is concerned with a review of multi-dimensional theoretical studies of in-cylinder mean flow and turbulence. The emphasis is on studies that include comparison with measurements, thus allowing evaluation of the accuracy of predictions. These and a few other important studies are reviewed within the text; others which are not of immediate interest are briefly summarised in Table 2.7. The 'zero' and 'one-dimensional' type methods are not included: these have been reviewed by Watkins [1977] and Johns [1980]. A survey of multi-dimensional methods

for simulation of in-cylinder flow and combustion is presented by Butler, et al. [1980]; it focuses primarily on methods originating from the Los Alamos Scientific Laboratory and includes a summary of the available computer codes and their capabilities.

In multi-dimensional methods, the combustion chamber is divided into discrete cells by a computational mesh and the differential conservation equations of mass, momentum, energy and those for the mathematical model of turbulence (see Chapter 3) are solved numerically over the whole chamber space and in time. The method thus provides detailed information about the spatial distribution and temporal variations of the in-cylinder velocities, temperature, turbulence parameters, etc.

The first multi-dimensional calculation of in-cylinder flow was performed by Watkins [1973], who solved the differential conservation equations of mass, momentum and energy for a laminar flow. A novel coordinate transformation, from an Eulerian to an Eulerian-Lagrangian coordinate frame, was improvised that allowed the finite-difference mesh to contract and expand with the piston motion, thus effectively confining the solution domain to the instantaneous cylinder volume. The differential equations were transformed into the new coordinates frame and were discretised, employing the fully-implicit temporal-differencing and the hybrid of central/upwind spatial-differencing schemes (see Chapter 4). The predicted pressure distribution for a one-dimensional isentropic compression/expansion was compared with the analytical solution and good agreement was found. The two-dimensional simulation of the flow induced by piston motion in a closed disc chamber during compression and expansion showed that the flow was mainly one-dimensional during both strokes, with the exception of the appearance of a toroidal vortex generated near the end of compression and suppressed early during expansion.

Boni, et al. [1976] predicted the flow and combustion in an axisymmetric representation of the Honda CVCC divided-chamber, stratified-charge engine. The compression and power strokes were simulated for an engine speed of 6000 rpm. The flow was considered turbulent and constant values of turbulent diffusivities for mass (species), momentum and energy were estimated from the experimental data of Witze [1975,1976a]. The equations for mass, momentum, internal energy and the species concentrations were solved using the Arbitrary Lagrangian Eulerian (ALE) numerical method of Hirt, et al. [1974]. A uni-directional axial flow in the cylinder and a vortex structure in the pre-chamber were predicted during the compression stroke.

The first serious attempt to predict turbulent flows in engines was by Watkins [1977]. He derived the governing differential equations for the ensemble-averaged quantities and employed the k-ε model of turbulence, modified to include the effects of compressibility, to calculate the turbulent stresses and other turbulent diffusion fluxes (see Chapter 3). The simulation of laminar and turbulent flows induced by piston motion in a closed disc chamber, performed on a 24×24 grid and with a time-step equivalent to $\Delta\theta = 6°$ CA, showed that, although both flows were one-dimensional over most of the compression and expansion strokes (as in the earlier Watkins [1973] study), a toroidal vortex was generated near TDC which differed in strength and sense of rotation between the two cases. He also performed a simulation of the induction and exhaust strokes for a laminar flow in a disc chamber engine with a central open-port, using a 30×30 grid. Comparisons were made with LDA measurements obtained in a plexiglass engine, operating at 10 rpm (Watkins [1977]): they showed that the main features of the flow, such as the spread of the intake jet near the piston and formation of a recirculation zone along the cylinder wall were relatively well predicted. However, weaker motions, especially a recirculation pattern near the cylinder head, were not predicted. The discrepancies were attributed to the assumed radial velocity profile at the inlet. Watkins [1977] also predicted the flow in a motored four-stroke disc-chamber engine with a centrally-located flush valve, for S = 1000 rpm to 3000 rpm and CR = 10 to 18. The predictions for S = 2000 rpm were compared with the single-point HWA measurements of Witze [1976b] in a similar engine: general agreement with the trends of variation of mean velocity and turbulence parameters were found during induction and exhaust, but not for the compression and expansion strokes. It was later found that the measurements for the latter phase over-estimated the true flow due to hot-wire calibration errors (Johns [1980]).

The general flow patterns during the engine cycle can be described as follows (see Figure 2.17). During induction, due to the small valve seat angle ($\psi = 30°$), the entering flow attaches to the cylinder head and wall, and derives a strong toroidal vortex within the interior (Figure 2.17). The mean velocity increases until mid-induction and thereafter falls rapidly until BDC, in accord with the measurement. This decay continues during the compression stroke, but the induction-generated vortex persists until TDC (Figure 2.17). Early during expansion, the residue vortex breaks up and flow becomes axially one-dimensional. A sink flow structure forms after the opening of the

exhaust valve that persists throughout the exhaust stroke.

During induction, turbulence is generated within the shear layers of the induction jet and the vortex, with maximum levels of u' being found in the former region and near the centre of the vortex towards the end of induction. The turbulence intensity decays near the end of induction and throughout compression; however, the decay rate is considerably smaller than that suggested by the measurement (during the phase that data are correct). During expansion, turbulence decays rapidly, and during the exhaust stroke, some turbulence is generated in the shear layers near the valve.

Other findings of this study were:

(i) The turbulence intensity at TDC compression generated by piston motion in a closed cylinder amounts to nearly 30% of that in a normal valved engine.

(ii) The variations of $\overline{U}$ and u' with engine speed are nearly linear at TDC compression.

(iii) $\overline{U}$ and u' are not influenced by changes in CR, except near TDC where both are reduced slightly by increase in CR.

Gosman, et al. [1979] demonstrated the extensive capabilities of multi-dimensional methods by simulating the flows in a range of axisymmetric engine configurations, including a disc chamber with a central valve, a Diesel chamber with a toroidal piston bowl and a pre-chamber Diesel configuration. The predicted $\overline{U}$ and u' for the disc chamber were compared with the single-point HWA measurements of Witze [1976b]. The results, disregarding the data for the late compression and expansion strokes which were shown to have been erroneous (Johns [1980]), were as follows:

(i) The general variation of $\overline{U}$ was in agreement with the data, although its magnitude was over-predicted by up to 100% during induction. It was shown that this could have been due in part to uncertainty about the incoming flow angle.

(ii) The predicted u' followed the measurement trend; however, its peak level was under-predicted by $\simeq$ 25%. The rapid decay near the end of induction was also under-predicted, resulting in larger predicted levels during compression (for the period where data are correct).

Gosman, et al. [1979] also calculated the flow evolution in the disc chamber, permanently-open central-valve model engine of Morse, et al. [1978a] and made comparisons with their LDA data obtained for a speed of 200 rpm. The comparison indicated:

(i) The structure and strength of the flow near the valve were reasonably well predicted; however, the strength of the vortex structure in the mid-cylinder region was strongly under-predicted.

(ii) The turbulence intensity in the inner part of the recirculation zone (near the cylinder axis) was well reproduced, but u' in the regions of induction jet and outer part of the recirculation zone (near the cylinder wall) was under-predicted and measured peaks associated with the flow structure was not predicted at all.

Jones [1980] predicted the mean flow and turbulence in the permanently-open central-valve disc chamber engine of Morse, et al. [1978b] with and without induction swirl, and the cylindrical bowl-in-piston configuration of Yianneskis [1977], and made comparisons with their LDA measurements. A computational grid of 30×30 in the former case and a 45×30 mesh, with 15 grids within the piston bowl, in the latter case were used. In general, he found that:

(i) The predicted mean flow structure during induction was in modest agreement with the data. The measured vortex structure near the cylinder head/wall was not predicted at all, and elsewhere the peaks in $\overline{U}$ were under-predicted and displaced.

(ii) The predicted turbulent intensities during induction were in good agreement with data in the region behind the valve, but were under-predicted in the induction jet and outer recirculation region (near the wall). The measured peaks in u' profiles corresponding to regions of strong shear were not predicted at all.

(iii) The predicted mean swirl velocity profiles during the induction and exhaust strokes were in good agreement with data.

With regard to (i) above, it was shown that the measured profiles of axial mean velocity close to the annular-orifice exit differed

considerably from the assumed plug flow distribution. This and additional uncertainties about the magnitude and shape of the radial velocity distribution at inlet were considered as important contributors to the discrepancy between the predictions and the data. Regarding (ii) above, the present study provides evidence (see Chapter 5) that the discrepancies have been largely due to the coarse grid used in these calculations.

Ramos, et al. [1981] predicted the mean flow and turbulence in a central-valve disc-chamber engine and made comparisons with their LDA measurements for an engine of 31 rpm. The predictions were performed on a 31×31 mesh and with a $\Delta\theta = 6°$ CA time-step. They obtained poor agreement during induction: the mean flow was largely over-predicted near the cylinder head and under-predicted towards the piston. The turbulence intensity was over-predicted and did not reproduce the measured peaks associated with regions of large shear. During compression, the mean velocities were well predicted but the (almost homogeneous) turbulence intensity was over-estimated by nearly 100%. During the expansion and exhaust strokes, the mean velocities were reasonably well reproduced, but the turbulence intensities were under-predicted.

Ahmadi-Befrui, et al. [1982] calculated the flow evolution in a central-valve disc-chamber model engine operating at 200 rpm and compression ratio of 3.5, and made comparisons with the LDA measurements of mean axial velocity and turbulence intensity. The predictions were performed with a variant of the RPM method (Watkins [1977]) on a relatively fine 45×45 grid and with a $\Delta\theta = 3°$ CA time-step. The measured flow structure was well reproduced by the calculations, but the strength of the central recirculation zone (near the axis) was under-predicted. The calculated turbulence intensity profiles contained peaks in regions of large shear, as in the measurements, but in general the levels were under-predicted. These discrepancies were associated with uncertainties in the boundary conditions at the valve exit.

The rapid decay of the mean flow and turbulence during late induction/early compression was under-predicted. Consequently, due to the persistence of the induction-generated vortex structure in the case of predictions, the agreement with data during compression (which showed a nearly uni-directional axial flow) was poor. However, the agreement in respect of both the homogeneity and level of turbulence intensity near the end of compression was good. The under-prediction of the rapid decay of the mean flow and turbulence intensity during late induction/early compression, observed also in other studies, can be in part due to the deficiency of the turbulence model, although the present study (Chapter 5)

shows that it is, in part, due to the (large) size of the computational time-step used.

Gosman, et al. [1984] were the first to predict the three-dimensional flow structures generated in a disc-chamber engine with an off-centre annular orifice or an off-centre poppet valve. The former predictions were compared with the LDA data of Morse, et al. [1980b] for the engine speed of 200 rpm. A novel numerical aspect was the use of a general non-iterative predictor-corrector technique for solving the implicit difference equations of the flow, that significantly reduced the computer time requirements over the previous RPM method. The calculations were performed on a $28 \times 18 \times 28$ mesh (grids in the radial, circumferential and axial directions, respectively) with a 1° CA time-step.

The results showed generation of a stratified swirling flow due to the valve eccentricity. The flow structure in the axial plane was similar to that for a central-valve configuration with circumferential variations due to the off-centre positioning. The comparison with measurements indicated that the mean flow structure was well predicted near the cylinder head, but agreement deteriorated towards the piston. The magnitudes of the mean velocities and the turbulence intensity, particularly in regions of peak values, were under-predicted.

2.3.2 Turbulence Modelling Aspect

The most common turbulence model employed in the multi-dimensional studies is the k-ε model, in the form originally derived by Watkins [1977] for the strongly compressible engine flows (see Chapter 3); although variants of this model have also been employed by, for example, Ramos & Sirignano [1980a,b] and Grasso & Bracco [1983a].

In addition to Watkins [1977], a few attempts have been made at deriving a suitable formulation of the k-ε model for application to engine flows, namely, by Reynolds [1980], Morel & Mansour [1982] and El Tahry [1983]: alternative forms were developed, with the differences residing in all instances in the form of the ε-transport equation (as discussed in detail in Chapter 3). The performances of these alternatives, in the cases of Morel & Mansour [1982] and El Tahry [1983], were compared by their developers with that of Watkins [1977] and showed substantial difference in the predictions, especially of the turbulence intensity and length-scale during the compression stroke. These studies, however, did not include simulation of the induction process and essentially involved quasi-one-dimensional compression/expansion of a homogeneous turbulence field. They also contained no comparison with data.

Therefore, in the absence of adequate application to the engine flows of the variants of the turbulence model (apart from the Watkins [1977] version) and assessment of their accuracy through comparison with data, no conclusions can be made as to which model is more suitable for engine applications.

2.4 CLOSURE

In this chapter, in the first instance, the uncertainty about the most suitable method for data reduction and characterisation of the non-stationary turbulent in-cylinder flows and the practices adopted by engine researchers have been discussed. It was concluded that the ensemble-average method is general and unambiguous, but may suppress important information; on the other hand, other methods involve a subjective data processing and their generality is questionable.

The important statistical parameters that characterise the spatial and temporal coherence of the turbulence, its energy spectrum and dissipation (life) time-scale have been identified and explained. The relation between certain measured parameters and those employed in the mathematical models of turbulence has been discussed. It was pointed out that, on the current evidence:

(i) The condition for validity of the Taylor hypothesis, commonly used to extract length-scale information from the time-scale measurements, is not in general satisfied during the compression stroke.
(ii) The micro-scale λ_χ has a significant influence on the combustion characteristics of engines.

The capabilities and deficiencies of hot-wire anemometry and laser-Doppler anemometry techniques in the engine context have been examined. It was found that the calibration difficulties of HWA can result in substantial error in the measurements of the mean velocity and turbulence parameters during the compression and expansion strokes. Furthermore, due to its direction-ambiguity and non-linearity, HWA can produce erroneous measurements of the mean velocity and turbulence in circumstances such as TDC compression. Thus, it was concluded that in spite of drawbacks associated with the non-continuous LDA signal (such as difficulties in measuring the turbulence scales), it is better suited for application to engine flows.

Experimental studies of the in-cylinder flow have been extensively reviewed. The flow characteristics of the induction system that affects

both the engine breathing capacity and the in-cylinder flow structure has been given proper attention. It was found that:

(i) The valve discharge coefficients under engine operating conditions are well presented by steady-flow measurements.
(ii) The flow behaviour at the inlet valve is complex and is strongly influenced by the valve design and lift. The intake jet velocity profile and angle of entry at the inlet-valve exit plane vary with valve lift and are influenced by the presence of the cylinder walls.

The flow evolution in disc-chamber engine configurations during the induction, compression and expansion strokes has been described and the effect of changes in the engine design and operating parameters pointed out. In general, it was found that:

(i) The in-cylinder flow during induction is strongly influenced by the design of inlet port/valve assembly. The flow structure is not affected by increase in engine speed, but the mean flow and turbulence intensity increase roughly linearly with speed. Overall, compression ratio has no significant effect on the flow.
(ii) The in-cylinder turbulence is generated within the shear layers of the induction jet and in other regions of large mean strain, and is strongly inhomogeneous. The turbulence advection into the cylinder is in comparison small.
(iii) The mean flow decays rapidly near the end of induction due to rapid fall-off of the inlet velocity. The turbulence intensity in the region of the intake jet also decays rapidly, but outside this region its decay is markedly slower, thus resulting in a rapid tendency towards homogeneity. This also indicates that the turbulence characteristics are different within the two regions and the single-point data, generally taken in the intake jet region, must not be generalised.
(iv) The induction-generated flow structure breaks up early during compression and flow becomes nearly one-dimensional in the axial plane. The flow memory in the diametrical plane is strong and swirl persists throughout the compression and expansion strokes.
(v) Turbulence intensity decays up to intake valve closure, and thereafter remains nearly constant until near the end of compression. Only in engines with an off-centre shrouded inlet valve has augmentation of turbulence during the compression stroke been observed. In all

cases, turbulence tends to decay as TDC is approached.

(vi) In the central-valve disc-chamber engine configuration, changes in the inlet valve seat angle and maximum lift have no significant effect on the mean flow and turbulence near TDC. However, in an off-centre valve arrangement, the mean flow induction history is prolonged and may persist to TDC. The TDC mean flow and turbulence intensity are not significantly affected by the compression ratio. The TDC mean velocity, in some cases, and the turbulence intensity, in most cases, are found to scale nearly linearly with engine speed.

(vii) Early during expansion, the mean flow is one-dimensional and turbulence remains homogeneous and decays.

Finally, the multi-dimensional model studies of the in-cylinder flow have been reviewed. In general, modest agreement with experiment has been observed. The main causes of discrepancies are believed to be the uncertainties in the boundary conditions, in particular the angle and profile of the inlet flow at the valve exit plane, and the coarseness of the computational grid and large time-steps used in many studies. These factors do not permit proper assessment of the performance of the turbulence model and of the numerical solution method. Furthermore, in the absence of an adequate assessment of the relative accuracy of the variants of the k-ε turbulence model, through comparison of the calculations with data, no conclusions can be made as to which model is more suitable for engine applications.

CHAPTER 3
THE MATHEMATICAL MODEL

3.1 INTRODUCTION

This chapter is concerned with assembling the differential equations that govern the in-cylinder flow and heat transfer, in a form suitable for the present study. In Section 3.2, the instantaneous conservation equations are introduced in the Cartesian tensor notation. Section 3.3 deals with recasting these equations in terms of statistical averaged quantities: the averaging procedures that may be applied to the non-stationary and compressible engine flows are examined and the most suitable one is adopted. The averaging process gives rise to additional unknown terms, containing correlations of the fluctuating components, that need to be determined with the aid of 'turbulence modelling'. In Section 3.4, the choice of a turbulence model is discussed; the differential equations of the selected k-ε model of turbulence are presented; and arguments concerning the effects of flow compressibility and complexity are put forward. Then, a general form of the differential equations is presented in Section 3.5 and is expressed in the cylindrical-polar coordinates frame that is employed in the remainder of the study.

The mathematical model is completed in Section 3.6 by specifying the boundary conditions for the differential equations.

3.2 THE INSTANTANEOUS EQUATIONS

The fundamental equations that govern a general compressible, non-reacting flow are the instantaneous conservation equations of mass, momentum and stagnation energy, together with the equation of state of gas. In the case of reacting flows, additional equations are required for the concentrations of the chemical species and for their rate of formation/decomposition (see, for example, Ahmadi-Befrui, et al. [1981]).

The differential equations for conservation of mass and momentum are given, in Cartesian tensor notation, as (Bird, et al. [1966])

$$\frac{\partial}{\partial t}(\rho) + \frac{\partial}{\partial x_j}(\rho U_j) = 0 \tag{3.1}$$

$$\frac{\partial}{\partial t}(\rho U_i) + \frac{\partial}{\partial x_j}(\rho U_j U_i) = -\frac{\partial P}{\partial x_j}\delta_{ij} + \frac{\partial}{\partial x_j}\tau_{ij} \tag{3.2}$$

where ρ, U, P and τ are, respectively, the density, velocity, static pressure and viscous stress tensor. In these equations, the Cartesian-tensor summation convention is used, in which repeated indices are to be

summed over all three coordinates, and δ_{ij} is the 'Kroneker delta' which is unity if $i = j$ and zero if $i \neq j$. τ_{ij} for a Newtonian fluid is defined as (Bird, et al. [1966])

$$\tau_{ij} = \mu \left(\frac{\partial U_i}{\partial x_j} + \frac{\partial U_j}{\partial x_i}\right) - \frac{2}{3} \mu \frac{\partial U_\ell}{\partial x_\ell} \delta_{ij} \tag{3.3}$$

where μ is the fluid's molecular viscosity.

The equation for the conservation of energy can be written in terms of the specific internal energy, e, as (Bird, et al. [1966])

$$\frac{\partial}{\partial t} \left[\rho \left(e + \frac{U_i^2}{2}\right)\right] + \frac{\partial}{\partial x_j} \left[\rho U_j \left(e + \frac{U_i^2}{2}\right)\right]$$

$$= \frac{\partial}{\partial x_j} \left(k \frac{\partial T}{\partial x_j}\right) - \frac{\partial}{\partial x_j} \left(P U_j\right) + \frac{\partial}{\partial x_j} \left(\tau_{ij} U_i\right) \tag{3.4}$$

where T and k are the temperature and the coefficient of conductivity, respectively, or in terms of the stagnation enthalpy, h_s, as

$$\frac{\partial}{\partial t} \left(\rho h_s\right) + \frac{\partial}{\partial x_j} \left(\rho U_j h_s\right) = \frac{\partial}{\partial x_j} \left(\frac{\mu}{\sigma_h} \frac{\partial h_s}{\partial x_j}\right) + \frac{\partial P}{\partial t}$$

$$+ \frac{\partial}{\partial x_j} \left[\left(\mu - \frac{\mu}{\sigma_h}\right) \frac{\partial}{\partial x_j} \left(\frac{U_i^2}{2}\right)\right] + \frac{\partial}{\partial x_j} \left(\mu U_i \frac{\partial U_j}{\partial x_i}\right)$$

$$- \frac{2}{3} \frac{\partial}{\partial x_j} \left(\mu U_j \frac{\partial U_\ell}{\partial x_\ell}\right) \tag{3.5}$$

where σ_h is the Prandtl number, and h_s, defined by

$$h_s = e + \frac{U_i^2}{2} + \frac{P}{\rho} \tag{3.6}$$

is the sum of the internal, kinetic and potential energies. The last three terms on the right hand side (hereafter abbreviated as rhs) of equation (3.5) represent the viscous transformation of the mechanical energy into heat and are negligibly small in the present circumstances.

The equation of state of gas is

$$P = R \rho T \tag{3.7}$$

where R is the gas constant.

The foregoing conservation equations and those for other scalar quantities, such as species concentrations, possess the common form

$$\frac{\partial}{\partial t} \left(\rho \Phi\right) + \frac{\partial}{\partial x_j} \left(\rho U_j \Phi\right) = \frac{\partial}{\partial x_j} \left(\Gamma_\Phi \frac{\partial \Phi}{\partial x_j}\right) + S_\Phi \tag{3.8}$$

where Φ is the dependent variable in question, Γ_Φ is the 'diffusion coefficient', and S_Φ represents the additional 'source terms'.

3.3 THE STATISTICAL APPROACH

Although the turbulent in-cylinder flows are governed by the fundamental conservation equations of the preceding section, the small time and length scale of the turbulent motions renders their direct simulation unfeasible in the context of the present day numerical solution methods. This problem is tackled, in the same manner as in experimental data processing, by adopting a statistical averaging procedure that allows calculation of the mean quantities, thus bypassing the need for direct simulation of the turbulence.

The statistical averaging procedures that have been adopted by experimentalists for application to engine flows, as outlined in Section 2.2.1, are the ensemble and the hybrid ensemble/time averaging schemes, entailing decomposition of the instantaneous quantities, respectively, according to equation (2.4) or equation (2.7). As shown in Appendix A, the general decomposition of equation (2.7) can be implemented through formal ensemble/time averaging of the instantaneous governing equations, resulting in sets of equations for the ensemble and time-averaged properties that require simultaneous solution. However, the problems in achieving this are: the large storage and additional computational time, the difficulty of arriving at a non-arbitrary time interval, and the turbulence modelling uncertainties, rendering this procedure unviable (furthermore, limited experimental data for comparison with the predictions are available). Therefore, the ensemble-averaging procedure is selected, thus the solutions of the equations represent statistical means over a large number of engine cycles.

3.3.1 The Ensemble-Averaged Equations

(i) Unweighted averaging

The usual approach for deriving the differential equations for the averaged quantities is to decompose the variables according to equation (2.4) and then apply the averaging procedure, equation (2.5), to all components of the differential equations (Watkins [1977]). Thus, introducing

$$\Phi = \overline{\Phi} + \phi' \tag{3.9}$$

where $\overline{\Phi}$ and ϕ' represent ensemble-mean and fluctuating components, respectively, and ensemble-averaging the conservation equations gives,

according to Watkins [1977],

$$\frac{\partial}{\partial t}(\bar{\rho}) + \frac{\partial}{\partial x_j}(\bar{\rho}\bar{U}_j + \overline{\rho' u_j'}) = 0$$

$$\frac{\partial}{\partial t}(\bar{\rho}\bar{U}_i + \overline{\rho' u_i'}) + \frac{\partial}{\partial x_j}(\bar{\rho}\bar{U}_j\bar{U}_i + \bar{\rho}\,\overline{u_j' u_i'} + \bar{U}_j\overline{\rho' u_i'} + \bar{U}_i\overline{\rho' u_j'} + \overline{\rho' u_j' u_i'})$$

$$= -\frac{\partial \bar{P}}{\partial x_i} + \frac{\partial}{\partial x_j}\bar{\tau}_{ij}$$

$$\frac{\partial}{\partial t}(\bar{\rho}\bar{\Phi} + \overline{\rho'\phi'}) + \frac{\partial}{\partial x_j}(\bar{\rho}\bar{U}_j\bar{\Phi} + \bar{\rho}\,\overline{u_j'\phi'} + \bar{U}_j\overline{\rho'\phi'} + \bar{\Phi}\overline{\rho' u_j'} + \overline{\rho' u_j'\phi'})$$

$$= \frac{\partial}{\partial x_j}\left(\bar{\Gamma}_\Phi \frac{\partial \bar{\Phi}}{\partial x_j}\right) + \bar{S}_\Phi \qquad (3.10)$$

where $\bar{S}_\Phi$ is the ensemble-averaged source term. The terms containing the fluctuating components, e.g. $\bar{\rho}\,\overline{u_j' u_i'}$, $\bar{\rho}\,\overline{u_j'\phi'}$, etc., are additional unknowns generated by the averaging process, and are taken to represent the transport of momentum, energy, etc., due to turbulence.

(ii) Density weighted averaging

The averaging procedure outlined, although straightforward for the case of incompressible flows, complicates the governing equations due to the additional terms that it generates, containing the density fluctuations, e.g. $\bar{U}_j\overline{\rho'\phi'}$, $\overline{\rho' u_j'\phi'}$. These terms can be significant in both reacting (Libby & Bray [1977]) and compressible non-reacting flows (Bradshaw & Ferriss [1971]). Since the replacement of these terms by calculable quantities is difficult and uncertain (Syed [1977]), it is best avoided if possible.

The latter objective can be achieved using an alternative approach, advocated for compressible flows, that introduces the notion of density-weighted properties (Favre [1969], Bilger [1975], Jones [1979]). In this, the density-weighted ensemble-averaged (hereafter DWEA) value, $\tilde{\Phi}$, is defined as

$$\tilde{\Phi}(\theta) = \frac{1}{\bar{\rho}(\theta)}\left[\lim_{N\to\infty}\frac{1}{N}\sum_{i=1}^{N}\rho(\theta,i)\,\Phi(\theta,i)\right] \qquad (3.11)$$

where $\bar{\rho}$ is the ensemble-averaged density, θ is the crank angle of interest, and i is the number of observations (engine cycles). (Hereafter, the overbar '—' will denote an unweighted ensemble-average and the DWEA values will be indicated either by '~' or '≃', the latter being used for terms containing several fluctuating components.)

The instantaneous variable Φ thus can be decomposed into its

DWEA value $\tilde{\Phi}$ and 'fluctuations' ϕ'' about this as

$$\Phi = \tilde{\Phi} + \phi'' \tag{3.12}$$

The comparison of equations (2.5) and (3.11) yields the following relation between $\tilde{\Phi}$, the ensemble-averaged $\overline{\Phi}$ and ϕ'

$$\tilde{\Phi} = \overline{\Phi} + \frac{\overline{\rho' \phi'}}{\overline{\rho}} \tag{3.13}$$

Therefore, application of the DWEA procedure precludes explicit appearance of (hence the need for treatment of) the correlations containing ρ'.

Some additional properties of the density-weighted variables, their relation with unweighted quantities, and details of the derivation of the differential governing equations of the flow in terms of DWEA variables are given in Appendix B. The resulting equations are summarised below.

$$\begin{aligned}
&\frac{\partial}{\partial t}(\overline{\rho}) + \frac{\partial}{\partial x_j}(\overline{\rho}\,\tilde{U}_j) = 0 \\
&\frac{\partial}{\partial t}(\overline{\rho}\,\tilde{U}_i) + \frac{\partial}{\partial x_j}(\overline{\rho}\,\tilde{U}_j\tilde{U}_i + \overline{\rho\,u_j''u_i''}) = -\frac{\partial \overline{P}}{\partial x_i} + \frac{\partial}{\partial x_j}\overline{\tau}_{ij} \\
&\frac{\partial}{\partial t}(\overline{\rho}\,\tilde{\Phi}) + \frac{\partial}{\partial x_j}(\overline{\rho}\,\tilde{U}_j\tilde{\Phi} + \overline{\rho\,u_j''\phi''}) = \frac{\partial}{\partial x_j}\left(\overline{\Gamma}_{\Phi}\frac{\partial \overline{\Phi}}{\partial x_j}\right) + \overline{S}_{\Phi}
\end{aligned} \tag{3.14}$$

The equation of state of gas reads

$$\overline{P} = R\,\overline{\rho}\,\tilde{T} \tag{3.15}$$

The molecular transport terms $(\partial/\partial x_j)\,\overline{\tau}_{ij}$ and $(\partial/\partial x_j)\left(\overline{\Gamma}_{\Phi}\,(\partial\overline{\Phi}/\partial x_j)\right)$ on the rhs of equations (3.14) can be neglected for high Reynolds number flows since, in virtually all turbulent flows, these terms are negligible except in the viscous sublayer region of wall boundary layers (Bradshaw [1973]).

3.4 TURBULENCE MODELLING

As evidenced above, the differential equations for the statistically averaged properties contain additional unknown terms, involving correlations of the fluctuating components, e.g. $\overline{\rho\,u_j''u_i''}$ and $\overline{\rho\,u_j''\phi''}$, and hence do not constitute a closed set. These correlations, commonly interpreted as representing additional diffusional fluxes of momentum, energy, etc., due to the turbulent motions, play a significant rôle in determining the flow behaviour; as the statistical effects of turbulence

is expressed through them. Their determination, therefore, is one of the main problems in calculating turbulent flows.

The instantaneous conservation equations can be manipulated to derive differential transport equations for these quantities (for example, see Appendix C for the transport equation of $\overline{\rho u_j'' u_i''}$). However, due to the non-linearity of the former equations, additional unknown terms arise involving higher order correlations of the fluctuating components, e.g. $\overline{\rho u_k'' u_j'' u_i''}$. The objective of 'turbulence modelling' is to resolve this 'closure problem' by relating the unknown turbulence correlations to known or calculable quantities, involving mean flow variables and statistical turbulence parameters, and thus 'close' the differential equation set.

3.4.1 The Nature of Turbulence

Prior to the discussion of the turbulence modelling practices, it is useful to examine some relevant details of the turbulence. This summary is drawn from material presented by Batchelor [1960], Rodi [1978] and Tennekes & Lumley [1980].

Turbulence can be conceived of as a tangle of vortices or 'eddies', with a wide range of size scales or frequencies, whose vorticity vectors can lie in all directions and are highly unsteady. The largest eddies, which are associated with the low frequency fluctuations, are determined by the boundary conditions and are of the same order of magnitude in size as the characteristic linear dimensions of the flow domain (i.e. the combustion chamber in the present case). The smallest eddies, which are associated with high frequency fluctuations, are determined by the amount of energy they extract from interaction with larger eddies and by the viscous forces.

The turbulent eddies interact with the (large scale) 'mean' motion and with each other, thereby extracting kinetic energy from the mean flow and passing it through to the smallest eddies where it is dissipated into heat by the viscous forces. The interaction of eddies is predominantly inertial and can be understood in terms of a vortex stretching mechanism, whereby the eddies aligned with the strain rate domain of the mean flow and/or the larger eddies are stretched, thereby gaining energy in order to conserve their angular momentum. The extraction of kinetic energy from the mean flow is principally done by larger eddies since these are most effectively stretched by the 'mean' flow strain rates. The kinetic energy of these 'energy containing' eddies is then transferred to smaller eddies, through their mutual

inertial interactions. The effect of the inertia forces is therefore to spread the energy over an increasingly wide spectrum of eddy sizes and effectively direct it - in a statistical term - towards the high frequency part of the spectrum, where the energy density is lowest, i.e. where the dissipation of kinetic energy by viscous forces is dominant. This process, however, is not controlled by the viscous forces: the inertial interactions determine the rate of energy transfer across the spectrum and the smallest scales adjust their velocity and length scale in order to dissipate this energy at the required rate. This statistical transfer of energy across the spectrum is known as the 'energy cascade'.

Due to their strong interaction with the mean motion, the large scales are strongly anisotropic, i.e. the statistical parameters such as turbulence intensity and length scale are direction-dependent. The effect of the inertia and pressure forces is to redistribute the turbulence energy between its directional components, therefore leading to isotropy at the higher frequencies. The 'energy cascade' is thus accompanied by a loss of the 'order' or information contained in the transferred energy (Batchelor [1960]). At high Reynolds numbers, the directional character is entirely lost and the dissipative eddies are isotropic (this is referred to as 'local isotropy'); furthermore, the rate of energy transfer from the 'energy-containing' eddies is identical to the dissipation rate by the smallest eddies ε*, implying that the viscous forces can be neglected for all but the small-scale dissipative motions. Under these conditions, the statistical characteristics of the dissipative eddies (i.e. the 'Kolmogorov' scales; see Chapter 2) are uniquely determined by the parameters ν (dynamic viscosity) and ε: this is known as the 'universal equilibrium hypothesis'. Batchelor [1960] shows that the condition for existence of the 'universal equilibrium' is that $Re_\ell^{\frac{3}{4}} >> 1$, where $Re_\ell = (u' \ell)/\nu$ is the Reynolds number of the energy-containing eddies.

Since the dynamics of the turbulence is independent of fluid viscosity, the flow is insignificantly affected by molecular diffusion: instead, diffusion due to turbulent motions are important. It is mainly the large-scale eddies that transport momentum, heat, etc., and contribute to the turbulence correlations $\overline{\tilde{u}_j'' u_i''}$ and $\overline{\tilde{u}_j'' \phi''}$. Hence, it is the large scales that have to be simulated in a turbulence model for

---

* This renders $\varepsilon \propto k \cdot (k^{1/2}/\ell) \propto k^{3/2}/\ell$, where ℓ is the length scale of the 'energy-containing' eddies (Batchelor [1960]).

determination of these quantities, and the length and velocity scales introduced in turbulence models must be statistical parameters that characterise them.

3.4.2 Choice of a Turbulence Model

There are numerous alternative turbulence modelling approaches of varying degrees of complexity; a number of reviews are available on their development and application, for example by Launder & Spalding [1972], Mellor & Herring [1973], Reynolds [1976], Rodi [1978], and Bradshaw, et al. [1981]. These models are often classified on the basis of the closure method for the Reynolds stresses $\overline{\rho}\,\widetilde{u_j'' u_i''}$, and the number of transport equations they solve for the turbulence parameters. The following presents a brief review of these models, and the rather different 'large eddy simulation' technique.

3.4.2.1 Mean flow or eddy viscosity type closures

These incorporate Boussinesq's [1877] turbulent (or eddy) viscosity concept and assume that analogous to viscous stresses, the Reynolds stresses are proportional to the mean flow strain rates. For a general compressible flow, this can be expressed through the Newtonian-type relationship:

$$-\overline{\rho}\,\widetilde{u_i'' u_j''} = \mu_T \left(\frac{\partial \tilde{U}_i}{\partial x_j} + \frac{\partial \tilde{U}_j}{\partial x_i}\right) - \frac{2}{3}\left(\mu_T \frac{\partial \tilde{U}_\ell}{\partial x_\ell} + \rho\, k\right) \delta_{ij} \qquad (3.16)$$

where μ_T is the turbulent or eddy viscosity. The 'turbulent viscosity' is a fictitious quantity defined by the above relation and is a flow property (as opposed to the molecular viscosity which is a fluid property). In this class of closure method, in analogy with the molecular viscosity theory, μ_T is related to the characteristic velocity (v) and length (ℓ) scales of (large scale) turbulence (Prandtl [1925]) via dimensional analysis

$$\mu_T \propto \overline{\rho}\, v\, \ell \qquad (3.17)$$

The turbulence parameters v and ℓ need to be determined, and according to the number of differential equations that are solved for them, this class of closure models are often further classified as zero-, one- or two-equation models (Launder & Spalding [1972], Reynolds [1976]).

(i) Zero-equation models: These models include variants of the Prandtl [1925] mixing length theory, in which the length scale ℓ_m

is postulated to be a simple algebraic function of the flow geometry, usually boundary layer width (see, for example, Launder & Spalding [1972]) and ν is expressed in terms of the mean shear, for a simple shear flow, as:

$$\nu \propto \ell_m \left|\frac{\partial \overline{U}}{\partial y}\right| \tag{3.18}$$

These models offer economy but fail to handle more complex flows (for example, involving curvature, flow acceleration, etc.) due to their neglect of the process of transport of turbulence (see, for example, Reynolds [1976], Rodi [1978]).

(ii) One-equation models: These models overcome some of the drawbacks of the zero-equation models, such as the neglect of the transport of turbulence and the postulate expressed by relation (3.18), by solving a transport equation for the turbulence velocity scale*. Following Kolmogorov [1942] and Prandtl [1945], the velocity scale ν is characterised by $\sqrt{k}$, where k is the turbulence energy. This is a physically meaningful scale and since the turbulence energy is mainly contained in the large scale motions, $\sqrt{k}$ is velocity scale of the large-scale turbulence. The resulting Kolmogorov-Prandtl expression for μ_T is:

$$\mu_T = C'_\mu \overline{\rho} \sqrt{k}\, \ell \tag{3.19}$$

where C'_μ is an empirical constant. The turbulence energy is obtained from solution of its modelled differential equation (to be presented later in this study) and ℓ is prescribed (see, for example, Launder & Spalding [1972], Reynolds [1976], Rodi [1978]). The main drawbacks with these models are the difficulties in specifying the length scale distribution in complex recirculating flows (such as those occurring in the engine cylinder) and their neglect of the convection and diffusion of the length scale.

(iii) Two-equation models: These models overcome the problem of specifying the length scale by solving a differential transport equation for ℓ (Rotta [1951]) or any dependent variable of the form

---

* The exception is Bradshaw & Ferriss's [1973] one-equation model for shear layers that solves a differential equation for the shear stress $\overline{u v}$, and does not employ the eddy-viscosity concept (see, for example, Rodi [1978]).

$z = k^m \ell^n$, where m and n are constants: since k is known, ℓ can be obtained from solution of the z-equation. In this respect, equations have been proposed for the dissipation rate $\varepsilon \propto k^{3/2}/\ell$ (Harlow & Nakayama [1968], Jones & Launder [1972]), $k\ell$ (Rodi & Spalding [1970]), frequency $\delta = k^{\frac{1}{2}}/\ell$ (Kolmogorov [1942]), and vorticity $w = k/\ell^2$ (Spalding [1971]) (see, for example, the summary of Launder & Spalding [1972] and Rodi [1978]). Of these, the equation for the dissipation rate ε is the most widely adopted, due to (i) ε appears directly in the transport equation for k; (ii) an exact transport equation for ε can be derived, with relative ease, from the Navier-Stokes equations; and (iii) this is the only equation that does not require a near-wall correction (Launder & Spalding [1974]).

In terms of these variables, the eddy viscosity relation (3.17) can be written

$$\mu_T = C_\mu \overline{\rho}\, k^2/\varepsilon \qquad (3.20)$$

where C_μ is an empirical coefficient, usually taken as a constant $C_\mu = 0.09$, determined from experiments in thin shear layer flows (Launder & Spalding [1972], Rodi [1978]).

The k-ε model has been tested in a wide range of shear and recirculating flows (for example, see Launder, et al. [1972], Launder & Spalding [1974], Gosman, Khalil & Whitelaw [1977]) and also has successfully been applied to the unsteady compressible in-cylinder flows (for example, Watkins [1977], Johns [1980]). These tests have shown that the model provides an adequate prediction of the flow for engineering purposes.

In general, the k-ε model offers a good compromise between the width of applicability, accuracy and computational economy (Rodi [1978]). However, certain aspects of the model are shown to be crude for application to complex flows (Rodi [1975,1978], Bradshaw [1973]) and strongly compressible flows (Watkins [1977]).

3.4.2.2 Reynolds stress closures

This class of models discards Boussinesq's hypothesis, equation (3.16), and solves the modelled differential transport equations for the Reynolds stresses $\overline{\rho}\,\widetilde{u_i'' u_j''}$ (the Reynolds stress models) or simplified versions of them (the algebraic stress models).

(i) The Reynolds stress models (RSM): These models solve

modelled versions* of the RS differential transport equations, thus allowing for the transport of the individual Reynolds stresses (for example, Launder, et al. [1975], Gibson, et al. [1981a]). As a dimensional necessity, the models also require a transport equation for the turbulence length scale, for which usually the ε-equation is used. These models are more physically based and offer more (potential) universality than the two-equation models, although it has been shown that their accuracy is affected by the deficiencies of the ε-transport equation (for example, Launder, et al. [1975], Launder & Morse [1979], Gibson, et al. [1981a]).

The use of the RSM method requires, for a general three-dimensional flow, solution of seven differential equations (six for the Reynolds stresses and one for the dissipation rate) in addition to the equations of the mean flow. Thus, the computational requirements, in terms of storage and time, are large. Therefore, their adoption can only be justified if the lower class models are proved to produce inadequate predictions.

(ii) Algebraic stress models (ASM): The complexity and computational cost of the RSM has provided an incentive to exploit any simplifications that the application warrants. Algebraic stress modelling (Rodi [1976]) is such an approach, in which the transport of $\widetilde{u_i'' u_j''}$ is assumed to be proportional to that of k: thus, the RS differential equations are reduced to a system of algebraic equations that are then solved in conjunction with the differential transport equations for k and ε (Rodi [1976]). The method therefore discards the eddy viscosity concept in favour of algebraic relations for $\widetilde{u_i'' u_j''}$, thus allowing more realism than the k-ε model. However, the assumptions involved in obtaining ASM require that the ratio $\widetilde{u_i'' u_j''}/k$ to be either constant or vary slowly within the flowfield. This condition is not satisfied in turbulent flows in engines. Moreover, for complex three-dimensional flows, solution of the coupled quadratic (and higher order) algebraic equations of the ASM sometimes proves to be more difficult and expensive than the solution of the parent differential equations (McGuirk [1983], Ghobadian [1983]).

---

* For a review of the modelling and various versions of the RS equations, see, for example, Reynolds [1976], Rodi [1978], Gibson, et al. [1978], and Jones [1979].

3.4.2.3 Multiple time-scale closure

This closure model has been proposed by Hanjalic & Launder [1978] in order to overcome some of the deficiencies of a single transport equation for the length scale used in the k-ε and RS closure models. The model attempts to account for the fact that turbulence energy production and dissipation occur within different ranges of turbulence eddy scales and the processes that affect the former (e.g. stretching by the mean shear) do not directly influence the latter. This is achieved by dividing the turbulence energy spectrum into energy-containing, energy-transfer and dissipation ranges, which are linked according to the 'energy cascade': two sets of modelled versions of the k-ε transport equations, for the energy-containing and transfer ranges, are then solved simultaneously.

The model, however, is in its development stage and, as yet, has not been applied to recirculating flows. Furthermore, Hanjalic, et al. [1979] have shown that it does not always produce an improvement over the single time-scale closures. Therefore, at present, its adoption for application to engine flows is not warranted.

3.4.2.4 Large eddy simulation

In this method, which is quite different from those described so far, the flow variables are decomposed into 'resolvable' and 'subgrid' scale components. The turbulent motions with scales larger than the size of the computational grid are obtained directly by solving the spatially-averaged Navier-Stokes equations. The 'subgrid-scale' Reynolds stresses are modelled, usually using the eddy viscosity concept, as a function of the 'resolvable' scale field (see, for example, Deardorff [1973], Schumann [1975], Clark, et al. [1979], or a brief overview by Reynolds [1980]).

This approach is potentially superior to the statistical flux models, inasmuch as (i) the small-scale turbulence is far more universal (i.e. independent of the gross characteristics of the flow) than large scales, and hence can be represented by relatively simple models, and (ii) the details of the 'subgrid-scale' turbulence model are far less influential on the flow behaviour than in the case of the statistical closure models. However, the application of this method, for an acceptable grid resolution, requires prohibitive computer time and storage; moreover, it is at present in an early stage of development. Therefore, for such time as advances in computers and further model development permit, its adoption for engineering purposes is unfeasible.

3.4.2.5 Choice of model

It is evident from the present review that the choice of a model for application to engine flows should be made between the k-ε and the Reynolds stress models. In such a decision, apart from the general criteria of universality, economy and ease of application, it is also necessary to take note of the extent to which the models have been developed and assessed in the presence of the phenomena (such as large compression and dilatation) that occur in engine circumstances.

In this context, the Reynolds stress model is considered to possess the following drawbacks and is rejected:

(a) The closure assumptions, for example for the velocity-pressure gradient correlation $[\overline{u_j''(\partial P'/\partial x_i)} + \overline{u_i''(\partial P'/\partial x_j)}]$, are uncertain for strongly compressible flows.

(b) Considerable uncertainty exists about the formulation of a suitable ε-transport equation for strongly compressible, confined flows in engines.

(c) The computational requirements are large.

Therefore, for the reasons that have already been discussed, the k-ε turbulence model is chosen for this study.

3.4.3 The k-ε Model of Turbulence

3.4.3.1 The k-transport equation

A transport equation for the DWEA turbulence kinetic energy k can be derived through manipulation of the continuity and Navier-Stokes equations. The details are presented in Appendix C, and the results are given here as:

$$\frac{\partial}{\partial t}(\bar{\rho}\,k) + \frac{\partial}{\partial x_j}(\bar{\rho}\,\tilde{u}_j\,k) = \underbrace{-\frac{\partial}{\partial x_j}\left(\bar{\rho}\,\widetilde{\frac{u_j''\,u_i''^2}{2}}\right)}_{\text{I}} \underbrace{-\frac{\partial}{\partial x_j}(\overline{P'\,u_j''})}_{\text{II}} + \frac{\partial}{\partial x_j}(\overline{u_i''\,\tau_{ij}'}) - \underbrace{\bar{\rho}\,\widetilde{u_j''\,u_i''}\frac{\partial \tilde{u}_i}{\partial x_j}}_{\text{III}} - \underbrace{\overline{u_i''}\frac{\partial \bar{P}}{\partial x_i}}_{\text{IV}} + \underbrace{\overline{P'\frac{\partial u_i''}{\partial x_i}}}_{\text{V}} - \underbrace{\overline{\tau_{ij}'\frac{\partial u_i''}{\partial x_j}}}_{\text{VI}} \tag{3.21}$$

All the terms in the above are similar to their counterparts for incompressible flows, with the exception of the terms labelled IV and V.

The terms on the rhs of the equation are not calculable as presented and require modelling. Following Bilger [1975] and Jones [1979], they are modelled here in a similar fashion as their incompressible flow counterparts. The physical significance and the closure treatments (where appropriate) of all the terms are as follows:

(i) I represents the rate of change plus advection of turbulence energy and requires no modelling.

(ii) The three components of II represent turbulent diffusion and are collectively modelled by the gradient expression (Watkins [1977], Jones [1979]):

$$II = \frac{\partial}{\partial x_j}\left(\frac{\mu_T}{\sigma_k}\frac{\partial k}{\partial x_j}\right) \tag{3.22}$$

where the Prandtl number, $\sigma_k = 1$, is determined by reference to experiment.

(iii) III represents production of turbulence energy due to interaction of the Reynolds stresses with the mean flow gradients. In conformity with Boussinesq's hypothesis for the Reynolds stresses (equation (3.16)), this term is modelled as:

$$III = \mu_T\left(\frac{\partial \tilde{u}_i}{\partial x_j}+\frac{\partial \tilde{u}_j}{\partial x_i}\right)\frac{\partial \tilde{u}_i}{\partial x_j} - \frac{2}{3}\left(\mu_T\frac{\partial \tilde{u}_\ell}{\partial x_\ell} + \bar{\rho}\,k\right)\frac{\partial \tilde{u}_\ell}{\partial x_\ell} \tag{3.23}$$

This will be referred to hereafter as the production term P.

(iv) Concerning IV, the quantity $\overline{u_i''}$ which it contains can be written as (see Appendix B):

$$\overline{u_i''} = -\frac{\overline{\rho' u_i'}}{\bar{\rho}} = -\frac{\overline{\rho' u_i''}}{\bar{\rho}} \tag{3.24}$$

Thus, term IV is the product of density-velocity fluctuation correlation with the mean pressure gradient and is of importance in combusting flows (Jones [1979], Bradshaw, et al. [1981]). Jones [1979] proposes that it be evaluated with the aid of an additional differential or algebraic equation for $\overline{\rho' u_i''}$; although he notes that the modelling of this equation, with guidelines based on the knowledge from constant density flows, involves empirical coefficients that in the absence of data cannot be determined. Jones also shows that under severe assumptions, that involve ignoring the mean pressure gradients and mean strain rates, the algebraic equation for $\overline{\rho' u_i''}$ can be reduced to

$$- \overline{\rho' u_i''} = \frac{1}{C_{\phi 1}} \frac{k}{\varepsilon} \overline{u_j'' u_i''} \frac{\partial \bar{\rho}}{\partial x_j} \tag{3.25}$$

with $C_{\phi 1} = 4.3$, indicating that it partly represents turbulence generation due to density gradients. Bradshaw, et al. [1981] have proposed a gradient approximation model of the form

$$- \overline{\rho' u_i''} = \frac{\mu_T}{\bar{\rho}\, \sigma_T} \frac{\partial \bar{\rho}}{\partial x_i} \tag{3.26}$$

which is a simplified version of equation (3.25); no suggestion has been made for the value of σ_T. However, Jones [1984] has found that use of this model (with $\sigma_T = 1$) does not significantly influence predictions of the combusting flows; concluding that it is far too simplified to account for the physical processes. In view of these factors, this term has been neglected in the present work.

(v) Term V, identically zero for constant density flows, has been associated with noise generation (Bilger [1976]) and is considered to be negligibly small, at least in low Mach number flows (Jones [1979]).

(vi) VI is the viscous dissipation correlation and, according to the definition of the dissipation rate ε, it can be rewritten as

$$\overline{\tau'_{ij} \frac{\partial u_i''}{\partial x_j}} = \bar{\rho}\, \varepsilon \tag{3.27}$$

When the above practices are incorporated in equation (3.21), the final modelled transport equation for k reads

$$\frac{\partial}{\partial t}(\bar{\rho} k) + \frac{\partial}{\partial x_j}(\bar{\rho} \tilde{u}_j k) = \frac{\partial}{\partial x_j}\left(\frac{\mu_T}{\sigma_k} \frac{\partial k}{\partial x_j}\right) + \mu_T \left(\frac{\partial \tilde{u}_i}{\partial x_j} + \frac{\partial \tilde{u}_j}{\partial x_i}\right) \frac{\partial \tilde{u}_j}{\partial x_i} - \frac{2}{3}\left(\mu_T \frac{\partial \tilde{u}_\ell}{\partial x_\ell} + \bar{\rho} k\right) \frac{\partial \tilde{u}_\ell}{\partial x_\ell} - \bar{\rho}\, \varepsilon \tag{3.28}$$

3.4.3.2 The ε-transport equation

In order to understand the deficiencies of the ε-transport equation and, in particular, the problems associated with obtaining a suitable modelled form of the equation for the present study, it is beneficial to examine this equation in some detail. Therefore, in

the present discussion, the exact and modelled equations for the constant-density flows are first presented. This is followed by consideration of the modifications necessary for compressible flows, particularly in the engine context.

(i) Incompressible flows: The counterpart of relation (3.27) for constant-density flows is

$$\overline{\tau'_{ij} \frac{\partial u'_i}{\partial x_j}} \equiv \mu \overline{\left(\frac{\partial u'_i}{\partial x_j} + \frac{\partial u'_j}{\partial x_i}\right) \frac{\partial u'_i}{\partial x_j}} = \bar{\rho}\,\varepsilon \tag{3.29}$$

This, for high Reynolds number flows, reduces to

$$\mu \overline{\left(\frac{\partial u'_i}{\partial x_j} \frac{\partial u'_i}{\partial x_j}\right)} \equiv \mu \overline{\left(\frac{\partial u'_i}{\partial x_j}\right)^2} = \bar{\rho}\,\varepsilon \tag{3.30}$$

since at high Reynolds numbers the small-scale turbulence is isotropic and, therefore, the cross-correlation terms in (3.29) are zero (Hinze [1975]).

The exact equation for the dissipation rate, as defined by equation (3.30), can be derived through manipulation of the Navier-Stokes equations for the fluctuating vorticity, following Harlow & Nakayama's [1968] approach. The result is the following equation (for example, Gibson, et al. [1978])

$$\frac{\partial}{\partial t}\varepsilon + \bar{U}_j \frac{\partial \varepsilon}{\partial x_j} = - \frac{\partial}{\partial x_j}\left[\nu \overline{u'_j \left(\frac{\partial u'_i}{\partial x_j}\right)^2} + \frac{2\nu}{\bar{\rho}} \overline{\frac{\partial p'}{\partial x_i} \frac{\partial u'_j}{\partial x_i}} - \nu \frac{\partial \varepsilon}{\partial x_j}\right]$$

I II

$$- 2\nu \frac{\partial \bar{U}_i}{\partial x_j}\left[\overline{\frac{\partial u'_i}{\partial x_\ell} \frac{\partial u'_j}{\partial x_\ell}} + \overline{\frac{\partial u'_\ell}{\partial x_i} \frac{\partial u'_\ell}{\partial x_j}}\right] - 2\nu \overline{u'_j \frac{\partial u'_i}{\partial x_\ell}} \frac{\partial^2 \bar{U}_i}{\partial x_j \partial x_\ell}$$

III

$$- 2\nu \overline{\frac{\partial u'_i}{\partial x_j} \frac{\partial u'_i}{\partial x_\ell} \frac{\partial u'_j}{\partial x_\ell}} - 2 \overline{\left(\nu \frac{\partial^2 u'_i}{\partial x_j \partial x_\ell}\right)^2} \tag{3.31}$$

IV V

The physical significance, order of magnitude and closure treatment of these terms are as follows:

(i) I represents the rate of change and convection of ε and requires no modelling.

(ii) The components of II represent diffusion by velocity and pressure

fluctuations and molecular viscosity: compared with the terms on the left hand side, the first component is of order unity and the rest are of order Re^{-1} ($Re = (u'\ell)/\nu$). These are collectively modelled as (Jones & Launder [1972])

$$II \equiv \frac{\partial}{\partial x_j}\left(\frac{\mu_T}{\overline{\rho}\,\sigma_\varepsilon}\frac{\partial \varepsilon}{\partial x_j}\right) \tag{3.32}$$

where the coefficient $\sigma_\varepsilon \simeq 1.3$ is obtained by reference to experiments.

(iii) The components of III represent generation by the mean motion and are of order $Re^{-\frac{1}{2}}$. They are small for high Reynolds number flows and are modelled together with IV.

(iv) IV represents generation due to self-stretching of vortices and is of order $Re^{\frac{1}{2}}$. Its closure model is discussed in the following.

(v) V represents viscous destruction and is of order $Re^{\frac{1}{2}}$. Its closure model is also discussed in the following.

Consideration of the orders of magnitude given above shows that for large Reynolds numbers, IV ≃ V, since both terms increase as $Re^{\frac{1}{2}}$ and become infinitely large compared with the rest of the terms. Thus, it appears that the ε-transport equation is of no use, since neither the rate of change (I) nor the diffusion (II) or production by the mean flow (III) play any rôle in it. Rodi [1971] analysed this behaviour and showed that IV - V is independent of the Reynolds number and thus is of the order of the convection and diffusion terms: hence, he concluded that these two terms should be modelled together. Accordingly, the generation and viscous destruction terms are modelled as (Jones & Launder [1972])

$$III + IV - V \equiv \frac{\varepsilon}{k}\left[C_{\varepsilon 1} P - C_{\varepsilon 2}\,\varepsilon\right] \tag{3.33}$$

in which P is the turbulence energy production rate and, $C_{\varepsilon 1} = 1.44$ and $C_{\varepsilon 2} = 1.92$ are empirical constants, obtained by reference to experiments. The modelled transport equation for ε, for a general incompressible flow, can therefore be written as (Jones & Launder [1972])

$$\frac{\partial}{\partial t}(\overline{\rho}\,\varepsilon) + \frac{\partial}{\partial x_j}(\overline{\rho}\,\overline{u}_j\,\varepsilon) = \frac{\partial}{\partial x_j}\left(\frac{\mu_T}{\sigma_\varepsilon}\frac{\partial \varepsilon}{\partial x_j}\right) + C_{\varepsilon 1}\frac{\varepsilon}{k}P - C_{\varepsilon 2}\,\overline{\rho}\,\frac{\varepsilon^2}{k} \tag{3.34}$$

where P is given by equation (3.23).

(ii) Compressible flows: As equations (3.27) and (3.29)

show, the definition of the dissipation rate of turbulence energy ε for density-weighted and conventional averaged quantities is slightly different. Therefore, for consistency, a transport equation for the dissipation rate ε for variable density flows, obtained using the density-weighting approach, must be derived. This, however, is difficult and so far has not been attempted. Jones [1979] argues that since the closure assumptions for modelling of the ε-transport equation essentially rest on qualitative physical arguments and dimensional analysis, there is little point in attempting to derive the exact equation, for the density-weighted quantities, for variable density flows. The approach generally adopted is to assume that similar form of the modelled ε-transport equation, as obtained for constant density flows, can be used in variable density flows with substitution of the conventional averaged quantities with their density-weighted counterparts (for example, Jones [1979], Bradshaw, et al. [1981]). This approach, which implies the models based on the two forms of averaging can be treated identically (Bradshaw, et al. [1981]) is followed in the present study.

Jones [1979] proposes that for variable density flows, the additional term $C_{\varepsilon 3}\,\bar{\rho}\,(\partial\tilde{U}_\ell/\partial x_\ell)$ and $C_{\varepsilon 4}\,(\varepsilon/k)\,(\overline{\rho' u_i''}/\bar{\rho})\,(\partial\bar{P}/\partial x_i)$ (the counterpart of the same term in the k-transport equation) also be added to equation (3.34); although he notes that in the absence of data, coefficients $C_{\varepsilon 3}$ and $C_{\varepsilon 4}$ cannot be determined. The latter term is not of significance in the present study and is neglected, as in the k-transport equation, due to the absence of a proper closure model. However, the former term, which represents generation due to compression, is important in strongly compressible engine flows and on this term, attention is focused in the following.

Watkins [1977], following Harlow & Nakayama's [1968] procedure, derived the ε-transport equation for variable density flows directly from the Navier-Stokes equations adopting a semi-rigorous approach: conventional (density unweighted) averaging method was used and the correlations containing density fluctuations were neglected. He showed that the term $\bar{\rho}\,\varepsilon\,(\partial\bar{U}_\ell/\partial x_\ell)$ appears as a natural product of the derivation*, implying that $C_{\varepsilon 3} = 1$. Accordingly, the following form of the ε-transport equation was adopted by him.

---

* The equation also contained additional correlation for which no guidance was available as to how to model them. These were neglected.

$$\frac{\partial}{\partial t}(\bar{\rho}\,\varepsilon) + \frac{\partial}{\partial x_j}(\bar{\rho}\,\tilde{u}_j\,\varepsilon) = \frac{\partial}{\partial x_j}\left(\frac{\mu_T}{\sigma_\varepsilon}\frac{\partial \varepsilon}{\partial x_j}\right)$$
$$+ C_{\varepsilon 1}\frac{\varepsilon}{k}\left[\mu_T\left(\frac{\partial \tilde{u}_i}{\partial x_j}+\frac{\partial \tilde{u}_j}{\partial x_i}\right)\frac{\partial \tilde{u}_i}{\partial x_j} - \frac{2}{3}\left(\mu_T\frac{\partial \tilde{u}_\ell}{\partial x_\ell} + \bar{\rho}\,k\right)\frac{\partial \tilde{u}_\ell}{\partial x_\ell}\right]$$
$$+ C_{\varepsilon 3}\,\bar{\rho}\,\varepsilon\,\frac{\partial \tilde{u}_\ell}{\partial x_\ell} - C_{\varepsilon 2}\,\bar{\rho}\,\frac{\varepsilon^2}{k} \qquad (3.35)$$

with σ_ε, $C_{\varepsilon 1}$ and $C_{\varepsilon 2}$ as in the constant density flow version, and $C_{\varepsilon 3} = 1$.

Subsequently, Reynolds [1980] examined the ε-transport equation (3.35) for the case of a homogeneous turbulence field under 'rapid' spherical compression. He argued that under rapid distortion, the angular momentum of the turbulent eddies (i.e. the product $u'\,\ell$) is conserved. Thus, using equations (2.13) and (3.20)

$$u'\,\ell = \sqrt{\frac{3}{2}k}\,\frac{C_\mu^{3/4}\,k^{3/2}}{\varepsilon} = \sqrt{\frac{3}{2}}\,C_\mu^{3/4}\,\frac{k^2}{\varepsilon} = \sqrt{\frac{3}{2}}\,C_\mu^{-1/4}\,\frac{\mu_T}{\bar{\rho}} = const. \qquad (3.36)$$

For constant C_μ, differentiation of the above gives

$$\frac{d\varepsilon}{dt} = 2\,\frac{\varepsilon}{k}\,\frac{dk}{dt} \qquad (3.37)$$

For a spherical compression, with the mean velocity field $U(r) = \beta r$, the production term P (equation (3.23)) has a simple form:

$$P = -\frac{2}{3}\,\bar{\rho}\,k\,\mathcal{D} \qquad (3.38)$$

where $\mathcal{D}$ is the velocity divergence*

$$\mathcal{D} \equiv \frac{\partial \tilde{u}_\ell}{\partial x_\ell} = -\frac{1}{\bar{\rho}}\frac{d\bar{\rho}}{dt} \qquad (3.39)$$

For a homogeneous turbulence, the convection and diffusion of k are zero, and assuming 'rapid distortion' the dissipation rate can be neglected (see Crow [1968]). Thus, equation (3.28) reduces to

$$\bar{\rho}\,\frac{dk}{dt} = -\frac{2}{3}\,\bar{\rho}\,k\,\mathcal{D} \qquad (3.40)$$

Combining equations (3.37) and (3.40) gives

---

* For spherical compression with $\tilde{U}(r) = \beta r$, $\mathcal{D} = (1/r^2)\,(\partial r^2\,\tilde{U}/\partial r) = 3\beta$.

$$\bar{\rho}\,\frac{d\varepsilon}{dt} = -\frac{4}{3}\,\bar{\rho}\,\varepsilon\,\mathcal{D} \tag{3.41}$$

This is the desired form of the ε-equation that satisfies the constraints (3.36) for this type of compression. For these conditions, the ε-transport equation (3.35) reduces to, neglecting the dissipation term $C_{\varepsilon 2}\,\bar{\rho}\,(\varepsilon^2/k)$

$$\bar{\rho}\,\frac{d\varepsilon}{dt} = \left(-\frac{2}{3}\,C_{\varepsilon 1} + C_{\varepsilon 3}\right)\bar{\rho}\,\varepsilon\,\mathcal{D} \tag{3.42}$$

Therefore, for the ε-transport equation to produce the 'proper' behaviour in rapid spherical compression, $C_{\varepsilon 3}$ must have the value $C_{\varepsilon 3} = \frac{2}{3}(C_{\varepsilon 1} - 2)$: since $C_{\varepsilon 1} = 1.44$, this yields $C_{\varepsilon 3} \simeq -0.373$.

Morel & Mansour [1982] (hereafter referred to as MM), following Reynolds' [1980] analysis, showed that using equations (3.39), (3.40) and (3.42), the variations of the turbulence length scale during a rapid spherical compression is given by

$$\ell\,\bar{\rho}^{-\left(\frac{2}{3}C_{\varepsilon 1} - 1 - C_{\varepsilon 3}\right)} = const. \tag{3.43}$$

A physically plausible behaviour for the length scale is to decrease under the compression, thus requiring the exponent to be positive, i.e. $C_{\varepsilon 3} < \frac{2}{3}C_{\varepsilon 1} - 1$ (for $C_{\varepsilon 1} = 1.44$, this gives $C_{\varepsilon 3} < -0.04$). Assuming that during a rapid spherical compression any small element of turbulence simply compresses with the fluid volume change, they invoked the constraint

$$\bar{\rho}\,\ell^3 = const. \tag{3.44}$$

Combining equations (3.43) and (3.44), MM found $C_{\varepsilon 3} = \frac{2}{3}(C_{\varepsilon 1} - 2)$. This is identical to the value obtained by Reynolds by invoking the constraint (3.36). A constraint of the form

$$\bar{\rho}\,\ell^3\left(\frac{k^2}{\varepsilon}\right) = const. \tag{3.45}$$

rendered the same value of $C_{\varepsilon 3}$.

MM further examined the production term P for different types of unidirectional compression (spherical, cylindrical-radial and axial) and found that it reduces to different forms, depending on the type of compression. They noted that, as a consequence, the three constraints, equations (3.36), (3.44) and (3.45), do not produce the same

results for all types of compression. Therefore, they invoked a general form of the constraint

$$\rho^p \, \ell^n \, \left(\frac{k^2}{\varepsilon}\right)^m = const. \tag{3.46}$$

where p, n and m were to be determined. This analysis rendered, taking $C_{\varepsilon 3} = 1$ (the 'accepted' value), the production term in the ε-transport equation (3.35) as

$$\frac{\varepsilon}{k}\left[C_{\varepsilon 1}\,\mu_T\left(\frac{\partial \tilde{u}_i}{\partial x_j}+\frac{\partial \tilde{u}_j}{\partial x_i}\right)\frac{\partial \tilde{u}_i}{\partial x_j}\right] - \frac{2}{3}C'_{\varepsilon 1}\,\mu_T\left(\frac{\partial \tilde{u}_\ell}{\partial x_\ell}\right)^2 - \frac{2}{3}C''_{\varepsilon 1}\,\bar{\rho}\,k\,\frac{\partial \tilde{u}_\ell}{\partial x_\ell} \tag{3.47}$$

in which the coefficients $C'_{\varepsilon 1}$ and $C''_{\varepsilon 1}$ depend on the type of compression and the exponents p, n and m.

In final analysis, in the absence of conclusive experimental evidence, MM chose $p = 1$ and $m = 0$, obtaining the following expressions for $C'_{\varepsilon 1}$ and $C''_{\varepsilon 1}$:

$$\begin{aligned} C'_{\varepsilon 1} &= C_{\varepsilon 1} + a\,(C_{\varepsilon 1} - 1.5) \\ C''_{\varepsilon 1} &= 3 + \frac{3}{2n} \end{aligned} \tag{3.48}$$

with a and n related to the mean strain tensor $S_{ij} = \frac{1}{2}[(\partial \tilde{u}_i/\partial x_j) + (\partial \tilde{u}_j/\partial x_i)]$ via the following algebraic relations:

$$\begin{aligned} a &= \frac{3\,(S_{11}^2 + S_{22}^2 + S_{33}^2)}{(|S_{11}| + |S_{22}| + |S_{33}|)^2 - 1} \\ n &= 3 - \sqrt{2a} \end{aligned} \tag{3.49}$$

The validity of the 'rapid' compression assumption in engine circumstances was examined by MM by comparing the turbulence dissipation time-scale τ_d (equation (2.27)) with the time scale of the mean flow $1/\mathcal{D}$. However, in their study, the dissipation time-scale was incorrectly taken as $\tau_d = k/(C_\mu \varepsilon)$ (instead of k/ε) and was estimated from rather inappropriate assumptions (such as the proportionality of the turbulence length scale ℓ and engine stroke S_t in the form $\ell/S_t \simeq O(10^{-1})$, at bottom dead centre of induction, which will be shown later (Chapters 5 and 6) to be incorrect). Here, the condition for the validity of the 'rapid' compression assumption is re-examined, using a similar approach but with more appropriate estimates of the scales.

The k-transport equation for a general unidirectional

compression can be written as

$$\bar{\rho}\,\frac{\mathcal{D}k}{\mathcal{D}t} = \frac{2}{3}\,a\,\mu_T\,\mathcal{D}^2 - \frac{2}{3}\,\bar{\rho}\,k\,\mathcal{D} - \bar{\rho}\,\varepsilon \qquad (3.50)$$

where the value of a depends on the type of compression, and $\mathcal{D}$, defined by equation (3.39), is the strain rate caused by the compression. This equation may be written as:

$$\bar{\rho}\,\frac{\mathcal{D}k}{\mathcal{D}t} = \frac{2}{3}\,a\,C_\mu\,\bar{\rho}\,\varepsilon\,T^2 - \frac{2}{3}\,\bar{\rho}\,\varepsilon\,T - \bar{\rho}\,\varepsilon \qquad (3.51)$$

where T is the ratio of the turbulence dissipation time-scale to time-scale of the distortion, given by

$$T = \frac{k/\varepsilon}{1/\mathcal{D}} = \frac{k\,\mathcal{D}}{\varepsilon} \qquad (3.52)$$

The rapid distortion assumption requires that the generation terms be much larger than the dissipation term, i.e.

$$\frac{2}{3}\,a\,C_\mu\,T^2 - \frac{2}{3}\,T - 1 \;>>\; 0 \qquad (3.53)$$

For a unidirectional axial compression (a = 2), this renders

$$T \;>>\; 6.78 \qquad (3.54)$$

Taking $\mathcal{D}$ as the average strain rate during compression

$$\mathcal{D} = \frac{\overline{V}_p}{S_t} = \frac{1}{2T_{cycle}} \qquad (3.55)$$

where $\overline{V}_p$ and T_{cycle} are, respectively, the mean piston speed and the period for one engine cycle, the predictions of the in-cylinder flow (presented in Chapters 5 and 6) show that the value of T, within the bulk of the flow, at the beginning of the compression stroke, is

$$T \simeq 0.1 - 0.2$$

and is nearly independent of the engine speed. Therefore, the assumption of rapid compression cannot be applied to engine flows.

In another study, El Tahry [1983] derived an exact transport equation for ε for variable density flows, adopting the conventional averaging method and retaining the correlations containing

fluctuations of density and molecular viscosity. He carried out an order of magnitude analysis of this equation and concluded that a number of terms in the ε-transport equation that were neglected by Watkins [1977] are not negligible. He further showed that the ensemble of compressibility terms can be modelled, without the introduction of additional empirical coefficients, as

$$C_{\varepsilon 3}\,\bar{\rho}\,\varepsilon\,\frac{\partial \tilde{U}_\ell}{\partial x_\ell} + \frac{\bar{\rho}\,\varepsilon}{\bar{\mu}}\frac{\partial \bar{\mu}}{\partial t} + \bar{\rho}\,\tilde{U}_j\,\frac{\varepsilon}{\bar{\nu}}\frac{\partial \bar{\nu}}{\partial x_j} - \frac{\mu_T}{\sigma_\varepsilon\,\bar{\nu}}\frac{\partial \bar{\nu}}{\partial x_j}\frac{\partial \varepsilon}{\partial x_j} - \frac{\mu_T}{\sigma_\varepsilon\,\bar{\rho}}\frac{\partial \bar{\rho}}{\partial x_j}\frac{\partial \varepsilon}{\partial x_j} \qquad (3.56)$$

where $C_{\varepsilon 3} = -1/3$, $\sigma_\varepsilon \simeq 1.3$, and $\bar{\mu}$ and $\bar{\nu}$ are the molecular and kinematic viscosities. In the above, the last three terms are of importance only in the presence of combustion (causing strong thermal stratification) and can be neglected in non-combusting flows. It is noteworthy that El Tahry's value of the coefficient $C_{\varepsilon 3}$ is very close to that obtained by Reynolds [1980].

It should also be mentioned that in some calculations with the k-ε model (using equations (3.28) and (3.35)), other values of $C_{\varepsilon 3}$ have been used: Ramos & Sirignano [1980a,b] set $C_{\varepsilon 3} = 0$, and Grasso & Bracco [1983a] used $C_{\varepsilon 3} = -1$. The former specification invokes the constant density form the equation; the reasoning for the latter choice is not given.

In the present study, three variants of the ε-transport equation, namely those of Watkins [1977], Morel & Mansour [1982] and El Tahry [1983], are employed and their predictions are rigorously examined (see Chapter 5). These can be collectively represented by an equation of the form

$$\begin{aligned}\frac{\partial}{\partial t}(\bar{\rho}\,\varepsilon) + \frac{\partial}{\partial x_j}(\bar{\rho}\,\tilde{U}_j\,\varepsilon) &= \frac{\partial}{\partial x_j}\left(\frac{\mu_T}{\sigma_\varepsilon}\frac{\partial \varepsilon}{\partial x_j}\right) + \frac{\varepsilon}{k}\left[C_{\varepsilon 1}\,\mu_T\left(\frac{\partial \tilde{U}_i}{\partial x_j}+\frac{\partial \tilde{U}_j}{\partial x_i}\right)\frac{\partial \tilde{U}_i}{\partial x_j}\right.\\ &\quad \left. - \frac{2}{3}\frac{\partial \tilde{U}_\ell}{\partial x_\ell}\left(C'_{\varepsilon 1}\,\mu_T\frac{\partial \tilde{U}_\ell}{\partial x_\ell} + C''_{\varepsilon 1}\,\bar{\rho}\,k\right)\right]\\ &\quad + C_{\varepsilon 3}\,\bar{\rho}\,\varepsilon\frac{\partial \tilde{U}_\ell}{\partial x_\ell} + C_{\varepsilon 4}\frac{\bar{\rho}\,\varepsilon}{\bar{\mu}}\frac{\partial \bar{\mu}}{\partial t} - C_{\varepsilon 2}\frac{\bar{\rho}\,\varepsilon^2}{k}\end{aligned} \qquad (3.57)$$

where values of the coefficients $C_{\varepsilon 1}$, $C'_{\varepsilon 1}$, etc., corresponding to each version are given in Table 3.1.

3.4.3.3 The scalar quantities

In direct analogy with the treatment of the Reynolds stresses, the second order correlations of velocity and scalar fluctuations ($\overline{\rho\,u''_j\,\phi''}$) that represent turbulent diffusional fluxes of energy, species,

etc., are expressed in terms of gradients of the mean variables, as in laminar flows (Launder & Spalding [1972]). Thus:

$$- \overline{\rho}\ \overline{u_j'' \phi''} = \Gamma_{\Phi,T} \frac{\partial \tilde{\Phi}}{\partial x_j} \tag{3.58}$$

Here, $\Gamma_{\Phi,T}$ - the turbulent (eddy) diffusivity - is evaluated, in accordance with the Reynolds analogy, from the relation (Launder & Spalding [1972])

$$\Gamma_{\Phi,T} = \frac{\mu_T}{\sigma_{\Phi,T}} \tag{3.59}$$

where $\sigma_{\Phi,T}$ is a turbulent Prandtl/Schmidt number. Experiments have shown that $\sigma_{\Phi,T}$ is not strongly flow-dependent (Rodi [1978]), thus it is usually assigned a constant value (of order unity) determined from experiment. The values employed in this study are given in Table 3.2.

3.4.4 Shortcomings of Model for Complex Compressible Flow Applications

This section examines some aspects of the assumptions incorporated in the k-ε model of turbulence and their validity in engine flow circumstances. These involve the invocation of Boussinesq's [1877] hypothesis (equation (3.16)) and the closure models for strongly compressible flows, and the assumption of an isotropic eddy viscosity, implied by relation (3.20), in complex flows*.

(i) Compressibility effects: The principle that is used to justify the application of 'constant density' turbulence models to compressible flows is Morkovin's hypothesis (cited in Bradshaw & Ferriss [1971]) which states that turbulence is unaffected by random fluctuations in pressure or density as long as they are small compared with the mean pressure or density. This is satisfied at all non-hypersonic speeds (Mach number $\lesssim 3$). However, Bradshaw & Ferris [1971] note that this hypothesis makes no reference to the pressure gradients that would be expected in the presence of shock waves or large dilatations ($div\ \tilde{U} \equiv \partial \tilde{U}_\ell / \partial x_\ell$) and would likely cause changes in turbulence structure, so the hypothesis is likely to fail in these circumstances.

---

* Bradshaw [1973] defines a 'complex flow' as a 'simple shear flow' that incorporates (or is subjected to) an 'extra rate of strain' due to flow curvature, longitudinal acceleration, lateral convergence/divergence and bulk compression/dilatation.

Bradshaw [1973,1975,1977] states that compression and dilatation strongly affect the turbulence, due to the extra rate of strain they produce, with compression increasing and dilatation decreasing the Reynolds stresses. This is supported by the experiments of Narashima & Viswanath [1975] and Muck & Smits [1983] that respectively show, in turbulent simple shear flows, bulk dilatation (expansion) greatly reduces and bulk (rapid) compression (through flow interaction with shock waves) greatly increases, the Reynolds stresses. Bradshaw [1973] also argues that the effect of the extra rate of strain on the turbulence energy production is much larger (of order 10) than is accounted for in equations (3.16) and (3.23)*.

However, measurements of the in-cylinder turbulence during the compression stroke do not show large increases of the Reynolds stresses and the turbulence intensity; rather, they tend simply to decay slowly (e.g. Bicen [1983], Arcoumanis [1983]). Therefore, it may be argued that for the compression rates characteristic of engine flows, the effect of the extra rate of strain on the turbulence energy production rate is not as large as is suggested by Bradshaw [1973]; although it is possible that the larger dissipation rate of turbulence energy in the circumstances where the irrotational strains are of significance (Hanjalic & Launder [1980]), as in the case of in-cylinder flow under compression, is responsible for this behaviour.

The capability of the k-ε model to, at least, qualitatively simulate the compression effects can be tested by considering the degenerate forms of the transport equations for the case of a general unidirectional compression/expansion process acting on a homogeneous turbulence field. For this case, equation (3.51) and its corresponding ε-equation reduce to:

$$\frac{\mathcal{D}k}{\mathcal{D}t} = \frac{2}{3}\, a\, C_\mu \frac{k^2}{\varepsilon}\mathcal{D}^2 - \frac{2}{3}\, k\, \mathcal{D} - \varepsilon$$

$$\frac{\mathcal{D}\varepsilon}{\mathcal{D}t} = \frac{\varepsilon}{k}\left[\frac{2}{3}\, C_{\varepsilon 1}\,(1+a)\, C_\mu \frac{k^2}{\varepsilon}\mathcal{D}^2 - \frac{2}{3}\, C'_{\varepsilon 1}\, C_\mu \frac{k^2}{\varepsilon}\mathcal{D}^2 - \left(\frac{2}{3}\, C''_{\varepsilon 1} - C_{\varepsilon 3}\right) k\, \mathcal{D}\right] + C_{\varepsilon 4}\frac{\varepsilon}{\mu}\frac{d\mu}{dt} - C_{\varepsilon 2}\frac{\varepsilon^2}{k} \qquad (3.60)$$

The k-equation shows that for compression ($\mathcal{D} < 0$), the 'production' term associated with the compressibility effect ($-\frac{2}{3}k\mathcal{D}$) is positive and tends

---

* The general argument applies to any extra rate of strain imposed on a 'simple shear flow' in a 'complex flow'.

to increase k, while for expansion it is negative and reduces k: thus, the physically correct behaviour is reproduced by the model. The ε-equation shows the same dependence on the compressibility term (for $C_{\varepsilon 3} < \frac{2}{3} C''_{\varepsilon 1}$), and also contains a dependence on the inverse of the dissipation time-scale ($\tau_d^{-1} = \varepsilon/k$). Thus, under the condition where τ_d is relatively large, the effect of compressibility on the dissipation rate is small. However, the term $(\varepsilon/\bar{\mu})\ (d\bar{\mu}/dt) \propto -\varepsilon \mathcal{D}$, which is independent of τ_d, tends to augment the dissipation rate during compression and reduce it during expansion. As pointed out earlier, in engine flow circumstances τ_d is relatively small compared with the time scale of compression ($\tau_d/T_{cycle} \simeq 0\ (10^{-1})$), and thus the effect of compression on the dissipation rate would be expected not to be small.

(ii) 'Flow complexity' effects: The value of $C_\mu = 0.09$ (equation (3.20)), generally used in the k-ε model of turbulence, has been obtained from measurements of thin shear layers, in which the transport of Reynolds stresses is negligible and turbulence is in local equilibrium (i.e. $P \simeq \rho\varepsilon$) (see, for example, Launder & Spalding [1972], Rodi [1978]). Rodi [1975] showed, by analysing measurements in various self-preserving shear flows, that C_μ is not a universal constant. Furthermore, he showed, by simplifying the transport equation for Reynolds stress $\overline{u'v'}$ for thin shear layer flows, that C_μ depends on:

(i) the ratio (transport of $\overline{u'v'}$/production of $\overline{u'v'}$);
(ii) the ratio $\overline{v'^2}/k$;
(iii) the production of $\overline{u'v'}$ (arising from the closure model for the pressure-strain rate correlation).

Thus, constancy of C_μ requires all three quantities identified above to be constant within the flow, a condition which is not generally satisfied.

Subsequently, Rodi [1976], through the Algebraic Stress Modelling (ASM) approach, derived the following algebraic expression

$$\overline{u'_i u'_j} = k \left[\frac{2}{3} \delta_{ij} + \frac{1-\gamma}{C_1} \frac{P_{ij}/\varepsilon - \frac{2}{3}\delta_{ij} P/\varepsilon}{1 + 1/C_1\ (P/\varepsilon - 1)} \right] \qquad (3.61)$$

in which P_{ij} and P are the turbulence energy production by the Reynolds stress $\overline{u'_i u'_j}$ and the total turbulence energy production, respectively, and C_1 and γ are the coefficients associated with the 'pressure-strain rate' closure model. Rodi [1976] further showed that for the Reynolds stress $\overline{u'v'}$ in shear layers, combination of equations (3.16), (3.20) and (3.61) yields

$$C_\mu = \frac{2}{3}\frac{1-\gamma}{\gamma}\left[1 - \frac{1}{C_1}\left(1 - \gamma\frac{P}{\varepsilon}\right)\right]\Big/\left[1 + \frac{1}{C_1}\left(\frac{P}{\varepsilon} - 1\right)\right]^2 \qquad (3.62)$$

which exhibits a dependence of C_μ on the ratio P/ε. Furthermore, since in general P_{ij} differs for different components of $\overline{u_i' u_j'}$, C_μ is anisotropic. In the present study, due to the non-stationary and complex nature of the flow, an invariably dominant Reynolds stress component, for which equation (3.62) can be used to obtain an appropriate C_μ, does not exist. Therefore, in spite of its drawbacks, a constant $C_\mu = 0.09$ is used.

3.5 GENERAL TRANSPORT EQUATION

The differential equations for momentum, stagnation enthalpy, turbulence energy and dissipation rate are similar in structure and can all be expressed in terms of the following general transport equation for an entity Φ (note that hereafter the averaging overbars are omitted for convenience).

$$\frac{\partial}{\partial t}(\rho\,\Phi) + \frac{\partial}{\partial x_j}(\rho\,U_j\,\Phi) = \frac{\partial}{\partial x_j}\left(\Gamma_\Phi\frac{\partial\Phi}{\partial x_j}\right) + S_\Phi \qquad (3.63)$$

where the diffusion coefficient Γ_Φ and the source term S_Φ for individual variables are given in Table 3.3. This representation is exploited in Chapter 4 to simplify the presentation of the solution procedure for the equations.

Equation (3.63) is now recast into cylindrical-polar coordinates (r,z,θ) which are more suitable for generally cylindrical combustion chambers to which the model will be applied:

$$\frac{\partial}{\partial t}(\rho\,\Phi) + \frac{\partial}{\partial z}(\rho\,U\,\Phi) + \frac{1}{r}\frac{\partial}{\partial r}(r\,\rho\,V\,\Phi) + \frac{1}{r}\frac{\partial}{\partial\theta}(\rho\,W\,\Phi)$$
$$= \frac{\partial}{\partial z}\left(\Gamma_\Phi\frac{\partial\Phi}{\partial z}\right) + \frac{1}{r}\frac{\partial}{\partial r}\left(r\,\Gamma_\Phi\frac{\partial\Phi}{\partial r}\right) + \frac{1}{r}\frac{\partial}{\partial\theta}\left(\frac{\Gamma_\Phi}{r}\frac{\partial\Phi}{\partial\theta}\right) + S_{\Phi(r,z,\theta)} \qquad (3.64)$$

Here, U, V and W are the axial, radial and circumferential (tangential) velocity components, respectively, and $S_{\Phi(r,z,\theta)}$ is the transformed S_Φ. The continuity equation can be derived directly from equation (3.14), or obtained from equation (3.64) by setting $\Phi = 1$ and the right hand side of the equation to zero, thus

$$\frac{\partial}{\partial t}(\rho) + \frac{\partial}{\partial z}(\rho\,U) + \frac{1}{r}\frac{\partial}{\partial r}(r\,\rho\,V) + \frac{1}{r}\frac{\partial}{\partial\theta}(\rho\,W) = 0 \qquad (3.65)$$

Attention hereafter is restricted to axisymmetric problems addressed in this study, for which $\partial/\partial\theta = 0$. In these circumstances, the continuity, equation (3.65), and the general transport equation (3.64) reduce to

$$\frac{\partial}{\partial t}(\rho) + \frac{\partial}{\partial z}(\rho U) + \frac{1}{r}\frac{\partial}{\partial r}(r \rho V) = 0 \qquad (3.66)$$

$$\frac{\partial}{\partial t}(\rho \Phi) + \frac{\partial}{\partial z}(\rho U \Phi) + \frac{1}{r}\frac{\partial}{\partial r}(r \rho V \Phi)$$

$$= \frac{\partial}{\partial z}\left(\Gamma_\Phi \frac{\partial \Phi}{\partial z}\right) + \frac{1}{r}\frac{\partial}{\partial r}\left(r \Gamma_\Phi \frac{\partial \Phi}{\partial r}\right) + S_{\Phi(r,z)} \qquad (3.67)$$

The definitions of the diffusion coefficient Γ_Φ and the source term $S_{\Phi(r,z)}$ in the above, corresponding to individual variables, are given in Table 3.4.

3.6 BOUNDARY CONDITIONS

The complete description of a particular engine in mathematical terms requires specification of initial conditions and the conditions at boundaries, for all variables. The former are only of influence during the transient period and the latter determine the cyclically repeating solutions (of the governing equations) that characterise the steady operating state. The boundary conditions can be grouped as conditions at the solid walls; at the symmetry axis; and at the planes of inlet and exhaust apertures.

3.6.1 Wall Boundary Conditions

In turbulent flows, the near wall region is distinguished by (i) steep non-linear gradients of the flow variables; (ii) the prominent influence of molecular viscosity on the production, diffusion and dissipation of turbulent energy (Tennekes & Lumley [1980]); and (iii) anisotropy of the turbulence and other modifications to its structure due to the presence of the wall (see, for example, Reynolds [1974], Tennekes & Lumley [1980]). Therefore, within the framework of the present method, the near wall region could be treated according to either of the following approaches:

(I) by modifying the turbulence model to allow for the low Reynolds number effects (Jones & Launder [1973]) and using sufficiently fine grids to accurately evaluate the steep gradients in this region;

(II) by using 'wall-functions' that describe the (supposed) near-universal characteristics of the flow near the wall and to

'bridge' this region (see, for example, Launder & Spalding [1972,1974]).

The use of the former approach is generally computationally unviable in the context of elliptic flow calculations. Therefore, in the present study, the latter approach is adopted.

According to the 'wall-function' method, the flow conditions in the interior, fully turbulent region are linked to the conditions at the wall, through semi-empirical relations derived from experimental data and Couette flow analyses of the wall region (see, for example, Patankar & Spalding [1970], Launder & Spalding [1972]). These relations give the variations of the flow and turbulence quantities across the wall-layer as functions of the dimensionless distance y^+ from the wall (which can also be interpreted as a local Reynolds number), defined as follows:

$$y^+ = \frac{\rho U_\tau Y}{\mu} \tag{3.68}$$

where Y is the normal distance from the wall and the 'friction velocity' U_τ is defined as:

$$U_\tau = \sqrt{\frac{\tau_w}{\rho}} \tag{3.69}$$

in which τ_w is the wall shear stress.

It should be remarked that the validity of these relations for the unsteady, recirculating and strongly curved flows occurring in engines is open to question and their application can only be justified on the grounds of absence of an alternative. For example, the study of Gibson, et al. [1981b] of the effect of some of these complexities on the wall heat transfer behaviour indicates that they may have considerable impact.

In the fully turbulent, inertial sublayer region (defined as $y^+ \geq 11.63$), the Couette flow velocity variation is described by the logarithmic 'law of the wall' as (Schlichting [1968], Tennekes & Lumley [1980])

$$\underline{U} = \frac{U_\tau}{\kappa} \log_e (E\, y^+) \tag{3.70}$$

where κ (= 0.4187) and E (= 9.793) are constants.

The (uniform) shear stress in the wall layer is given by

$$\tau_w \simeq \tau = \mu_T \frac{d\underline{U}}{dy} \tag{3.71}$$

In this region, turbulence is in local equilibrium (i.e. $P \simeq \rho \varepsilon$) and the

turbulence energy transport equation reduces to

$$\mu_T \left(\frac{dU}{dy}\right)^2 = \rho \varepsilon \tag{3.72}$$

The above relations, along with the turbulence model equation (3.20), yield (see, for example, Ideriah [1977] and Johns [1980] for details)

$$\tau_w = C_\mu^{\frac{1}{2}} \rho k = \rho U_\tau^2 = \frac{\rho \kappa C_\mu^{\frac{1}{4}} k^{\frac{1}{2}} U}{\log_e (E y^+)} \tag{3.73}$$

It also follows that substitution of U_τ from equation (3.73) in equation (3.68) gives the following alternative expression for y^+:

$$y^+ = \frac{\rho C_\mu^{\frac{1}{4}} k^{\frac{1}{2}} y}{\mu} \tag{3.74}$$

The dissipation rate in the wall-layer is obtained by combining equation (3.20) with equations (3.71) and (3.70) to give

$$\varepsilon = \frac{C_\mu \rho k^2}{\kappa y} \frac{U_\tau}{\tau_w} \tag{3.75}$$

Substituting for U_τ and τ_w from equations (3.70) and (3.73) gives

$$\varepsilon = \frac{C_\mu^{3/4} k^{3/2}}{\kappa y} \tag{3.76}$$

The wall function for the heat flux across the inertial sublayer ($y^+ \geq 11.63$) employed in this study is due to Jayatillaka [1969] and has the form

$$\dot{q}_w = \frac{\mu y^+}{\sigma_{h,T}} \left[\frac{1}{\kappa} \log_e (E y^+) + P_{\sigma_h}\right]^{-1} \frac{dT_w}{dy} \tag{3.77}$$

with P_{σ_h} defined as

$$P_{\sigma_h} = 9.0 \left(\frac{\sigma_h}{\sigma_{h,T}} - 1\right) \left(\frac{\sigma_h}{\sigma_{h,T}}\right)^{-\frac{1}{4}} \tag{3.78}$$

Here, T_w is the wall temperature, and σ_h and $\sigma_{h,T}$ are the laminar and turbulent Prandtl numbers, respectively.

In the viscous sublayer region ($y^+ < 11.63$), the wall shear stress is given by (see Tennekes & Lumley [1980])

$$\tau_w = \mu \frac{dU}{dy} \tag{3.79}$$

and the heat transfer rate is obtained from

$$\dot{q}_w = \frac{\mu}{\sigma_h} \frac{dT_w}{dy} \tag{3.80}$$

In practical engine circumstances, the wall temperature and heat flux are time- and location-dependent and oscillate during the engine cycle. However, these transient temperature variations are damped by the thermal inertia of the cylinder (Sitkei [1974], Watkins [1977]) and are usually small compared with the gas-to-wall temperature difference. Therefore, insofar as the in-cylinder processes are concerned, the wall temperature can be assumed as steady.

3.6.2 Symmetry Axis

At the axis of symmetry, the radial velocity component and the gradients of all other dependent variables in the radial direction are equal to zero.

3.6.3 Planes of Inlet and Exhaust Apertures

In order to simulate the complete four stroke engine cycle, a treatment is required for the intake and exhaust processes. This requires considerable care, in view of the complexity of the valve flow characteristics and their influence on the engine breathing capacity and the in-cylinder flow structure, as reviewed earlier in Chapter 2. Therefore, a procedure is needed that incorporates both generality, allowing a wide range of application, and the important characteristics of the valve flow.

An appropriate procedure could be the extension of the solution domain through the valve opening and into the inlet port. However, the complicated port/valve assembly geometry would require the use of non-orthogonal grids and a substantial number of additional mesh points, rendering the method computationally complex and expensive. The only viable alternative is to employ the well-established orifice-type analysis for the mass flow rate that is generally used for the engine cycle simulation (e.g. Streit & Borman [1971], Watson & Janota [1982]) and utilise whatever knowledge is available of the details of the valve flow characteristics to define the boundary conditions. This is the approach adopted in this study. It is similar to those hitherto used with the present method (Watkins [1977], Johns [1980]), except that more consideration is given to the detailed specification of the inflow characteristics.

(i) Mass flow rate: The orifice equations employed are as follows:

(I) For subsonic flows, with

$$\frac{P_d}{P_u} > \left(\frac{2}{\gamma+1}\right)^{\gamma/\gamma-1} \tag{3.81}$$

the mass flow rate is

$$\dot{m} = C_D A_M \rho_u \sqrt{\gamma R_g T_u} \sqrt{\frac{2}{(\gamma-1)} \left(\frac{P_d}{P_u}\right)^{2/\gamma} \left[1 - \left(\frac{P_d}{P_u}\right)^{\gamma-1/\gamma}\right]} \tag{3.82}$$

(II) For sonic flow, with

$$\frac{P_d}{P_u} \leq \left(\frac{2}{\gamma+1}\right)^{\gamma/\gamma-1} \tag{3.83}$$

$$\dot{m} = C_D A_M \rho_u \sqrt{\gamma R_g T_u} \sqrt{\left(\frac{2}{\gamma+1}\right)^{\gamma+1/\gamma-1}} \tag{3.84}$$

Here, $\dot{m}$ is the mass flow rate through the valve; A_M is the minimum (throat) valve area given by relations (2.36) as a function of valve lift; C_D is the valve discharge coefficient (corresponding to the area A_M); P and T are pressure and temperature, respectively; and the subscripts u and d denote upstream and downstream values (e.g. during intake, u and d denote manifold and cylinder values, respectively).

The review of experimental data presented earlier in Chapter 2 (Section 2.2.5.1) revealed that C_D is in general a function of the geometry of the port/valve assembly, the valve lift and the pressure drop across the valve; although it becomes insensitive to pressure drop when the latter becomes large. In the present study, C_D is obtained from the following relations, derived by fitting the experimental data of Bicen [1983] for the engine being simulated, in a piece-wise-linear fashion.

$$\begin{aligned}
C_D &= 0.93 + 2.6923\ L/D && \text{for} && L/D < 0.052 \\
C_D &= 1.07 - 0.8623\ (L/D - 0.052) && \text{for} && 0.052 \leq L/D < 0.113 \\
C_D &= 1.0174 + 0.9494\ (L/D - 0.113) && \text{for} && 0.113 \leq L/D < 0.2 \\
C_D &= 1.1 - 1.7\ (L/D - 0.2) && \text{for} && 0.2 \leq L/D
\end{aligned} \tag{3.85}$$

Here, D is the valve diameter and L is the instantaneous valve lift. In the case of engine simulation studies that were performed prior to the

above data becoming available, the discharge coefficient C_D was obtained from the experimental data of Kastner, et al. [1963-64] in a similar fashion. For this case, the C_D~lift relations are

$$\begin{aligned} C_D &= 1.0 - L/D && \text{for} && L/D \leqslant 0.15 \\ C_D &= 1.1875 - 2.25\ L/D && \text{for} && 0.15 < L/D \leqslant 0.27 \\ C_D &= 0.37 + 0.77\ L/D && \text{for} && 0.27 < L/D \end{aligned} \qquad (3.86)$$

In both cases, the effect of the pressure difference across the valve, which is negligibly small compared with that of the lift, is ignored.

(ii) Inlet velocity: The profile and angle of entry of the flow at the exit plane of valve are not in general known and, as the review of the experimental data in Chapter 2 (Section 2.2.5.1) showed, they depend on such factors as the valve geometry and lift, and vary according to the mode of the flow (characterised by the formation of regions of flow reversal due to flow separation in the seat passage). In the present study, whenever detailed data were not available, a plug flow distribution was considered and the exit velocity (normal to the plane of the valve aperture) was obtained from

$$U_{in} = \frac{\dot{m}}{2\pi\ D\ L} \qquad (3.87)$$

The measurements of Bicen [1983] indicate that apart from in regions of separated flow*, this is a reasonable assumption; however, the effect of reduction in the flow area must be taken into consideration. The practice thus adopted is to base the exit (normal) velocity calculation on the peripheral outflow area of the valve:

$$U_{in} = \frac{\dot{m}}{2\pi\ D\ (L - Z_{sep})} \qquad (3.88)$$

where Z_{sep} is the width of the reverse flow region at the valve exit plane (Figure 3.1). The width of the reverse flow region Z_{sep} for the engine being simulated is derived from the experiments of Bicen [1983] as

$$\begin{aligned} Z_{sep} &= 0.62 \text{ mm} && \text{for } 0.113 < L/D \leqslant 0.117 \\ Z_{sep} &= 1.86 \text{ mm} && \text{for } 0.117 < L/D \end{aligned} \qquad (3.89)$$

---

* The engine being simulated has a medium 'maximum valve lift', in which case flow separation only occurs at the valve head (see Section 2.2.5.1).

The axial velocity component at the valve exit is obtained from the following relation, assuming that flow enters the cylinder at the valve seat angle, as

$$U = U_{in} \tan \psi \tag{3.90}$$

The measurements of Vafidis & Whitelaw [1984] show that this assumption is valid only for small valve lifts: for larger values and in particular when flow separation occurs at the valve exit, the exit angle deviates from the seat angle. Because this information has only recently become available, it is not accounted for in the present study.

(iii) Turbulence parameters: Concerning the turbulence parameters k and ε, for which no detailed measurements are available, the boundary conditions are estimated from the pipe flow data of Reynolds [1974] and the Prandtl mixing length relation for plane jets (Launder & Spalding [1972]), as

$$\begin{aligned} k &= 0.01\, U_{in}^2 \\ \varepsilon &= \frac{C_\mu^{3/4}\, k^{3/2}}{0.045\, L} \end{aligned} \tag{3.91}$$

where L is the instantaneous valve lift and U_{in} is the inlet/exhaust velocity. The validity of these relations is open to question. The measurements of Bicen [1983] and Vafidis & Whitelaw [1984] show that the flow separation and the transient effects due to the piston motion both increase the turbulence intensity at the valve exit. However, the measurements of Vafidis & Whitelaw [1984] show that turbulence is mainly generated in the shear layers of the jet-like flow downstream of the valve and the level of turbulence intensity at the exit plane of the valve is negligible compared with the levels downstream. The calculations show the same feature and also indicate that the downstream turbulence levels are rather insensitive to substantial changes (e.g. an increase of 200% in k) in these boundary conditions.

(iv) Stagnation enthalpy: The boundary condition for the enthalpy equation is a prescribed (ambient) uniform inlet temperature.

3.7 CLOSURE

In this chapter, the differential equations that govern the turbulent in-cylinder flow processes are derived in density-weighted ensemble-averaged terms, suitable for application to the compressible and non-

stationary flows occurring in engines. The turbulent diffusional fluxes are obtained with the aid of the k-ε model of turbulence, for which the additional k- and ε-transport equations, in the form suitable for engine applications, are derived. Three variants of the ε-transport are selected for later application and evaluation. Also, the effect of strong compressibility on turbulence, and consequences with regard to the selected model, are discussed.

The governing equations are cast into a general differential equation and then expressed in cylindrical-polar coordinates suitable for application to cylinder geometry.

The boundary conditions for in-cylinder flow calculations, in particular the treatments of the solid boundaries and inlet/exhaust valves, are discussed.

CHAPTER 4
THE NUMERICAL SOLUTION METHOD

4.1 INTRODUCTION

This chapter describes the numerical procedure employed for solving the differential conservation/transport equations of mass, momentum, etc., derived in the preceding chapter, within a time-dependent solution domain.

Section 4.2 describes the method for confining the solution domain to the instantaneous cylinder volume, irrespective of the piston position, by introducing a flexible coordinate frame that moves in a manner determined by the piston and the valve motions.

Section 4.3 contains the derivation of the discretised equations. The 'finite-volume' method is used, involving a combination of formal integration of the differential equations over discrete computational 'cells' and time, and the introduction of spatial and temporal differencing approximations.

The procedure that links the continuity, momentum and enthalpy equations in order to obtain the pressure field is described in Section 4.4.

Section 4.5 deals with the implementation of the boundary conditions. Finally, Section 4.6 outlines the algorithm for solving the finite-difference equations.

4.2 TRANSFORMATION TO MOVING COORDINATE FRAME

4.2.1 The Transformation Relations

The transport equations of the preceding chapter are for an Eulerian coordinate frame. Here, following the approach devised by Watkins [1973] and adopted by almost all engine researchers (for example, Diwakar, et al. [1976], Watkins [1977], Johns [1980], Ramos, et al. [1981]), these equations are transformed into a Lagrangian-Eulerian coordinate frame that contracts and expands in accord with the motion of the moving boundaries (e.g. the piston and the inlet/exhaust valves). This, in effect, confines the solution domain to the instantaneous cylinder volume, irrespective of the piston and the valve motions.

The transformation is achieved by replacing the coordinate set (r,z,t) with the set (r,ξ,t), in which

$$\xi \equiv f(z,t) \tag{4.1}$$

is the new axial coordinate system. The definition of ξ depends on the chamber geometry considered, as illustrated in the following.

For the case of protruding valve geometry, simulated in the present study, two cases are distinguished and treated differently. These are:

(i) The low compression ratio case(s), for which the clearance gap at the top dead centre (TDC) of induction z_{TDC} is larger than the maximum valve lift L_{max} ($z_{TDC} > L_{max}$).
(ii) The high compression ratio case(s), for which $z_{TDC} \leq L_{max}$.

In the former case, the solution domain is divided into three distinct regions, as shown in Figure 4.1, namely:

Region I; confined between the cylinder head and the valve face, that contracts and expands with the valve movement. In this region, ξ is defined as

$$\xi = \frac{z}{z_v(t)} \qquad \text{for } 0 \leq z \leq z_v(t) \tag{4.2}$$

where $z_v(t)$ is the instantaneous distance of the valve face from the cylinder head ($z_v(t) \equiv$ valve lift L). Differentiation of this expression with respect to time gives the coordinate frame velocity as

$$\frac{d\xi}{dt} = -\frac{\xi}{z_v(t)} \frac{dz_v(t)}{dt} \qquad \text{for } 0 \leq z \leq z_v(t) \tag{4.3}$$

This gives the velocity of the contracting/expanding computational grid in the Eulerian coordinate frame u_G (see Figure 4.3 and also Section 4.3) as:

$$u_G = \xi \frac{dz_v(t)}{dt} \qquad \text{for } 0 \leq z \leq z_v(t) \tag{4.4}$$

Region II; is bounded by the valve face and a 'stationary arbitrary plane' z_o (see Figure 4.1) which is positioned such that $L_{max} < z_o < z_{TDC}$. This arrangement allows easy control of the grid distribution in the vicinity of the valve. The appropriate expressions for ξ and u_G are

$$\begin{aligned} \xi &= \frac{z - z_v(t)}{z_o - z_v(t)} && \text{for } z_v(t) < z \leq z_o \\ u_G &= (1 - \xi) \frac{dz_v(t)}{dt} && \text{for } z_v(t) < z \leq z_o \end{aligned} \tag{4.5}$$

Region III; confined between the 'arbitrary plane' z_o and the piston face $z_p(t)$ (see Figure 4.1) that contracts and expands with the piston motion. For this region,

$$\begin{aligned} \xi &= \frac{z - z_o}{z_p(t) - z_o} \qquad \text{for } z_o < z \leqslant z_p(t) \\ u_G &= \xi \frac{dz_p(t)}{dt} \qquad \text{for } z_o < z \leqslant z_p(t) \end{aligned} \tag{4.6}$$

The above arrangement cannot be applied to high compression ratio engines (Case (ii)), since a stationary arbitrary plane cannot be found such that $L_{max} < z_o < z_{TDC}$. In this case, the arbitrary plane z_o is discarded and, as shown in Figure 4.2, the solution domain is divided into two regions, viz.:

Region I; confined between the cylinder head and the valve face, as for Region I in Case (i), for which ξ and u_G are defined by equations (4.2) and (4.4).

Region II; confined between the valve face and the piston, which contracts and expands in accord with the relative motion between these two. For this region, ξ and u_G are defined by:

$$\begin{aligned} \xi &= \frac{z - z_v(t)}{z_p(t) - z_v(t)} \qquad \text{for } z_v(t) < z \leqslant z_p(t) \\ u_G &= (1 - \xi) \frac{dz_v(t)}{dt} + \xi \frac{dz_p(t)}{dt} \end{aligned} \tag{4.7}$$

The comparison of equations (4.2) to (4.7) shows that all the foregoing relations can be derived from the following general expression for ξ, and the corresponding relations for the coordinate frame and the grid velocities.

$$\begin{aligned} \xi &= \frac{z - z_o(t)}{z_1(t) - z_o(t)} \qquad \text{for } z_o(t) \leqslant z \leqslant z_1(t) \\ \frac{d\xi}{dt} &= -\frac{(1 - \xi)}{z_1(t) - z_o(t)} \frac{dz_o(t)}{dt} - \frac{\xi}{z_1(t) - z_o(t)} \frac{dz_1(t)}{dt} \\ u_G &= (1 - \xi) \frac{dz_o(t)}{dt} + \xi \frac{dz_1(t)}{dt} \end{aligned} \tag{4.8}$$

Here, $z_o(t)$ and $z_1(t)$ are the instantaneous distances, from the cylinder

head (the origin of the Eulerian coordinate frame), of the boundaries of the region of interest.

4.2.2 Transformed General Transport Equation

The transformed general transport equation is derived following Watkins [1977] and Johns [1980], by obtaining the transformation formulae for the derivatives $\partial/\partial r$, $\partial/\partial z$ and $\partial/\partial t$ between the two coordinate systems. Employing the general transformation equation (4.8), these are obtained as

$$\begin{aligned}
&\frac{\partial \phi}{\partial r} \rightarrow \frac{\partial \phi}{\partial r} \\
&\frac{\partial \phi}{\partial z} \rightarrow \frac{\partial \phi}{\partial \xi}\frac{\partial \xi}{dz} = \frac{1}{z_1(t) - z_0(t)}\frac{\partial \phi}{\partial \xi} \\
&\frac{\partial \phi}{\partial t} \rightarrow \frac{\partial \phi}{\partial t} + \frac{\partial \phi}{\partial \xi}\frac{\partial \xi}{dt} \\
&\quad = \frac{\partial \phi}{\partial t} - \left[\frac{(1-\xi)}{z_1(t) - z_0(t)}\frac{dz_0(t)}{dt} + \frac{\xi}{z_1(t) - z_0(t)}\frac{dz_1(t)}{dt}\right]\frac{\partial \phi}{\partial \xi}
\end{aligned} \tag{4.9}$$

Substitution of the above in the general transport equation (3.67), after some manipulation, renders

$$\begin{aligned}
&\frac{1}{z_H}\frac{\partial}{\partial t}(z_H \rho \phi) + \frac{1}{z_H}\frac{\partial}{\partial \xi}(\rho \hat{U} \phi) + \frac{1}{r}\frac{\partial}{\partial r}(r \rho V \phi) \\
&= \frac{1}{z_H}\frac{\partial}{\partial \xi}\left(\frac{\Gamma_\phi}{z_H}\frac{\partial \phi}{\partial \xi}\right) + \frac{1}{r}\frac{\partial}{\partial r}\left(r \Gamma_\phi \frac{\partial \phi}{\partial r}\right) + S_{\phi(r,\xi)}
\end{aligned} \tag{4.10}$$

in which

$$\begin{aligned}
z_H &= z_1(t) - z_0(t) \\
\hat{U} &= U - U_G = U - \left[(1-\xi)\frac{dz_0(t)}{dt} + \xi\frac{dz_1(t)}{dt}\right]
\end{aligned} \tag{4.11}$$

Thus, $\hat{U}$ is the local axial velocity of the fluid relative to the grid. The expressions for the transformed source terms $S_{\phi(r,\xi)}$ for the individual variables are given in Table 4.1.

4.3 THE METHOD OF DISCRETISATION

An overview of the discretisation methods for the numerical solution of the fluid flow problems is given by Lai [1983]. In the present study, the 'finite-volume' approach, as described by Gosman, et al. [1969] and others, is adopted. In this approach, macroscopic conservation/transport equations are derived through integration of the differential equations over a finite-volume, and are then expressed in an algebraic form. The discretised equations thus represent the conservation principles for the

selected volumes.

In accordance with this approach, the combustion chamber is here divided into a finite number of contiguous discrete volumes or 'cells' by a computational grid. The selected grid, which consists of arbitrarily-spaced planes of constant ξ and r, is shown in Figure 4.3.

4.3.1 Derivation of the General Difference Equation

Figure 4.4 illustrates a portion of the computational grid. Following Johns [1980], all scalar quantities (including pressure, density, viscosity, enthalpy, k and ε) and angular velocity are located at the centre of the cells (denoted in Figure 4.4 by capitals *PNSEW*, etc.). Following the well-established practice of 'staggered' variable arrangement (see, for example, Caretto, et al. [1972], Patankar [1980]), the axial and radial velocities, designated by arrows, are displaced to lie on the cell boundaries (denoted by *nsew*, etc.). The main advantage of this arrangement is to avoid decoupling of the adjacent velocities and pressures (Patankar [1980]); further benefits are that (i) the velocities are in a convenient position to calculate the convective fluxes of scalar variables, and (ii) evaluation of the pressure gradient terms in the momentum equations is straightforward.

The numerical values of the dependent variables are calculated at the centre of their respective control volumes. These, for the scalar variables and the axial and radial velocities (which have their separate control volumes), are shown in Figure 4.4. These volumes are formed by rotating the areas shown through unit angle about the axis of symmetry.

The discretised transport equations are derived by integrating the differential equations over the appropriate control volume and over a finite increment of time δt, and applying Gauss's Divergence theorem. By way of illustration, the integration of the general transport equation (4.8), for the entity ϕ located at P (Figure 4.4), gives:

$$\frac{1}{\delta t}\int_{t}^{t+\delta t}\Big\{\underbrace{\int_{V_P}\rho\,\phi\,dV}_{\text{I}}+\underbrace{\int_{r_s}^{r_n}\Big[\rho\,\hat{U}\,\phi-\frac{\Gamma_\phi}{z_H}\frac{\partial\phi}{\partial\xi}\Big]_{\xi_w}^{\xi_e} r\,dV}_{\text{II}}$$

$$+\underbrace{\int_{\xi_w}^{\xi_e}\Big[r\,\rho\,V\,\phi-r\,\Gamma_\phi\frac{\partial\phi}{\partial r}\Big]_{r_s}^{r_n} z_H\,d\xi}_{\text{III}}-\underbrace{\int_{V_P} S_\phi\,dV}_{\text{IV}}\Big\}\,dt \;=\; 0 \qquad (4.12)$$

where

$$\int_{V_P} dV \equiv \int_{\xi_w}^{\xi_e} \int_{r_s}^{r_n} z_H \, r \, dr \, d\xi$$

and from relation (4.8)

$$z_H \, d\xi \equiv (z_1(t) - z_0(t)) \, d\xi = dz \tag{4.13}$$

The individual terms in equation (4.10) are then approximated, following Watkins [1977] as follows.

Term I is approximated, to the first order accuracy, by assuming that the values of variables at nodes represent average over the cells, as:

$$\frac{1}{\delta t} \int_t^{t+\delta t} \{ \int_{V_P} \rho \, \phi \, dV \} \, dt \simeq \frac{(\rho \, \phi)_P^n \, V_P^n - (\rho \, \phi)_P^o \, V_P^o}{\delta t} \tag{4.14}$$

where the superscripts n and o denote the 'new' and 'old' time levels, respectively, separated by the time interval δt.

Term II represents total convective and diffusive fluxes of ϕ across the cell faces nw-sw and ne-se in the axial direction. This term can be represented as

$$F_\xi = \int_{r_s}^{r_n} \left[\rho \, \hat{U} \, \phi - \frac{\Gamma_\phi}{z_H} \frac{\partial \phi}{\partial \xi} \right]_w^e r \, dr$$

$$= \left[(\rho \, \hat{U} \, \phi \, a)_e - (\frac{\Gamma_\phi \, a}{z_H} \frac{\partial \phi}{\partial \xi})_e \right] - \left[(\rho \, \hat{U} \, \phi \, a)_w - (\frac{\Gamma_\phi \, a}{z_H} \frac{\partial \phi}{\partial \xi})_w \right] \tag{4.15}$$

where the square-bracketed quantities are averages over the cell faces, and $a_e = a_w = (r_n^2 - r_s^2)/2$ are the cell boundary areas. If a linear variation of ϕ is assumed between the adjacent cell nodes W, P and E, the first-order differential terms may be approximated as:

$$(\frac{\partial \phi}{\partial \xi})_e \simeq \frac{\phi_E - \phi_P}{\xi_E - \xi_P} = \frac{\phi_E - \phi_P}{\delta \xi_{E-P}}$$

$$(\frac{\partial \phi}{\partial \xi})_w \simeq \frac{\phi_P - \phi_W}{\xi_P - \xi_W} = \frac{\phi_P - \phi_W}{\delta \xi_{P-W}} \tag{4.16}$$

Thus giving, when substituted into equation (4.15):

$$F_\xi = (\rho \hat{U} a)_e \left[\phi_e - \frac{\phi_E - \phi_P}{Pe_e}\right] - (\rho \hat{U} a)_w \left[\phi_w - \frac{\phi_P - \phi_W}{Pe_w}\right] \tag{4.17}$$

Here, Pe_e and Pe_w are cell-boundary Peclet numbers that measure the ratio of convective and diffusive fluxes and are defined as

$$\begin{aligned} Pe_e &= \frac{(\rho \hat{U})_e}{\Gamma_{\phi_e}/z_H \, \delta\xi_{E-P}} = \frac{(\rho \hat{U})_e}{\Gamma_{\phi_e}/\delta z_{E-P}} \\ Pe_w &= \frac{(\rho \hat{U})_w}{\Gamma_{\phi_w}/z_H \, \delta\xi_{P-W}} = \frac{(\rho \hat{U})_w}{\Gamma_{\phi_w}/\delta z_{P-W}} \end{aligned} \tag{4.18}$$

in which the values of ρ and Γ_ϕ at the cell boundaries e and w are evaluated, through linear interpolation, from their values at cell nodes W, P and E.

The cell-boundary values of ϕ (i.e. ϕ_e and ϕ_w) appearing in equation (4.17) are expressed in terms of nodal values as

$$\begin{aligned} \phi_e - \frac{\phi_E - \phi_P}{Pe_e} &= (1 - \alpha_e)\, \phi_E + \alpha_e \, \phi_P \\ \phi_w - \frac{\phi_P - \phi_W}{Pe_w} &= \alpha_w \, \phi_W + (1 - \alpha_w)\, \phi_P \end{aligned} \tag{4.19}$$

where the quantities α_e and α_w are spatial difference functions, whose evaluation will be discussed later.

The integration is completed through introduction of a temporal difference factor β ($0 \leq \beta \leq 1$), whose specification will be given later, so that the time-average F_ξ is evaluated as a weighted mean of 'old' and 'new' levels $F_\xi^{\,o}$ and $F_\xi^{\,n}$, respectively, thus:

$$\frac{1}{\delta t} \int_t^{t+\delta t} F_\xi \, dt \simeq \beta \, F_\xi^{\,n} + (1 - \beta)\, F_\xi^{\,o} \tag{4.20}$$

With the aid of the foregoing, the final expression for term II of equation (4.12) can be represented as:

$$\begin{aligned} &\frac{1}{\delta t} \int_t^{t+\delta t} \int_{r_s}^{r_n} \left[\rho \hat{U} \phi - \frac{\Gamma_\phi}{z_H} \frac{\partial \phi}{\partial \xi}\right]_{\xi_w}^{\xi_e} r \, dr \, dt \\ &\simeq \beta \left\{(\rho \hat{U} a)_e \left[(1 - \alpha_e)\, \phi_E + \alpha_e \, \phi_P\right] - (\rho \hat{U} a)_w \left[\alpha_w \phi_W + (1 - \alpha_w)\, \phi_P\right]\right\}^n \\ &+ (1-\beta) \left\{(\rho \hat{U} a)_e \left[(1-\alpha_e)\, \phi_E + \alpha_e \, \phi_P\right] - (\rho \hat{U} a)_w \left[\alpha_w \phi_W + (1-\alpha_w)\, \phi_P\right]\right\}^o \end{aligned} \tag{4.21}$$

where the superscripts n and o apply to all terms within the curly brackets.

Term III is treated in the same manner, giving

$$\frac{1}{\delta t}\int_{t}^{t+\delta t}\int_{\xi_w}^{\xi_e}\left[r\,\rho\,V\,\phi - r\,\Gamma_\phi\,\frac{\partial\phi}{\partial r}\right]_{r_s}^{r_n} z_H\,d\xi\,dt$$

$$\simeq \beta\left\{(\rho V a)_n\left[(1-\alpha_n)\,\phi_N + \alpha_n\,\phi_P\right] - (\rho V a)_s\left[\alpha_s\,\phi_S + (1-\alpha_s)\,\phi_P\right]\right\}^n$$

$$+ (1-\beta)\left\{(\rho V a)_n\left[(1-\alpha_n)\,\phi_N + \alpha_n\,\phi_P\right] - (\rho V a)_s\left[\alpha_s\,\phi_S + (1-\alpha_s)\,\phi_P\right]\right\}^o \qquad (4.22)$$

The form of the source term IV in equation (4.12) depends on the variable under consideration. It is represented at this stage as:

$$\frac{1}{\delta t}\int_{t}^{t+\delta t}\int_{V_P} S_\phi\,dV\,dt = S_P \qquad (4.23)$$

Substitution of the above approximations into equation (4.12) gives the general discretised equation as:

$$\frac{(\rho\,\phi)_P^n\,V_P^n - (\rho\,\phi)_P^o\,V_P^o}{\delta t}$$

$$+ \beta\left\{(\rho\,\hat{u}\,a)_e\left[(1-\alpha_e)\,\phi_E + \alpha_e\,\phi_P\right] - (\rho\,\hat{u}\,a)_w\left[\alpha_w\,\phi_W + (1-\alpha_w)\,\phi_P\right]\right\}^n$$

$$+ (1-\beta)\left\{(\rho\,\hat{u}\,a)_e\left[(1-\alpha_e)\,\phi_E + \alpha_e\,\phi_P\right] - (\rho\,\hat{u}\,a)_w\left[\alpha_w\,\phi_W + (1-\alpha_w)\,\phi_P\right]\right\}^o$$

$$+ \beta\left\{(\rho V a)_n\left[(1-\alpha_n)\,\phi_N + \alpha_n\,\phi_P\right] - (\rho V a)_s\left[\alpha_s\,\phi_S + (1-\alpha_s)\,\phi_P\right]\right\}^n$$

$$+ (1-\beta)\left\{(\rho V a)_n\left[(1-\alpha_n)\,\phi_N + \alpha_n\,\phi_P\right] - (\rho V a)_s\left[\alpha_s\,\phi_S + (1-\alpha_s)\,\phi_P\right]\right\}^o$$

$$- S_P = 0 \qquad (4.24)$$

The finite-volume mass conservation equation can be similarly derived as:

$$\frac{\rho_P^n\,V_P^n - \rho_P^o\,V_P^o}{\delta t} + \beta\left\{(\rho\,\hat{u}\,a)_e - (\rho\,\hat{u}\,a)_w + (\rho V a)_n - (\rho V a)_s\right\}^n$$

$$+ (1-\beta)\left\{(\rho\,\hat{u}\,a)_e - (\rho\,\hat{u}\,a)_w + (\rho V a)_n - (\rho V a)_s\right\}^o = 0 \qquad (4.25)$$

Subtraction of this equation, after multiplication by ϕ_P^n, from equation (4.24) yields the final form of the general transport equation as:

$$\frac{(\rho\ V)_P^o\ [\phi_P{}^n - \phi_P{}^o]}{\delta t}$$

$$+ \beta \{\dot{m}_e\ (1-\alpha_e)\ [\phi_E-\phi_P] - \dot{m}_w\ \alpha_w\ [\phi_W-\phi_P] + \dot{m}_n\ (1-\alpha_n)\ [\phi_N-\phi_P] - \dot{m}_s\ \alpha_s\ [\phi_S-\phi_P]\}^n$$

$$+ (1-\beta) \{\dot{m}_e\ (1-\alpha_e)\ [\phi_E-\phi_P] - \dot{m}_w\ \alpha_w\ [\phi_W-\phi_P] + \dot{m}_n\ (1-\alpha_n)\ [\phi_N-\phi_P] - \dot{m}_s\ \alpha_s\ [\phi_S-\phi_P]\}^o$$

$$- (1 - \beta)\ [\phi_P{}^n - \phi_P{}^o]\ \{\dot{m}_e - \dot{m}_w + \dot{m}_n - \dot{m}_s\}^o - S_P = 0 \qquad (4.26)$$

Here, $\dot{m}_e$, $\dot{m}_n$, etc., are the cell-boundary mass flow rates, which are defined in terms of nodal values of density as, for example:

$$\begin{aligned} \dot{m}_e &= [\delta_1\ \rho_P + (1 - \delta_1)\ \rho_E]\ a_e\ \hat{u}_e \\ \dot{m}_n &= [\delta_2\ \rho_P + (1 - \delta_2)\ \rho_N]\ a_n\ v_n \end{aligned} \qquad (4.27)$$

where δ_1 and δ_2 are linear interpolation factors:

$$\begin{aligned} \delta_1 &= \delta\xi_{E-e}/\delta\xi_{E-P} \\ \delta_2 &= \delta n_{N-n}/\delta n_{N-P} \end{aligned} \qquad (4.28)$$

Equation (4.26) can now be re-written in the following final compact form

$$A_P{}^n\ \phi_P{}^n = \sum_C A_C{}^n\ \phi_C{}^n + A_P{}^o\ \phi_P{}^o + \sum_C A_C{}^o\ (\phi_C{}^o - \phi_P{}^o) + S_\phi \qquad (4.29)$$

in which $\sum_C$ denotes summation over the surrounding points N, S, E, W, and the coefficients are defined as:

$$\begin{aligned} A_P{}^n &= \sum_C A_C{}^n + A_P{}^o \\ A_E{}^n &= \beta\ \dot{m}_e{}^n\ (\alpha_e{}^n - 1) \\ A_W{}^n &= \beta\ \dot{m}_w{}^n\ \alpha_w{}^n \\ A_N{}^n &= \beta\ \dot{m}_n{}^n\ (\alpha_n{}^n - 1) \\ A_S{}^n &= \beta\ \dot{m}_s{}^n\ \alpha_s{}^n \end{aligned} \qquad (4.30)$$

$$
\begin{aligned}
A_E^{\,o} &= (1-\beta)\,\dot{m}_e^{\,o}\,(\alpha_e^{\,o}-1)\\
A_W^{\,o} &= (1-\beta)\,\dot{m}_w^{\,o}\,\alpha_w^{\,o}\\
A_N^{\,o} &= (1-\beta)\,\dot{m}_n^{\,o}\,(\alpha_n^{\,o}-1)\\
A_S^{\,o} &= (1-\beta)\,\dot{m}_s^{\,o}\,\alpha_s^{\,o}\\
A_P^{\,o} &= \frac{\rho_P^{\,o}\,V_P^{\,o}}{\delta t} - (1-\beta)\sum_C \dot{m}_C^{\,o}
\end{aligned}
\qquad (4.30)
$$

4.3.2 Treatment of Momentum Equations

Equations (4.29) and (4.30) hold for all the dependent variables. However, for the particular case of the axial and radial velocities, the definitions of the terms in equation (4.29) slightly differ, since, as shown in Figure 4.4, the control volumes for these variables are displaced from the main-node cells. These special cases are detailed below.

(i) Axial velocity, $\hat{U}$: The labelling convention adopted here for the velocities is that they assume the label of the grid nodes at which they point. Thus, for the $\hat{U}_P$ velocity centred by the '*nww-n-s-sww*' control volume in Figure 4.4, the associated finite-volume equation is

$$
A_P^{\,n}\,\hat{U}_P^{\,n} = \sum_C A_C^{\,n}\,\hat{U}_C^{\,n} + A_P^{\,o}\,\hat{U}_P^{\,o} + \sum_C A_C^{\,o}\,(\hat{U}_C^{\,o}-\hat{U}_P^{\,o}) + S_P \qquad (4.31)
$$

where $A_P^{\,n}$, $A_C^{\,n}$'s, $A_C^{\,o}$'s and $A_P^{\,o}$ are defined by equations (4.30), but the cell-boundary mass flow rates appearing in these coefficients are now given by:

$$
\dot{m}_e = \rho_P\, a_{n-s}\left(\frac{\hat{U}_P+\hat{U}_E}{2}\right) \qquad (4.32)
$$

$$
\dot{m}_n = [\delta_2\,\rho_P + (1-\delta_2)\,\rho_N]\,a_{n-nw}\,V_N + [\delta_2\,\rho_W + (1-\delta_2)\,\rho_{NW}]\,a_{nw-nww}\,V_{NW}
$$

in which $\delta_2 = \delta r_{N-n}/\delta r_{N-P}$. Similar definitions apply to $\dot{m}_w$ and $\dot{m}_s$.

The associated cell-boundary (in this case) Reynolds numbers are defined as:

$$Re_e = \frac{\rho_P \, (\hat{U}_P + \hat{U}_E)/2}{\mu_P / z_H \; \delta\xi_{e-w}}$$

$$Re_n = \frac{\rho_{nw} \, V_{nw}}{\mu_{nw} / \delta r_{N-P}} \qquad (4.33)$$

etc., where

$$\rho_{nw} = \delta_1 \, [\delta_2 \, \rho_W + (1 - \delta_2) \, \rho_{NW}] + (1 - \delta_1) \, [\delta_2 \, \rho_P + (1 - \delta_2) \, \rho_N]$$

$$\mu_{nw} = \delta_1 \, [\delta_2 \, \mu_W + (1 - \delta_2) \, \mu_{NW}] + (1 - \delta_1) \, [\delta_2 \, \mu_P + (1 - \delta_2) \, \mu_N] \qquad (4.34)$$

$$V_{nw} = \delta_1 \, V_{NW} + (1 - \delta_1) \, V_N$$

and

$$\delta_1 = \delta\xi_{p-w} / \delta\xi_{p-W}$$

Finally, the term $(\rho_P^{\,o} \, V_P^{\,o})/\delta t$ in the expression for $A_P^{\,o}$ is defined as the summation of the two overlapping scalar-cell values, i.e.

$$\frac{1}{2\delta t} \, (\rho_W^{\,o} \, V_W^{\,o} + \rho_P^{\,o} \, V_P^{\,o}) \qquad (4.35)$$

It must be noted that the absolute velocity U is required for evaluation of some of the source terms of the independent variables presented in Table 4.1. In such cases, U is obtained from the solution of equation (4.31) for the relative axial velocity $\hat{U}$, with the aid of equation (4.11).

(ii) Radial velocity: If the aforementioned labelling convention is adopted, then the finite-volume equation for the radial velocity V_P, surrounded by the control volume 'e-ss e-ss w-w' in Figure 4.4, is

$$A_P^{\,n} \, V_P^{\,n} = \sum_C A_C^{\,n} \, V_C^{\,n} + A_P^{\,o} \, V_P^{\,o} + \sum_C A_C^{\,o} \, (V_C^{\,o} - V_P^{\,o}) + S_P \qquad (4.36)$$

where $A_P^{\,n}$, $A_C^{\,n}$'s, $A_C^{\,o}$'s and $A_P^{\,o}$ are as defined in equation (4.30) with the following amendments. Firstly, the cell-boundary mass flow rates are now given by, for example:

$$\dot{m}_e = [\delta_1 \rho_P + (1-\delta_1)\rho_E]\, a_{e-se}\, \hat{U}_E + [\delta_1 \rho_S + (1-\delta_1)\rho_{SE}]\, a_{se-sse}\, \hat{U}_{SE}$$
$$\dot{m}_n = \rho_P\, a_{e-w}\, \left(\frac{V_N + V_P}{2}\right) \tag{4.37}$$

with $\delta_1 = \delta\xi_{E-e}/\delta\xi_{E-P}$. Secondly, the cell-boundary Reynolds numbers are defined as:

$$Re_e = \frac{\rho_{se}\, \hat{U}_{se}}{\mu_{se}/z_H\, \delta\xi_{E-P}}$$
$$Re_n = \frac{\rho_P\, (V_N + V_P)/2}{\mu_P/\delta n_{n-s}} \tag{4.38}$$

etc., where, for example

$$\rho_{se} = \delta_2\, [\delta_1 \rho_S + (1-\delta_1)\rho_{SE}] + (1-\delta_2)\, [\delta_1 \rho_P + (1-\delta_1)\rho_E] \tag{4.39}$$

with $\delta_2 = \delta n_{P-s}/\delta n_{P-S}$. Finally, the term $(\rho_P^{\,o} V_P^{\,o})/\delta t$ is evaluated as

$$\frac{1}{2\delta t}\, (\rho_S^{\,o} V_S^{\,o} + \rho_P^{\,o} V_P^{\,o}) \tag{4.40}$$

4.3.3 The Differencing Schemes

(i) Temporal differencing: The value of the temporal difference factor β, introduced in equation (4.20), determines the relative contributions of 'old' and 'new' time-level quantities in the finite-volume equations. The optimum value of β depends on factors such as the variations of F_ξ in time and space and the time-interval δt (Patankar & Baliga [1978]); however, in finite-difference methods the following three schemes are most commonly adopted (Patankar & Baliga [1978], Johns [1980]).

The explicit scheme assumes $\beta = 0$ (e.g. see Richtmyer & Morton [1967]); thus, the 'new' time-level values ϕ^n in equation (4.29) depend only on the 'old' time-level values (see equation (4.30)) and can be obtained by direct substitution. However, this scheme suffers from the well-known Courant-Friedrich-Lewy time-step restriction (Courant, et al. [1967]) that requires $\delta t \leqslant \Delta z/|U|$ (throughout the solution domain) for numerical stability. Therefore, its application to engine flows, involving regions of high local velocity, requires the use of excessively small time steps that render it computationally expensive (for example,

from the results presented in Chapter 5, it can be shown that in the region of the intake valve $\delta t \leqslant 0.07°$ CA).

The time-centred Crank-Nicolson [1947] scheme assumes $\beta = \frac{1}{2}$, i.e. a linear variation of the variable between the two time levels. This method, although unconditionally stable in the mathematical sense* (i.e. the error has a finite upper bound at all times and diminishes as the solution proceeds) and accurate for small time steps, for large steps produces erroneous, physically unrealistic oscillatory (i.e. unbounded) solutions whose amplitude increases with the size of δt (Patankar & Baliga [1978], Johns [1980]).

The fully-implicit scheme, which assumes $\beta = 1$ (Roache [1976]), is unconditionally stable and produces physically realistic (bounded) solutions, even for arbitrarily large time steps, although it is less accurate than the Crank-Nicolson scheme for small steps (Patankar & Baliga [1978]). Johns [1980] examined the relative merits of both schemes for engine flow calculations and concluded that for time-steps larger than $\delta t \simeq 1°$ CA, the implicit scheme is superior on the grounds of the unconditional 'boundedness' of the solution. A further advantage of this scheme is that choice of $\beta = 1$ removes all references to 'old' time-level coefficients in equations (4.29) and (4.30); thus, it is more efficient, especially in respect of computer storage.

The 'boundedness' of different schemes (i.e. not producing oscillatory, physically unrealistic solutions) can be ascertained through examination of the sign of the coefficients in equation (4.30). Sufficient condition for a 'bounded' solution is that all the coefficients should have the same (positive) sign (Lai [1983]). This constraint also forms part of the 'diagonal dominance' requirement for stability (convergence) of certain iterative solution schemes (Verga [1962]). It is evident that only $\beta = 1$ ensures the desired positivity of the coefficients; for $\beta < 1$, the coefficient A_P^o may become negative (which is why the Crank-Nicolson scheme may produce oscillatory solutions).

On the grounds of the foregoing considerations, the fully-implicit scheme ($\beta = 1$) is adopted for the present study.

(ii) Spatial differencing: The spatial difference function α introduced in equation (4.19) is a measure of the relative importance of the convection and diffusion processes as represented in the discretised

---

* Patankar & Baliga [1978] state that the condition for 'unconditional stability' is $\frac{1}{2} \leqslant \beta \leqslant 1$.

transport equation. The choice of α, in numerical schemes for the solution of fluid flow problems, is of great importance for it affects the accuracy and stability of the scheme.

The assumption of a piecewise linear variation of ϕ between adjacent cell nodes, when introduced into equation (4.19), yields:

$$\alpha = (\frac{1}{2} + \frac{1}{Pe}) \tag{4.41}$$

This 'central difference' formulation gives 'second order' accuracy by the well-known Taylor series truncation error analysis (see, for example, McGuirk, et al. [1981]). However, it has been shown that (Runchal [1976]) unless fine, probably uneconomical, computational meshes are used, the 'order' of a scheme is not a reliable indicator of its accuracy. In fact, numerous studies have shown that for $|Pe| > 2$, use of this formulation leads to erroneous unrealistic results (Spalding [1972]) or failure to obtain convergence (Runchal [1972]). This can be explained by the fact that for $|Pe| > 2$, the coefficients in equation (4.30) may become negative, undermining the 'boundedness' condition.

A method which does not suffer from this problem is the 'upwind' or 'donor-cell' differencing scheme (Courant, et al. [1952]) that assumes

$$\alpha = \begin{cases} 1 & Pe \geqslant 0 \\ 0 & Pe < 0 \end{cases} \tag{4.42}$$

Although this approach ensures 'boundedness' (and hence stability of the numerical scheme), it lacks, for $|Pe| < 2$, the accuracy of the 'central-difference' scheme.

The 'hybrid-difference' scheme proposed by Spalding [1972] incorporates the advantages of both schemes in the form

$$\alpha = \begin{cases} \frac{1}{2} + \frac{1}{Pe} & \text{for } |Pe| \leqslant 2 \\ 1 & \text{for } Pe > 2 \\ 0 & \text{for } Pe < -2 \end{cases} \tag{4.43}$$

This evidently reduces to, and gives the accuracy of, the 'central-difference' scheme for $|Pe| \leqslant 2$ and, by ensuring a positive and diagonally dominant matrix of coefficients by switching to the 'upwind' scheme for $|Pe| > 2$, gives unconditional boundedness and stability.

The hybrid-difference scheme produces accurate results for the

entire range of cell Pe if the flow is aligned with the computational grid (Patankar [1980]). However, in multi-dimensional flows, this condition is not, in general, possible to satisfy and where misalignment occurs, the hybrid scheme suffers from inaccuracies due to the so-called 'false' or 'numerical' diffusion (Patankar [1980]).

There has been misunderstanding with regard to the origin of 'false diffusion': some investigators (e.g. McGuirk, et al. [1981]) have associated it with the first order accuracy of upwind-differencing, but others (e.g. Patankar [1980]) have shown that it lies in the fact that interpolation is performed along the grid lines rather than streamlines. Several investigators (see, for example, Lai [1983]) have recognised this problem and proposed schemes for its remedy. These schemes extend the 'computational molecule' to a nine-point one, by incorporating values of ϕ at corner nodes NW, NE, SE and SW (Figure 4.4). However, Lai's [1983] survey of these schemes indicates that they generally suffer from possibility of negative coefficients, giving rise to instability or oscillatory unbounded solutions.

On the foregoing grounds, and the fact that the task of incorporation and testing of recent schemes is beyond the scope of the present study, the hybrid 'central/upwind' difference scheme is employed here.

4.3.4 Differencing of the Source Terms

The final stage in the assembly of the difference equations for the individual variables is the approximation of the source integral S_P, through the application of equation (4.23) to the individual source terms presented in Table 4.1

The general approach adopted here is to use the fully-implicit formulation $\beta = 1$ (with the exception of S_{h_s} whose treatment will be described) for the source integrals and to manipulate them into a linearised form as

$$S_P = S_I \, \phi_P^n + S_E \qquad (4.44)$$

where S_I and S_E, representing implicit and explicit dependence (where they exist) on ϕ, contain the negative and positive elements of the source term, respectively. S_I is then included into the coefficient A_P^n in equation (4.30). The purpose of this formulation is to further increase the diagonal dominance of the coefficients' matrix and thus promote stability (Watkins [1977], Johns [1980]).

The differencing of the source terms, with the exception of

that for h_s and the centrifugal component $(\rho W^2)/r$ in the V-momentum equation, is similar and therefore only a representative example, here for the $\hat{U}$-momentum equation, is considered. The special cases referred to above are explained thereafter.

(i) Axial momentum equation, $\hat{U}$: The integration of the source term for $\hat{U}_P$ (Table 4.1) over the control volume 'nww-n-s-sww' in Figure 4.4 yields, following the practice outlined above:

$$S_I = 0$$

$$\begin{aligned} S_E = {} & (P_W - P_P)\, a_{nw-sw} + \left\{\left[\left(\frac{\mu_T}{z_H}\frac{\partial U}{\partial \xi}\right)_P - \left(\frac{\mu_T}{z_H}\frac{\partial U}{\partial \xi}\right)_W\right]/z_H\ \delta\xi_{P-W}\right\}\ \delta V_w \\ & + \left\{\frac{1}{r_w}\left[\left(\frac{r\,\mu_T}{z_H}\frac{\partial V}{\partial \xi}\right)_{nw} - \left(\frac{r\,\mu_T}{z_H}\frac{\partial V}{\partial \xi}\right)_{sw}\right]/\delta r_{nw-sw}\right\}\ \delta V_w \qquad (4.45) \\ & - \left\{\frac{2}{3}\left[(\mu_T\, \nabla.\underline{U} + \rho\, k)_P - (\mu_T\, \nabla.\underline{U} + \rho\, k)_W\right]/z_H\ \delta\xi_{P-W}\right\}\ \delta V_w \\ & - A_P^{\,o}\,(U_G - U_G^{\,o})_w - A_E\,(U_{G_w} - U_{G_e}) - A_W\,(U_{G_w} - U_{G_{ww}}) \end{aligned}$$

Here, with the exception of $A_P^{\,o}$ and $U_G^{\,o}$, all variables relate to the 'new' time-level (the superscript n has been omitted for convenience); the coefficients A_P, A_E and A_W are given in equation (4.30); U_G is the grid velocity defined in equation (4.11) and δV_w is the 'new' time-level cell volume. The first order differentials in the above are approximated as, for example:

$$\left(\frac{1}{z_H}\frac{\partial U}{\partial \xi}\right)_P \simeq \frac{U_E - U_P}{(z_H\,\xi)_e - (z_H\,\xi)_w} = \frac{U_E - U_P}{\delta z_{e-w}} \qquad (4.46)$$

(ii) Radial momentum equation: The derivation of all components of the radial momentum source, with the exception of the centrifugal force term $(\rho W^2)/r$, is similar to the above. However, if the latter term is inserted explicitly into S_E, then for large values of swirl and/or small radii, it can become a dominant contributor to the local momentum balance, reducing the dependence on the surrounding values and causing numerical instability (Johns [1980]). Therefore, this term is linearised in an implicit fashion according to the method of Gosman, et al. [1976] as:

$$\frac{\rho W^2}{r}\left(1 + \frac{\delta}{W}\left(V^i + V^{i+1}\right)\right) \qquad (4.47)$$

in which δ is an under-relaxation factor with recommended value around $\simeq 0.3$ (Johns [1980]) and superscript i refers to the ith iteration level.

The V_p source term can thus be written as:

$$S_I = -2\frac{\mu_T}{r_s^2}\delta V_s - \frac{\delta}{W_s}\frac{\rho_s W_s^2}{r_s}\delta V_s$$
$$S_E = (P_S - P_P)\, a_{sw\text{-}se} + \left(1 + \frac{\delta V_P}{W_s}\right)\frac{\rho_s W_s^2}{r_s}\delta V_s + \text{other terms} \qquad (4.48)$$

where δV_s is the volume of the 'ssw-w-e-sse' control volume (Figure 4.4).

(iii) Stagnation enthalpy: The pressure-work term $\partial P/\partial t$ is of considerable importance in the engine flow circumstances, and its correct formulation is fundamental to the accurate calculation of the in-cylinder pressure and temperature (Watkins [1977], Johns [1980]). Watkins [1977] and Johns [1980] showed that a simple (temporal) central-difference formulation of this term would not correctly reproduce a reversible variation of the in-cylinder pressure and temperature for an adiabatic compression and expansion, and proposed semi-empirically determined formulations that satisfied this reversibility requirement. The formulation due to Johns [1980] is employed in the present study, and can be expressed as

$$S_I = 0$$
$$S_E = \left(\frac{P_P^n - P_P^o}{\delta t}\right)\left(\frac{\rho_P^o}{\rho_P^n}\right)^{\frac{1}{2}}\delta V_P^o \qquad (4.49)$$

where the superscripts o and n denote 'old' and 'new' time-levels.

4.4 PRESSURE CALCULATION

In the context of engine flows, the pressure variations are the consequence of two distinct processes, brought about by the piston motion: (i) the bulk pressure variation due to the cylinder volume change, and (ii) the spatial variations due to the fluid motion induced by the piston movement. Following the practice of Watkins [1977] and Johns [1980], a two-stage pressure calculation procedure, which first adjusts the global pressure and density in order to satisfy the overall continuity balance and then corrects the spatial pressure distribution to simultaneously satisfy the local continuity and momentum equations, is employed in the present study.

(i) Overall pressure adjustment procedure: Following Watkins [1977] and Johns [1980], this is derived by invoking the overall continuity balance (over the cylinder volume) as described below.

The prevailing fields of pressure and density, prior to adjustment, are denoted by the superscript '*' and the overall correction to be made to the pressure field is defined as P''. The associated correction to the density field is connected to P'' through the equation of state, thus

$$\rho = \rho^* + \left(\frac{\partial \rho}{\partial P}\right)^*_T P'' = \rho^* + \gamma^* P'' \qquad (4.50)$$

An equation for the overall mass conservation is obtained through summation of the discretised local continuity equation (4.25) over the entire solution domain. In fully-implicit form, it is

$$\sum_V \left(\frac{\rho_P^{\,n} V_P^{\,n} - \rho_P^{\,o} V_P^{\,o}}{\delta t}\right) + \sum_B \dot{m}_b^{\,n} = 0 \qquad (4.51)$$

where $\sum_V$ and $\sum_B$ denote summation over the volume and the boundaries of the solution domain, respectively (the inter-cell mass fluxes cancel out). Substitution of the corrected density field from equation (4.50) into equation (4.51) gives

$$\sum_V \frac{(\rho^* V^n)_P - (\rho^o V^o)_P}{\delta t} + P'' \sum_V \frac{(\gamma^* V^n)_P}{\delta t} + \sum_B \dot{m}_b^* + P'' \sum_B \gamma_A^* a_A U_A = 0 \qquad (4.52)$$

where a_A and U_A are the areas and velocities at the inlet/exhaust aperture, respectively. An expression for the overall pressure adjustment can be obtained from the above, thus:

$$P'' = \frac{-\left\{\sum_V \frac{(\rho^* V^n)_P - (\rho^o V^o)_P}{\delta t} + \sum_B \dot{m}_B^*\right\}}{\sum_V \frac{(\gamma^* V^n)_P}{\delta t} + \sum_B \gamma_A^* a_A U_A} \qquad (4.53)$$

The studies of Johns [1980] showed that a variant of this scheme, proposed by Watkins [1977], which provides for simultaneous adjustment of pressure and temperature by further invoking the overall energy conservation does not yield an improvement over this scheme.

(ii) Field pressure correction equation: Following the approach of Chorin [1968] and later workers (e.g. Caretto, et al. [1972], Patankar & Spalding [1972]), the pressure field is calculated according to a 'guess and correct' procedure, via relations derived by combining the discretised

continuity and momentum equations. The method is often referred to as the SIMPLE (Semi-Implicit Method for Pressure-Linked Equations) algorithm.

Following the work of Watkins [1977] and Johns [1980], the pressure correction equation is derived by expressing the pressure, density and velocities in terms of an approximation, labelled by the superscript (*), and a correction value, denoted by the superscript (');

thus:

$$\begin{aligned} P &= P^* + P' \\ \rho &= \rho^* + \left(\frac{\partial \rho}{\partial P}\right)_T P' = \rho^* + \gamma^* P' \\ \hat{U} &= \hat{U}^* + \hat{U}' \\ V &= V^* + V' \end{aligned} \tag{4.54}$$

The solution of the momentum equations obtained with the approximate pressure field P^* satisfy, for example for the axial component

$$A^n_{P,\hat{U}} \hat{U}^*_P = \sum_C A^n_{C,\hat{U}} \hat{U}^*_C + A^o_{P,\hat{U}} \hat{U}_P{}^o - (P^*_P - P^*_W)\, a_{n-s} + R_{P,\hat{U}} \tag{4.55}$$

where the pressure gradient term has been extracted from the source term $S_{\hat{U}}$ given in equation (4.45) (note that equation (4.55) and all other equations employed here are in fully-implicit form). The 'correct' pressure and velocity fields will satisfy

$$A^n_{P,\hat{U}} \hat{U}_P{}^n = \sum_C A^n_{C,\hat{U}} \hat{U}_C{}^n + A^o_{P,\hat{U}} \hat{U}_P{}^o - (P_P{}^n - P_W{}^n)\, a_{n-s} + R_{P,\hat{U}} \tag{4.56}$$

Substitution of relations (4.54) into the above equation, and subtraction of equation (4.55) gives

$$A^n_{P,\hat{U}} \hat{U}'_P = \sum_C A^n_{C,\hat{U}} \hat{U}'_C - (P'_P - P'_W)\, a_{n-s} \tag{4.57}$$

Omission of the first term on the right hand side of the above (the grounds for this will be explained later) permits the 'correction' velocity $\hat{U}'_P$ to be locally expressed in terms of the 'correction' pressures that drive it; thus:

$$\hat{U}'_P = \frac{-(P'_P - P'_W)\, a_{n-s}}{A^n_{P,\hat{U}}} \tag{4.58}$$

Hence, according to relations (4.54)

$$\hat{U}_P = \hat{U}^*_P - \frac{(P'_P - P'_W)\, a_{n-s}}{A^n_{P,\hat{U}}} \tag{4.59}$$

Similarly, for the radial velocity component

$$V_P = V^*_P - \frac{(P'_P - P'_S)\, a_{se-sw}}{A^n_{P,V}} \tag{4.60}$$

The fully-implicit continuity equation is (from equation (4.25))

$$\frac{\rho_P^{\,n} V_P^{\,n} - \rho_P^{\,o} V_P^{\,o}}{\delta t} + (\rho \hat{U} a)^n_e - (\rho \hat{U} a)^n_w + (\rho V a)^n_n - (\rho V a)^n_s = 0 \tag{4.60}$$

Introduction of relations (4.54), (4.59) and (4.60) into the above yields, after manipulation and omission of second-order correction terms

$$\frac{(\gamma^* P' V^n)_P}{\delta t} + a^n_{ne-se}\left[(\hat{U}^* \gamma^* P')_e - \rho^*_e \frac{a^n_{ne-se}}{A^n_{e,\hat{U}}}(P'_E - P'_P)\right]$$

$$- a^n_{nw-sw}\left[(\hat{U}^* \gamma^* P')_w - \rho^*_w \frac{a^n_{nw-sw}}{A^n_{w,\hat{U}}}(P'_P - P'_W)\right]$$

$$+ a^n_{nw-ne}\left[(V^* \gamma^* P')_n - \rho^*_n \frac{a^n_{nw-ne}}{A^n_{n,V}}(P'_N - P'_P)\right]$$

$$- a^n_{sw-se}\left[(V^* \gamma^* P')_s - \rho^*_s \frac{a^n_{sw-se}}{A^n_{s,V}}(P'_P - P'_S)\right]$$

$$= -\left\{\frac{(\rho^* V^n - \rho^o V^o)_P}{\delta t} + (\rho^* \hat{U}^* a^n)_e - (\rho^* \hat{U}^* a^n)_w\right.$$

$$\left. + (\rho^* V^* a^n)_n - (\rho^* V^* a^n)_s\right\} \tag{4.62}$$

where $A^n_{e,\hat{U}}$, $A^n_{w,\hat{U}}$, etc., are the centre-node coefficients $A_P^{\,n}$ for the velocities located at e, w, etc., expressed in this manner to avoid confusion. The right hand side of the equation represents the local mass inbalance (that tends to zero as ρ^*, U^*, etc., tend to correct values ρ^n, U^n, etc.). Cell-face Mach numbers are now defined, for example:

$$Ma_e^{\,2} = \frac{\hat{U}^*_e \gamma^*_e A^n_{e,\hat{U}}}{\rho^*_e a^n_{ne-se}} \tag{4.63}$$

Introduction of the above into equation (4.62) gives, upon incorporating the right hand side into a 'source' term S_P:

$$\frac{(\gamma^* P' V^n)_P}{\delta t} + (\hat{U}^* \gamma^* a)_e \left[P'_e - \frac{P'_E - P'_P}{Ma_e^2}\right] - (\hat{U}^* \gamma^* a)_w \left[P'_w - \frac{P'_P - P'_W}{Ma_w^2}\right]$$

$$+ (V^* \gamma^* a)_n \left[P'_n - \frac{P'_N - P'_P}{Ma_n^2}\right] - (V^* \gamma^* a)_s \left[P'_s - \frac{P'_P - P'_S}{Ma_s^2}\right] = S_P \qquad (4.64)$$

By analogy with equation (4.19), the cell-face values of P' are now expressed in terms of the nodal values as, for example:

$$P'_e - \frac{P'_E - P'_P}{Ma_e^2} = (1 - \alpha_e)\, P'_E + \alpha_e\, P'_P \qquad (4.65)$$

Introduction of these relations into equation (4.64) and subtraction of the following relation (which is exact only in the limit $P'_P \to 0$)

$$[(\hat{U}^* \gamma^* a)_e - (\hat{U}^* \gamma^* a)_w + (V^* \gamma^* a)_n - (V^* \gamma^* a)_s]\, P'_P \simeq 0 \qquad (4.66)$$

from equation (4.64) finally gives the pressure correction equation as

$$\frac{(\gamma^* P' V^n)_P}{\delta t} + (\hat{U}^* \gamma^* a)_e\, (1 - \alpha_e)\, [P'_E - P'_P] - (\hat{U}^* \gamma^* a)_w\, \alpha_w\, [P'_W - P'_P]$$

$$+ (V^* \gamma^* a)_n\, (1 - \alpha_n)\, [P'_N - P'_P] - (V^* \gamma^* a)_s\, \alpha_s\, [P'_S - P'_P] = S_P \qquad (4.67)$$

The above equation may be written, analogous to equation (4.29), in the following compact form

$$A_P^n\, P'_P = \sum_C A_C^n\, P'_C + S_P \qquad (4.68)$$

with the coefficient defined as

$$\begin{aligned} A_P^n &= \sum_C A_C^n + \frac{(\gamma^* V^n)_P}{\delta t} \\ A_E^n &= (U^* \gamma^* a^n)_e\, (\alpha_e - 1) \\ A_W^n &= (U^* \gamma^* a^n)_w\, \alpha_w \\ A_N^n &= (V^* \gamma^* a^n)_n\, (\alpha_n - 1) \\ A_S^n &= (V^* \gamma^* a^n)_s\, \alpha_s \end{aligned} \qquad (4.69)$$

$$S_P = -\{\frac{(\rho^* V^n - \rho^o V^o)_P}{\delta t} + (\rho^* \hat{U}^* a^n)_e - (\rho^* \hat{U}^* a^n)_w + (\rho^* V^* a^n)_n - (\rho^* V^* a^n)_s\} \quad (4.69)$$

Following Watkins [1977] and Johns [1980], the spatial difference functions α_e, α_w, etc., are defined to give a similar hybrid of central/donor-cell differencing as in the other equations; thus

$$\alpha = \begin{cases} \frac{1}{2} + \frac{1}{Ma^2} & \text{for } |Ma^2| \leq 2 \\ 1 & \text{for } Ma^2 > 2 \\ 0 & \text{for } Ma^2 < -2 \end{cases} \quad (4.70)$$

It should be noted that in the process of deriving equation (4.68), certain approximations were introduced. This is permitted for the source term S_P of the equation is the local mass imbalance and both P' and S_P become zero as the solution converges. Thus, the pressure correction equation serves only as a temporary link between the pressure, density and velocity fields, so that ultimately they satisfy the continuity and momentum equations simultaneously. Therefore, any approximation made in deriving the P' equation is acceptable, as long as it does not impede convergence.

In the latter stages of this study, it was found that for a particular case examined (to be described in Chapter 6), at high engine speeds ($\geq$ 3000 rpm, corresponding to maximum valve exit Mach number $\geq$ 0.72), this procedure lead to a tendency towards divergence of the solutions of the continuity and momentum equations, that could only be prevented by using unacceptably small under-relaxation factors for the pressure-correction and momentum equations. The analysis of the solutions of the P' equation (4.68) indicated that relation (4.63) is not an exact representative of the local Mach number: for the maximum valve exit $Ma \approx 0.7$, the local Mach number defined according to relation (4.63) attained the value $Ma^2 \geq 2$ along the path of the inlet jet, causing the P' coefficients (equation (4.69)) to be evaluated in an upwind fashion along the path of the inlet jet. This practice undermines the link with the momentum equation, that is represented through the terms, for example, $\rho^*_e a_{ne-se} (P'_E - P'_P)/A_{e,\hat{U}}$ in equation (4.62).

The omission of the terms $(U^* \gamma^* P')_e$, $(U^* \gamma^* P')_w$,

etc., in equation (4.62), that originate from the density~pressure correction relation (see equation (4.54)), causes the coefficients of the pressure correction equation to be independent of the local Mach number; but use of this formulation did not alleviate the divergence problem. A number of factors were believed to be responsible, including (i) the presence of a pressure wave that was suppressed by the global pressure adjustment procedure, and (ii) the strong perturbances produced by sudden variations in the inlet boundary and local velocities, as a result of simulation of flow separation at the valve (see Section 3.6.3). However, due to the shortage of time, investigation of the causes of the problem and means of its remedy was not pursued.

4.5 IMPLEMENTATION OF THE BOUNDARY CONDITIONS

The boundary conditions are incorporated in the numerical calculations by appropriately modifying the transport equations at the cells adjoining the boundary in question. This is done by setting the coefficient A_C^n's in equation (4.30) that link the internal grid node to that at the boundary equal to zero, and inserting in equation (4.29) the boundary conditions as fictitious source terms. These 'sources', like their real counterparts, are linearised according to equation (4.44) as

$$S_B = S_I \, \phi_P^n + S_E \tag{4.71}$$

where S_I and S_E represent the implicit and explicit contributions, respectively. Details will now be given.

4.5.1 Wall Boundary Conditions

(i) Momentum equations: The momentum 'source' due to the wall shear stress τ_w for a tangential velocity component adjacent to the wall is calculated as, for example for a 'north' wall

$$(S_{\hat{U}})_N = \tau_{w_N} a_N = \mu_{eff} a_N \frac{U_N - U_P}{y_P} \tag{4.72}$$

where a_N is the 'north' area of the cell, y_P is the normal distance from the cell-centre to the wall, and μ_{eff} is, from equations (3.73) and (3.79),

$$\begin{aligned} \mu_{eff} &= \mu && \text{for } y_P^+ \leqslant 11.63 \\ \mu_{eff} &= \frac{C_\mu^{\frac{1}{4}} \kappa \rho_P k_P^{\frac{1}{2}}}{\log_e (E \, y_P^+)} y_P && \text{for } y_P^+ > 11.63 \end{aligned} \tag{4.73}$$

with y_P^+ defined by equation (3.74) as

$$y_P^+ = \frac{C_\mu^{\frac{1}{4}} \rho_P k_P^{\frac{1}{2}}}{\mu} y_P$$

$(S_{\hat{U}})_N$ is then linearised, according to equation (4.71), as

$$\begin{aligned} S_I &= -\frac{\mu_{eff} a_N}{y_P} \\ S_E &= \frac{\mu_{eff} a_N}{y_P} \hat{U}_N \end{aligned} \tag{4.74}$$

Similar expressions may be derived for other boundary orientations.

(ii) Stagnation enthalpy: The enthalpy 'source' due to heat transfer for a main cell adjacent to, for example, a 'north' wall is:

$$(S_h)_N = \left(\frac{\mu}{\sigma_h}\right)_{eff} a_N \frac{T_N - T_P}{y_P} \tag{4.75}$$

where $(\mu/\sigma_h)_{eff}$ is, from equations (3.77) and (3.80),

$$\begin{aligned} \left(\frac{\mu}{\sigma_h}\right)_{eff} &= \frac{\mu}{\sigma_h} && \text{for } y_P^+ \leq 11.63 \\ \left(\frac{\mu}{\sigma_h}\right)_{eff} &= \frac{C_\mu^{\frac{1}{4}} \rho_P k_P^{\frac{1}{2}}}{T^+} y_P && \text{for } y_P^+ > 11.63 \end{aligned} \tag{4.76}$$

in which $$T^+ = \sigma_{h,T} \left[\frac{1}{\kappa} \log_e (E\, y_P^+) + P_{\sigma_h}\right] \tag{4.77}$$

(iii) Turbulence energy, k : For a cell adjacent to a wall, the expression for the shear stress contribution to the turbulence energy production term is modified to take account of the near-wall turbulence characteristics. Thus, in calculation of the turbulence production (term P_1 in Table 4.1), the approximation is made that, for the stress parallel, for example, to a 'north' wall

$$\mu_{T_P} \left[\left(\frac{1}{z_H} \frac{\partial V}{\partial \xi}\right)_P + \left(\frac{\partial U}{\partial n}\right)_P\right]^2 \simeq \tau_{w_N} \frac{U_N - U_P}{y_P} \tag{4.78}$$

and similar expressions are derived for other orientations.

(iv) Dissipation rate, ε: The level of ε for the cell adjacent to a wall is fixed according to the local equilibrium relation (3.75) as:

$$\varepsilon_P = \frac{C_\mu^{3/4} k_P^{3/2}}{\kappa y_P} \tag{4.79}$$

(v) Pressure correction, P': At boundaries where the normal velocity is prescribed, the finite-difference equation for local pressure correction (4.68) must be modified so that this velocity is not changed. This is done, for example for the cell adjacent to a 'north' wall, by setting $A_N = 0$. This amounts to prescription of zero normal gradient on P', as may be deduced from equations (4.68) and (4.69).

4.5.2 Axis of Symmetry

For the cells adjacent to the symmetry axis, the condition of zero normal gradient is implemented by setting A_S and the boundary 'source' S_B in the finite-volume equations of all the dependent variables except radial velocity, to zero. In the case of radial velocity, V_S and S_B are set to zero.

4.5.3 Planes of Inlet and Exhaust Apertures

For the circumstances of inflow, the profiles of all the dependent variables must be specified in the plane of the aperture, as remarked in Section 3.6.3. The mass flow rate $\dot{m}$ is determined from the orifice equations (3.82) and (3.84), using the discharge coefficient C_D for the following cases as:

(i) In one case, in which no treatment is made for the flow separation at valve, $C_D \sim L$ is given by equation (3.86).

(ii) For all other cases, in which the flow separation at valve is simulated, $C_D \sim L$ is given by equation (3.85).

The 'normal' inlet velocities U_{in} at the plane of inlet aperture are obtained for the case (i) from equation (3.87). In the cases (ii), the effect of flow separation on the inlet velocity is simulated as follows: having obtained $\dot{m}$ based on the minimum flow area A_M for the actual valve lift L (and the measured C_D), the valve is positioned such that it corresponds to a lift of $z_V = L - z_{sep}$ (see Figure 3.1), with z_{sep} given by equation (3.89), and the normal inlet velocity at the plane of valve U_{in}

is calculated from equation (3.88). The radial and axial (from equation (3.90)) velocity components at the valve inlet plane are then fixed accordingly. Thus, for the cells adjacent to the aperture, A_w in equation (4.68) is set to zero (implying $\partial P'/\partial \xi = 0$) so that these velocities are not changed.

For the circumstances of outflow, the mass flow rate and the normal velocity at the plane of the valve are determined according to the procedure outlined above. The profiles of the other variables at the valve need not be specified because, due to the 'donor-cell' differencing scheme employed, they do not enter into calculations. If required, their exit values can be equated to the corresponding values at the nearest upwind node.

4.6 SOLUTION PROCEDURE

The method of solution starts from fields of initial values and marches forward in increments of time Δt (or equivalently crank angle $\Delta\theta$), at every interval iteratively solving the coupled finite-volume equations for the dependent variables, until the desired period is covered.

At each time-interval, the method updates the fields of variables from the preceding interval in the following sequence:

(i) The position of piston (from the cylinder head) and its velocity is calculated from the following relations

$$z_p(\theta) = z_{TDC} + \frac{St}{2}\left[1 - \cos\theta + \frac{2L_{cr}}{St}\left(1 - \sqrt{1 - \left(\frac{St}{2L_{cr}}\right)^2 \sin^2\theta}\right)\right] \qquad (4.80)$$

$$U_p(\theta) = \frac{St}{2}\,\omega\left\{\sin\theta + \frac{1}{2}\left(\frac{St}{2L_{cr}}\right)\left[1 - \left(\frac{St}{2L_{cr}}\right)^2 \sin^2\theta\right]^{-\frac{1}{2}} \sin 2\theta\right\} \qquad (4.81)$$

in which z_{TDC} is the clearance distance at TDC induction, St is the engine stroke, L_{cr} is the connecting rod length, ω is the engine angular velocity, and θ is the crank angle measured from the TDC induction.

(ii) The valve lift L is obtained from the (experimental) valve diagram and its velocity is approximated as

$$U_{valve} \simeq \frac{z_v(\theta) - z_v(\theta-\Delta\theta)}{\Delta t} \qquad (4.82)$$

where $z_v = L - z_{sep}$ and z_{sep} is obtained from equation (3.89).

(iii) The new grid configuration and the grid-line velocities are

then determined from relations (4.8).

(iv) The mass flow rate through the valve is calculated, for the prevailing pressure drop across the valve, via equations (3.82) and (3.84). The (time-dependent) boundary conditions at the plane of the inlet/exhaust valves are then determined, as outlined in Section 3.6.3, and implemented as described in Section 4.5.3.

(v) The momentum equations (4.31) and (4.36) are solved, using the prevailing fields of variables.

(vi) The overall pressure adjustment is calculated from equation (4.53) and the overall density is adjusted according to equation (4.50). The local pressure corrections are obtained by solving equation (4.68) and the fields of pressure, density and velocities are corrected using equation (4.54).

(vii) The difference equation (4.29) for stagnation enthalpy is solved; then the temperatures are determined and the densities are re-calculated from the equation of state (3.7).

(viii) The difference equation (4.29) for the turbulence quantities k (equation (3.28)) and ε (equation (3.57)) are solved and the turbulent viscosity μ_T field is determined from equation (3.20).

The above process is repeated from steps (iv) to (viii) until convergence is obtained. The procedure then advances to the next time-level and recommences from sequence (i), with the just-obtained fields now becoming the 'old' time-level values.

The simultaneous equations for the independent variables are solved iteratively by an alternating-direction line-by-line iterative method, employing the Tri-Diagonal Matrix Algorithm (TDMA) solution procedure (see, for example, Watkins [1977]). The stability and convergence of the numerical method is enhanced through incorporation of the dynamic under-relaxation method of Johns [1980].

4.7 CLOSURE

In this chapter, the method of solution has been described, starting with the transformation of the general transport equation into a coordinates frame that expands and contracts according to the piston and

the valve motions. The discretisation of this equation has then been carried out, and the method of discretisation and linearisation of the individual source terms of the dependent variables outlined. The procedure for determining the pressure field has been described and the discretised pressure-correction equation has been derived. The method of implementing the boundary conditions has then been described. Finally, the solution algorithm has been outlined.

CHAPTER 5
ASSESSMENT OF THE CALCULATION METHOD AND THE TURBULENCE MODELS

5.1 INTRODUCTION

This chapter is concerned with the assessment of the performance of the present method in conjunction with the selected variants of the k-ε turbulence model described earlier in Chapter 3. This is achieved through simulation of the flow in a four-stroke, central-valve, disc-chamber model engine and detailed comparison with two sets of data, pertaining to the operating conditions of 200 rpm and compression ratios of 3.5 and 6.7, respectively. The turbulence model variants employed are those of Watkins [1977], Morel & Mansour [1982] and El Tahry [1983].

Section 5.2 presents the details of the two test cases, including the engine geometry and operating conditions. Also provided is information relevant to the computation, such as the grid arrangements.

In Section 5.3, the numerical solutions are tested for grid- and time-interval independence and the values employed in this study are selected. In Section 5.4, the influence of the inlet conditions on the predictions of the mean flow and turbulence is examined by comparing the results for two different inlet flow specifications with in-cylinder measurements. The better of the two treatments is selected for the later studies.

Section 5.5 presents the predictions for the two test cases. The structure and evolution of the flow is first analysed with the aid of plots of the velocity field and selected turbulence parameters, namely, intensity, dissipation length and time-scales and eddy viscosity. Further insight into the characteristics of the turbulence evolution is provided through analysis of the volume-integral balances of the k- and ε-transport equations during the engine cycle. The predictions obtained with the different versions of the turbulence model are then compared with the measurements of the axial mean velocity and turbulence intensity and are assessed in the light of findings.

Section 5.6 presents a further assessment of the turbulence model variants based on the physical plausibility and compatibility of the predicted variations of the aforementioned turbulence parameters, during the engine cycle. The version deemed to be most suitable for application to engine flows is then selected for the later studies. Finally, the conclusions are presented in Section 5.7.

5.2 DETAILS OF THE TEST CASES

The two test cases involve flow in an axisymmetric model engine with a disc-shaped combustion chamber, equipped with a cam-operated single central valve. Extensive measurements in such a configuration have been made by researchers in the Fluids Section, Imperial College, as was discussed earlier in Chapter 2. (The data for the present study were reported by Arcoumanis, et al. [1981a], and Ahmadi-Befrui, et al. [1982].) The geometrical and operating details are as follows.

	Case I (Ahmadi-Befrui, et al. [1982])	Case II (Arcoumanis, et al. [1981a])
Bore	75 mm	75 mm
Stroke	94 mm	94 mm
Connecting-rod length	363.5 mm	363.5 mm
Compression ratio	3.5	6.7
Speed	200 rpm	200 rpm
Mean piston speed	0.6267 m/sec	0.6267 m/sec
Maximum valve lift (L_{max})	7.3 mm	8 mm
Valve diameter (D_v)	34 mm	34 mm
L_{max}/D_v	0.21	0.24
Seat angle	60°	60°
Intake valve opens at*	- 6° CA	- 6° CA
closes at	224° CA	224° CA
Exhaust valve opens at	496° CA	496° CA
closes at*	6° CA	6° CA

The valve lift diagram is given in Figure 5.1.

The data consist, for Case I, of temporal measurements during the induction and compression strokes at a fixed location in the cylinder and for both cases, of radial profiles at several axial locations and selected crank angles, of the ensemble-mean axial velocity $\overline{U}$ and root-mean-square (rms) fluctuations u', both normalised by the piston mean speed $\overline{V}_p$. The measurements were obtained by laser-Doppler anemometry (Arcoumanis [1983]) and are believed to be accurate to ±5% for the mean velocity and ±10% for the rms component (although, according to the findings of Arcoumanis, et al. [1982b], the error in the measurements of the rms component, in the regions of large velocity gradient during induction, can be as large as

---

* Extrapolated crank angle from intake and exhaust lift diagrams.

±20%). The mean cylinder pressure data, as a function of crank angle, were also reported.

The computational grid arrangements employed for the two cases are illustrated in Figures 5.2 (Case I) and 5.3 (Case II). In the Case I arrangement, the plane EH is stationary: the grid in the regions ABCD and ADEH contract and expand axially according to the valve motion and the grid in the EFGH region follows the piston motion. The position of EH and the grid distribution were optimised in order to obtain good resolution near the valve and acceptable grid aspect and expansion ratios for the three regions throughout the engine cycle. For Case II (Figure 5.3) with its higher compression ratio, the plane EH is discarded due to smallness of the clearance gap. Thus, here, the grid in the region DFGA follows the relative motions of the piston and valve.

The wall temperatures were estimated (no measurements were available for these) to be:

	Case I	Case II
Cylinder wall	340°K	350°K
Cylinder head and valve	340°K	350°K
Piston	360°K	370°K

The induction air and the initial in-cylinder temperature and pressure (at the start of the induction) were assumed to be 295°K and 1.01×10^5 N/m^2, respectively.

5.3 EFFECTS OF THE GRID DENSITY AND TIME-STEP SIZE

5.3.1 *Grid Density*

Figures 5.4(a) and (b) show, respectively, the radial distributions of the predicted axial velocity ($\overline{U}$) and turbulence energy (k) at different axial locations, at θ = 36° CA into the induction stroke, obtained from computations on 30×26 and 45×45 grids. It is evident from Figure 5.4(a) that the magnitude and position of the peak velocity of the induction jet and its rate of spread are influenced by the grid density, as are the strength and size of the recirculation region near the cylinder axis.

Figure 5.3(b) illustrates the influence of the grid density on the magnitude and distribution of k. Evidently, this quantity exhibits greater sensitivity than the mean velocity. This is probably due to the non-linear dependence of the turbulence generation rate on the local mean strain rates (see equation (3.28)) and the fact that, as will be shown, the k-transport equation is dominated by the local generation and

dissipation rates. The results of the 45 × 45 grid clearly show the expected correspondence between regions of peak k and large velocity gradient, whereas those for the coarser grid are smeared.

It was not possible, within the constraints of the computer resources available in the present study, to ascertain the grid dependence of the solutions by further refinement. However, the studies of McGuirk, et al. [1981] and Jahanbakhsh [1984], that are, respectively, concerned with the prediction of the turbulent wake of a confined axisymmetric disc and the in-cylinder flow during induction, indicate that this degree of spatial grid resolution is adequate to reduce the truncation errors to tolerable levels.

The results to be presented hereafter are obtained using the 45 × 45 mesh.

5.3.2 Time-Step

Figures 5.5(a,b), 5.6(a,b), 5.7(a,b) and 5.8(a,b) present the predicted radial distributions of the $\overline{U}$ and k for time-steps equivalent to $\Delta\theta$ = 3° and 1° CA, respectively at crank angle positions 36, 90, 180 and 234 degrees. The results show that in the regions dominated by the intake jet, the reduction in $\Delta\theta$ has very small influence on the predicted $\overline{U}$ and k. However, the development of the downstream recirculation zone and the associated level of k are significantly affected. In particular, the results for $\Delta\theta$ = 1° CA show a stronger recirculation pattern and larger k levels at mid-induction (Figure 5.6(a,b)) and weaker mean flow and smaller k at bottom dead centre (Figure 5.7(a,b)), as compared with the results for $\Delta\theta$ = 3° CA. The latter finding indicates that the evolution of the mean flow and the rate of decay of turbulence near the end of induction (more details of which will be given later on) are sensitive to the choice of time-step, with $\Delta\theta$ = 1° CA predicting faster decay of both quantities. However, the results for θ = 234° CA (just after inlet valve closure) in Figure 5.8(a,b) show that the differences between the two time-steps diminish during compression.

The strong time-step dependence of $\overline{U}$ and u' in the region of the main vortex is due to accumulation of truncation errors (possibly also affected by the coarser grid in this region). The small sensitivity of the flow in the induction jet region is likely due to the small effect of $\Delta\theta$, in these two cases, on the induction mass flow rate (and hence the inlet velocity).

The results to be presented later on and in Chapter 6 are all obtained using $\Delta\theta$ = 3° CA. This compromise was again imposed by the

considerable computational overheads of the calculations. For instance, the simulation of the induction and compression strokes, with $\Delta\theta = 3°$ CA, requires almost 3 hours CPU time on an IBM 360/195 computer; this increases by a factor of nearly 3 for $\Delta\theta = 1°$ CA. Fortunately, however, comparisons with measurements in the region of the induction jet will not be affected by this compromise nor, to some extent, those late in the compression stroke, when the sensitivity to $\Delta\theta$ can be expected to have further diminished.

5.4 THE INFLUENCE OF INLET CONDITIONS

A major area of uncertainty and cause of discrepancy between the predictions of multi-dimensional methods and the measurements is the specification of the inlet flow boundary conditions (see the review of theoretical studies in Chapter 2). In this study, two different treatments of the valve flow are adopted and their influence on the predictions is assessed through comparison with data. The calculations are performed for the Case I engine and employ the Watkins [1977] version of the turbulence model.

The 'old approach', as it will hereafter be termed, uses discharge coefficient relations (3.86) derived from the measurements of Kastner, et al. [1963-64] and obtains the inlet velocity according to relation (3.87), thus making no allowance for flow separation in the seat passage. The 'new approach' employs the measured (for this engine) discharge coefficient relations (3.85) reported by Bicen [1983] and calculates the inlet velocity from relation (3.88), hence taking the effect of reduction in the flow area at the valve exit plane into effect. Also, the valve lift is modified such that it corresponds to the width of the flow area (see Subsection 4.5.3).

Figure 5.9 presents the predicted induction mass flow rate and inlet velocity variations with crank angle, for the two boundary condition treatments. The results show small differences in mass flow rate, but flow separation produces considerably larger inlet velocities. The increase is not uniform throughout induction, because the width of the region of reverse flow Z_{sep} (see Figure 3.1) does not scale with the valve lift (see relations (3.89) and Subsection 2.2.5.1). Figure 5.10 presents the measured and predicted variations of the mean cylinder pressure during the compression and early expansion strokes: the best agreement is

obtained with the 'new' treatment*. However, considering the accuracy of the data and uncertain wall temperatures, both predictions are in acceptable accord with the data. Figure 5.11 compares the measured and predicted variations of $\overline{U}/\overline{V}_p$ and $u'/\overline{V}_p$† for the location Z = 15 mm and r = 25 mm. Insofar as the influence of boundary condition is concerned, these results indicate that the new inlet treatment (i) apparently gives the poorest prediction of the mean velocity during induction, (ii) produces the highest turbulence intensity (the increase of 50% over the old treatment is roughly proportional to the corresponding increase in the intake jet velocity), and (iii) gives the fastest rate of turbulence decay during late induction and compression strokes, such that as TDC is approached both treatments give $u'_{TDC} \simeq 0.6\ \overline{V}_p$.

Further insight into the effects of inlet boundary condition can be gained from Figures 5.12, 5.13, 5.14 and 5.15, presenting radial profiles of $\overline{U}/\overline{V}_p$ and $u'/\overline{V}_p$ at θ = 90°, 270°, 324° and 360° CA, respectively (for an impression of the flow structure and evolution, see Figures 5.16(a,b)). Figure 5.12 shows that contrary to the impression gained from Figure 5.11, the new treatment improves the overall prediction of both the mean flow and the turbulence intensity. The effect of increase in the intake jet velocity due to flow separation at valve (in the new treatment) is to produce a stronger and larger recirculation region behind the valve, in agreement with the experimental data of Arcoumanis, et al. [1982c]. The discrepancy for the new treatment between the predicted and measured location of the peak velocity is believed to be due to the assumption that the intake jet enters the cylinder at valve seat angle. As pointed out earlier in Chapter 2, the recent measurements of Vafidis & Whitelaw [1984] show that the entry angle varies with the valve lift and the occurrence of the flow separation. (This information was not available at the time the present calculations were performed.) The discrepancies in Figure 5.11, noted earlier, may therefore be due in part to the fact that the measurement location is within the path of the induction jet and thus sensitive to the entry angle.

Figure 5.13 shows that the differences for the two inlet treatments persist until mid-compression (θ = 270° CA). Thereafter, however, the

---

* For this case, the inlet valve was assumed to have closed for $L/L_{max} \leq 5 \times 10^{-2}$; this can have a small effect on the mean pressure during compression.

† In the case of calculations, $u' = \sqrt{2/3\ k}$, for which isotropy is assumed. Hereafter, u' will be referred to as turbulence intensity.

predicted mean flows become identical and the differences in the level of $u'/\overline{V}_p$ diminish continuously, as shown by Figures 5.14 and 5.15; thus rendering the flow at TDC almost independent of the inlet treatment. This behaviour is in accord with the experimental findings of Arcoumanis, et al. [1982c], regarding the effect of inlet conditions on TDC flow.

It is concluded that the 'new' treatment is the preferred one and it is thus employed for all the predictions to be presented.

5.5 PREDICTIONS AND COMPARISON WITH EXPERIMENTAL DATA

This section presents and discusses the features of the calculated in-cylinder flow evolution and compares the predictions based on the three variants of the turbulence model with each other and the measurements.

The flow evolution is depicted with the aid of vector plots of the ensemble-mean velocity field and contour plots of the distributions of selected turbulence parameters; namely, intensity (u'), dissipation length-scale ($\ell = C_\mu^{3/4} k^{3/2}/\varepsilon$), dissipation time-scale ($\tau_d = k/\varepsilon = \sqrt{2/3}\, C_\mu^{-3/4}\, \ell/u'$) and viscosity ($\mu_T = C_\mu \overline{\rho} k^2/\varepsilon$), respectively normalised by mean piston speed ($\overline{V}_p$), cylinder bore (B), engine cycle time (T_{cycle}) and molecular viscosity (μ) (calculated at the inlet temperature).

Also provided is a term-by-term analysis of the volume-integrals of the k- and ε-transport equations. The individual terms (i.e. inertia $\rho\, \partial/\partial t$, transport and sources) are integrated numerically over the cylinder volume, at every time-step, throughout the engine cycle. These results are based on the Morel & Mansour [1982] turbulence model variant. (The differences between the predictions of the model variants, in particular with regard to the turbulence parameters, will be discussed later.)

5.5.1 Test Case I (Ahmadi-Befrui, et al. [1982])

5.5.1.1 The predicted flow evolution

Figure 5.16(a) presents the velocity field and Figures 5.16(b), (c), (d) and (e), respectively, present the turbulence intensity ($u'/\overline{V}_p$), length-scale (ℓ/B), time-scale (τ_d/T_{cycle}) and viscosity (μ_T/μ) fields, at selected crank angles during the induction, compression and early expansion strokes.

Diagrams (a) show that the annular intake jet separates at the valve seat and head early during induction, forming a ring vortex in the cylinder head/wall corner and a main toroidal vortex behind the valve (θ = 36° CA), with large levels of turbulence generated within the shear layers of the induction jet and transported downstream towards the piston. The diffusion of turbulence towards the cylinder

axis is small, resulting in low levels of u' in the region of valve wake (diagram (b), θ = 36° CA).

The dissipation length-scale (diagram (c)) within the induction jet region is small, in accord with its expected scaling with the valve lift, but it is much larger in the region of valve wake, where it apparently is controlled by the clearance gap. The distribution of τ_d (diagram (d)) is consistent with those of u' and ℓ: it is small ($\tau_d \simeq 10^{-2}\ T_{cycle}$) in the region of the induction jet and increases by one order of magnitude in the valve wake. The implications are that (i) the induction jet turbulence is in a quasi-steady state, compared with the time-scale of the induction process ($\tau_d \simeq 7°$ CA), and (ii) its τ_d is of order of the travel time of the intake jet ($\overline{u}_{in}/Z_p$) and therefore it decays rapidly as it is transported into regions of small local turbulence energy production.

The distribution of μ_T (diagram (e), θ = 36° CA) is dissimilar to those of other parameters and shows circular contours in the region of the induction jet, increasing in magnitude towards the location of flow impingement on the cylinder wall. This distribution is in accord with the predictions of the plane jet impingement with the standard k-ε model (Looney [1982]). However, the over-estimation of the turbulence intensity in this region observed in the latter study indicates that this feature may physically be incorrect. In this connection, the studies of Hanjalic & Launder [1980] and Rodi & Schenerer [1983a] show that this is a consequence of the deficiency of the k-ε mode in flows with appreciable 'normal' strain rates and adverse pressure gradient, and modification of the model by sensitising the ε-transport equation to account for the larger dissipation rate associated with the normal strain rates reduces the turbulent viscosity in these circumstances.

Figure 5.16(a) shows that later during induction (θ = 72° CA), the main vortex intensifies and grows by entraining the induction flow (see the measurements of Arcoumanis, et al. [1982a]) and is displaced and stretched by the descending piston. This causes the deflection of the intake jet and its impingement on the cylinder wall, which effectively restricts the growth of the ring vortex in the cylinder head/wall corner during the rest of induction.

The distribution of u' at θ = 72° CA (diagram (b)) is similar to that at θ = 36° CA, except for the high turbulence levels in the region of jet impingement and formation of a region of moderately varying u' within the main vortex. The average level of u' over the cylinder volume is nearly 25% larger than at θ = 36° CA, roughly proportional to

the increase (≃ 35%) in the intake jet velocity (Figure 5.9(b)).

The distribution of ℓ at θ = 72° CA (diagram (c)) shows a structure in which ℓ within the region of induction jet is still of the order of the valve lift, and outside is controlled by the cylinder walls. In this respect, a lack of correspondence between the mean flow structure and the distribution of ℓ outside the jet region, and the location of the largest scale behind the valve are of interest. The level of ℓ throughout the cylinder is nearly 14% smaller than at θ = 36°, showing a small dependence on the Reynolds number of the intake jet (which has increased).

The distribution of τ_d at θ = 72° CA (diagram (d)) corresponds to that of u', with the smallest values occurring within the induction jet. A region of relatively small τ_d exists in the core of the main vortex: it increases by nearly five-fold towards the cylinder axis and the position of the largest τ_d, which is near the piston. This distribution indicates that the induction jet is the source of the turbulence, and, although the turbulence energy production in the main vortex contributes to its sustainment, it decays rapidly as it is transported into the regions of weak mean strain rate (compared with that of the induction jet), with a characteristic increase of the time-scale (Batchelor [1960]).

The level of τ_d over the whole cylinder at θ = 72° CA is nearly 50% smaller than at θ = 36° CA. This can be explained by considering that the induction jet turbulence is in a 'quasi-steady' state and in 'quasi-equilibrium': thus, τ_d is roughly inversely proportional to the (momentary) mean strain rates* of the induction jet. This emphasises the dynamics of the induction-generated flow and its dependence on the characteristics of the intake jet.

The distribution of μ_T at θ = 72° CA (diagram (e)) shows two high-level regions at the location of the jet impingement on the cylinder wall and in the valve wake. The arguments concerning the validity of the former were presented previously. The latter could be due to the same deficiencies of the standard k-ε model in flows with relatively large normal strain rates (Rodi & Scheuerer [1983a]), although

---

* For turbulence in 'local equilibrium' (i.e. production ≃ dissipation), equation (3.28), neglecting the compressibility terms, gives

$$\tau_d = C_\mu^{\frac{1}{2}} \left[\left(\frac{\partial \tilde{u}_i}{\partial x_j} + \frac{\partial \tilde{u}_j}{\partial x_i} \right) \frac{\partial \tilde{u}_i}{\partial x_j} \right]^{-\frac{1}{2}}$$

it may also be due to its shortcomings in flows with strong streamline curvature (Leschziner & Rodi [1981], Rodi & Scheuerer [1983b]). In this connection, the study of Leschziner & Rodi [1981] shows that modifications to the model to allow for the effects of streamline curvature and normal strains (Hanjalic & Launder [1980]) both reduce the predicted turbulent viscosity in the recirculation region of separating flows and improve the accuracy of the predictions. Although, as noted by Leschziner & Rodi [1981], these modifications act differently in reducing μ_T: the former gives a dependence of the coefficient C_μ on the streamline curvature and causes it to reduce within the recirculation region; the latter increases the dissipation rate and thereby reduces ℓ. These authors did not conclude which behaviour is more physically realistic. Therefore, the implication in respect of the present predictions is that the large levels of ℓ in the recirculation region behind the valve may be over-estimated.

The mean flow at mid-induction (Figure 5.16(a), $\theta = 90°$ CA) is similar to that at $\theta = 72°$ CA, except that the main vortex is larger and stronger. The distributions of the turbulence parameters are similar to those at $\theta = 72°$ CA and the level of u' has scarcely changed. However, τ_d and ℓ are larger due to the reduction in the intake jet velocity, although the increase in ℓ can also be due to the larger valve lift. The average level of μ_T at $\theta = 90°$ CA is larger by 30%, compared with that at $\theta = 72°$ CA, in accord with the variations of u' and ℓ, and there is evidence of formation of a region of large viscosity within the centre of the main vortex.

Figure 5.16(a) at $\theta = 126°$ shows continuous growth of the main vortex through entrainment of the intake mass flow and its stretching by piston. Also evident is a new region of flow separation in the cylinder wall/piston corner, due to adverse pressure gradient acting on the cylinder wall boundary layer. The strength of the main vortex is slightly reduced, compared with that at $\theta = 90°$ CA, due to the reduction of the intake jet momentum and the increase in μ_T (nearly 70%), producing considerably higher shear stresses in this region.

The distribution of u' at $\theta = 126°$ (diagrams (b)) is different from that at $\theta = 90°$ CA and shows the formation of a second region of large turbulence level within the main vortex. The largest levels in the jet are nearly 7% smaller than at $\theta = 90°$ CA, indicating a dependence on the intake jet momentum (note that according to Figures 5.9(a,b), the inlet velocities at $\theta = 90°$ and 126° CA are similar, but the mass flow rate is reduced by nearly 20%, resulting in a 20% reduction in the momentum). However, comparison of the u' levels in the region of the

main vortex shows nearly a 30% increase. A similar trend of variation (which has gone unnoticed) can be detected in the detailed measurements of Bicen [1983] and Arcoumanis [1983] in a similar engine with a permanently open valve. This behaviour can be explained with the aid of the distribution of μ_T at θ = 126° CA (diagrams (e)) which shows the largest levels of viscosity (nearly 3 to 8 times those within the induction jet) are situated near the centre of the main vortex. This is a consequence of the different length scales within the two regions (see diagrams (c)).

The distribution of ℓ at θ = 126° CA (diagrams (c)) is similar to that at θ = 90° CA, except for the changes near the centre of the main vortex, indicating an increase of nearly 70% in this region; elsewhere, ℓ is larger by nearly 20%. The increase of ℓ in the intake jet, despite the reduction in the valve lift, indicates that because of its strong interaction with the vortex structure, the intake jet cannot preserve a self-similar character.

The distribution of τ_d at θ = 126° CA (diagrams (d)) is similar to that at θ = 90° CA, with the region of small and moderately increasing τ_d coinciding with the region of turbulence generation in the main vortex. The levels are everywhere larger than at θ = 90° CA, indicating that even in the main vortex, the increase of ℓ (nearly 70%) is more substantial than that of u' (nearly 30%). The implication, thus, is that the turbulence generated within the main vortex has a longer life-time than that of the induction jet. The increase in ℓ results in larger levels of μ_T at θ = 126° CA, particularly in the region of the main vortex where the largest levels are attained (due to the increase in both ℓ and u').

The velocity field at θ = 162° CA (Figure 5.16(a)) shows further weakening of the mean flow, due to the rapid fall of the intake jet momentum and the increasing level of μ_T (diagram (e)), and formation of a third vortex in the cylinder wall/piston corner, in accord with the measurements of Bicen [1983]. The intake jet turbulence intensity is nearly 17% smaller than at θ = 126° CA, while the u' level in the main vortex is reduced only by 5% (the latter is not evident in diagram (b) because of the scaling of the contour levels). In connection with the latter feature, examination of the intermediate results (not shown) revealed that the turbulence intensity is actually sustained during most of the interval 126° to 162° CA and only tends to decay near the end of the interval. The variation of u' in the main vortex from the time of formation of an identifiable structure in this region (θ = 108° CA) indicates that it is independent of the intake jet turbulence level and

thus is determined by the local turbulence generation.

The predicted behaviour, in respect of the different rates of decay of turbulence within the intake jet and the main vortex, is in qualitative agreement with the measurements of Bicen [1983] and Arcoumanis [1983]. However, the data show a larger decay of the u' level in the main vortex (for the interval θ = 144° to 170° CA) than the calculations suggest. This can be attributed to the effect of the time-step and the shortcomings of the k-ε model in recirculating flows discussed earlier.

The distribution of ℓ at θ = 162° CA (diagram (c)) is as at θ = 126° CA; but its level in the cylinder head/wall vortex is considerably reduced, due to the weakening of the flow and increased influence of the cylinder wall on the turbulence in this region, whereas it is increased by nearly 30% elsewhere. The rapid increase of the length scale during the latter part of induction (70% at θ = 126° CA and 30% at θ = 162°) is in accord with the reduced influence of the intake jet turbulence and the increased level of generation by the main vortex and indicates a transformation into a state in which turbulence is controlled by the local conditions.

The distribution of τ_d at θ = 162° CA (diagram (d)) is similar to that at θ = 126° CA, but the levels are larger by nearly 10% in the main vortex and 60% in the region of the third vortex. The increase in τ_d in the last-named region is due to the large increase in ℓ and consequently the reduction in the dissipation rate, and its small increase in the main vortex is because of the turbulence sustainment in this region. The rapid reduction in the rate of increase of τ_d in the main vortex (25% at θ = 126° CA and 10% at θ = 162° CA) indicates the tendency of the turbulence towards a quasi-equilibrium state (in which the dissipation rate is largely balanced by the mean flow generation).

The distribution of μ_T at θ = 162° CA is as at θ = 126°; however, its levels are larger by nearly 30% in the main vortex (proportional to increase in ℓ) and 70% in the region behind the valve, due to increase in both ℓ (30%) and turbulence intensity (see diagram (b), showing large turbulence levels behind the valve). As already noted, the latter could be a consequence of the deficiencies of the standard k-ε model in flows with streamline curvature and appreciable adverse pressure gradient.

The velocity field at the end of induction (Figure 5.16(a), θ = 180° CA) shows that the rapid fall-off and ultimate termination of the intake flow does not change the mean flow structure:

the vortex system persists under its inertia but continuously weakens due to the effect of the turbulent stresses, in agreement with the measurements of Bicen [1983] and Arcoumanis [1983].

The distribution of u' at $\theta = 180°$ (diagram (b)) shows the disappearance of the structure associated with the intake jet and the existence of three regions of high intensity: one is at the centre of the main vortex; a second is behind the valve and extending into the zone of strong shear between the main and the cylinder head/wall vortices; and a third is near the cylinder wall, at the location of flow stagnation, between the two vortices. Comparison of the levels with those at $\theta = 162°$ CA shows sustainment of the turbulence in the region behind the valve and nearly 15% decay in the main vortex. The former behaviour is a consequence of the probably incorrectly predicted large and increasing level of μ_T in this region.

The distribution of ℓ at $\theta = 180°$ CA is similar to that at $\theta = 162°$, except for the disappearance of the intake jet structure, and confirms that, as noted earlier, after formation of the structure associated with the main vortex, the turbulence in this region remains in a quasi-equilibrium state and is independent of the induction jet turbulence. The levels of ℓ are nearly 10% larger than at $\theta = 162°$ CA, due to the relaxation and decay of the turbulence (see Batchelor [1960]). (The increase in cylinder volume during this period is only 1.5%.) The largest level of ℓ, near the cylinder axis, is 0.07 times the cylinder diameter.

The distribution of τ_d at $\theta = 180°$ is, apart from the disappearance of the intake jet structure, similar to that at $\theta = 162°$ CA. However, the levels are larger by nearly 20% (except for a region near the piston/cylinder axis junction) in accordance with the decay of u' and increase in ℓ (Batchelor [1960]). The value of τ_d in the main vortex is nearly 0.06 times the engine cycle time ($\tau_d \simeq 20°$ CA).

The distribution of μ_T at $\theta = 180°$ CA is essentially as at $\theta = 162°$ CA; the levels are nearly 8% larger behind the valve and in the third vortex, but have remained nearly constant in the main vortex. The behaviour in the main vortex is consistent with that of the decay of the grid generated turbulence, in which the Reynolds number of the energy containing eddies ($Re = u' L_x/\nu$) remains constant during the decay (Batchelor [1960]). The increase of μ_T in the third vortex is due to substantial increase in ℓ subsequent upon its formation, while the increase behind the valve could be a result of the aforementioned deficiencies of the turbulence model.

The velocity field at θ = 198° CA shows continuous weakening of the induction generated mean flow structure due to the effect of the turbulent stresses. The piston-induced pressure gradients and the existence of a small amount of outflow, due to the in-cylinder pressure becoming larger than ambient level, do not seem to influence the vortex structure. The latter is probably due to the fact that the mass flow rate is small.

The distribution of u' at θ = 198° CA shows the generation of large turbulence levels in the shear layers of the outgoing jet near the valve exit; but most of this is convected out of the cylinder. Outside this region, the u' distribution is as at θ = 180° CA, but the levels are smaller by nearly 15%.

The distribution of ℓ at θ = 198° CA is similar to that at θ = 180° CA and shows the established structure due to the main vortex and the influence of the cylinder walls; however, its level is larger by nearly 7%, which is again consistent with the characteristics of the decay of turbulence (Batchelor [1960]). Similarly, the distribution of τ_d is as at θ = 180° CA and the levels are larger by nearly 10%.

The distribution of μ_T at θ = 198° CA is similar to that at θ = 180° CA but its levels are nearly 10% smaller in the main vortex and slightly larger behind the valve, consistent with the variations of u' and ℓ. The reduction of μ_T in the main vortex could be due to (i) the reduction in the rate of growth of ℓ due to compression, tending to reduce the length-scale (Townsend [1956], p. 68), and (ii) the controlling influence of the cylinder walls on ℓ. An additional reason could be the fact that the coefficient C_μ, which is taken to be a constant in the present models, in general depends on the ratio of the local turbulence energy production to dissipation rate (P/ε) and increases in the circumstances where $P < \varepsilon$ (Rodi [1976]). (The predicted balance of the k-transport equation to be presented later on shows that near the end of induction and during compression, over the cylinder volume $P < \varepsilon$.)

The velocity field at θ = 234°, just after inlet valve closure, shows the break-up of the vortex in the cylinder head/wall corner, the displacement of the third vortex by the piston and of the main vortex towards the cylinder head/wall corner, and continuous decay of the mean motion due to the effect of the turbulent stresses (note the change in the velocity scale in Figure 5.16(a)).

The distributions of u', ℓ, τ_d and μ_T at θ = 234° CA are similar to those at θ = 198° CA. The turbulence intensity levels have reduced by nearly 35% in the centre of the main vortex and 20% in the

region behind the valve. The location of the largest level and the smaller decay of u' behind the valve could be due to over-estimation of μ_T (arising from deficiency of the model in flows with appreciable streamwise velocity gradient (Rodi & Scheuerer [1983a])) and the contribution to turbulence production from the impingement of the flow near the axis on the cylinder head (see diagrams (a)).

The levels of ℓ at θ = 234° CA are only 4% larger than at θ = 198° CA, indicating a reduction in the rate of growth due to the increased effect of compression. A noteworthy point is that, despite the large decay of u' in the main vortex (35%), the increase in ℓ in this region is not proportionally larger, indicating that its growth is controlled by the cylinder walls.

The levels of τ_d at θ = 234° CA, compared with those at θ = 198° CA, have increased by 40% in the main vortex and 10% elsewhere, in accordance with the variations of u' and ℓ. The levels of μ_T have reduced by 30% in the main vortex and nearly 10% elsewhere, indicating that the effect of compression on the length-scale is larger than it is on density.

The velocity field at θ = 270° CA shows the remnants of the third vortex in the cylinder wall/piston corner and a considerable reduction in the size and strength of the main vortex. The distribution of u' shows the disappearance of the region of high turbulence intensity in the main vortex; considerable homogeneity in the radial direction; and the decay of turbulence by nearly 35% in the main vortex and 25% elsewhere, compared with the levels at θ = 234° CA. The implications are that the turbulence generation by the main vortex is rapidly falling (as is also evidenced by the volume-integral balance of the k-equation in Figure 5.17(c), to be discussed later on) and the turbulence is 'relaxing' into a structure predominantly controlled by the cylinder walls.

The distribution of ℓ at θ = 270° CA is similar to that at θ = 234° CA, but the levels are smaller by nearly 7% due to the effect of compression. The distribution of τ_d at θ = 270° CA shows considerable modifications in the regions of the main vortex, indicating the continuing process of relaxation of turbulence. Compared with the levels at θ = 234° CA, τ_d in the main vortex has increased by 20%, in accordance with the large decay of u', while in the region near the piston, it has reduced by 10% due possibly to the break-up of the third vortex, and turbulence generation by compression. (It must be recalled from Chapter 3 that with reduction in the turbulence production by the mean flow strains, the relative significance of the turbulence generation by

compression increases; furthermore, the overall effect of compression on the turbulence depends on the level of τ_d.) The distribution of μ_T is as at θ = 234° CA, but its levels have reduced by 10%.

The velocity field at θ = 324° CA shows further reduction in the size of the main vortex and a considerable weakening of the flow due to the reduction in the piston speed, and the complete break-up of the third vortex. The distributions of the turbulence parameters (Figures 5.16) show a continuous relaxation into a structure controlled by the combustion chamber geometry. The u' distribution shows a continuing decay and tendency towards homogeneity. The levels, compared with those at θ = 270° CA, have fallen by nearly 35% everywhere except near the piston, where it has reduced by 20% due to the larger τ_d and the contribution of turbulence generation by compression.

The distribution of ℓ at θ = 324° CA exhibits its total control by the cylinder walls. The levels are nearly 20% smaller than at θ = 270° CA, indicating a sudden and large influence of the cylinder head/piston gap on the length-scale, when the former becomes comparable with the cylinder diameter. The distribution of τ_d is consistent with the continuous relaxation of the turbulence and shows an increase of nearly 20% in the main vortex and a small reduction in the region near the piston, in accordance with the variations of u' and ℓ. The overall picture is one of decay of turbulence exceeding the reduction in the length-scale over most of the cylinder volume. Thus, the compression process is far from being 'rapid' in the sense invoked in Rapid Distortion Theory (see Townsend [1956], Crow [1968]), which has been supposed in some studies (see Chapter 3).

The distribution of μ_T at θ = 324° CA essentially reflects the cylinder geometry-controlled distributions of u' and ℓ. The levels, compared with at θ = 270° CA, are smaller by nearly 6% everywhere.

The velocity field at TDC compression (θ = 360° CA) shows a weak mean flow ($\overline{U}_{max} \simeq 0.4\ \overline{V}_p$) due to the persisting main vortex. The distribution of u' shows continuous tendency towards homogeneity and a decay of nearly 27%, compared with the levels at θ = 324°. The levels within the bulk of the cylinder are nearly $u'/\overline{V}_p \simeq 0.4$ to 0.5, indicating a decay of nearly 75% during the compression stroke (θ = 180° to 360° CA).

The distribution of ℓ at θ = 360° CA is as at θ = 324° and the levels are slightly smaller (nearly 3%), indicating that it is controlled by the cylinder head/piston clearance gap. The significant relaxation of the turbulence and control of engine geometry is clearly evidenced by the variations of ℓ: during early compression (θ = 180° to

270° CA), ℓ increases due to the turbulence decay process, that exceeds the effect of compression (in tending to reduce ℓ). But, during late compression (θ = 270° to 360° CA), despite the continuous decay of turbulence (at almost similar rates), ℓ decreases in a manner strongly influenced by the clearance distance, as TDC is approached.

The distribution of τ_d at θ = 360° CA is similar to that at θ = 324°, but the levels are 15% to 20% smaller due to the reduction of ℓ exceeding that of u'. Similarly, the distribution of μ_T is as at θ = 324° CA, but the levels are smaller by nearly 13%, due to the reduction in ℓ and u' exceeding the increase in density.

The velocity fields at θ = 378° CA and 414° CA show the destruction of the residual main vortex early during the expansion stroke and the establishment of a one-dimensional flow in the direction of the piston motion. The distributions of u' show increasing homogeneity of the turbulence, accompanied with increase in the rate of decay (u' falls by nearly 18% during θ = 360° to 378°): this is due to the effect of dilatation in suppressing the turbulence (Bradshaw [1973]). The length- and time-scale distributions preserve their forms and show total control of the chamber geometry on the turbulence structure. The levels of ℓ and τ_d are larger than their TDC averages by nearly 5% and 17%, respectively, at θ = 378° CA, and rapidly increase to 28% and 60% , respectively, at θ = 414° CA. The distributions of μ_T during expansion are also similar to that at TDC, with the levels falling due to the large reduction in u' and the density off-setting the increase in ℓ.

5.5.1.2 The integral balances of the k-ε transport equations

This section presents a term-by-term analysis of the volume-integral balances of the k- and ε-transport equations and provides an insight into the relative importance of the mechanisms that generate and sustain the turbulence, especially with regard to the induction and compression processes. The individual terms (i.e. 'inertia' $\rho\, \partial/\partial t$, transport and the production and dissipation 'sources') are integrated numerically over the cylinder volume at every time step during the engine cycle. The results over the entire induction, compression and early expansion strokes are plotted in Figures 5.17(a) and (b); while Figures 5.17(c) and (d) present the expanded results for the compression and early expansion strokes. Also shown in Figure 5.17(c) is the variation of the compressibility term $\nabla.\underline{U}$ due to the piston motion
(i.e. $\nabla.\underline{U} = -(1/\overline{\rho})(d\overline{\rho}/dt) = (1/Z_p)(dZ_p/dt)$).

The noteworthy general features concerning the k-

balance (Figure 5.17(a)) are that (i) the turbulence advection into the cylinder by the intake flow is negligible compared with the level of turbulence generation (within the cylinder), and (ii) during most of the induction phase, over the cylinder volume, the turbulence generation is balanced by dissipation. In respect of the ε-balance, Figures 5.17(b) and (d) show the expected generation ≃ dissipation balance of the ε-transport equation (discussed earlier in Chapter 3); however, note should be taken of the significant level of 'diffusion', during both the induction and compression strokes, which represents the (dissipative) influence of the cylinder walls. The details of the mechanism of turbulence evolution are described in the following.

Figure 5.17(a) shows that early during induction, the in-cylinder turbulence level increases, due to the shear production of turbulence energy G_S ($\equiv \int_V \mu_T \{(\partial\tilde{u}_i/\partial x_j) + (\partial\tilde{u}_j/\partial x_i)\} (\partial\tilde{u}_i/\partial x_j)\, dV$, $i \neq j$) and turbulence energy production by the normal strain rates G_N ($\equiv \int_V \mu_T \{(\partial\tilde{u}_i/\partial x_j) + (\partial\tilde{u}_j/\partial x_i)\} (\partial\tilde{u}_i/\partial x_j)\, dV$, $i = j$) of the induction jet. The rate of increase of k (i.e. $\partial k/\partial t$) and the levels of G_S and G_N increase initially proportional to the increase in the intake jet velocity; but consequent upon the flow separation at the valve and the intake jet impingement on the cylinder wall, G_S and G_N increase rapidly and $\partial k/\partial t$ reaches a maximum level at around $\theta \simeq 50°$ CA. However, ε increases rapidly almost at the same rate as G_N, indicating the near-equilibrium nature of the intake-generated turbulence (due to the smallness of the dissipation time-scale).

Thereafter, the rate of increase of k falls ($\theta \simeq 50°$ to 75° CA), despite the increasing levels of G_S, as a result of the reduction of G_N parallel with the fall of the inlet velocity (see Figure 5.9(b)), and the increased level of ε. A quasi-steady state is then reached ($\theta = 75°$ to 140° CA) whereby the total turbulence production is balanced by dissipation, both within the flow and due to the influence of the cylinder walls (which is manifested by the significant ε-diffusion contribution). During this phase, G_N reduces, closely following the variations of the intake jet velocity (Figure 5.9(b)); but G_S increases continuously and reaches a maximum level at around $\theta \simeq 120°$ to 150° CA, which corresponds to the time of formation of a turbulence structure in the main vortex. Therefore, it appears that G_N and G_S represent turbulence generation mainly by the intake jet and the vortex structure, respectively.

The turbulence decays near the end of induction ($\theta \simeq 150°$ to 180° CA) with the rapid reduction of G_S and G_N, due to the

rapid fall-off of the intake jet momentum and the decay of the mean flow. The turbulence decay continues, in spite of the increase in G_S and G_N due to turbulence generation in the outgoing flow during early compression ($\theta \simeq 180°$ to 215° CA), which as noted earlier is mainly convected out of the cylinder.

The expanded results for after intake valve closure (Figure 5.17(c)) show the rapid reduction of G_S and G_N during θ = 215° to 270° CA, indicating the extent of decay of the induction-generated mean flow, and continuous decay of turbulence throughout the compression stroke, despite the contribution from turbulence generation by compression G_C ($\equiv \int_V -2/3\,\rho\, k\, \nabla.\tilde{U}\, dV$). The level of G_C is relatively small and only becomes comparable with G_S and G_N near the end of compression ($\theta \simeq 270°$ to 340° CA): this corresponds to the phase of the largest weakening of the persisting main vortex (see Figure 5.16(a)) and also the maximum mean strain ($\nabla.\tilde{U}$) caused by piston motion. The turbulence generation by the piston-induced normal strains ($-2/3\,\mu_T\,\nabla.\tilde{U}^2$) is negligible throughout the compression stroke.

The rate of decay of turbulence and the level of dissipation rate continuously decrease during the compression stroke; but with the levels of G_N, G_S and G_C diminishing, turbulence tends towards a state of pure decay (i.e. $\rho\, \partial k/\partial t \simeq -\rho\, \varepsilon$) at TDC. The ε-balance (Figure 5.17(d)) shows that the reduction of ε during compression is due to the fall in the levels of ε-production (due to turbulence generation by the mean flow) and ε-diffusion (i.e. dissipation due to the cylinder walls). The ε-generation due to the effect of compression (i.e. $\int_V (-2/3\, C''_{\varepsilon 1} + C_{\varepsilon 3})\, \rho\, \varepsilon\, \nabla.\tilde{U}\, dV$) is almost negligible compared with the other terms, except near the end of compression ($\theta \simeq 300°$ to 340°).

5.5.1.3 Comparison with experimental data

The predictions obtained with the three variants of the turbulence model are now compared with the measurements of Ahmadi-Befrui, et al. [1982]. Figure 5.18 presents the measured and predicted normalised axial mean velocity $\overline{U}/\overline{V}_p$ and turbulence intensity $u'/\overline{V}_p$, at the fixed location Z = 15 mm, r = 25 mm. Also shown is the velocity at this location corresponding to the simple one-dimensional axial flow ($\overline{U}(z) = (z/z_p)\, U_p$) which would be generated by the piston motion alone, in the absence of induction and wall shear effects.

The measurements show a rapid increase of $\overline{U}$ and u' during the first half of the induction stroke and rapid decay of both during the latter half. The 'spikes' in the $\overline{U}$ curve are believed

to be a consequence of (i) variation in the angle of the intake jet with increase of the valve lift (Vafidis & Whitelaw [1984]), and (ii) its deflection by the growing vortex behind the valve. (As Figure 5.19 indicates, the measurement location is within the path of this jet and, thus, is sensitive to these effects.) However, the spike in the measured variations of u' at early induction ($\theta \simeq 30°$ CA) is due to another cause, this being measurement error due to crank angle broadening (Arcoumanis, et al. [1982b]). The predictions of the different turbulence models are almost identical and follow the trends of variations of the measurements, although they considerably under-predict the magnitudes. But, as Figure 5.19 shows, the discrepancies could be due in part to small errors in the predicted jet trajectory, arising from the sources identified earlier (in Section 5.4). This illustrates a pitfall in assessing predictions through comparisons with single-point measurements in regions of large gradients.

The measurements and the predictions alike show rapid reduction of the mean velocity, due to fall-off of the intake jet velocity, during late induction and early compression. However, although the u' decrease near the end of induction is well predicted, the level and rate of decay of turbulence during early compression is in gross disagreement with the measurements. This is partly due to the effects of the large computational time-step resulting in under-prediction of the decay of the mean flow and turbulence during this period (discussed in Section 5.3), although it may also be attributed to the over-prediction of the turbulence level in the main vortex due to the deficiencies of the turbulence model (in all forms investigated here) in flows with streamline curvature and varying levels of P/ε, discussed earlier.

The differences between the predictions of the turbulence model variants during compression and expansion are small. The results from the Morel & Mansour [1982] and El Tahry [1983] (hereafter referred to as MM and ET, respectively) versions are identical. The Watkins [1977] model produces slightly larger u' during the latter part of compression, that tends to deteriorate the agreement with the data. This is due to the significantly larger ℓ, τ_d and μ_T (indicating larger turbulence generation by the mean flow and longer decay time-scale) that this version produces. (The dependence of the turbulence parameters on the differences in turbulence models will be discussed later in Section 5.6.)

The variation of the axial mean velocity at the measurement location during the compression and expansion strokes

(θ = 225° to 450° CA) is identical to that predicted by the one-dimensional theory, and appears to be reasonably well reproduced by the numerical calculations.

The measurements show rapid decay of turbulence intensity during early compression, until the intake valve closure (IVC) (a decay of nearly 45% during θ = 180° to 225° CA). Thereafter, u' decays at considerably slower rates (a total decay of nearly 40% occurs over the interval θ = 225° to 360° CA), giving at TDC $u' \simeq 0.5\ \overline{V}_p$. The calculations show under-prediction of the rapid turbulence decay during θ = 180° to 225° CA (noted earlier); but thereafter, u' decays markedly fast (nearly 67% during θ = 225° to 330° CA), due to the weakening of the main vortex and strong influence of the cylinder wall on its turbulence (as was explained earlier in Section 5.5.1.1), producing good agreement with the measurements from $\theta \simeq$ 320° CA right through to θ = 450° CA of the expansion stroke. The latter agreement is due to the reduction in the predicted decay rate of u', as the turbulence within the main vortex relaxes into a structure controlled by the cylinder wall.

The measured and predicted radial profiles of the axial mean velocity and turbulence intensity for the axial location Z = 15 mm, at θ = 36° CA and 90° CA during induction, are presented in Figures 5.19(a) and (b), respectively. The predictions of all turbulence versions are identical, due to the absence of significant compressibility effects* during induction, for the present engine speed of 200 rpm. The measurements show a jet-like flow with recirculation regions near the cylinder wall and in the valve wake, consistent with the predicted pattern noted earlier in Section 5.5.1.1, with high levels of turbulence in the shear layers of the jet and in the recirculation zone near the cylinder wall.

The comparison at θ = 36° CA shows good qualitative and quantitative agreement between the measurements and the predictions. The main discrepancies are the under-prediction of the peak velocities and turbulence intensities of the induction jet and the recirculation zone near the cylinder wall. These discrepancies could be due to a variety of causes, including (i) the assumed plug velocity distribution of the intake jet, (ii) insufficient spatial resolution of the computational grid, and (iii) the deficiencies discussed earlier of the k-ε model in shear flows with extra rates of strain due to streamline curvature (Bradshaw [1973],

---

* As can be seen from equation (3.57), the model versions become identical when the dilatation term $\nabla.\tilde{U}$ and the temperature variations are small.

Rodi & Scheuerer [1983b]) and appreciable 'normal' strain rates (Rodi & Scheuerer [1983a]). The apparent large under-prediction of u' in the region of the jet can also be partly due to measurement over-estimation (by as much as 20%) arising from Doppler- and crank-angle broadening effects (Arcoumanis, et al. [1982b]). The good agreement, in respect of u', in the recirculation zone behind the valve shows that the predicted small convection and diffusion of turbulence outside the region of intake jet, discussed in Section 5.5.1.1, is correct.

The measurements at $\theta = 90°$ CA show a deflection of the induction jet towards the cylinder axis, due to the stretching of the main vortex by the piston, and an increase in its peak velocity to about $10.5\ \overline{V}_p$, accompanied by increases in the level of u'. Increase is also evident in the strength of the recirculating patterns and level of u' behind the valve, in general agreement with the predicted flow evolution depicted in Figures 5.16. The predictions of the turbulence models are again almost identical and, allowing for the discrepancy in the location of the peak jet velocity which is due to the assumed constant angle of entry of the intake flow (already discussed in Section 5.4), are in good agreement with the data. The under-prediction of the $\overline{U}$ and u' in the recirculation region behind the valve is partly due to the error in the prediction of the location and peak velocity of the induction jet; although it can also be attributed to the deficiencies of the k-ε model in recirculating flows. In this connection, it is pertinent to note that the study of Taylor [1981] of stationary recirculating flows behind axisymmetrical confined baffles shows considerable discrepancies between measurements and the predictions of the k-ε model in respect of both the strength and size of the recirculation zone and the level of turbulence intensity therein (which, except in the vicinity of baffle, is considerably under-predicted).

Figure 5.19(c) presents similar comparisons at mid-compression ($\theta = 270°$ CA) and provides evidence of the extent of decay of the intake-generated flow. According to the data, the mean flow at the measurement location ($Z = 15$ mm) is nearly one-dimensional, in the direction of the piston motion, except for a weak vortex near the cylinder wall, remaining from the intake stroke. The turbulence intensity has decayed to the level $u' \simeq 0.8\ \overline{V}_p$ and is virtually homogeneous. The predictions of the three turbulence models are almost identical and their comparison with the data shows that, as evidenced by Figure 5.18, the rapid decay of the mean flow and turbulence near the end of induction/early compression has been under-predicted by all versions, rendering a

larger and stronger vortex and higher level of u' than are measured (although the tendency towards homogeneity is well predicted). The under-prediction of the decay process is partly caused by the numerical effects due to the computational time-step, discussed in Section 5.3; other factors are the turbulence model deficiencies identified earlier. An additional and important factor is the suitability of the Couette flow based wall functions for unsteady recirculating flows; for instance, in the present conditions, a larger level of wall shear stress could produce a larger decay of the induction generated mean flow and turbulence (noting that, as discussed earlier, the level of u' is largely influenced by turbulence generation by the persisting main vortex).

The accurate prediction of the flow near the end of compression/early expansion is of particular importance due to its influence on the combustion process (see, for example, Cole & Swords [1980], Witze, et al. [1983b]). The results for this phase, in the form of radial profiles of $\overline{U}/\overline{V}_p$ and $u'/\overline{V}_p$ at several axial locations, are presented in Figures 5.20, 5.21 and 5.22 corresponding to θ = 324°, 360° and 380° CA, respectively. (Note the change of the scale in these figures.)

The measurements at θ = 324° CA show that the mean flow is dominated by the piston motion and is largely one-dimensional, although there are remnants of the main vortex in the cylinder head/wall corner. The apparent flow structure in the region near the cylinder head/axis is either (i) the remains of a vortex generated behind the valve by the outgoing flow during early compression, that has not been predicted, (ii) a weak recirculation generated near the end of compression, or (iii) a consequence of measurement errors in a strongly turbulent flow with small mean velocity (Bicen [1984]). The measurements of the turbulence intensity show a homogeneous structure with a mean level of $u' \simeq 0.6$ to $0.7\ \overline{V}_p$.

The predictions based on the different turbulence models are very similar: those of MM and ET are almost identical and the Watkins version produces slightly weaker mean flow and larger turbulence intensity. The agreement with the data, in respect of the mean flow, is impaired by the under-prediction of the decay of the main vortex (throughout the compression stroke). However, the turbulent intensities are in rather good agreement with the data, with the level of agreement depending on the (axial) location (Figure 5.20). The good agreement with regard to u', despite the large discrepancies in the mean flow, is due to (i) the small contribution of the turbulence generation by the persisting

main vortex to the turbulence energy balance (Figure 5.17(c)), and (ii) the controlling influence of the cylinder walls on the turbulence structure (explained in Section 5.5.1.1). However, the slight over-prediction of the turbulence intensity near the cylinder head indicates that the predictions are in some regions influenced by the turbulence generation due to the strain field caused by the persisting main vortex.

The measurements of Figure 5.21 (θ = 360° CA) show an almost quiescent flow and homogeneous turbulence of level $u' \simeq 0.55$ to $0.6\ \overline{V}_p$. The predictions of all turbulence models are similar, with, as before, the Watkins version producing slightly weaker mean flow and larger turbulence. Although the calculated vortex strength has considerably reduced compared with that at θ = 324° CA, its persistence is still sufficient to taint the agreement with the measurements.

The agreement in respect of the turbulence intensity continues to be good, and has especially improved near the cylinder head, due to the decay of the vortex structure. The performance of the turbulence models now depends on location: the MM and ET versions give excellent agreement with measurements near the cylinder head, while this is the case for the Watkins version near the piston.

The measurements of Figure 5.22, for early expansion (θ = 380° CA), show a one-dimensional mean flow in the direction of the piston motion and a homogeneous turbulence level of $u' \simeq 0.45\ \overline{V}_p$. The different turbulence models still give similar predictions, with the Watkins version producing slightly weaker mean flow and larger turbulence intensity. The predicted turbulence intensities are in excellent agreement with data. The agreement with the measured mean velocities is still poor because of the lingering effects of the main vortex.

The results presented in Figures 5.20, 5.21 and 5.22 show that the predictions of the mean flow and turbulence are not sensitive to the choice of the turbulence model in the present circumstances. This is due to the fact that, as will be discussed later in Section 5.6, the MM and ET versions produce almost identical turbulent viscosities, and although the Watkins version produces larger levels of μ_T during $\theta \simeq 235°$ to 395° CA (due to the larger levels of ℓ it predicts (Figure 5.28)), during this phase the mean flow is dominated by the piston-induced pressure gradients, and the strength and hence the contribution of turbulence generation by the persisting main vortex to the k-energy balance (Figure 5.17) are rapidly decreasing.

5.5.2 Test Case II (Arcoumanis, et al. [1981a])

5.5.2.1 The predicted flow evolution

Figure 5.23(a) presents plots of the velocity field for this case and Figures 5.23(b), (c), (d) and (e), respectively, show the distributions of the turbulent intensity ($u'/\overline{V}_p$), length-scale (ℓ/B), time-scale (τ_d/T_{cycle}) and viscosity (μ_T/μ) at selected crank angles during induction, compression and early expansion strokes. The predictions are obtained with the Morel & Mansour [1982] k-ε version.

The results show that during early induction (θ = 36° CA), the intake jet impinges on the piston and produces a different flow structure than in the lower compression ratio case (Figures 5.17), in agreement with the measurements of Arcoumanis, et al. [1982a] (also Bicen [1983]) in a similar engine. The distribution of u' (diagram (b), θ = 36° CA) shows the generation of large turbulence levels within the shear layers and the impingement location: the levels in the intake jet region are similar to those for Case I, but the levels in the main vortex are larger, in accord with the data of Bicen [1983].

The distribution of ℓ (diagram (c), θ = 36° CA) shows its growth along the axis of the induction jet, consistent with the characteristics of stationary jets (Looney [1982]), and two regions of large ℓ within the centres of the vortices. The levels within the intake jet and the vortex near the cylinder head/wall are almost identical to those for Case I, indicating dependence of the former on the valve lift and the strong influence of the chamber walls on the latter; but, in the main vortex, the influence of flow structure is evident. Similarly, the distribution and levels of τ_d (diagram (d), θ = 36° CA) in the regions of the intake jet and the vortex near the cylinder head/wall are similar to those for Case I, but are considerably different in the main vortex due to the larger transport of the induction jet turbulence (generated also at the impingement location) as a result of the reduced convection time-scale, and sustainment by the stronger mean strain rates in this region, for the present case.

The distribution of μ_T at θ = 36° CA shows the largest levels at the location of the jet impingement on the piston and near the centres of the vortices. With the exception of the main vortex, where the level of μ_T is expectedly larger than in Case I, the levels are similar in the two cases.

Later in the induction stroke (θ = 72° CA), the growth of the main vortex and its stretching and displacement by the descending piston causes outward deflection and impingement of the intake

jet on the cylinder wall and produces a similar flow structure to that for the low compression ratio Case I, in accord with the data of Arcoumanis, et al. [1982a] (also Bicen [1983]). The distribution of turbulence intensity (diagram (b)) shows generation of large levels of u' within the induction jet and at the location of impingement on the cylinder wall: the levels in the induction jet are as in Case I, but are larger by nearly 60% within the main vortex.

The distribution and levels of ℓ at θ = 72° CA, both within the intake jet and the main vortex, are almost identical to Case I. This illustrates the rapid transformation of the turbulence structure, from that at θ = 36° CA, and a similarity due to the dependence of ℓ within the main vortex on the cylinder geometry. The distribution of τ_d at 72° CA is similar to that for Case I, but the levels in the main vortex are nearly 50% smaller, in accordance with the predictions of u' and ℓ.

The pattern of distribution of μ_T is similar to that for the low compression ratio Case I, but the levels are similar only in the jet region, being larger by nearly 70% in the main vortex and 140% in the region behind the valve. The substantially larger level of μ_T in the last named region is believed to be a consequence of the deficiencies of the turbulence model, discussed earlier in Section 5.5.1.1.

The evolution of the mean flow during the rest of the induction stroke is similar to that for the low compression ratio Case I, except that in the present case the third vortex in the cylinder wall/piston corner is formed earlier in the stroke (at $\theta \simeq 90°$ CA) and is larger and stronger. Although the decay of the mean flow near the end of induction is faster due to the substantially larger levels of μ_T (see Figure 5.23(e)). These and other features noted above are consistent with the experimental study of Arcoumanis, et al. [1982a] and Bicen [1983] concerning the effects of the clearance gap on the flow structure during the induction stroke.

The evolution of the turbulence, as shown by the distributions of u' (Figure 5.23(b)), is similar to that for Case I: u' within the intake jet falls after θ = 90° CA in accord with the reduction in the intake jet momentum, and an identifiable turbulence structure is formed within the main vortex by θ = 108° CA. The turbulence intensity in the latter region initially increases (θ = 108° to 126° CA), and then decays (θ = 126° to 180° CA), as the mean flow weakens. The peak levels of u' in the shear layers of the induction jet and the impingement region on the cylinder wall are only slightly larger ($\simeq$ 10%) than in Case I, indicating that the turbulence level in these regions depends primarily on

the intake jet momentum which is almost identical for the two cases (see Chapter 6). However, there is an important influence of the early induction flow structure on the average turbulence levels, as evidenced by the considerably larger values ($\simeq$ 60%) within the main vortex. This is due to the considerably larger turbulent viscosities (nearly 70% to 100%) and thus higher levels of turbulence energy production in this region, in the present case. These higher turbulence levels, however, decay at faster rates during late induction than in Case I, due to the considerably smaller dissipation time-scales and larger weakening of the mean flow in this case, producing u' levels that are only 15% larger (than in Case I) by the end of induction at θ = 180° CA. These trends are in accord with the measurements of Bicen [1983].

The distribution and evolution of ℓ during θ = 72° to 180° CA are similar to that for Case I, except in the region of third vortex near the piston, where considerably larger (nearly 80% in this case) levels of ℓ evolve in accord with the previously discussed increase of ℓ in the vortex structure. The other significant difference between the two cases is that after the flow transformation at θ = 72° CA, ℓ within the main vortex, in the present case, tends towards slightly larger levels than in Case I, probably due to the stronger curvature effects, with the maximum difference of nearly 16% occurring at θ = 126° CA, when an identifiable structure in the main vortex is formed. The differences decrease, with the turbulence decay near the end of induction, to 10% at θ = 180° CA.

The distributions of τ_d (Figure 5.23(d)) are similar to those for Case I; however, the levels and the details of its development in the regions of the main and the third vortex (near the piston) are significantly different in the present case. The levels of τ_d, after the flow transformation at θ = 72° CA, are smaller than in Case I by nearly 40% in the main vortex and 70% near the piston, due to the larger mean strain rates and higher levels of u'. These differences remain almost constant, due to similar rates of increase of τ_d in the two cases, until θ = 126° CA. Thereafter, τ_d increases more rapidly in the present case, producing levels in the main vortex at the end of induction that are nearly 10% smaller than in Case I. This increase in the time-scale is consistent with the more rapid decay of the mean flow and turbulence intensity near the end of induction in the present case. However, in spite of a similarly large increase in τ_d in the region of the third vortex, the differences between the two cases (in the peak levels in this region) remain relatively large (τ_d is 20% to 40% smaller in this

case), due to a stronger vortex and dissimilar levels of ℓ in this region.

The overall distribution and evolution of μ_T (Figure 5.23(e)) during the period θ = 72° to 180° CA are similar to that for Case I, but the levels are larger in accordance with higher levels of u' in this case. The differences decrease near the end of induction, due to the larger decay of u' in Case II (for example, μ_T in the main vortex is larger than in Case I by nearly 100% at θ = 72° CA and 35% at θ = 180° CA).

The evolution of the mean flow during the compression stroke (Figure 5.23(a)) is similar to that in Case I: the ring vortex near the cylinder head/wall breaks up by the time of inlet valve closure (θ = 234° CA) and the (in this case, stronger) vortex near the piston decays and disintegrates after mid-compression (θ = 270° CA), with the mean vortex decaying to a lingering weak motion at θ = 360° CA. The most noteworthy quantitative difference is the appreciably more rapid decay of the main vortex during early compression (evident at θ = 234° CA) due to the larger turbulent viscosities and the consequent weaker remnants, than for Case I.

The distributions of u' during compression are similar for the two cases and show decay and tendency of turbulence towards homogeneity; however, the details of its evolution are slightly different. Here, the turbulence decays more rapidly during early compression than in Case I, due to the more rapid weakening of the mean flow and smaller levels of τ_d, producing about 15% lower levels of intensity at θ = 234° CA. Thereafter, the rate of decay becomes nearly similar to that for the lower compression ratio case, so that by TDC (θ = 360° CA), the level of u' ($\simeq 0.45\ \overline{V}_p$) is only 10% smaller than that of Case I.

The distributions of ℓ (Figure 5.23(c)) during compression are similar to those for Case I, except for in the region near the piston where the larger levels of ℓ associated with the third vortex are evident until θ = 270° CA. However, the temporal variation is different, even before the influence of the clearance gap becomes predominant. Comparison of the levels for the two cases at θ = 180° CA and θ = 198° CA shows that in the present case, ℓ is nearly 10% larger at BDC ($\ell \simeq 0.077\ B$) and, despite larger decay of u', the increase in ℓ during θ = 180° to 198° CA is smaller than in Case I. The likely explanations are that (i) the rapid decay of the mean flow reduces the influence of streamline curvature (which tends to increase ℓ in the recirculation region) such that it offsets the concurrent increase in ℓ due to the decay of turbulence, or (ii) the length-scale has reached a

limiting level controlled by the cylinder diameter. In connection with the latter explanation, the experiments of Prudnikov [1963] concerning the decay of grid-generated turbulence in tubes show that, for different grid geometries, the length-scale of the turbulence approaches a limiting level (the 'normal' scale of turbulence for the tube) with distance from the grid, and further decay of intensity proceeds without an increase in the length-scale. In this respect, it is interesting to note that the largest ℓ at θ = 180° CA near the cylinder axis exceeds by only 10% the mixing length* at the centre of a fully-developed turbulent pipe flow (Launder & Spalding [1982], p. 73).

The length-scale decreases moderately during θ = 198° to 270°, despite the continuous decay of turbulence, due to the effect of compression on the turbulent eddy size. However, as in Case I, the rate of reduction rapidly increases near the end of compression stroke (θ = 324° CA) as the influence of the clearance gap becomes predominant. The level of ℓ at TDC (θ = 360° CA) is nearly 68% of that for the low compression ratio case. This is larger than the ratio of the clearance gaps for the two cases ($\simeq$ 45%) and indicates that ℓ at TDC is not simply proportional to the geometrical parameters but also is influenced by the turbulence history.

The distribution and development of τ_d during compression (Figure 5.23(d)) is similar to that for Case I: it increases up to mid-compression (θ = 270° CA) due to the rapid decay of u' exceeding the effect of compression on ℓ; then it decreases during θ = 270° to 324° CA as the influence of the reduction in clearance gap on ℓ becomes predominant; finally, it tends to remain constant during θ = 324° to 360° CA as the rate of reduction in ℓ falls. The influence of the main vortex is evidenced by the more rapid (than elsewhere) increase of τ_d there, during θ = 180° to 270° CA (as in Case I); however, at θ = 324° CA, no apparent structure associated with the main vortex remains (this is also true for other turbulence parameters), indicating the relaxation of turbulence into a structure controlled by the engine geometry. The level of τ_d at TDC for the present case is nearly 70% of that for Case I. This is in accord with the measurements of Semenov [1963] (analysed by Dent & Salama [1975a]) and Dent & Salama [1975a] that show a reduction of λ_y (and thus τ_d, according to equation (2.26)) at TDC, with increase in the compression ratio.

---

* The dissipation length-scale as defined here is equivalent to the mixing length in the pipe flow.

The distributions of μ_T during compression are also as in Case I, with the largest levels near the cylinder axis behind the valve; but the levels are different. In the present case, μ_T (which is nearly 50% larger than in Case I at θ = 180° CA) falls rapidly due to the greater decay of u' during early compression: the result is similar levels for the two cases at θ = 270° CA. Thereafter, μ_T increases briefly during θ = 270° to 324° CA due to the reduction in the rate of decay of turbulence, as a result of significant contribution from turbulence generation by compression (see Section 5.5.2.2 and Figure 5.24(c)) and then reduces (θ = 324° to 360° CA) as the level of generation falls and the rate of decay of turbulence increases (Figure 5.24(c)). The level of μ_T at TDC is nearly 25% larger than for the low compression ratio.

During early expansion, the residual vortex structure breaks up more rapidly than in Case I, resulting in a one-dimensional flow at θ = 414° CA. The turbulence decays rapidly during the interval θ = 360° to 414° CA, at a similar rate to that for Case I (nearly 1% per CA degree); but the results for θ = 432° CA show considerable reduction in the rate of decay (to nearly 0.4% per CA degree) due to the rapid increase of τ_d. The length-scale during early expansion progressively increases at a larger rate than in Case I (70% during θ = 360° to 414° CA), due to the larger effect of expansion on the turbulence; the rate of increase falls later as the cylinder diameter again becomes the dominant geometrical constraint. This behaviour is consistent with the variations of the turbulence decay rate.

The dissipation time-scale (Figure 5.23(d)) increases rapidly in accordance with the variations of u' and ℓ. The turbulent viscosity (Figure 5.23(e)) falls rapidly during early expansion (nearly 54% during θ = 360° to 414° CA) but the rate of reduction decreases later on, as the turbulence decay slows down.

The distributions of all turbulence parameters during expansion show complete relaxation of the turbulence into a structure controlled by the engine geometry. Their comparison with diagrams for the compression stroke indicates that the influence of the persisting main vortex on the turbulence structure (during compression) is to establish the largest levels of ℓ and μ_T behind the valve (as discussed earlier, likely because of the relatively significant normal strain rates in this region) and to produce a region of small (and moderately varying) τ_d near its centre.

5.5.2.2 The integral balances of the k-ε transport equations

Figure 5.24 presents the term-by-term volume-integral balances of the components of the k- and ε-transport equations. The results for the induction, compression and early expansion strokes are given in Figures 5.24(a) and (b), while Figures 5.24(c) and (d) present the expanded results for the compression/early expansion strokes.

The general trends and the near-equilibrium (production ≈ dissipation) balance of the k and ε equations during induction are as in Case I; however, there are appreciable differences in the details, indicating the influence of the induction-generated mean flow on certain features of the turbulence evolution.

Figure 5.24(a) shows rapid increase of G_N and G_S during early induction ($\theta \simeq 30°$ to $50°$ CA) due to the intake jet impingement on the piston and considerable turbulence generation in the main vortex. The level of G_N is similar to that in Case I, but G_S is markedly larger (nearly 140%) due to the large levels of turbulent viscosity in the main vortex (nearly 110%) and stronger mean flow strains in this region. The turbulence level increases at a larger rate than in Case I, during the phase corresponding to the intake jet impingement on the piston.

After the mean flow transformation (to that in which the intake jet impinges on the cylinder wall) at $\theta \simeq 50°$ CA, G_S initially decreases ($\theta \simeq 50°$ to $90°$ CA) due to the reduced shear strain rates, and then increases to the same level as in Case I, at $\theta \simeq 125°$ CA, due to the formation of the turbulence structure within the main vortex. G_N rapidly increases initially ($\theta = 50°$ to $80°$ CA) to a level nearly 30% larger than in Case I, and remains nearly constant for the period $\theta = 80°$ to $130°$ CA. This, in view of the similar intake jet velocities in the two cases (see Figure 6.1), may be due to the considerable turbulence generation by the normal strain rates in the region of the valve wake (μ_T here is nearly 140% larger than in Case I), evidenced by the large levels of u' in this region in the present case (see Figure 5.23(b)). During this phase, turbulence is in a quasi-equilibrium state, whereby over the cylinder volume its production is balanced by dissipation.

The fall in the levels of G_S and G_N starts earlier near the end of induction (i.e. $\theta \simeq 120°$ CA) and is larger than in Case I, due to the already noted larger decay of the mean flow during this phase in Case II. Consequently, the decay of turbulence starts earlier and the rate of decay is throughout larger than in Case I.

The results for after intake valve closure (Figure

5.24(c)) show rapid reduction of G_N and G_S in the period θ = 210° to 270° CA. The levels are only 40% of those in Case I, confirming the larger decay of the intake-generated mean flow in the present case. The turbulence generation by compression G_C is relatively large (as opposed to Case I, here it exceeds G_N and G_S during most of the compression stroke) and tends to reduce the rate of decay of k during $\theta \simeq 270°$ to 320° CA (the period of largest $\nabla.\tilde{U}$). However, thereafter, with the reduction of G_C, the rate of decay of k increases (as opposed to its continuous reduction in Case I), reaching a maximum just before TDC ($\theta \simeq 350°$ CA). This is due to the ε-production by compression (see Chapter 3) that as both Figures 5.24(c) and (d) show tends to augment the level of ε near the end of compression.

According to Figure 5.24(c), at TDC, turbulence is in a state of pure decay ($\partial k/\partial t \simeq \varepsilon$). This condition is maintained during early expansion, with the rate of decay of k falling continuously in accord with the characteristics of the decay process (Batchelor [1960], Tsuge, et al. [1973]).

5.5.2.3 *Comparison with experimental data*

The comparison of the predictions obtained with the different turbulence models and the measurements, in the form of radial profiles of the normalised axial mean velocity $\overline{U}/\overline{V}_p$ and turbulence intensity $u'/\overline{V}_p$, are presented in Figures 5.25, 5.26 and 5.27, corresponding to θ = 324°, 360° and 378° CA, respectively.

The measurements at θ = 324° CA show a mean flow in the direction of the piston motion and a nearly homogeneous turbulence intensity of around $u' \simeq 0.5$ to $0.6\ \overline{V}_p$. The axial velocity is not uniform near the cylinder head (at Z = 10 mm) and exhibits a peak near the cylinder wall: comparison with the uniform velocity at this location due to the piston motion, obtained from the one-dimensional theory (i.e. $\overline{U}(z) = (z/z_p)\ U_p$), indicates a clear tendency towards formation of a vortex near the cylinder head. This feature has been overlooked by Arcoumanis, et al. [1981a], and in the absence of measurements during earlier phases of the compression stroke, its origin cannot be identified.

The almost quiescent flow at TDC (Figure 5.26) clearly shows the total dependence of the mean flow on the piston-induced pressure gradients. The turbulence intensity at TDC is nearly homogeneous with a level of $u' \simeq 0.45$ to $0.5\ \overline{V}_p$. Hence, the effect of the increase in compression ratio between Cases I and II is to slightly reduce u' at TDC.

The measurements at θ = 380° CA (Figure 5.27) show the emergence of a jet near the cylinder wall early during the expansion stroke, due to the rapid expansion of the entrapped air in the cylinder wall/piston crevice, resulting in considerably large velocity and high levels of u' (in the low compression ratio of Case I, this jet emerges later in the stroke (θ = 410° CA) and is weaker (Arcoumanis, et al. [1981a])). However, as is evident in Figure 5.27, the influence of the jet is confined to the region near the wall and the mean flow within the bulk of the cylinder remains essentially one-dimensional, with a uniform turbulence level of nearly $u' \simeq 0.35\ \overline{V}_p$.

The results presented in Figures 5.25 to 5.27 show that as in Case I, the predictions of the MM and ET versions are almost identical, whereas the Watkins version predicts slightly weaker mean flow (i.e. larger decay of the intake-generated main vortex) and higher levels of u'. Overall, the agreement between all predictions and the data, in respect of the mean velocity, is better than that for Case I, but still suffers from under-prediction of the decay of the induction-generated structure. The agreement improves towards the end of compression and, as Figure 5.26 shows, the essentially quiescent flow at TDC is reasonably well reproduced. The flow associated with the emergence of the wall-jet at θ = 380° (Figure 5.27) is not predicted since, in the computations, the clearance between the piston and the cylinder wall has not been represented; however, the agreement with measurements in the bulk of the flow is reasonably good.

The calculated turbulence intensities are in excellent agreement with the measurements, apart form in the region of the wall jet (at θ = 380° CA). In this respect, the agreement is better than in Case I, due here to the lessened influence of the weakened persisting vortex structure on the turbulence (as evidenced by the volume-integral balance of the k-equation in Figure 5.24(c)).

With regard to the relative accuracy of the turbulence models, the MM and ET versions produce superior agreement, than that of Watkins, with the measured turbulence intensities. However, the larger decay of the intake-generated flow structure predicted by the Watkins version renders better agreement in respect of the mean flow. Therefore, there is no clear-cut 'best' performer. Furthermore, the differences between the predictions are small and an assessment on the grounds of comparison with the data for the cases examined here cannot be conclusive, especially in view of the possible influence of the deficiencies (of all versions) of the turbulence model in such complex flows.

It should be pointed out that in the review of previous work in Chapter 2, larger differences between the predictions of u' during compression and expansion were observed in the studies of MM and ET between these and the Watkins model. However, these studies did not include simulation of the induction process and essentially involved compression/expansion of a homogeneous turbulence field: most significantly, they showed an increase in the level of u' during compression. The latter contrast with the findings of the present study is an indication of the unrepresentative initial conditions employed by the forementioned investigators for k and ε, as opposed to those generated by the present induction simulation. In particular, it is believed that their arbitrary choices have led to excessively large levels of τ_d ($\equiv k/\varepsilon$): this, on one hand, reduces the effect of turbulence energy production in augmenting the dissipation rate ε (as inspection of the ε-transport equation (3.57) will confirm, the 'production' terms are multiplied by τ_d^{-1}) and, on the other, increases the sensitivity of the ε-transport equation, and thus k, to the terms $C_3 \bar{\rho} \varepsilon (\partial \tilde{u}_\ell / \partial x_\ell)$ and $C_4 \bar{\rho} \varepsilon (\partial \bar{\mu} / \partial t)$ (which are independent of τ_d).

5.6 ASSESSMENT OF THE TURBULENCE MODELS

It is evident from the preceding section that in the present circumstances, the experimental data of Cases I and II do not provide a suitable testing ground for assessment of the relative merits of the turbulence model variants, since they all produce closely similar predictions of the measured quantities. Therefore, in the present section, the behaviour of further predicted flow parameters are examined and compared, with a view to identify which model yields the most consistent and physically plausible variations.

The predicted point values at the location Z = 15 mm, r = 25 mm of the normalised quantities $\bar{U}/\bar{V}_p$, $u'/\bar{V}_p$, ℓ/B, τ_d/T_{cycle} and μ_T for the three variants of the turbulence model are presented in Figure 5.28 for the conditions of Case I. Figure 5.29 contains similar plots for the conditions of Case II at the location Z = 10 mm, r = 25 mm*.

The results show that the turbulence models predict almost identical variations of all parameters during induction, since as pointed out earlier during this phase the effect of compressibility, for the (low) engine speed of 200 rpm, is small. However, during the compression and expansion

---

* In Case II, the results at Z = 15 mm are influenced by wall effects (of the piston) due to the small clearance gap at the TDC compression.

strokes, the variations of the parameters ℓ, τ_d and μ_T produced by the Watkins version are substantially different from those of the MM and ET variants, as will now be discussed.

The Watkins version predicts large increases of ℓ, τ_d and μ_T during the interval θ = 220° to 330° CA, followed by rapid falls of all three (except for τ_d in Case I which reduces relatively slowly) during θ = 330° to 450° CA. With regard to these variations, MM argue that the increase of ℓ during the compression stroke is physically implausible on the grounds that it can be expected that any element of the turbulence will physically contract with the compression of the fluid. However, as noted earlier, the increases in ℓ and τ_d are characteristics of the turbulence decay process (Batchelor [1960]) and thus this argument is not sufficient to prove the inadequacy of this model (since it may be argued that the decay process overwhelms the effect of compression on the turbulence). However, the predicted reductions of ℓ and τ_d during the expansion stroke are incompatible with the decay of turbulence intensity and the effect of expansion on turbulence (both tending to increase ℓ). Furthermore, the increase of ℓ near TDC compression (θ = 330° CA) with increase in compression ratio (evidenced by Figures 5.28 and 5.29) is physically incorrect (since it can lead to ℓ larger than the chamber dimensions, for higher compression ratios). Therefore, it must be concluded that the Watkins [1977] version is not suitable for application to engine flows.

The MM and ET versions predict similar trends for all turbulence parameters during the compression and expansion. According to these models, during compression ℓ decreases, τ_d increases and μ_T may decrease or increase moderately, depending on the variations of u', ℓ and the fluid density. The differences between the predictions are small, with the MM version producing smaller levels of both scales and the turbulent viscosity.

During expansion, ℓ increases initially (θ = 360° to 420° CA), due to the increase in the clearance gap and the effect of expansion, but thereafter tends towards an asymptotic value (which, in the case of MM, is similar to the level of ℓ during early compression), indicating the constraints imposed by the chamber walls on the growth of the length-scale. However, τ_d increases rapidly throughout (in accord with the characteristics of the turbulence decay) and μ_T falls. The differences between the predictions of the two models are larger than during compression, with the MM version producing greatest increases in ℓ and τ_d. This departure of the predictions of these two versions is due to the insignificant turbulence energy production by the mean flow and hence a

substantially larger rôle of the compressibility term in the balances of the k- and ε-transport equations (as evidenced in Figures 5.17 and 5.24). However, the predictions of both models are compatible and consistent.

It appears that on the basis of the above observations, either of the two variants could be selected for engine applications. However, the MM version predicts the growth of ℓ during expansion to a level similar to that at the beginning of the compression stroke (the asymptotic value predicted by the ET version is noticeably smaller) which is plausible on the grounds that only the chamber geometry imposes a constraint on the growth of ℓ during expansion. Therefore, on this basis, the MM version is marginally preferable. This version is thus employed in the studies presented in Chapter 6.

5.7 CLOSURE

This chapter has been concerned with the detailed analysis of the in-cylinder flow evolution and assessment of the performance of the calculation method and three variants of the k-ε turbulence model through comparison of the predictions with two sets of data.

In Section 5.3, the numerical solutions have been tested for the grid-size and time-step dependence. It was found that the predictions of the mean flow in the region of the induction jet were not strongly sensitive to the grid and time-step size; however, the strength and size of the downstream recirculating (vortex) pattern and the level of turbulence intensity throughout were greatly influenced. In particular, it was found that reduction of the computational time-step produces a stronger vortex and higher levels of u' during early induction and a faster decay of both near the end of induction/early compression, which is in closer agreement with the measurements. It was also found that, although the time-step could be made sufficiently small to reduce the temporal errors to acceptable levels, the same could not be done in respect of spatial errors, due to the rapid increase in computing costs with grid refinement. Nevertheless, it is believed that the accuracy is sufficient for the purposes of this study.

In Section 5.4, the influence of modifications to the inlet boundary conditions on the predictions has been assessed by comparing the results for two different treatments of the inlet flow with measurements. It was found that the influence on the predicted mean flow and turbulence level is appreciable during induction, but gradually diminishes to a small level by TDC compression.

In Section 5.5, the predicted evolution of the in-cylinder flow has

been analysed in depth. This analysis and detailed comparison with the known features of similar stationary and non-stationary flows revealed areas of uncertainty due most likely to known deficiencies of the turbulence models in flows with (a) strong streamline curvature, (b) significant normal strains and adverse pressure gradient, and (c) large variations in the ratio of the turbulence production to dissipation rate (P/ε).

In respect of the flow evolution in engines, it was found that:

(i) The induction jet separates at the valve head and seat and forms recirculating patterns within the cylinder, whose strength, size and development during the induction stroke are strongly influenced by the clearance gap, in agreement with experiment.

(ii) During early induction, high levels of turbulence, with length-scale of the order of the valve lift and dissipation time-scales $\tau_d \simeq 10^{-2}\ T_{cycle}$, are generated within the induction jet; but the transport of turbulence into other regions is limited, as evidenced also by the measurements, due to the smallness of τ_d compared with the time-scale of the transport processes.

(iii) The intake jet impingement on the piston early in the stroke for the higher compression ratio engine does not influence the intake jet turbulence, but produces considerably higher u' levels within the bulk of the flow, in agreement with the data.

(iv) The intake jet turbulence is in quasi-equilibrium and a quasi-steady state prevails compared with the time-scale of the induction process (i.e. the period of the induction stroke).

(v) During late induction, the intake jet u' falls but turbulence is generated within the main recirculation region in the valve wake, as evidence by the data. A turbulence structure is formed in this region whose development is largely independent of the induction jet turbulence and is influenced only by the cylinder walls.

(vi) Near the end of induction, with the rapid fall-off of the intake jet momentum, the mean flow and turbulence decay. However, the induction-generated vortex structure persists under its inertia and the decay of turbulence there is less rapid, again in accord with the measurements.

(vii) During compression, the induction-generated flow decays and, apart from the main vortex, disintegrates before TDC. The turbulence decays and tends towards homogeneity, and relaxes into

a structure predominantly controlled by the chamber geometry near the end of compression; although the turbulence at TDC still retains part of its induction history.

(viii) The length-scale is largely controlled by the cylinder diameter during early compression and the clearance gap near the end of the stroke.

(ix) During expansion, the flow is one-dimensional in the direction of the piston motion, in accord with measurements. The turbulence decays (especially rapidly during early expansion) and retains its cylinder geometry-controlled structure.

(x) The influence of an increase in compression ratio is to produce a stronger mean flow and higher turbulence levels during early induction that decay more rapidly during the late induction and the compression strokes, thereby producing weaker mean flow and slightly lower turbulence level near the TDC, in accord with the measurements.

The volume-integral balances of the k- and ε-transport equations during the induction and compression strokes have been analysed and it has been found that:

(xi) During early induction, the mean turbulence level increases with increase in the turbulence generation by the induction jet; but, due to the small dissipation time-scale of the induction turbulence, ε increases nearly as $P \geq \varepsilon$. A quasi-equilibrium state is then reached, in which turbulence generation is balanced by dissipation both within the flow and due to the effect of the cylinder walls. Near the end of induction, the mean turbulence decays with the rapid fall of the turbulence generation.

(xii) The turbulence advection into the cylinder by the intake flow is negligible, as is also shown in experiments.

(xiii) The intake jet impingement on the piston during early induction for higher compression ratio significantly increases the turbulence generation, especially in the recirculating flow in the valve wake.

(xiv) During compression, turbulence decays continuously, despite its generation by the persisting induction-generated flow and by compression. At TDC, the turbulence is in a state of pure decay.

(xv) Turbulence generation by compression contributes also to the sustainment of ε, and for higher compression ratio tends to

produce a relatively larger decay of turbulence near the end of compression.

(xvi) The turbulence generation due to piston-induced normal strains (i.e. $-2/3\,\mu_T\,\nabla.\tilde{U}^2$) is negligible.

(xvii) The level of turbulence dissipation due to the effect of cylinder walls is significant during both induction and compression.

The accuracy of the calculation method has also been assessed in Section 5.5, by comparing predictions based on three variants of the k-ε model with measurements. It was found that:

(xviii) For the cases of this study, the turbulence models produce closely similar predictions of the mean flow and turbulence intensity throughout the engine cycle.

(xix) During induction, the calculations are in good qualitative and moderate quantitative agreement with the measurements. The discrepancies are believed to be in part due to the assumed constant angle of entry of the intake flow in the calculations, which the recent measurements show varies during induction.

(xx) The decay of the mean flow and turbulence intensity during late induction/early compression is under-predicted, due in part to the effects of the computational time-step and grid and the known deficiencies of the turbulence model.

(xxi) During late compression/early expansion, the predicted turbulence intensities are in good agreement with the data, but the agreement in respect of the mean flow is impaired by longer persistence of the predicted induction-generated flow.

(xxii) Due to the close similarity of the predictions of the turbulence models and the lack of a clear pattern of agreement with the measured quantities, their relative merits cannot be assessed on the basis of this information alone.

In the light of the above findings, in Section 5.6 the predictions of further turbulence parameters have been analysed and compared, in order to identify which model yields the most consistent and physically plausible behaviour. It was found that on this basis, the Watkins [1977] version is not suitable for application to engine flows, but the Morel & Mansour [1982] and El Tahry [1983] versions are both suitable, with the former one marginally preferable.

CHAPTER 6
STUDY OF TURBULENT ENGINE FLOWS

6.1 INTRODUCTION

This chapter presents a study of the influence of variations in compression ratio, engine speed and valve-lift characteristics on the in-cylinder mean flow and turbulence in an axisymmetric, disc-chamber, central-valve model engine. The aims of this study are to identify the important features associated with these variations in operating conditions, and to ascertain whether the mathematical model accurately predicts the experimental trends.

Section 6.2 is concerned with the influence of compression ratio. Predictions for the operating conditions S = 200 rpm and CR = 10.5 are presented and compared with those for CR = 3.5 and 6.7, which have been presented in Chapter 5.

Section 6.3 presents a study of the influence of the intake valve lift on the induction-generated flow and its evolution. Predictions are presented and compared pertaining to the operating conditions of S = 200 rpm and CR = 10.5 for two different valve lift characteristics with L_{max}/D_v equal to 0.24 and 0.14.

The influence of variations in engine speed is studied in Section 6.4. Predictions are given for the operating conditions S = 200, 500 and 1000 rpm and compression ratio of 10.5.

The conclusions are presented in Section 6.5.

6.2 THE INFLUENCE OF VARIATIONS IN COMPRESSION RATIO

6.2.1 Mean Flow and Turbulence Parameters

The predictions of the mass flow rate through the valve ($\dot{m}$) and the inlet velocity (U_{in}) for the engine speed of 200 rpm and three compression ratios of 3.5, 6.7 and 10.5 are presented in Figure 6.1. The inlet and initial conditions and the wall temperatures for CR = 10.5 are as for CR = 6.7 (Case II) presented in Chapter 5. The results show that the increase in compression ratio has almost no effect on $\dot{m}$ and U_{in} for the present engine operating speed. The slightly larger $\dot{m}$ for CR = 3.5 is probably due to the lower cylinder wall temperatures (see Chapter 5) that result in less heating, and hence expansion, of the in-cylinder gas and thus slightly lower in-cylinder mean pressure.

Figure 6.2(a) presents plots of the velocity field and Figures 6.2(b), (c), (d) and (e), respectively, show the distributions of turbulence intensity ($u'/\overline{V}_p$), length-scale (ℓ/B), time-scale (τ_d/T_{cycle})

and viscosity (μ_T/μ) at selected crank angles during the engine cycle, for CR = 10.5. The variations of the normalised mean axial velocity ($U/\overline{V}_p$) and the turbulence parameters at the fixed monitoring locations Z = 10 mm, r = 25 mm for CR = 3.5 and 6.7, and Z = 9 mm, r = 25 mm for CR = 10.5 (in this case, Z = 10 mm is larger than the clearance gap at TDC) are given in Figures 6.3(a) to (e).

Comparison of the predicted flow for CR = 10.5 (Figures 6.2(a) to (e)) with those for CR = 3.5 and 6.7, presented, respectively, in Figures 5.16 and 5.23 (these have been extensively analysed and compared in Chapter 5), shows that the flow structure during induction is very similar to that for CR = 6.7. Therefore, it can be concluded that the marked influence of the reduction in the clearance gap with increase in compression ratio, evidenced for CR = 3.5 and 6.7, ceases once the clearance gap is sufficiently small to cause the intake jet impingement on the piston. In this respect, it is obvious that the inlet valve seat angle has an important rôle.

The main influence of the increase in CR on the mean flow is to cause the third vortex near the cylinder wall/piston corner to form earlier during induction and become larger and stronger, as was observed earlier for an increase in CR from 3.5 to 6.7. This constrains the displacement and growth of the main vortex (in the valve wake) and produces a stronger mean flow during most of the induction stroke ($\theta \simeq 70°$ to 120° CA), in accord with the measurements of Arcoumanis, et al. [1982a]. However, due to the higher levels of turbulent stresses (see diagram (e) for μ_T), the mean flow decays more rapidly near the end of induction, again in agreement with Arcoumanis, et al. [1982a], rendering a smaller and weaker main vortex at bottom dead centre (θ = 180°).

The increased compression ratio, CR = 10.5, also produces higher levels of turbulence intensity within the bulk of the cylinder, due to the longer lasting intake jet impingement on the piston and higher turbulence production by the stronger mean flow strain rates (evident in the volume-integral balances of the k-equation in Figure 6.4). The turbulence decays rapidly near the end of induction to levels nearly 14% smaller than those for CR = 6.7 at θ = 180° CA. Examination of the u' distribution for CR = 10.5 further reveals that, unlike for lower CR cases, there is no indication of formation of a region of large turbulence intensity in the main vortex during the latter part of induction (θ = 110° to 160° CA). This, as the distributions of u' and ℓ reveal, is because for CR = 10.5 the formation of a turbulence structure associated with the main vortex occurs earlier during induction ($\theta \simeq 90°$ CA).

The variations of $u'/\overline{V}_p$ at the monitoring locations (which, as the variations of $\overline{U}/\overline{V}_p$ (Figure 6.3(a)) indicate, are within the incoming jet) are similar for the three compression ratios, with a level of around $u' \simeq 3.0\ \overline{V}_p$ (Figure 6.3(b)), during most of induction. The average velocity for the same period is about $\tilde{U} \simeq 10\ \overline{V}_p$, thus giving the relative turbulence intensity nearly $u'/\tilde{U} \simeq 0.3$. This is slightly larger than that for plane jets ($u'/\tilde{U}_c = 0.2$) and round jets ($u'/\tilde{U}_c = 0.26$) issuing into still air (Rodi [1972]), but less than the measurements ($u'/\tilde{U} = 0.35$ to 0.5).

The distributions of ℓ for $CR = 10.5$ show that increased compression ratio produces smaller levels, outside the intake jet, during early induction, due either to the effect of the longer lasting intake jet impingement on the piston, or the smaller cylinder head/piston clearance gap. The levels of ℓ increase rapidly at $\theta \simeq 90°$ CA due to the formation of the turbulence structure within the main vortex to levels larger than for $CR = 6.7$; although the occurrence of this feature later in the stroke in the case of $CR = 6.7$ (i.e. at $\theta = 126°$ CA, according to Figure 5.23(c)) results in smaller ℓ for $CR = 10.5$ near the end of induction. The levels of ℓ in the induction jet are not influenced by the compression ratio, as shown in Figure 6.3(c) and also diagrams (e), apart from near the end of induction where it is affected by the development of the main vortex.

The distributions of ℓ at the end of induction ($\theta = 180°$ CA) for $CR = 3.5$, 6.7 and 10.5 are similar, except for the region of the third vortex, where the history effect of the induction flow is evident. The levels in the region of the main vortex are similar (the differences are less than 10%); there is no trend between the variations of ℓ and the increase in CR.

The higher compression ratio, $CR = 10.5$, produces smaller levels of τ_d during early induction, due to the larger mean flow strain rates and higher level of turbulence energy production, that increase more rapidly near the end of induction than for $CR = 6.7$ (due to the larger decay of the mean flow and turbulence), producing levels at $\theta = 180°$ CA similar to those for $CR = 6.7$. Comparison of the τ_d distributions at $\theta = 180°$ CA for $CR = 3.5$, 6.7 and 10.5 (Figures 5.16(d), 5.22(d) and 6.2(d), respectively) shows that, although their levels in the third vortex are different (in particular for $CR = 3.5$, due to the absence of the intake jet impingement on the piston), the levels in the main vortex are similar and average around $\tau_d \simeq 0.06$ to $0.07\ T_{cycle}$ (nearly 22° to 25° CA).

The distributions of μ_T for $CR = 10.5$ (Figure 6.2(e)) show lower levels during early induction, due to the effect of CR on ℓ noted

earlier. The levels of μ_T become larger than in the cases CR = 3.5 and 6.7 with the formation of the turbulence structure within the main vortex at $\theta \simeq 90°$ CA; but with the occurrence of this feature later in the stroke in the cases CR = 3.5 and 6.7, and the larger decay of u' near the end of induction here, μ_T falls to smaller levels than for CR = 6.7 at $\theta = 180°$ CA. The main influence of increase in CR on the μ_T distribution at the end of induction is the disappearance of the region of largest μ_T in the main vortex (Figures 5.16(e), 5.23(e) and 6.2(e)). Comparison of the levels at $\theta = 180°$ CA shows absence of a trend of variation with CR, due to the complicated behaviour of ℓ and u' in the main vortex during $\theta = 90°$ to 180° CA in the three cases.

The evolution of the flow during compression and the distributions of the turbulence parameters for CR = 10.5 are similar to those for CR = 6.7, except for differences in the region of the third vortex (principally because of the larger levels of ℓ) that disappear after mid-compression ($\theta = 270°$ CA) with the break-up of this structure. The main influence of increase in CR on the mean flow during compression is to produce a smaller and weaker main vortex. This is partly a consequence of the reduction of its size and strength during late induction and partly due to the reduced clearance gap near the end of compression.

The distributions of u' for CR = 10.5 show continuous decay and tendency of turbulence towards homogeneity. The mean u' levels near the end of compression (θ = 234° to 360° CA), for CR = 10.5, are nearly 10% smaller than for CR = 6.7. Thus, the predicted effect of increase in compression ratio in the range CR = 3.5 to 10.5 is to reduce the turbulence intensity near the end of (and at TDC) compression (Figure 6.3(b)). This trend, it should be noted, is in accord with the data presented in Chapter 5 (i.e. for CR = 3.5 and 6.7) and also the measurements of Vafidis & Whitelaw [1984b] in the same model engine, for CR = 7.7. The absence of such compression ratio effects in some experiments reviewed in Chapter 2 (see Table 2.6) could be due to factors such as the three-dimensionality of the flow and/or the method of data processing. Another reason could be that the smallness of the effect (the'mean' TDC turbulence level varies between u' = 0.5 to 0.4 $\overline{V}_p$ for variations of CR = 3.5 to 10.5) is within the error tolerances of the measurement techniques employed.

The predictions of ℓ (diagrams (c) and Figure 6.3(c)) show that the levels and variations of ℓ during early compression slightly differ between CR = 3.5, 6.7 and 10.5, due to the influence of CR on the evolution of the induction-generated mean flow and turbulence during late induction/early compression. In this connection, Figures 6.4(c) and

6.4(d), respectively, show larger levels of turbulence energy production by the mean flow and considerably smaller rate of decay of the 'mean' turbulence during early compression for CR = 3.5. However, the noteworthy point is that in all three cases, the maximum levels (near the cylinder axis) are around $\ell \simeq 0.07$ to 0.08 B, confirming the already noted influence of the cylinder diameter on the length scale during this phase (see Chapter 5).

The effect of increase in CR is to reduce ℓ near the end of compression (θ = 324° to 360° CA), as shown in Figure 6.3(c)*, due to both the augmentation of the effect of compression on turbulence and the decrease of the clearance gap (Z_{TDC}). The ratios ℓ/Z_{TDC} at TDC for CR = 3.5, 6.7 and 10.5 are 0.114, 0.173 and 0.175, respectively. The smaller relative size of ℓ for CR = 3.5 is consistent with the less decay of turbulence in this case and indicates the influence of the turbulence generation by the persisting induction-generated flow on the turbulence structure (as evidenced by the behaviour of ℓ during early compression). The similarity of ℓ/Z_{TDC} for the cases CR = 6.7 and 10.5 may be coincidental (noting the differences at θ = 180° CA); although it may be a true effect, indicating a complete relaxation of the turbulence into a structure controlled by the engine geometry near the end of compression (due to the markedly larger decay of the intake-generated flow in these cases).

The predictions of τ_d for CR = 3.5, 6.7 and 10.5 (Figures 5.16(d), 5.23(d) and 6.2(d)) show that the levels in the main vortex at θ = 180° CA are similar, but their variations during early compression are significantly influenced by the development of the mean flow. The levels of τ_d in the main vortex during the θ = 180° to 270° CA period are smallest in the case of CR = 3.5 and largest for CR = 10.5, in accord with the higher level of turbulence production and smaller decay of u' in the former case. Thereafter, however, this trend changes (see Figure 6.3(d)) due to the overriding effect of compression on the ℓ. Thus, the level of τ_d near the end of compression (θ = 324° to 360° CA) decreases with increase in CR, in accord with the augmentation of the dissipation rate (evidenced in Figures 6.5) due to the reduction of the length-scale. As noted earlier in Chapter 5, this trend is in accord with the experimentally observed reduction of λ_y with increase in CR (see Table 2.6).

The effect of CR on the level and variations of μ_T during

---

* Note that the excessive reduction of ℓ near TDC for CR = 10.5 is due to the influence of the piston proximity.

compression is complicated by its influence on the decay of the induction-generated flow (and hence the variations of u' and ℓ) and the differences in the rate of increase of ρ: thus, there is no trend of variation of μ_T with CR (see diagrams (e) and Figure 6.4(e)). The most noteworthy effect of CR is to tend to increase the level of μ_T during $\theta = 270°$ to $330°$, due to the reduction in the rate of decay of k during this phase caused by the relatively larger levels of turbulence energy production by compression (see Figure 6.5).

The effect of increase in CR on the flow during expansion is to produce a more rapid break-up of the remnants of the main vortex. The rate of decay of u' during early expansion increases with CR, consistent with the smaller levels of τ_d at TDC; but it rapidly decreases and becomes similar for all the cases later in the stroke ($\theta = 414°$ CA). There is evidence of turbulence generation within the cylinder wall shear layer (see Figure 6.2(b)) later during expansion ($\theta \simeq 414°$ to $450°$ CA); this, however, is confined to the cylinder wall boundary layer and does not influence the turbulence decay elsewhere (see Figure 6.3(b)).

The length-scale ℓ increases more rapidly in the case of higher CR, but by mid-expansion reaches a limiting value identical for the three compression ratios (Figure 6.3(c)), indicating its control by the cylinder diameter. Also, the rate of increase of τ_d during expansion increases with CR (Figure 6.3(d)) due to the larger rates of decay of u' and growth of ℓ. The turbulent viscosity falls and approaches a similar level for the three CR by mid-expansion, in accordance with the variations of u' and ℓ.

6.2.2 Turbulence Energy Balance

Figures 6.4(a), (b), (c) and (d), respectively, present the variations of the cylinder volume-integrals of the turbulence energy K ($\equiv \int_V \rho\, k\, dV$), dissipation rate E ($\equiv \int_V \rho\, \varepsilon\, dV$), shear turbulence energy production G_S ($\equiv \int_V \mu_T \left[\left(\partial \tilde{u}_i/\partial x_j\right) + \left(\partial \tilde{u}_j/\partial x_i\right)\right] \left(\partial \tilde{u}_i/\partial x_j\right) dV$ for $i \neq j$) and normal strain turbulence energy production G_N ($\equiv \int_V \mu_T \left[\left(\partial \tilde{u}_i/\partial x_j\right) + \left(\partial \tilde{u}_j/\partial x_i\right)\right] \left(\partial \tilde{u}_i/\partial x_j\right)$ for $i = j$) during the engine cycle, for the three compression ratios.

The large differences between the results for $CR = 3.5$ and those for $CR = 6.7$ and 10.5 during induction are, as noted earlier in Chapter 5, due to the intake jet impingement on the piston during early induction, producing markedly larger levels of turbulence viscosity and stronger mean strain rates and thus higher levels of turbulence energy production by the mean flow. These clearly illustrate the influence of

the early induction flow structure on the mean turbulence level.

The results for $CR = 10.5$ show a similar trend but markedly larger levels of G_S during $\theta = 65°$ to 115° CA than for $CR = 6.7$. This is due to the longer lasting intake jet impingement on the piston and stronger mean strain rates (including the region of the third vortex), and the early formation of the turbulence structure in the main vortex evidenced by an increase in G_S at $\theta \simeq 90°$ CA. In both cases, the extent of influence of the early induction flow structure is indicated by the reduction of G_S, at around $\theta \simeq 55°$ to 70° CA, with the transformation of the flow to that in which the intake jet impinges on the cylinder wall. The differences in G_S during late induction ($\theta \simeq 115°$ to 180° CA) are due to the late formation of the turbulence structure in the main vortex (at $\theta \simeq 135°$ CA) in the cases of $CR = 3.5$ and 6.7 (a weaker effect is also evident in the case of $CR = 10.5$). The considerably larger decay of the mean flow near the end of induction/early compression for higher CR is clearly evidenced by the larger reduction of G_S (Figure 6.4(c)).

The levels and variations of G_N during induction for $CR \simeq 6.7$ and 10.5 are similar, but substantially differ from those for $CR = 3.5$. It has been noted in Chapter 5 that there is a strong correlation between the variations of G_N and the intake jet velocity in the case of $CR = 3.5$. Therefore, in view of the similar inlet velocities for the three CR, the larger levels of G_N during the interval $\theta \simeq 75°$ to 135° CA in the cases of $CR = 6.7$ and 10.5 may be due to the larger levels of μ_T and thus higher turbulence generation by the normal strains in the regions of impingement on the cylinder wall and the valve wake.

Overall, comparison of the results presented in Figures 6.4(a) to (d) indicates a stronger correlation during induction between the variations of K with G_S and between E with G_N. This can be explained by noting that the τ_d levels in the regions of G_N production (i.e. the induction jet and impingement regions on the piston/cylinder wall) are quite small and thus the turbulence dissipates rapidly, or, more fundamentally, that the induction jet turbulence is in quasi-equilibrium. Also evident is the larger decay of K for higher CR near the end of induction, due to the increased decay of the intake-generated mean flow. Therefore, the effect of increase in CR is to produce lower levels of K and G_S at the end of induction.

The integral balance of the k-transport equation during the compression and expansion strokes for $CR = 3.5$, 6.7 and 10.5 are presented in Figures 6.5(a), (b) and (c), respectively, and show the reduction of G_S and G_N (due to the weaker mean flow) for higher compression ratios. The

effect of increase in CR is to reduce the rate of decay of k during late compression (θ = 290° to 320° CA) due to the larger contribution from turbulence generation by compression G_C. However, for higher CR, the rate of decay of k near the end of compression (θ = 320° to 360° CA) increases, due to the similar effect of compression in augmenting the level of ε (see Chapter 3). Thus, it is evident that in the present circumstances, the effect of an increase in CR is to reduce the TDC turbulence intensity. Therefore, it can be concluded that higher levels of TDC turbulence can only be achieved through generation of mean flow structures that persist throughout the compression stroke and are capable of turbulence energy production.

6.3 THE INFLUENCE OF VALVE LIFT

6.3.1 Mean Flow and Turbulence Parameters

The engine operating conditions for this study are S = 200 rpm and CR = 10.5. The lift diagrams for the two cases studied, viz. the standard valve (L_{max}/D_v = 0.24) and a valve with 0.57 times its lift (i.e. L_{max}/D_v = 0.14) (hereafter referred to as Cases III and IV, respectively) are presented in Figure 6.6. In both cases, the discharge coefficient C_D and the flow separation data are obtained, for the instantaneous lift, from relations (3.85) and (3.89), respectively. The mass flow rate ($\dot{m}$) and the inlet velocity through the valve (U_{in}) are calculated according to the 'new' valve treatment procedure, outlined in Chapters 3 and 4.

The predicted $\dot{m}$ and U_{in} are presented in Figures 6.7(a) and (b), respectively, and show that $\dot{m}$ for the two valves are identical, except for slight differences associated with the occurrence of flow separation. This is because for the low engine speed of 200 rpm, both lifts are sufficiently large to give a 100% volumetric efficiency throughout the induction (see, for example, the absence of mean cylinder pressure variations for Case III in Figure 6.12(c)). Consequently, U_{in}, which is inversely proportional to the valve exit area (equation (3.88)) is larger in Case IV for small lifts associated with early induction. However, since flow separation occurs at different crank angles for the two valves, at larger lifts it causes additional less systematic differences between the inlet velocities (see Figure 6.7(b)).

The predicted velocity fields and the distributions of the normalised turbulence parameters $u'/\overline{V}_p$, ℓ/B, τ_d/T_{cycle} and μ_T/μ for the small lift case are given in Figures 6.8(a), (b), (c), (d) and (e), respectively (the results for the standard lift have already been

presented in Figures 6.2(a) to (e)). The temporal variations of the normalised mean axial velocity $\tilde{U}/\overline{V}_p$ and the turbulence parameters at the fixed monitoring location Z = 5 mm, r = 25 mm for the two cases are presented in Figures 6.9(a) to (e).

The predicted velocity fields (Figure 6.8(a)) show that the mean flow during induction is similar to that for the standard lift (Figure 6.2(a)), but is stronger here due to the larger inlet velocities; furthermore, the different timing of the flow separation at the valve exit influences the development of the flow structure. Figure 6.8(a) shows that the effect of rapid increase in U_{in} due to the occurrence of the flow separation during the period $\theta \simeq 80°$ to 120° CA (see Figure 6.7(b)) is to displace the main vortex towards the cylinder wall and suppress the development of the third vortex near the piston. This produces a larger and markedly stronger main vortex during the rest of the induction stroke.

The distributions of u' (Figure 6.8(b)) during early induction (i.e. θ = 36° to 72° CA) are similar to those for Case III, but, as would be expected, the levels are larger (nearly 11%) due to the larger U_{in}. The pattern at θ = 90° CA is of interest and shows generation of large turbulence in the vicinity of the intake valve, due to the rapid increase in U_{in} consequent upon the flow separation. There is no evidence of similar increases within the bulk of the flow, and indeed the results for θ = 126° CA show a slight reduction in the average level of u'. The explanation for this is that the rapid increase of U_{in} disrupts the formation and development of the turbulence structure associated with the main vortex (as clearly evidenced by the distributions of ℓ during θ = 90° to 126° CA in Figure 6.8(c)) which is responsible for large turbulence energy production within the bulk of the flow (in Case III, this occurs around $\theta \simeq 90°$ CA). This structure, in the present case, is formed later during θ = 126° to 162° CA (after flow re-attachment at the valve at $\theta \simeq 120°$ CA), as evidenced by the distributions of u' and ℓ that show the formation of a region of large u' accompanied by a marked growth of ℓ, within the main vortex. Consequently, in the present case, the average u' level at the end of induction (θ = 180° CA) is nearly 30% larger than in Case III.

The distributions of ℓ (Figure 6.8(c)) indicate smaller levels within the intake jet, in accord with the smaller lift; but the levels within the vortex structure early during induction (θ = 36° to 72° CA) are unaffected by the reduction of the valve lift, due most likely to the strong effects of the jet impingement, flow curvature and the cylinder walls on the turbulence in these regions. The flow separation at the

valve, as already noted, markedly influences the distribution and growth of ℓ within the main vortex, resulting in nearly 20% smaller levels at θ = 126° CA than in Case III. However, these differences rapidly diminish near the end of induction with the formation of the turbulence structure in the main vortex, producing similar levels of ℓ for the two cases at θ = 180° CA; although the level in the third vortex is nearly 15% smaller.

The distributions of τ_d (Figure 6.8(d)) throughout induction are similar for the two cases. The effect of flow separation during $\theta \simeq 80°$ to 120° CA is to produce smaller τ_d within the main vortex (in accord with the smaller ℓ) than in Case III. These differences do not diminish near the end of induction (for the development of the turbulence structure in the main vortex is accompanied by turbulence generation and higher levels of u') and at θ = 180° CA, the τ_d levels in the main vortex are nearly 20% smaller than in Case III. The τ_d levels in the third vortex at θ = 180° CA are similar.

The distributions of μ_T (Figure 6.8(e)) show that the levels in the main vortex are nearly 35% smaller than in Case III during θ = 90° to 126° CA, due to the effect of flow separation on the u' and ℓ in this region. However, μ_T increases rapidly near the end of induction, and the levels in the main vortex at θ = 180° CA are nearly 20% larger than in Case III; but the levels in the third vortex are smaller throughout θ = 90° to 180° CA.

The flow evolution and the distributions of the predicted turbulence parameters during the compression stroke are similar to those for the standard valve (Figures 6.2(a) to (e)), except for the differences in the region of the third vortex that disappear after its break-up around $\theta \simeq 270°$ CA. In the present case, the main vortex is stronger and slightly larger during θ = 180° to 270° CA, but decays rapidly during θ = 270° to 324° CA, due to the overriding influence of the clearance gap. The mean flows near the end of compression (θ = 324° to 360° CA) are almost identical in the two cases (see Figure 6.9(a)).

The levels of u' are larger by nearly 30% at θ = 180° and 234° CA, 20% at θ = 270° CA, 9% at θ = 234° CA and become almost identical to that for the standard valve at TDC (see Figure 6.9(b)). This is in general agreement with the experimental study of Arcoumanis, et al. [1982c] in a similar engine configuration (there are certain differences in respect of the variations of u' during compression that may be attributed to the presence of induction swirl in the experimental case and under-prediction of the turbulence decay during early compression).

The levels of ℓ, apart from in the third vortex during early compression, are almost identical in the two cases (see Figure 6.9(c)). The levels of τ_d are expectedly smaller in the present case, in accordance with the higher levels of u' during early compression (θ = 180° to 270° CA), but thereon the differences rapidly diminish: τ_d is nearly 9% smaller at θ = 324° CA and becomes identical to that for the standard valve at TDC (Figure 6.9(d)). The levels of μ_T are also larger in the present case during θ = 180° to 270° CA, but, as with the other parameters, these differences diminish to insignificant levels near the end of compression (Figure 6.9(e)).

The noteworthy implications in respect of the combustion process are that the effects of the intake valve are still present at the time of ignition ($\theta \simeq$ 330° to 340° CA). These effects could prove to be significant, in view of the numerous studies showing a strong dependence of the flame propagation speed on the turbulence intensity and scales at the time of ignition (e.g. Andrews, et al. [1975], Groff & Matekunas [1980]).

The velocity field and the distributions and levels of the predicted turbulence parameters are, as would be expected, identical in the two cases during the expansion stroke (Figures 6.8(a) to (e) and 6.9(a) to (e)).

6.3.2 Turbulence Energy Balance

Figures 6.10(a), (b), (c) and (d), respectively, present the variations of the volume-integrals of the turbulence energy K, dissipation rate E and shear (G_S) and normal (G_N) strain rate turbulence generation during the engine cycle, for the two cases. These show higher levels of K, E, G_S and G_N during early induction, due to the larger u_{in} in the present case. The effect of flow separation at the valve during $\theta \simeq$ 90° to 120° CA is evidenced by a rapid and substantial increase of G_N and G_S that is balanced by a similar increase of E, indicating the equilibrium nature of the induction jet turbulence. The increase in G_S near the end of induction (θ = 126° to 144° CA) is due to the formation of the turbulence structure associated with the main vortex in the present case. This produces higher levels of G_N (because of the increase of μ_T in the main vortex) and K than for the standard valve.

The volume-integral balance of the k-transport equation for the compression and expansion phases, for the present case, is given in Figure 6.11. Comparison with the results for the standard valve (Figure 6.5) shows higher levels of G_N, G_S and G_C (in the last instance, because

of the higher levels of k) for the period $\theta \simeq 210°$ to 300° CA: thereafter, the two cases become identical. The close correspondence between the level and variations of k and those of G_S and G_N confirms the finding of Section 6.1, that the induction-generated flow is the main agent for sustaining higher levels of turbulence during compression.

6.4 THE INFLUENCE OF ENGINE SPEED

6.4.1 Mean Flow and Turbulence Parameters

Figures 6.12(a), (b) and (c), respectively, present the influence of engine speed on the intake mass flow rate ($\dot{m}$), inlet velocity (u_{in}) and the cylinder mean pressure (P_{cyl}) during induction and early compression (i.e. until inlet valve closure), for the speed range S = 200 to 1000 rpm. Figures 6.12(a) and (b) show increases in the magnitudes of $\dot{m}$ and u_{in}, with increase in S, without alteration of the patterns of their variation during the induction stroke. Figure 6.12(c) reveals the absence of a significant cylinder pressure drop for the low speed of S = 200 rpm, indicating effectively 100% volumetric efficiency throughout induction. For higher engine speeds, P_{cyl} drops rapidly during early induction (θ = 0° to 45° CA) and recovers steadily during the rest of the stroke. The variations for S = 1000 rpm is similar to the measurements of Kastner, et al. [1963-64], reviewed in Chapter 2.

Figures 6.13(a) and (b) present the variations of the normalised intake mass flow rate $\dot{m}/(\rho_{in} A_p \overline{V}_p)$ and inlet velocity $u_{in}/\overline{V}_p$ (where ρ_{in} is the inlet air density, A_p is the piston area, and $\overline{V}_p$ is the mean piston speed) for the three engine speeds. The results are almost identical during induction and show that $\dot{m}$ and u_{in} vary linearly with S, over this range. The differences during the outflow phase (θ = 180° to 220° CA) could be due to non-linear variations of the wall heat transfer with the engine speed (influencing the mean cylinder density and pressure).

(a) Engine speed of 500 rpm: Figures 6.14(a), (b), (c), (d) and (e), respectively, present the plots of the velocity field and distributions of normalised turbulence parameters ($u'/\overline{V}_p$), length-scale (ℓ/B), dissipation time-scale (τ_d/T_{cycle}) and viscosity (μ_T/μ) during the engine cycle. These show that the increase in engine speed does not change the flow structure, in agreement with the experimental data reviewed in Chapter 2: the evolution of the mean flow and distributions of the turbulence parameters are similar to those for the engine speed of 200 rpm (Figures 6.2(a) to (e)).

Figure 6.14(a) shows scaling of the mean flow during induction

with engine speed (note that the velocity vectors are scaled with $\overline{V}_p$), but a larger and stronger main vortex near the end of induction (θ = 162° to 180° CA) is predicted in the present case. In view of the small and rapidly falling intake jet momentum during this phase, it may be concluded that this difference is a consequence of the differences in the turbulent stresses due to the formation and development of the turbulence structure associated with the main vortex.

Figure 6.14(b) shows an almost linear increase of u' with engine speed, except close to the very beginning (θ = 36° CA) and near the end of induction (θ = 162° to 180° CA). The lack of such a dependence near the beginning of the stroke could be a consequence of the initial values ascribed to the turbulence parameters (which were not scaled with the engine speed) or the smallness of the clearance gap being insufficient for development of the intake jet to its self-similar structure (as indicated by the smaller ℓ in this region) before impinging on the piston (see Looney [1982]). The distributions of u' near the end of induction (θ = 162° to 180° CA) differ slightly from those for S = 200 rpm and show the formation of a region of relatively high turbulence in the main vortex. The $u'/\overline{V}_p$ levels in the main vortex at bottom dead centre (θ = 180° CA) are nearly 20% to 30% larger in the present case, but the levels in the third vortex near the piston are smaller.

The levels of ℓ during induction are similar to those for the engine speed of 200 rpm (about 20% smaller at θ = 36° CA, with the differences rapidly diminishing to nearly 10% at θ = 72° CA and 5% at θ = 90° CA), indicating insensitivity of the length-scale on engine speed. This is in agreement with the measurements of Witze [1977] that show L_x (measured in the induction jet) is nearly independent of engine speed. The growth of ℓ in the main vortex near the end of induction (i.e. θ = 162° to 180° CA) is slightly faster in the present case, producing nearly 10% larger levels near its centre at θ = 180° CA; but the levels in the third vortex near the piston are smaller.

Figure 6.14(d) shows similar levels of τ_d/T_{cycle} during induction to those for S = 200 rpm, indicating that τ_d is nearly inversely proportional to engine speed. This may be explained as either a consequence of the linear variation of u' and lack of dependence of ℓ on engine speed, or, more fundamentally, as an indicator of the quasi-equilibrium turbulence, for which τ_d is inversely proportional to the mean flow strain rates (that increase mostly proportional to speed). However, in the main vortex at θ = 180° CA, τ_d/T_{cycle} is nearly 20% smaller than for S = 200 rpm, in accordance with the stronger mean flow

and higher level of u' in the present case.

The distributions of μ_T (Figure 6.14(e)) are, as would be expected, similar to those for the lower engine speed, except near the end of induction (θ = 162° to 180° CA) where the formation of a region of large μ_T within the main vortex is evident. The increase in μ_T is not proportional to engine speed throughout the induction stroke: the ratios of the average levels for the two speeds increase from nearly 1.6 at θ = 36° CA to 2.9 (in the main vortex) at θ = 180° CA. This non-proportionality during early induction is also evident in the induction jet, indicating that the predicted behaviour is less likely a consequence of the prescribed initial conditions, but rather a characteristic of the induction jet. In this connection, the detailed measurements of Morse, et al. [1979] for the speed range S = 100 to 300 rpm show differences in the rate of spread of the induction jet (and size and strength of the main vortex) that may be taken as an indication of its non-self-similarity.

The mean flow evolution and the distributions of the turbulence parameters during compression are similar for S = 200 and 500 rpm (Figures 6.2(a) to (e) and 6.14(a) to (e)). The main vortex in the present case is larger and stronger during θ = 180° to 270° CA; but, thereafter, the differences rapidly diminish due to the suppression of the main vortex by the piston, as TDC is approached.

The turbulence levels in the main vortex are also higher in this case. The normalised levels ($u'/\overline{V}_p$) are larger than for S = 200 rpm by nearly 30% at θ = 180° CA, 50% at θ = 234° CA and 40% at θ = 270° CA, indicating a considerable reduction of the rate of decay of turbulence during early compression due to the turbulence energy production by the stronger main vortex. This difference rapidly diminishes near the end of the stroke to 25% at θ = 324° CA and 10% at θ = 360° CA. The larger-than-linear increase of u' near the end of compression (around the time of ignition) is of considerable importance in respect of the combustion process, as discussed earlier. The predicted nearly linear increase of the TDC turbulence with engine speed is in agreement with the majority of the experimental data reviewed in Chapter 2 (see Table 2.6). A noteworthy influence of increase in engine speed, evidenced by Figure 6.14(b), is the enhanced homogeneity of the turbulence near the end of compression, due to the larger levels within the main vortex.

The levels of ℓ (Figure 6.14(c)) in the main vortex are similar to those for S = 200 rpm; although they are smaller in the third vortex during θ = 180° to 270° CA. The length-scales near the end of compression (θ = 324° to 360° CA) are identical and show complete independence of this

parameter from the engine speed. This is in accord with the measurements of Lancaster [1976] and Witze [1977] regarding L_x (see Table 2.6).

Figure 6.14(d) shows smaller levels of τ_d/T_{cycle}, especially in the main vortex, during θ = 180° to 270° CA, in accordance with the higher levels of $u'/\overline{V}_p$ in the present case. These differences rapidly diminish during late compression: the levels of τ_d/T_{cycle} are nearly 15% smaller at θ = 324° and become identical to those for S = 200 rpm at θ = 360° CA. Thus, τ_d at TDC is inversely proportional to engine speed.

Figure 6.14(e) shows the expected larger levels of μ_T in the main vortex during the early part of compression; the increases in the levels with the engine speed are similar to those of u', due to the insignificant influence of speed on the length scale. The ratios of average μ_T levels for the two speeds near the end of compression (θ = 324° to 360° CA) are about 2.9, which is larger than a linear increase would produce (i.e. 2.5).

The mean flow evolution, during the expansion stroke, follow the same patterns for the two speeds, but there is evidence of a 'longer-lived' main vortex residue for S = 500 rpm. Consequently, although the evolution of the turbulence parameters is identical to that for the lower speed, their distributions differ slightly within this region. Elsewhere, the levels of $u'/\overline{V}_p$, ℓ/B and τ_d/T_{cycle} are almost identical to those for S = 200 rpm, throughout θ = 360° to 450° CA.

(b) Engine speed of 1000 rpm: Figures 6.15(a) to (d) present the plots of the velocity field and the distributions of the normalised turbulence parameters $u'/\overline{V}_p$, ℓ/B, τ_d/T_{cycle} and μ_T/μ during the engine cycle, for this speed. These show that the mean flow structure and evolution during the induction stroke follows the pattern of the lower engine speeds. The distributions of u' and other turbulence parameters and their pattern of development are also similar to those for the lower speeds.

The levels of $u'/\overline{V}_p$ in the present case are slightly smaller during early induction and larger after the formation of the turbulence structure in the main vortex (θ = 126° to 162° CA), decaying to similar levels as for the lower speeds at the end of induction. The levels of ℓ are smaller near the beginning of the stroke, but the differences diminish quickly, resulting in identical levels to those for S = 200 and 500 rpm at θ = 180° CA. This confirms the independence of ℓ at the end of induction from engine speed. In respect of the τ_d variations, except for early induction, the normalised levels are nearly identical to those for the

lower speeds, confirming its inverse proportionality with engine speed. The levels of μ_T at θ = 180° CA indicate an approximately linear increase with engine speed.

During compression, as Figure 6.16(a) indicates, the main vortex is stronger at this speed. The development of the turbulence intensity follows the usual pattern, but due to the stronger mean flow the rate of decay of turbulence during θ = 180° to 270° CA is smaller, such that $u'/\overline{V}_p$ at mid-compression is nearly 18% larger than for S = 500 rpm. The difference reduces to nearly 13% at θ = 234° CA and 10% at the TDC.

The turbulence length and time-scales follow the previous patterns of, in the former case, independence from engine speed, and, in the latter, a linear reduction with engine speed. The turbulence viscosity follows the variations of u', and near the end of compression is approximately linearly proportional to speed.

The flow evolution during expansion is almost identical to that for S = 500 rpm, except for the slight differences in the distributions of $u'/\overline{V}_p$ due to the persistence of the larger levels in the main vortex at TDC.

(c) Results for the three engine speeds: Figures 6.16(a) to (c) present the temporal variations of the normalised axial mean velocity and turbulence parameters at the monitoring location Z = 5 mm, r = 25 mm, for the three engine speeds of S = 200, 500 and 1000 rpm. Figure 6.16(a) shows similar trends of variation but suggests a larger-than-linear dependence of the mean velocity on engine speed. In view of the earlier evidence of a linear increase of the intake velocity with engine speed in the present circumstances, the differences may be attributed to the variations in the rate of spread of the intake jet (to which the monitoring location is sensitive) due to the non-linear increase of μ_T with speed discussed earlier.

The results for the compression stroke also show a larger-than-linear increase of the mean velocity, that is due to the influence of speed on the development of the main vortex during induction. The differences decrease near the end of compression with the rapid decay of the main vortex, but appear to persist until it disintegrates early during expansion ($\theta \simeq$ 414° CA). The predicted larger-than-linear increase of mean velocity with speed during compression is in accord with the measurements of Semenov [1963], Lancaster [1976] and Liou, et al. [1984] (for a disc-chamber engine with non-shrouded intake valve).

Figure 6.16(b) shows a nearly linear increase of u' with speed

during induction. However, this does not hold during most of the compression stroke, due to the influence of speed on the strength and level of turbulence energy production in the main vortex during late induction and compression. This influence is evidenced by the markedly larger levels of u' for S = 500 and 1000 rpm at the start of the compression stroke, which are due to the formation of the turbulence structure in the main vortex near the end of induction (evidenced by the increase in G_S around θ = 140° CA in Figures 6.17(b) and (c)) in these cases. (Note that the apparent increase in u' is due to convection of the large levels in the main vortex towards the monitoring location.) As noted earlier, the differences rapidly diminish near the end of compression, due to overriding influence of the engine geometry on the flow: the result is a nearly linear increase of the TDC turbulence intensity with engine speed, in accord with the findings of almost all experimental studies (see Table 2.6).

Figures 6.16(c) and (d), respectively, confirm that to a good approximation, ℓ is independent of speed (in agreement with some of the experimental data regarding L_x, presented in Table 2.6) and τ_d decreases linearly with it. Figure 6.16(d) shows the proportional increase of μ_T with engine speed, in accord with the variation of u'.

6.4.2 Turbulence Energy Balance

Figures 6.17(a), (b) and (c) present the volume-integral balance of the k-transport equation for the engine speeds of 200, 500 and 1000 rpm, respectively. These show similar trends of variations of the components of the k-equation during induction, except for the marked increase in the level of G_S near the end of induction ($\theta \simeq 140°$ CA), with increase in speed. This, as noted earlier, is due to the turbulence generation and formation of the turbulence structure in the main vortex.

The balances of the k-equation provide an explanation for the predicted behaviour of the turbulence parameters. The condition that would produce the variations of $u' \sim S$, $\tau_d \sim S^{-1}$ and ℓ independent of speed is that $k \sim S^2$ and $\varepsilon \sim S^3$. This, in the absence of significant variations of ρ with speed, requires that $\rho\, \partial k/\partial t$, $\rho\, \varepsilon$ and (in view of the quasi-equilibrium turbulence) G_S and G_N in the k-transport equation to vary proportional to S^3. Comparison of the results indicates that this condition prevails during induction and roughly P ($\equiv G_N + G_S$) and $\rho\, \varepsilon \sim S^3$.

The results for the compression stroke show significant increase in the relative levels of G_N and G_S with increase in the engine speed, due to the stronger main vortex. Comparison of the levels after

the intake valve closure (θ = 210° CA) shows increases in $P \sim S^{3.5-4.5}$ and turbulence production by compression $G_C \sim S^{3.2-3.7}$ for the three engine speeds. Therefore, as evidenced by Figures 6.17(a) to (c), the effect of increasing speed is to augment the turbulence generation by the mean flow at a higher rate and thus to reduce the relative significance of the compressibility effect in the balance of the k-equation.

6.5 CLOSURE

This chapter has been concerned with the prediction of the influence of the compression ratio, inlet valve lift and engine speed on the in-cylinder mean flow and turbulence. In Section 6.2, the effect of compression ratio was studied. This confirmed the findings of Chapter 5 and further showed that:

(i) The intake mass flow rate is almost independent of CR.

(ii) Beyond some CR, impingement of the induction jet on piston occurs, promoting formation of the vortex near the piston and producing a stronger mean flow and higher turbulence levels that decay more rapidly (for higher CR) near the end of induction, in accord with the experimental data.

(iii) Although the development of the mean flow and turbulence structure is influenced by the increase in CR, the basic flow structure at the end of induction is not altered.

(iv) The higher the CR, the weaker is the (persisting) intake-generated mean flow during compression and the slightly smaller are the u' levels near the end of compression (θ = 324° to 360° CA), as evidenced by the measurements.

(v) The length-scale ℓ and dissipation time-scale τ_d near the end of compression decrease with increase in CR. The latter is consistent with the reduction of λ_χ with increase of CR, evidenced by the data.

(vi) The level of u' during compression depends on the level of turbulence generation by the persisting intake-generated vortex structure and hence its strength.

Section 6.3 was concerned with the influence of the reduction in the intake valve lift (L) and the findings were:

(vii) The intake mass flow rate is not influenced by the reduction of L for the low engine speed of 200 rpm; however, the intake jet

velocity is greatly influenced, due to the dependence of the flow separation in the valve passage on L.

(viii) The reduction in L influences the development of the flow (but not its basic structure), producing a stronger recirculating pattern in the valve wake and higher levels of u' near the end of induction. The increase in the level of u' is due to the larger turbulence production by the vortex structure.

(ix) During compression, the induction-generated flow is stronger and the turbulence levels are larger for the smaller lift. The differences diminish near the end of compression, due to the overriding influence of the engine geometry on the flow, and the two valves produce nearly identical levels of u' at TDC, in accord with the data. However, the effect of lift on u' and τ_d at the time of ignition is still significant in respect of the combustion process.

(x) The turbulence length-scale ℓ in the main vortex at the end of induction and throughout compression is not influenced by the valve lift.

In Section 6.4, the effect of engine speed was investigated and the main findings were:

(xi) The intake mass flow rate and inlet jet velocity increase linearly with engine speed, for the range considered (S = 200 to 1000 rpm).

(xii) The basic flow structure during induction is not altered by changes in engine speed, in accordance with the experimental data. However, the relative strength and size of the vortices and the development and level of turbulence in these regions are influenced.

(xiii) During induction, the 'mean' turbulence is in quasi-equilibrium, with the levels of turbulence production and dissipation rate increasing nearly proportional to S^3.

(xiv) During early compression, u' increases larger-than-linear with engine speed, due to the influence of the intake-generated vortex structure. However, the rapid decay of the mean flow and turbulence near the end of induction yields nearly linear variation of u' with speed at TDC in accord with the experimental data.

(xv) During and specifically near the end of compression, the

turbulence length-scale is independent of speed; the dissipation time-scale decreases nearly inversely with speed; and turbulent viscosity increases nearly proportionally with speed.

The predictions also provide evidence that:

(xvi) The turbulence length-scale during compression is largely controlled by the engine geometry, especially by the clearance gap near the end of the stroke.

(xvii) The strength, and thus the level of turbulence production by the induction-generated flow strongly influences the level of turbulence intensity during compression; although the clearance gap has an overriding effect on both the mean flow and turbulence near the end of compression.

(xviii) The turbulence generation by compression does not increase the level of turbulence intensity near TDC, due to its similar contribution towards augmentation of the dissipation rate.

CHAPTER 7
CONCLUSIONS

7.1 MAIN FINDINGS AND ACHIEVEMENTS

This chapter outlines the main findings and achievements of the present study and puts forward suggestions for future research. Detailed findings have been summarised at the end of each chapter and are not repeated here.

In respect of the contribution of this work to the multi-dimensional mathematical method, calculations have been performed in a central-valve disc-chamber model engine and the performances of three variants of the k-ε model have been assessed through comparison of predictions with two sets of data and the analysis of the key turbulence parameters produced by these models. It was found that in the conditions examined in the present study, all models produced closely similar predictions of the measured (axial mean velocity and turbulence intensity) quantities. Overall, the predictions were in moderate agreement with data. The agreement in respect of the distribution and level of turbulence intensity near the end of compression and during early expansion was good; but that in respect of the mean flow during compression was impaired by longer persistence, in the case of computations, of the intake-generated flow structure. A further analysis of the predicted variations of the key turbulence parameters, as produced by the different models, has lead to a conclusion that the Watkins [1977] version fails to produce a consistent and physically plausible variation of these parameters in the engine circumstances, but the Morel & Mansour [1982] and El Tahry [1983] versions are both suitable candidates for application to engine flows.

Additionally, the predictions of the mean flow and key turbulence parameters have been analysed in depth and the areas of uncertainty have been identified. This study pointed to likely deficiencies of the k-ε model, in the forms employed in this study, due to the effects of (a) streamline curvature, (b) appreciable normal strain rates, and (c) the turbulence decay process (i.e. $P/\varepsilon < 1$). These effects are of various degrees of importance during the engine cycle.

The influence of the inlet flow boundary conditions on the predictions has also been assessed. It was found that the influence on the calculated mean flow and turbulence intensity is appreciable during induction, but gradually diminishes to a small level at TDC compression.

In respect of the contribution to the advancement of the knowledge of flow in reciprocating engines, the thesis presents an in-depth analysis of

the evolution of the in-cylinder mean flow and turbulence. It has been found that:

(i) The intake jet turbulence is in quasi-equilibrium and a quasi-steady state compared with the time-scale of the induction process, i.e. the period of the induction stroke.

(ii) The structure and development of the turbulence within the induction-generated vortex structure is markedly influenced by features such as intake jet impingement on the piston/cylinder wall during early induction, but is independent of the intake jet turbulence near the end of induction and is determined by the local turbulence generation.

(iii) The volume-averaged turbulence during most of induction is in near-equilibrium, i.e. the generation within the intake jet and other regions of significant mean strains is roughly balanced by its dissipation; although the former predominates during early induction and the latter near its end. The amount of turbulence advection into the cylinder by the intake flow is, in comparison, negligible.

(iv) During compression, the intake-generated mean flow decays. Turbulence decays and relaxes into a structure predominantly controlled by the combustion chamber geometry near TDC.

(v) The main contributions towards the sustainment of turbulence are the turbulence generation by the persisting induction-generated flow structure and that due to compression. However, the former diminishes to a small level near the end of compression, due to the overriding effect of engine geometry on the flow.

(vi) Throughout the engine cycle, the turbulence dissipation due to the effect of the cylinder walls is substantial.

The influence of variations in the engine design and operating conditions, namely, the inlet valve lift, engine speed and compression ratio, on the in-cylinder flow has been analysed. It has been found that:

(vii) These variations influence the development and the relative size and strength of the intake-generated vortices and thus the structure and level of turbulence during early- to mid-induction. However, the flow structure at the end of induction is similar, and the differences diminish during the compression stroke as a result of the continuous decay of the mean flow and turbulence

and the overriding influence of the combustion chamber geometry on the flow near TDC.

(viii) The turbulence generation by compression does not increase the level of TDC turbulence, due to its similar augmentation of the dissipation rate. Therefore, generation of a vortex structure that persists during the compression stroke and is capable of turbulence generation is the only means of increasing the turbulence levels near TDC.

(ix) The effect of engine speed is to produce a larger-than-linear increase of turbulence intensity at the end of induction, due to its influence on the development of the turbulence structure associated with vortices. This tends towards a linear dependence near the end of compression. Also, the effect of speed is to cause a proportional reduction in the turbulence dissipation time-scale near the end of compression. The turbulence length-scale during compression is independent of speed.

7.2 SUGGESTIONS FOR FUTURE WORK

In the first instance, there is an obvious need for more accurate numerical discretisation, such as nine-point schemes (see, for example, Lai [1983]), in order to reduce the numerical diffusion errors and allow grid-independent solutions to be obtained at the level of grid refinement employed in this study. In respect of the temporal differencing practice, in view of the numerical oscillations of higher order methods such as the time-centred Crank-Nicolson scheme (Johns [1980]), the best approach for improving the accuracy of the method seems to be: since, as this study indicates, the k- and ε-transport equations are strongly source dominated, central-differencing of the source terms could prove advantageous.

In respect of turbulence modelling, there is limited scope for remedying all the deficiencies of the k-ε model in the context of the non-stationary, complex flows in engines. This is due to the fact that the flow complexities are numerous and vary in significance during the engine cycle, making the task of unravelling the modelling errors very complex. However, since the major cause of the discrepancies between the calculations and the data is the under-prediction of the decay of the vortex structure and its turbulence level, it is advisable in the first instance that the model be modified to take account of curvature Leschziner & Rodi [1981]) and the turbulence decay (Rodi [1976]) effects.

In the meantime, the development of a suitable formulation of the Reynolds stress models for strongly compressible flows and the feasibility of its application to engine flows should seriously be examined.

In respect of the method of data analysis, a hybrid ensemble/time-averaging scheme that allows evaluation of the cycle-to-cycle variations has been developed and the differential governing equations of the ensemble-mean flow quantities and cycle-to-cycle variations have been assembled. This statistical scheme can be adopted in the present calculation method. The present study provides the necessary guidelines regarding the suitable averaging time interval, during the engine cycle, over which turbulence may be assumed to be stationary.

REFERENCES

AHMADI-BEFRUI, B., GOSMAN, A.D., LOCKWOOD, F.C., and WATKINS, A.P. [1981]
"Multi-dimensional Calculation of Combustion in an Idealised Homogeneous Charge Engine: A Progress Report",
Trans. SAE, Paper 810151.

AHMADI-BEFRUI, B., ARCOUMANIS, C., BICEN, A.F., GOSMAN, A.D., JAHANBAKHSH, A., and WHITELAW, J.H. [1982]
"Calculation and Measurements of the Flow in a Motored Engine and Implications for Open-Chamber, Direct-Injection Engines",
Proc. ASME Symp. on Three-Dimensional Turbulent Shear Flows, St. Louis.

ALCOCK, J.F. [1934]
"Air Swirl in Oil Engines",
Proc. IMechE, 128, 123-193.

ANDREWS, G.E., BRADLEY, D., and LWAKABAMBA, S.W. [1975]
"Turbulence and Turbulent Flame Propagation - A Critical Appraisal",
Combustion and Flame, 24, 285-304.

ANNAND, W.J.P. [1969]
"Engine Breathing",
Automobile Engineer, 59, 50-55.

ARCOUMANIS, C., BICEN, A.F., and WHITELAW, J.H. [1981a]
"Influence of Compression Ratio on the Flow Characteristics in a Four-Stroke Model Engine",
Imperial College, Mechanical Engineering Department, Report FS/81/26.

ARCOUMANIS, C., BICEN, A.F., VLACHOS, N.S., and WHITELAW, J.H. [1982a]
"Effects of Flow and Geometry Boundary Conditions on Fluid Motion in a Motored IC Model Engine",
Proc. IMechE, 196, No. 4.

ARCOUMANIS, C., BICEN, A.F., and WHITELAW, J.H. [1982b]
"Application of LDA to Four-Stroke Motored Model Engine",
Presented at Symp. on LDA Applications to Fluid Mechanics, Lisbon.

ARCOUMANIS, C., BICEN, A.F., and WHITELAW, J.H. [1982c]
"Effect of Inlet Parameters on the Flow Characteristics in a Four-Stroke Model Engine",
SAE Paper 820750 (also Arcoumanis, et al. [1981b], Imperial College, Mechanical Engineering Department, Report FS/81/12).

ARCOUMANIS, C., BICEN, A.F., and WHITELAW, J.H. [1982d]
"Measurements in a Motored Four-Stroke Reciprocating Model Engine",
J. Fluids Engng., 104, 235-241.

ARCOUMANIS, C. [1983]
"Velocity and Concentration Fields in Reciprocating Model Engines", PhD Thesis, University of London.

ARCOUMANIS, C., BICEN, A.F., and WHITELAW, J.H. [1983]
"Squish and Swirl-Squish Interactions in Motored Model Engines", *J. Fluids Engng.*, 105, 105-111.

ARCOUMANIS, C., BICEN, A.F., VAFIDIS, C., and WHITELAW, J.H. [1984]
"Three-Dimensional Flow Field in Four-Stroke Model Engines", SAE Paper 841360 (also Arcoumanis, et al. [1984], Imperial College, Mechanical Engineering Department, Report FS/84/5).

ARNOLD, M.J., TINDAL, M.J., and WILLIAMS, T.J. [1972]
"Measurement of Induction Gas Velocities in a Reciprocating Engine Cylinder",
SAE Paper 720115.

BATCHELOR, G.K. [1960]
"The Theory of Homogeneous Turbulence",
Cambridge University Press.

BERNARD, P.S. [1981]
"Computation of Turbulent Flow in an Internal Combustion Engine During Compression",
J. Fluids Engng., 103, 75-81.

BICEN, A.F., and VLACHOS, N.S. [1980]
"The influence of Stroke and Clearance on the Flow Patterns in Motored Piston-Cylinder Assemblies",
Imperial College, Mechanical Engineering Department, Report FS/80/28.

BICEN, A.F. [1983]
"Air Flow Characteristics of Model Internal-Combustion Engines", PhD Thesis, University of London.

BICEN, A.F. [1984]
Private communication.

BICEN, A.F., VAFIDIS, C., and WHITELAW, J.H. [1984]
"Intake Valve and In-Cylinder Flow in a Reciprocating Engine", Imperial College, Mechanical Engineering Department, Report FS/84/9.

BILGER, R.W. [1975]
"A Note on Favre Averaging in Variable Density Flows",
Comb. Sci. Tech., 11, 215-217.

BILGER, R.W. [1976]
"Turbulent Jet Diffusion Flames",
Prog. Energy Comb. Sci., 1, No. 2/3, 87.

BIRD, R.B., STEWARD, W.E., and LIGHTFOOD, E.N. [1966]
"Transport Phenomena",
J. Wiley, New York.

BLUMBERG, P.N., LAVOIE, G.A., and TABACZYNSKI, R.J. [1979]
"Phenomenological Models for Reciprocating Internal Combustion Engines",
Prog. Energy Comb. Sci., 5, 123-167.

BONI, A.A., CHAPMAN, M., COOK, J.L., and SCHNEYER, G.P. [1976]
"Computer Simulation of Combustion in a Stratified Charge Engine",
Proc. 16th Symp. (Int.) on Combustion, 1527-1541.

BOUSSINESQ, J. [1877]
"Théorie de l'écoulement Tourbillant",
Mém. Prés. par Div. Savants à l'acad. Sci., 23, Paris.

BRADSHAW, P. [1971]
"An Introduction into Turbulence and its Measurement",
Pergamon Press, London.

BRADSHAW, P., and FERRISS, D.H. [1971]
"Calculation of Boundary Layer Development Using the Turbulent Energy Equation: Compressible Flow on Adiabatic Walls",
J. Fluid Mech., 46, Pt. 1, 83-110.

BRADSHAW, P. [1973]
"Effects of Streamline Curvature on Turbulent Flow",
AGARD, AG-169.

BRADSHAW, P., and FERRISS, D.H. [1973]
"Application of a General Method of Calculating Turbulent Shear Layers",
J. Basic Eng., Trans. ASME, Series D, 94, 345.

BRADSHAW, P. [1975]
"Review, Complex Turbulent Flows",
J. Fluids Engng., 71, 146.

BRADSHAW, P. [1977]
"Complex Turbulent Shear Flows",
Ann. Rev. Fluid Mech., 9, 33.

BRADSHAW, P., CEBECI, T., and WHITELAW, J.H. [1981]
"Engineering Calculation Methods for Turbulent Flows",
Academic Press, London.

BRANDL, F., REVERENCIC, I., CARTELLIERI, W., and DENT, J.C. [1979]
"Turbulent Air Flow in the Combustion Bowl of a DI Diesel Engine and its Effect on Engine Performance",
SAE Paper 790040.

BRANDSTATTER, W., and JOHNS, R.J.R. [1983]
"The Implication of a Probability Method to Engine Combustion Modelling",
Proc. IMechE Int. Conf. on Combustion in Engineering, I, Paper C58/83, 113-124.

BUTLER, T.D., CLOUTMAN, L.D., DUKOWICZ, T.K., and RAMSHAW, T.D. [1979]
"CONCHAS: An Arbitrary Lagrangian-Eulerian Computer Code for Multi-Component Chemically Reactive Fluid Flow at All Speeds",
Los Alamos Scientific Laboratories, Report LA-8129-MS.

BUTLER, T.D., CLOUTMAN, L.D., DUKOWICZ, T.K., and RAMSHAW, T.D. [1980]
"Multi-Dimensional Numerical Simulation of Reactive Flow in Internal Combustion Engines",
Los Alamos Scientific Laboratories, Report LA-UR-80-2762.

CARETTO, L.S., GOSMAN, A.D., PATANKAR, S.V., POTTER, R., and SPALDING, D.B. [1972]
"Two Numerical Procedures for Three-Dimensional Recirculating Flows",
Proc. Int. Conf. on Numerical Methods in Fluid Dynamics, II, 60, Paris.

CHOMIAK, J. [1979]
"Basic Considerations in the Turbulent Flame Propagation in Premixed Gases",
Prog. Energy Comb. Sci., 5, 207-221.

CHONG, M.S., MILKINS, E.E., and WATSON, H.C. [1976]
"The Prediction of Heat and Mass Transfer During Compression and Expansion in IC Engines",
SAE Paper 760761.

CHORIN, A.J. [1968]
"Numerical Solution of the Navier-Stokes Equations",
Math. Comp., 22, 745.

CLARK, R.A., FERZIGER, J.H., and REYNOLDS W.C. [1979]
"Evaluation of Subgrid-Scale Models Using an Accurately Simulated Turbulent Flow",
J. Fluid Mech., 91, Pt. 1, 1-16.

CLERK, . [1912]
Fifth Report of the Gaseous Explosions Committee, cited in Bone, W.A., and Townend, D.T.A. [1927], "Flame and Combustion in Gases",
Longman, Green & Company, London.

COGHE, A., and GHEZZI, U. [1981]
"Measurement and Analysis of Turbulence in Internal Combustion Engines",
Proc. First IEA Conf. on New Energy Conservation Technology and Their Commercialisation, Berlin.

COLE, J.B., and SWORDS, M.D. [1980]
"An Investigation of the Ignition Process in a Lean-Burning Engine Using Conditionally Sampled Laser-Doppler Anemometry",
SAE Paper 800043.

CORRSIN, S. [1962]
Phys. Fluids, 5, 1301.

COURANT, R., ISSACSON, E., and REES, M. [1952]
"On the Solution of Non-Linear Hyperbolic Differential Equations by Finite Differences",
Comms. Pure Appl. Math., 5, 243.

COURANT, R., FRIEDRICHS, K., and LEWY, H. [1967]
"On the Partial Difference Equations of Mathematical Physics",
IBM Journal 2.

CRANK, J., and NICOLSON, P. [1947]
"A Partial Method for Numerical Evaluation of Solutions of Partial Differential Equations of the Heat-Conduction Type",
Proc. Cambridge Phil. Soc., 43, 50-67.

CROW, S.C. [1968]
"Viscoelastic Properties of Fine-Grained Incompressible Turbulence",
J. Fluid Mech., 33, Pt. 1, 1-20.

DANESHYAR, H., and FULLER, D.E. [1981]
"Mixture Motion in an Engine Cylinder",
Cambridge University, Engineering Department, Report CUED/A-Thermo/TR15.

DEARDORFF, J.W. [1973]
"The Use of Subgrid Turbulence Equations in a Three-Dimensional Model of Atmospheric Turbulence",
J. Fluids Engng., 429-438.

DENT, J.C., and SALAMA, N.S. [1975a]
"The Measurement of the Turbulence Characteristics in an Internal Combustion Engine Cylinder",
SAE Paper 750886.

DENT, J.C., and SALAMA, N.S. [1975b]
"Turbulence Structure in the Spark Ignition Engine",
I.Mech.E., Paper C83/75.

DENT, J.C. [1980]
"In-Cylinder Air Motion and Fuel Distribution Using Hot-Wire Anemometry and Interferometric Methods",
Proc. Symp. SRC/UnICEG, 116-130.

DIWAKAR, R., ANDERSON, J.D., GRIFFIN, M.D., and JONES, E. [1976]
"Invisid Solutions of the Flow Field in an Internal Combustion Engine",
AIAA Journal, 14, No. 12, 1667-1668.

EKCHIAN, A., and HOULT, D.P. [1979]
"Flow Visualisation Study of the Intake Process of an Internal Combustion Engine",
SAE Paper 790095.

EL TAHRY, S.H. [1982]
"A Numerical Study on the Effects of Fluid Motion at Inlet-Valve Closure on Subsequent Fluid Motion in a Motored Engine",
SAE Paper 820035.

EL TAHRY, S.H. [1983]
"k-ε Equation for Compressible Reciprocating Engine Flows",
AIAA Journal of Energy, 7, No. 4, 345-353.

FAVRE, A. [1969]
"Statistical Equations of Turbulent Gases",
in "Problems of Hydrodynamics and Continuum Mechanics", *Soc. Indust. Appl. Math.*, 231-266.

FUKUTANI, I., and WATANABE, E. [1982]
"Air Flow Through Poppet Inlet Valves - Analysis of Static and Dynamic Flow Coefficients",
SAE Paper 820154.

GERBER, A. [1982]
"Transient Flows in Piston Engines",
PhD Thesis, École de Lyons (English translation, AERE Harwell, 1983).

GHOBADIAN, A. [1983]
Private communication.

GIBSON, M.M. [1978]
"An Algebraic Stress and Heat-Flux Model for Turbulent Shear Flow with Streamline Curvature",
Int. J. Heat Mass Transfer, 21, 1609-1617.

GIBSON, M.M., McGUIRK, J.J., JONES, W.P., and WHITELAW, J.H. [1978]
"Outline Lecture Notes on Fundamentals of Turbulence and Their Application in Calculation Methods",
Imperial College, Mechanical Engineering Department, Report FS/78/27.

GIBSON, M.M., JONES, W.P., and YOUNIS, B.A. [1981a]
"Calculation of Turbulent Boundary Layers on Curved Surfaces",
Phys. Fluids, 24, No. 3, 386-395.

GIBSON, M.M., VERRIOPOULOS, C.A., and NAGANO, Y. [1981b]
"Measurements in Heated Turbulent Boundary Layer on a Mildly Curved Convex Surface",
in "Turbulent Shear Flows 3", Springer-Verlag, 80-89.

GOSMAN, A.D., PUN, W.M., RUNCHAL, A.K., SPALDING, D.B., and WOLFSTEIN, M. [1969]
"Heat and Mass Transfer in Recirculating Flows",
Academic Press, London.

GOSMAN, A.D., KOOSINLIN, M.L., LOCKWOOD, F.C., and SPALDING, D.B. [1976]
"Transfer of Heat in Rotating Systems",
ASME, Paper 76/GT/25.

GOSMAN, A.D., KHALIL, E.E., and WHITELAW, J.H. [1977]
"The Calculation of Two-Dimensional Turbulent Recirculating Flows",
Proc. First Symp. on Turbulent Shear Flows, Pennsylvania, 13.35-13.45.

GOSMAN, A.D., and JOHNS, R.J.R. [1978]
"Development of a Predictive Tool for In-Cylinder Gas Motion in Engines",
SAE Paper 780315.

GOSMAN, A.D., JOHNS, R.J.R., TIPLER, W., and WATKINS, A.P. [1979]
"Computer Simulation of In-Cylinder Flow, Heat Transfer and Combustion: A Progress Report",
Presented at 13th CIMAC Conference, Vienna (also Imperial College, Mechanical Engineering Department, Report FS/78/38).

GOSMAN, A.D., and JOHNS, R.J.R. [1980]
"Computer Analysis of Fuel-Air Mixing in Direct-Injection Engines",
SAE Paper 800091.

GOSMAN, A.D., JOHNS, R.J.R., and WATKINS, A.P. [1980]
"Development of Prediction Methods for In-Cylinder Processes in Reciprocating Engines",
in "Combustion Modelling in Reciprocating Engines", (eds. J.N. Mattavi and C.A. Amann), Plenum Press, New York.

GOSMAN, A.D., and HARVEY, P.S. [1982]
"Computer Analysis of Fuel-Air Mixing and Combustion in an Axisymmetric DI Engine",
SAE Paper 820036.

GOSMAN, A.D. [1984]
"Flow Processes in Cylinders",
To be published.

GOSMAN, A.D., TSUI, Y.Y., and WATKINS, A.P. [1984]
"Calculation of Three-Dimensional Air Motion in Motored Engines", SAE Paper 840229.

GOSMAN, A.D., TSUI, Y.Y., and VAFIDIS, C. [1984b]
"Flow in a Motored Engine with a Shrouded Valve - A Combined Experimental and Computational Study",
Imperial College, Mechanical Engineering Department, Report FS/84/22 (also Gosman, et al. [1985], to be published as SAE Paper 850498).

GRASSO, F., and BRACCO, F.V. [1983a]
"Computed and Measured Turbulence in Axisymmetric Reciprocating Engines",
AIAA Journal, 21, No. 4, 601-607.

GRASSO, F., and BRACCO, F.V. [1983b]
"Sensitivity of Chamber Turbulence to Intake Flows in Axisymmetric Reciprocating Engines",
AIAA Journal, 21, No. 4, 637-640.

GRIFFIN, M.D., ANDERSON, J.D., and DIWAKAR, R. [1976]
"Navier-Stokes Solutions of the Flow Field in an Internal Combustion Engine",
AIAA Journal, 14, No. 12, 1665-1666.

GROFF, E.G., and MATEKUNAS, F.A. [1980]
"The Nature of Turbulent Flame Propagation in a Homogeneous Spark-Ignition Engine",
SAE Paper 800133.

HANJALIC, K., and LAUNDER, B.E. [1978]
"Basic Multi-Scale Model Development and its Application to Thin Shear Flows",
University of California, Davis, Mechanical Engineering Department, Report TF/78/8.

HANJALIC, K., LAUNDER, B.E., and SCHIESTEL, R. [1979]
"Multiple-Time-Scale Concepts in Turbulent Transport Modelling",
in "Turbulent Shear Flows 2", Springer-Verlag, 36-49.

HANJALIC, K., and LAUNDER, B.E. [1980]
"Sensitising the Dissipation Equation to Irrotational Strains",
J. Fluids Engng., 102, 34-40.

HARLOW, F.H., and NAKAYAMA, P.I. [1968]
"Transport of Turbulence Energy Decay Rate",
Los Alamos Scientific Laboratories, Report LA-3854.

HINZE, P.O. [1975]
"Turbulence",
2nd edition, McGraw-Hill.

HIRES, S.D., TABACZYNSKI, R.J., and NOVAK, J.M. [1978]
"The Prediction of Ignition Delay and Combustion Intervals for a Homogeneous Charge, Spark Ignition Engine",
SAE Paper 780232.

HIROTOMI, T., NAGAYAMA, I., KOBAYASHI, S., and YAMAMASU, M. [1981]
"Study of Induction Swirl in a Spark Ignition Engine",
SAE Paper 810496.

HIRT, C.W., AMSDEN, A.A., and COOK, J.L. [1974]
"An Arbitrary Lagrangian-Eulerian Computing Method for All Flow Speeds",
J. Comp. Phys., 14, No. 3, 227-253.

IDERIAH, F.J.K. [1977]
"Turbulent Natural and Forced Convection in Plumes and Cavities",
PhD Thesis, University of London.

ISSA, R.I. [1982]
"Solution of the Implicitly Discretised Fluid Flow Equations by Operator-Splitting",
Imperial College, Mineral Resources Engineering Department,
Report 65:65P20.

JAHANBAKHSH, A. [1984]
Private communication.

JAMES, E.H., and LUCAS, G.G. [1975]
"Turbulent Flow in Spark Ignition Engine Combustion Chamber",
SAE Paper 750885.

JAYATILLAKA, C.V.L. [1969]
"The Influence of Prandtl Number and Surface Roughness on the Resistance of the Laminar Sub-Layer to Momentum and Heat Transfer",
in "Progress in Heat and Mass Transfer, Vol. 1", Pergamon Press, London.

JOHNS, R.J.R. [1980]
"Prediction of Flow in Diesel Engine Cylinders",
PhD Thesis, University of London.

JOHNSTON, S.C., ROBINSON, C.W., RORKE, W.S., SMITH, J.R., and WITZE, P.O. [1979]
"Application of Laser Diagnostics to an Injected Engine",
SAE Paper 790092.

JONES, W.P., and LAUNDER, B.E. [1972]
"The Prediction of Laminarisation with a Two-Equation Model of Turbulence",
Int. J. Heat Mass Transfer, 15, 301-314.

JONES, W.P., and LAUNDER, B.E. [1973]
"The Calculation of Low-Reynolds-Number Phenomena with a Two-Equation Model of Turbulence",
Int. J. Heat Mass Transfer, 16, 1119-1130.

JONES, W.P. [1979]
"Models for Turbulent Flows with Variable Density and Combustion",
Von Karman Inst. for Fluid Dynamics, Lecture Series 1979-2.

JONES, W.P. [1984]
Private communication.

KASTNER, L.J., WILLIAMS, T.J., and WHITE, J.B. [1963-64]
"Poppet Inlet Valve Characteristics and Their Influence on the Induction Process",
Proc. IMechE., 178, Pt. 1, No. 36, 955-975.

KOLMOGOROV, A.N. [1942]
"Equations of Turbulent Motion in an Incompressible Fluid",
Izv. Akad. Nauk. USSR, Seria Fizicheska Vi., No. 1-2, 56-58
(English translation, Imperial College, Mechanical Engineering Department, Report ON/6, 1968).

KUO, A.Y.S., and CORRSIN, S. [1971]
J. Fluid Mech., 50, 285.

LAI, K.Y.M. [1983]
"Numerical Analysis of Fluid Transport Phenomena",
PhD Thesis, University of London.

LANCASTER, D.R. [1976]
"Effects of Engine Variables on Turbulence in a Spark-Ignition Engine",
SAE Paper 760159.

LANCASTER, D.R., KRIEGER, R.B., SORENSON, S.C., and HULL, W.L. [1976]
"Effects of Turbulence on Spark-Ignition Engine Combustion",
SAE Paper 760160.

LAUNDER, B.E., and SPALDING, D.B. [1972]
"Lectures in Mathematical Models of Turbulence",
Academic Press, London.

LAUNDER, B.E., MORSE, A., RODI, W., and SPALDING, D.B. [1972]
"The Prediction of Free Shear Flows - A Comparison of the Performance of Six Turbulence Models",
NASA SP-321, 1, 361-426 (also Imperial College, Mechanical Engineering Department, Report TM/TN/B/19).

LAUNDER, B.E., and SPALDING, D.B. [1974]
"The Numerical Computation of Turbulent Flow",
Comp. Meth. in Appl. Mech. and Eng., 3, 269.

LAUNDER, B.E., REECE, G.J., and RODI, W. [1975]
"Progress in the Development of a Reynolds Stress Turbulence Closure",
J. Fluid Mech., 68, Pt. 3, 537-566.

LAUNDER, B.E., and MORSE, A. [1979]
"Numerical Prediction of Axisymmetric Shear Flows with a Reynolds Stress Closure",
in "Turbulent Shear Flows 1", Springer-Verlag, 279-293.

LESCHZINER, M.A., and RODI, W. [1981]
"Calculation of Annular and Twin Parallel Jets Using Various Discretisation Schemes and Turbulence-Model Variations",
J. Fluids Engng., 103, 352-359.

LIBBY, P.A., and BRAY, K.N.C. [1977]
"Variable Density Effects in Premixed Turbulent Flames",
AIAA Journal, 15, No. 8, 1186.

LIOU, T.M., and SANTAVICCA, D.A. [1982]
"Cycle Resolved Measurements in a Motored IC Engine",
Presented at Symp. on Flows in Internal Combustion Engines, ASME Winter Annual Meeting, Phoenix.

LIOU, T.M., and SANTAVICCA, D.A. [1983]
"Cycle Resolved Turbulence Measurements in a Ported Engine with and without Swirl",
SAE Paper 830419.

LIOU, T.M., HALL, M., SANTAVICCA, D.A., and BRACCO, F.V. [1984]
"Laser-Doppler Velocimetry Measurements in Valved and Ported Engines",
SAE Paper 840375.

LOONEY, M.K. [1982]
"Numerical Modelling of the Transport Equations for Two-Dimensional Free and Impinging Jet Flows",
PhD Thesis, University College, Dublin.

MacCORMACK, R.W. [1969]
"The Effect of Viscosity in Hypervelocity Impact Cratering",
AIAA Paper 69-354.

McGUIRK, J.J., TAYLOR, A.M.K.P., and WHITELAW, J.H. [1981]
"The Assessment of Numerical Diffusion in Upwind Difference Calculations of Turbulent Recirculating Flows",
in "Turbulent Shear Flows 3", Springer-Verlag, 206-224.

McGUIRK, J.J. [1983]
Private communication.

MARKATOS, N.C., and MUKERJEE, T. [1981]
"Three-Dimensional Computer Analysis of Flow and Combustion in Automotive Internal Combustion Engines",
Trans. IMACS, 23, No. 4, 354.

MELLOR, G.L., and HERRING, H.J. [1973]
"A Survey of the Mean Turbulent Field Closure Models",
AIAA Journal, 11, No. 5, 590-598.

MONAGHAN, M.L., and PETTIFER, H.F. [1981]
"Air Motion and its Effect on Diesel Performance and Emissions",
SAE Paper 810225.

MOREL, T., and MANSOUR, N.N. [1982]
"Modelling of Turbulence in Internal Combustion Engines",
SAE Paper 820040.

MORSE, A.P. [1977]
"The Effect of Crank-Angle Broadening on Laser-Doppler Measurements in Reciprocating Engines",
Imperial College, Mechanical Engineering Department, Report FS/77/18.

MORSE, A.P., WHITELAW, J.H., and YIANNESKIS, M. [1978a]
"Turbulent Flow Measurements by Laser-Doppler Anemometry in a Motored Reciprocating Engine",
Imperial College, Mechanical Engineering Department, Report FS/78/24.

MORSE, A.P., WHITELAW, J.H., and YIANNESKIS, M. [1979]
"The Effect of Engine Speed on the Flow Pattern in Reciprocating Engines",
Imperial College, Mechanical Engineering Department, Report FS/79/12.

MORSE, A.P., WHITELAW, J.H., and YIANNESKIS, M. [1980a]
"The Influence of Swirl on the Flow Characteristics of a Reciprocating Piston-Cylinder Assembly",
ASME, Paper 80-WA/FE-8 (also Morse, et al. [1978b], Imperial College, Mechanical Engineering Department, Report FS/78/41).

MORSE, A.P., WHITELAW, J.H., and YIANNESKIS, M. [1980b]
"The Flow Characteristics of a Piston-Cylinder Assembly with an Off-Centre, Open Port",
Proc. IMechE., 194, No. 31, 291-299.

MORSE, A.P., and WHITELAW, J.H. [1981]
"Measurements of the In-Cylinder Flow of a Motored Four-Stroke Reciprocating Engine",
Proc. R. Soc. Lond., A337, 309-321.

MUCK, K.C., and SMITS, A.J. [1983]
"The Behaviour of Compressible Boundary Layer Under Incipient Separation Conditions",
Proc. Fourth Symp. on Turbulent Shear Flow, 2.15-2.20.

MUKERJEE, T., PRZEKWAS, A.J., SINGHAL, A.K., DUGGAL, V.K., and KUO, T.W. [1984]
"Three-Dimensional Modelling of In-Cylinder Processes in DI Diesel Engine",
SAE Paper 840227.

NAMAZIAN, M., HANSEN, S., LYFORD-PIKE, E., SANCHEZ-BARSSE, J., HEYWOOD, J., and RIFE, J. [1980]
"Schlieren Visualisation of the Flow and Density Fields in the Cylinder of a Spark-Ignition Engine",
SAE Paper 800044.

NARASHIMA, R., and VISWANATH, P.R. [1975]
"Reverse Transition at an Expansion Corner in Supersonic Flow",
AIAA Journal, 13, 693.

PATANKAR, S.V., and SPALDING, D.B. [1970]
"Heat and Mass Transfer in Boundary Layers",
2nd edition, Intertex Books, London.

PATANKAR, S.V., and SPALDING, D.B. [1972]
"A Calculation Procedure for Heat, Mass and Momentum Transfer in Three-Dimensional Parabolic Flows",
Int. J. Heat Mass Transfer, 15, 1787.

PATANKAR, S.V., and BALIGA, B.R. [1978]
"A New Finite-Difference Scheme for Parabolic Differential Equations",
Num. Heat Transfer, 1, 27-37.

PATANKAR, S.V. [1980]
"Numerical Heat Transfer and Fluid Flow",
McGraw-Hill, New York.

PRANDTL, L. [1925]
"Bericht über Untersuchungen zur Ausgebildeten Turbulenz",
ZAMN, 5, 136.

PRANDTL, L. [1945]
"Über ein Neues Formelsystem für die Ausgebildeten Turbulenz",
Nachr. Akad. Wiss, Göttingen, Math.-Phys. Klasse, S.6.

PRUDNIKOV, A.G. [1963]
"Some Measurements of the Turbulence of Air Flows in Industrial Tubes", NASA Tech. Trans. F-97, 85-96.

RAMOS, J.I., and SIRIGNANO, W.A. [1980a]
"Axisymmetric Flow Model with and without Swirl in a Piston-Cylinder Arrangement with Idealised Valve Operation", SAE Paper 800284.

RAMOS, J.I., and SIRIGNANO, W.A. [1980b]
"Axisymmetric Flow Model in a Piston-Cylinder Arrangement with Detailed Analysis of the Valve Region", SAE Paper 800286.

RAMOS, J.I., GANY, A., and SIRIGNANO, W.A. [1981]
"Study of Turbulence in a Motored Four-Stroke Internal Combustion Engine", *AIAA Journal*, 19, No. 5, 595-600.

RASK, R.B. [1979]
"Laser-Doppler Anemometry Measurements in an Internal Combustion Engine", SAE Paper 790094.

RASK, R.B. [1981]
"Comparison of Window, Smoothed-Ensemble and Cycle-by-Cycle Data Reduction Techniques for Laser-Doppler Anemometer Measurements of In-Cylinder Velocity", *Proc. ASME Symp. on Fluid Mechanics of Combustion Systems*, Boulder.

REYNOLDS, O. [1895]
"On the Dynamical Theory of Incompressible Viscous Fluids and the Determination of the Criterion", *Phil. Trans. R. Soc. Lond.*, 186, 123.

REYNOLDS, A.J. [1974]
"Turbulence Flows in Engineering", John Wiley & Sons, London.

REYNOLDS, W.C. [1976]
"Computation of Turbulent Flows", *Ann. Rev. Fluid Mech.*, 8, 183-208.

REYNOLDS, W.C. [1980]
"Modelling of Fluid Motions in Engines - An Introductory Overview", in "Combustion Modelling in Reciprocating Engines", (eds. J.N. Mattavi and C.A. Amann), Plenum Press, New York.

RICARDO, H.H. [1922]
"Recent Research Work on the Internal Combustion Engine",
Trans. SAE, 17, Pt. 1.

RICHTMYER, R.D., and MORTON, K.W. [1967]
"Difference Methods for Initial Value Problems",
John Wiley & Sons, London.

ROACHE, P.J. [1976]
"Computational Fluid Dynamics",
Hermosa Publishers, Albuquerque.

RODI, W., and SPALDING, D.B. [1970]
"A Two Parameter Model of Turbulence and its Applications to Free Jets",
Warne und Stoffübertragung, 3, 85.

RODI, W. [1971]
"On the Equation Governing the Rate of Turbulent Energy Dissipation",
Imperial College, Mechanical Engineering Department, Report TM/TN/A/14.

RODI, W. [1972]
"The Prediction of Free Turbulent Boundary Layers by Use of a Two-Equation Model of Turbulence",
PhD Thesis, University of London.

RODI, W. [1975]
"A Note on the Empirical Constant in the Kolmogorov-Prandtl Eddy-Viscosity Expression",
J. Fluids Engng., 386-389.

RODI, W. [1976]
"A New Algebraic Relation for Calculating the Reynolds Stresses",
ZAMM, 56, 219-221.

RODI, W. [1978]
"Turbulence Models and Their Application in Hydraulics - A State of the Art Review",
University of Karlsruhe, Report SFB 80/T/127.

RODI, W., and SCHEUERER, G. [1983a]
"Scrutinising the k-ε Model Under Adverse Pressure Gradient Condition",
Proc. Fourth Symp. on Turbulent Shear Flow, 2.8-2.14.

RODI, W., and SCHEUERER, G. [1983b]
"Calculation of Curved Shear Layers with Two-Equation Turbulence Models",
Phys. Fluids, 26, No. 6, 1422-1436.

ROTTA, J. [1951]
"Statistische Theorie Nichthomogeuer Turbulenze",
Zietsch. für Physik, 129, 547, and 131, 51 (English translation, Imperial College, Mechanical Engineering Department, Reports TWF/TN/38 and TWF/TN/39, 1968).

RUNCHAL, A.K. [1972]
"Convergence and Accuracy of Three Finite Difference Schemes for a Two-Dimensional Conduction and Convection Problem",
Int. J. Num. Meth. Eng., 4, 541-550.

RUNCHAL, A.K. [1976]
"Comparative Criteria for Finite Difference Formulation for Problems of Fluid Flow",
Dames and Moore Advanced Technology Group, Report ATG/ES/1.

SCHLICHTING, H. [1968]
"Boundary-Layer Theory",
6th edition, McGraw-Hill.

SCHOCK, H.J., SOSOKA, D.J., and RAMOS, J.I. [1983]
"Numerical Studies of the Formation and Destruction of Vortices in a Motored Four-Stroke Piston-Cylinder Configuration",
Proc. AIAA 21st Aerospace Sciences Meeting, Paper AIAA-83-0497.

SCHUMANN, U. [1975]
"Subgrid Scale Model for Finite Difference Simulations of Turbulent Flows in Plane Channels and Annuli",
J. Comp. Phys., 18, No. 4, 376-404.

SEMENOV, E.S. [1963]
"Studies of Turbulent Gas Flow in Piston Engines",
NASA Tech. Trans. F-97, 122-147.

SITKEI, G. [1974]
"Heat Transfer and Thermal Loading in Internal Combustion Engines",
Akademiai Kiado, Budapest.

SMITH, J.R. [1982]
"Turbulent Flame Structure in a Homogeneous-Charge Engine",
SAE Paper 820043.

SPALDING, D.B. [1971]
"The kw Model of Turbulence",
Imperial College, Mechanical Engineering Department, Report TM/TN:A/16.

SPALDING, D.B. [1972]
"A Novel Finite-Difference Formulation for Differential Formulations Involving Both First and Second Derivatives",
Int. J. Num. Meth. Eng., 4, 551-559.

SPALDING, D.B. [1980]
"A General Computer Program for Fluid Flow, Heat Transfer and Chemical Reaction Processes",
Int. FEM Congress, Baden-Baden.

STREIT, E.E., and BORMAN, G.C. [1971]
"Mathematical Simulation of a Large Turbocharged Two-Stroke Diesel Engine",
SAE Paper 710176.

TABACZYNSKI, R.J. [1979]
"Turbulence and Turbulent Combustion in Spark-Ignition Engines",
in "Progress in Energy and Combustion Science", Student Edition 1, (ed. N.A. Chigier), Pergamon Press.

TABACZYNSKI, R.J., TRINKER, F.H., and SHANNON, Ben A.S. [1980]
"Further Refinement and Validation of a Turbulent Flame Propagation Model for Spark-Ignition Engines",
Combustion and Flame, 39, 111-121.

TANNAKA, K. [1929]
"Air Flow Through Suction Valve of a Conical Seat",
Tokyo Imperial University, Aeronautical Research Institute Report, 4, No. 50, 260.

TAYLOR, A.M.K.P. [1981]
"Confined Isothermal and Combusting Flows Behind Axi-Symmetric Baffles",
PhD Thesis, University of London.

TENNEKES, H. [1968]
Phys. Fluids, 11, 669.

TENNEKES, H., and LUMLEY, J.L. [1980]
"A First Course in Turbulence",
6th edition, MIT Press.

TINDAL, M.J., WILLIAMS, T.J., and EL KHAFIJI, A.H.A. [1974]
"Gas Flow Measurements in Engine Cylinders",
SAE Paper 740719.

TINDAL, M.J., and WILLIAMS, T.J. [1977]
"An Investigation of Cylinder Gas Motion in the Direct Injection Diesel Engine",
SAE Paper 770405.

TOWNSEND, A.A. [1956]
"The Structure of Turbulent Shear Flow",
1st edition, Cambridge University Press.

TOWNSEND, A.A. [1980]
"The Structure of Turbulent Shear Flow",
2nd edition, Cambridge University Press.

TSUGE, M., HIROYUKI, K., and YANAGIHARA, H. [1973]
"Decay of Turbulence in a Closed Vessel: First Report, Decay of Turbulence Intensity",
Bulletin of JSME, 16, No. 92, 244-251.

VAFIDIS, C. [1984]
"Influence of Induction Swirl and Piston Configuration on Air Flow in a Four-Stroke Model Engine",
Proc. IMechE., 198C, No. 4.

VAFIDIS, C., and WHITELAW, J.H. [1984]
"Steady and Pulsating Air Flow Through a Stationary Valve of a Reciprocating Engine",
Imperial College, Mechanical Engineering Department, Report FS/84/04.

VAFIDIS, C., and WHITELAW, J.H. [1984b]
"Valve and In-Cylinder Flow in Reciprocating Engines",
Imperial College, Mechanical Engineering Department, Report FS/84/21.

VERGA, R.S. [1962]
"Matrix Iterative Analysis",
Prentice-Hall Int., London.

VLACHOS, N.S. [1977]
"Blood Flow in Small Diameter Duct, Particularly in Venules",
PhD Thesis, University of London.

WAKISAKA, T., HAMAMOTO, Y., OHIGASHI, S., and HASHIMOTO, M. [1979]
"Measurements of Air Swirl and its Turbulence Characteristics in the Cylinder of an Internal Combustion Engine",
Proc. IMechE., Paper C91/79.

WALLACE, W.B. [1967-68]
"High-Output, Medium-Speed Diesel Engine Air and Exhaust System Flow Losses",
Proc. IMechE., 182, Pt. 3D.

WATKINS, A.P. [1973]
"Calculation of Flow and Heat Transfer in the Combustion Chamber of a Reciprocating Engine",
MSc Thesis, University of London.

WATKINS, A.P. [1977]
"Flow and Heat Transfer in Piston/Cylinder Assemblies",
PhD Thesis, University of London.

WATSON, N., and JANOTA, M.S. [1982]
"Turbocharging the Internal Combustion Engine",
Macmillan Press.

WIGLEY, G., and HAWKINS, M.G. [1978]
"Three-Dimensional Velocity Measurements by Laser-Doppler Anemometry in a Diesel Engine Cylinder Under Steady-State Inlet Flow Conditions",
SAE Paper 780060.

WIGLEY, G., PATTERSON, A.C., and RENSHAW, J. [1981]
"Swirl Velocity Measurements in a Firing Production Diesel Engine by Laser Anemometry",
Proc. ASME Conf. on Fluid Mechanics of Combustion Systems, Boulder.

WILLIAMS, T.J., and TINDAL, M.J. [1979]
"The Prediction and Measurement of Gas Flow in the Combustion Chambers of Direct Injection Diesel Engines",
CIMAC 13th Int. Cong. on Combustion Engines, Vienna, Paper D24.

WILLIAMS, T.J., and TINDAL, M.J. [1981]
"Gas Flow Studies in Direct Injection Diesel Engines with Re-Entrant Combustion Chambers",
SAE Paper 800027.

WINSOR, R.E., and PATTERSON, D.J. [1973]
"Mixture Turbulence - A Key to Cyclic Combustion Variation",
SAE Paper 730086.

WITZE, P.O. [1975]
"Hot-Wire Turbulence Measurements in a Motored Internal Combustion Engine",
Sandia National Laboratories, Report SAND 75-8641.

WITZE, P.O. [1976a]
"Hot-Wire Measurements of the Turbulence in a Motored Spark-Ignition Engine",
Presented at AIAA 14th Aerospace Sciences Meeting, Washington, D.C., Paper 76-37.

WITZE, P.O. [1976b]
"Preliminary Hot-Wire Measurements in a Motored Engine with an Axisymmetric Cylinder Geometry",
cited in Watkins [1977], "Flow and Heat Transfer in Piston Cylinder Assemblies".

WITZE, P.O. [1977]
"Measurements of the Spatial Distribution and Engine Speed Dependence of Turbulent Air Motion in an IC Engine",
SAE Paper 770220.

WITZE, P.O. [1978]
"Application of Laser Velocimetry to a Motored Internal Combustion Engine",
Presented at Third Int. Workshop on Laser Velocimetry, Purdue University.

WITZE, P.O. [1979]
"A Critical Comparison of Hot-Wire Anemometry and Laser-Doppler Velocimetry for IC Engine Applications",
Sandia National Laboratories, Report SAND 79-8683 (also Witze [1980], SAE Paper 800132).

WITZE, P.O., MARTIN, J.K., and BORGNAKKE, C. [1983a]
"Conditionally-Sampled Velocity and Turbulence Measurements in a Spark-Ignition Engine",
Sandia National Laboratories, Report SAND 83-8794.

WITZE, P.O., MARTIN, J.K., and BORGNAKKE, C. [1983b]
"Fluid Motion During Flame Propagation in a Spark Ignition Engine",
Sandia National Laboratories, Report SAND 83-8761.

WOODS, W.A., and KHAN, S.R. [1965-66]
"An Experimental Study of Flow Through Poppet Valves",
Proc. IMechE., 180, Pt. 3N, 32-41.

YIANNESKIS, M. [1977]
"Flow Patterns in Internal Combustion Engines",
MSc Thesis, University of London.

APPENDIX A

DIFFERENTIAL EQUATIONS FOR ENSEMBLE-AVERAGED QUANTITIES AND CYCLE-TO-CYCLE VARIATIONS

The instantaneous equations of conservation of mass and transport of a dependent variable Φ (equation (3.8)) are:

$$\begin{aligned} &\frac{\partial}{\partial t}(\rho) + \frac{\partial}{\partial x_j}(\rho U_j) = 0 \\ &\frac{\partial}{\partial t}(\rho \Phi) + \frac{\partial}{\partial x_j}(\rho U_j \Phi) = \frac{\partial}{\partial x_j}\left(\Gamma \frac{\partial \Phi}{\partial x_j}\right) + S_\Phi \end{aligned} \tag{A.1}$$

We require to derive equations for averaged properties defined according to the decomposition:

$$\Phi = \overline{\Phi} + \hat{\Phi} + \phi' \tag{A.2}$$

in which $\overline{\Phi}$ ≡ ensemble-averaged value

$\hat{\Phi}$ ≡ time-average of $(\Phi - \overline{\Phi})$ over Δt, where Δt is a time increment over which the turbulence can be assumed to be stationary

ϕ' ≡ turbulent fluctuations

If there is no cycle-to-cycle variation, $(\Phi - \overline{\Phi})$ would only include the turbulent fluctuations about $\overline{\Phi}$ and hence $\hat{\Phi}$ would be zero. Therefore, $\hat{\Phi}$ is a measure of cycle-to-cycle variations.

We assume that there is no cycle-to-cycle variation of density and also density fluctuations are small, thus $\rho = \overline{\rho}$. If we first decompose Φ as

$$\Phi = \overline{\Phi} + \phi'' \tag{A.3}$$

where, it will be recalled, ϕ'' represents fluctuations about $\overline{\Phi}$, then equation (A.1) can be written, with viscous diffusion neglected, as:

$$\begin{aligned} &\frac{\partial}{\partial t}(\overline{\rho}) + \frac{\partial}{\partial x_j}(\overline{\rho}\,\overline{U}_j + \overline{\rho}\,\overline{u_j''}) = 0 \\ &\frac{\partial}{\partial t}(\overline{\rho}\,\overline{\Phi} + \overline{\rho}\,\overline{\phi''}) + \frac{\partial}{\partial x_j}(\overline{\rho}\,\overline{U}_j\,\overline{\Phi} + \overline{\rho}\,\overline{U}_j\,\overline{\phi''} + \overline{\rho}\,\overline{u_j''}\,\overline{\Phi} + \overline{\rho}\,\overline{u_j''\phi''}) = \overline{S} + S' \end{aligned} \tag{A.4}$$

If the above equations are now ensemble-averaged, they become

$$\frac{\partial}{\partial t}(\bar{\rho}) + \frac{\partial}{\partial x_j}(\bar{\rho}\,\bar{U}_j) = 0$$
$$\frac{\partial}{\partial t}(\bar{\rho}\,\bar{\Phi}) + \frac{\partial}{\partial x_j}(\bar{\rho}\,\bar{U}_j\bar{\Phi} + \overline{\rho\,u_j''\phi''}) = \bar{S} \qquad (A.5)$$

Equations (A.5) describe the variation of the ensemble-averaged (mean flow) properties $\bar{U}_j$ and $\bar{\Phi}$.

In order to derive the equations for the time-averaged properties, equation set (A.5) is subtracted from set (A.4) to give

$$\frac{\partial}{\partial x_j}(\bar{\rho}\,u_j'') = 0$$
$$\frac{\partial}{\partial t}(\bar{\rho}\,\phi'') + \frac{\partial}{\partial x_j}(\bar{\rho}\,\bar{U}_j\phi'' + \bar{\rho}\,\bar{\Phi}\,u_j'' + \bar{\rho}\,u_j''\phi'' - \overline{\rho\,u_j''\phi''}) = S'' \qquad (A.6)$$

Substitution for u_j'' and ϕ'' according to the definitions (A.2) and (A.3) gives

$$\frac{\partial}{\partial x_j}(\bar{\rho}\,\hat{U}_j + \bar{\rho}\,u_j') = 0$$
$$\frac{\partial}{\partial t}(\bar{\rho}\,\hat{U}_j + \bar{\rho}\,\phi') + \frac{\partial}{\partial x_j}(\bar{\rho}\,\bar{U}_j\hat{\Phi} + \bar{\rho}\,\bar{U}_j\phi' + \bar{\rho}\,\bar{\Phi}\,\hat{U}_j + \bar{\rho}\,\bar{\Phi}\,u_j' + \bar{\rho}\,\hat{U}_j\hat{\Phi} \qquad (A.7)$$
$$+ \bar{\rho}\,\hat{U}_j\phi' + \bar{\rho}\,u_j'\hat{\Phi} + \bar{\rho}\,u_j'\phi' - \overline{\rho\,u_j''\phi''}) = \hat{S} + S'$$

Time-averaging of set (A.7) produces

$$\frac{\partial}{\partial x_j}(\hat{\bar{\rho}}\,\hat{U}_j) = 0$$
$$\frac{\Delta\bar{\rho}}{\Delta t}\hat{U}_j + \frac{\partial}{\partial x_j}(\hat{\bar{\rho}}\,\hat{\bar{U}}_j\hat{\Phi} + \hat{\bar{\rho}}\,\hat{\bar{\Phi}}\,\hat{U}_j + \hat{\bar{\rho}}\,\hat{U}_j\hat{\Phi} + \hat{\bar{\rho}}\,\hat{u_j'\phi'} - \hat{\bar{\rho}}\,\hat{\overline{u_j''\phi''}}) = \hat{S} \qquad (A.8)$$

in which the hat-overbar '$\hat{\bar{}}$' represents time-mean values (over Δt) of the ensemble-averaged properties.

Therefore, calculation of the ensemble-averaged quantities $\bar{U}$ and $\bar{\Phi}$, the cycle-to-cycle variations $\hat{U}$ and $\hat{\Phi}$, and the statistical parameters $\hat{u_j'\phi'}$ associated with the 'true' turbulence entails the following sequence of operations.

(i) Solve the continuity, momentum and Φ-transport equations in the form represented by equation (A.5) to obtain $\bar{\rho}$, $\bar{U}_j$, $\bar{\Phi}$ and $\overline{\rho\,u_j''\phi''}$; then store these quantities.

(ii) Take the time-mean of these quantities over a time interval Δt, during which the turbulence can be assumed to be nearly stationary (in experiments, $\Delta\theta \simeq 10° - 45°$ CA has been used).

(iii) Insert the time-mean values $\hat{\bar{\rho}}$, $\hat{\bar{U}}_j$, $\hat{\bar{\Phi}}$ and $\overline{u_j'' \hat{\phi}''}$ in equation set (A.8) and solve for $\hat{U}_j$ and $\hat{\Phi}$ ($\hat{u_j' \phi'}$ is obtained with the aid of turbulence modelling).

APPENDIX B
INTRODUCTION OF DENSITY-WEIGHTED AVERAGING AND DERIVATION OF THE GOVERNING DIFFERENTIAL EQUATIONS FOR DWEA PROPERTIES

The ensemble-averaging (EA) and the density-weighted ensemble-averaging (DWEA) processes, denoted here by { } and < > respectively, are defined as

$$\{\Phi(X,t)\} = \lim_{N\to\infty} \frac{1}{N+1} \sum_{i=0}^{N} \Phi(X,t+iT_0) = \overline{\Phi} \tag{B.1}$$

$$\langle\Phi(X,t)\rangle = \frac{1}{\overline{\rho}} \{\rho(X,t)\ \Phi(X,t)\} = \frac{1}{\overline{\rho}} \overline{\rho\ \Phi} = \tilde{\Phi} \tag{B.2}$$

in which i is the number of observations (e.g. engine cycles) and T_0 is the period. The instantaneous value of a variable Φ can be decomposed according to either approach, thus

$$\begin{aligned} \Phi &= \overline{\Phi} + \phi' \\ &= \tilde{\Phi} + \phi'' \end{aligned} \tag{B.3}$$

From the above definitions, the following relations can be deduced (Jones [1979]):

$$\begin{aligned} \{\phi'\} &= \overline{\phi'} = 0 \\ \langle\phi''\rangle &= \frac{1}{\overline{\rho}} \overline{\rho\ \phi''} = 0 \\ \{\phi''\} &= \overline{\phi''} \neq 0 \\ \{\rho\ \Phi\} &= \overline{\rho}\ \tilde{\Phi} \\ \{\rho\ \phi''\} &= \overline{\rho}\ \tilde{\phi''} = 0 \\ \{\tilde{\Phi}\} &= \tilde{\Phi} \end{aligned} \tag{B.4}$$

The relationship between DWEA and EA 'mean' properties can be obtained as follows: let

$$\Phi = \overline{\Phi} + \phi'$$

then multiply by ρ and take ensemble average

$$\{\rho\ \Phi\} = \overline{\rho}\ \overline{\Phi} + \overline{\rho'\ \phi'}$$

thus
$$\tilde{\Phi} = \overline{\Phi} + \frac{\overline{\rho'\ \phi'}}{\overline{\rho}} \qquad (B.5)$$

The relationship between the fluctuating DWEA and EA components can be derived from equation (B.5) as follows

$$\Phi - \phi'' = \Phi - \phi' + \frac{\overline{\rho'\ \phi'}}{\overline{\rho}}$$

thus
$$\phi'' = \phi' - \frac{\overline{\rho'\ \phi'}}{\overline{\rho}} \qquad (B.6)$$

The following further useful relations can be derived from equations (B.5) and (B.6):

$$\overline{\phi''} = -\frac{\overline{\rho'\ \phi'}}{\overline{\rho}}$$

$$\phi'' = \phi' + \overline{\phi''}$$

$$\overline{\Phi} = \tilde{\Phi} + \phi''$$

$$\overline{\rho'\ \phi''} = \overline{\rho'\ \phi'} \qquad (B.7)$$

$$\overline{\rho'\ \phi''} = -\overline{\rho}\ \overline{\phi''}$$

$$\overline{\rho\ \phi_1''\ \phi_2''} = \overline{\rho}\ \overline{\phi_1''\ \phi_2''}$$

$$\overline{\phi_1'\ \phi_2'} = \overline{\phi_1''\ \phi_2''} - \frac{\overline{\rho'\ \phi_1''\ \phi_2''}}{\overline{\rho}} + \overline{\phi_1''}\ \overline{\phi_2''}$$

(Note that $\tilde{=}$ is equivalent to $\tilde{}$: the use of the overbar is to denote correlations between the fluctuating components.)

The governing differential equations for DWEA properties are derived by using a combined EA and DWEA decomposition. The instantaneous density and pressure are decomposed into their EA values and fluctuations as

$$\rho = \overline{\rho} + \rho'$$

$$P = \overline{P} + p' \qquad (B.8)$$

All other variables are decomposed into their DWEA values and the

fluctuations $(\tilde{\Phi} + \phi'')$ if they are contained in the 'convection' terms, and into their EA values and the fluctuations $(\overline{\Phi} + \phi')$ if they are included in the diffusion terms. The governing equations (3.1), (3.2) and (3.8) thus can be written, within this framework, as:

(i) Continuity:

$$\frac{\partial}{\partial t}(\overline{\rho} + \rho') + \frac{\partial}{\partial x_j}(\rho \tilde{U}_j + \rho u_j'') = 0 \tag{B.9}$$

Ensemble-averaging gives

$$\frac{\partial}{\partial t}(\overline{\rho}) + \frac{\partial}{\partial x_j}(\overline{\rho}\, \tilde{U}_j) = 0 \tag{B.10}$$

(ii) Momentum:

$$\frac{\partial}{\partial t}(\rho \tilde{U}_j + \rho u_j'') + \frac{\partial}{\partial x_j}(\rho \tilde{U}_j \tilde{U}_i + \rho u_j'' \tilde{U}_i + \rho \tilde{U}_j u_i'' + \rho u_i'' u_j'')$$

$$= -\frac{\partial}{\partial x_j}(\overline{P} + p') + \frac{\partial}{\partial x_j}(\overline{\tau_{ij}} + \tau'_{ij}) \tag{B.11}$$

where

$$\begin{aligned} \overline{\tau_{ij}} &= \overline{\mu}\left(\frac{\partial \overline{U}_i}{\partial x_j} + \frac{\partial \overline{U}_j}{\partial x_i}\right) - \frac{2}{3}\overline{\mu}\frac{\partial \overline{U}_\ell}{\partial x_\ell}\delta_{ij} \\ \tau'_{ij} &= \overline{\mu}\left(\frac{\partial u'_i}{\partial x_j} + \frac{\partial u'_j}{\partial x_i}\right) - \frac{2}{3}\overline{\mu}\frac{\partial u'_\ell}{\partial x_\ell}\delta_{ij} \end{aligned} \tag{B.12}$$

Ensemble-averaging gives

$$\frac{\partial}{\partial t}(\overline{\rho}\, \tilde{U}_i) + \frac{\partial}{\partial x_j}(\overline{\rho}\, \tilde{U}_j \tilde{U}_i + \overline{\rho u_i'' u_j''}) = -\frac{\partial \overline{P}}{\partial x_i} + \frac{\partial}{\partial x_j}\overline{\tau_{ij}} \tag{B.13}$$

(iii) Scalar transport:

$$\frac{\partial}{\partial t}(\rho \tilde{\Phi} + \rho \phi'') + \frac{\partial}{\partial x_j}(\rho \tilde{U}_j \tilde{\Phi} + \rho u_j'' \tilde{\Phi} + \rho \tilde{U}_j \phi'' + \rho u_j'' \phi'')$$

$$= \frac{\partial}{\partial x_j}\left[\overline{\Gamma}_\Phi\left(\frac{\partial \overline{\Phi}}{\partial x_j} + \frac{\partial \phi'}{\partial x_j}\right)\right] + \tilde{S}_\Phi + S''_\phi \tag{B.14}$$

Ensemble-averaging gives

$$\frac{\partial}{\partial t}(\overline{\rho}\, \tilde{\Phi}) + \frac{\partial}{\partial x_j}(\overline{\rho}\, \tilde{U}_j \tilde{\Phi} + \overline{\rho u_j'' \phi''}) = \frac{\partial}{\partial x_j}\left(\overline{\Gamma}_\Phi \frac{\partial \overline{\Phi}}{\partial x_j}\right) + \tilde{S}_\Phi \tag{B.15}$$

For high Reynolds number turbulent flows, the molecular diffusion is

negligible, and therefore the diffusion terms on the right hand side of the equations, containing the EA 'mean' values, can be dropped. Consequently, the equations would only contain the DWEA values.

APPENDIX C
TRANSPORT EQUATIONS FOR THE REYNOLDS STRESSES AND THE TURBULENCE KINETIC ENERGY

Here, the general DWEA form of the transport equation for the Reynolds stresses $\bar{\rho}\,\widetilde{u_i'' u_j''}$ are derived. The transport equation for k can be simply obtained by contraction, thus

$$\tfrac{1}{2}\,\bar{\rho}\,\widetilde{u_i'' u_i''} \equiv \bar{\rho}\left(\frac{\widetilde{u_1''^2} + \widetilde{u_2''^2} + \widetilde{u_3''^2}}{2}\right) = \bar{\rho}\,k \tag{C.1}$$

For brevity here, the transport equation for $R \equiv u_i'' u_j''$ is first derived and then is substituted. It will be recalled that, according to the definition of density-weighted averaging

$$\langle \rho\, R \rangle = \bar{\rho}\left\{\frac{\rho\, R}{\bar{\rho}}\right\} = \bar{\rho}\,\tilde{R} \tag{C.2}$$

Accordingly, the DWEA total derivative of R is given by

$$\begin{aligned}
\left\langle \rho \frac{DR}{Dt} \right\rangle &= \left\langle \rho \frac{\partial R}{\partial t} + \rho\, U_k \frac{\partial R}{\partial x_k} \right\rangle \\
&= \left\langle \frac{\partial}{\partial t}(\rho\, R) + \frac{\partial}{\partial x_k}(\rho\, U_k\, R) \right\rangle - \underbrace{\left\langle R \left(\frac{\partial \rho}{\partial t} + \cancel{\frac{\partial}{\partial x_k}}^{\,0}(\rho\, U_k)\right)\right\rangle}_{\text{cont.}} \\
&= \left\langle \frac{\partial}{\partial t}(\rho\, R) + \frac{\partial}{\partial x_k}(\rho\, U_k\, R) \right\rangle
\end{aligned} \tag{C.3}$$

since the second term on the right hand side is zero due to continuity (equation (3.1)). Equation (C.3) can also be written as

$$\left\langle \rho \frac{DR}{Dt} \right\rangle = \left\langle \rho \frac{\partial R}{\partial u_i''} \frac{Du_i''}{Dt} + \rho \frac{\partial R}{\partial u_j''} \frac{Du_j''}{Dt} \right\rangle \tag{C.4}$$

An equation for Du_i''/Dt in terms of U_i and $\tilde{U}_i$ can be derived as follows

$$\begin{aligned}
\frac{DU_i}{Dt} &= \frac{\partial U_i}{\partial t} + U_k \frac{\partial U_i}{\partial x_k} \\
&= \frac{\partial \tilde{U}_i}{\partial t} + \tilde{U}_k \frac{\partial \tilde{U}_i}{\partial x_k} + u_k'' \frac{\partial \tilde{U}_i}{\partial x_k} + \frac{\partial u_i''}{\partial t} + \tilde{U}_k \frac{\partial u_i''}{\partial x_k} \\
&= \frac{\partial \tilde{U}_i}{\partial t} + \tilde{U}_k \frac{\partial \tilde{U}_i}{\partial x_k} + u_k'' \frac{\partial \tilde{U}_i}{\partial x_k} + \frac{Du_i''}{Dt}
\end{aligned}$$

Thus

$$\frac{\mathcal{D}u_i''}{\mathcal{D}t} = \frac{\mathcal{D}U_i}{\mathcal{D}t} - \left(\frac{\partial \tilde{U}_i}{\partial t} + \tilde{U}_k \frac{\partial \tilde{U}_i}{\partial x_k} + u_k'' \frac{\partial \tilde{U}_i}{\partial x_k}\right) \tag{C.5}$$

Multiplying equation (C.5) by ρ gives

$$\rho \frac{\mathcal{D}u_i''}{\mathcal{D}t} = \rho \frac{\mathcal{D}U_i}{\mathcal{D}t} - \left(\rho \frac{\partial \tilde{U}_i}{\partial t} + \rho\, \tilde{U}_k \frac{\partial \tilde{U}_i}{\partial x_k} + \rho\, u_k'' \frac{\partial \tilde{U}_i}{\partial x_k}\right) \tag{C.6}$$

Introduction of equation (C.6) into equation (C.4) and expression of $\langle \rho\, (\mathcal{D}R/\mathcal{D}t) \rangle$ according to equation (C.3) gives

$$\frac{\partial}{\partial t}\left(\bar{\rho}\, \tilde{R}\right) + \frac{\partial}{\partial x_k}\left(\bar{\rho}\, \tilde{U}_k \tilde{R}\right) + \left\langle \frac{\partial}{\partial x_k}\left(\rho\, u_k'' R\right)\right\rangle$$

$$= \left\langle \frac{\partial R}{\partial u_i''}\left[\rho \frac{\mathcal{D}U_i}{\mathcal{D}t} - \rho \frac{\partial \tilde{U}_i}{\partial t} - \rho\, \tilde{U}_k \frac{\partial \tilde{U}_i}{\partial x_k} - \rho\, u_k'' \frac{\partial \tilde{U}_i}{\partial x_k}\right]\right\rangle$$

$$+ \left\langle \frac{\partial R}{\partial u_j''}\left[\rho \frac{\mathcal{D}U_j}{\mathcal{D}t} - \rho \frac{\partial \tilde{U}_j}{\partial t} - \rho\, \tilde{U}_k \frac{\partial \tilde{U}_i}{\partial x_k} - \rho\, u_k'' \frac{\partial \tilde{U}_j}{\partial x_k}\right]\right\rangle \tag{C.7}$$

$\rho\, (\mathcal{D}U_i/\mathcal{D}t)$ can be written from the momentum equation for U_i (equation (3.2)) as

$$\rho \frac{\mathcal{D}U_i}{\mathcal{D}t} = -\frac{\partial P}{\partial x_k}\delta_{ik} + \frac{\partial}{\partial x_k}\tau_{ik} \tag{C.8}$$

Introduction of equation (C.8) into equation (C.7) gives

$$\frac{\partial}{\partial t}\left(\bar{\rho}\, \tilde{R}\right) + \frac{\partial}{\partial x_k}\left(\bar{\rho}\, \tilde{U}_k \tilde{R}\right) + \left\langle \frac{\partial}{\partial x_k}\left(\rho\, u_k'' R\right)\right\rangle$$

$$= \left\langle \frac{\partial R}{\partial u_i''}\left[-\frac{\partial P}{\partial x_k}\delta_{ik} + \frac{\partial}{\partial x_k}\tau_{ik} - \rho \frac{\partial \tilde{U}_i}{\partial t} - \rho\, \tilde{U}_k \frac{\partial \tilde{U}_i}{\partial x_k} - \rho\, u_k'' \frac{\partial \tilde{U}_i}{\partial x_k}\right]\right\rangle$$

$$+ \left\langle \frac{\partial R}{\partial u_j''}\left[-\frac{\partial P}{\partial x_k}\delta_{jk} + \frac{\partial}{\partial x_k}\tau_{jk} - \rho \frac{\partial \tilde{U}_j}{\partial t} - \rho\, \tilde{U}_k \frac{\partial \tilde{U}_j}{\partial x_k} - \rho\, u_k'' \frac{\partial \tilde{U}_j}{\partial x_k}\right]\right\rangle \tag{C.9}$$

Introduction of $R \equiv u_i'' u_j''$ and its derivatives

$$\frac{\partial R}{\partial u_i''} = u_j''$$

$$\frac{\partial R}{\partial u_j''} = u_i''$$

into equation (C.9) gives

$$\frac{\partial}{\partial t}\left(\overline{\rho}\,\overline{u_i''\tilde{u}_j''}\right) + \frac{\partial}{\partial x_k}\left(\overline{\rho}\,\tilde{u}_k\,\overline{u_i''\tilde{u}_j''}\right) + \frac{\partial}{\partial x_k}\left(\overline{\rho\,u_k''\tilde{u}_i''u_j''}\right)$$

$$= \left\langle -u_j''\frac{\partial P}{\partial x_k}\delta_{ik} + u_j''\frac{\partial}{\partial x_k}\tau_{ik} - \underbrace{\rho\,u_j''\frac{\partial \tilde{u}_i}{\partial t}}_{\text{cont.}} - \rho\,\tilde{u}_k u_j''\frac{\partial \tilde{u}_i}{\partial x_k}\,(\to 0) - \rho\,u_k''u_j''\frac{\partial \tilde{u}_i}{\partial x_k}\right\rangle$$

$$+ \left\langle -u_i''\frac{\partial P}{\partial x_k}\delta_{jk} + u_i''\frac{\partial}{\partial x_k}\tau_{jk} - \underbrace{\rho\,u_i''\frac{\partial \tilde{u}_j}{\partial t}}_{\text{cont.}} - \rho\,\tilde{u}_k u_i''\frac{\partial \tilde{u}_j}{\partial x_k}\,(\to 0) - \rho\,u_k''u_i''\frac{\partial \tilde{u}_j}{\partial x_k}\right\rangle \qquad \text{(C.10)}$$

The pressure and the stress tensor are decomposed into their ensemble-averaged 'mean' and the fluctuating components, neglecting the fluctuations of the laminar viscosity, as

$$P = \overline{P} + p'$$

$$\tau_{ik} = \overline{\mu}\left(\frac{\partial \overline{U}_i}{\partial x_k} + \frac{\partial \overline{U}_k}{\partial x_i} - \frac{2}{3}\frac{\partial \overline{U}_\ell}{\partial x_\ell}\delta_{ik}\right) + \overline{\mu}\left(\frac{\partial u_i'}{\partial x_k} + \frac{\partial u_k'}{\partial x_i} - \frac{2}{3}\frac{\partial u_\ell'}{\partial x_\ell}\delta_{ik}\right) \qquad \text{(C.11)}$$

Equation (C.10) can now be recast using the above relations as

$$\frac{\partial}{\partial t}\left(\overline{\rho}\,\overline{u_i''\tilde{u}_j''}\right) + \frac{\partial}{\partial x_k}\left(\overline{\rho}\,\tilde{u}_k\,\overline{u_i''\tilde{u}_j''}\right) = -\left(\overline{\rho\,u_k''\tilde{u}_j''}\frac{\partial \tilde{u}_i}{\partial x_k} + \overline{\rho\,u_k''\tilde{u}_i''}\frac{\partial \tilde{u}_i}{\partial x_k}\right)$$

I

$$-\frac{\partial}{\partial x_k}\overline{\rho}\,\overline{u_k''\tilde{u}_i''u_j''}$$

II

$$-\left(\overline{u_j''}\frac{\partial \overline{P}}{\partial x_i} + \overline{u_i''}\frac{\partial \overline{P}}{\partial x_j}\right) - \left(\overline{u_j''\frac{\partial p'}{\partial x_i}} + \overline{u_i''\frac{\partial p'}{\partial x_j}}\right)$$

III IV

$$+\left(\overline{u_j''}\frac{\partial}{\partial x_k}\overline{\tau_{ik}} + \overline{u_i''}\frac{\partial}{\partial x_k}\overline{\tau_{jk}}\right)$$

V

$$+\left(\frac{\partial}{\partial x_k}\overline{u_j''\tau_{ik}'} + \frac{\partial}{\partial x_k}\overline{u_i''\tau_{jk}'}\right) - \left(\overline{\tau_{ik}'\frac{\partial u_j''}{\partial x_k}} + \overline{\tau_{jk}'\frac{\partial u_i''}{\partial x_k}}\right) \qquad \text{(C.12)}$$

VI VII

For high Reynolds number turbulent flows, the mean viscous stress $\overline{\tau_{ik}}$ and viscous diffusion of the Reynolds stresses $(\partial/\partial x_k)\,\overline{u_j'' \tau_{ik}'}$ are negligible and, therefore, terms V and VI can be dropped (Jones [1979]). The correlation between the fluctuating velocity and fluctuating pressure gradient, term IV, is conventionally separated into two parts (see Jones [1979]) as

$$\overline{u_j'' \frac{\partial p'}{\partial x_i}} + \overline{u_i'' \frac{\partial p'}{\partial x_j}} = \frac{\partial}{\partial x_i}(\overline{p' u_j''}) + \frac{\partial}{\partial x_j}(\overline{p' u_i''}) - \overline{p'\left(\frac{\partial u_j''}{\partial x_i} + \frac{\partial u_i''}{\partial x_j}\right)} \qquad (C.13)$$

Equation (C.12) can finally be written as

$$\frac{\partial}{\partial t}(\bar{\rho}\,\overline{\tilde{u_i'' u_j''}}) + \frac{\partial}{\partial x_k}(\bar{\rho}\,\tilde{u}_k\,\overline{\tilde{u_i'' u_j''}}) = -(\bar{\rho}\,\overline{\tilde{u_k'' u_j''}}\frac{\partial \tilde{u}_i}{\partial x_k} + \bar{\rho}\,\overline{\tilde{u_k'' u_i''}}\frac{\partial \tilde{u}_j}{\partial x_k})$$

$$- \frac{\partial}{\partial x_k}\bar{\rho}\,\overline{\tilde{u_k'' u_i'' u_j''}} - (\overline{u_j''}\frac{\partial \bar{P}}{\partial x_i} + \overline{u_i''}\frac{\partial \bar{P}}{\partial x_j})$$

$$- (\frac{\partial}{\partial x_i}(\overline{p' u_j''}) + \frac{\partial}{\partial x_j}(\overline{p' u_i''})) + \overline{p'\left(\frac{\partial u_j''}{\partial x_i} + \frac{\partial u_i''}{\partial x_j}\right)}$$

$$+ (\frac{\partial}{\partial x_k}\overline{u_j'' \tau_{ik}'} + \frac{\partial}{\partial x_k}\overline{u_i'' \tau_{jk}'})$$

$$- (\overline{\tau_{ik}'\frac{\partial u_j''}{\partial x_k}} + \overline{\tau_{jk}'\frac{\partial u_i''}{\partial x_k}}) \qquad (C.14)$$

The transport equation for turbulence kinetic energy is obtained by 'contracting' the above, i.e. by replacing the tensor subscript j with i, and then multiplying equation (C.14) by $\frac{1}{2}$. These then result:

$$\frac{\partial}{\partial t}(\bar{\rho}\,k) + \frac{\partial}{\partial x_k}(\bar{\rho}\,\tilde{u}_k\,k) = \bar{\rho}\,\overline{\tilde{u_k'' u_i''}}\frac{\partial \tilde{u}_i}{\partial x_k} - \frac{\partial}{\partial x_k}(\bar{\rho}\,\overline{\tilde{u_k''}\frac{u_i''^2}{2}})$$

$$- \overline{u_i''}\frac{\partial \bar{P}}{\partial x_i} - \frac{\partial}{\partial x_i}(\overline{p' u_i''}) + \overline{p'\frac{\partial u_i''}{\partial x_i}}$$

$$+ \frac{\partial}{\partial x_k}(\overline{u_i'' \tau_{ik}'}) - \overline{\tau_{ik}'\frac{\partial u_i''}{\partial x_k}} \qquad (C.15)$$

The physical significance of these terms and the comparison of equation (C.15) with its constant density flow counterpart are presented in Chapter 3.

TABLE 2.1

Experimental Investigations

Author(s)	Engine & Operating Conditions	Technique	Main Findings
Semenov [1963]	Disc-chamber; S = 600-1200 rpm; CR = 4-9.5; η_v = 0.24-0.71	HWA; T/E ave. $\Delta\theta$ = 24°CA	Intake generated velocity gradients are the main source of turbulence. The mean flow and turbulence decay during late induction/IVC, but remain almost constant during the second half of compression. The turbulence energy spectrum markedly changes during the engine cycle. (Also see Tables 2.2 to 2.6.)
Kastner, et al. [1963-64]	Steady and unsteady air flow through valves	Pressure probes	Four different modes of the valve flow with increasing lift, together with discontinuities in C_D. Rounding-off of the valve and seat corners increase C_D. Valve movement may increase or decrease C_D depending on cam (engine) speed.
Woods & Khan [1965-66]	Steady air flow through inlet and exhaust valves	Pressure probes	The effective area (hence C_D) is independent of pressure drop across the valve for small lifts, but for high lifts, increases with increase in ΔP.
Annand [1969]	Steady air flow through valves	Pressure probes	Similar findings to those of Kastner, et al. [1963-64]. A bi-stable flow at small lifts is observed. Valves with 30° and 45° seat angles are superior to the 60° seat.
Arnold, et al. [1972]	Hemispherical-chamber; S = 1200-1500 rpm; study of swirl and valve masking	HWA	Swirl generation is determined by cylinder head design and position of valve mask. Swirl increases less-than-linear with engine speed.

TABLE 2.1 (continued)

Author(s)	Engine & Operating Conditions	Technique	Main Findings
Winsor & Patterson [1973]	Disc-chamber; S = 500-1500 rpm	HWA; low-pass filter	There is no mean motion near TDC and turbulence is isotropic and homogeneous. The TDC u' increase almost linearly with S.
Tindal, et al. [1974]	Disc-chamber; S = 1000-1400 rpm; CR = 6.7-10; study of swirl and valve masking	HWA	The induction flow pattern depends on the position of the valve mask. During compression, swirl tends towards solid body. Large swirl reduces cyclic variation and u'. Swirl velocity increases less-than-linear with speed and is not influenced by CR.
Dent & Salama [1975a]	Heron- & wedge-chamber; S = 1000-3500 rpm; CR = 8.9-9	HWA; T/E ave. $\Delta\theta$ = 10°CA	Continuous decay of $\overline{U}$ and u' during compression, in absence of squish generation. Marked changes of turbulence energy spectrum during engine cycle. λ_t is not strongly dependent on the gas mean velocity during compression. (Also see Tables 2.2 to 2.6.)
Dent & Salama [1975b]	Heron- & wedge-chamber; S = 1000-3500 rpm; CR = 9; study of the influence of inlet turbulence promoters	HWA; T/E ave. $\Delta\theta$ = 10°CA	The effect of engine speed and valve throttle on $\overline{U}$ and u' is not uniform and tends to decrease during compression. The effect of all inlet modifications, except for valve masking, on $\overline{U}$ diminishes near the end of compression. Near TDC, $\lambda_t \simeq$ 0.1-0.25 msec for a wide range of design and operating conditions. (Also see Tables 2.2 to 2.6.)

TABLE 2.1 (continued)

Author(s)	Engine & Operating Conditions	Technique	Main Findings
James & Lucas [1975]	Squish- & disc-chambers; S = 700-1450 rpm; CR = 3.9-8.88; study of turbulence energy spectrum (f = 200-5800 Hz)	HWA; band-filters; T/E ave. $\Delta\theta$ = 10°CA	Variations of $\overline{U}$ with S is not uniform during compression, but at TDC $\overline{U}$ varies linearly with S. Increase in speed increases the fluctuation velocity of all frequency components. During compression, the turbulence energy is mainly contained in low frequency fluctuations f < 700 Hz. The main influence of squish chamber is to increase the fluctuation velocity in the range f < 1600 Hz, higher frequencies remain relatively unaffected.
Lancaster [1976]	Disc-chamber; shrouded and non-shrouded inlet valves; S = 1000-2000 rpm; CR = 6.8-10.5; η_v = 25%-75%	HWA; T/E ave.; $\Delta\theta$ = 45°CA EA	Large over-estimation of EA u' during compression due to cycle-to-cycle variations. $\overline{U}$ and u' in the non-shrouded engine remain nearly constant after IVC, but markedly decay near TDC (θ = 330°-360°CA). The turbulence frequency spectrum markedly changes during the engine cycle. During compression, turbulence tends towards isotropy. Swirl (shrouded valve) increases u' level at TDC. (Also see Tables 2.2 to 2.6.)
Witze [1976a] (Revised data)	L-head, flat piston; S = 2000 rpm; CR = 7.25	HWA; EA	Throughout induction and compression, $u'/\overline{U} \simeq 0.5$. During θ = 260°-360°CA, $\lambda_t \simeq 0.1$ msec and $L_t \simeq 1$ msec, and nearly constant; therefore, $L_x/\lambda_x \simeq 10$.
Tindal & Williams [1977]	DI diesel engine; study of different helical and directed inlet ports	HWA; rotating vane	The in-cylinder flow patterns depend on the port design and valve lift. Swirl distribution is stratified along the cylinder axis.

TABLE 2.1 (continued)

Author(s)	Engine & Operating Conditions	Technique	Main Findings
Witze [1977]	L-head, flat piston; S = 500-2500 rpm; CR = 7.25	HWA; EA	Except during early induction, $\overline{U}$ and u' do not scale linearly with S: $\overline{U}/\overline{V}_p$ and $u'/\overline{V}_p$ during compression increase with S. During induction and compression, $u'/\overline{U} \simeq 0.5$, nearly independent of S. $L_t \simeq 2°CA$ during induction and increases to $\simeq 12°CA$ during compression nearly independent of speed (i.e. $L_t(sec)$ is inversely proportional with S). L_χ depends on geometry and is nearly independent of S. (Also see Tables 2.2 to 2.6.)
Witze [1978]	L-head, flat piston; S = 600 rpm; CR = 10.5	LDA and HWA; EA	During intake and early compression, HWA and LDA results are similar, but during IVC-EVO (θ = 270°-480°CA) HWA produces erroneous results due to the changes in the gas temperature and pressure.
Wigley & Hawkins [1978]	DI diesel engine; steady air flow through directed and helical ports	LDA and HWA	The flow structure depends on the intake port design. Helical port produces a more ordered bulk flow. Swirl is axially stratified. The level and distribution of w' do not correspond to $\overline{W}$.
Ekchian & Hoult [1979]	Water model of the intake process; S = 750-2500 rpm; $(L_{max}/D)_v$ = 0.07-0.21; (B/S_t) = 0.74-1.35	Flow visualisation	The flow structure is not influenced by engine speed. The vortices velocities scale with flow velocity at the valve. The development, size and location of the vortex in the valve wake scale with piston displacement. Longer strokes cause earlier break-up of the vortex structure near the end of induction.

TABLE 2.1 (continued)

Author(s)	Engine & Operating Conditions	Technique	Main Findings
Rask [1979]	L-head engine; motored and firing; S = 270-800 rpm; full and half throttle	LDA; EA	Mean velocity $\overline{w}$ roughly scales with S during induction and compression and is not affected by the valve throttle. Turbulence w' does not scale with S during induction, but does during compression. The decay of w' during compression is small. There is an apparent increase in w' at flame arrival. (Also see Tables 2.2 to 2.6.)
Wakisaka, et al. [1979]	Disc-chamber; S = 600-1200 rpm; CR = 4.1; study of inlet valve masking	HWA; T/E ave. $\Delta\theta$ = 43°CA	Swirl resembles solid body rotation during compression. Mean velocity $\overline{w}$, w', L_t and L_χ at TDC depend on the valve mask orientation, but λ_t is not influenced. There is large variation of $w'/\overline{w}$, L_t and L_χ across the cylinder at TDC, but λ_t and λ_χ are nearly uniform. At TDC, $L_\chi/\lambda_\chi \simeq$ 2.5-5 depending on location. (Also see Tables 2.4 to 2.6.)
Johnston, et al. [1979]	Disc-chamber, side intake (shrouded) valve; fuel-injection; S = 460 rpm	LDA EA	During compression, swirl is axisymmetric, not stratified axially and decays nearly exponentially. Fuel injection strongly interacts with the flow.
Brandl, et al. [1979]	DI diesel engine, flat and bowl pistons; 3 different inlet ports; S = 1100-2400 rpm; CR = 18; with combustion	HWA T/E ave.	The mean flow and turbulence structure near TDC depend on the inlet port design. There are considerable axial stratification of swirl and spatial variations in u' and λ_χ near TDC. In general, around TDC, u' and λ_χ increase with engine speed, but their sensitivity to S differs for different intake ports. The combustion characteristics depend on the inlet port. (Also see Tables 2.4 to 2.6.)

TABLE 2.1 (continued)

Author(s)	Engine & Operating Conditions	Technique	Main Findings
Morse, et al. [1979]	Disc-chamber, central-valve model engine; S = 100-335 rpm	LDA; EA	The induction flow structure is almost unaffected by speed. The mean velocity $\bar{u}$ and u' scale linearly with speed.
Witze [1979] and [1980]	L-head engine; S = 600 rpm; CR = 5.1	LDA and HWA; EA	The mean velocity and turbulence intensity are largely over-estimated by HWA during compression and expansion, due to calibration errors. The level of error increases with probe temperature. For engine applications, LDA is superior to HWA.
Williams & Tindal [1979]	DI diesel engine; CR = 16; helical and directed inlet ports	HWA	The flow pattern during induction is strongly dependent on the port design and valve lift. Helical port produces a more ordered flow pattern, but similar turbulence levels.
Morse, et al. [1980a]	Disc-chamber, central open-valve, model engine; pre-swirl vanes; S = 200 rpm	LDA; EA	Imparting swirl to the intake flow influences the formation, strength and size of the vortices (in the axial plane) during induction.
Morse, et al. [1980b]	Disc-chamber, off-centre open-valve, model engine; S = 200 rpm	LDA; EA	The flow in the axial plane is structured by the annular intake jet. In the tangential plane, a twin-vortex system is generated. The flow is considerably asymmetric, stratified along the cylinder axis and evolves during induction.

TABLE 2.1 (continued)

Author(s)	Engine & Operating Conditions	Technique	Main Findings
Bicen & Vlachos [1980] (also Arcoumanis, et al. [1982a])	Disc-chamber, central open-valve, model engine; S = 200 rpm; study of the effects of clearance gap and valve seat angle on the intake flow	LDA; EA	Clearance gap influences the development of the vortex structure and produces higher u' level due to intake jet impingement on the piston during early induction, but the mean flow and turbulence levels at the end of induction are similar. The valve seat angle significantly influences induction-generated flow structure.
Cole & Swords [1980]	Spark-ignition engine; S = 420-800 rpm; combustion	LDA conditional-sampling	There is a strong correlation between the mean flow near the spark-plug at the time of ignition and the peak (combustion) pressure. A much weaker dependence of peak pressure on turbulence intensity variations is noted.
Williams & Tindal [1980]	DI diesel engine; S = 1000 rpm; study of toroidal and re-entrant piston bowls	HWA	Swirl velocity in the re-entrant bowl is larger and squish effects are more pronounced. Also swirl is retained in the re-entrant bowl for a longer time during expansion.
Morse & Whitelaw [1981]	Disc-chamber; toroidal bowl; masked inlet valve (open and operating); S = 325-675 rpm; CR = 17.5	LDA; EA	During induction, w' is uniform and does not correspond to $\overline{W}$ profiles. The flow during induction is similar for compressing and non-compressing engines. During compression, swirl relaxes into a solid body rotation.

TABLE 2.1 (continued)

Author(s)	Engine & Operating Conditions	Technique	Main Findings
Arcoumanis, et al. [1981a] (also Arcoumanis, et al. [1982b])	Disc-chamber, central valve model engine; with and without pre-swirl inlet valve; S = 200 rpm; CR = 3.5 and 6.7	LDA; EA	During compression, turbulence is homogeneous and isotropic and decays very slowly. Increase in CR influences the decay of the intake-generated vortex structure; but in the presence or absence of induction swirl, it has no effect on turbulence intensities during compression.
Coghe & Ghezzi [1981]	Disc-chamber; combustion; S = 600-1800 rpm; CR = 11	LDA; EA	During compression, $\overline{U}$ and u' are nearly constant. The level of decay of u' during compression (IVC to TDC) increase with engine speed. The TDC turbulence intensity increases linearly with speed. Flame speed scales with u' at the time of ignition.
Hirotomi, et al. [1981]	Disc-chamber; study of directional ports with swirl promoters; combustion	Flow visualisation	Off-centre location of inlet port produces swirl. For directed ports, a twin-vortex structure is formed in the tangential plane that is stratified along the cylinder axis. The strength, arrangement and evolution of the vortex structure depend on the port design and the valve lift. The combustion characteristics depend on the induction system design.
Rask [1981]	L-head engine; S = 300 rpm; study of window, smoothed-ensemble and cycle-by-cycle data reduction methods	LDA	The basic mean flow repeats itself, and cycle-to-cycle variations occur in the higher frequency components. A strong, directed mean flow reduces cyclic variations. During compression, cycle-to-cycle variation represents a substantial fraction of EA turbulence intensity.

TABLE 2.1 (continued)

Author(s)	Engine & Operating Conditions	Technique	Main Findings
Wigley, et al. [1981]	DI diesel engine; motored and combustion; S = 1000-2800 rpm	LDA	Prior to fuel injection, the swirl profiles are similar in the motored and firing cases. After combustion, the swirl velocity is always less than in the motoring case. The onset of combustion causes a sharp increase in turbulence intensity.
Daneshyar & Fuller [1981]	Disc-chamber, shrouded and non-shrouded valves; S = 260 rpm; CR = 4; Ricardo E6 Engine; S = 500-1500 rpm	HWA T/E ave. $\Delta\theta$ = 30°CA	There are large cycle-to-cycle variations of the (time-averaged) $\overline{U}$ and u'. The generation of swirl increases u' during compression; with the level depending on the peak valve lift. During compression, turbulence energy is contained in the low frequency components. Increase in S increases energy of all the turbulence frequency components and a shift of the peak of the spectrum to higher frequencies. u' increases linearly with S.
Arcoumanis, et al. [1982c]	Disc-chamber, central-valve model engine; S = 200 rpm; CR = 3.5; study of the influence of induction swirl, valve seat angle and maximum lift	LDA; EA	The mean flow and turbulence during induction are strongly influenced by valve seat angle, but the differences diminish during compression. Reduction in valve lift strongly influences mean flow and turbulence during induction; the differences in $\overline{U}$, u' and w' diminish to a small level during compression, but swirl profiles are different. Induction swirl reduces u' level during compression. During compression, turbulence is homogeneous with a nearly constant level of $u' \simeq 0.5$ to $0.7\ \overline{V}_p$.

TABLE 2.1 (continued)

Author(s)	Engine & Operating Conditions	Technique	Main Findings
Arcoumanis, et al. [1982d]	Disc-chamber, central-valve model engine; S = 200 rpm; CR = 3.5; study of the effect of piston bowls	LDA; EA	The flow structure during induction is dominated by the inlet geometry with small dependence on piston configuration. In general, small effect of cylindrical piston bowl on the mean flow and turbulence during compression and expansion is observed. For re-entrant bowl, substantial squish occurs during late compression, with no apparent effect on u', and reverse squish during expansion, producing locally high levels of u'.
Liou & Santavicca [1982]	Two-stroke, ported model engine; S = 1200-2400 rpm; data for 60°CA around TDC	LDA; EA and cycle-resolved	During compression, turbulence energy is contained in the low frequency components and a frequency for separating turbulence and cycle-to-cycle variations cannot be determined from the frequency spectrum. The ensemble-averaged u'_E and cycle-resolved u'_c vary similarly, but u'_E is 50%-100% over-estimated due to cycle-to-cycle variations. Both u'_E and u'_c scale linearly with speed.
Gerber [1982]	Renault 16TS engine (hemispherical chamber); S = 500-2000 rpm	HWA and LDA; EA	There is a strong correlation between the turbulence level and the mean velocity gradients during induction. Turbulence is isotropic during induction and compression, and is nearly constant during compression. During expansion, the mean flow is disordered and the turbulence anisotropic. The mean flow and turbulence intensities u',v' and $u'+v'$ do not scale with engine speed during both induction and compression. Cyclic variations in mean velocity are smallest during induction and largest during compression, and increase with S. (Also see Tables 2.2 to 2.6.)

TABLE 2.1 (continued)

Author(s)	Engine & Operating Conditions	Technique	Main Findings
Liou & Santavicca [1983]	Two-stroke, ported model engine; S = 1200-2400 rpm; with and without induction swirl; data for 30° BTDC - 30° ATDC	LDA; EA and cycle-resolved	Swirl reduces cycle-to-cycle variations in mean velocity. Swirl increases the TDC u' by 25% to 50%. The ensemble mean velocity does not scale with S, but u' for both swirl and non-swirl cases increases linearly with speed. Cyclic variations result in over-estimation of u' and L_t. Cyclic variations increase linearly with S. Turbulence energy is mainly contained in low frequency fluctuations. (Also see Tables 2.4 to 2.6.)
Witze [1983a]	Disc-chamber, side-valve model engine; combustion	LDA; conditional-sampling	The flame arrival time (at measuring point) correlates with u' in the unburned gas: higher u' produces faster burns. An increase in u' in the pre-flame gas by combustion is indicated in both the conditionally and non-conditionally sampled data.
Arcoumanis, et al. [1984]	Model engine with axisymmetric and off-centre intake/exhaust valve; S = 200 rpm; CR = 6.7; pre-valve swirl vanes and shrouded valve; cylindrical and re-entrant piston bowls	LDA; EA	The off-centre valve without swirl vanes produces a double-vortex structure during induction that later collapses. When swirl is enhanced by port vanes, the induction vortex structure is transformed during compression into a single eccentric vortex. The axi-symmetric port with the shrouded valve produces a rolling vortex, with markedly higher turbulence levels at TDC, compared with the off-centre valve with or without swirl vanes.
Vafidis [1984]	Four-stroke, central-valve model engine; S = 200 rpm; CR = 6.7; pre-valve swirl vanes of 30° and 60°; flat and re-entrant piston bowl	LDA; EA	Swirl level and profile during induction and compression is strongly dependent on the intake design. Higher swirl reduces turbulence intensity at TDC for flat piston and a more complex vortex pattern inside the re-entrant piston bowl.

TABLE 2.1 (continued)

Author(s)	Engine & Operating Conditions	Technique	Main Findings
Vafidis & Whitelaw [1984]	Steady and pulsating flow through and downstream of intake valve	LDA; EA	Four different modes of flow with increase in lift, caused by flow separation at valve head and seat and accompanied by large variations in C_D. The angle of entry and the inlet velocity profile varies with lift. C_D and inlet velocity profiles are similar for steady and unsteady flows; cylinder confinement and off-centre valve location does not affect C_D but influences the flow entry angle. The flow downstream of the valve differs for steady and unsteady conditions. Turbulence levels at valve exit are larger for the unsteady case, but are negligible compared with the levels generated in the intake jet immediately downstream of the valve.
Liou, et al. [1984]	Disc-chamber model engine; ported and valved intake; S = 600-2400 rpm; results for -45° to 30° CA around TDC	LDA; EA and cycle-resolved	Mean (ensemble-averaged) velocity scales with engine speed for flow with swirl; no such trend in either engine without induction swirl. In all cases, turbulence is nearly homogeneous and isotropic, and nearly $u' \sim S$. The turbulence intensity is overestimated by 100% in ported engine and 300% in valved engine without swirl, and by 10% in the former engine with swirl, due to cycle-to-cycle variations. Cyclic variations increase with speed.

TABLE 2.2

Measured Values of Turbulence Scales Within Motored IC Engine Chambers During Induction

Investigator	Experimental Details	Combustion Chamber Shape	Compression Ratio	Engine Speed	Volumetric Efficiency	u'	L_t (msec)	L_x (mm)	λ_t (msec)	λ_x (mm)	Miscellaneous
Semenov [1963]	HWA, Ensemble-time average, $\Delta\theta$ = 24° CA, frequency filter < 300 Hz	Disc	4-9.5	600-1200	0.24-0.71	5-10 m/sec		1.8			Turbulence energy in frequency range 1000-3500 Hz.
Dent & Salama [1975a]	HWA, Ensemble-time average, frequency filter, $\Delta\theta$ = 10° CA	Wedge	9	1000	Open throttle	2.5-0.8 m/sec			0.14-0.16	0.7-0.4	Turbulence energy in frequency range 700-3000 Hz (wedge).
		Heron	8.9	1000	1/3 throttle	0.8 m/sec			0.18	0.5-0.4	
Dent & Salama [1975b]	HWA, Ensemble-time average, low frequency filter, $\Delta\theta$ = 10° CA	Wedge	9	1000-1500	Open throttle	5-12 m/sec (θ = 120°)			0.1-0.2 (at 1000 rpm)		λ_t depends on the intake manifold design.
		Heron	8.9	1000	1/10-1/4 throttle	0.2-0.75 m/sec (θ = 120°)					
Lancaster [1976]	HWA, non-stationary time-Ensemble average, $\Delta\theta$ = 45° CA	Disc non-shrouded valve	8.7 (6.8-10.5)	1500 (1000-2000)	50% (25%-75%)	3-5 m/sec	0.3-0.4	3-5	0.07-0.1	0.5-1	
		Shrouded valve	8.7 (6.8-10.5)	1500 (1000-2000)	50% (25%-75%)	5-10 m/sec	0.35	4-8	0.07	0.7-1.5	
Witze [1977]	HWA, Ensemble-average	L-head squish chamber	7.25	500-2500		0.5-1.5 * $\bar{U}_p$ (0.5 * $\bar{U}$) $_p$	0.7-0.1 (2° CA)	2-3			$\bar{U}_p$ ≡ mean piston speed.
Rask [1979]	LDA, Ensemble-average	L-head	7	270-800	Open throttle	2-10 * $\bar{U}_p$					
					1/2 throttle	2-8 * $\bar{U}_p$					
Gerber [1982]	HWA, LDA, Ensemble-average	Hemispherical flat piston		1500 500-2500		2-7 m/sec	0.4 1.0-0.2 (4° CA)	3-7 3-10			

TABLE 2.3

Measured Influence of Increase in Engine Speed, Compression Ratio and Volumetric Efficiency on the Mean Velocity and Turbulence Parameters During Induction†

Investigator	Experimental Details	$\bar{U}$			u'			L_t			L_x			λ_t			λ_x			Miscellaneous
		S	CR	η_v	S	CR	η_v	S	CR	η_v	S	CR	η_v	S	CR	η_v	S	CR	η_v	
Semenov [1963]	HWA, Ensemble-time average, frequency filter < 300 Hz, $\Delta\theta$ = 24° CA	linear		↑	linear		linear													Increase in η_v influencing $\bar{U}$ during θ = 60° - 180°.
Dent & Salama [1975b]	HWA, Ensemble-time average, low frequency filter, $\Delta\theta$ = 10° CA	↑		↑	↑		↑													
Lancaster [1976]	HWA, Ensemble-average	≃ linear	constant	↑* ↓	≃ linear	constant	↑* ↓													* For shrouded valve and 50%-75% volumetric efficiency.
Witze [1977]	HWA, Ensemble-average	≤ linear			≤ linear			↓ ≃ linear			constant									
Rask [1979]	HWA, Ensemble-average	≃ linear		constant	↑§		↑													
Gerber [1982]	HWA, LDA, Ensemble-average	↑§			↑§			↓ ≃ linear			no trend									$\bar{U}$ and u' do not scale with engine speed.

† See Table 2.2 for operating conditions.

§ No consistent trend

TABLE 2.4

Measured Values of Turbulence Scales Within Motored IC Engine Chambers During Compression

Investigator	Experimental Details	Combustion Chamber Shape	Compression Ratio	Engine Speed	Volumetric Efficiency	u'	l_t (msec)	l_x (mm)	λ_t (msec)	λ_x (mm)	Miscellaneous
Semenov [1963]	HWA, Ensemble-time average, $\Delta\theta$ = 24° CA, frequency filter < 300 Hz	Disc	4-9.5	600-1200	0.24-0.71	0.2-0.8 m/sec (at TDC)				0.3* at TDC (900 rpm)	Turbulence energy in frequencies < 500 Hz.
Dent & Salama [1975a]	HWA, Ensemble-time average, low frequency filter, $\Delta\theta$ = 10° CA	Wedge	9	1000	Open throttle	2.5-0.5 m/sec		7-4	0.2-0.16	0.3-0.7	l_y = (3-4) λ_y (at TDC). Energy spectrum peak at 700 Hz.
		Heron	8.9	1000	1/3 throttle	0.8-0.2 m/sec		0.6-0.4	0.18-0.2	0.5-0.15	
		Flat	6-8	1000						0.5-0.3	
Dent & Salama [1975b]	HWA, Ensemble-time average, $\Delta\theta$ = 10° CA	Wedge	9	1000-1500	Open throttle	0.9-1.8 m/sec (at TDC)			0.18-0.25 (at TDC, for different intake manifold designs)		l_x = (3-5) λ_y.
		Heron	8.9	1000	1/10-1/4 throttle	0.05-0.15 m/sec (at TDC)					
Lancaster [1976]	HWA, non-stationary time-Ensemble average, $\Delta\theta$ = 45° CA	Disc non-shrouded valve	8.7 (6.8-10.5)	1500 (1000-2000)			0.4-0.8	4	0.1-0.2	0.7	+ At TDC, it drops to ≈ 1.2 mm. 80% of turbulence energy in frequencies below 1 kHz. l_x = 4 λ_x.
		Shrouded valve	8.7 (6.8-10.5)	1500 (1000-2000)			0.3-0.6	7-14	0.07-0.12	1.5-2.0+	
Witze [1977]†	HWA, Ensemble-average	L-head	7.25	500-2500		0.5 * $\bar{U}_p$	1-4.5 0.2-0.7 (2°-12° CA)	1.5-4			
Wakisaka, et al. [1979]	HWA, Ensemble-time average, $\Delta\theta$ = 43° CA	Disc (swirl)	4.1	900 (600-1200)		1-1.5 m/sec (0.15-0.25 * $\bar{U}$)	0.5-1.5	5-15	0.2	2	The results are for TDC and depend on the valve shroud position. l_x = (2.5-5) λ_x.
Rask [1979]	LDA, Ensemble-average	L-head	7	270-800	Open throttle 1/2 throttle	1.5-1 * $\bar{U}_p$					
Brandl, et al. [1979]	HWA, Ensemble-time average	Disc bowl-in-piston	18	1100-2400						0.5-1.5 0.5-2.5	
Daneshyar & Fuller [1981]	HWA, Ensemble-time average, $\Delta\theta$ = 30° CA	Disc non-shrouded valve	4	260		0.35-0.4 m/sec					Turbulence energy is in frequencies < 300 Hz.
		Shrouded valve				0.5-0.7 m/sec					
Wakisaka, et al. [1982]	HWA, Ensemble-time average, $\Delta\theta$ = 43° CA	Disc side valve	3.2	600-1200			0.5-2		0.1-0.35		
		Overhead valve	4.1								
Gerber [1982]	HWA, LDA, Ensemble-average	Hemispherical flat piston		1500 500-2500		2 m/sec	0.5-2 10-2 (30°-10°CA)	3-8 5-12			
Liou & Santavicca [1983]	LDA, cycle resolved data analysis	Disc, 2 stroke model engine		1200-2400		0.7-0.5 * $\bar{U}_p$	0.6-0.2§	6-4			§ l_t = 0.6-1 with ensemble-averaging.

* Dent & Salama's [1975] re-analysis.

† Results only for θ = 180° - 270° CA; beyond this, results are suspected of HWA calibration error.

TABLE 2.5

Measured Variations of Flow Parameters During Compression Stroke

Investigator	Experimental Details	Combustion Chamber Shape	Compression Ratio	Engine Speed	$\bar{u}$	u'	L_t	L_x	λ_t	λ_x	Miscellaneous
Semenov [1963]	HWA, Ensemble-time average, $\Delta\theta$ = 24° CA, frequency filter < 300 Hz	Disc	4-9.5	600-1200	constant, decreasing near TDC					decrease*	
Dent & Salama [1975]	HWA, Ensemble-time average, frequency filter, $\Delta\theta$ = 10° CA	Wedge	9	1000	increase/ decrease	as $\bar{u}$		decrease	constant	increase/ decrease	Weak dependence of λ_t on $\bar{u}$.
		Heron	8.9	1000	decrease	as $\bar{u}$		decrease	constant	decrease	
Lancaster [1976]	HWA, non-stationary time-Ensemble average, $\Delta\theta$ = 45° CA	Disc non-shrouded valve	8.7 (6.8-10.5)	1500 (1000-2000)		constant	increase	constant	increase	constant	
		Shrouded valve	8.7 (6.8-10.5)	1500 (1000-2000)		increase/ decrease	increase	increase/ decrease	increase	increase/ decrease	
Witze [1977]	HWA, Ensemble-average	L-head	7.25	500-2500	constant	as $\bar{u}$	increase	increase			Results for θ = 180° - 270° CA.
Wakisaka, et al. [1979]	HWA, Ensemble-time average, $\Delta\theta$ = 43° CA	Disc (swirl)	4.1	900 (600-1200)	linear increase	as $\bar{u}$	moderate increase	increase	constant	constant	Results for θ = 310° - 360° CA.
Rask [1979]	LDA, Ensemble-average	L-head	7	270-800	constant, decreasing near TDC	as $\bar{u}$					
Brandl, et al. [1975]	HWA, Ensemble-time average	Disc	18	1100-2400		decrease				decrease	The variations depend on the measurement location.
		Bowl-in-piston				increase				increase	
Coghe & Ghezzi [1981]	LDA, Ensemble-average	Disc	11	600-1800	constant	as $\bar{u}$					
Daneshyar & Fuller [1981]	HWA, Ensemble-time average, $\Delta\theta$ = 30° CA	Disc non-shrouded valve	4	260	constant	as $\bar{u}$					
		Shrouded valve			increase	as $\bar{u}$					
Gerber [1982]	HWA, LDA, Ensemble-average	Hemispherical flat piston		500-2500	increase/ decrease near TDC	constant	increase/ decrease	increase/ decrease			
Liou & Santavicca 1983	LDA, cycle resolved data analysis	Disc (without swirl)		1200-2400	decrease	increase	increase				Results for θ = 330° - 360° CA.
		(swirl)			decrease	moderate decrease	moderate decrease	decrease			

* Re-analysis of data by Dent & Salama [1975a].

TABLE 2.6

Measured Influence of Increase in Speed, Compr ession Ratio and Volumetric Efficiency on the Mean Velocity, and Turbulence Parameters During Compression

Investigator	Experimental Details	$\bar{U}$			u'			L_t			L_x			λ_t			λ_x			Miscellaneous
		S	CR	η_v	S	CR	η_v	S	CR	η_v	S	CR	η_v	S	CR	η_v	S	CR	η_v	
Semenov [1963]	HWA, Ensemble-time average, frequency filter < 300 Hz, $\Delta\theta$ = 24° CA	$\uparrow$ ($\bar{u}$-S$^{2.1}$)	↑	linear	$\uparrow$ (u'-S$^{1.5}$)	const.	linear													The increase in speed increases turbulence energy at all frequencies; for CR, the energy of 2-4 kHz range increases.
Dent & Salama [1975a]	HWA, Ensemble-time average, low frequency filter, $\Delta\theta$ = 10° CA													const.			↑	↑		
Dent & Salama [1975b]	HWA, Ensemble-time average, $\Delta\theta$ = 10° CA	↑		↑	↑		↑				↑		↑	const.			↑		↑	λ_t = 0.12-0.22 msec for numerous engine designs and operating conditions.
Lancaster [1976]	HWA, non-stationary time-Ensemble average, $\Delta\theta$ = 10° CA	↑		no trend	linear	const.	linear (small)	↑* linear		↑* (small)	↑* shrouded valve const. non-shrouded valve		↑*	↓	const.	const.	no trend	no trend	no trend	λ_t = 0.10-0.25 msec, decreasing with increase in $\bar{U}$, at TDC.
Witze [1977]	HWA, Ensemble-average	> linear			linear			↓			const.									Results for θ = 180° - 270° CA.
Wakisaka, et al. [1979]	HWA, Ensemble-time average, $\Delta\theta$ = 43° CA	linear			linear			↓			↑			↓ moderate			↑ moderate			Results at θ = 360° CA.
Rask [1979]	LDA, Ensemble-average	≥ linear		const.	linear		const.													
Brandl, et al. [1979]	HWA, Ensemble-time average	↑			↑												↑			
Coghe & Ghezzi [1981]	LDA, Ensemble-average	linear			linear															
Wakisaka, et al. [1982]	HWA, Ensemble-time average, $\Delta\theta$ = 43° CA							no trend						↓						λ_t/L_t decreases with increase in mean velocity.
Gerber [1982]	HWA, LDA, Ensemble-average	↑†			↑†			↓			no trend									No scaling of $\bar{U}$ and u' with engine speed.
Liou & Santavicca [1983]	LDA, cycle resolved data processing	↑†			linear			↓												

* Lancaster, D.R. [1975], "Effect of Turbulence on Spark Ignition Engine Combustion", PhD Thesis, University of Illinois (cited in Tabaczynski [1979]).

† No consistent trend.

TABLE 2.7

Multi-Dimensional Theoretical Studies

Author(s)	Flow Configuration	Modelling Aspects	Findings
Chong, et al. [1976]	Axisymmetric cylindrical chamber (flat and bowl-in-piston); compression and expansion strokes.	Similar to Watkins [1973]; grid (10 axial × 5 radial).	A toroidal vortex at TDC for low engine speeds (100 rpm) and a totally one-dimensional axial flow for higher speeds are predicted.
Griffin, et al. [1976]	Axisymmetric disc-chamber; inlet and exhaust valves; four-stroke.	Coordinate transformation similar to Watkins [1973]; solution by the fully-explicit finite difference scheme of MacCormack [1969]; grid (10 × 9).	The flow during compression and expansion is one-dimensional axial.
Diwakar, et al. [1976]	Axisymmetric disc-chamber; inlet and exhaust valves; four-stroke.	Identical to Griffin, et al. [1976]; inviscid solutions.	A toroidal vortex is generated during induction that persists throughout engine cycle; it is destroyed during the exhaust stroke.
Gosman & Johns [1978]	Axisymmetric; cylindrical, re-entrant and toroidal bowl-in-piston; with swirl.	Curvilinear-orthogonal grid; grid translation in the bowl and contraction/expansion within the cylinder; axisymmetric swirl velocity; all other aspects identical to Watkins [1977].	The flow structurein the bowl, at TDC compression, is strongly influenced by the level of swirl and interaction with squish flow.

TABLE 2.7 (continued)

Author(s)	Flow Configuration	Modelling Aspects	Findings
Ramos & Sirignano [1980a]	Axisymmetric disc-chamber; central orifice in open/closed arrangement; without and with swirl.	Identical to Watkins [1977] and Johns [1980]; k-ε turbulence model.	Inclusion of the compressibility term in the Reynolds stress model increases u' at TDC by 25%. The induction swirl increases the turbulent intensity. The swirl profile tends to solid body during compression stroke.
Ramos & Sirignano [1980b]	Axisymmetric disc-chamber; central thin-plate valve; CR = 7, 8.5 and 10.1; speed 500, 1000, 1500 rpm.	Identical to Watkins [1977]; grid (30 axial × 22 radial).	Peak turbulence levels during induction occur in the regions of large shear. Turbulence is homogeneous during compression. The turbulence energy at TDC increases linearly with engine speed and with CR.
Gosman & Johns [1980]	Axisymmetric cylindrical chamber; toroidal piston bowl; swirl; fuel injection.	Identical to Watkins [1977] and Johns [1980]; discrete droplet model (DDM) for the spray.	The spray induces large velocities and high turbulence intensities, comparable with those produced by the squish flow.

TABLE 2.7 (continued)

Author(s)	Flow Configuration	Modelling Aspects	Findings
Gosman, et al. [1980]	Axisymmetric disc and bowl-in-head chambers; closed-cylinder, central pipe, annular orifice and valve; S = 10-2000 rpm; CR = 3-14; seven test cases.	Similar to Watkins [1977]; grid (22 × 22) and (30 × 30); $\Delta\theta$ = 6°CA.	For laminar flow, good agreement with the analytical solutions for compression/expansion strokes are found. The qualitative behaviour of the induction flow and stronger motions are predicted with moderate accuracy, but weaker vortices are not well predicted. The average u' levels are in moderate agreement, but the measured peaks are not reproduced. The errors are in part due to uncertainties in the inlet boundary conditions.
Bernard [1981]	Axisymmetric disc-chamber; compression stroke.	Equations for the mean and variance of the turbulent vorticity field; standard five-point spatial difference; explicit temporal difference.	The piston motion generates two vortices in the cylinder wall/piston during compression stroke stroke. The strength of this vortex and its turbulence level at TDC increases with increase in the stroke/bore ratio.
El Tahry [1982]	Axisymmetric cylindrical chamber; disc and bowl-in-piston; CR = 10:1; with and without swirl.	CONCHAS computer code of Butler, et al. [1979]; k-ε turbulence model.	The mean motion and turbulence at TDC are sensitive to the level and distribution of initial swirl velocity at IVC. The turbulence at TDC is influenced by the initial levels at IVC in the absence of swirl, and is not influenced in the presence of swirl.

TABLE 2.7 (continued)

Author(s)	Flow Configuration	Modelling Aspects	Findings
Grasso & Bracco [1983a]	Axisymmetric cylindrical chamber; flat and bowl-in-piston; with and without swirl; compression stroke; S = 1000-4000 rpm; η_v = 0.25-0.75; CR = 6.5-16.	CONCHAS computer code; k-ε turbulence model.	In the absence of swirl, the turbulence intensity at TDC depends on the initial diffusivity (k^2/ε) and not on the initial values of k and ε. For the swirling flow, initial values of the turbulence parameters are unimportant. In the absence of swirl, the TDC turbulence intensity and diffusivity increase linearly with speed and load, and decrease with increase in CR; for swirling flow, u' and diffusivity are insensitive to load.
Grasso & Bracco [1983b]	Axisymmetric cylindrical chamber; disc and bowl-in-piston; swirl and without swirl; compression stroke; speed 1700 rpm; CR = 10:1.	CONCHAS computer code; k-ε turbulence model.	The turbulence intensity and diffusivity at TDC compression are insensitive to the initial levels, but non-uniformities depend on the details of the initial field. The turbulence relaxation crank angle is ≈100°CA, in the absence of strong mean flow, and is independent of engine speed.

TABLE 2.7 (continued)

Author(s)	Flow Configuration	Modelling Aspects	Findings
Schock, et al. [1983]	Axisymmetric disc-chamber; four-stroke; speed 1000 rpm; CR = 7:1; thin-plate modelling of valve.	Identical to Watkins [1977].	The details of the flow in the inlet port has a significant effect on the flow structure and turbulence during induction that persists during compression stroke. For small bore-to-stroke ratios, the intake-generated flow structure persists longer during the compression stroke.
Mukerjee, et al. [1984]	Axisymmetric cylindrical chamber; cylindrical and toroidal bowl-in-piston; compression and expansion strokes (270°-375°CA); speed 2600 rpm; CR = 15.47:1.	The PICALO computer code of Markatos & Mukerjee [1981] based on the PHOENICS code of Spalding [1980]; three-dimensional; fuel injection; 1440 computational cells and 6°CA time-step.	The penetration and mixing of the injected liquid fuel strongly depends on the level of the swirl velocity.
Gosman, et al. [1984]	Disc-chamber; off-centre, open annular orifice and operating valve; speed 200 rpm.	The RPM code of Watkins [1977] with the non-iterative PISO predictor-corrector method of Issa [1982]; three-dimensional; grids 28 × 16 × 28; 1°CA time-step.	The predictions are in good qualitative agreement with the data but accuracy is low for the moderate mesh densities. The off-centre position gives rise to considerable flow complexity during induction, that rapidly decay beyond the end of induction.

TABLE 2.7 (continued)

Author(s)	Flow Configuration	Modelling Aspects	Findings
Gosman, et al. [1984b]	Disc-chamber; central shrouded valve; S = 200 rpm.	Similar to Gosman, et al. [1984].	The shrouded valve produces a strong long-lived tumbling vortex. During compression, the tumbling vortex produces high turbulence generation and level, but the mean flow and turbulence decay rapidly near TDC. The mean u' level at TDC is 1.2 $\overline{V}_p$ which is markedly larger than in non-shrouded case ($\simeq$0.5 $\overline{V}_p$). The accuracy of the computer model is at best moderate.

TABLE 3.1

Values of the Coefficients Appearing in Variants of the ε-Transport Equation (3.57)

Version	$C_{\varepsilon 1}$	$C'_{\varepsilon 1}$	$C''_{\varepsilon 1}$	$C_{\varepsilon 2}$	$C_{\varepsilon 3}$	$C_{\varepsilon 4}$
Watkins [1977]	1.44	1.44	1.44	1.92	1.0	0.0
Morel & Mansour [1982]	1.44	$\delta\ (\partial\tilde{U}_i/\partial x_j)$ 1.32 - 1.44	$\delta\ (\partial\tilde{U}_i/\partial x_j)$ 3.5 - 4.5	1.92	1.0	0.0
El Tahry [1983]	1.44	1.44	1.44	1.92	-1/3	1.0

TABLE 3.2

Values of the Turbulence Model Constants

Constant	Value
C_μ	0.09
κ	0.4187
E	9.793
$\sigma_{h,T}$	0.9
σ_k	1.0
σ_ε	$\dfrac{\kappa^2}{C_\mu^{\frac{1}{2}}\,(C_{\varepsilon 2} - C_{\varepsilon 1})} \simeq 1.3$

TABLE 3.3

ϕ	Γ_ϕ	S_ϕ
u_i	μ_T	$-\frac{\partial P}{\partial x_i} + \frac{\partial}{\partial x_j}\left(\mu_T \frac{\partial u_j}{\partial x_i}\right) - \frac{2}{3}\frac{\partial}{\partial x_i}\left(\mu_T \frac{\partial u_\ell}{\partial x_\ell} + \rho k\right)$
h	$\frac{\mu_T}{\sigma_{h,T}}$	$\frac{\partial P}{\partial t}$
k	$\frac{\mu_T}{\sigma_k}$	$\mu_T \left(\frac{\partial u_i}{\partial x_j} + \frac{\partial u_j}{\partial x_i}\right)\frac{\partial u_i}{\partial x_j} - \frac{2}{3}\left(\mu_T \frac{\partial u_\ell}{\partial x_\ell} + \rho k\right)\frac{\partial u_\ell}{\partial x_\ell} - \rho \varepsilon$
ε	$\frac{\mu_T}{\sigma_\varepsilon}$	$\frac{\varepsilon}{k}\left[C_{\varepsilon 1}\,\mu_T \left(\frac{\partial u_i}{\partial x_j} + \frac{\partial u_j}{\partial x_i}\right)\frac{\partial u_i}{\partial x_j} - \frac{2}{3}\left(C'_{\varepsilon 1}\,\mu_T \frac{\partial u_\ell}{\partial x_\ell} + C''_{\varepsilon 1}\,\rho k\right)\frac{\partial u_\ell}{\partial x_\ell}\right]$ $+ C_{\varepsilon 3}\,\rho\,\varepsilon \frac{\partial u_\ell}{\partial x_\ell} + C_{\varepsilon 4}\frac{\rho\,\varepsilon}{\mu}\frac{\partial \mu}{\partial t} - C_{\varepsilon 2}\frac{\rho\,\varepsilon^2}{k}$

TABLE 3.4

ϕ	Γ_ϕ	$S_\phi(r,z)$
U	μ_T	$-\frac{\partial P}{\partial z} + \frac{\partial}{\partial z}\left(\mu_T \frac{\partial U}{\partial z}\right) + \frac{1}{r}\frac{\partial}{\partial r}\left(r\,\mu_T \frac{\partial V}{\partial z}\right) - \frac{2}{3}\frac{\partial}{\partial z}\left(\mu_T\, \nabla.\underline{U} + \rho\, k\right)$
V	μ_T	$-\frac{\partial P}{\partial r} + \frac{\partial}{\partial z}\left(\mu_T \frac{\partial U}{\partial r}\right) + \frac{1}{r}\frac{\partial}{\partial r}\left(r\,\mu_T \frac{\partial V}{\partial r}\right) + \frac{\rho\, W^2}{r} - 2\mu_T \frac{V}{r^2}$ $- \frac{2}{3}\frac{\partial}{\partial r}\left(\mu_T\, \nabla.\underline{U} + \rho\, k\right)$
W	μ_T	$-\rho\frac{V\,W}{r} - \mu_T \frac{W}{r^2} - \frac{W}{r}\frac{\partial \mu_T}{\partial r}$
h_s	$\frac{\mu_T}{\sigma_{h,T}}$	$\frac{\partial P}{\partial t}$
k	$\frac{\mu_T}{\sigma_k}$	$P_1 - \frac{2}{3}\left(\mu_T\, \nabla.\underline{U} + \rho\, k\right) \nabla.\underline{U} - \rho\,\varepsilon$
ε	$\frac{\mu_T}{\sigma_\varepsilon}$	$C_{\varepsilon 1}\frac{\varepsilon}{k} P_1 - \frac{2}{3}\left(C'_{\varepsilon 1}\,\mu_T\, \nabla.\underline{U} + C''_{\varepsilon 1}\,\rho\, k\right)\frac{\varepsilon}{k}\nabla.\underline{U}$ $+ C_{\varepsilon 3}\,\rho\,\varepsilon\,\nabla.\underline{U} + C_{\varepsilon 4}\frac{\rho\,\varepsilon}{\mu}\frac{\partial \mu}{\partial t} - C_{\varepsilon 2}\frac{\rho\,\varepsilon^2}{k}$

Note: $\nabla.\underline{U} = \frac{\partial U}{\partial z} + \frac{1}{r}\frac{\partial}{\partial r}(r\,V)$

$$P_1 = 2\mu_T\left[\left(\frac{\partial U}{\partial z}\right)^2 + \left(\frac{\partial V}{\partial r}\right)^2 + \left(\frac{V}{r}\right)^2\right] + \mu_T\left(\frac{\partial V}{\partial z} + \frac{\partial U}{\partial r}\right)^2 + \mu_T\left[r\frac{\partial}{\partial r}\left(\frac{W}{r}\right)\right]^2 + \mu_T\left(\frac{\partial W}{\partial z}\right)^2$$

TABLE 4.1

ϕ	$S_\phi(r, \xi, t)$
$\hat{U}$	$-\frac{1}{z_H}\frac{\partial P}{\partial \xi} + \frac{1}{z_H}\frac{\partial}{\partial \xi}\left(\frac{\mu_T}{z_H}\frac{\partial U}{\partial \xi}\right) + \frac{1}{r}\frac{\partial}{\partial r}\left(\frac{r\,\mu_T}{z_H}\frac{\partial V}{\partial \xi}\right)$ $-\frac{2}{3}\frac{1}{z_H}\frac{\partial}{\partial \xi}\left(\mu_T \nabla.\underline{U} + \rho k\right) - \frac{1}{z_H}\left(z_H \rho U_G\right) - \frac{1}{z_H}\frac{\partial}{\partial \xi}\left(\rho \hat{U} U_G - \frac{1}{z_H}\frac{\partial U_G}{\partial \xi}\right)$ $-\frac{1}{r}\frac{\partial}{\partial r}\left(r \rho V U_G - r \mu_T \frac{\partial U_G}{\partial r}\right)$
V	$-\frac{\partial P}{\partial r} + \frac{1}{z_H}\frac{\partial}{\partial \xi}\left(\mu_T \frac{\partial U}{\partial r}\right) + \frac{1}{r}\frac{\partial}{\partial r}\left(r \mu_T \frac{\partial V}{\partial r}\right) + \rho\frac{W^2}{r} - 2\mu_T\frac{V}{r^2}$ $-\frac{2}{3}\frac{\partial}{\partial r}\left(\mu_T \nabla.\underline{U} + \rho k\right)$
W	$-\rho\frac{V W}{r} - \mu_T\frac{W}{r^2} - \frac{W}{r}$
h_s	$\frac{\partial P}{\partial t} - \frac{U_G}{z_H}\frac{\partial P}{\partial \xi}$
k	$P_1 - \frac{2}{3}\left(\mu_T \nabla.\underline{U} + \rho k\right)\nabla.\underline{U} - \rho \varepsilon$
ε	$C_{\varepsilon 1}\frac{\varepsilon}{k}P_1 - \frac{2}{3}\left(C'_{\varepsilon 1}\mu_T \nabla.\underline{U} + C''_{\varepsilon 1}\rho k\right)\frac{\varepsilon}{k}\nabla.\underline{U} + C_{\varepsilon 3}\rho\varepsilon\nabla.\underline{U}$ $+ C_{\varepsilon 4}\frac{\rho\varepsilon}{\mu}\left(\frac{\partial \mu}{\partial t} - \frac{U_G}{z_H}\frac{\partial \mu}{\partial \xi}\right) - C_{\varepsilon 2}\frac{\rho\varepsilon^2}{k}$

Note: $\nabla.\underline{U} = \frac{1}{z_H}\frac{\partial U}{\partial \xi} + \frac{1}{r}\frac{\partial}{\partial r}(r V)$

$$P_1 = 2\mu_T\left[\left(\frac{1}{z_H}\frac{\partial U}{\partial \xi}\right)^2 + \left(\frac{\partial V}{\partial r}\right)^2 + \left(\frac{V}{r}\right)^2\right] + \mu_T\left(\frac{1}{z_H}\frac{\partial V}{\partial \xi} + \frac{\partial U}{\partial r}\right)^2 + \mu_T\left[r\frac{\partial}{\partial r}\left(\frac{W}{r}\right)\right]^2 + \mu_T\left(\frac{1}{z_H}\frac{\partial W}{\partial \xi}\right)^2$$

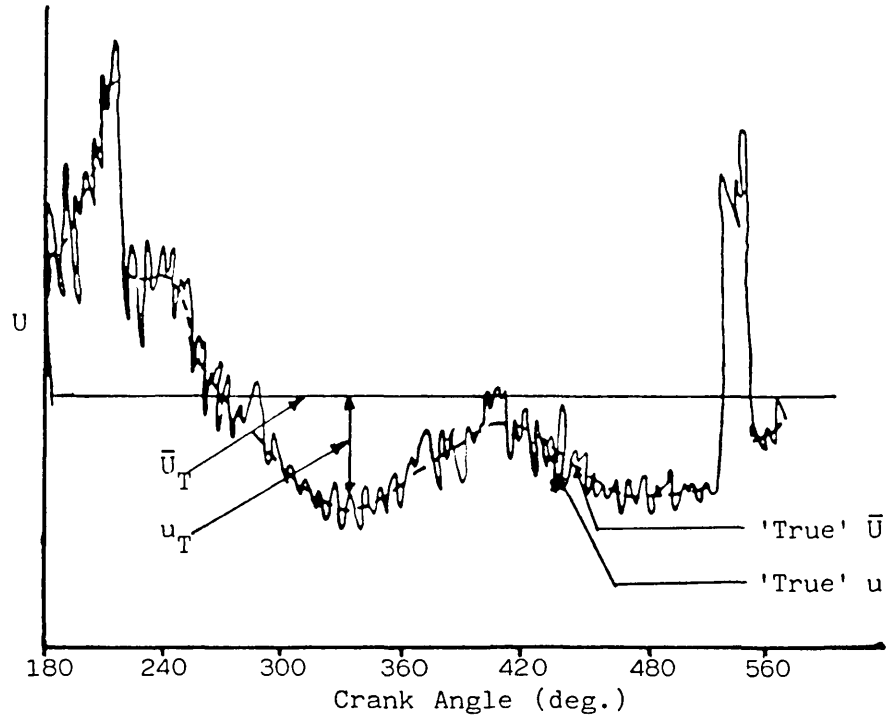


Figure 2.1: A typical instantaneous velocity record at a monitoring location, 'True' mean velocity $\bar{U}$ and Time-mean velocity $\bar{U}_T$

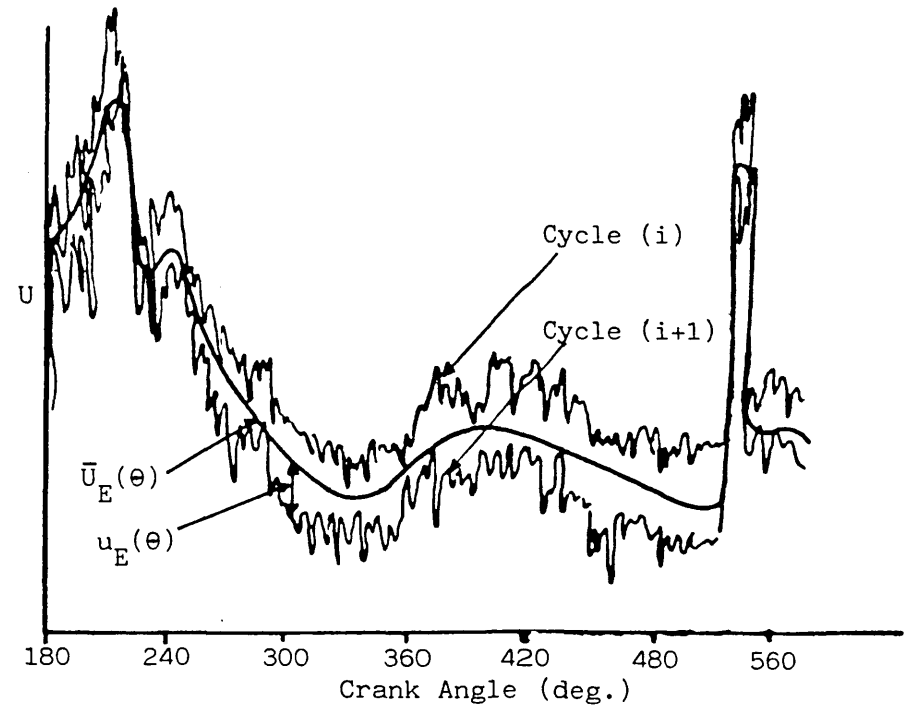


Figure 2.2: The effect of cycle-to-cycle variations on the ensemble-mean velocity and turbulence

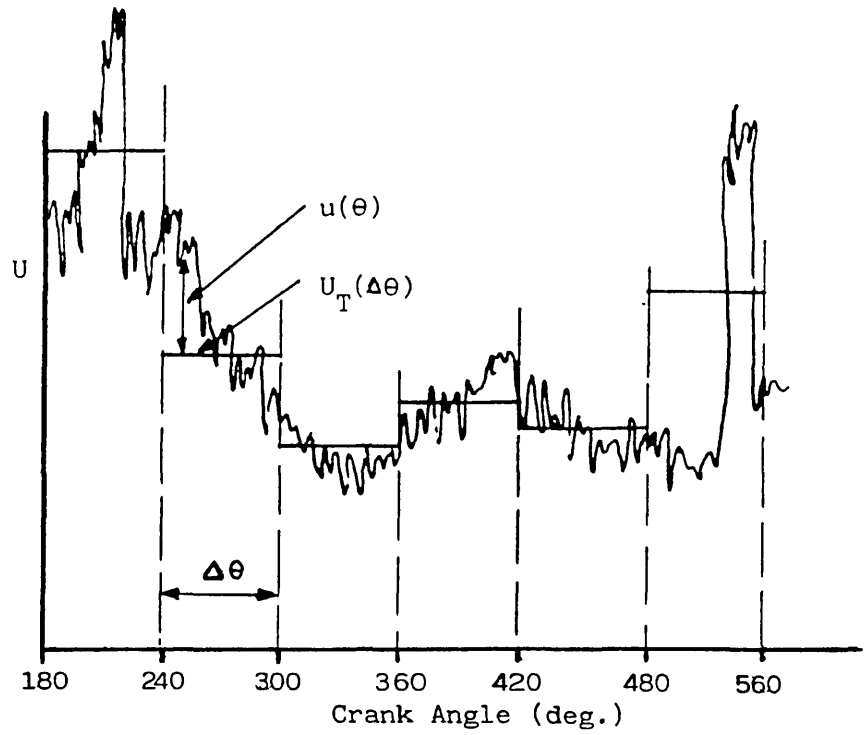


Figure 2.3: Time-average mean velocity and turbulence intensity over finite Δθ interval

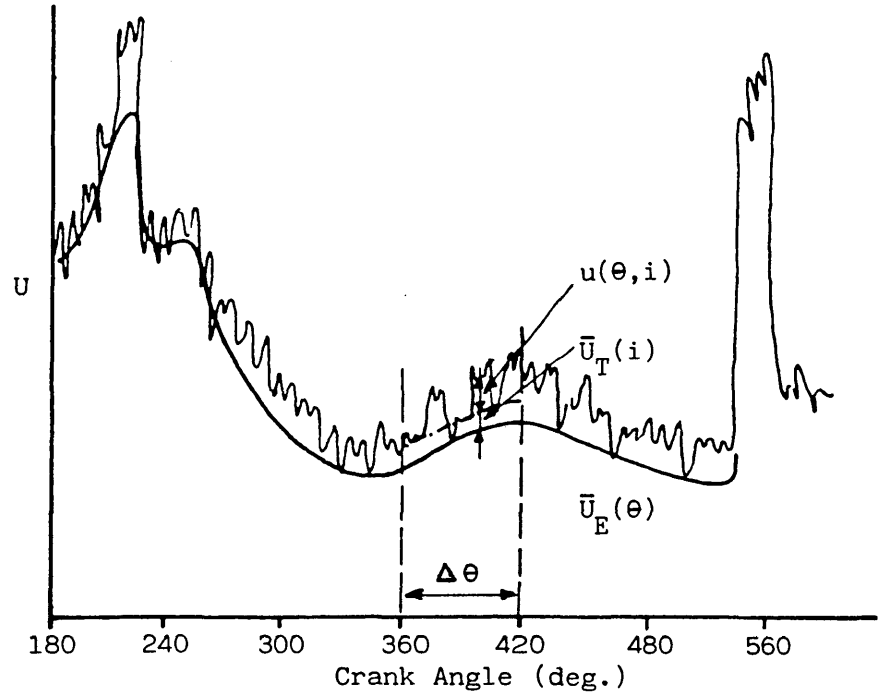


Figure 2.4: Components of the instantaneous velocity according to the non-stationary analysis of Lancaster [1976]

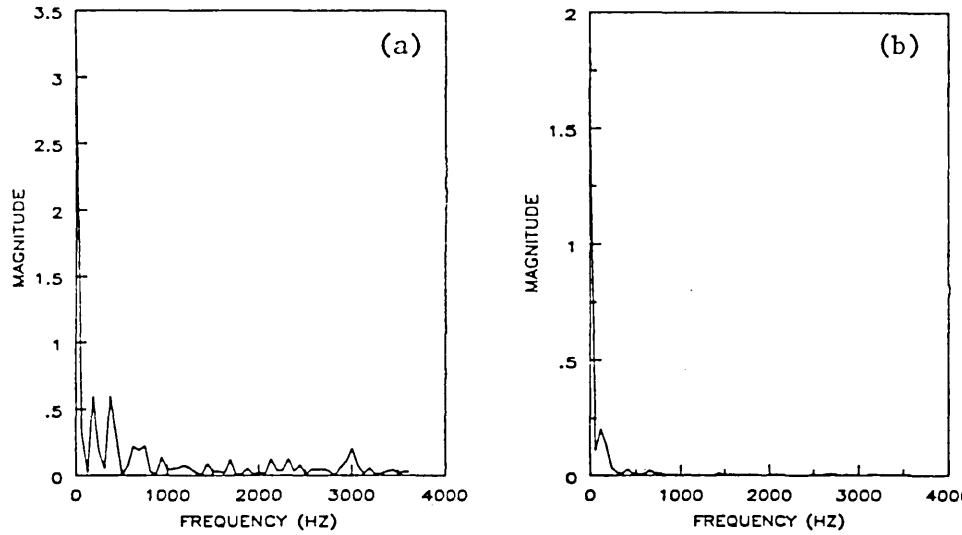


Figure 2.5: Frequency spectrum of (a) instantaneous velocity and (b) ensemble-mean velocity, for the interval θ = 330° - 390° CA (data of Liou & Santavicca [1982])

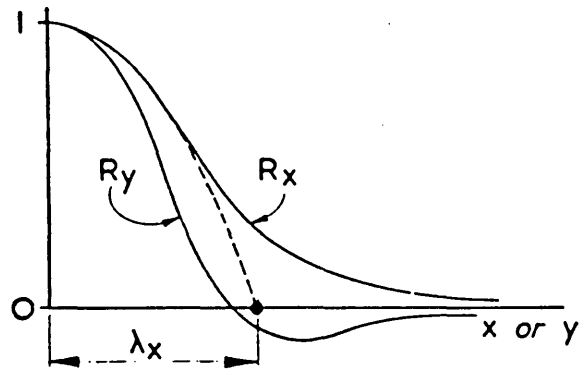


Figure 2.6: The correlation coefficients R_x and R_y and the micro-length scale λ_x

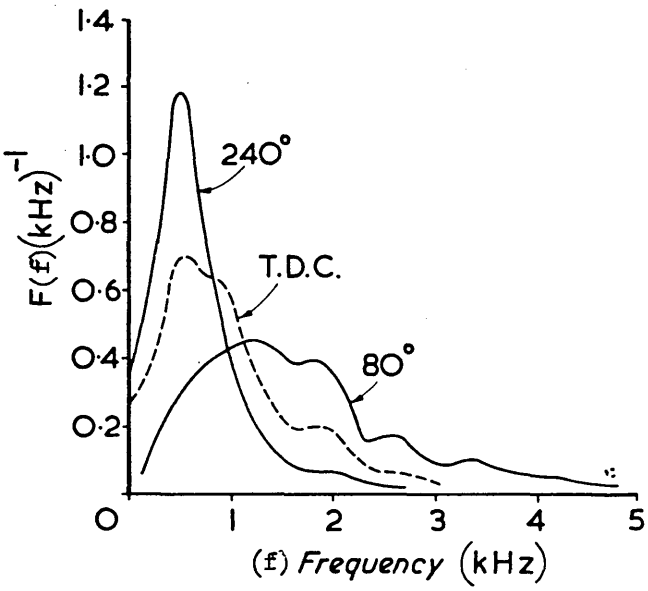


Figure 2.7: The turbulence energy spectrum at three stages in the engine cycle (data of Dent & Salama [1975a])

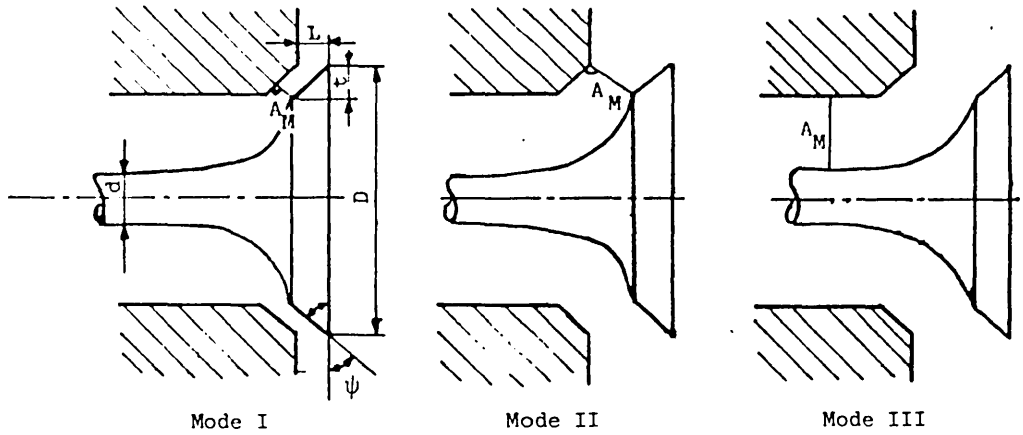


Figure 2.8: The valve geometry and notation and variations of the minimum flow area A_M with lift

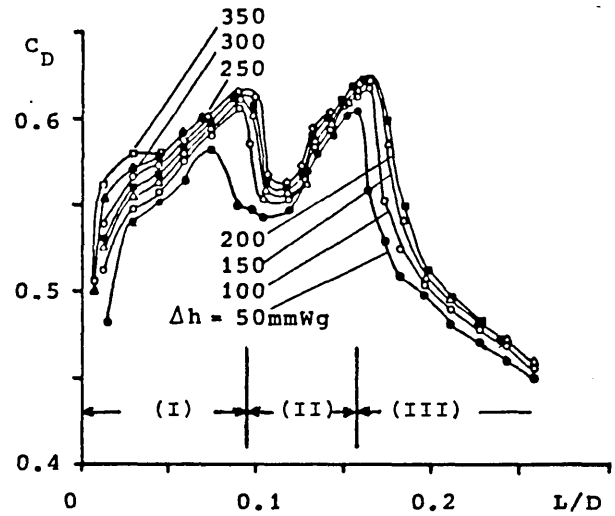


Figure 2.9: Variations of the valve discharge coefficient with lift and pressure drop (data of Vafidis & Whitelaw [1984])

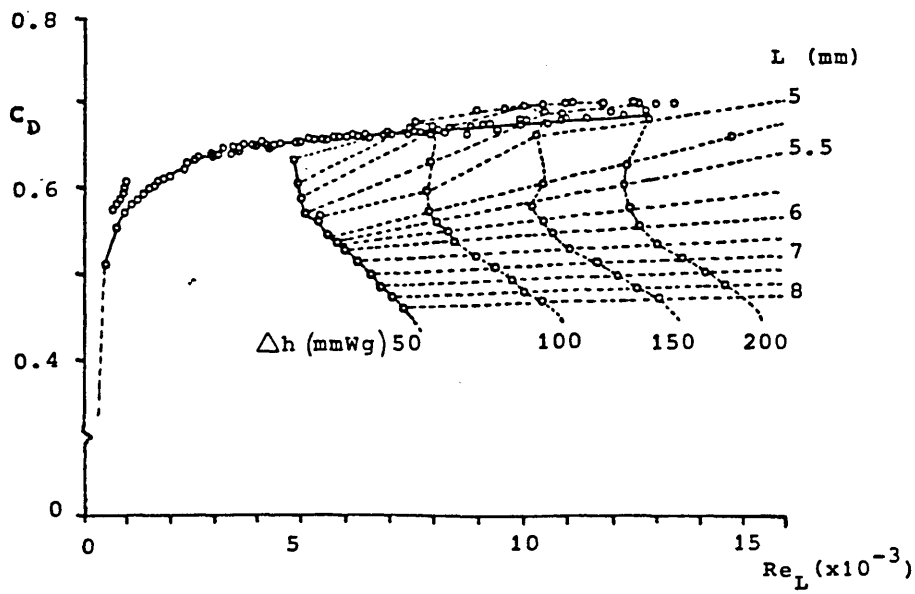


Figure 2.10: Variations of the valve discharge coefficient with flow Reynolds number (data of Vafidis & Whitelaw [1984])

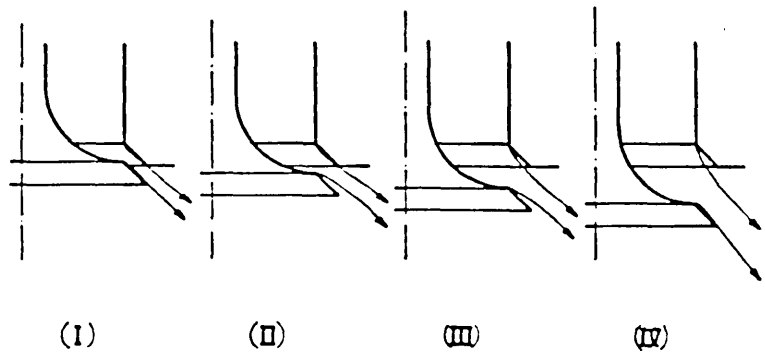


Figure 2.11: Flow patterns at the valve exit (data of Kastner, et al. [1963-64])

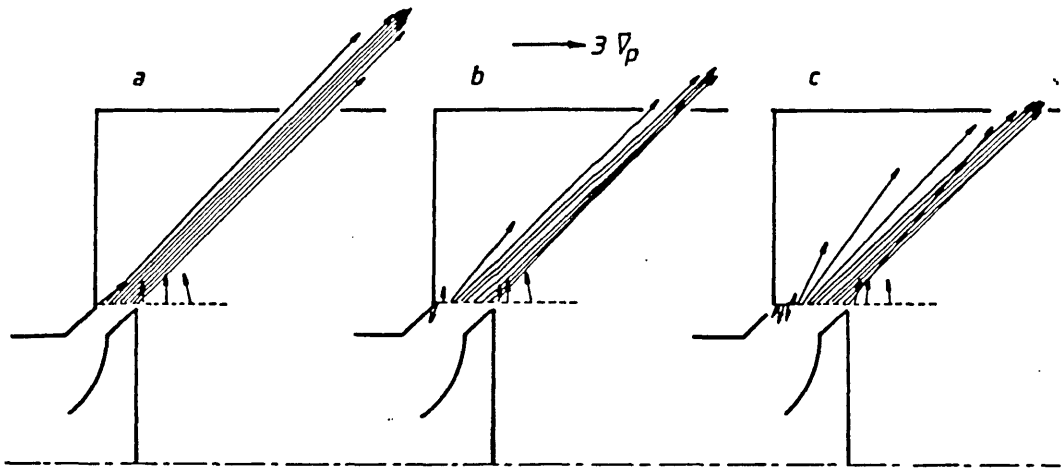


Figure 2.12: Variations of the velocity profile and angle of entry with valve lift (data of Vafidis & Whitelaw [1984])

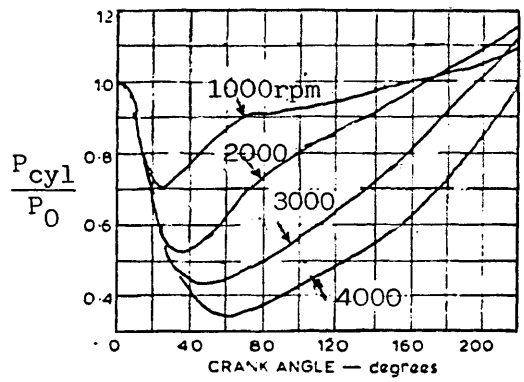


Figure 2.13: Variations of the cylinder mean pressure during induction (data of Kastner, et al. [1963-64])

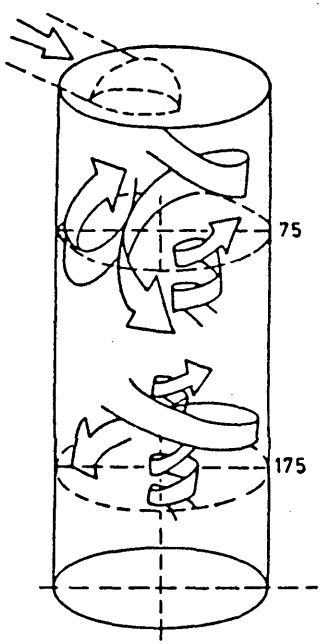


Figure 2.14: In-cylinder flow structure during induction for a directed port (data of Wigley & Hawkins [1981])

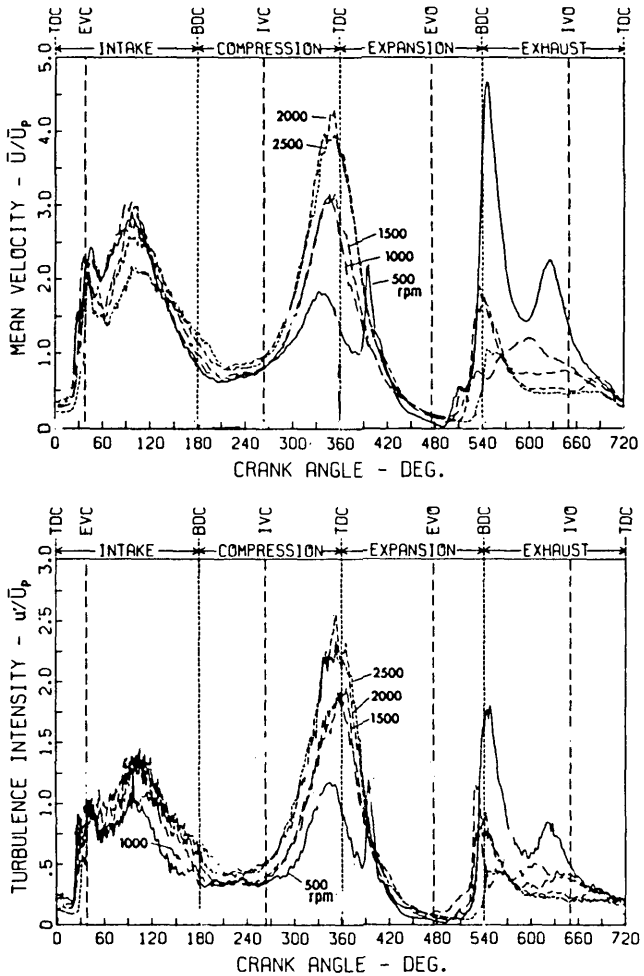


Figure 2.15: Variations with engine speed of the normalised ensemble-mean velocity and turbulence intensity (data of Witze [1977])

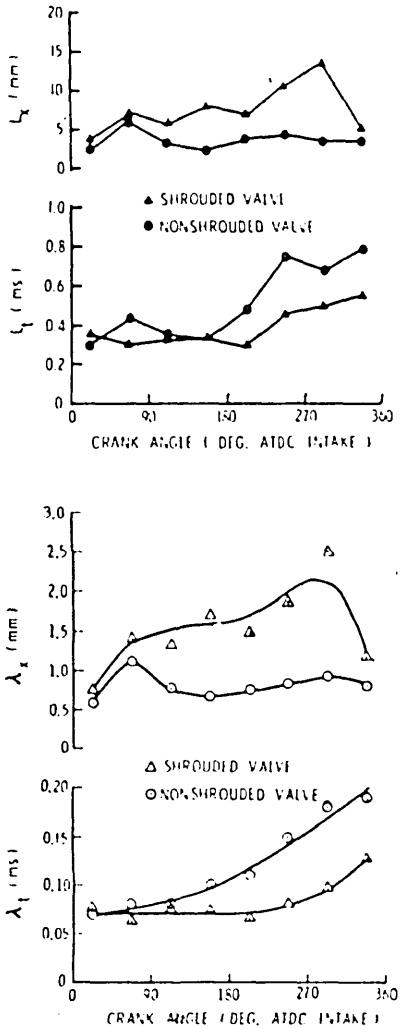


Figure 2.16: Variations of the turbulence time and length scales (data of Lancaster [1976])

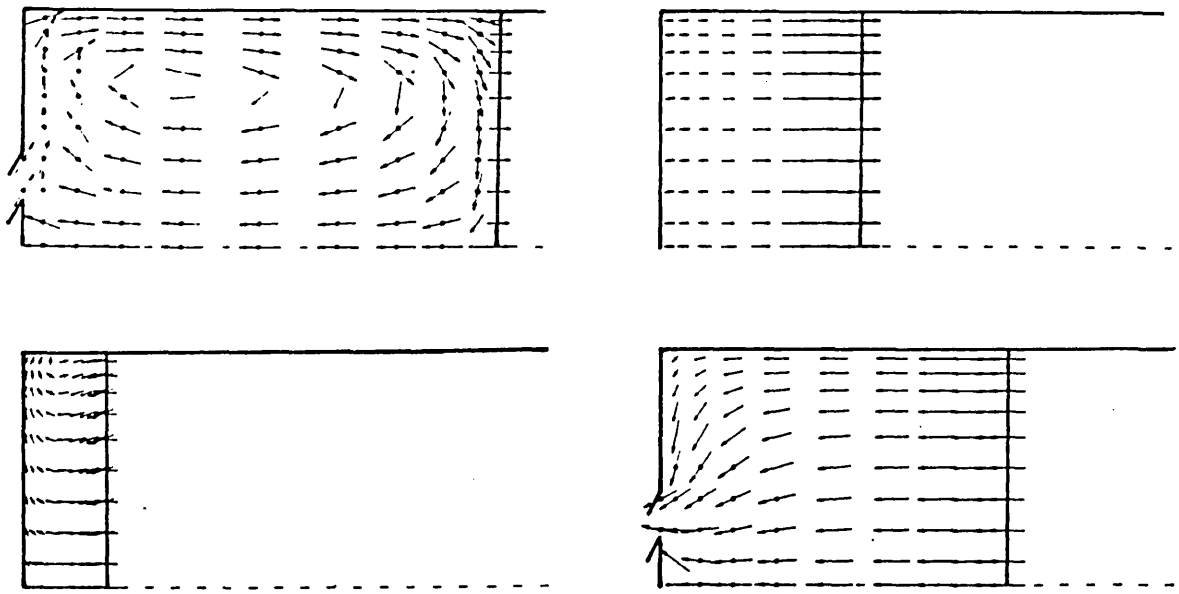


Figure 2.17: The predicted evolution of the mean flow in an engine with 30° seat angle (Watkins [1977])

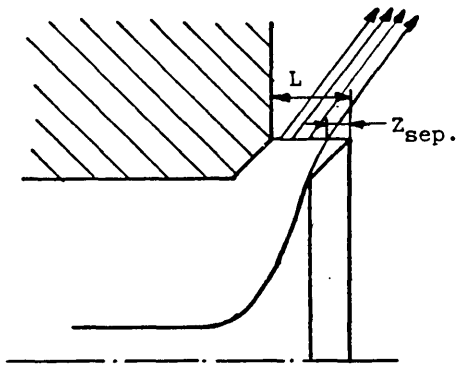


Figure 3.1: Schematic illustration of width of reverse flow region at valve exit Z_{sep}

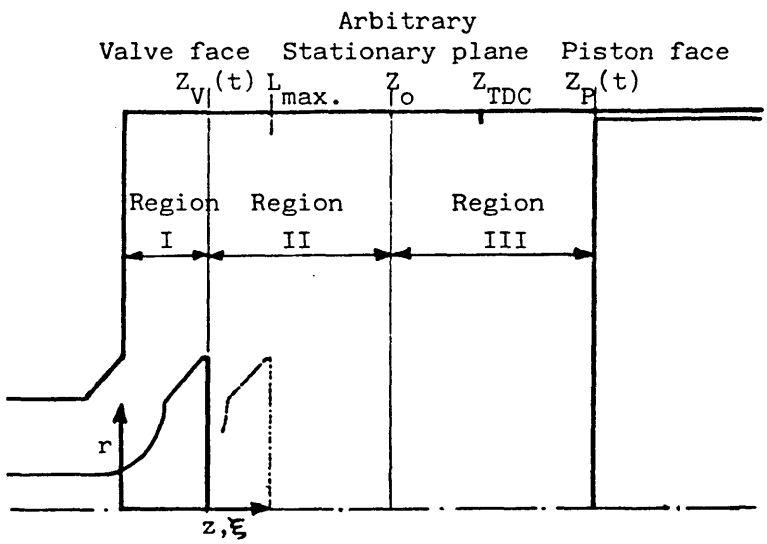


Figure 4.1: Subdivisions of the solution domain for the case of low compression ratio engine

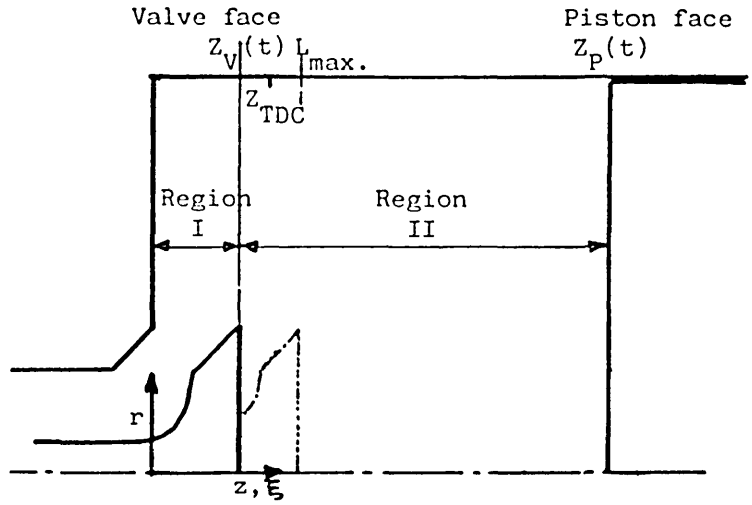


Figure 4.2: Subdivisions of the solution domain for the case of high compression ratio engine

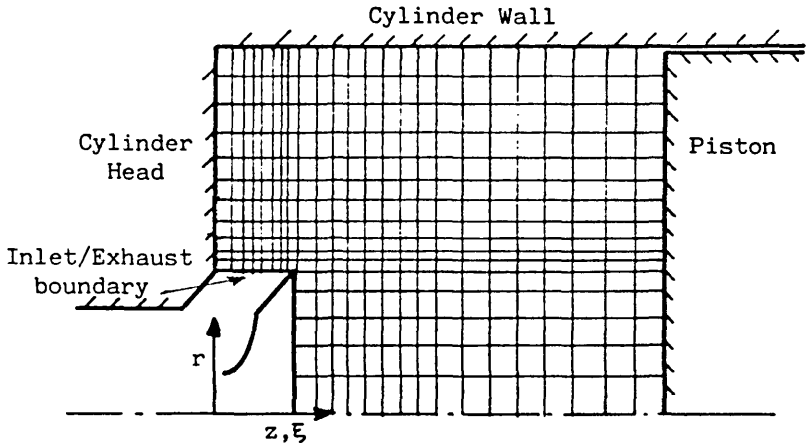


Figure 4.3: Schematic illustration of the computational grid and boundaries of the solution domain

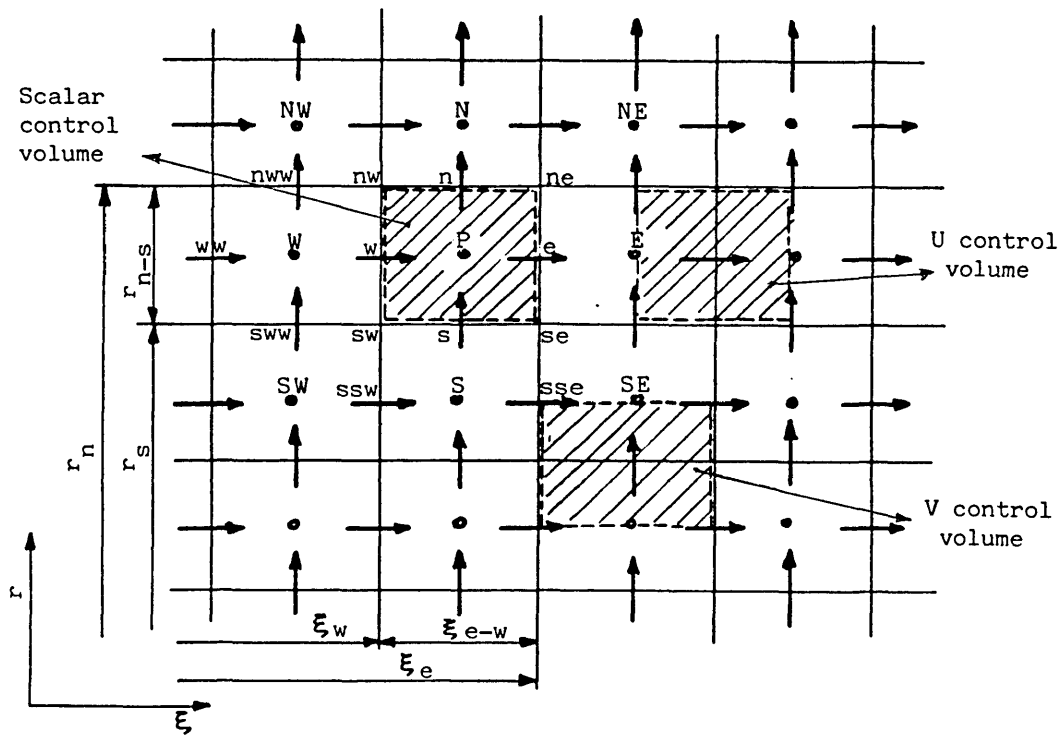


Figure 4.4: Computational grid, notation and control volumes of scalar variables and axial and radial velocities

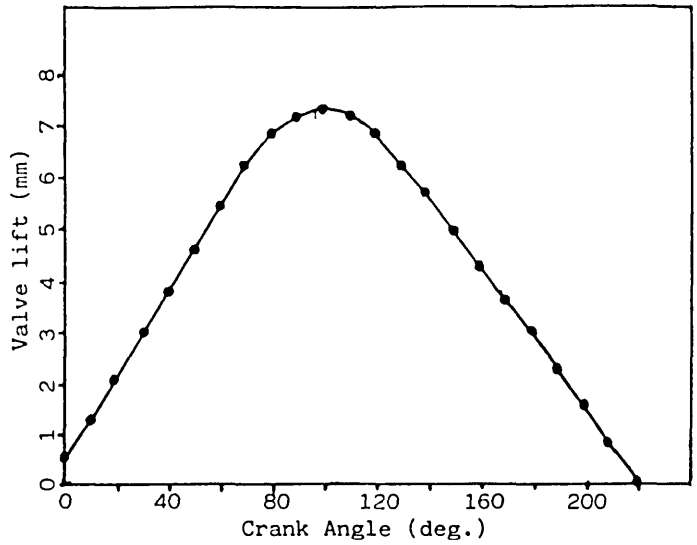


Figure 5.1: Valve lift diagram of the model engine

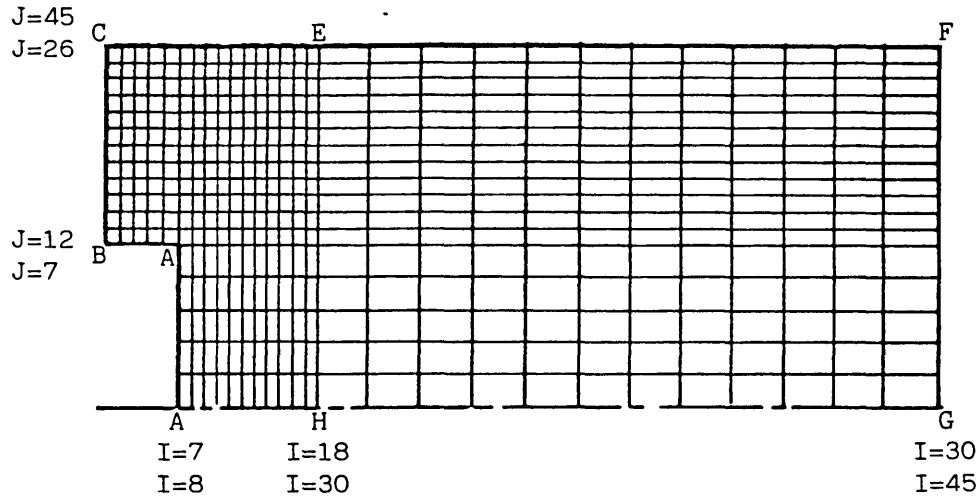


Figure 5.2: Grid arrangements for the test Case I

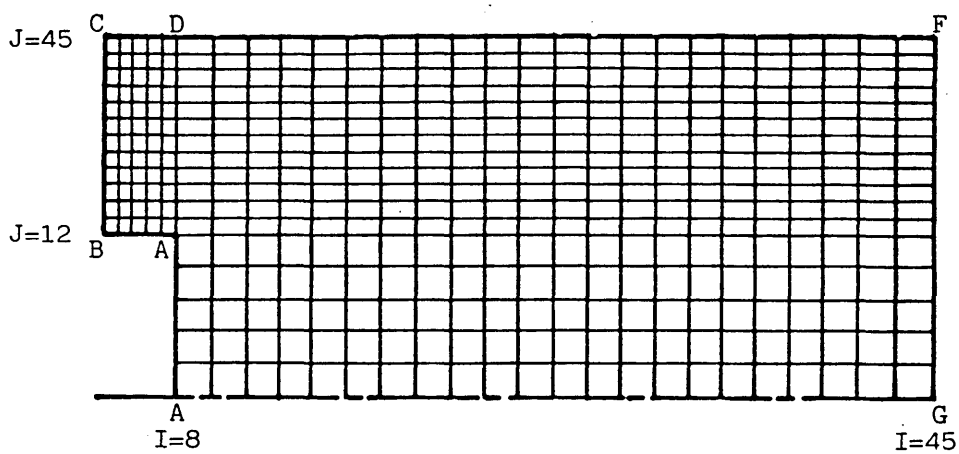


Figure 5.3: Grid arrangement for the test Case II

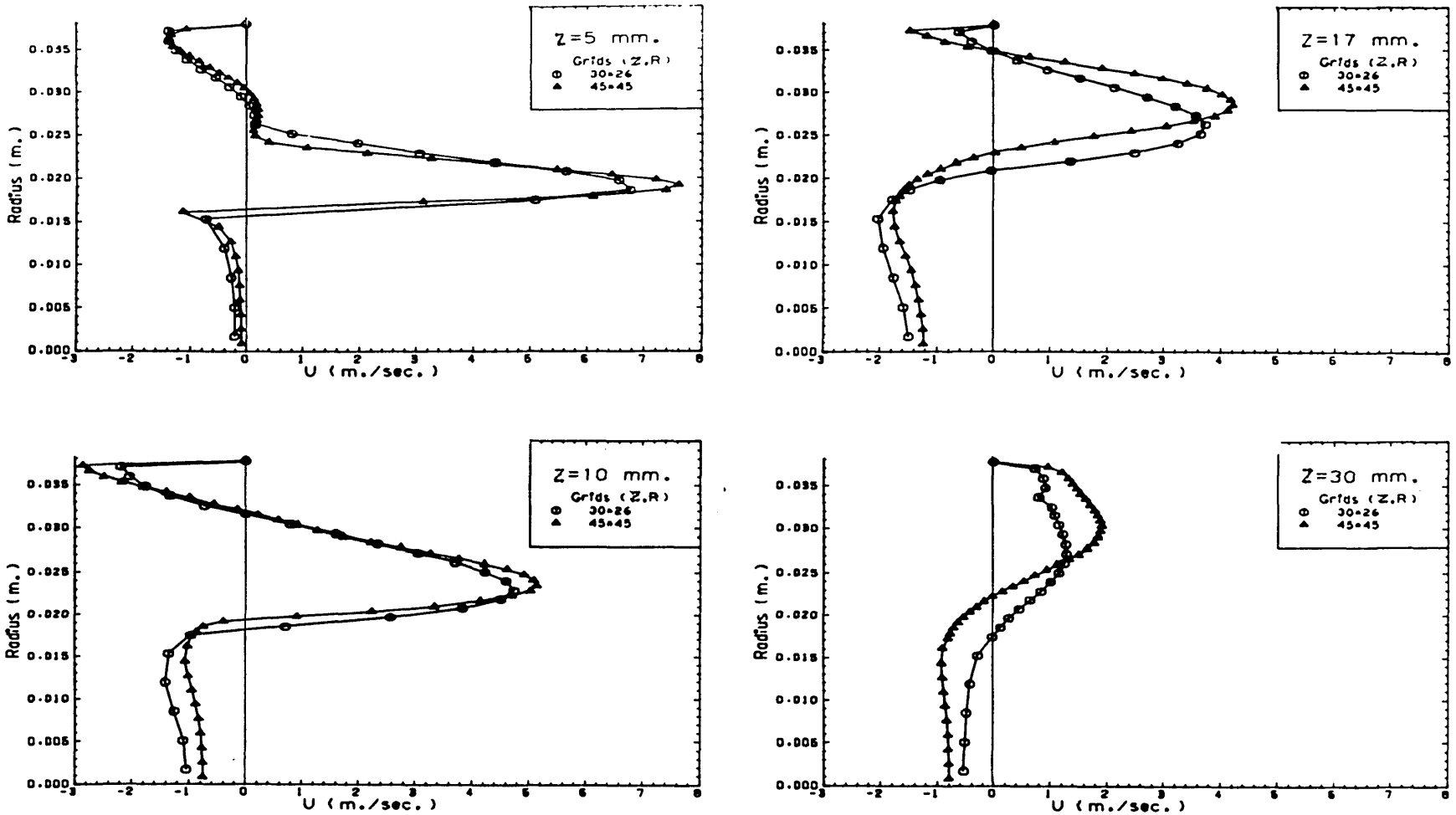


Figure 5.4(a): The effect of grid refinement on the mean axial velocity distributions at different axial locations, at θ = 36° CA

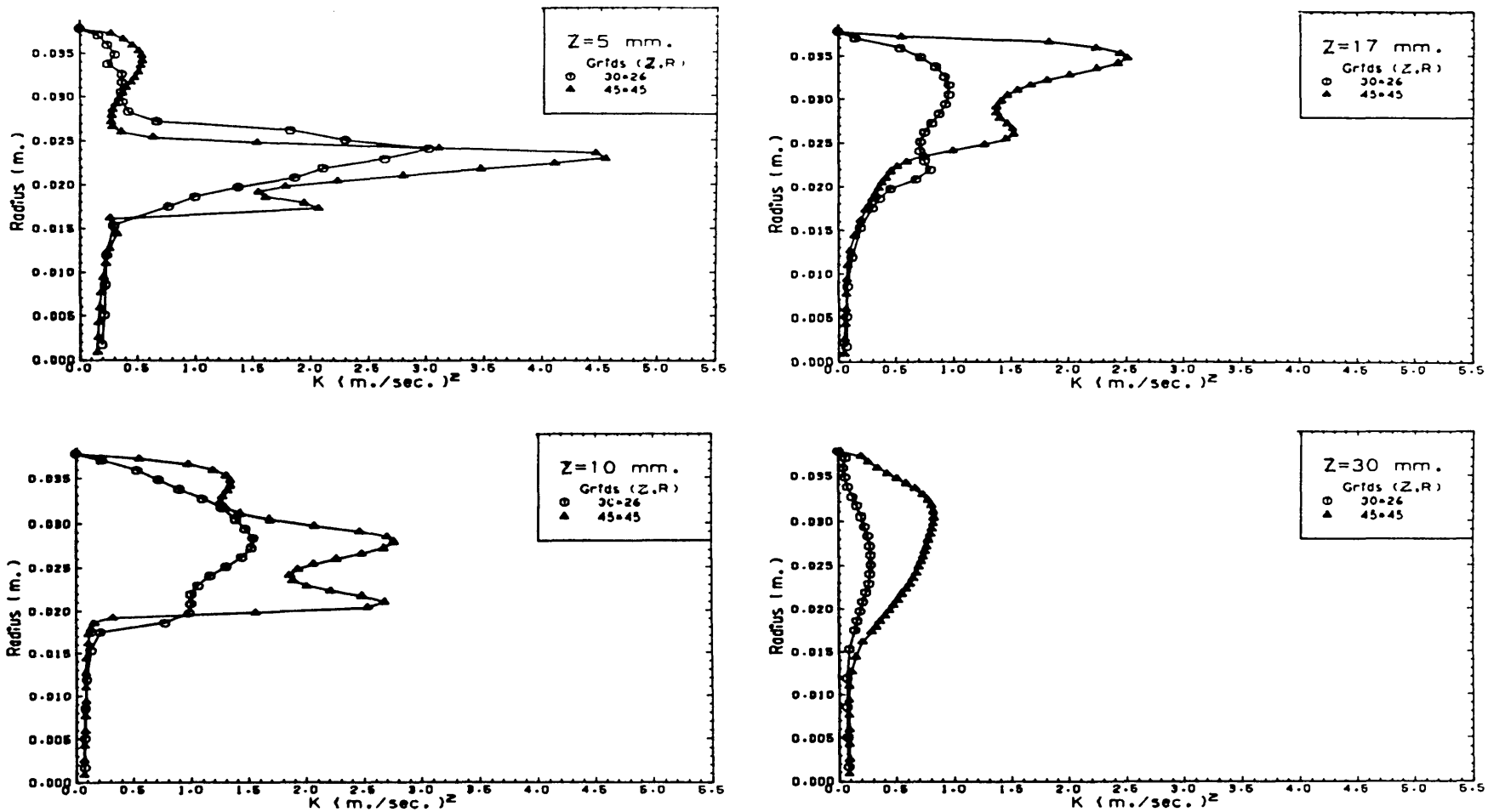


Figure 5.4(b): The effect of grid refinement on the turbulence energy distributions at different axial locations, at θ = 36° CA

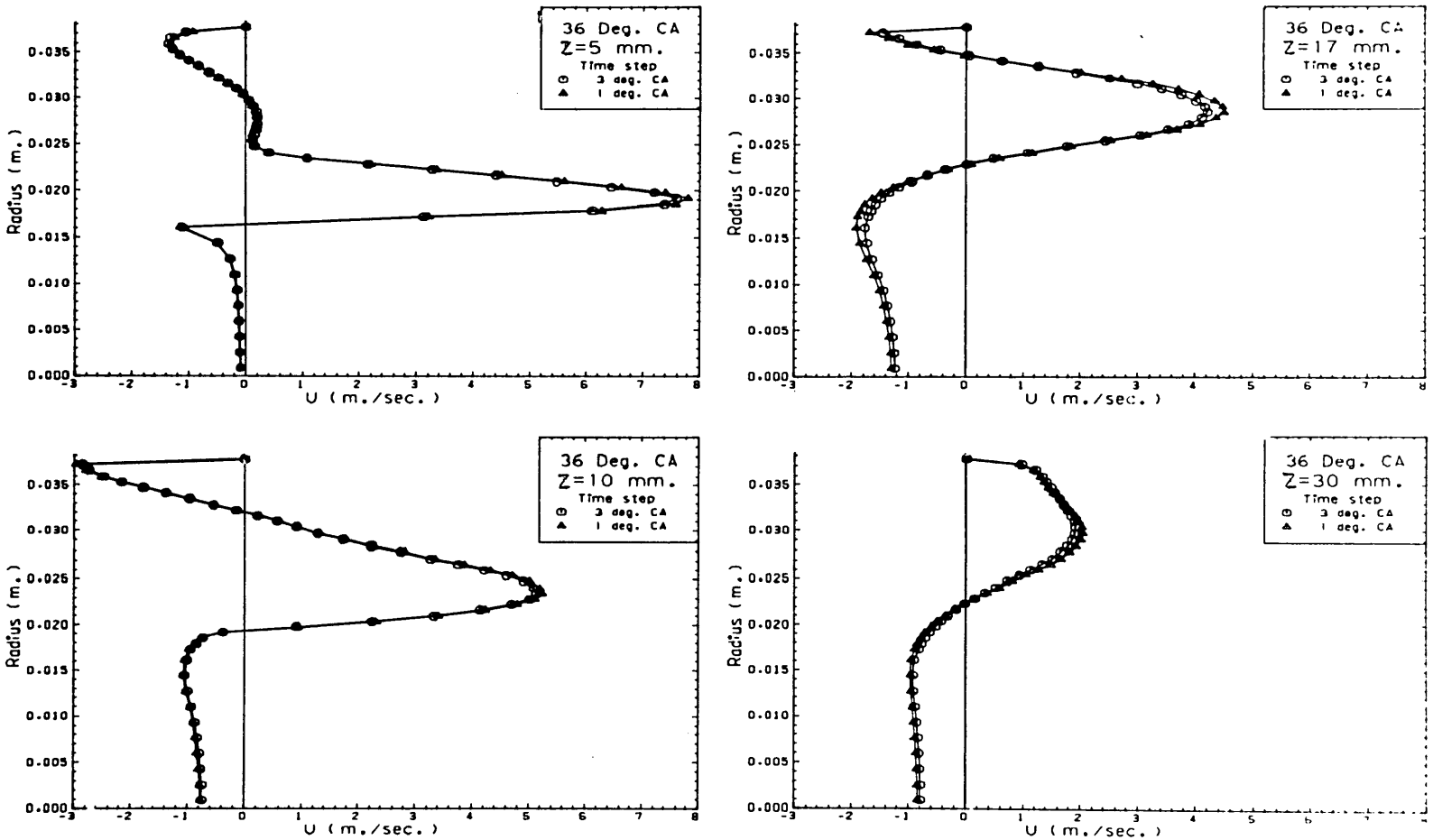


Figure 5.5(a): The effect of time-step on the mean axial velocity distributions at different axial locations, at θ = 36° CA

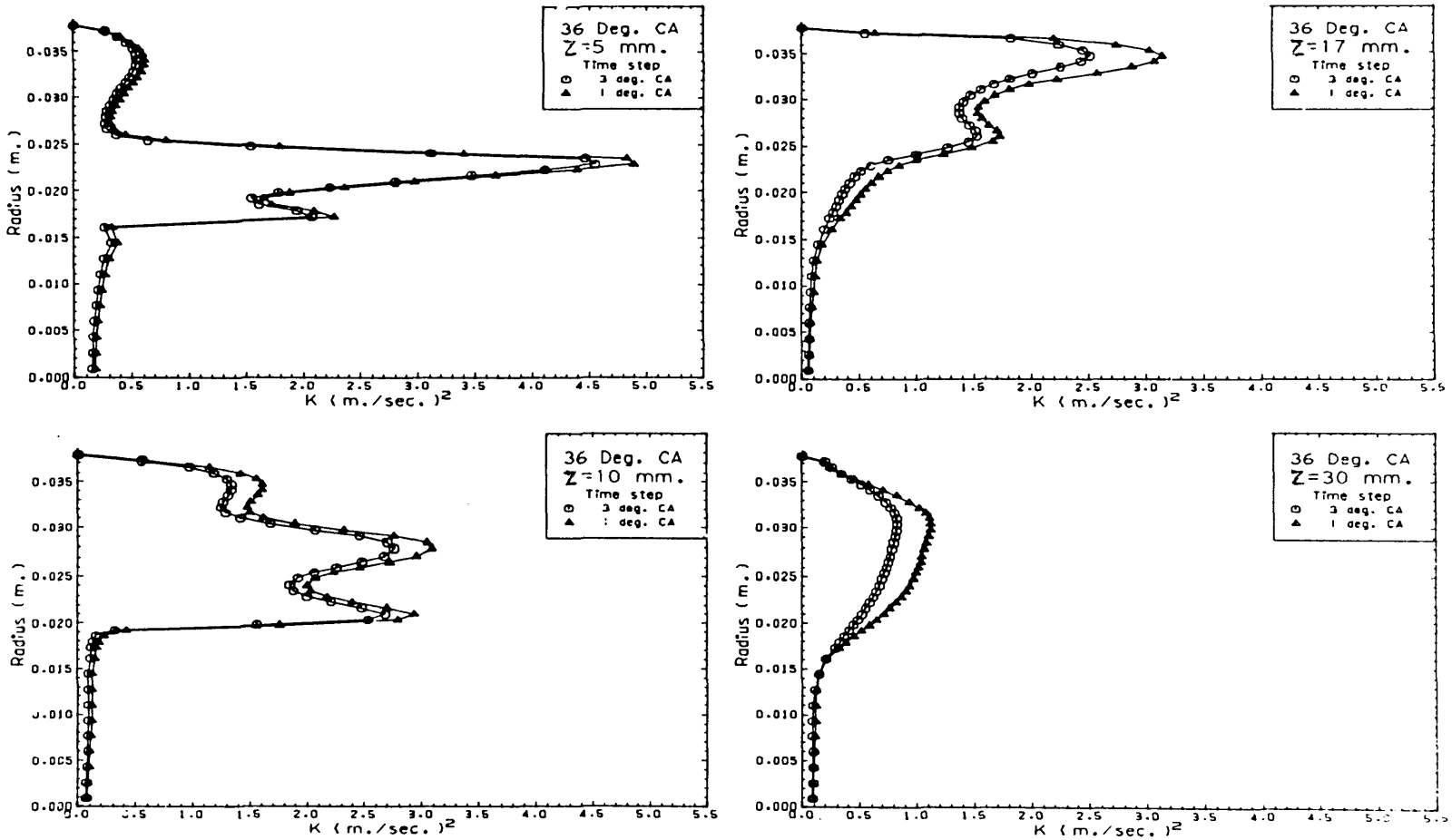


Figure 5.5(b): The effect of time-step on the turbulence energy distributions at different axial locations, at θ = 36° CA

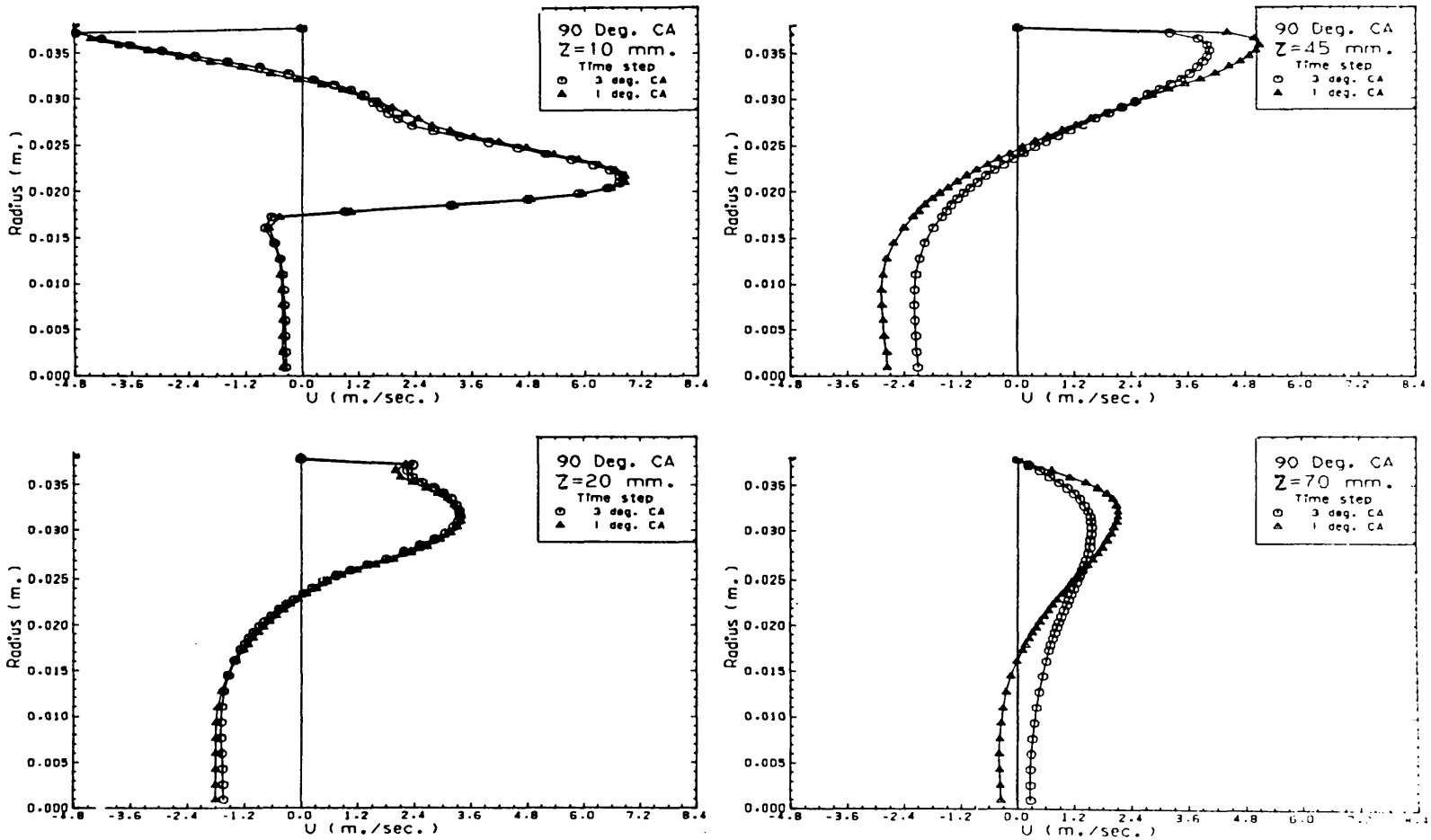


Figure 5.6(a): The effect of time-step on the mean axial velocity distributions at different axial locations, at θ = 90° CA

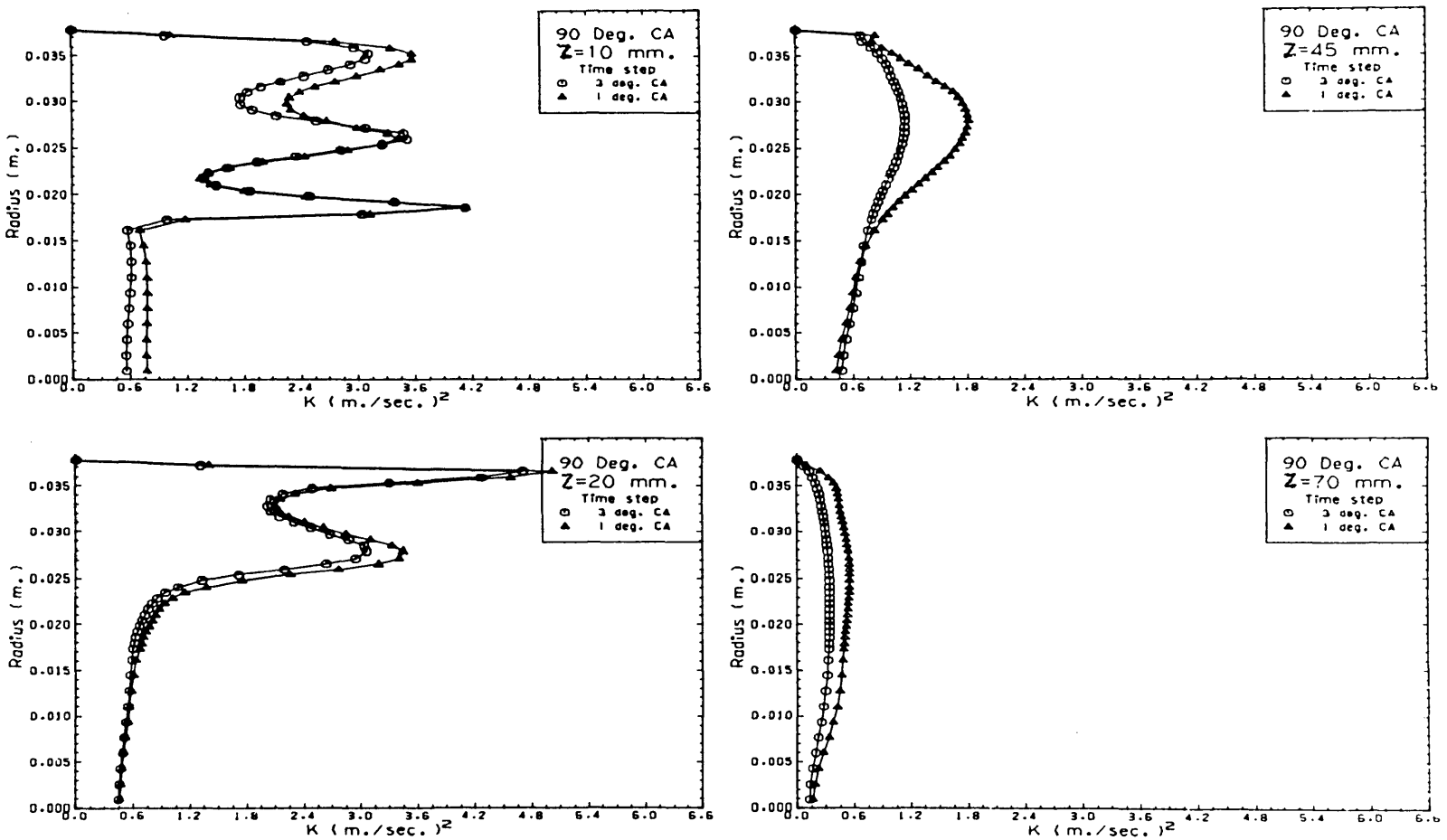


Figure 5.6(b): The effect of time-step on the turbulence energy distributions at different axial locations, at θ = 90° CA

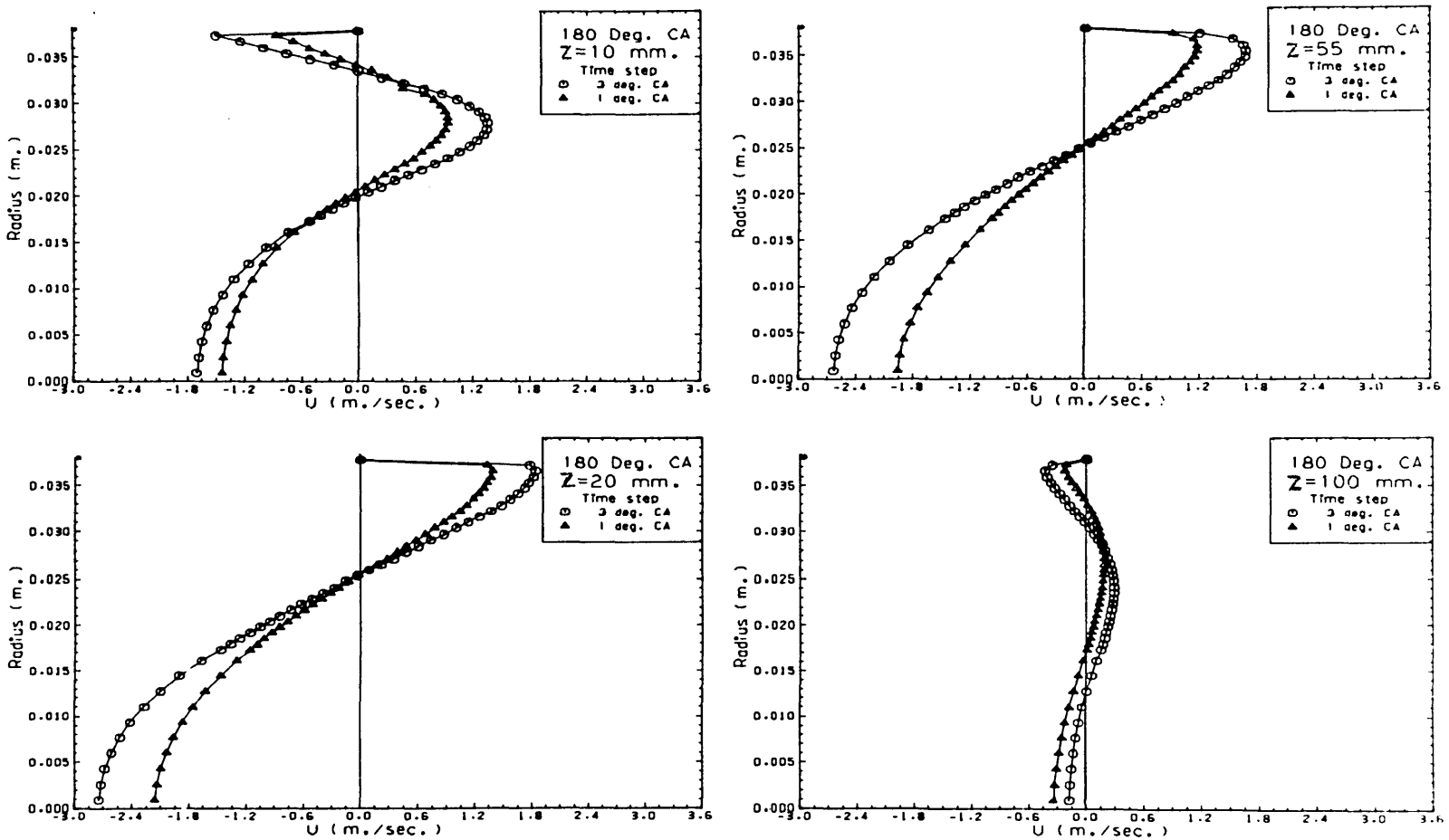


Figure 5.7(a): The effect of time-step on the mean axial velocity distributions at different axial locations, at θ = 180° CA

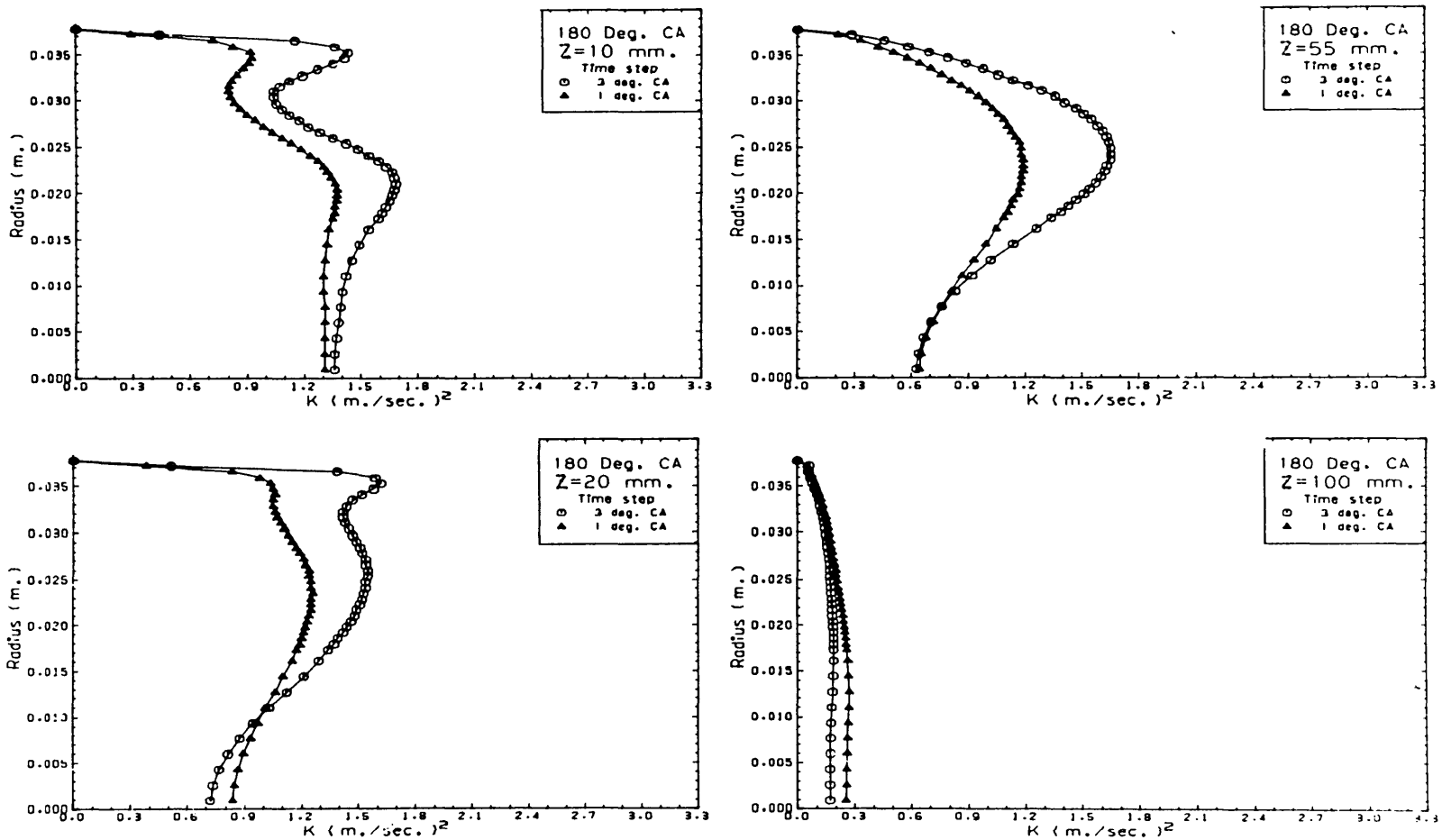


Figure 5.7(b): The effect of time-step on the turbulence energy distributions at different axial locations, at θ = 180° CA

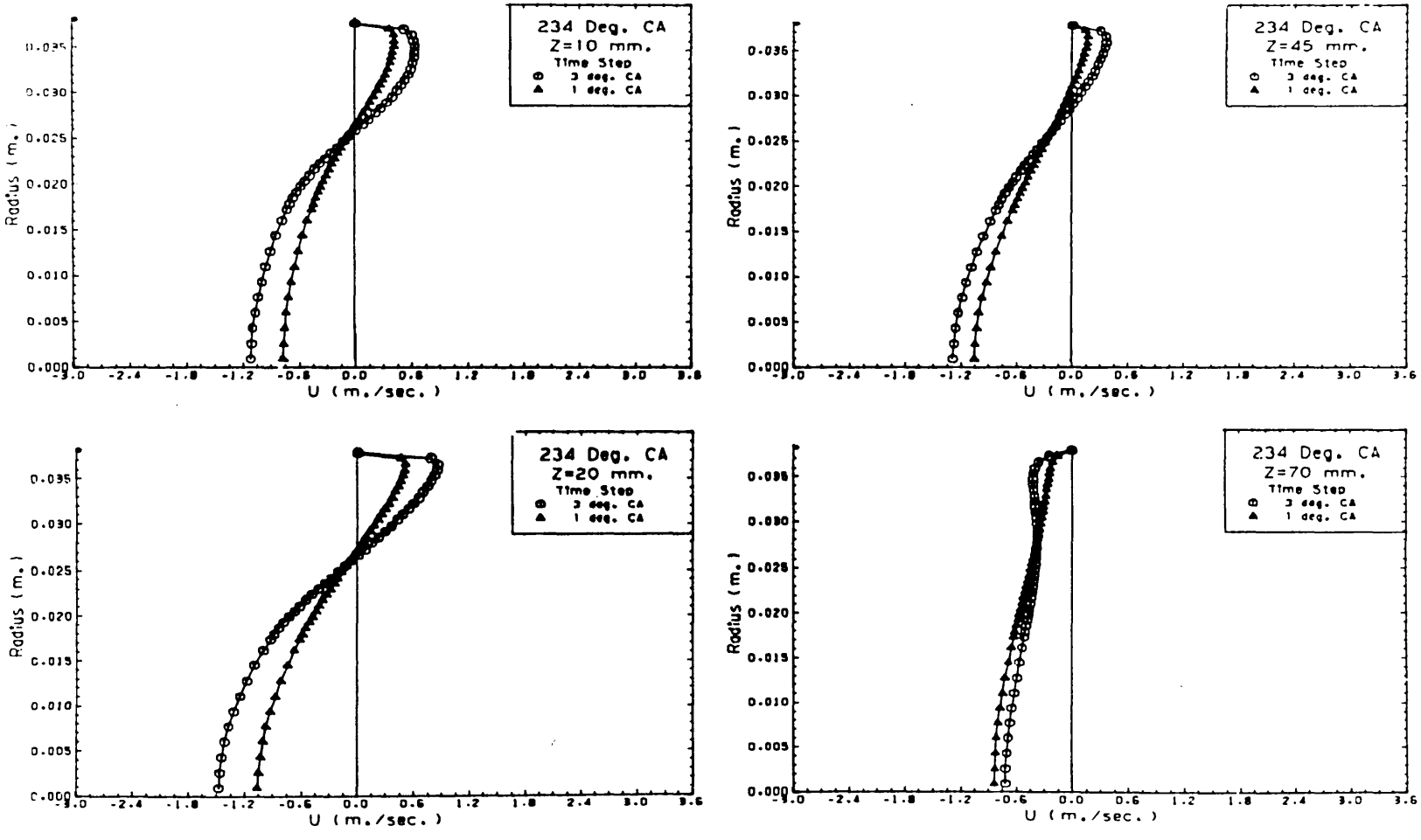


Figure 5.8(a): The effect of time-step on the mean axial velocity distributions at different axial locations, at θ = 234° CA

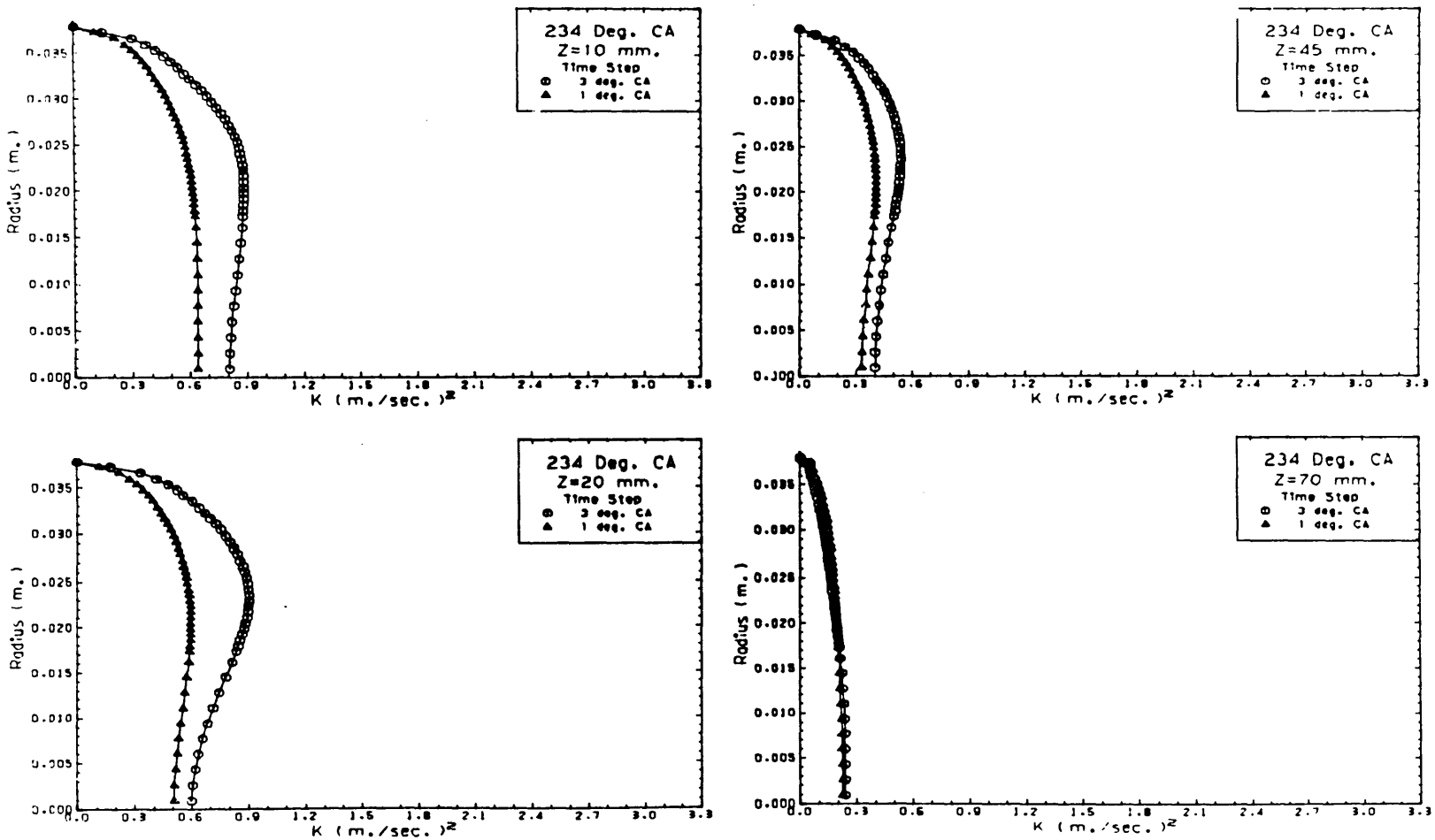


Figure 5.8(b): The effect of time-step on the turbulence energy distributions at different axial locations, at θ = 234° CA

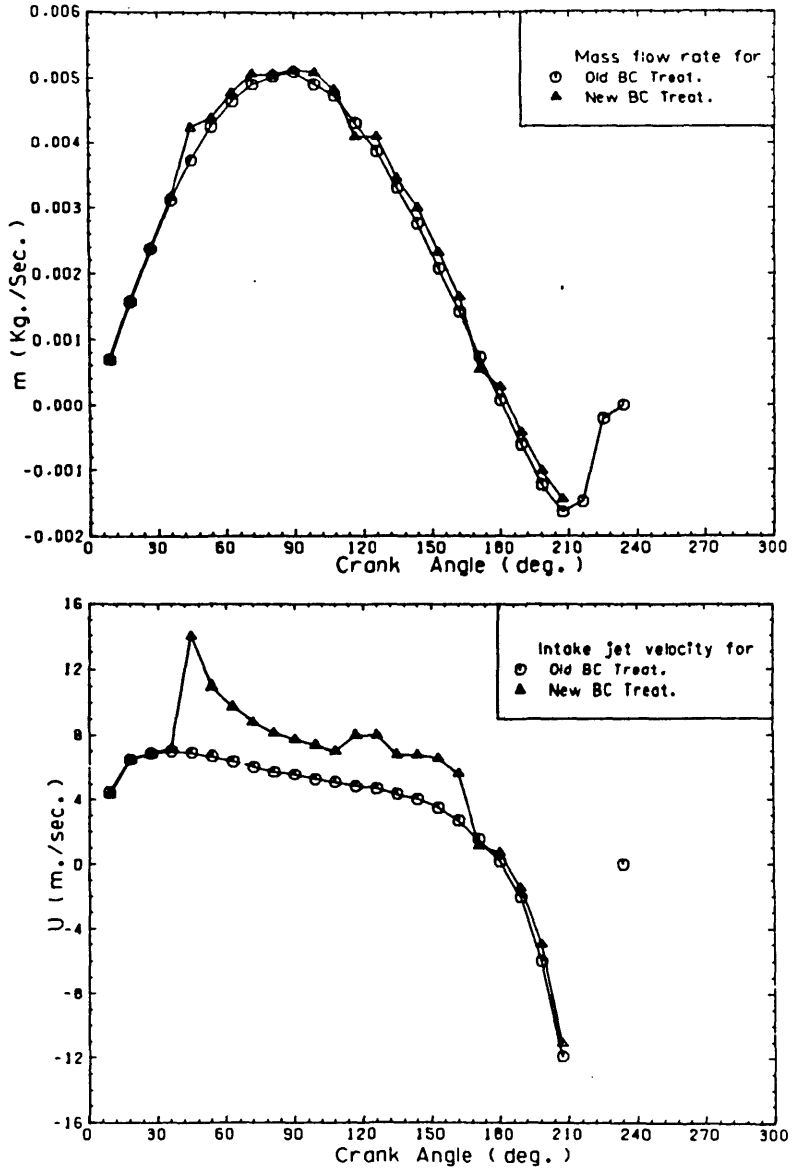


Figure 5.9: The mass flow rates and inlet velocities for the two inlet flow boundary condition treatments; test Case I

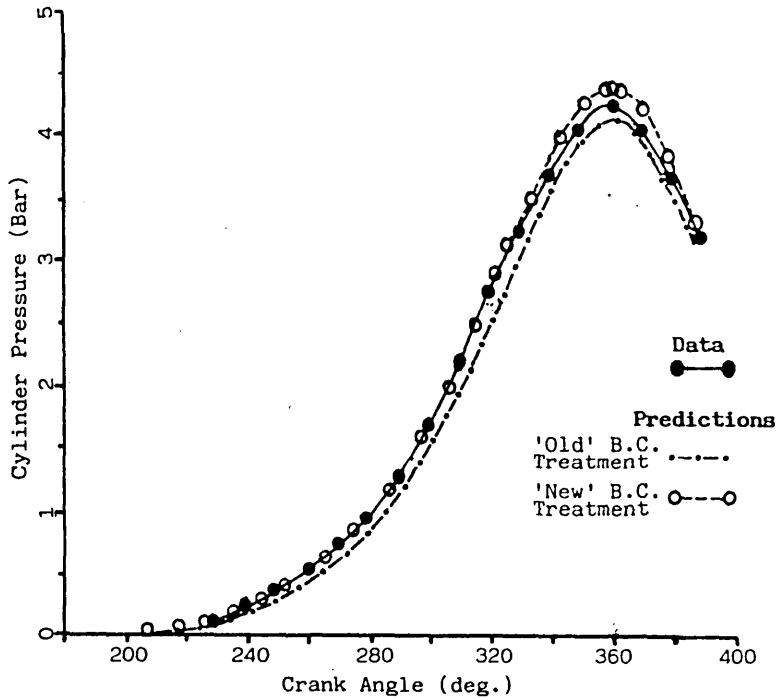


Figure 5.10: The measured and predicted mean cylinder pressure variations for the two inlet flow boundary condition treatments; test Case I

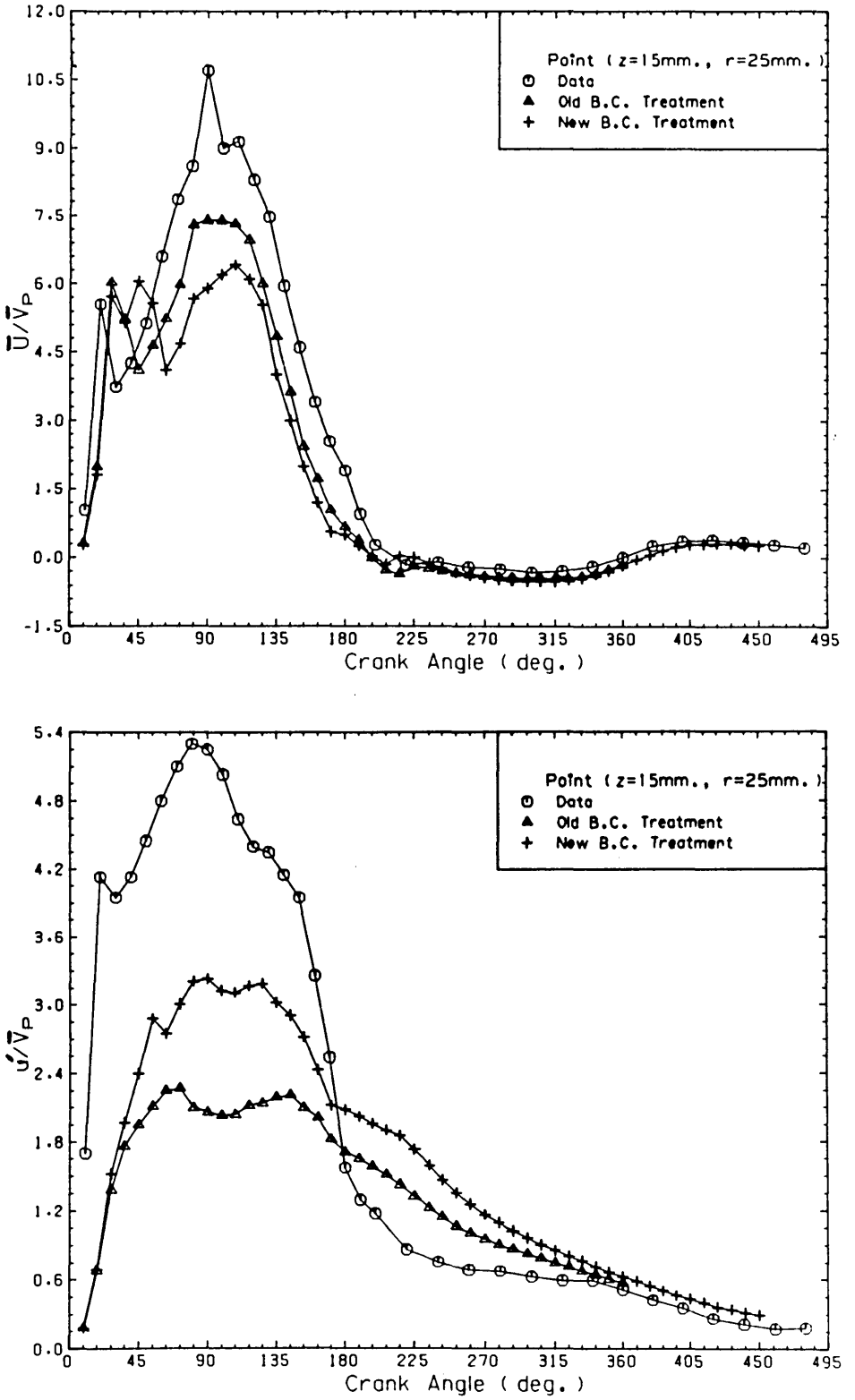


Figure 5.11: The measured and predicted mean axial velocity and turbulence intensity at the monitoring location Z = 15 mm, r = 25 mm for the two inlet flow boundary condition treatments; test Case I

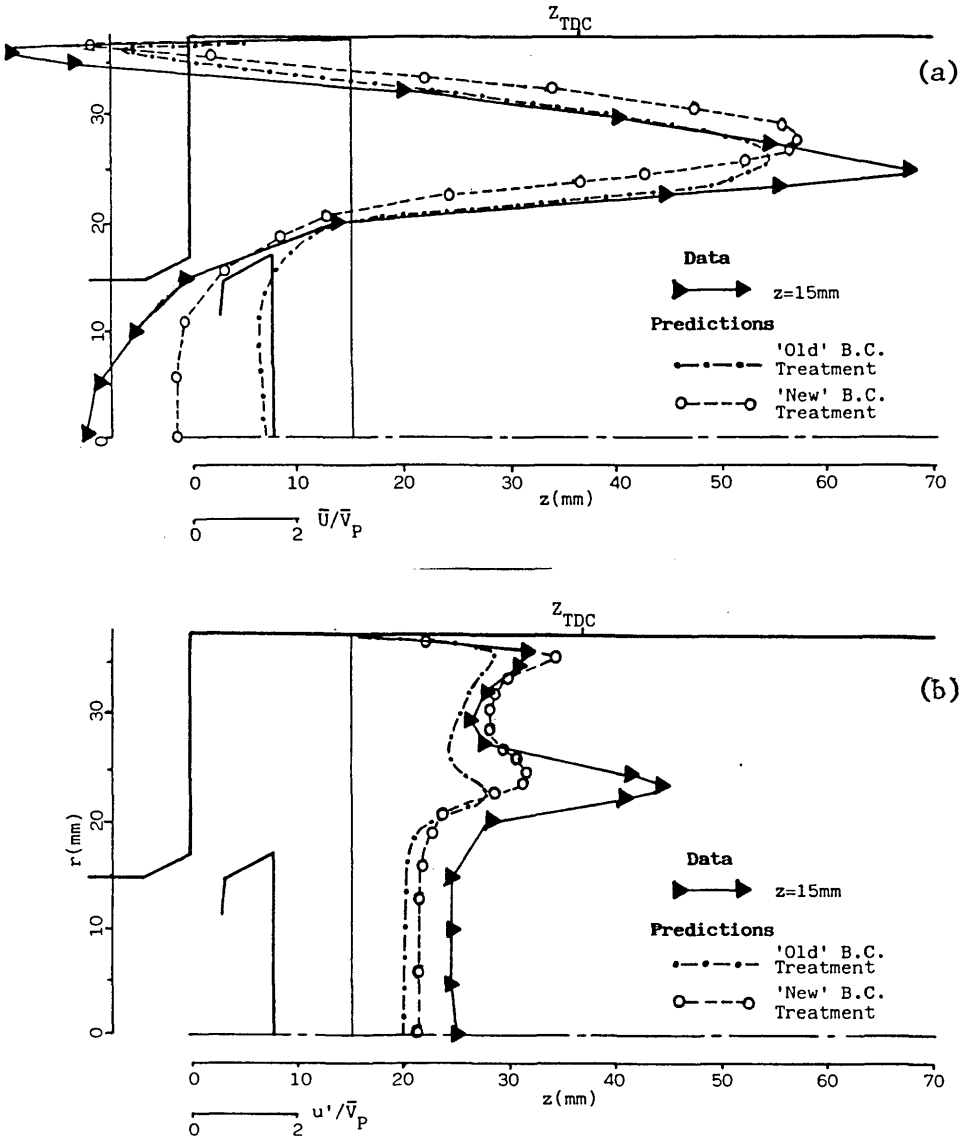


Figure 5.12: The measured and predicted radial profiles of $\bar{U}/\bar{V}_p$ and $u'/\bar{V}_p$ for the two BC treatments at θ = 90° CA; test Case I

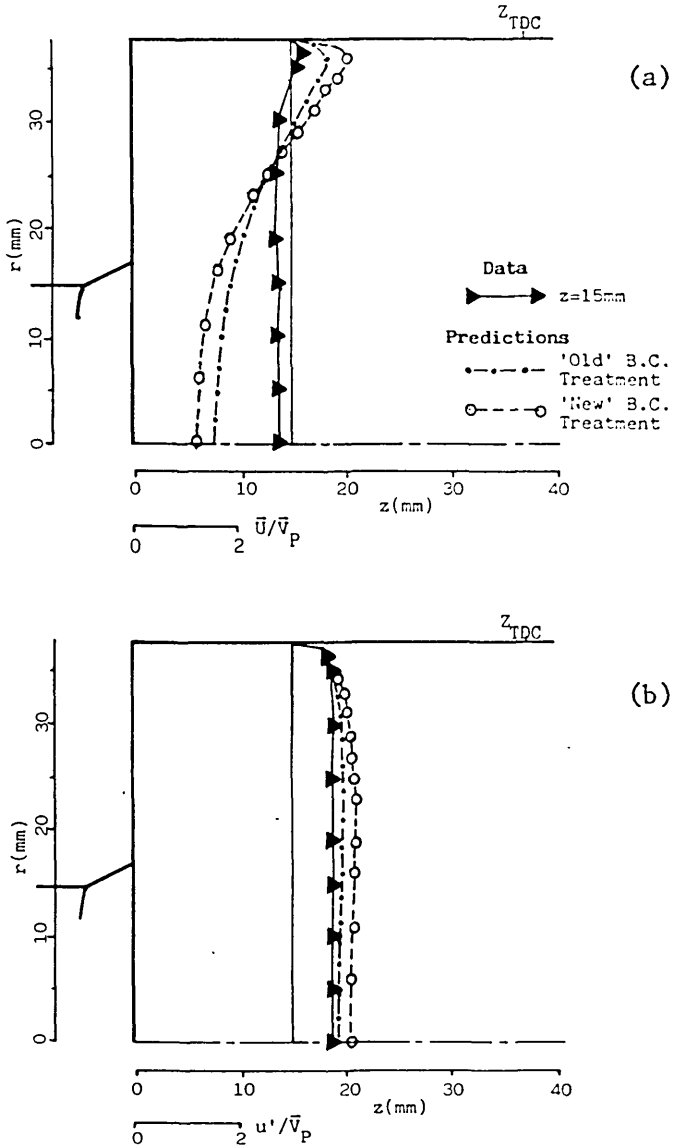


Figure 5.13: The measured and predicted radial profiles of $\bar{U}/\bar{V}_p$ and $u'/\bar{V}_p$ for the two BC treatments at θ = 270° CA; test Case I

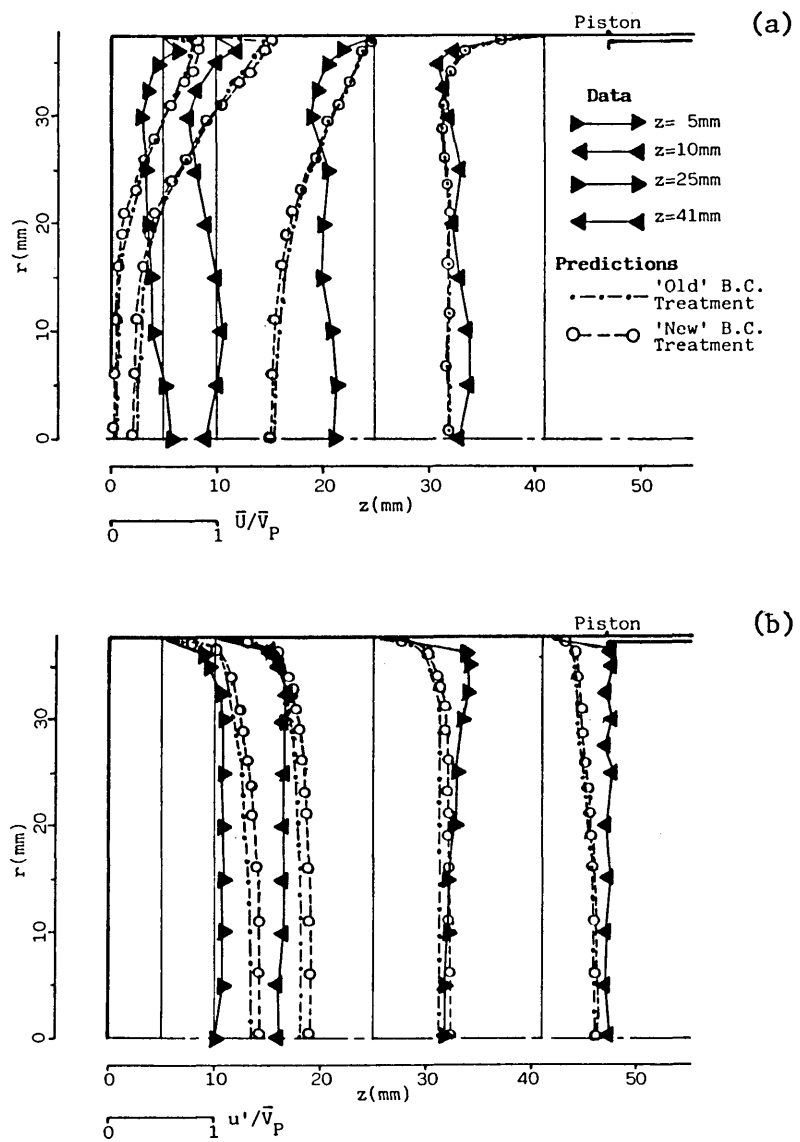


Figure 5.14: The measured and predicted radial profiles of $\overline{U}/\overline{V}_p$ and $u'/\overline{V}_p$ for the two BC treatments at θ = 324° CA; test Case I

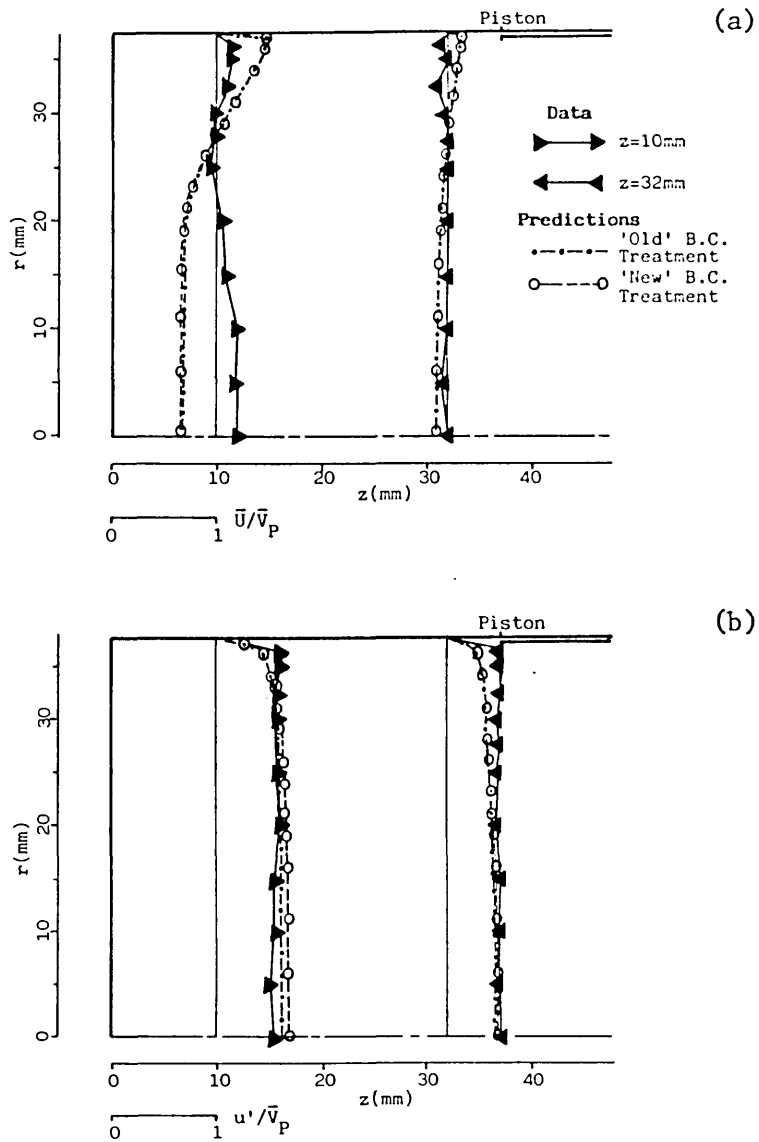


Figure 5.15: The measured and predicted radial profiles of $\overline{U}/\overline{V}_p$ and $u'/\overline{V}_p$ for the two BC treatments at θ = 360° CA; test Case I

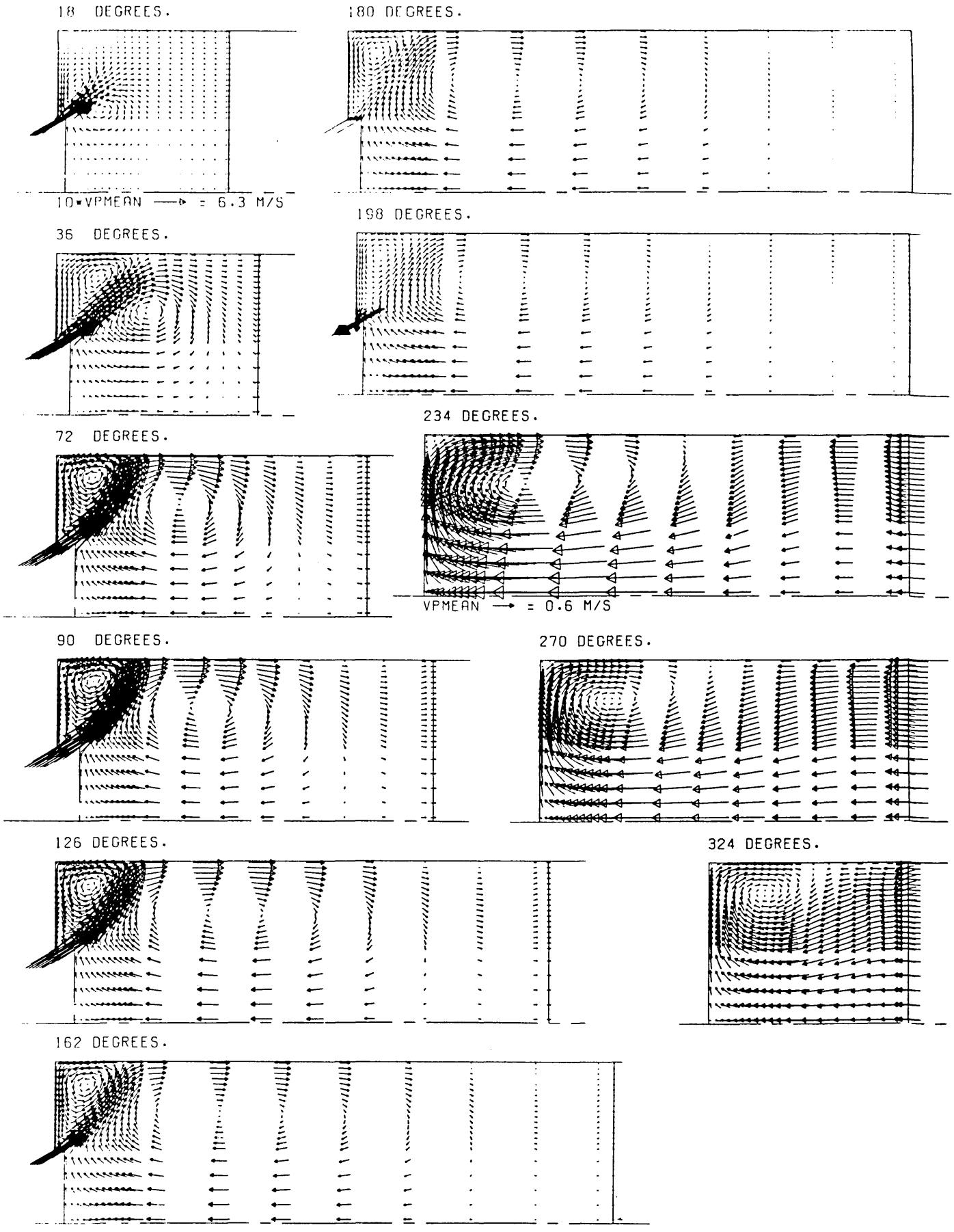


Figure 5.16(a): Predictions of the velocity field for the test Case I

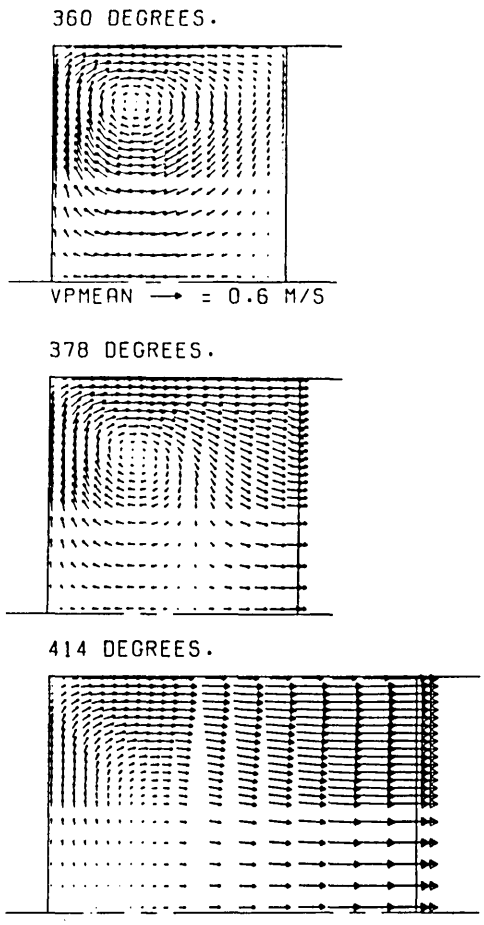


Figure 5.16(a): Continued

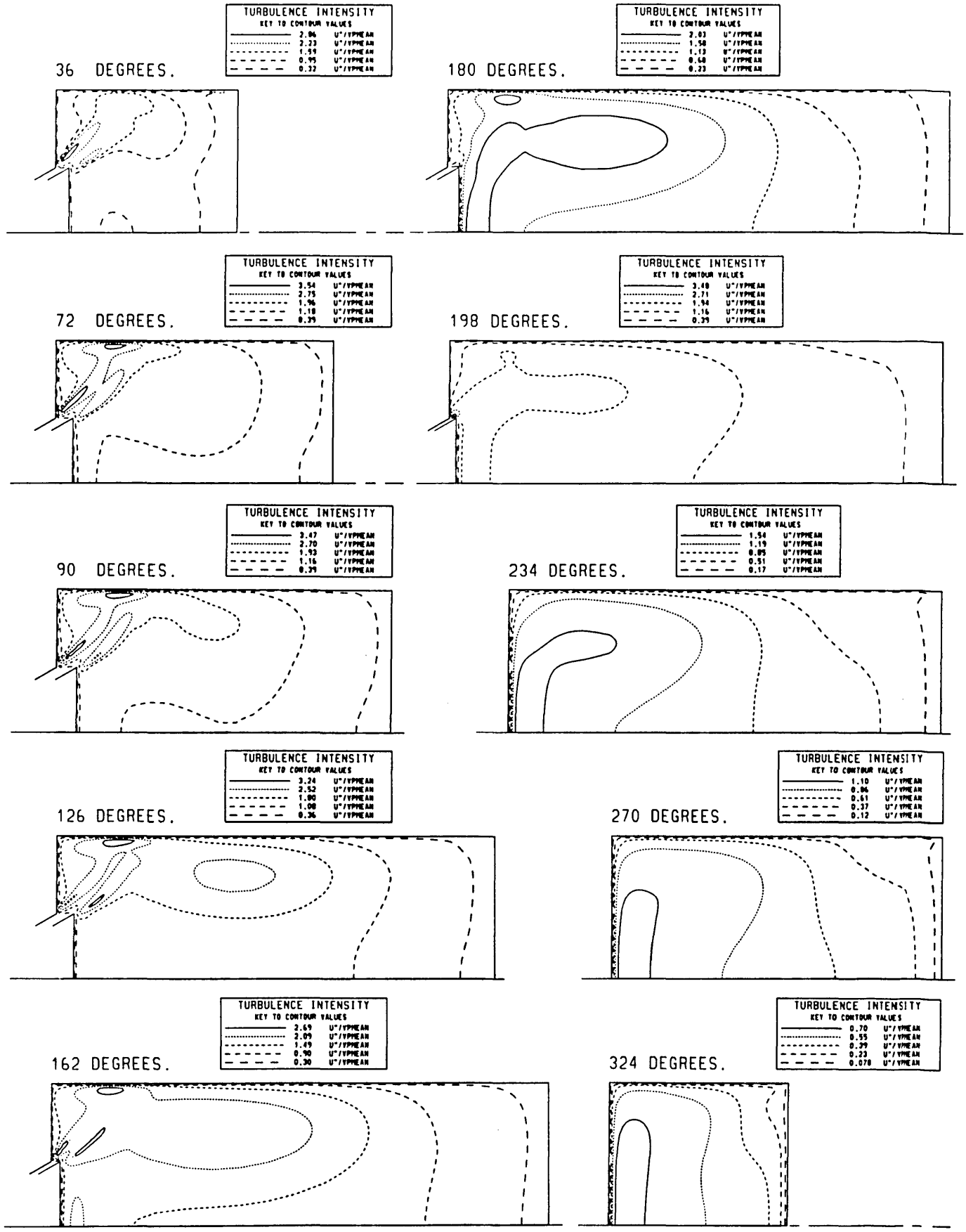


Figure 5.16(b): Predictions of the turbulence intensity distribution for the test Case I

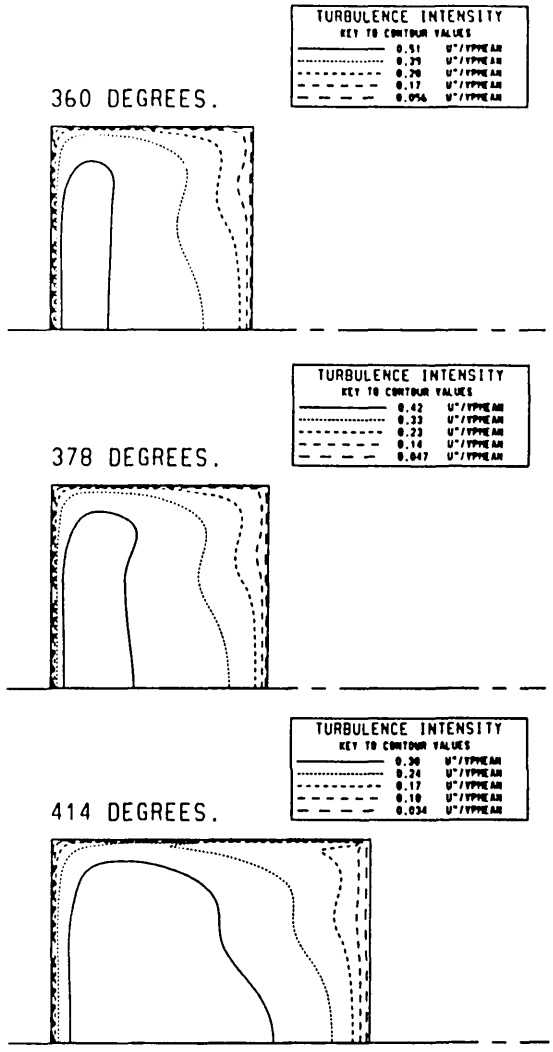


Figure 5.16(b): Continued

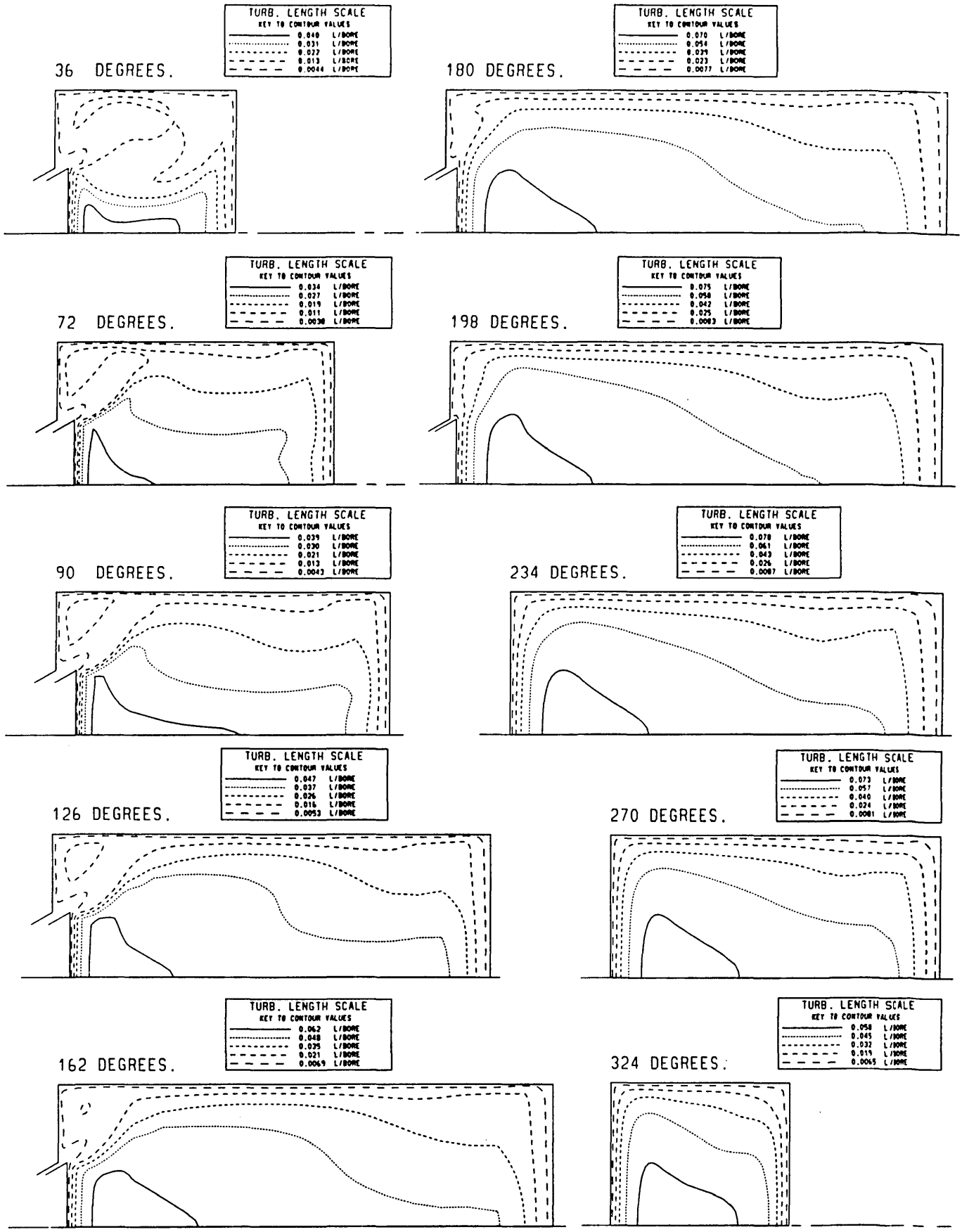


Figure 5.16(c): Predictions of the length scale distribution for the test Case I

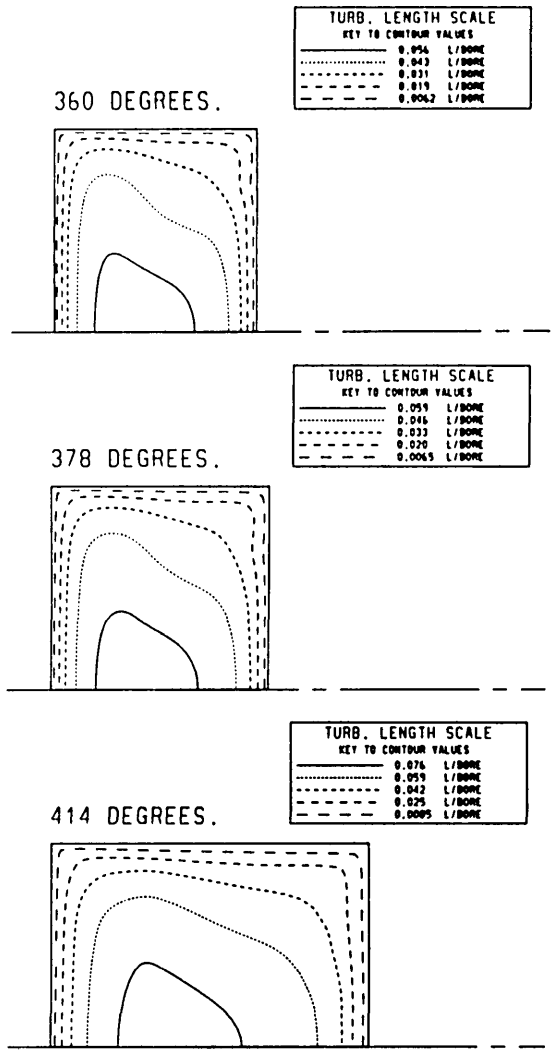


Figure 5.16(c): Continued

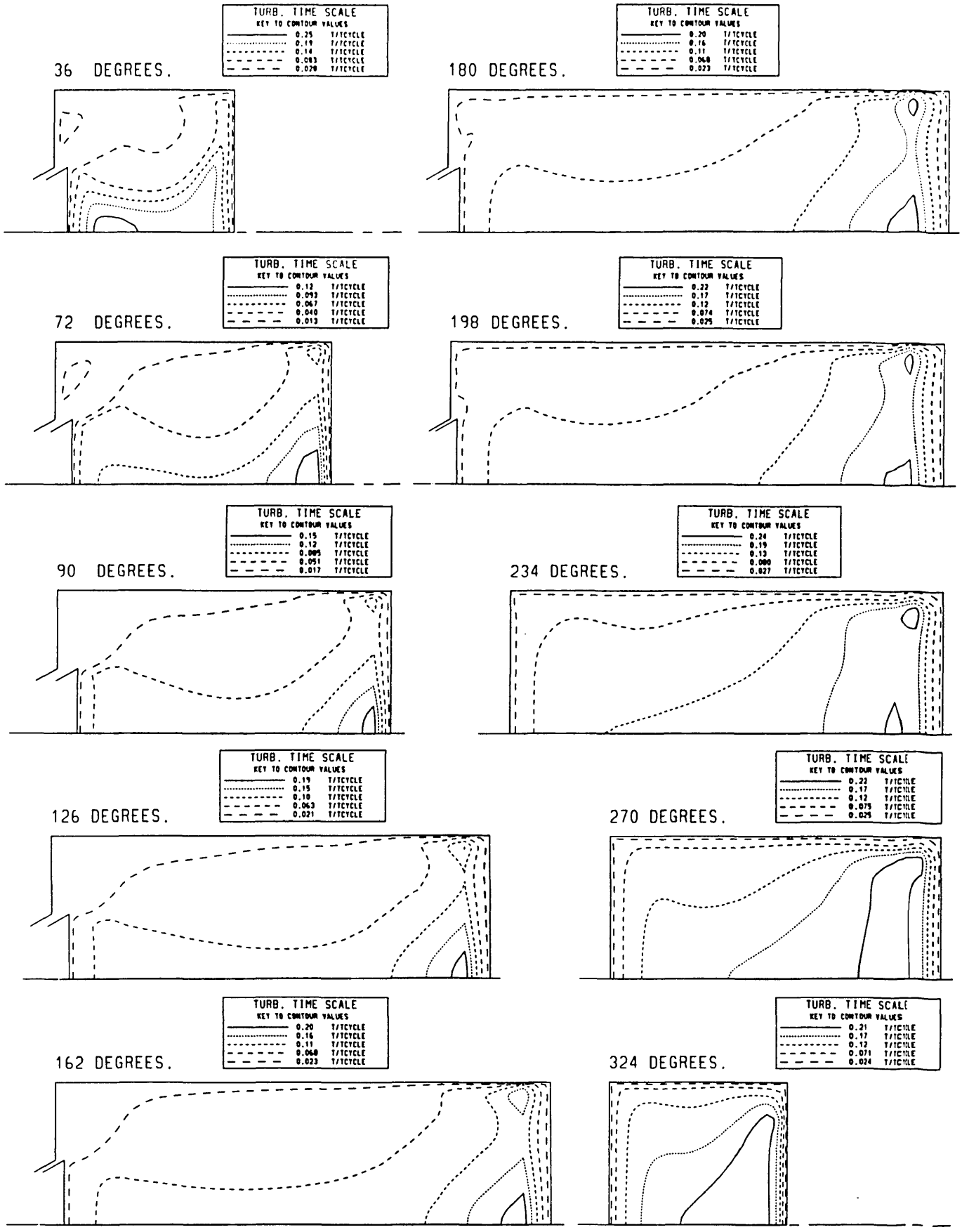


Figure 5.16(d): Predictions of the dissipation time scale distribution for the test Case I

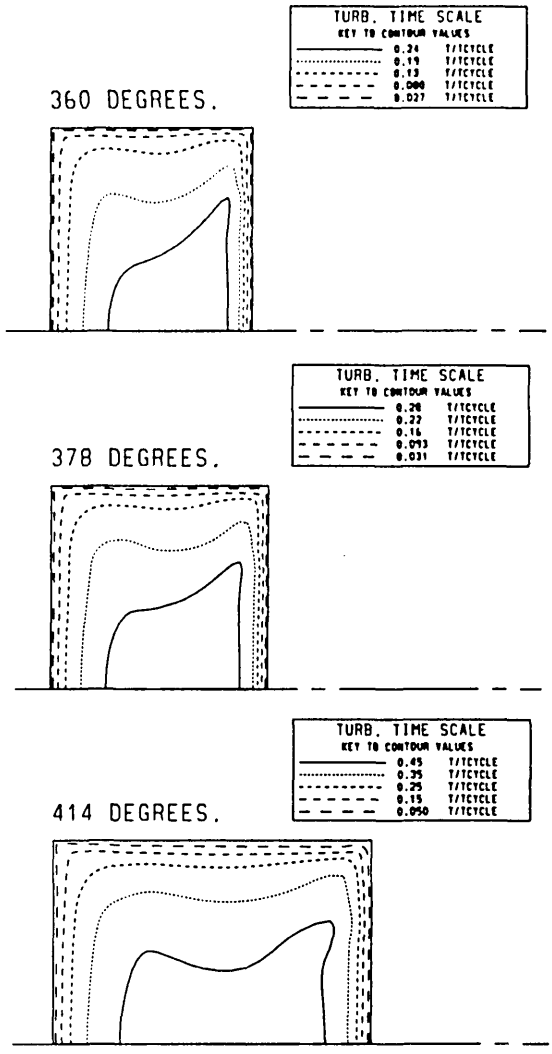


Figure 5.16(d): Continued

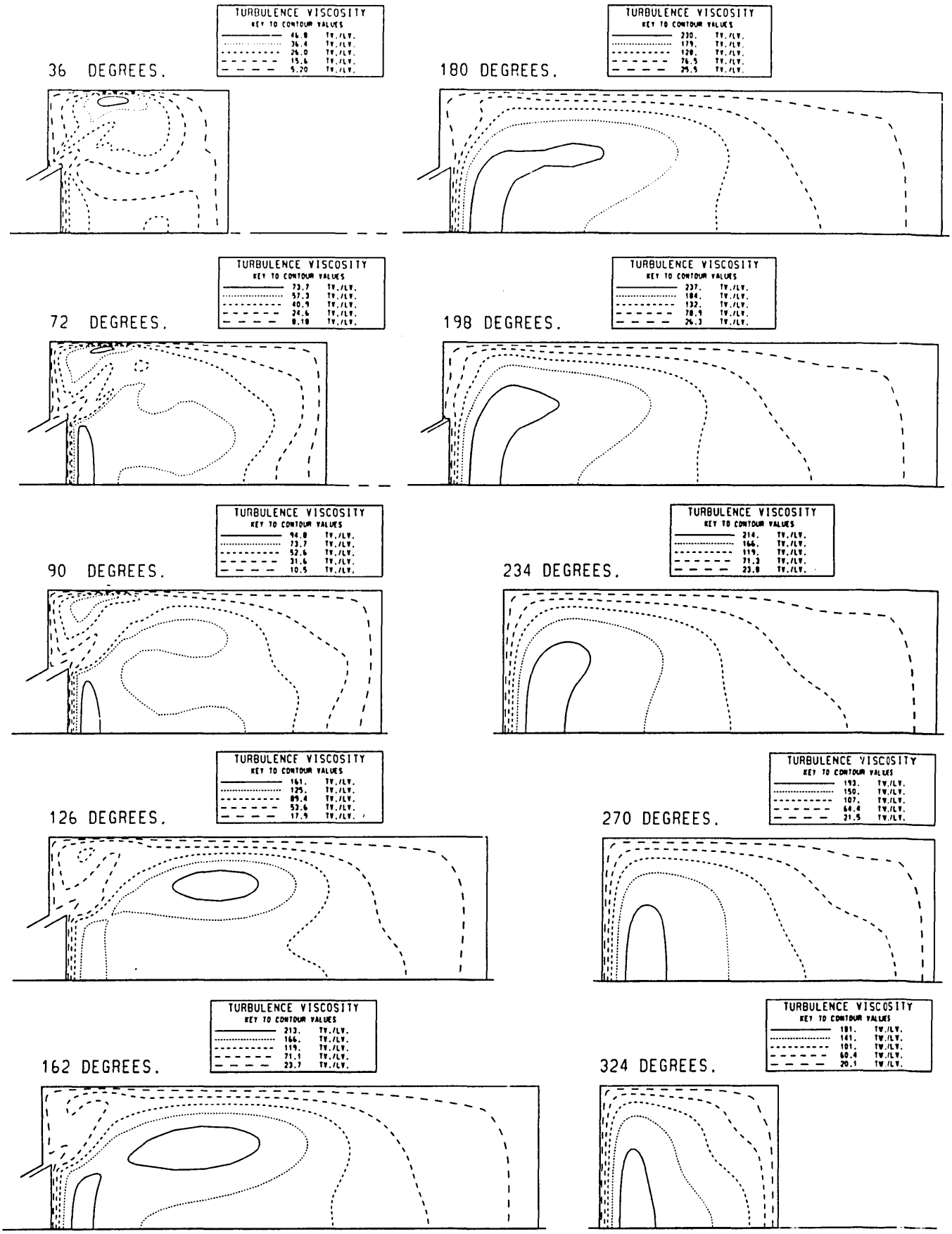


Figure 5.16(e): Predictions of the turbulent viscosity distribution for the test Case I

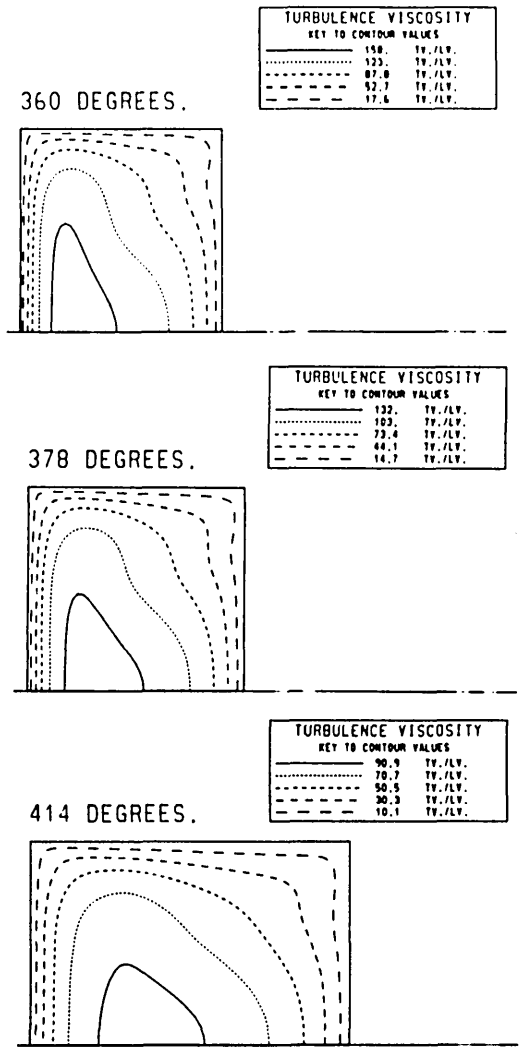


Figure 5.16(e): Continued

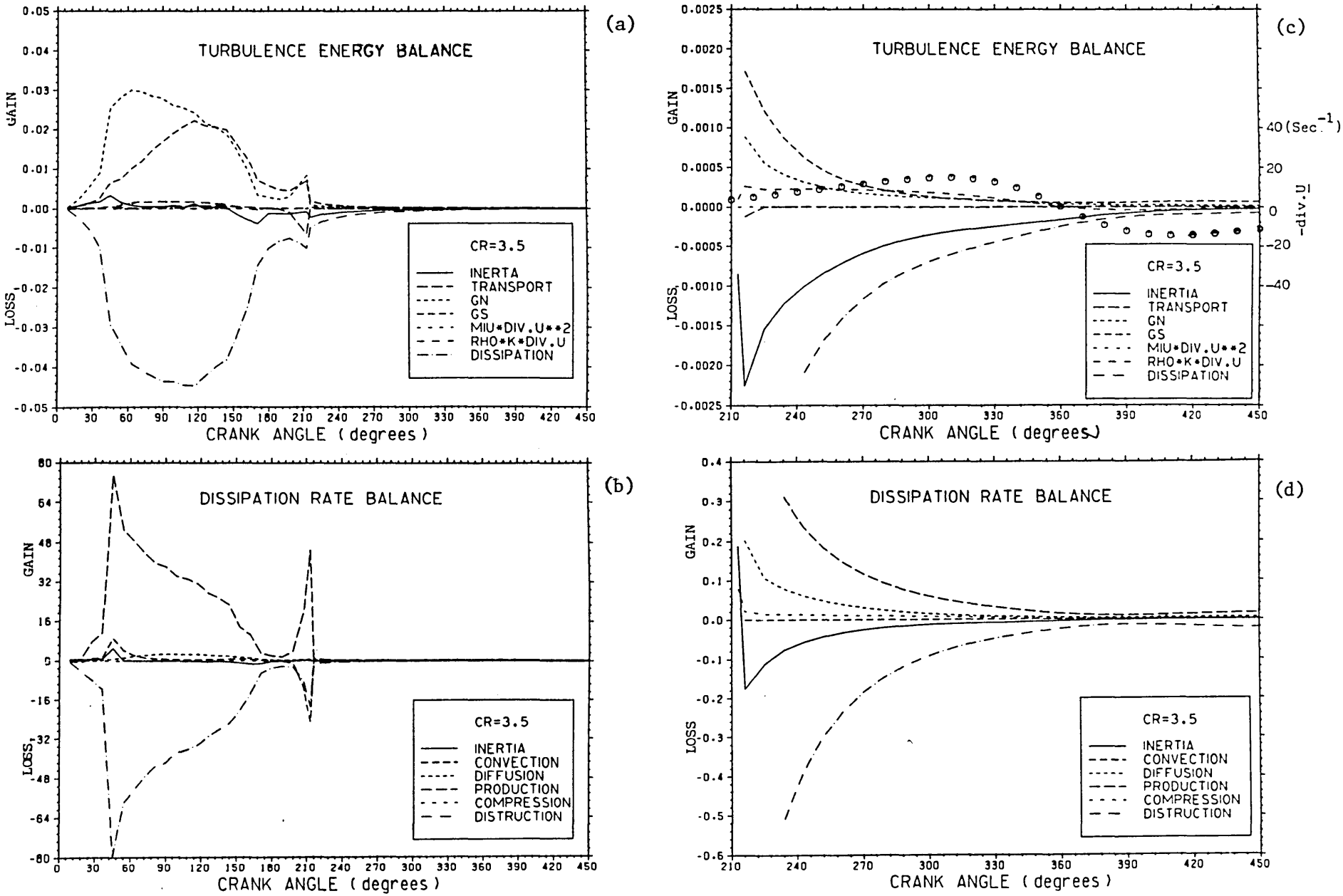
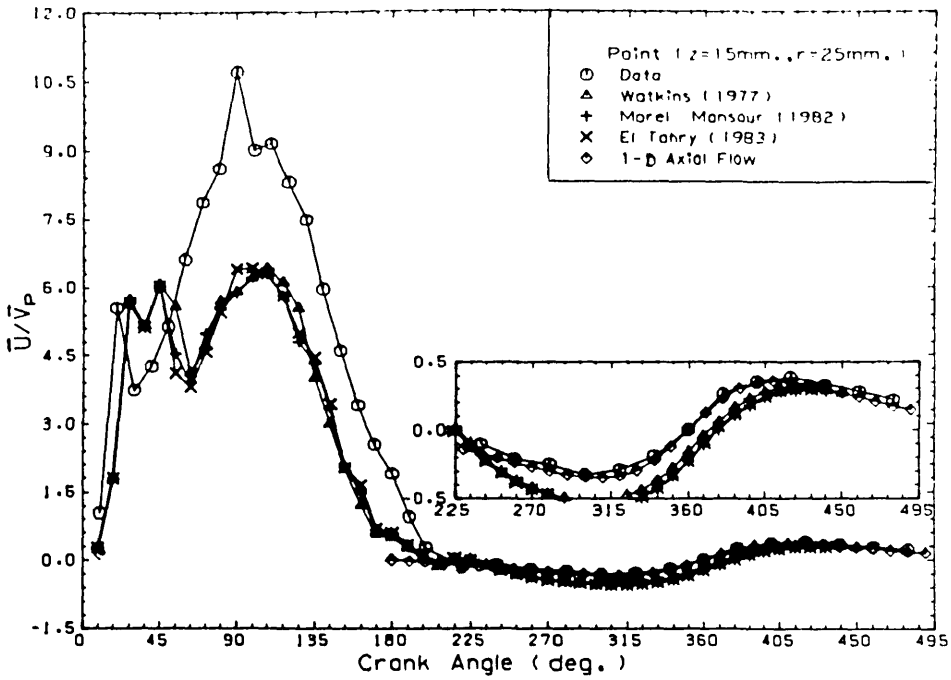
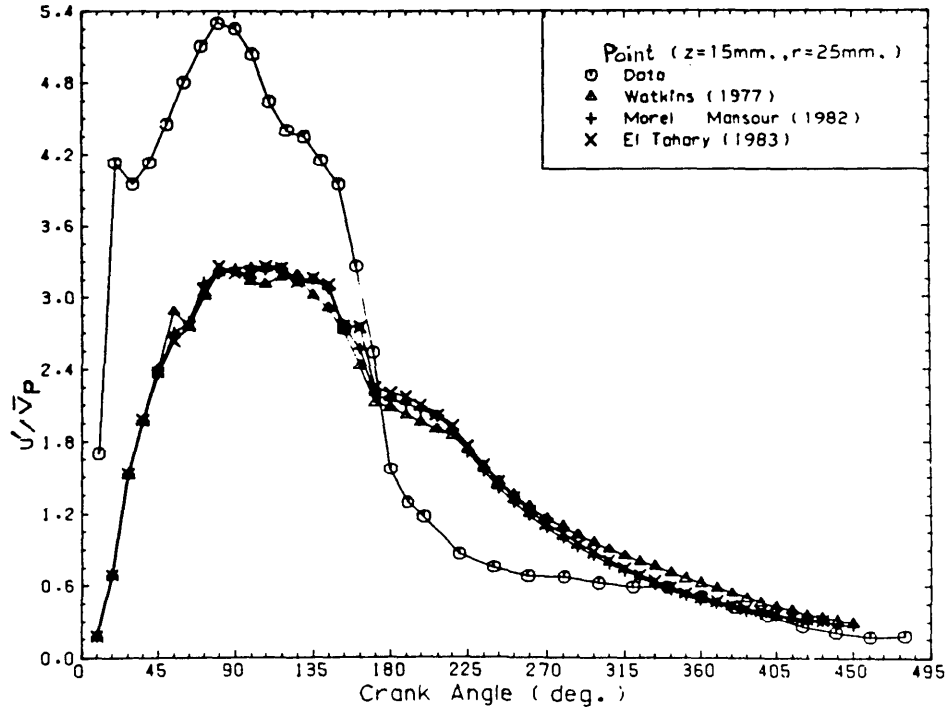


Figure 5.17: The volume-integral balances of the k- and ε-transport equations for the test Case I



(a)



(b)

Figure 5.18: The measured and predicted mean axial velocity and turbulence intensity at the monitoring location Z = 15 mm, r = 25 mm; test Case I

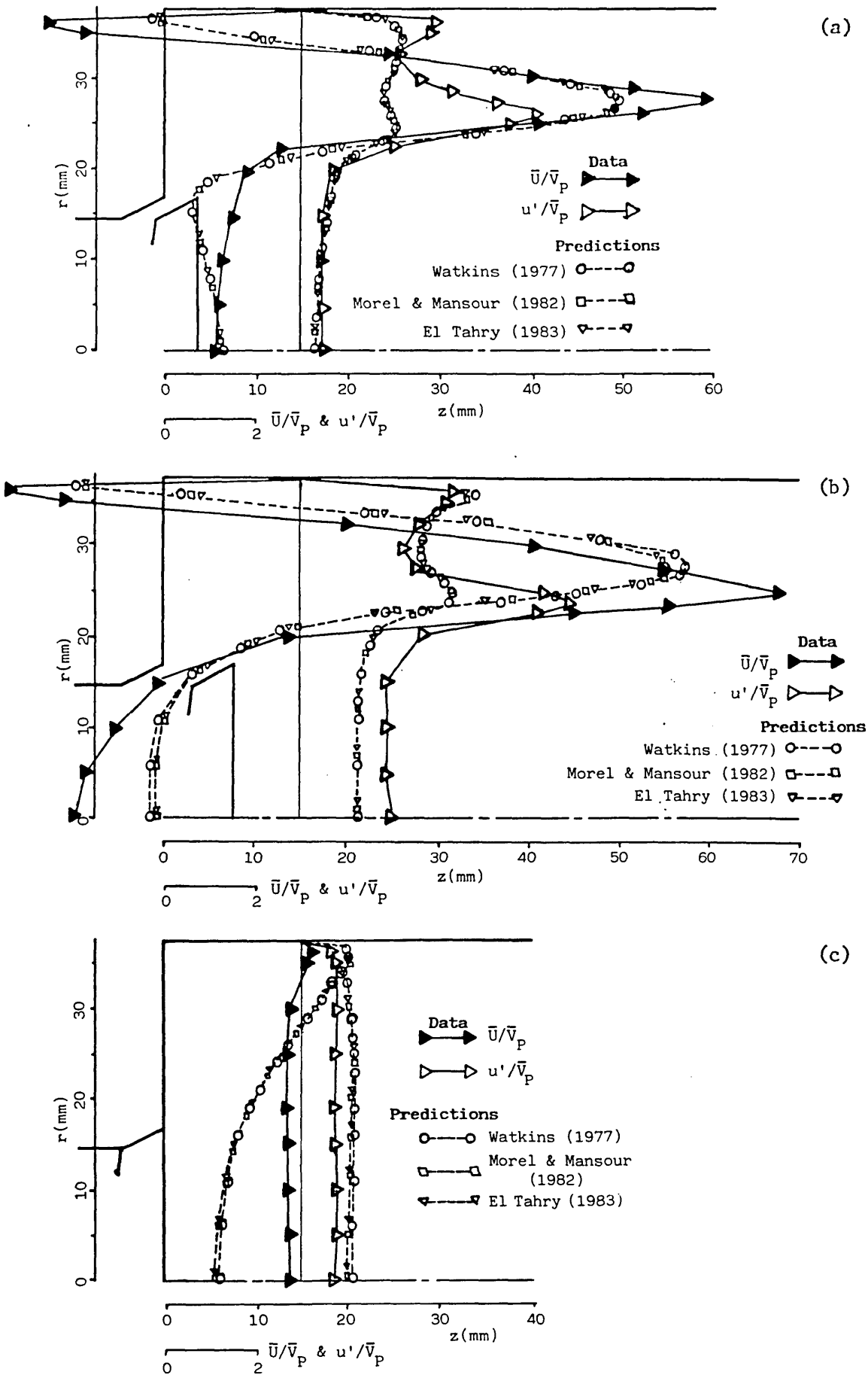


Figure 5.19: The measured and predicted profiles of $\bar{U}/\bar{V}_p$ and $u'/\bar{V}_p$ for the axial location Z = 15 mm at (a) θ = 36° CA, (b) θ = 90° CA and (c) θ = 270° CA; test Case I

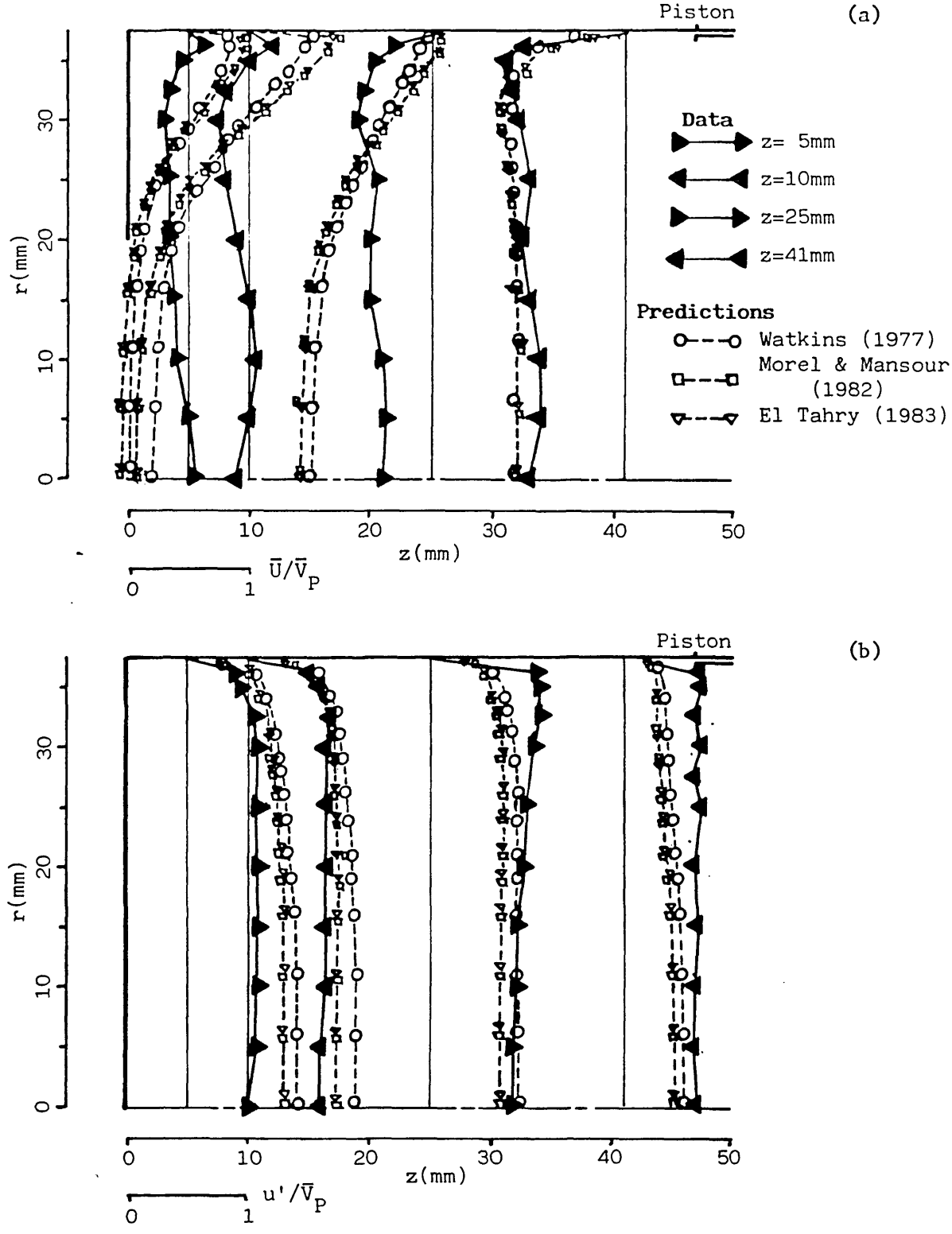


Figure 5.20: The measured and predicted radial profiles of $\bar{U}/\bar{V}_p$ and $u'/\bar{V}_p$ at θ = 324° CA; test Case I

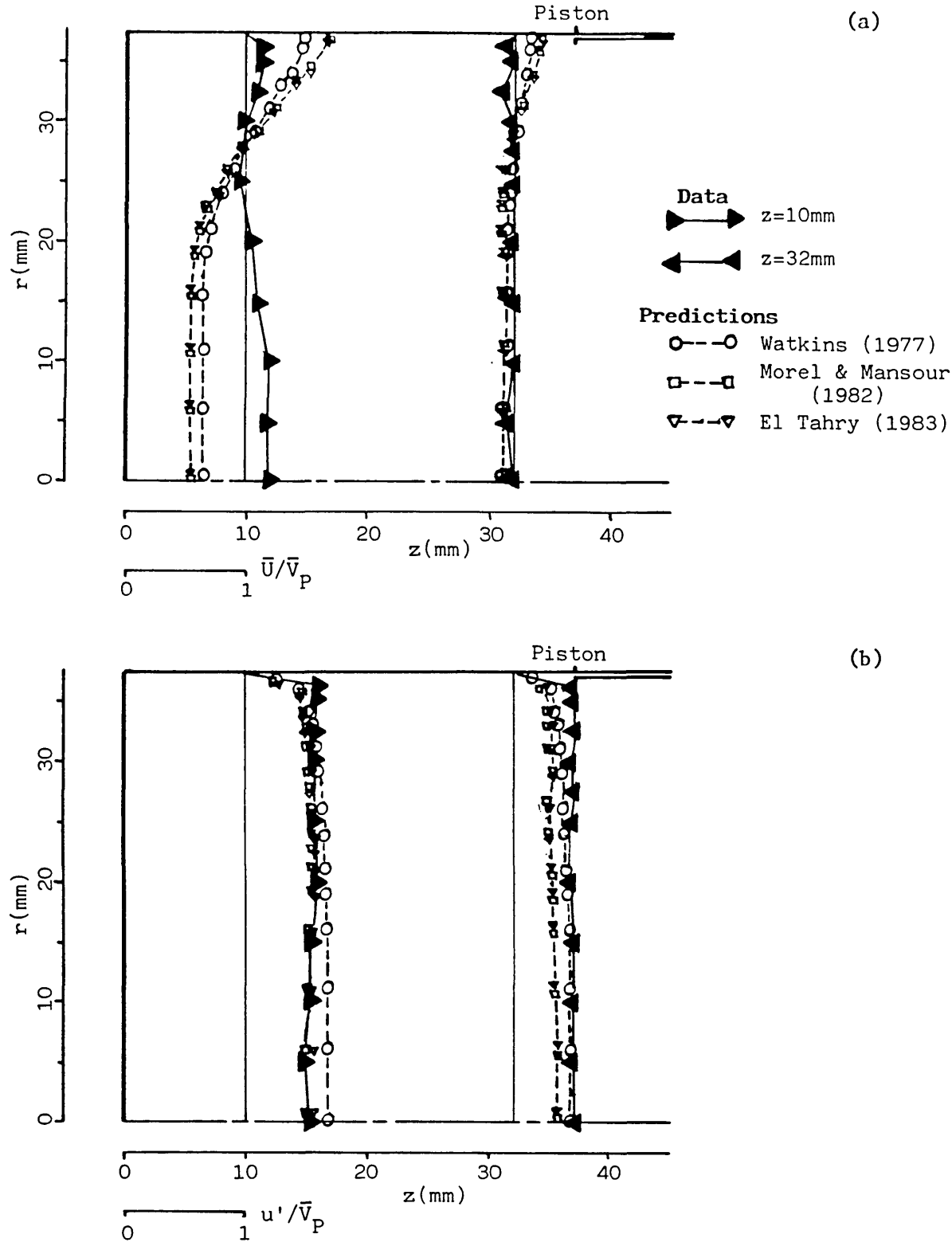


Figure 5.21: The measured and predicted radial profiles of $\bar{u}/\bar{v}_p$ and $u'/\bar{v}_p$ at θ = 360° CA; test Case I

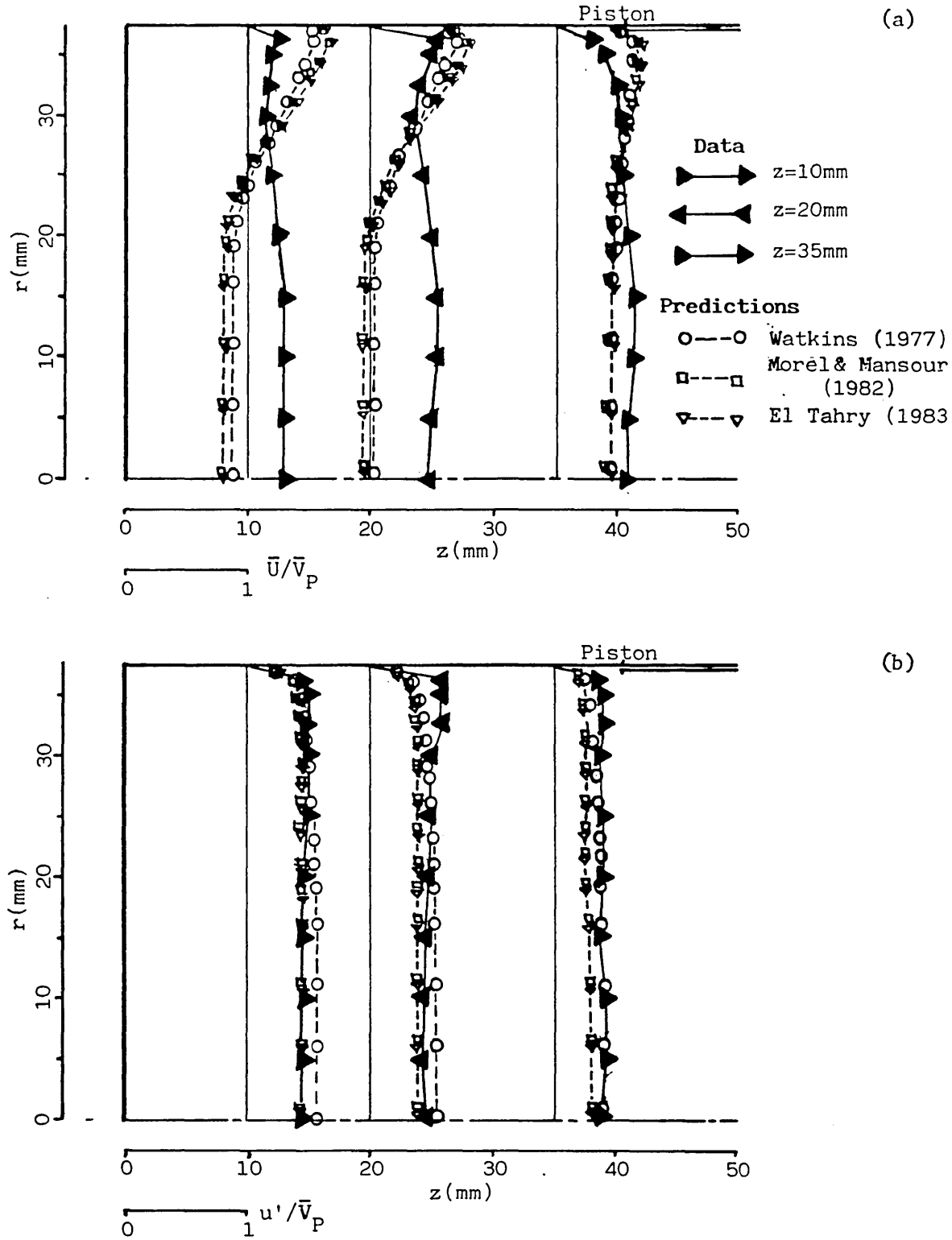


Figure 5.22: The measured and predicted radial profiles of $\overline{U}/\overline{V}_p$ and $u'/\overline{V}_p$ at θ = 380° CA; test Case I

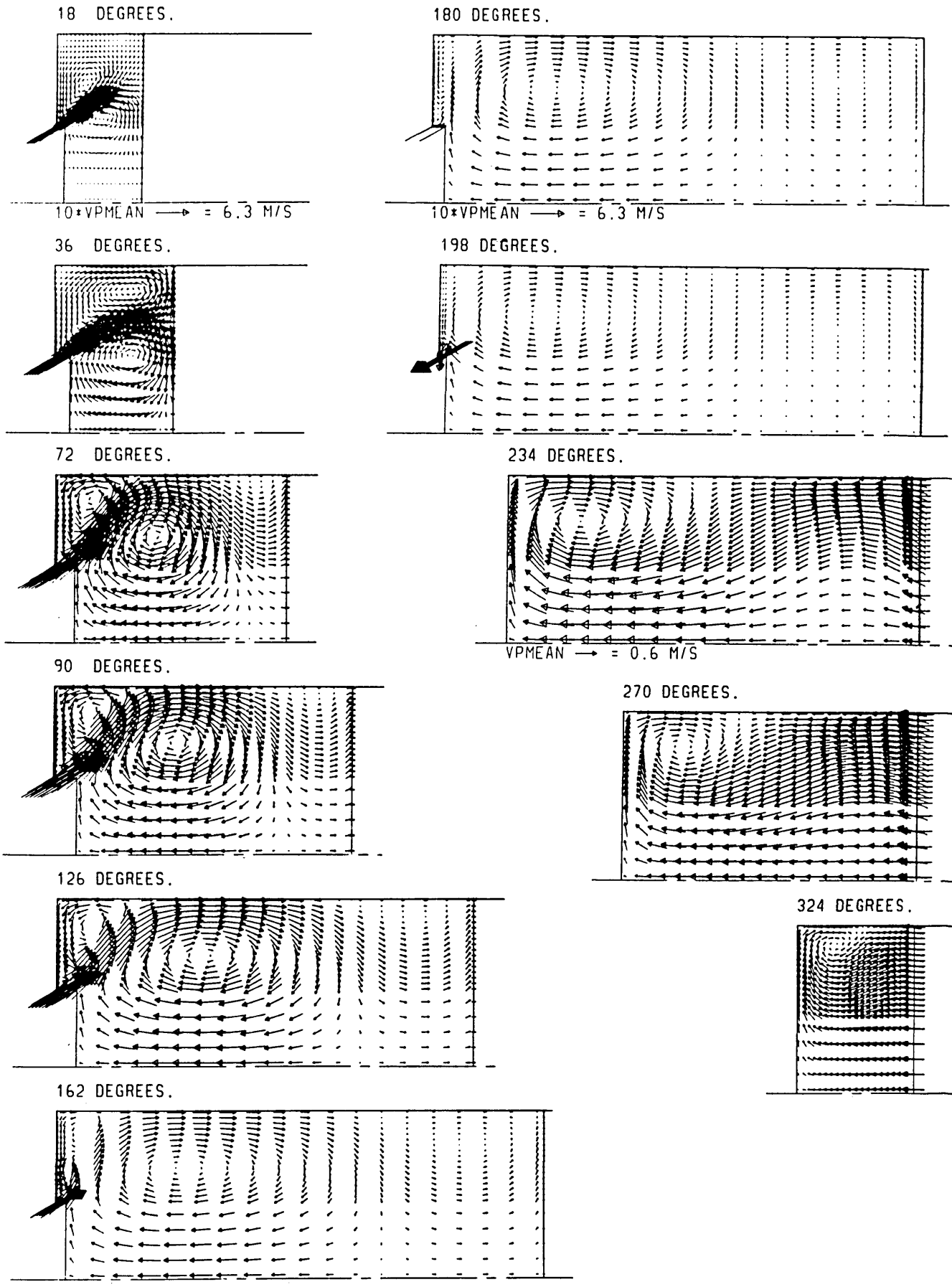


Figure 5.23(a): Predictions of the velocity field for the test Case II

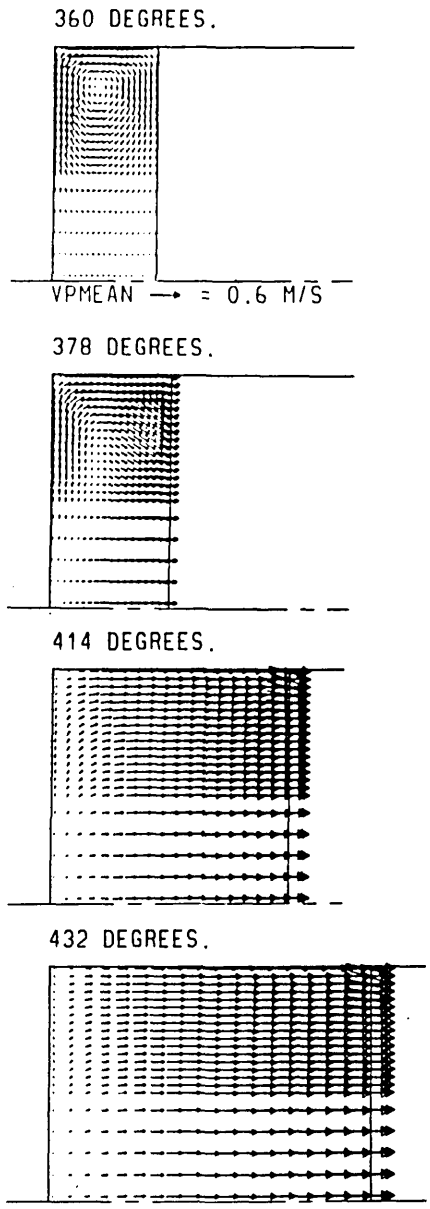


Figure 5.23(a): Continued

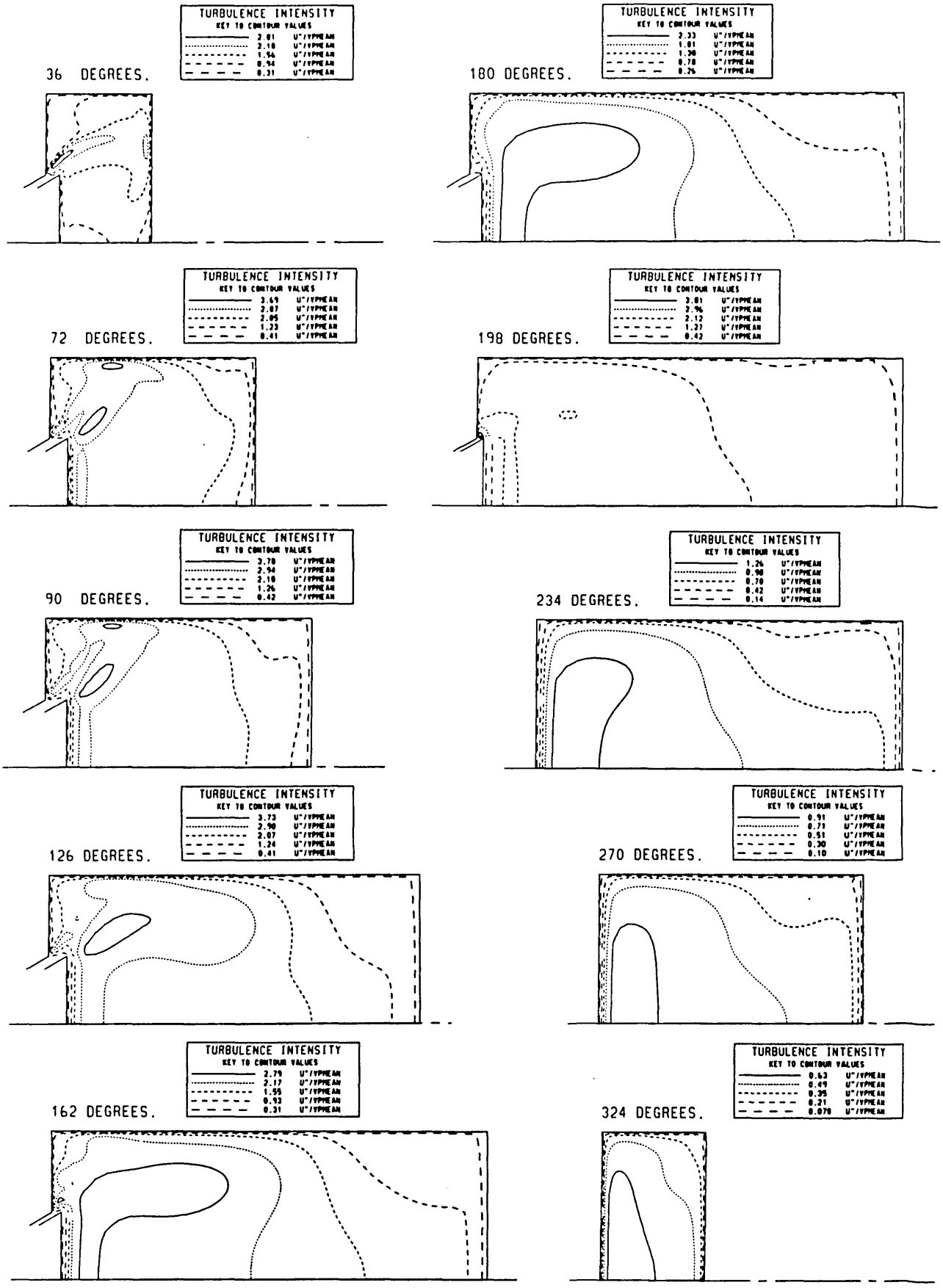


Figure 5.23(b): Predictions of the turbulence intensity distribution for the test Case II

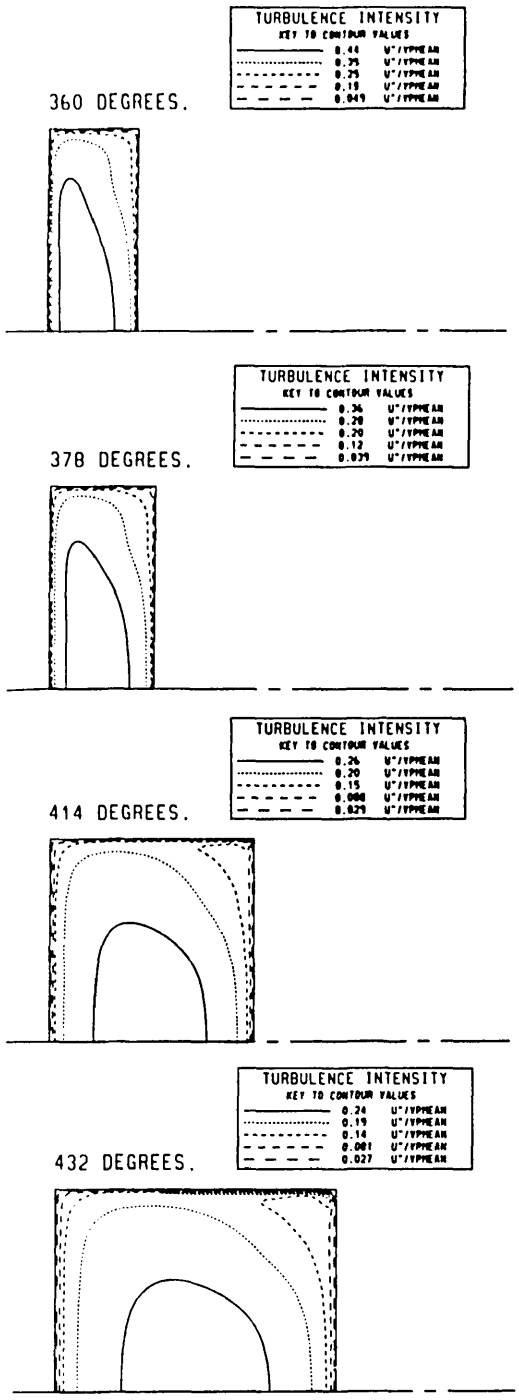


Figure 5.23(b): Continued

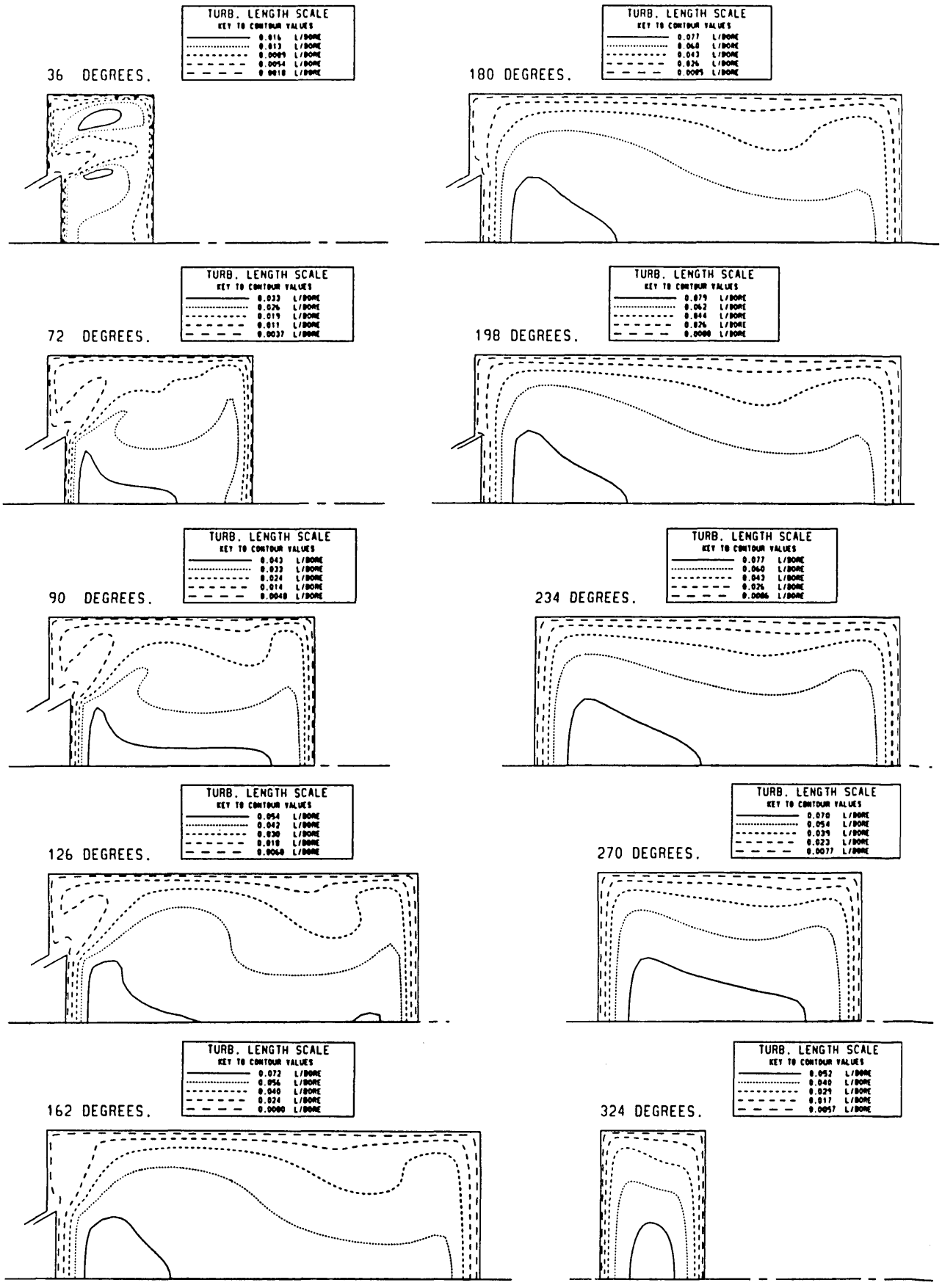


Figure 5.23(c): Predictions of the length scale distribution for the test Case II

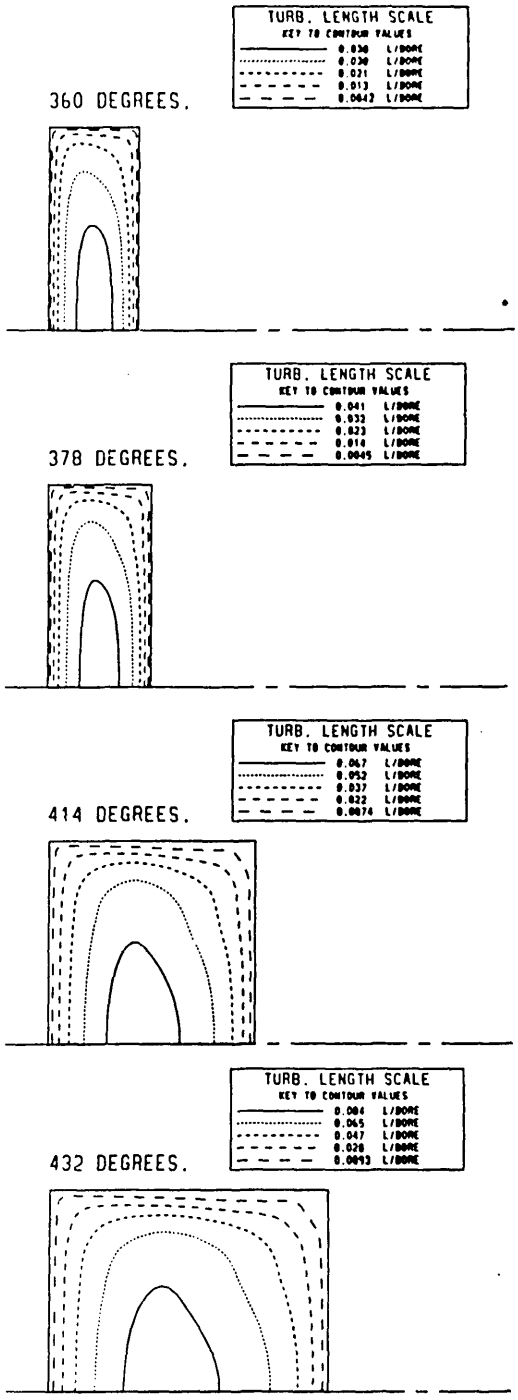


Figure 5.23(c): Continued

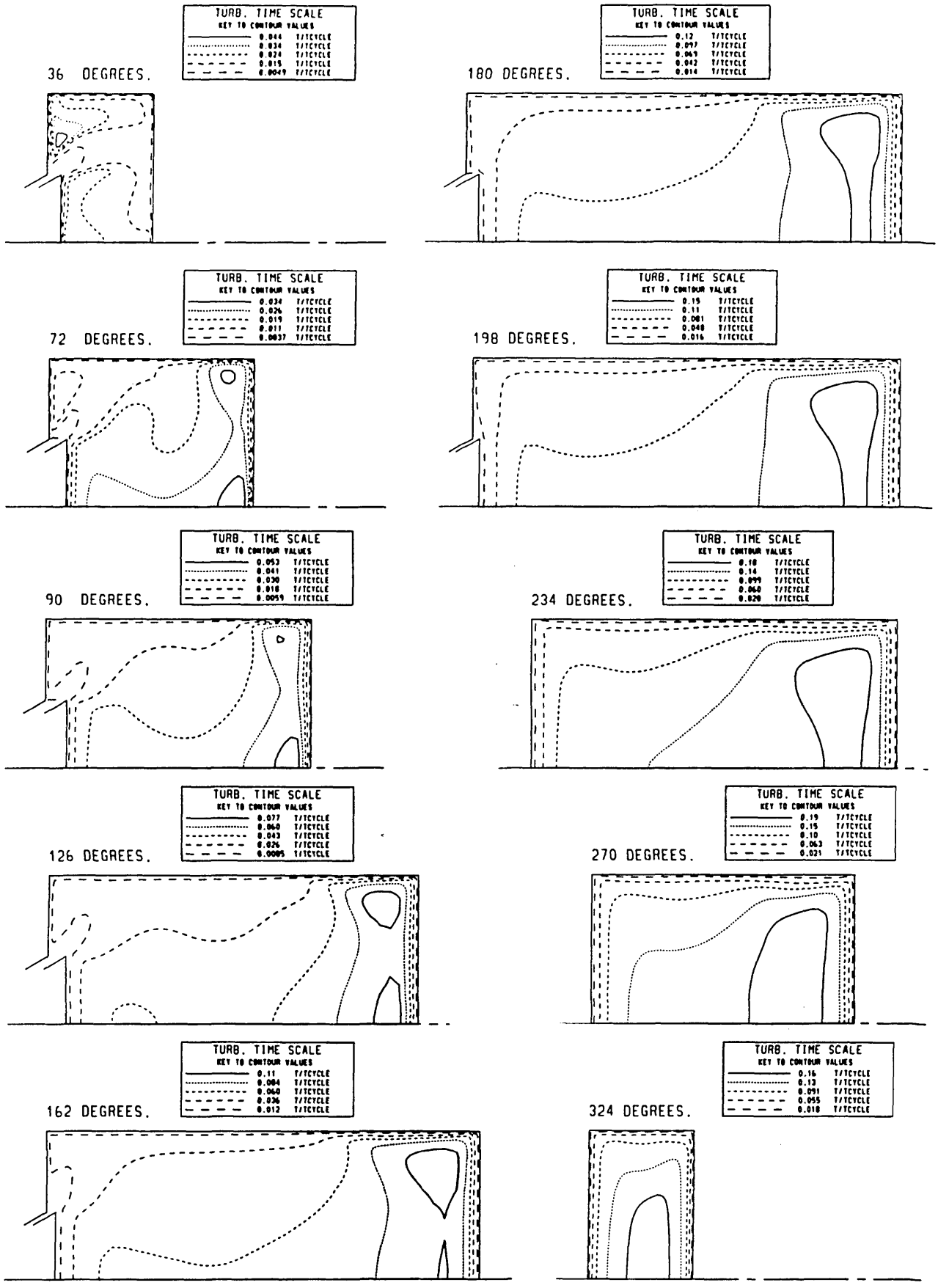


Figure 5.23(d): Predictions of the dissipation time-scale distribution for the test Case II

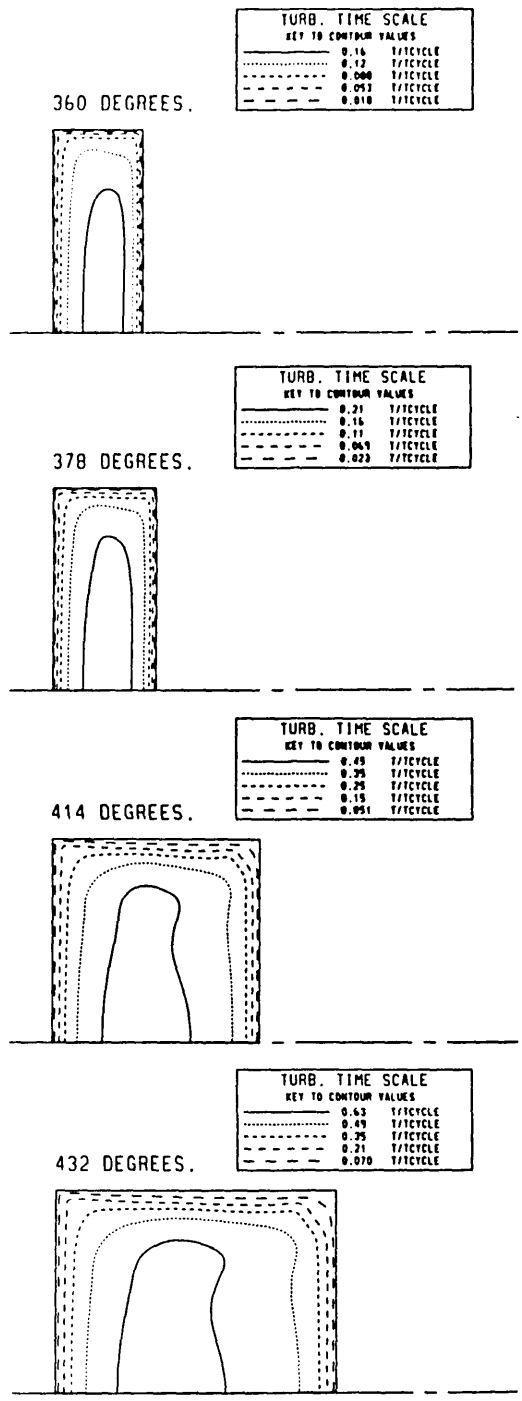


Figure 5.23(d): Continued

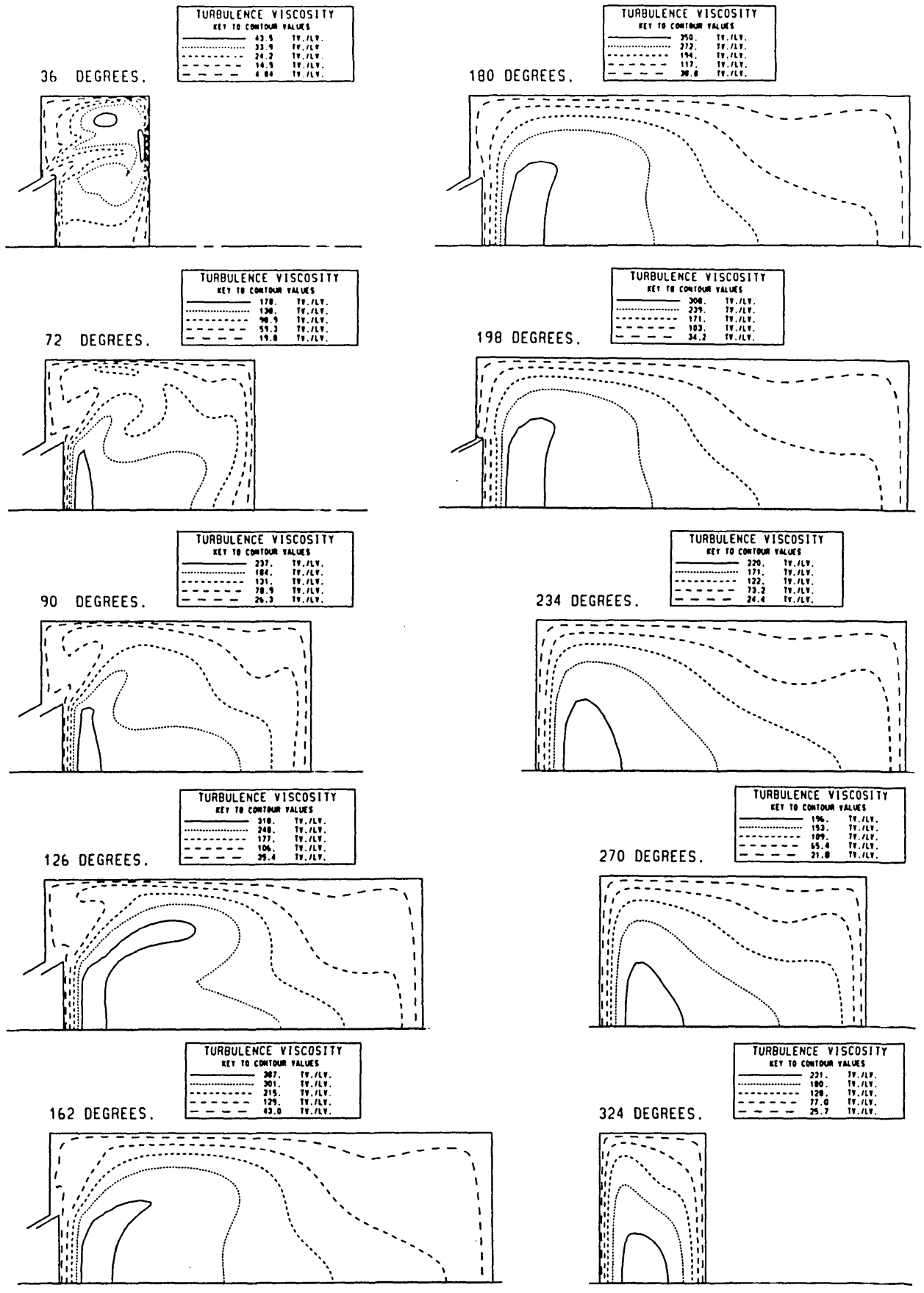


Figure 5.23(e): Predictions of the turbulent viscosity distribution for the test Case II

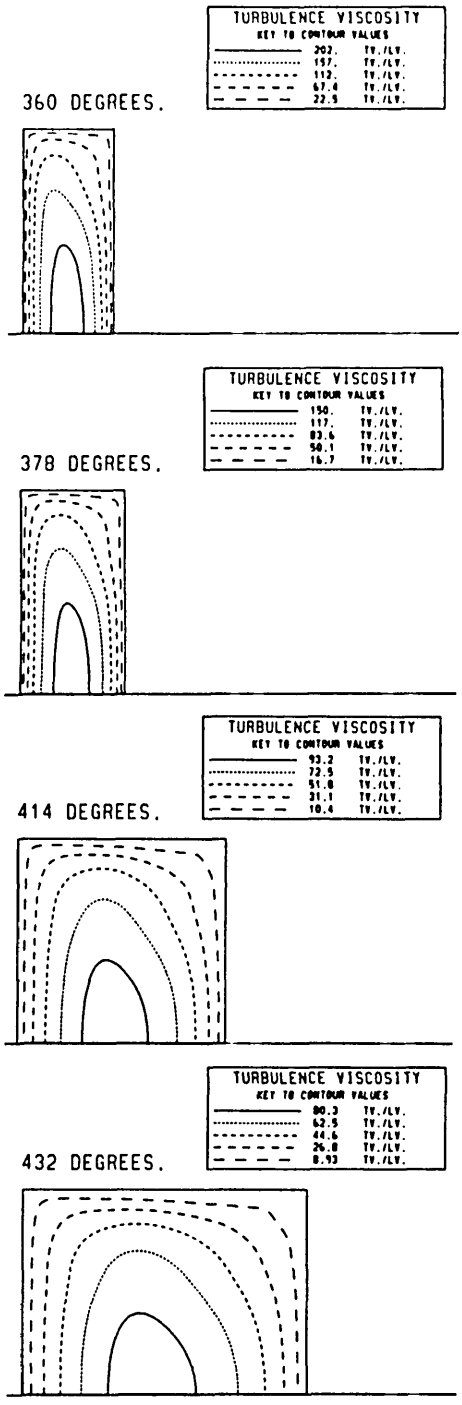


Figure 5.23(e): Continued

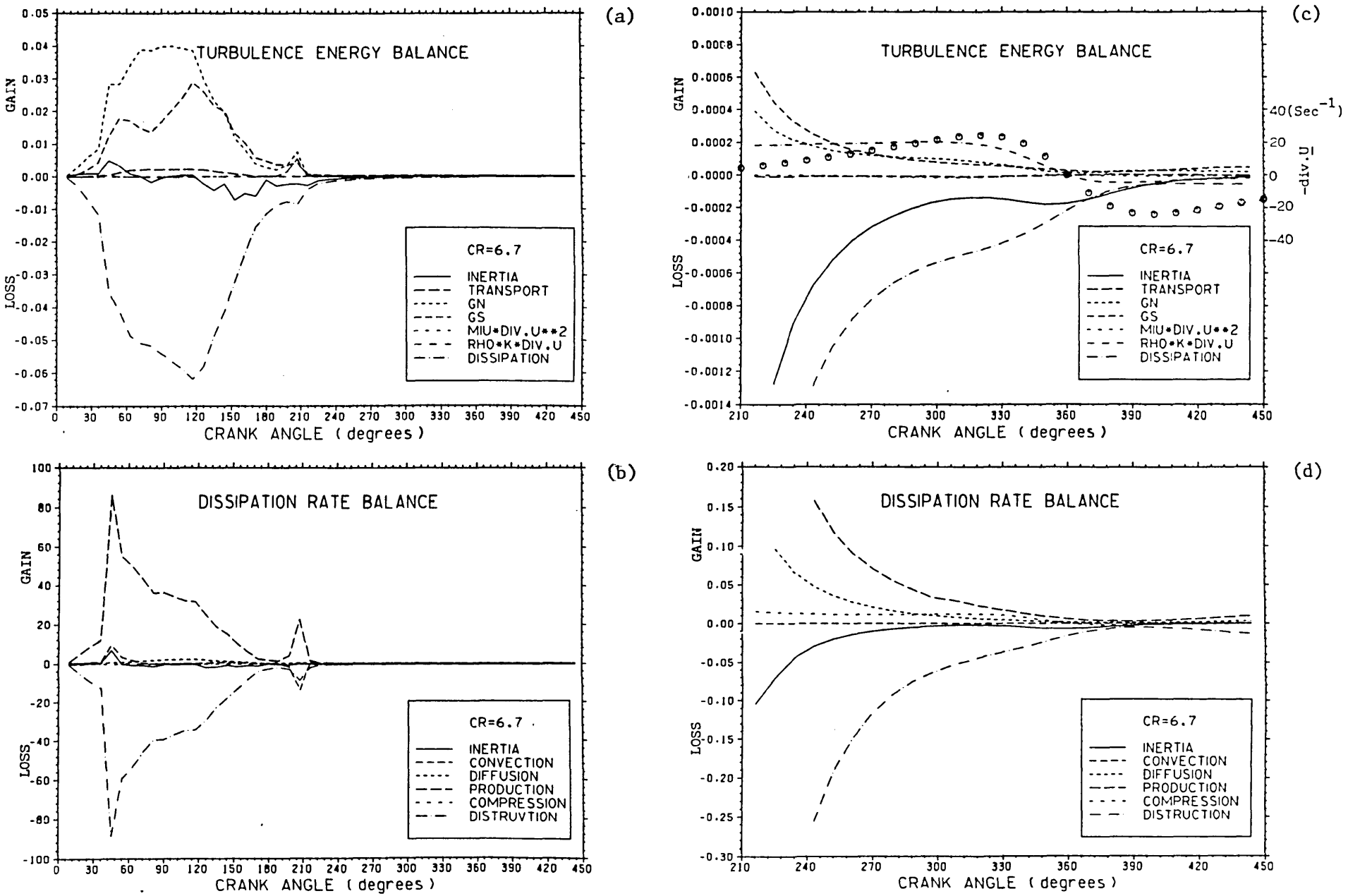


Figure 5.24: The volume-integral balances of the k- and ε-transport equations for the test Case II

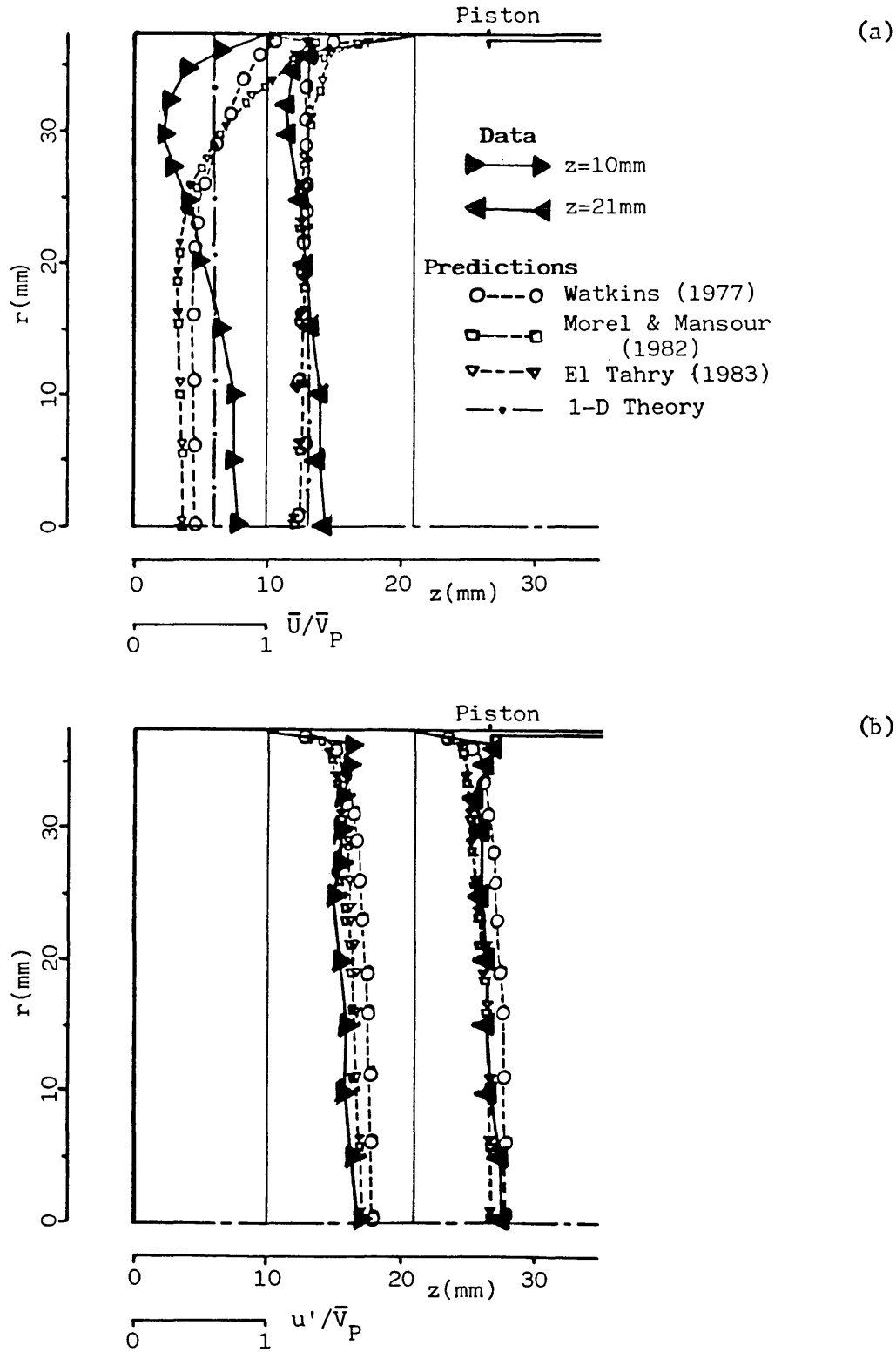


Figure 5.25: The measured and predicted radial profiles of $\overline{u}/\overline{v}_p$ and $u'/\overline{v}_p$ at θ = 324° CA; test Case II

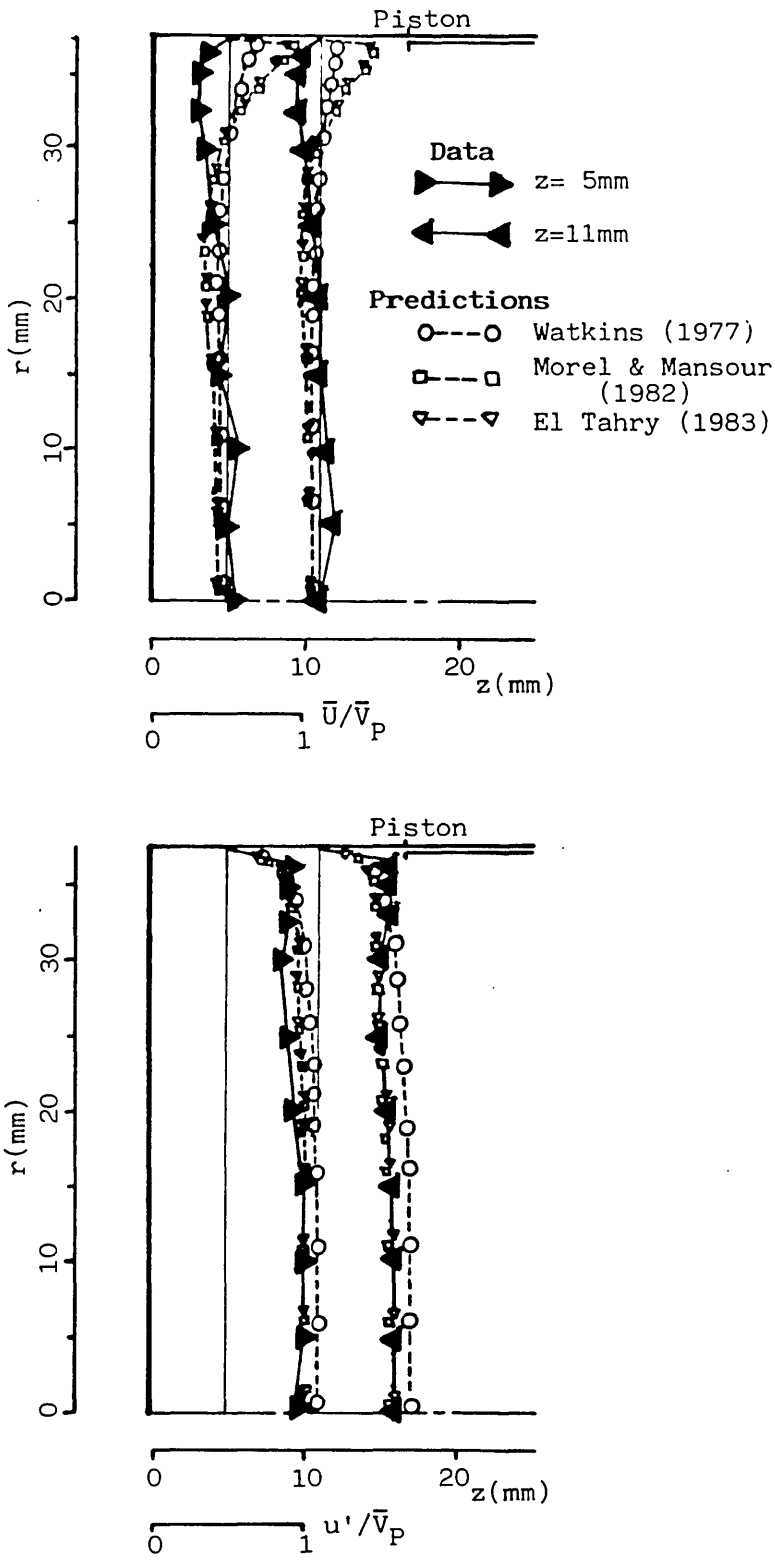


Figure 5.26: The measured and predicted radial profiles of $\overline{U}/\overline{V}_p$ and $u'/\overline{V}_p$ at θ = 360° CA; test Case II

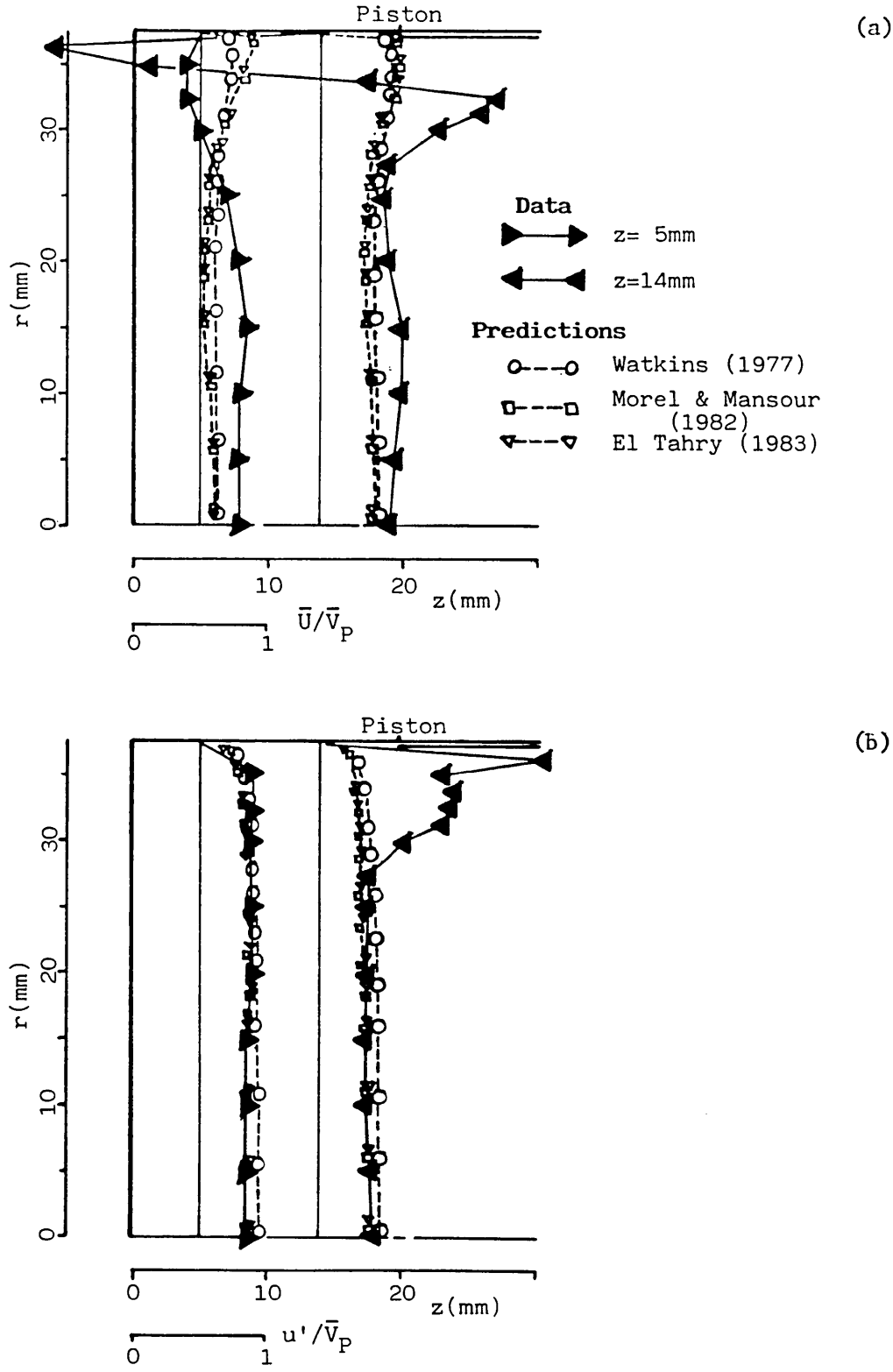


Figure 5.27: The measured and predicted radial profiles of $\overline{U}/\overline{V}_p$ and $u'/\overline{V}_p$ at θ = 380° CA; test Case II

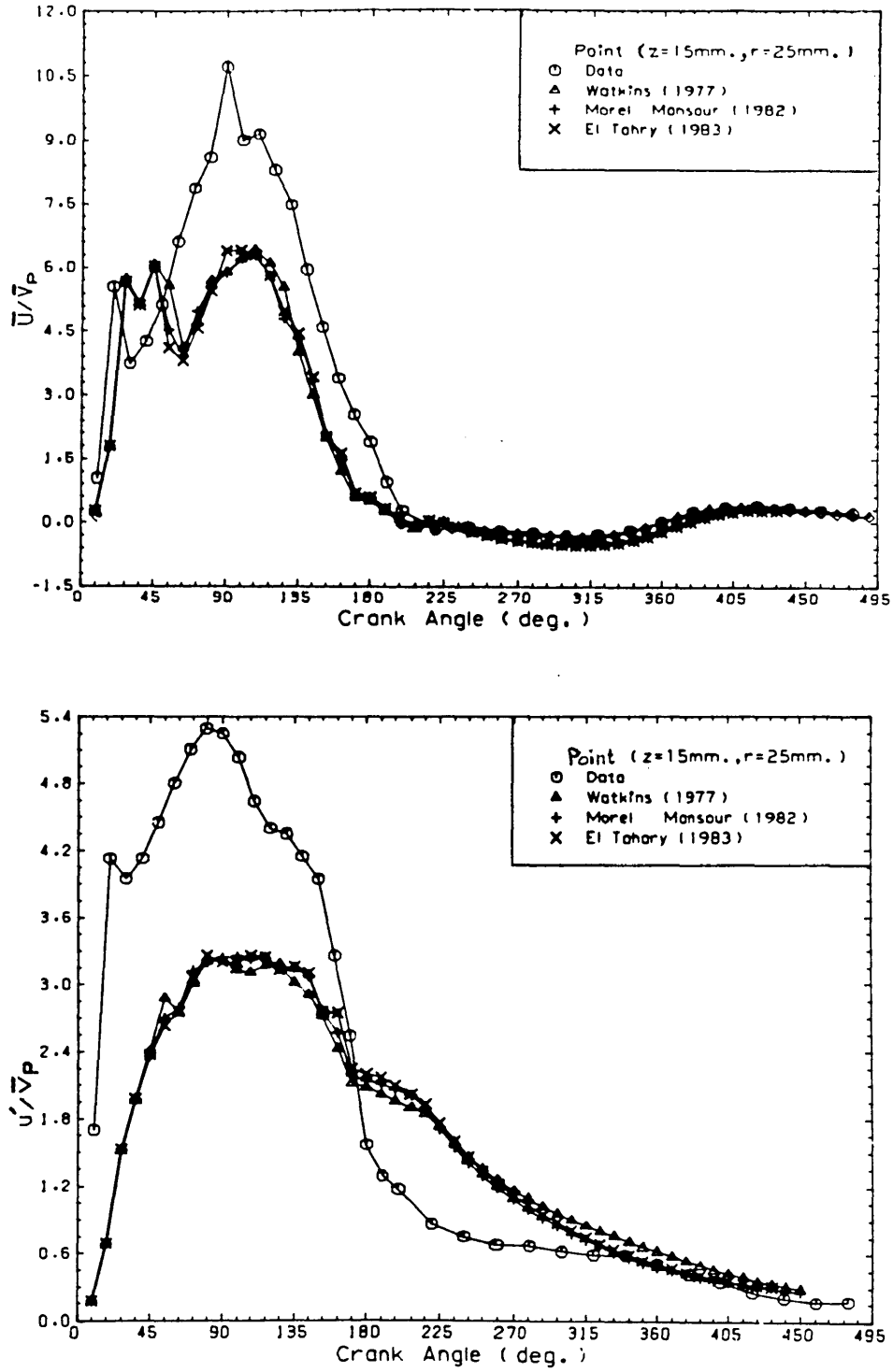
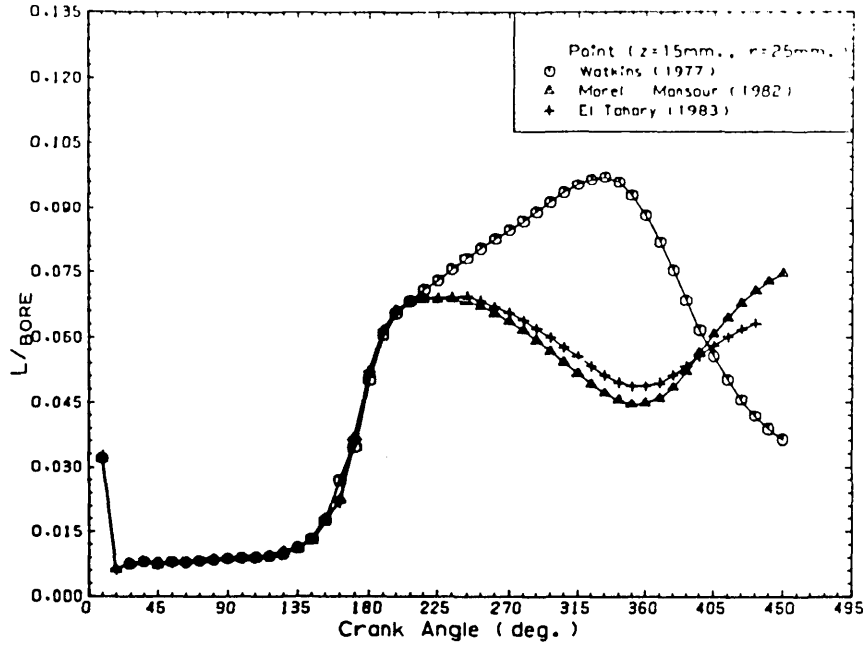
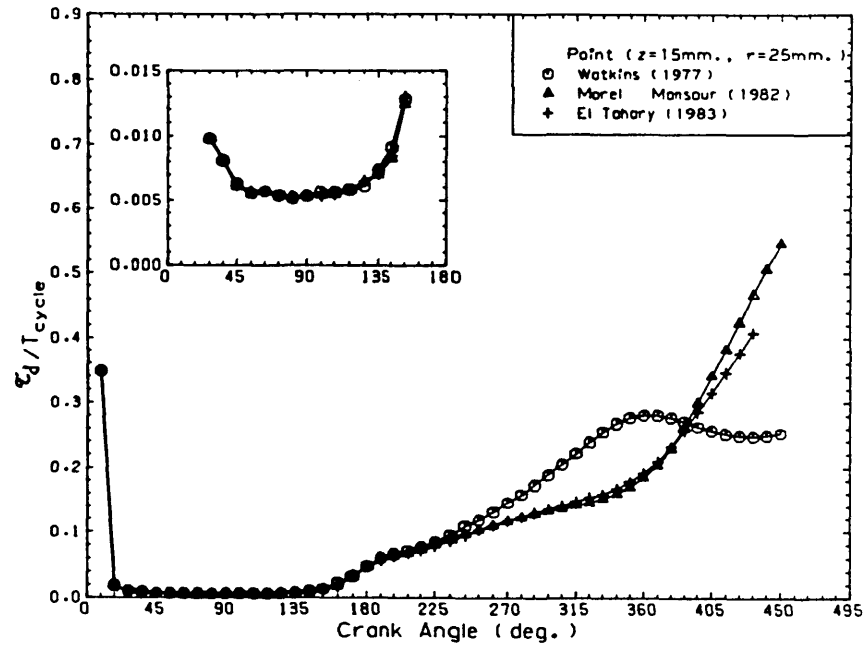


Figure 5.28: The predicted variations of the mean velocity and turbulence parameters at monitoring location Z = 15 mm, r = 25 mm; test Case I





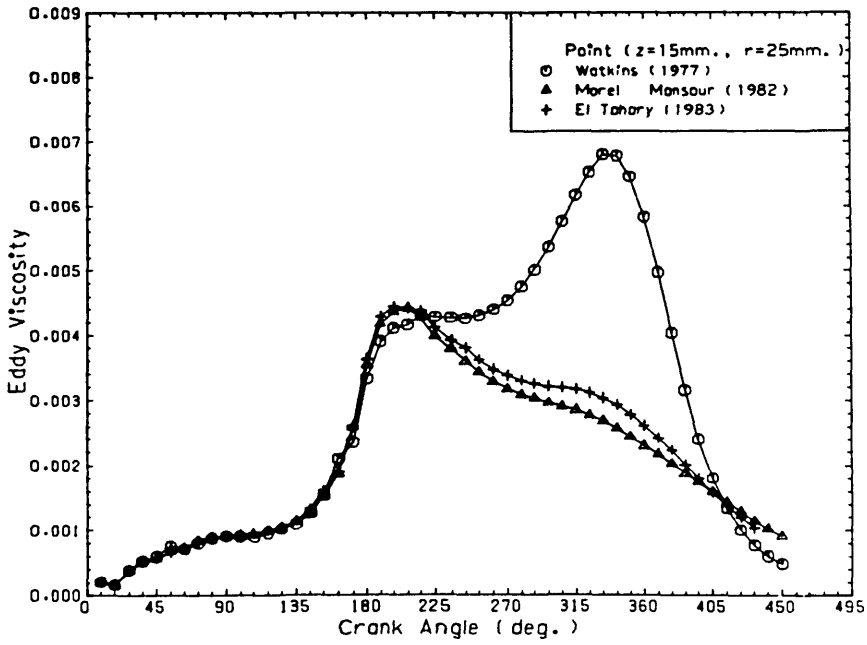


Figure 5.28: Continued

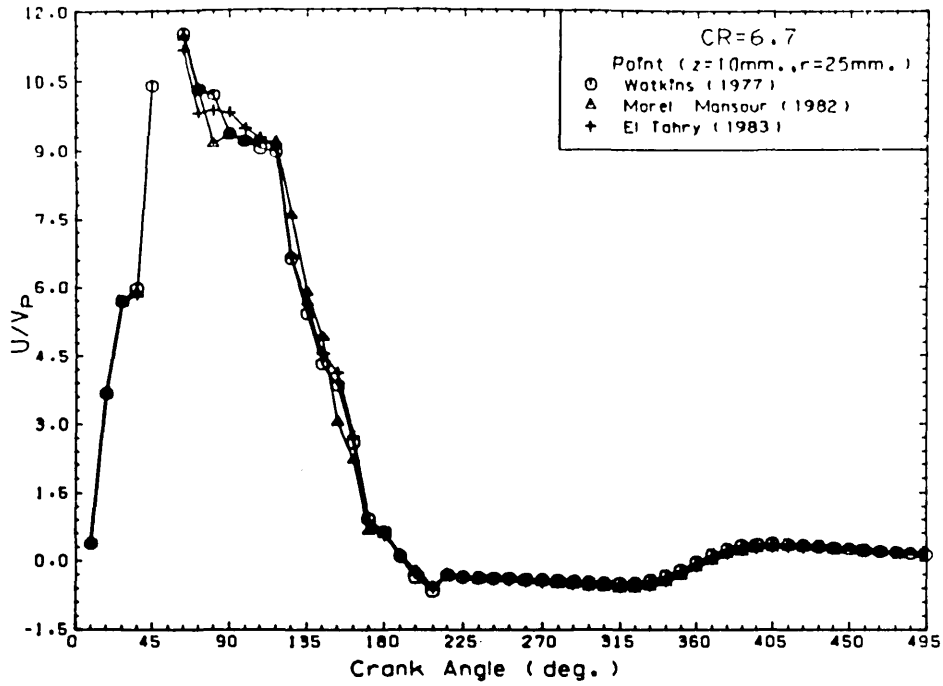
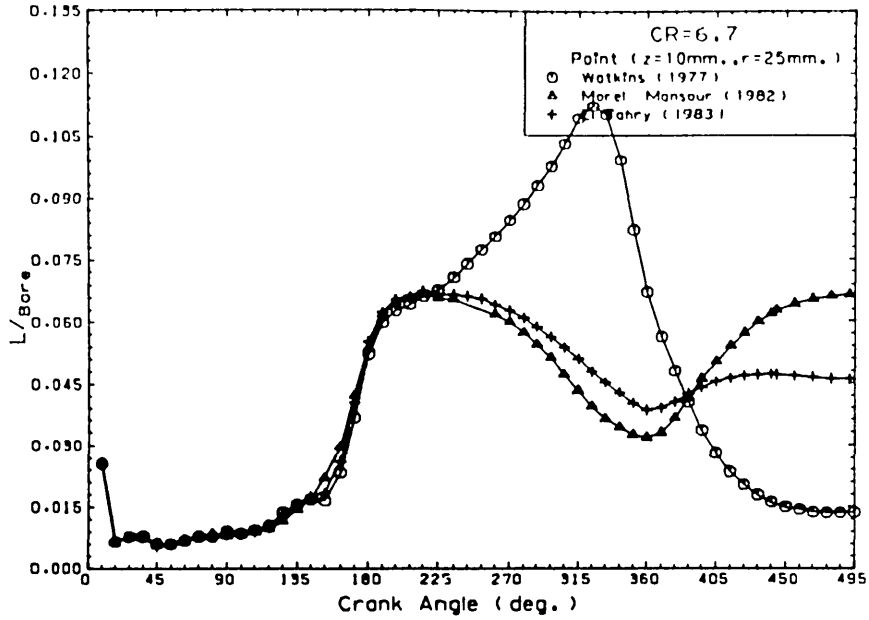
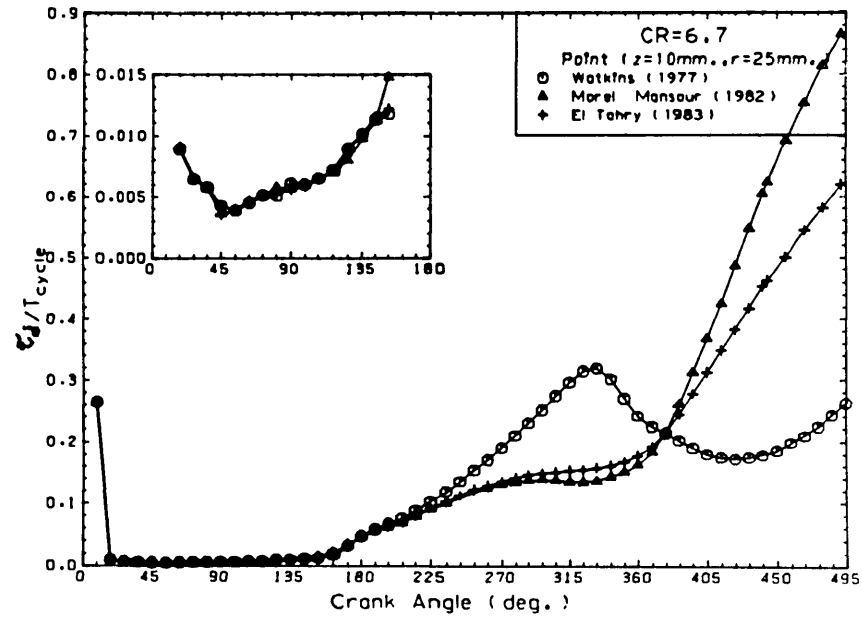


Figure 5.29: The predicted variation of the mean axial velocity and turbulence parameters at monitoring location Z = 10 mm and r = 25 mm; test Case II





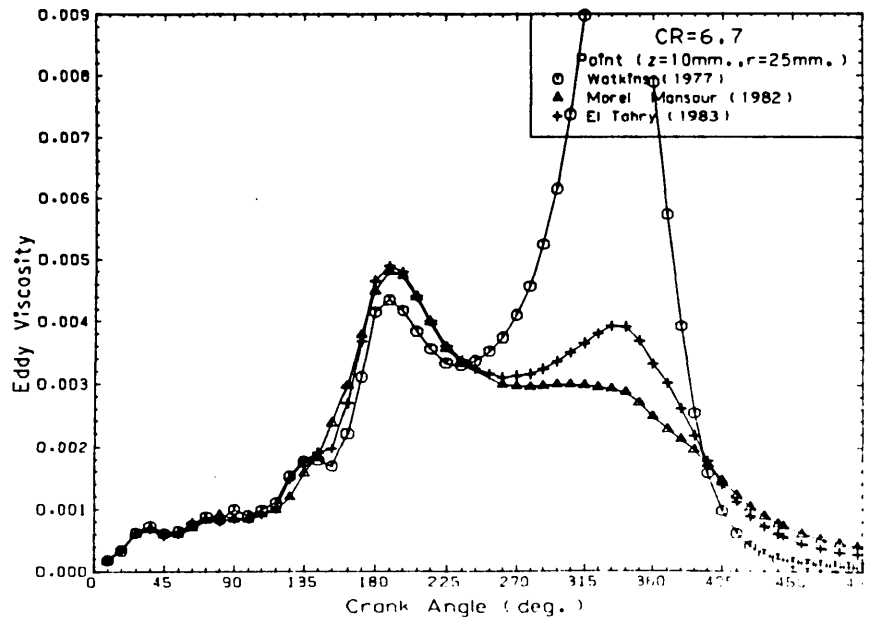
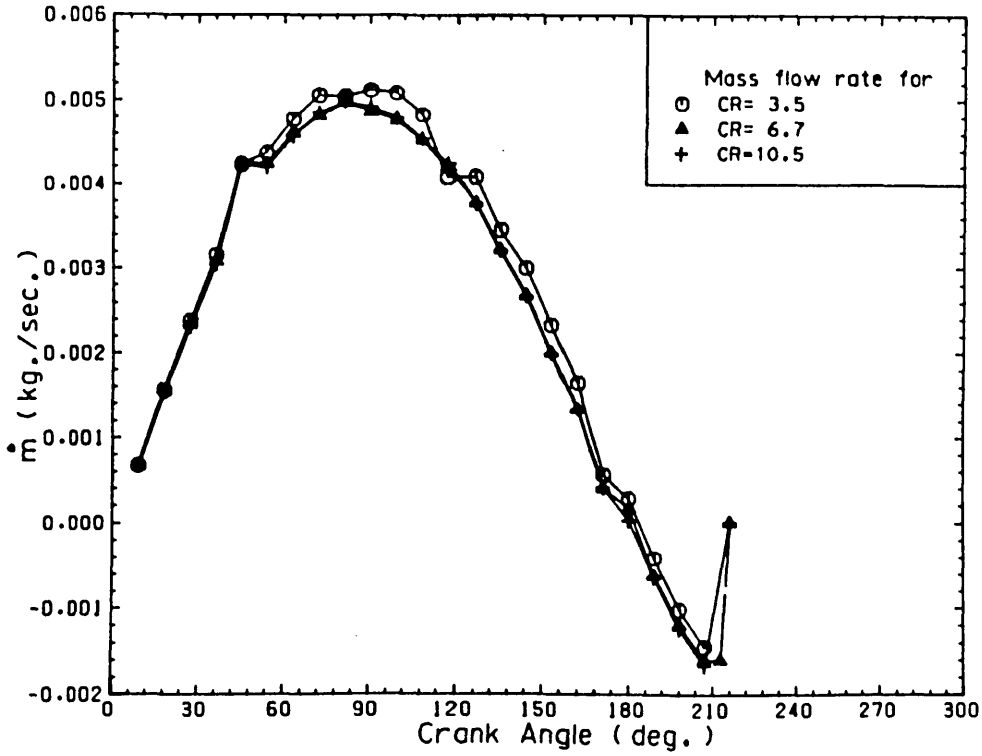


Figure 5.29: Continued



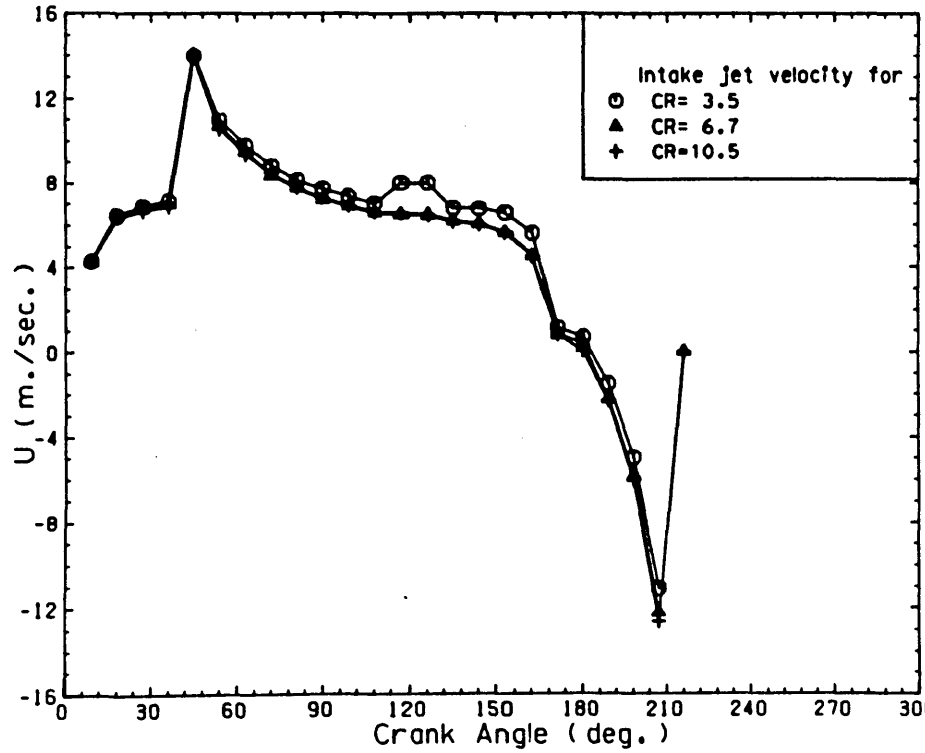


Figure 6.1: Effect of compression ratio on the (a) intake mass flow rate and (b) inlet velocity through the valve

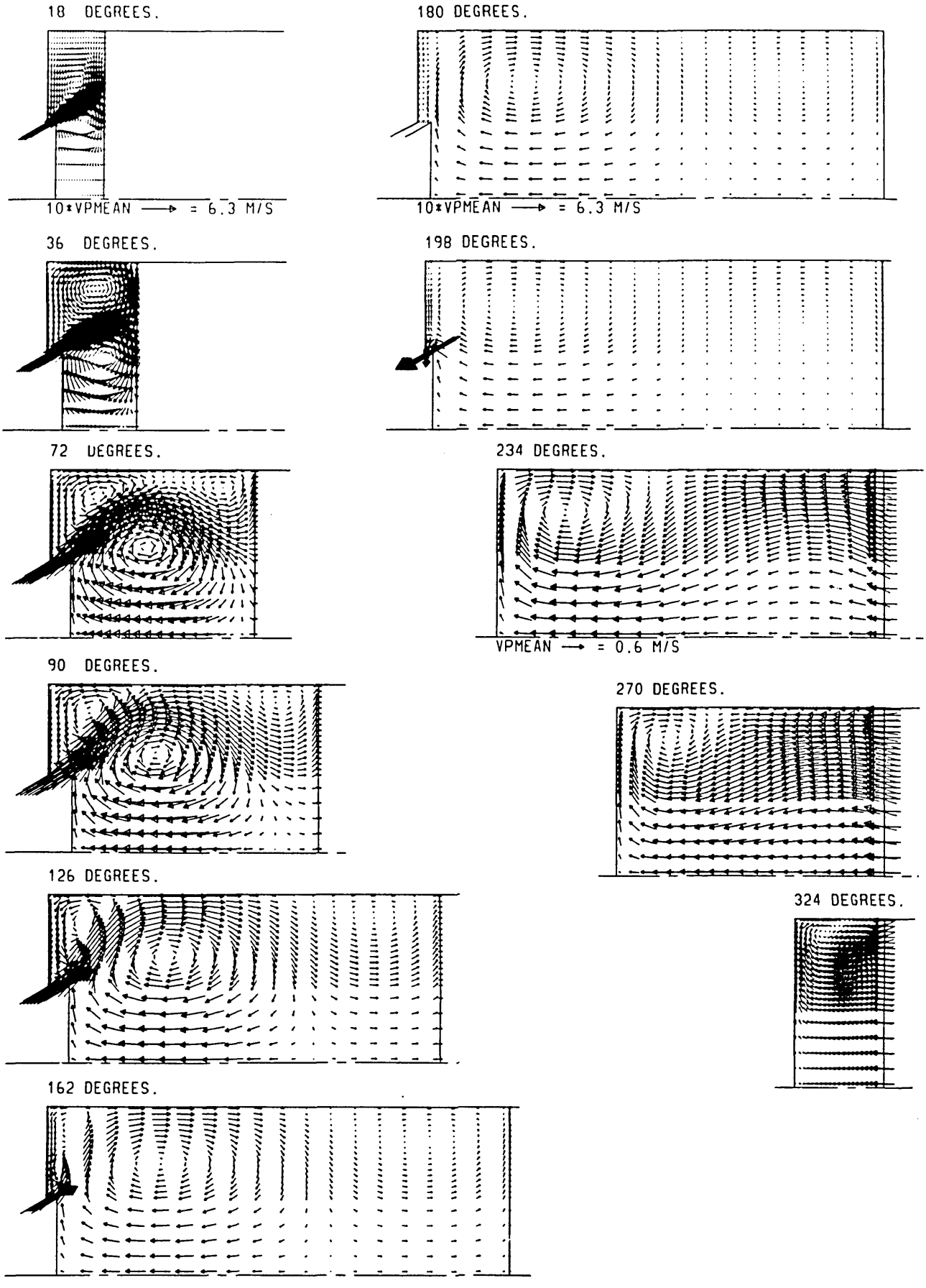


Figure 6.2(a): Predictions of the velocity field for operating condition CR = 10.5 and S = 200 rpm

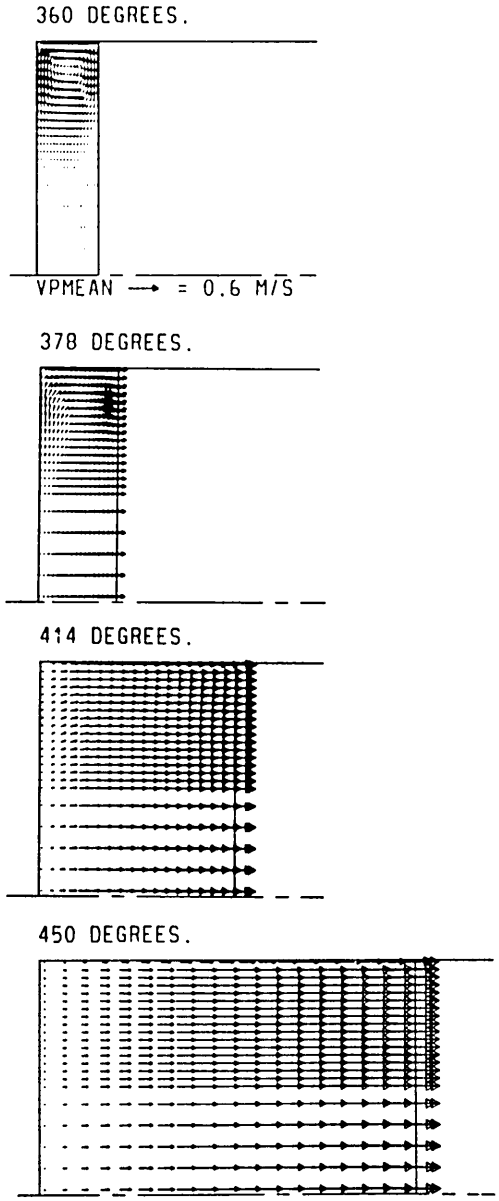


Figure 6.2(a): Continued

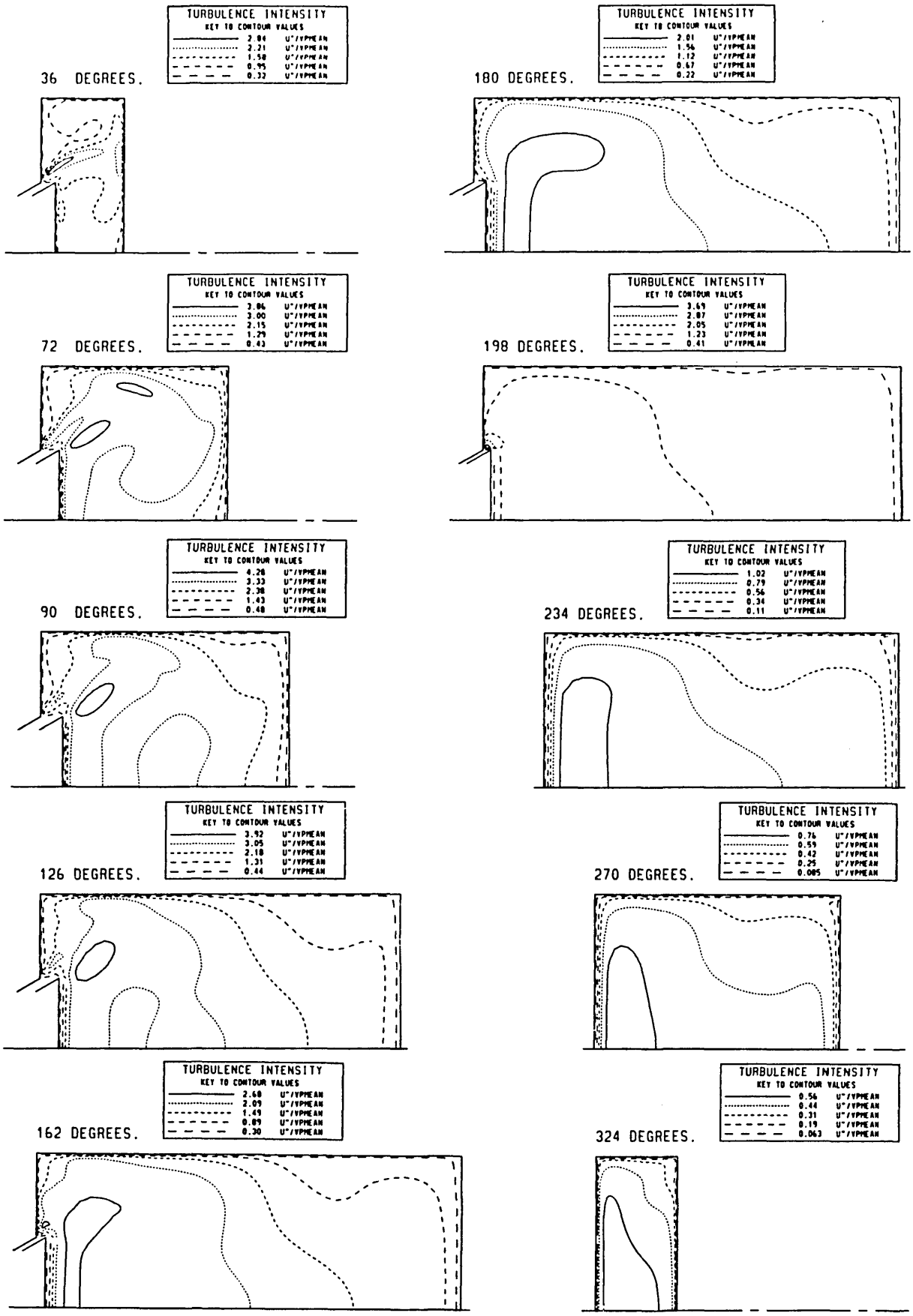


Figure 6.2(b): Predictions of the turbulence intensity distribution for operating condition CR = 10.5 and S = 200 rpm

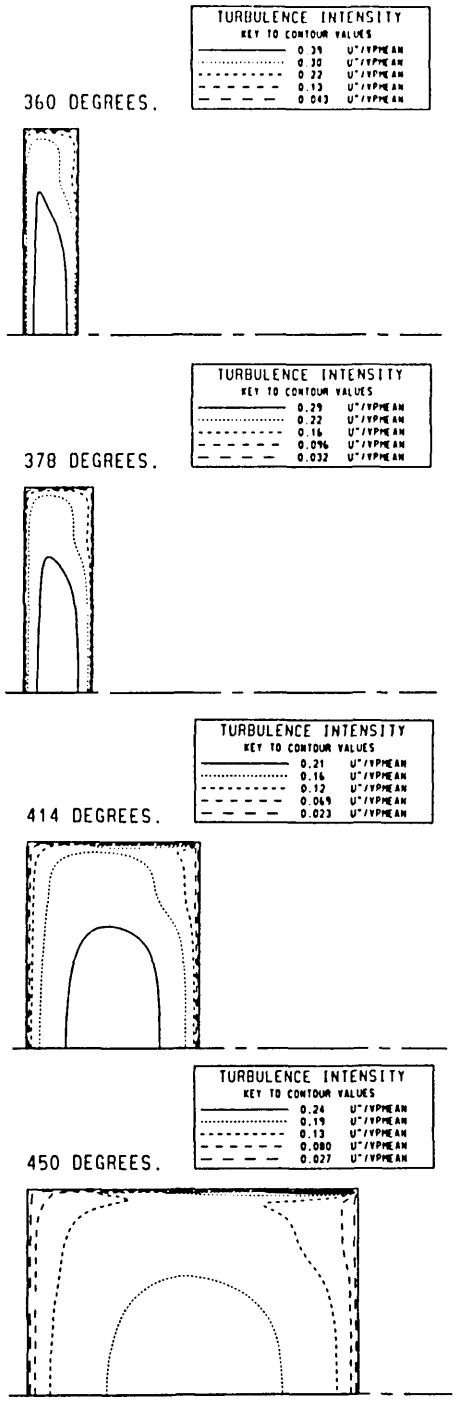


Figure 6.2(b): Continued

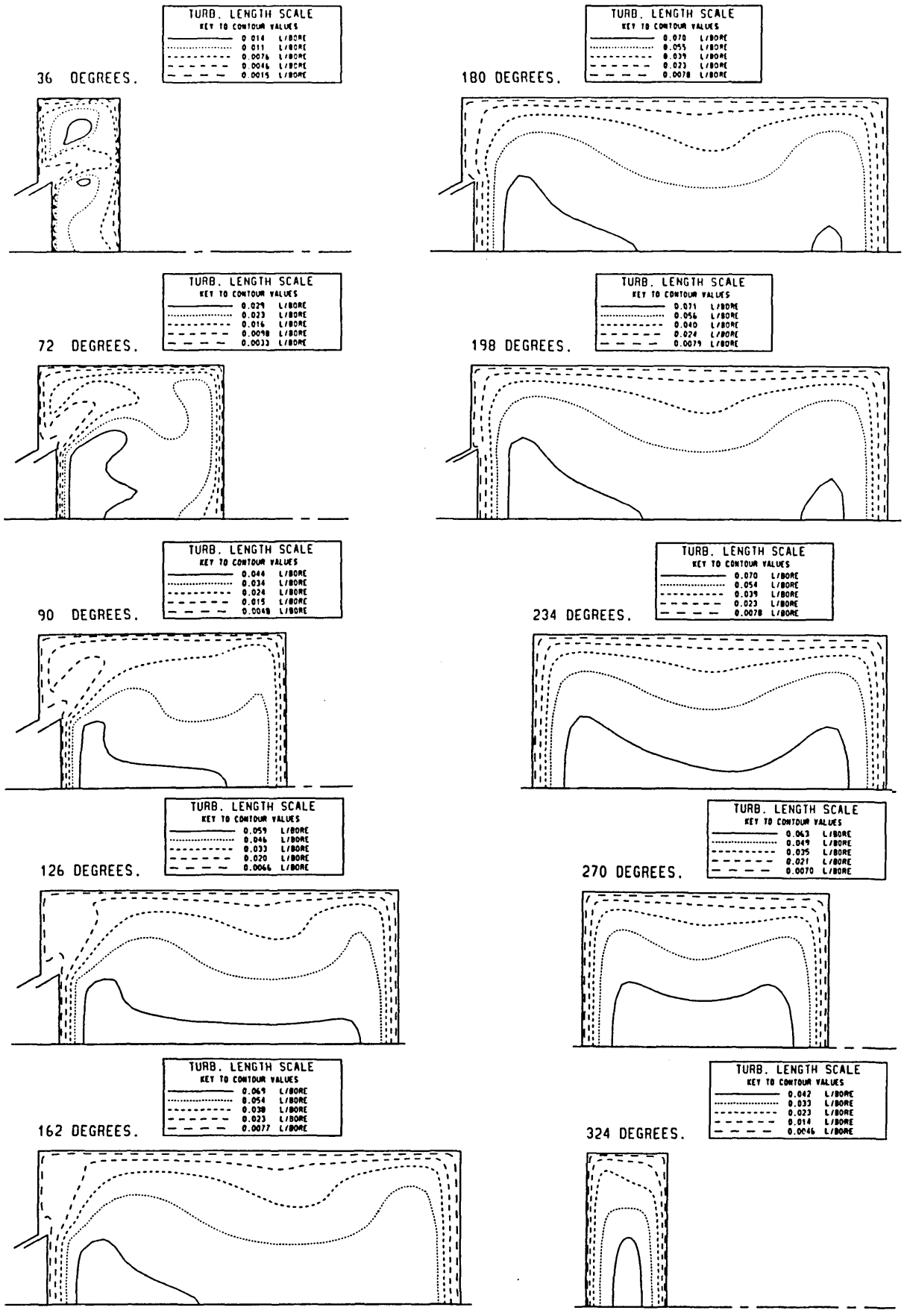


Figure 6.2(c): Predictions of the length scale distribution for operating condition CR = 10.5 and S = 200 rpm

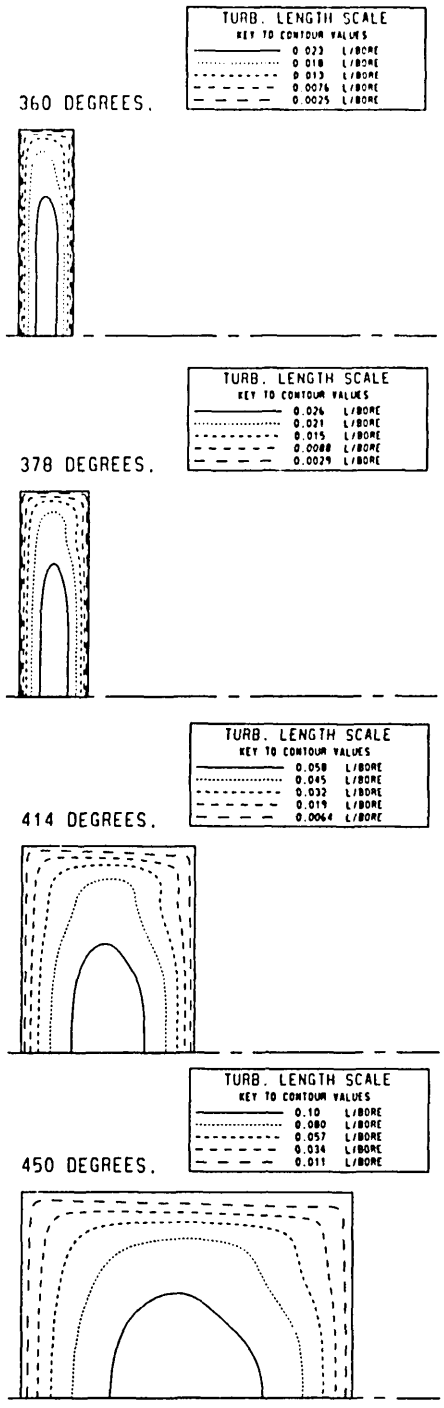


Figure 6.2(c): Continued

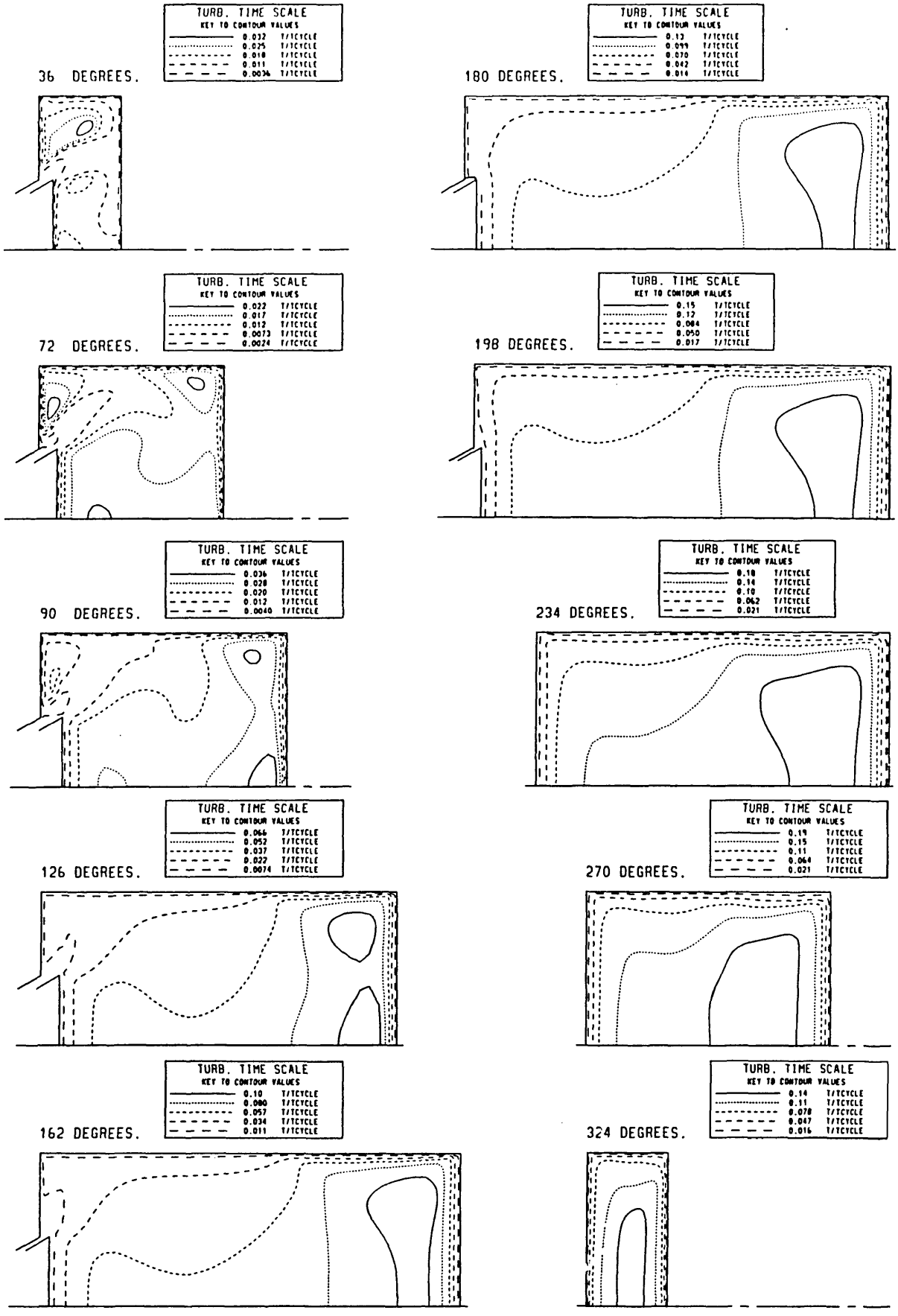


Figure 6.2(d): Predictions of the dissipation time-scale distribution for operating condition CR = 10.5 and S = 200 rpm

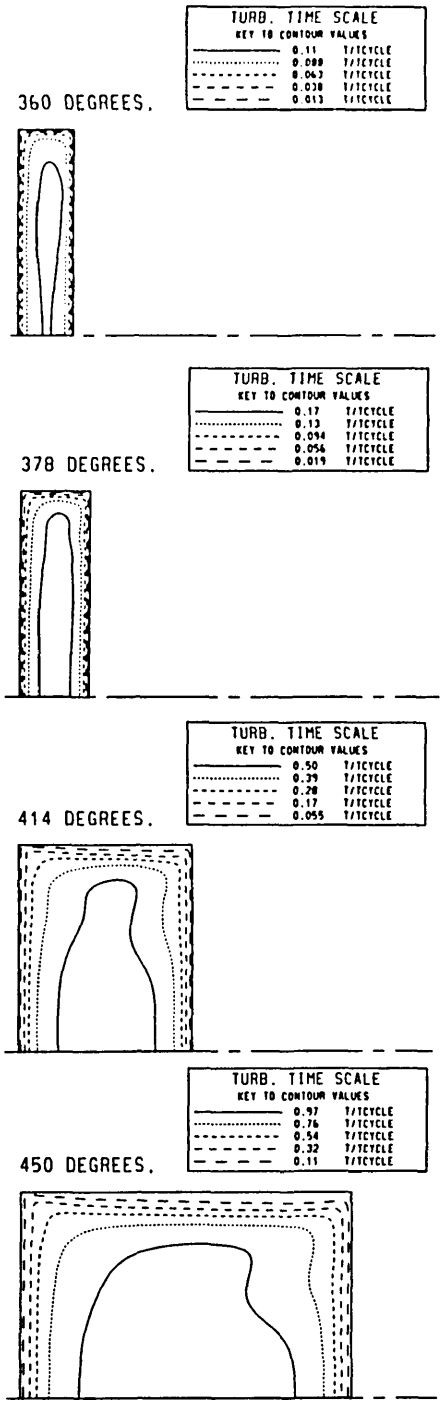


Figure 6.2(d): Continued

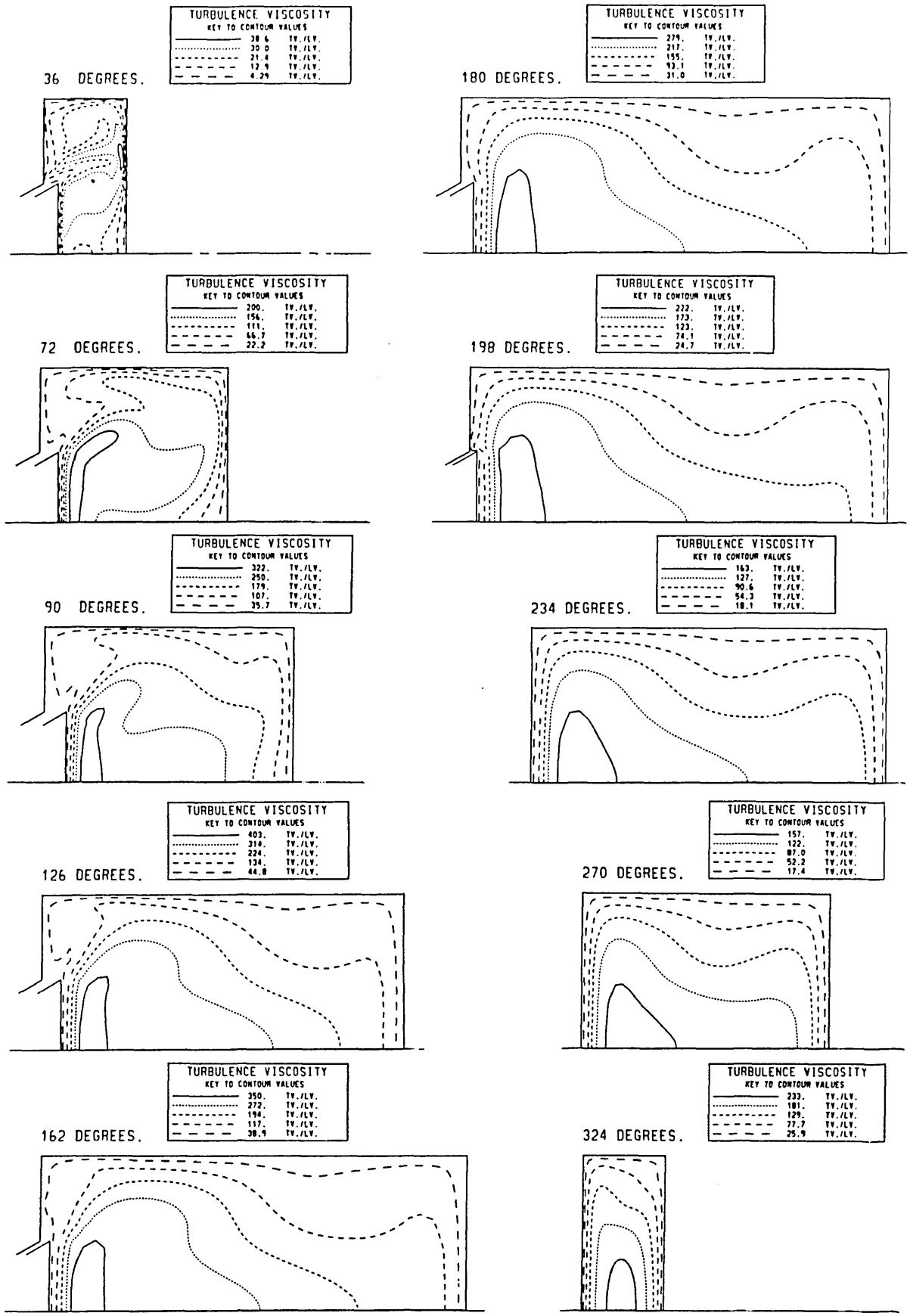


Figure 6.2(e): Predictions of the turbulent viscosity distribution for operating condition CR = 10.5 and S = 200 rpm

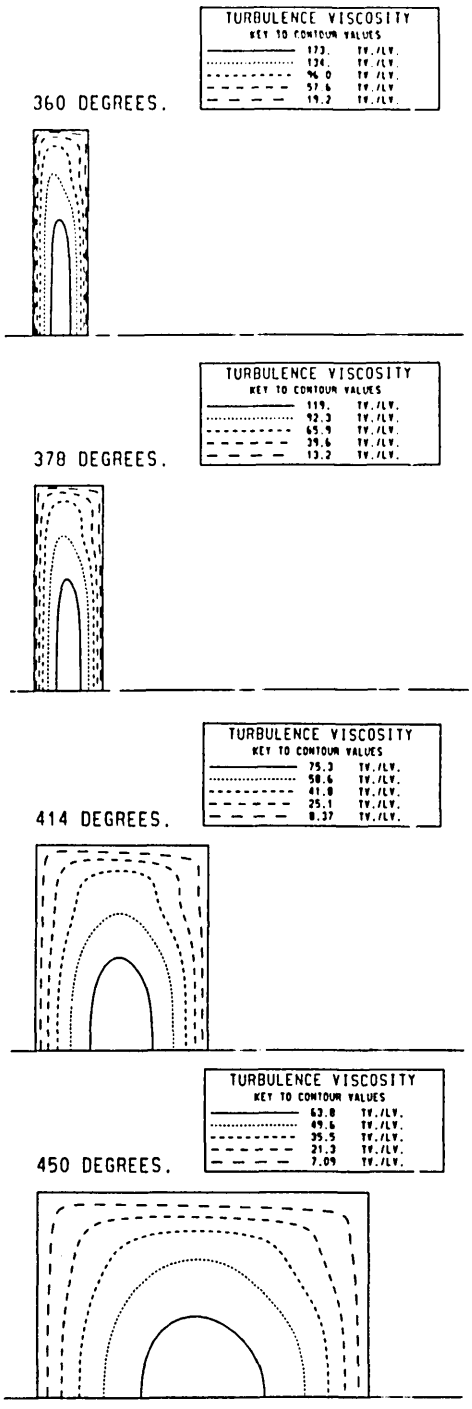


Figure 6.2(e): Continued

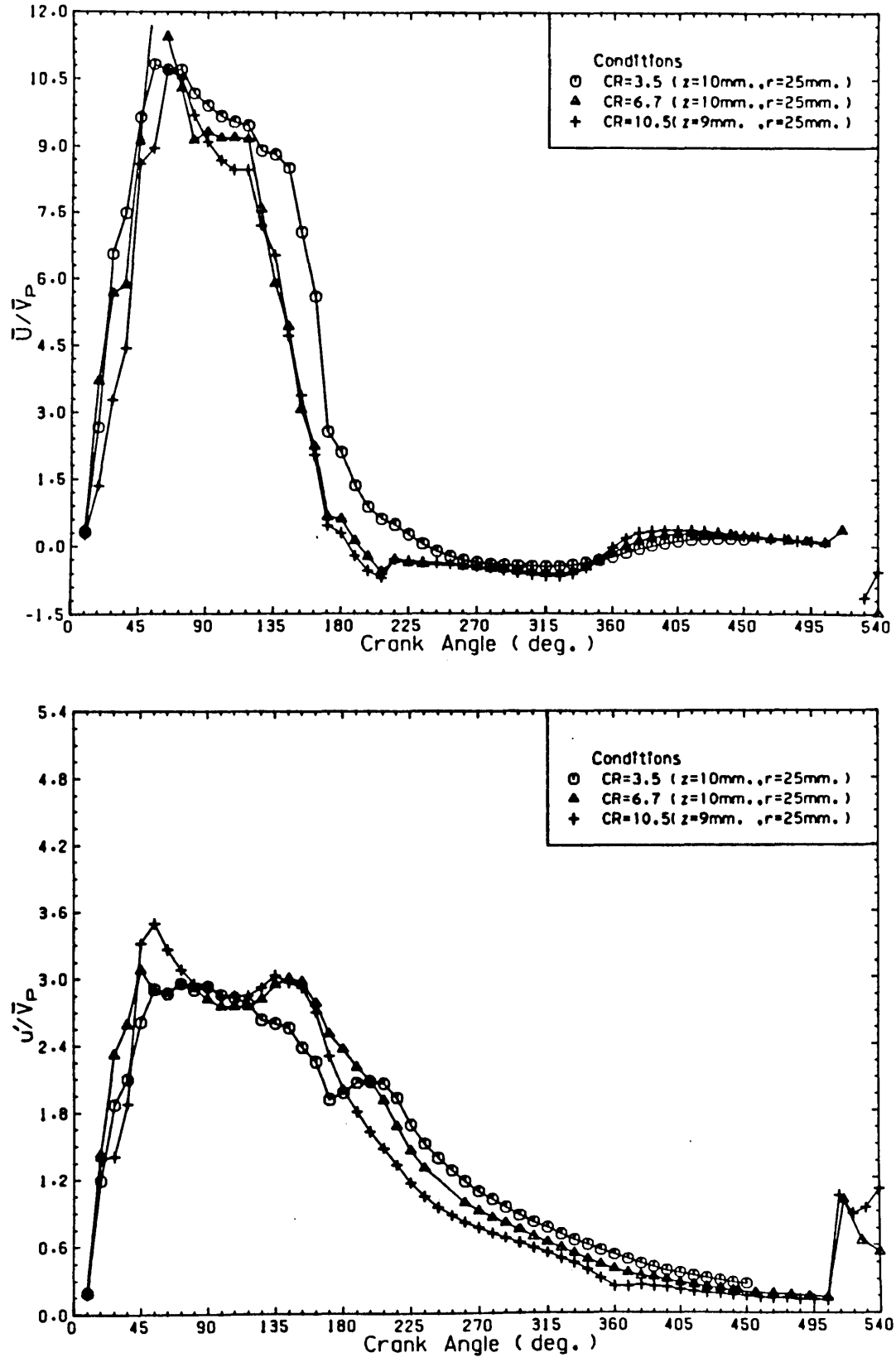
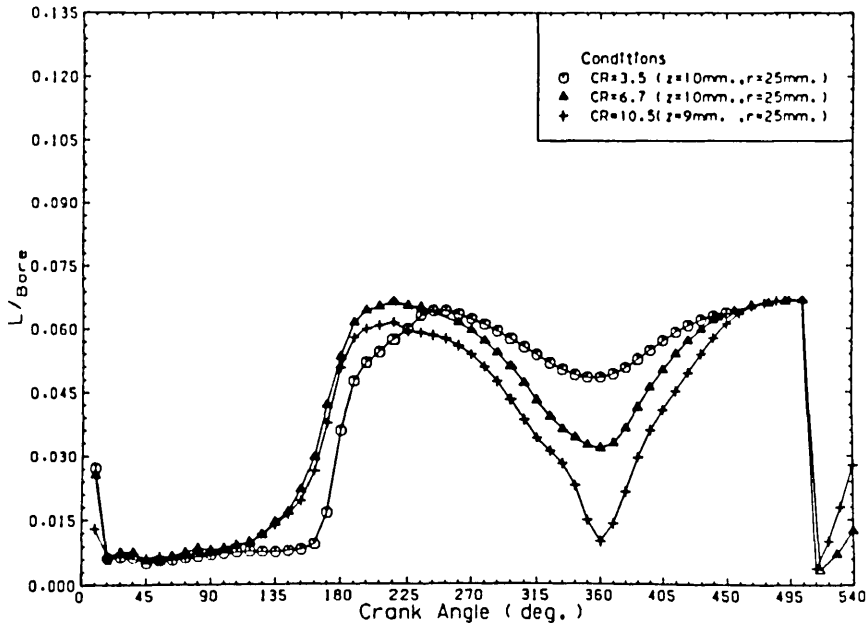
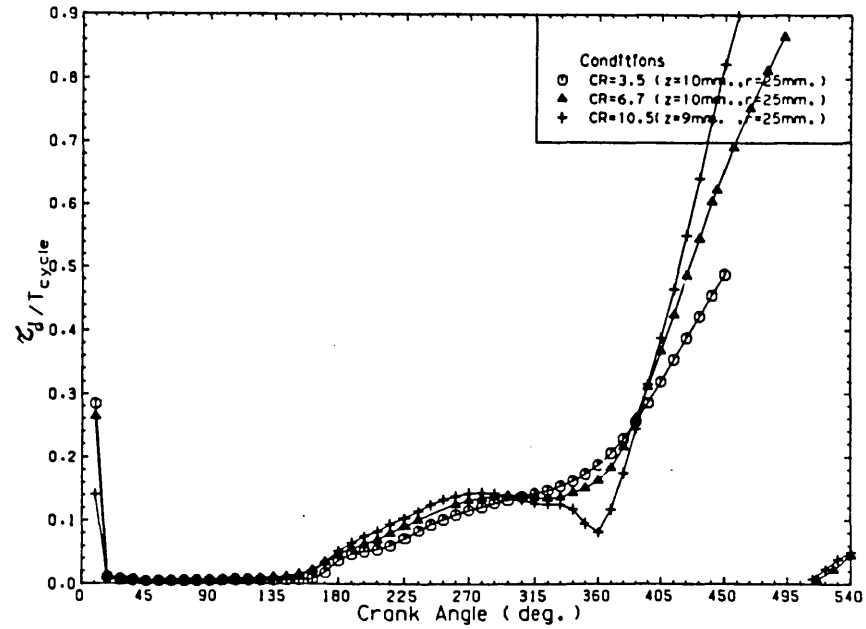


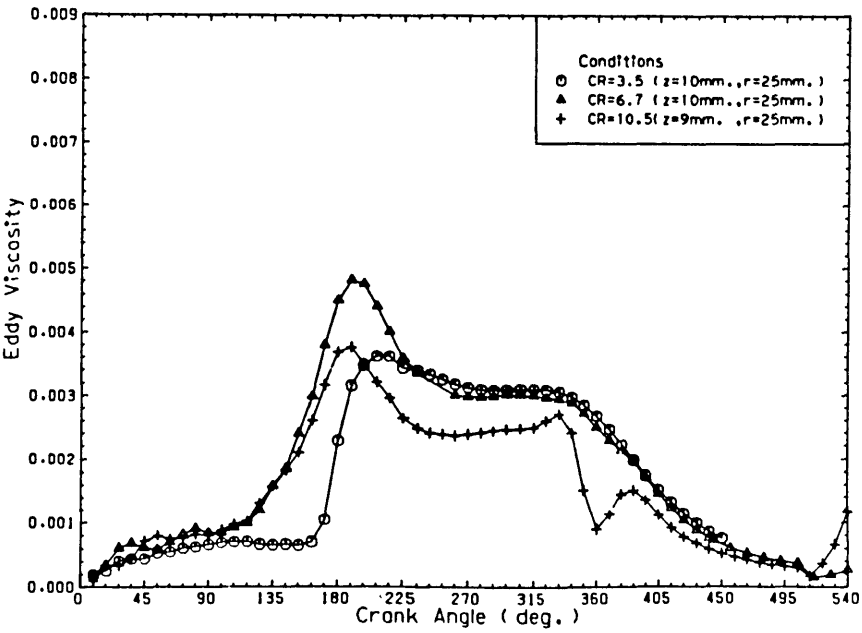
Figure 6.3: Influence of compression ratio on temporal variations of the mean axial velocity and turbulence parameters at fixed monitoring locations



(c)



(d)



(e)

Figure 6.3: Continued

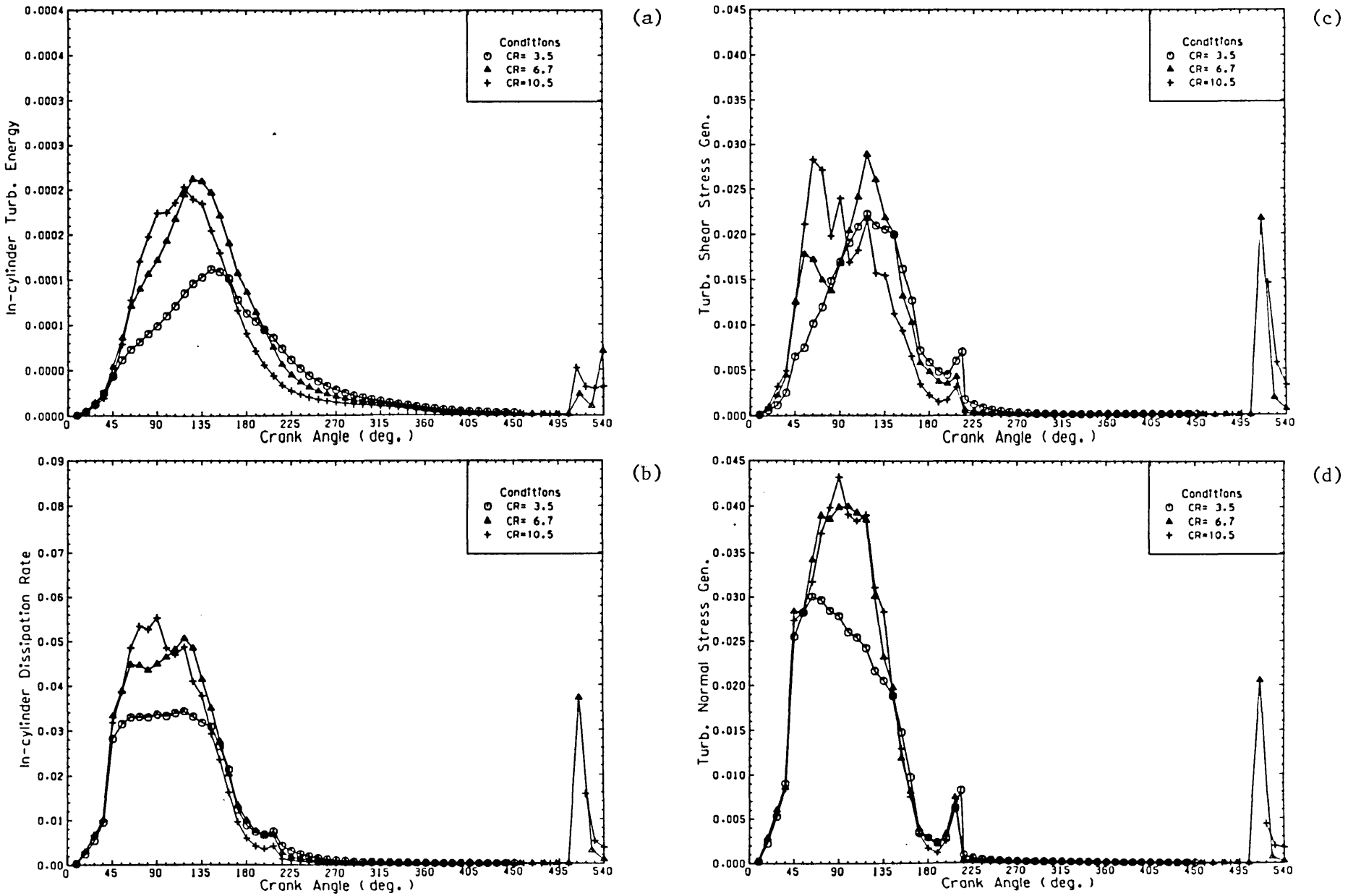
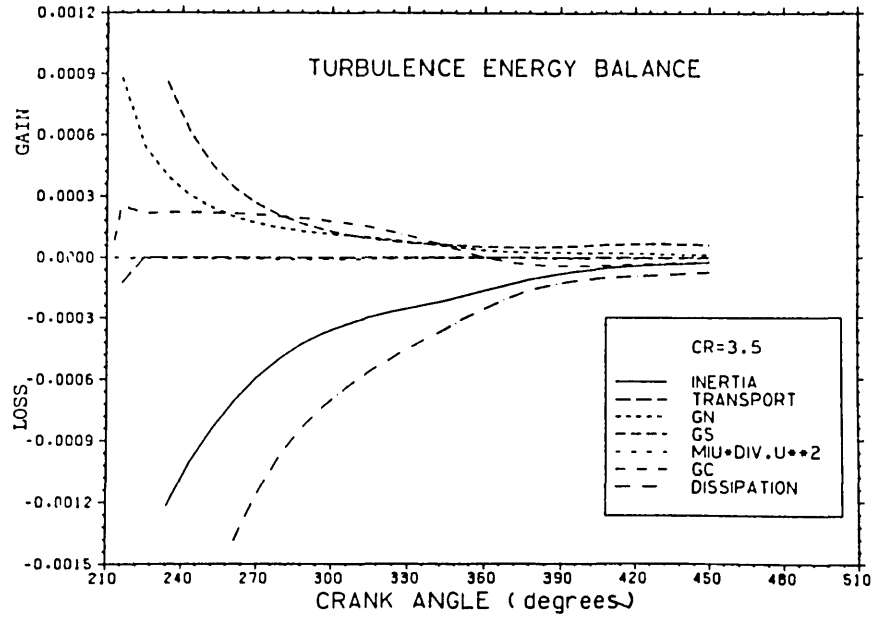
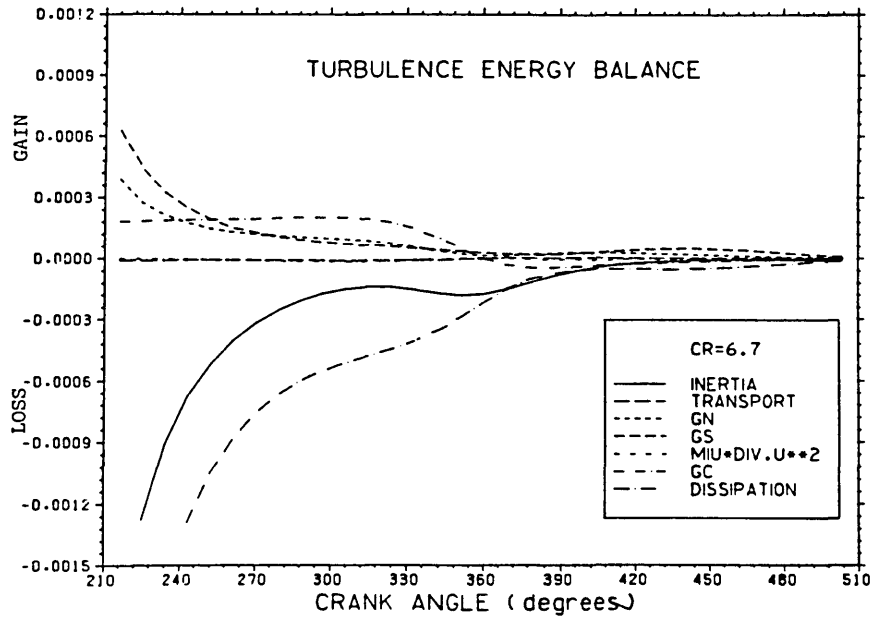


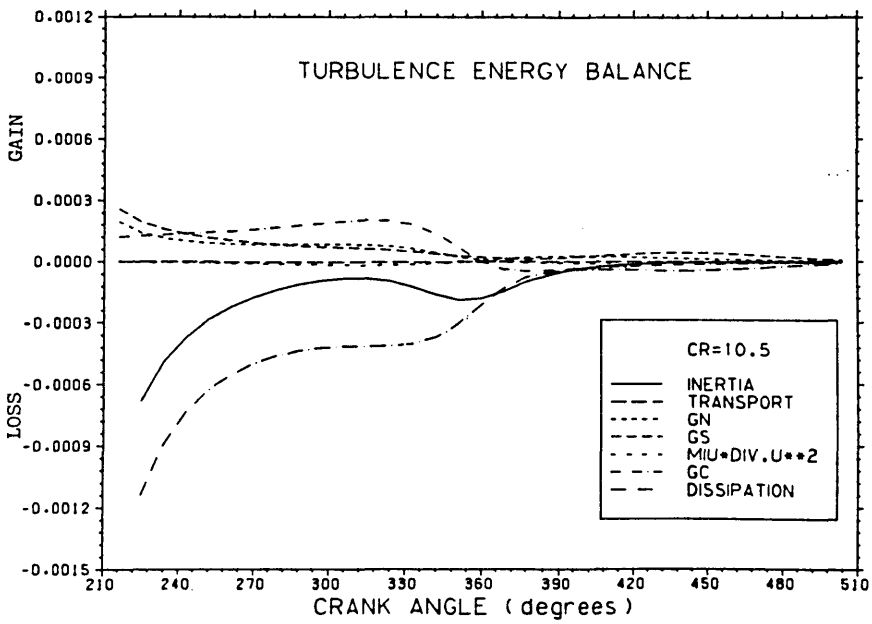
Figure 6.4: Influence of compression ratio on the volume-integral turbulence energy K, dissipation rate E, G_S and G_N



(a)



(b)



(c)

Figure 6.5: Influence of compression ratio on the volume-integral balances of the k-transport equation

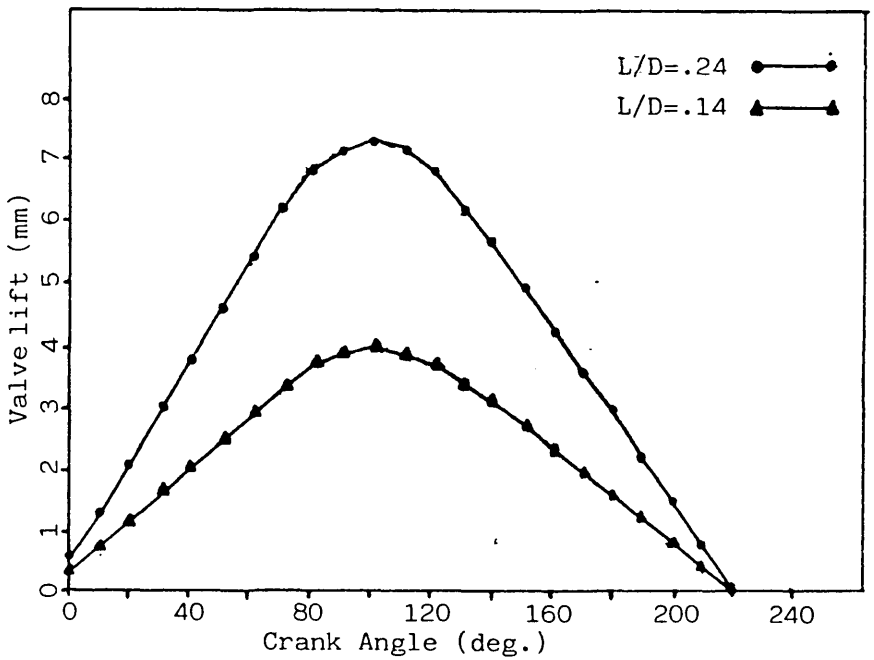


Figure 6.6: The valve lift diagrams for the valves L_{max}/D = 0.24 and 0.14

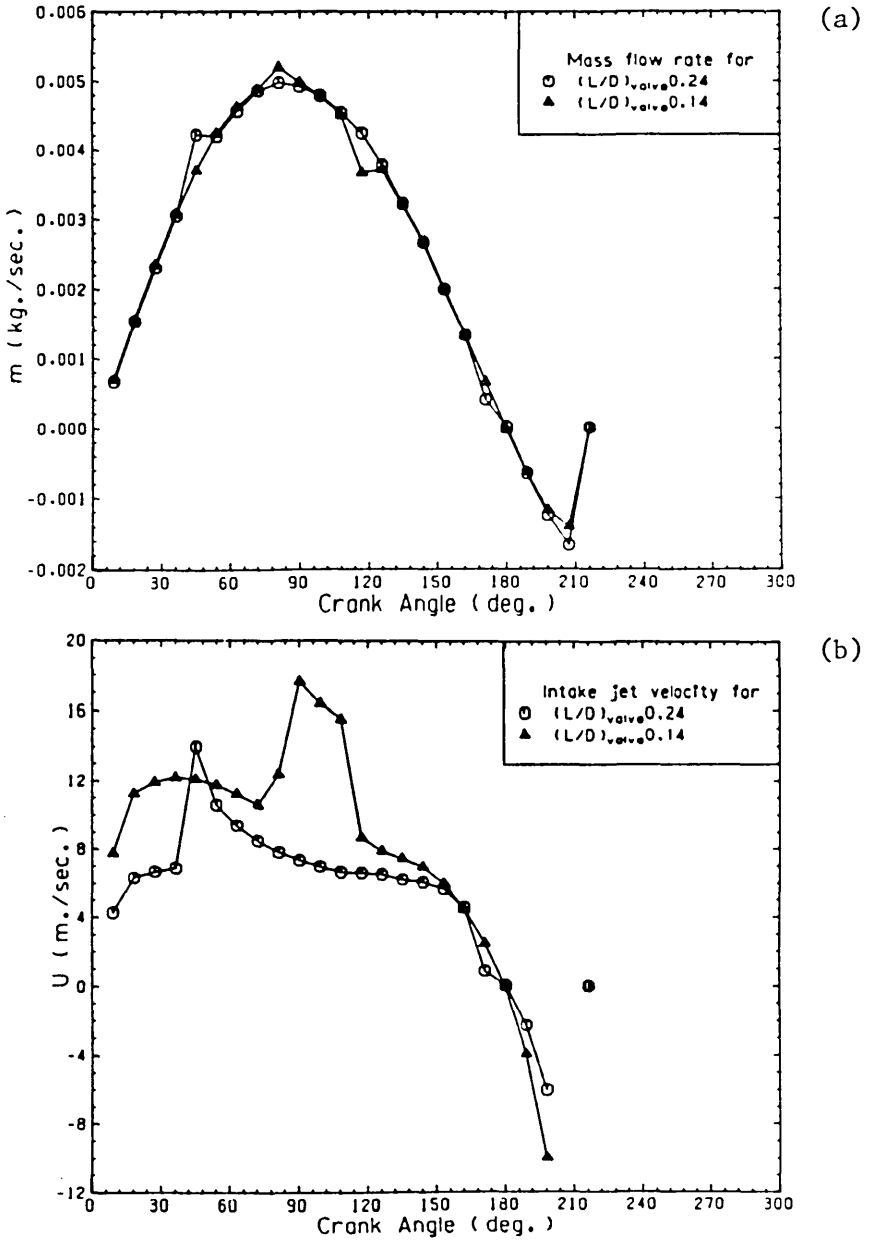


Figure 6.7: The influence of valve lift on (a) intake mass flow rate and (b) inlet velocity through the valve

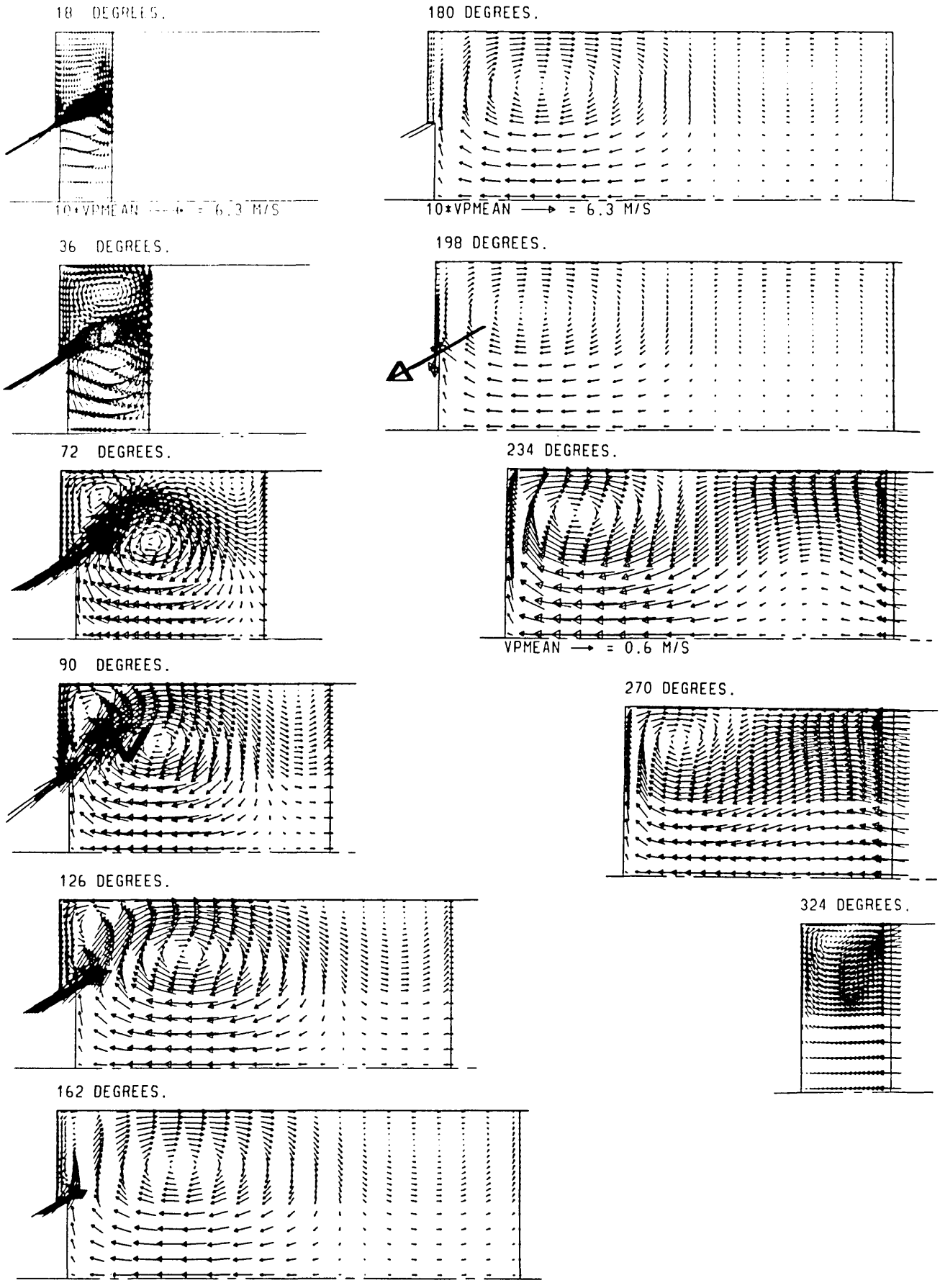


Figure 6.8(a): Predictions of the velocity field for the intake valve lift L_{max}/D = 0.14 (CR = 10.5, S = 200 rpm)

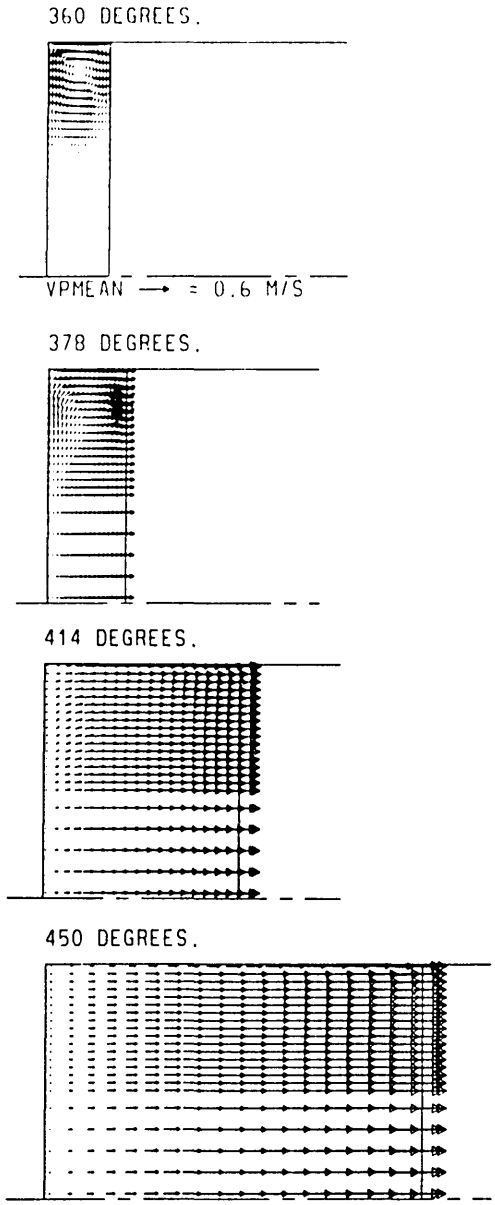


Figure 6.8(a): Continued

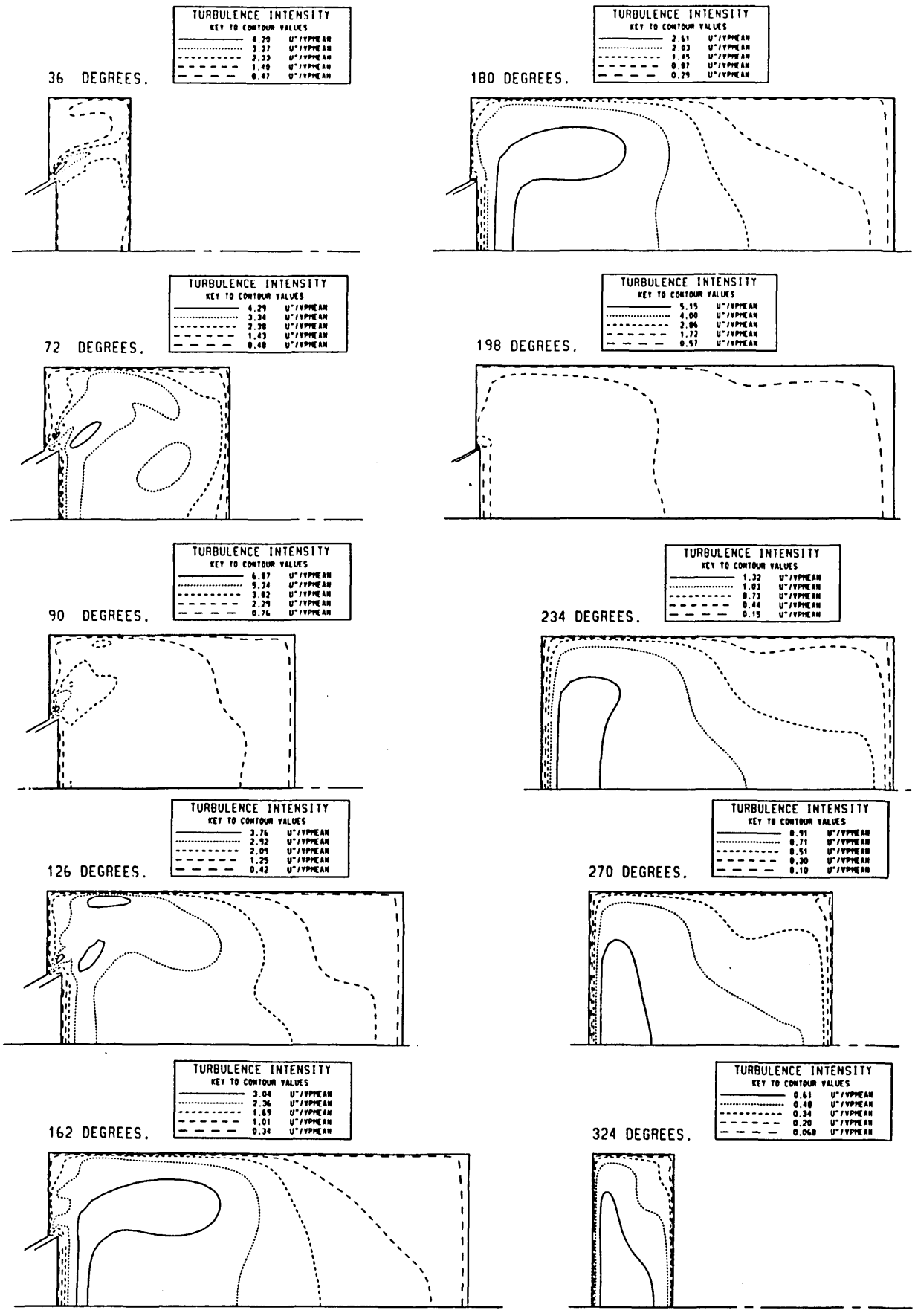


Figure 6.8(b): Predictions of the turbulence intensity distributions for the intake valve lift L_{max}/D = 0.14 (CR = 10.5, S = 200 rpm)

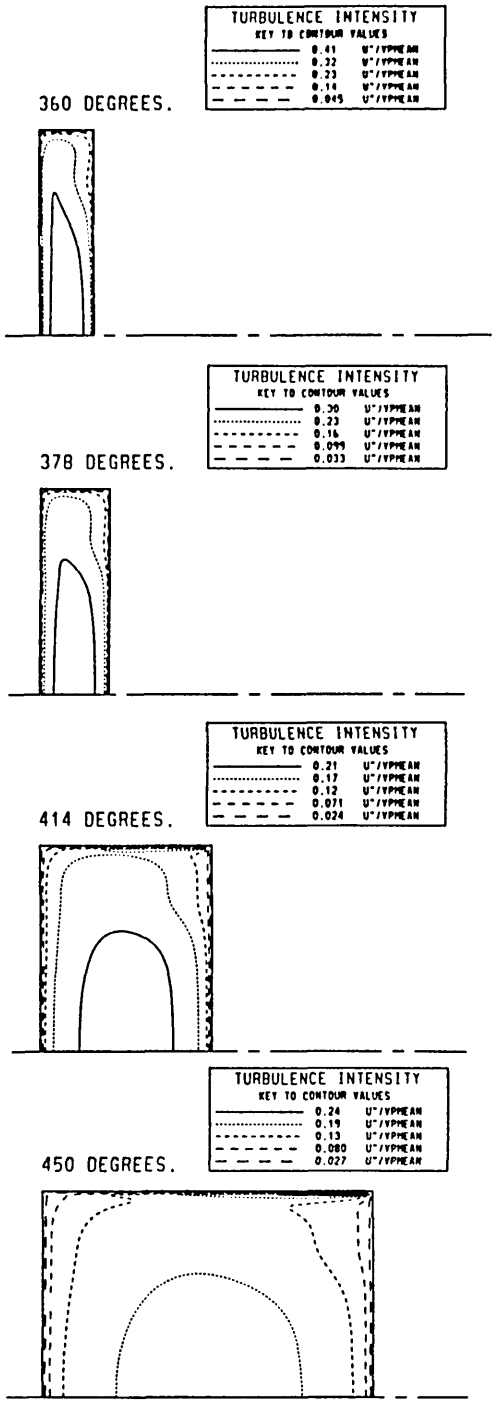


Figure 6.8(b): Continued

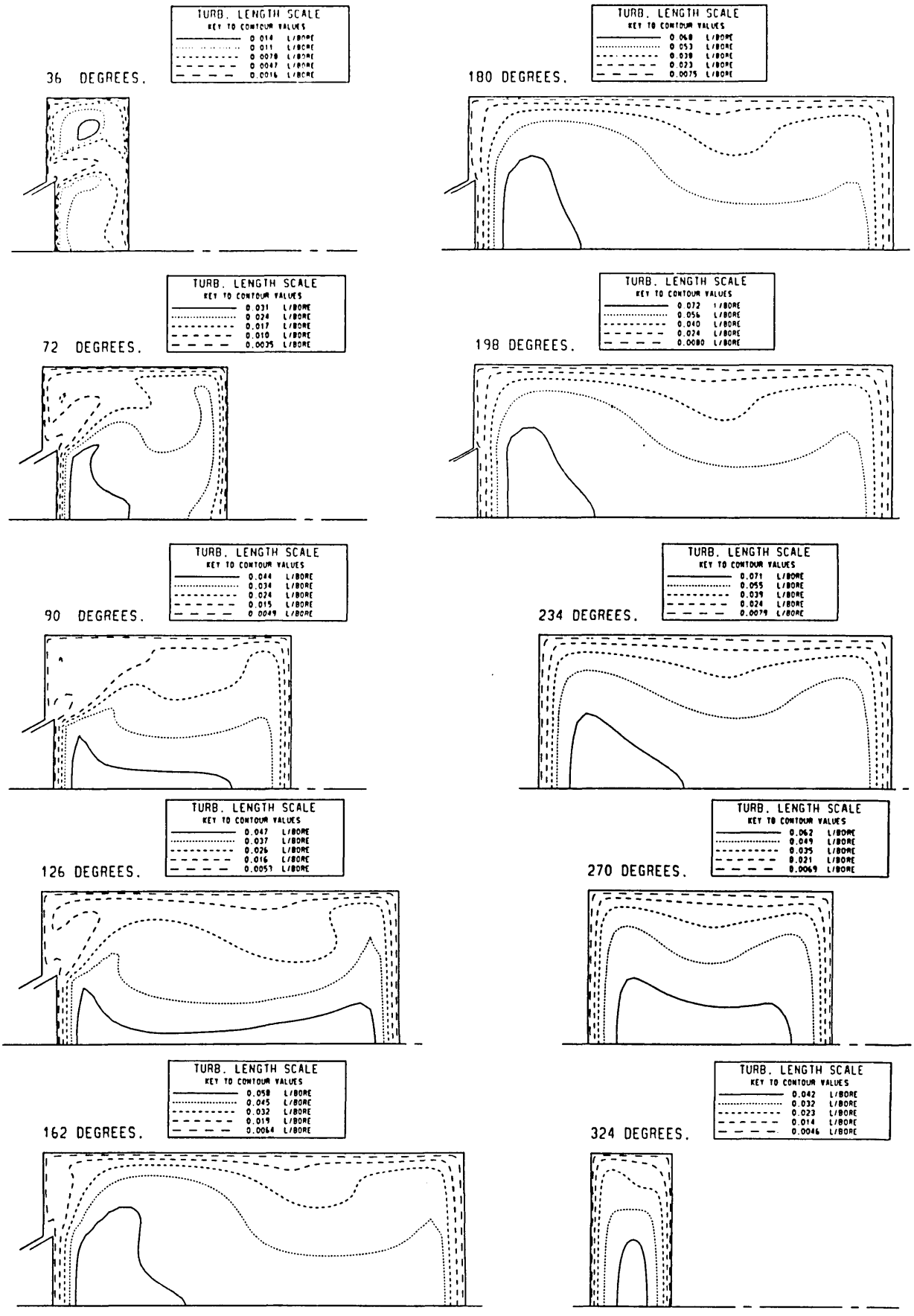


Figure 6.8(c): Predictions of the length scale distributions for the intake valve lift L_{max}/D = 0.14 (CR = 10.5, S = 200 rpm)

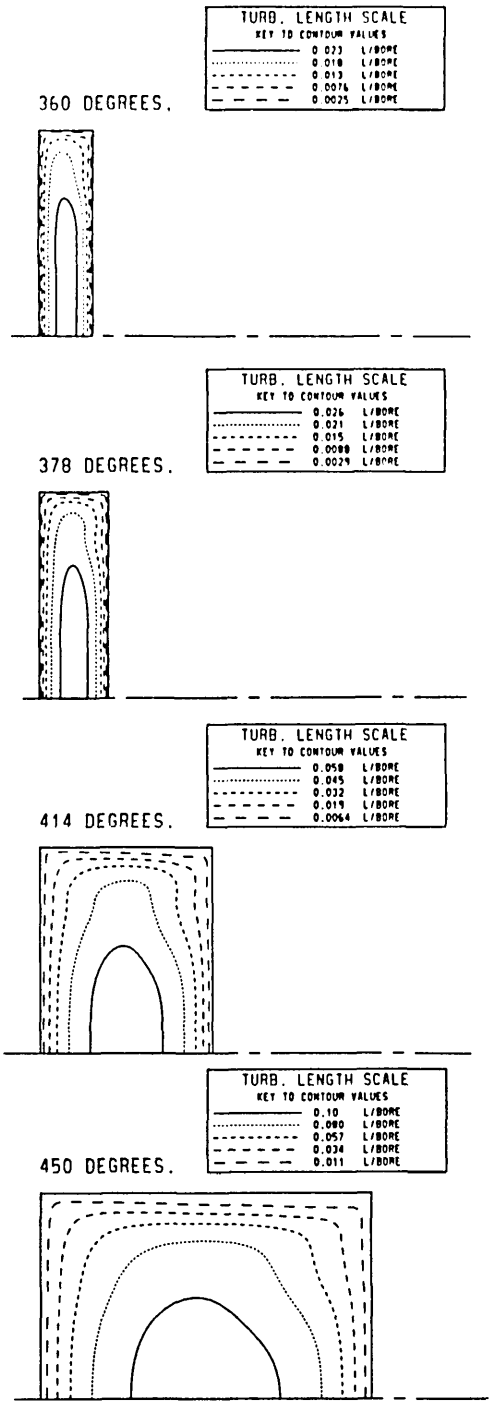


Figure 6.8(c): Continued

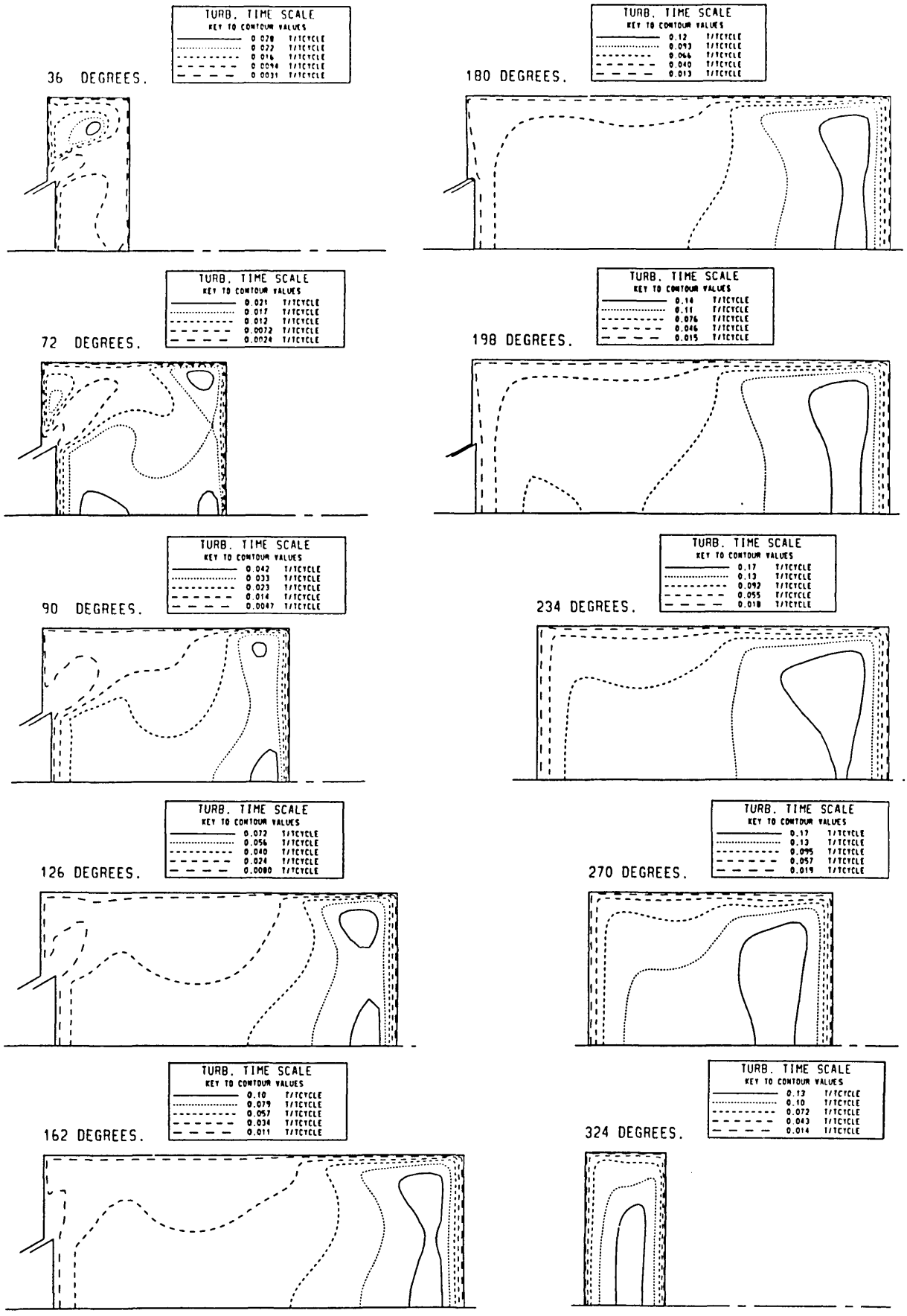


Figure 6.8(d): Predictions of the time-scale distributions for the intake valve lift L_{max}/D = 0.14 (CR = 10.5, S = 200 rpm)

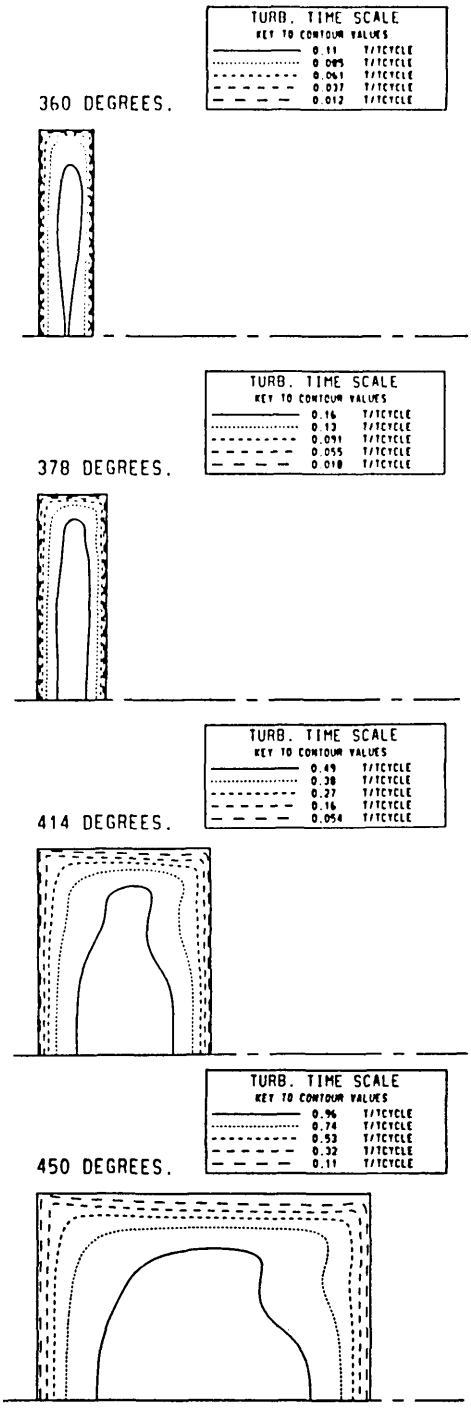


Figure 6.8(d): Continued

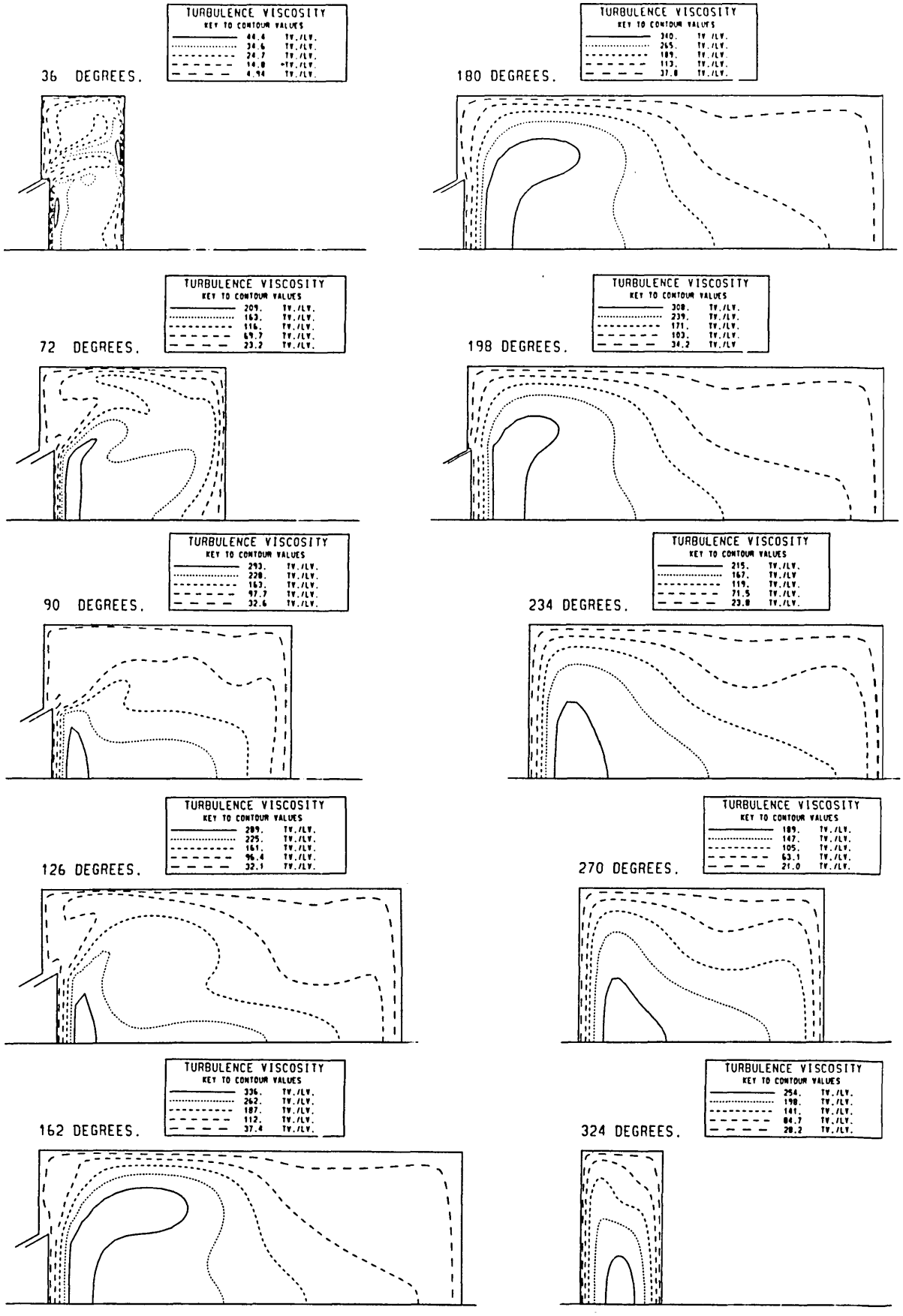


Figure 6.8(e): Predictions of the turbulent viscosity distributions for the intake valve lift L_{max}/D = 0.14 (CR = 10.5, S = 200 rpm)

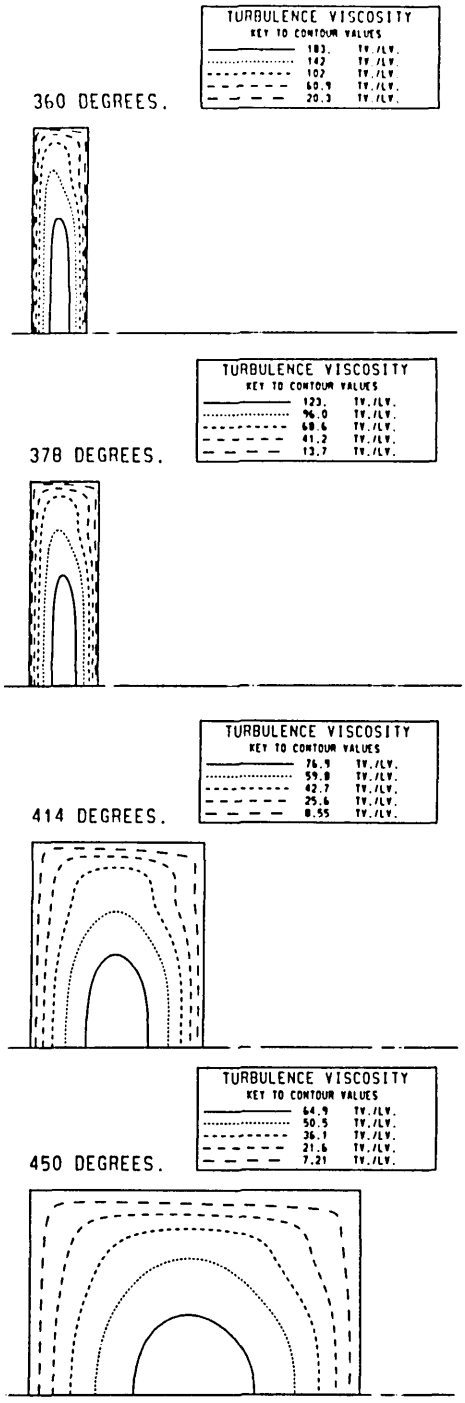


Figure 6.8(e): Continued

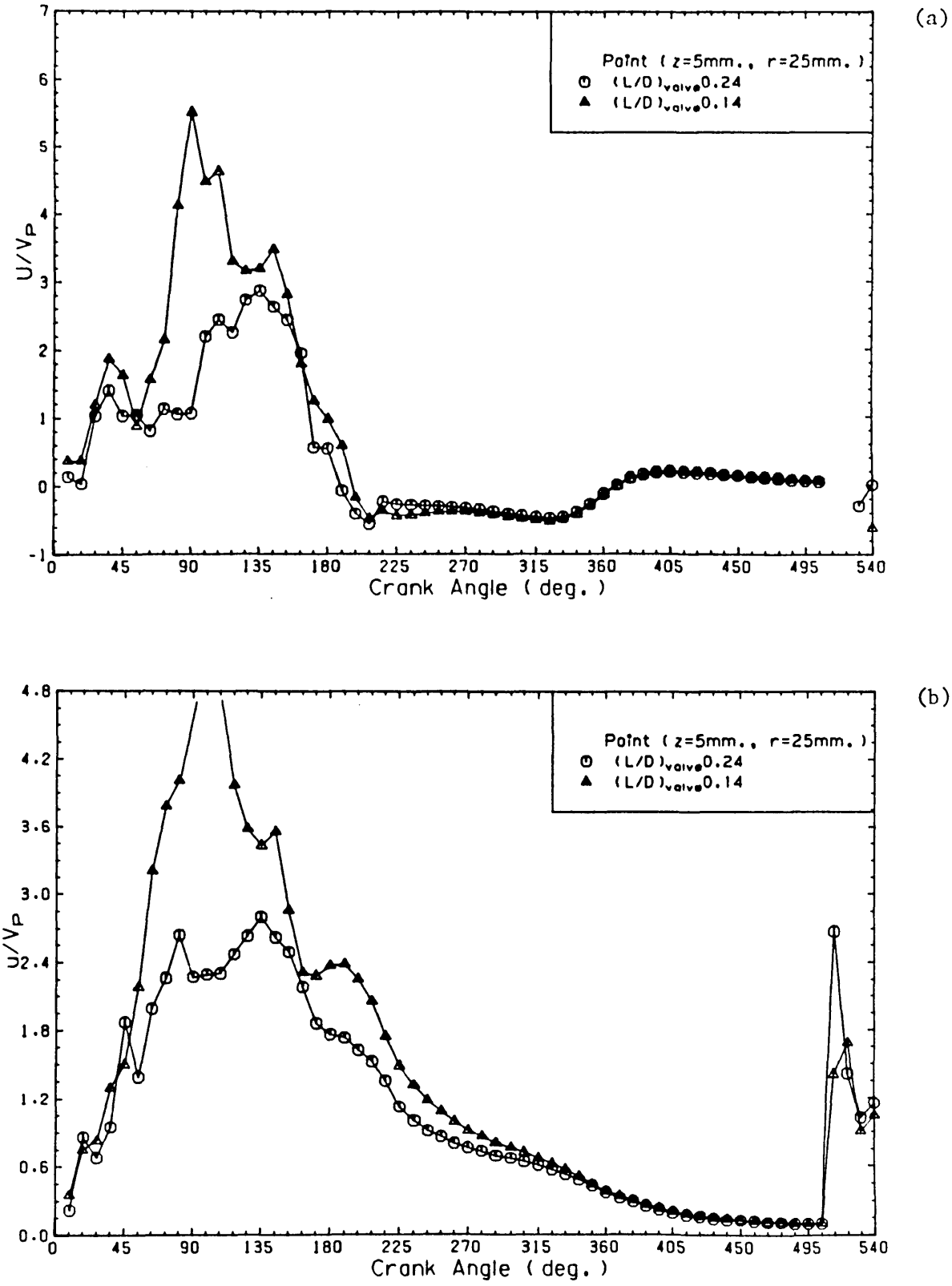
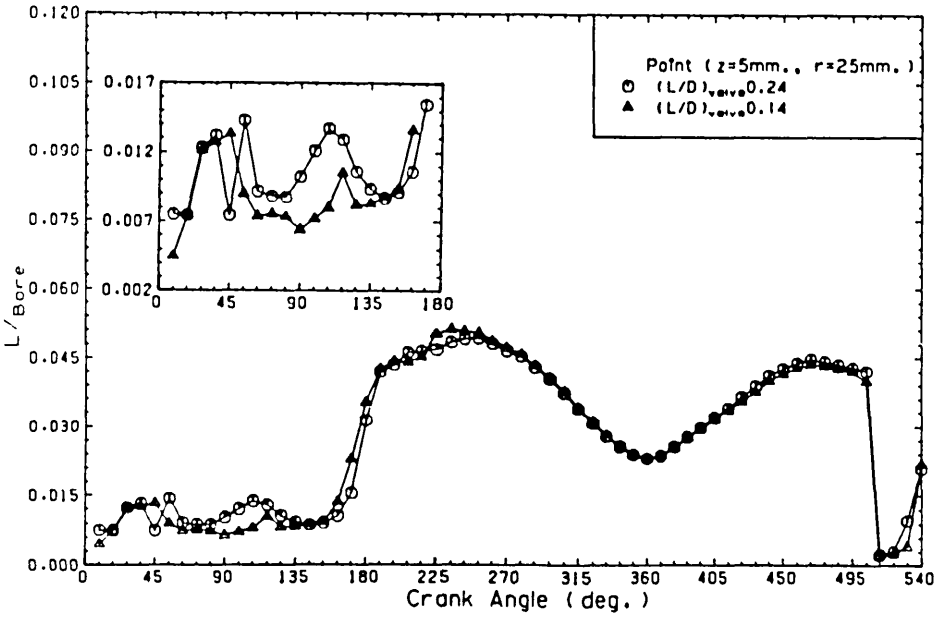
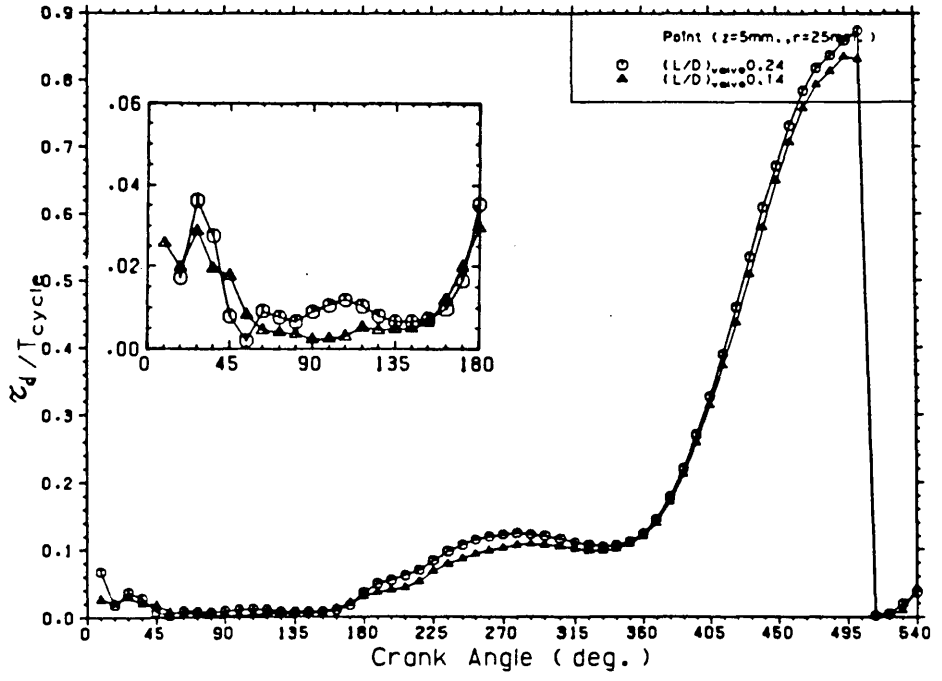


Figure 6.9: Influence of valve lift on the temporal variations of the mean axial velocity and turbulence parameters at a monitoring location





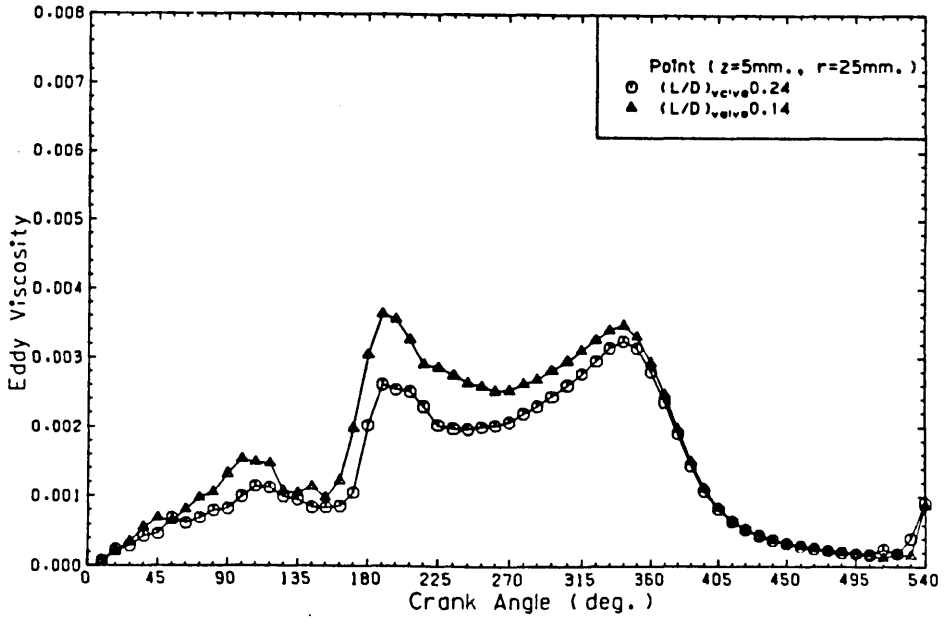


Figure 6.9: Continued

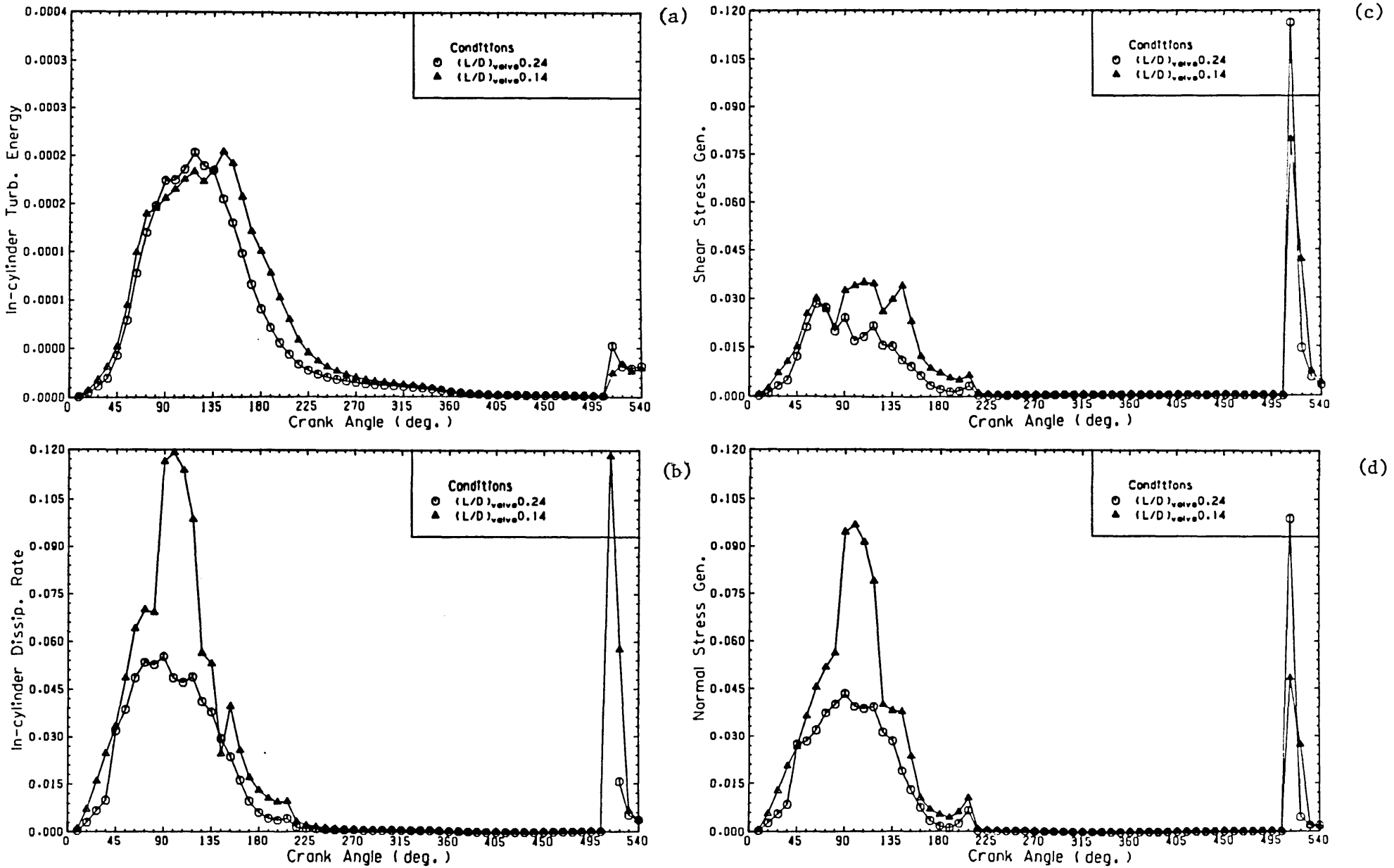


Figure 6.10: Influence of valve lift on the volume-integral turbulence energy K, dissipation rate E, G_S and G_N

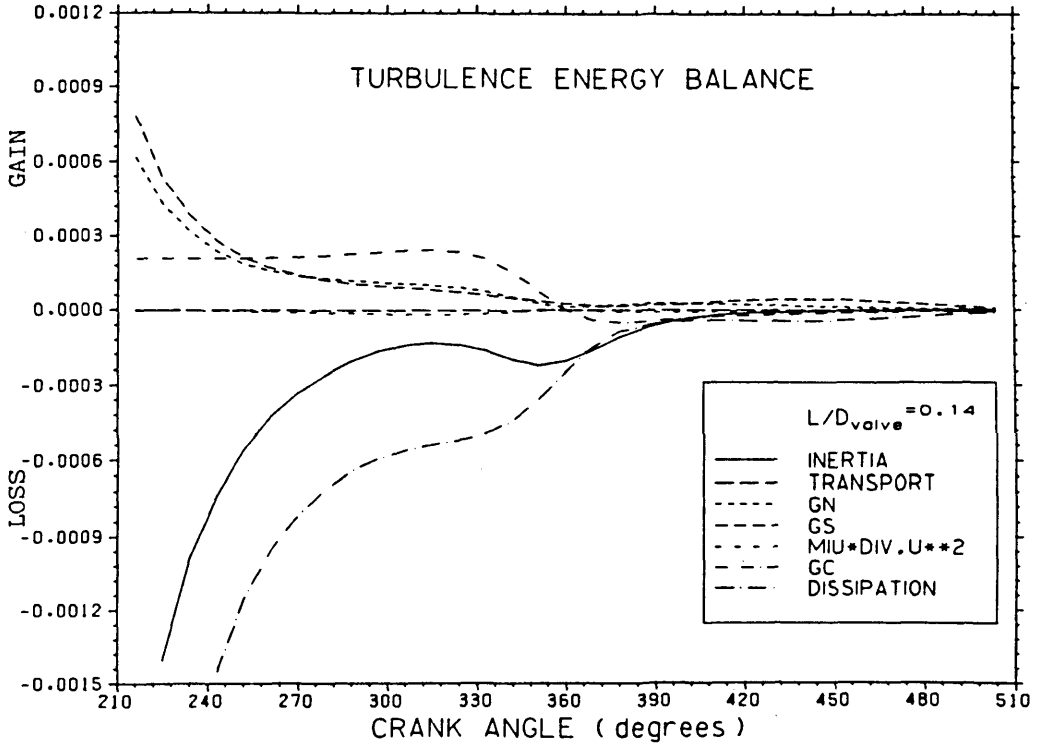
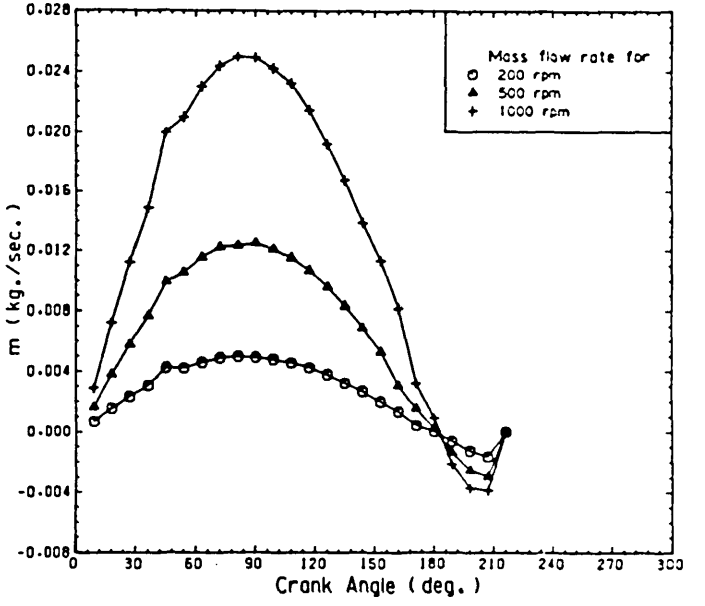


Figure 6.11: The volume-integral balance of the k-transport equation for the valve lift L_{max}/D = 0.14

(a)



(b)

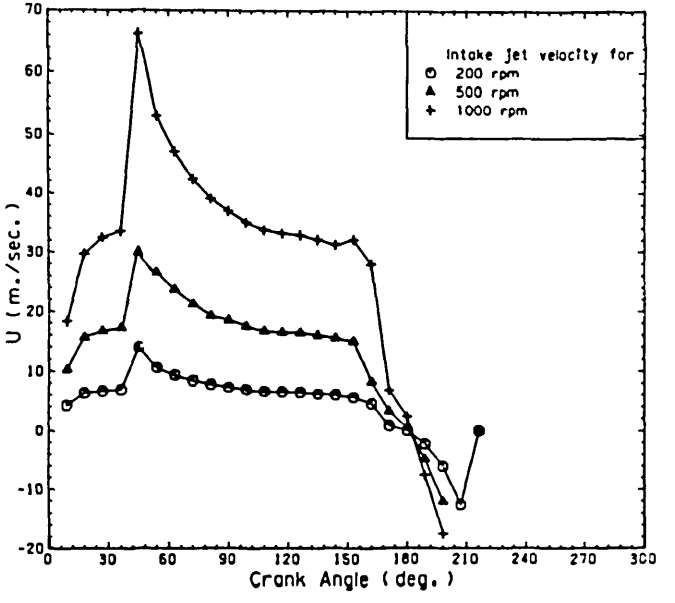
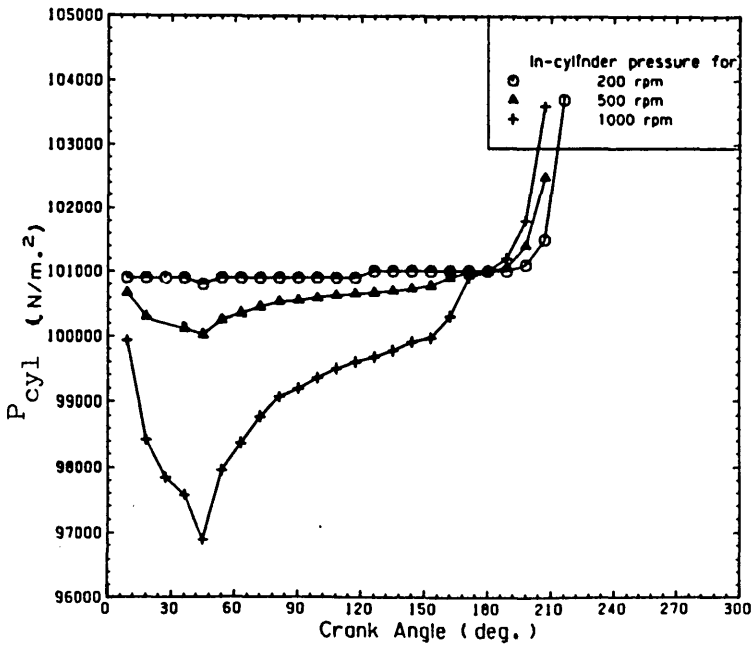


Figure 6.12: The influence of engine speed on (a) intake mass flow rate, (b) inlet velocity and (c) mean cylinder pressure



(c)

Figure 6.12: Continued

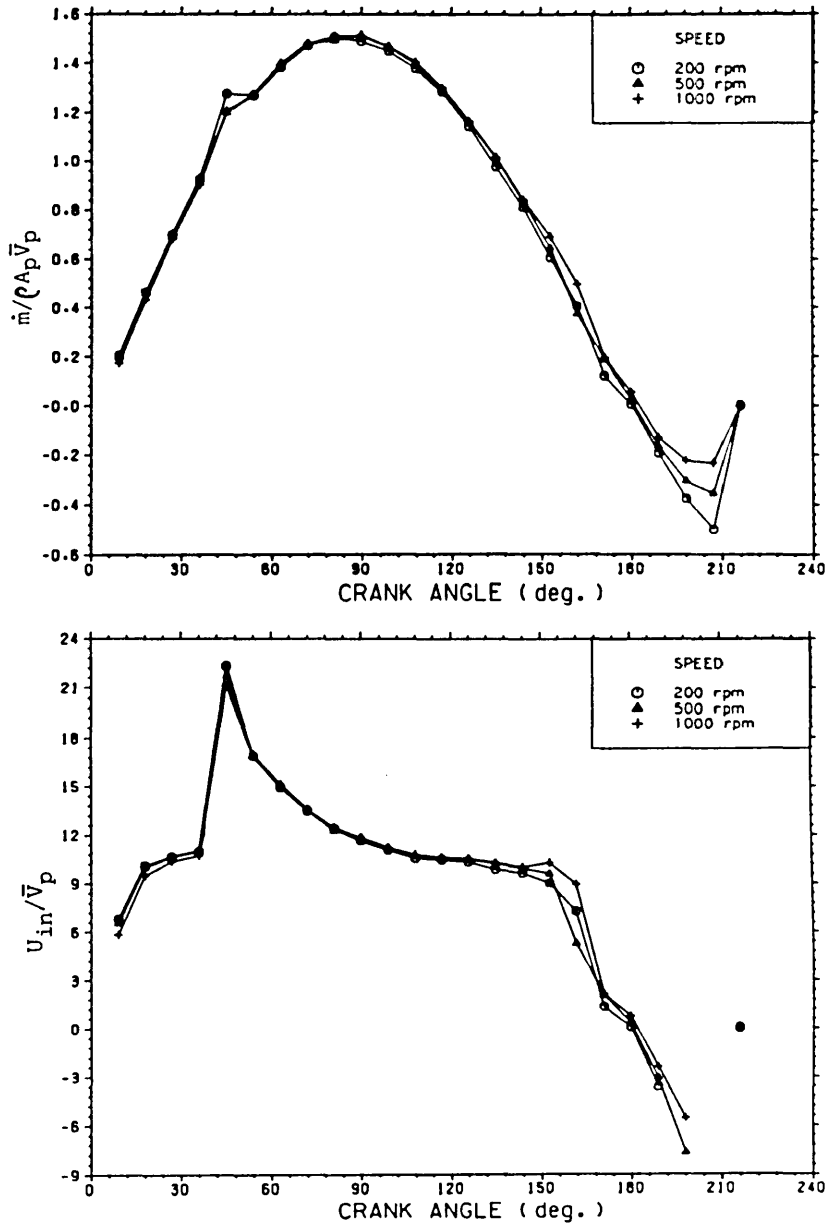


Figure 6.13: The influence of engine speed on the normalised intake mass flow rate and inlet velocity

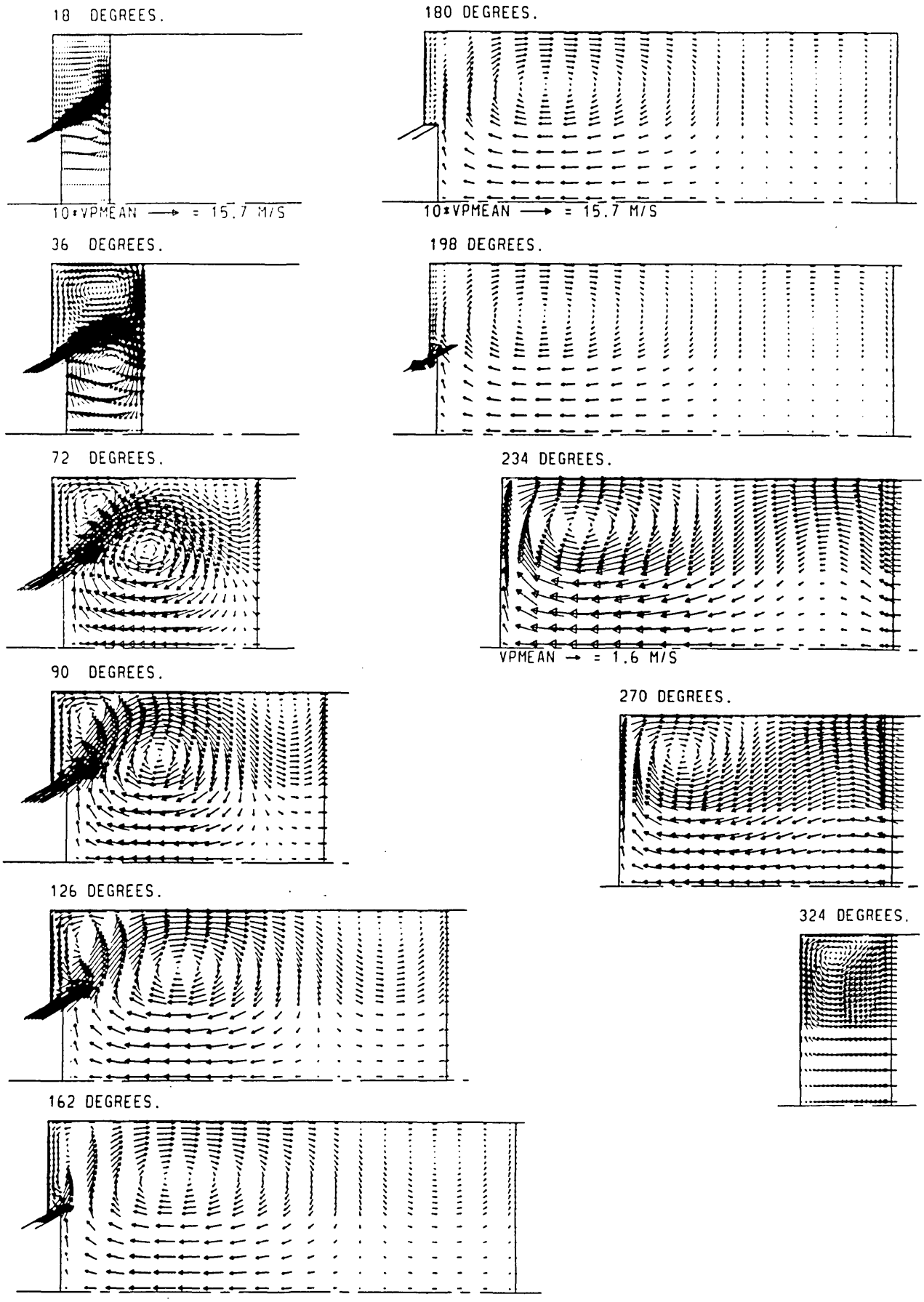


Figure 6.14(a): Predictions of the velocity field for operating condition CR = 10.5 and S = 500 rpm

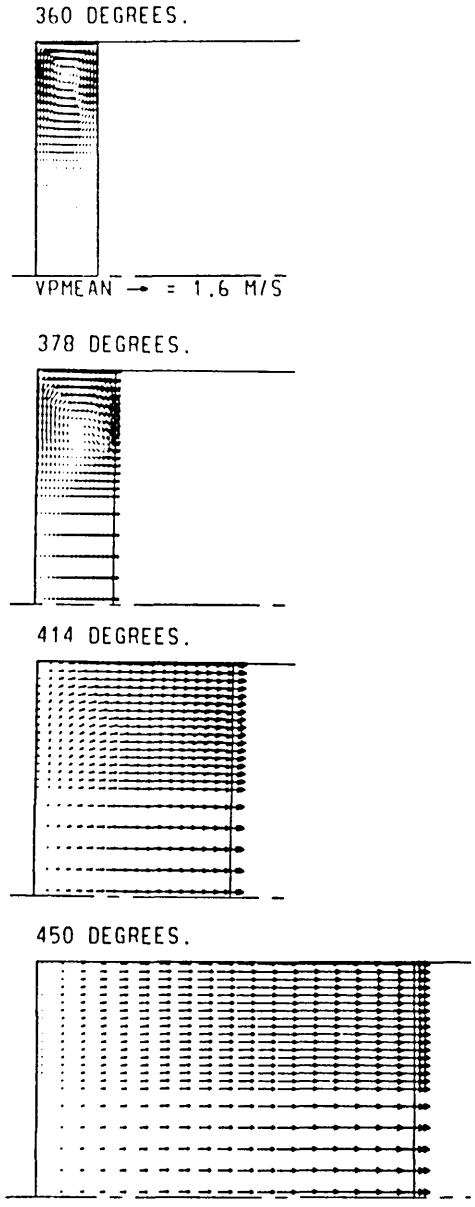


Figure 6.14(a): Continued

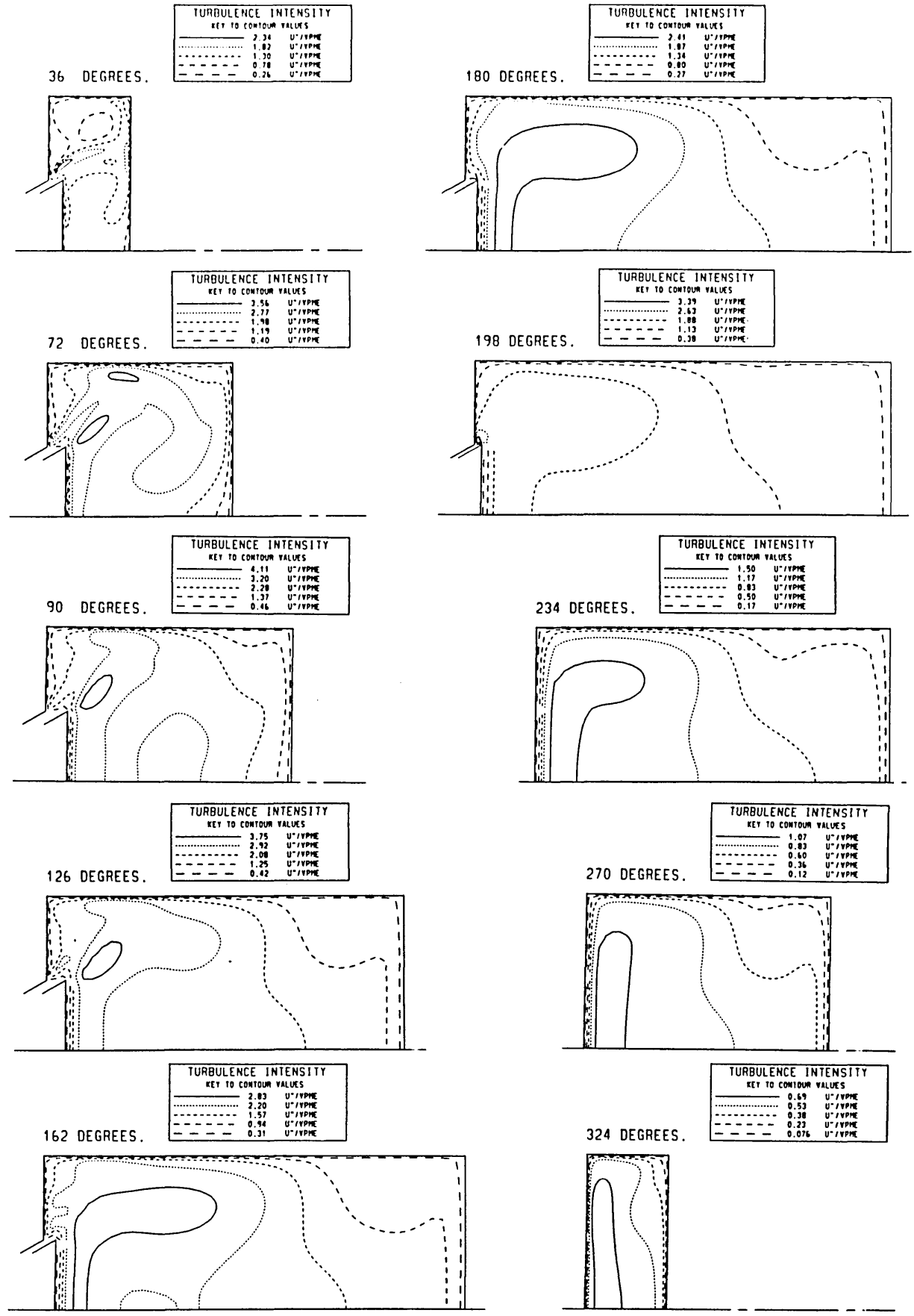


Figure 6.14(b): Predictions of the turbulence intensity distribution for operating condition CR = 10.5 and S = 500 rpm

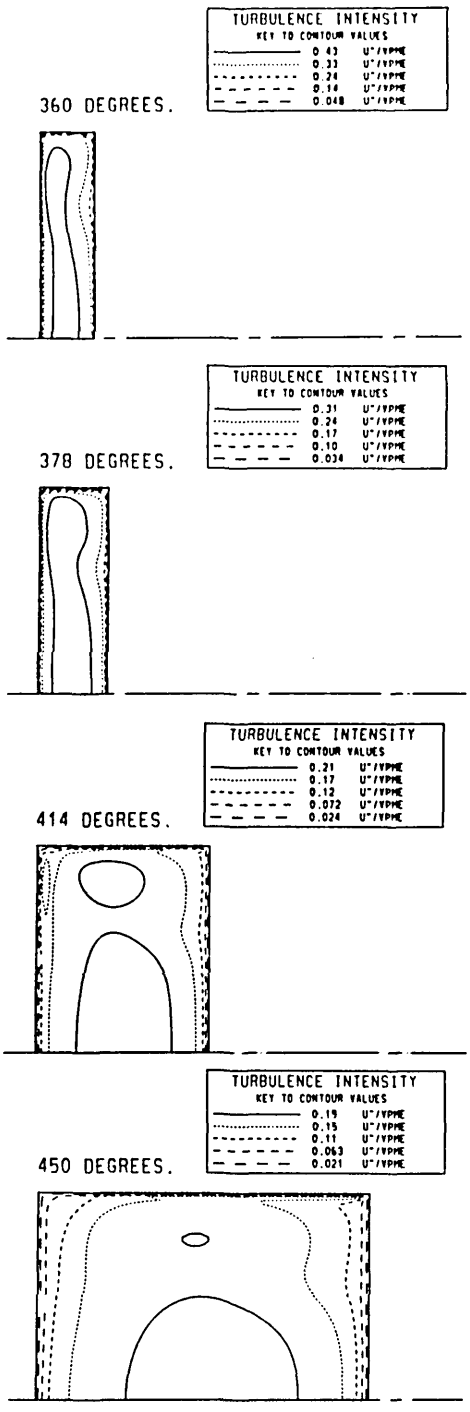


Figure 6.14(b): Continued

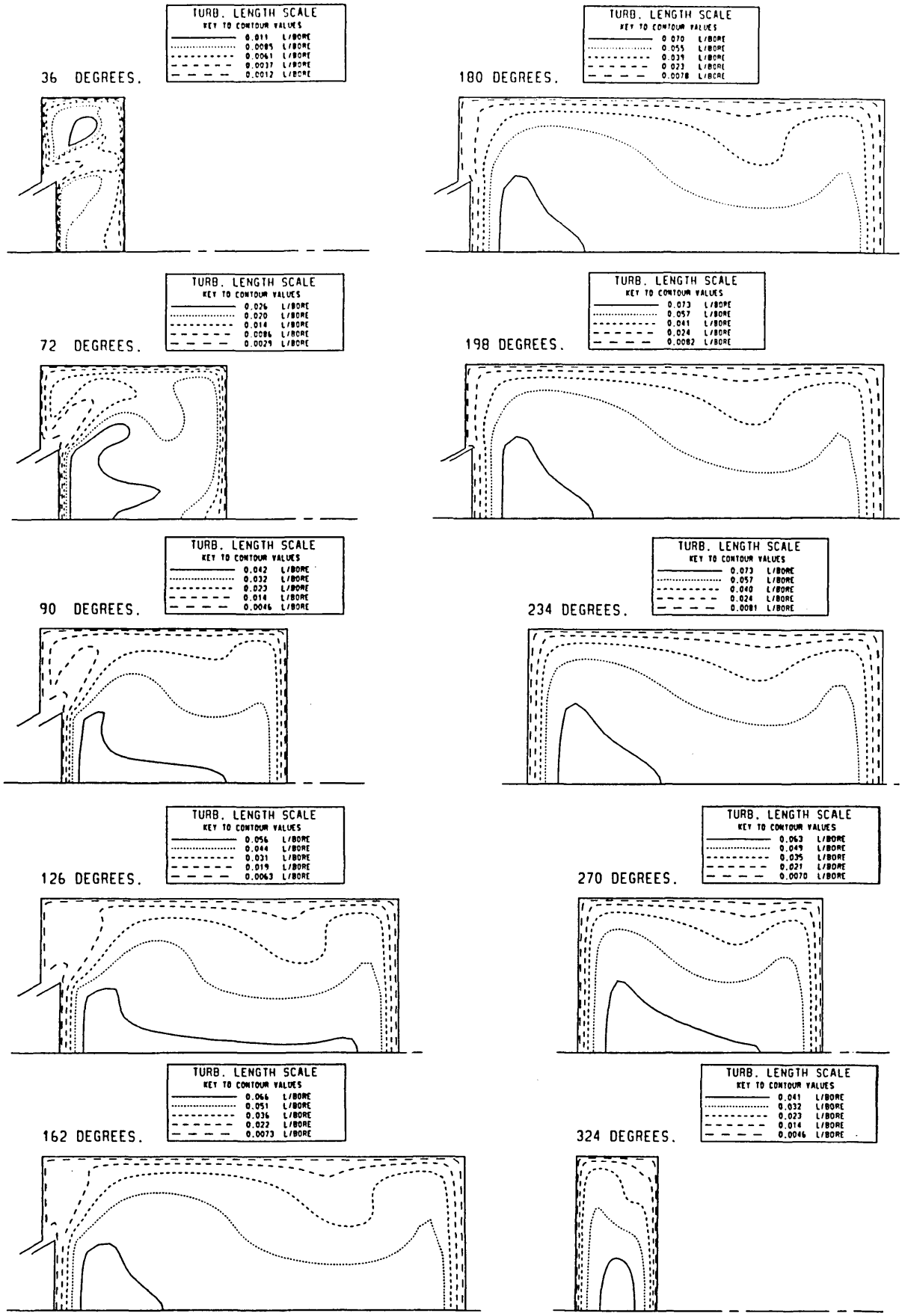


Figure 6.14(c): Predictions of the length scale distribution for operating condition CR = 10.5 and S = 500 rpm

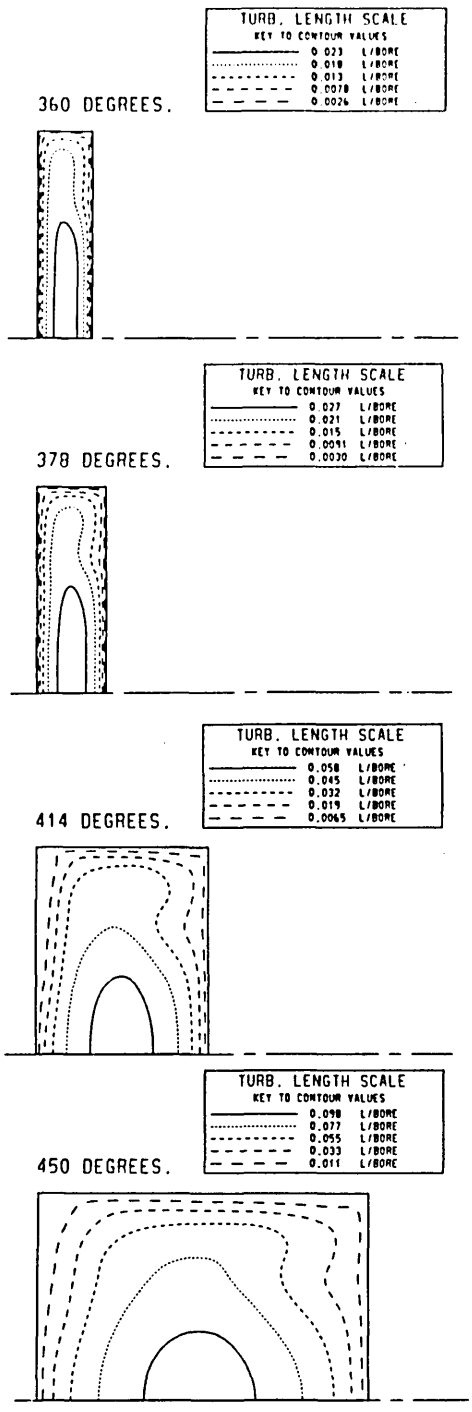


Figure 6.14(c): Continued

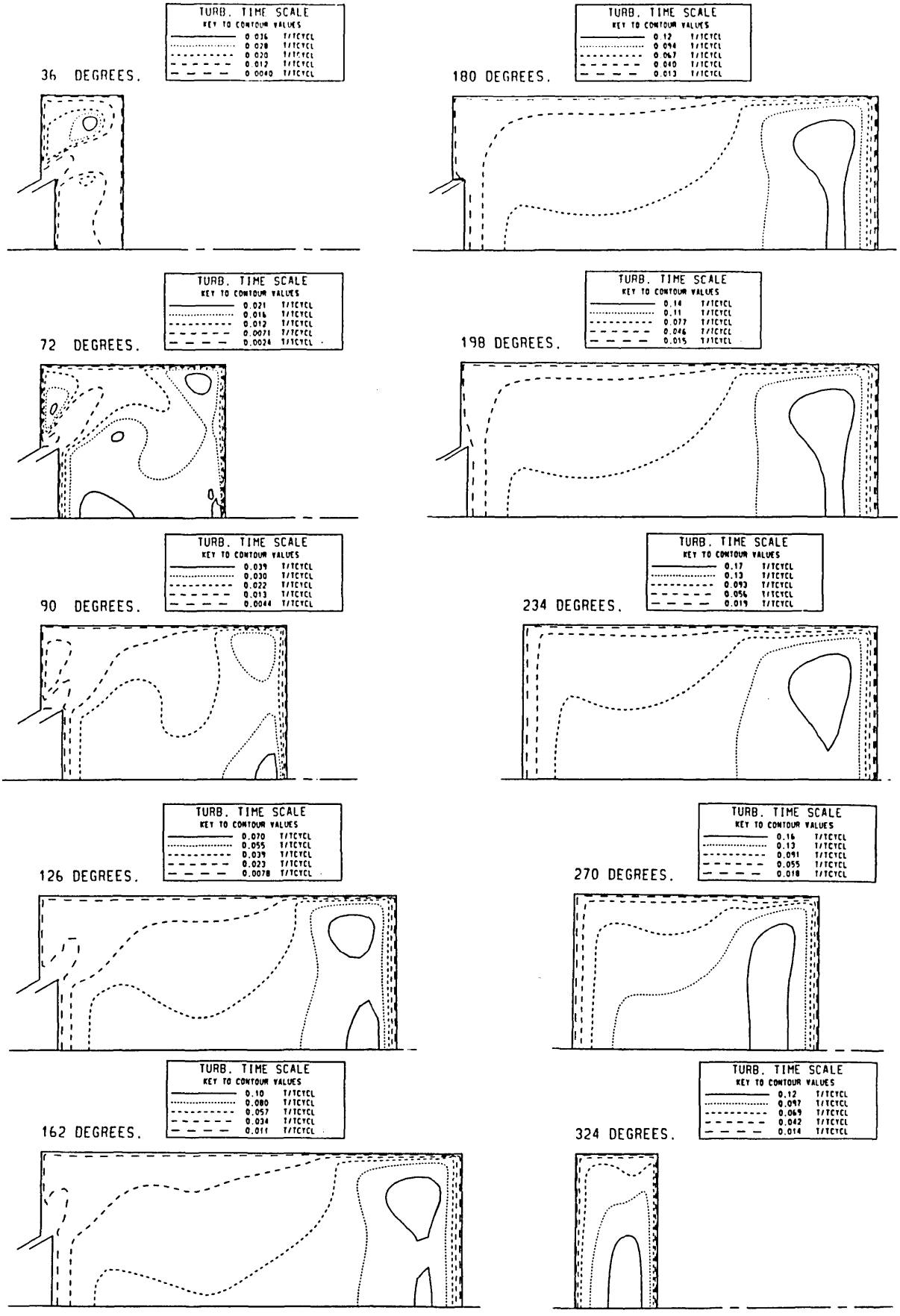


Figure 6.14(d): Predictions of the dissipation time-scale distribution for operating condition CR = 10.5 and S = 500 rpm

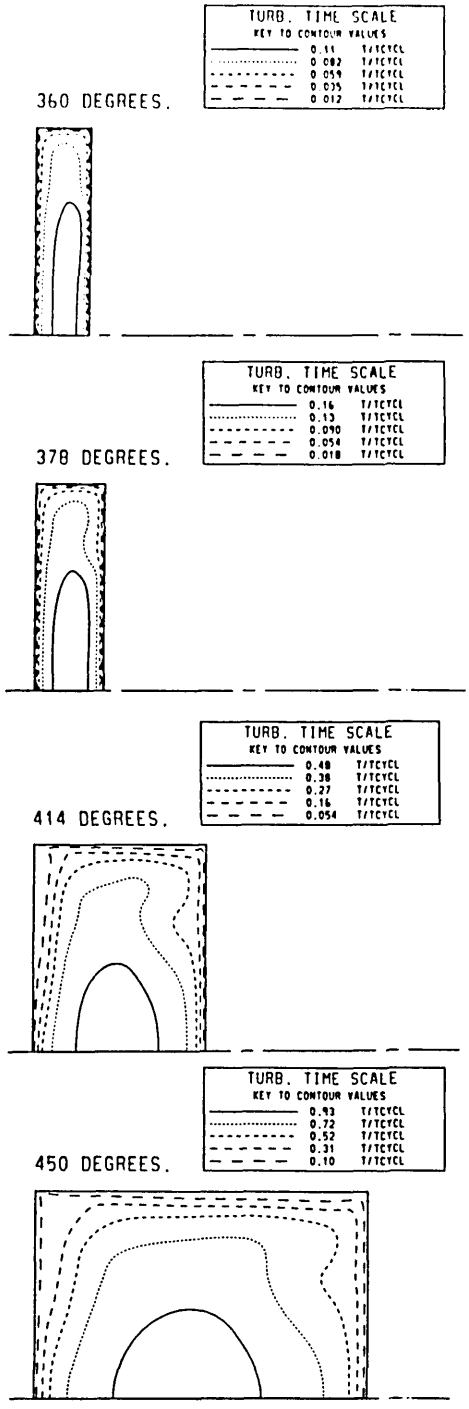


Figure 6.14(d): Continued

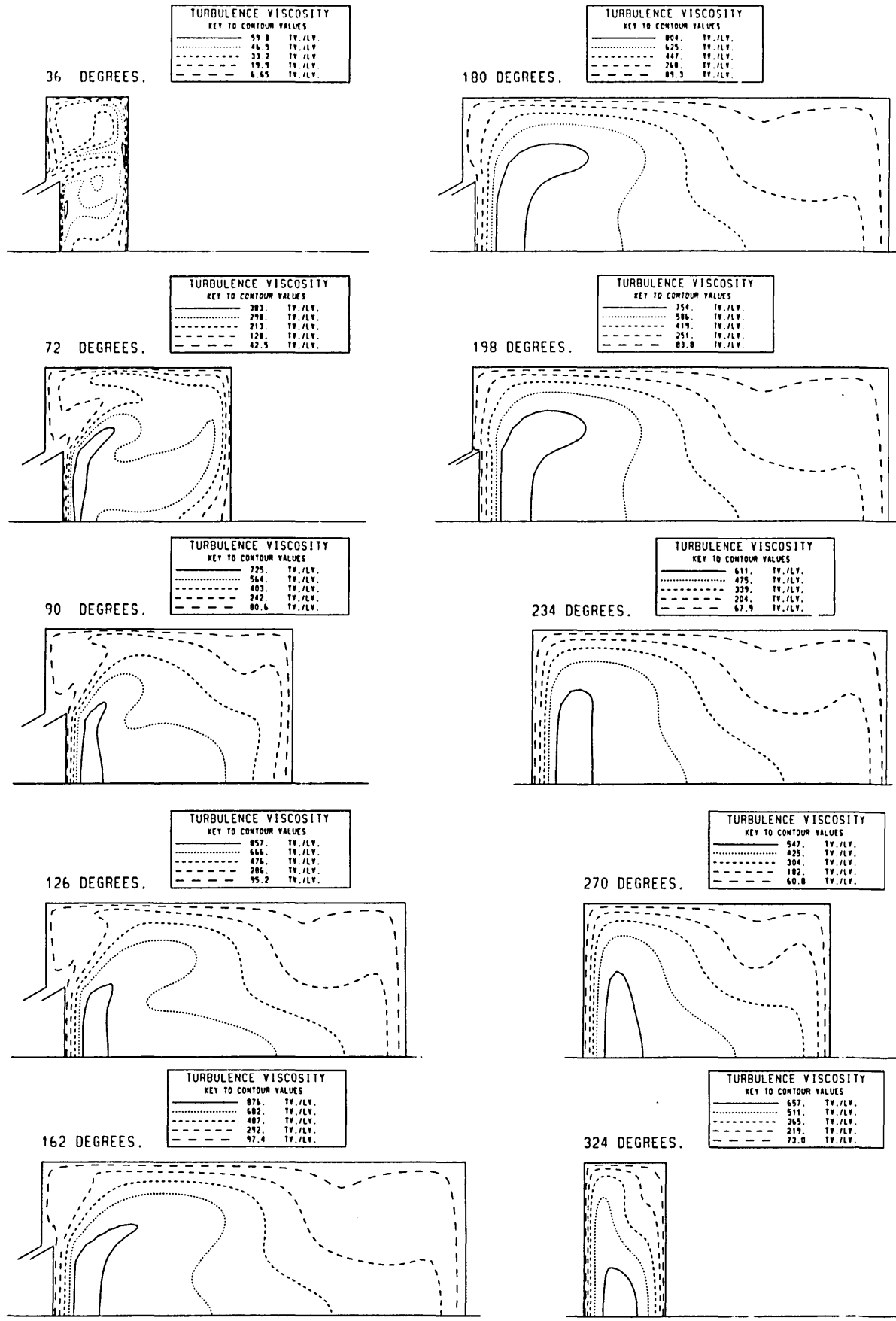


Figure 6.14(e): Predictions of the turbulent viscosity distribution for operating condition CR = 10.5 and S = 500 rpm

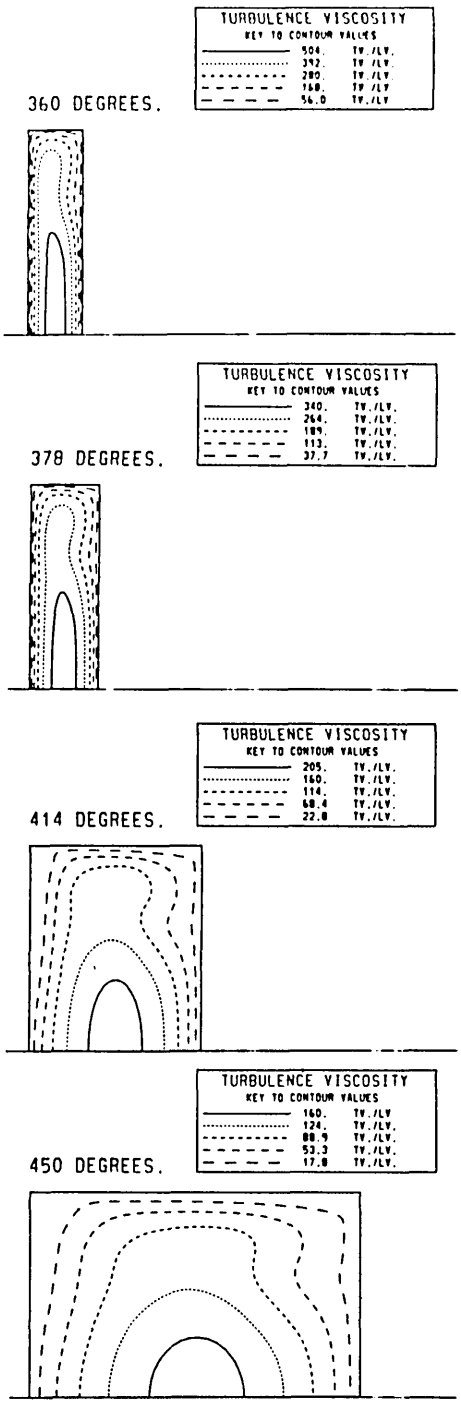


Figure 6.14(e): Continued

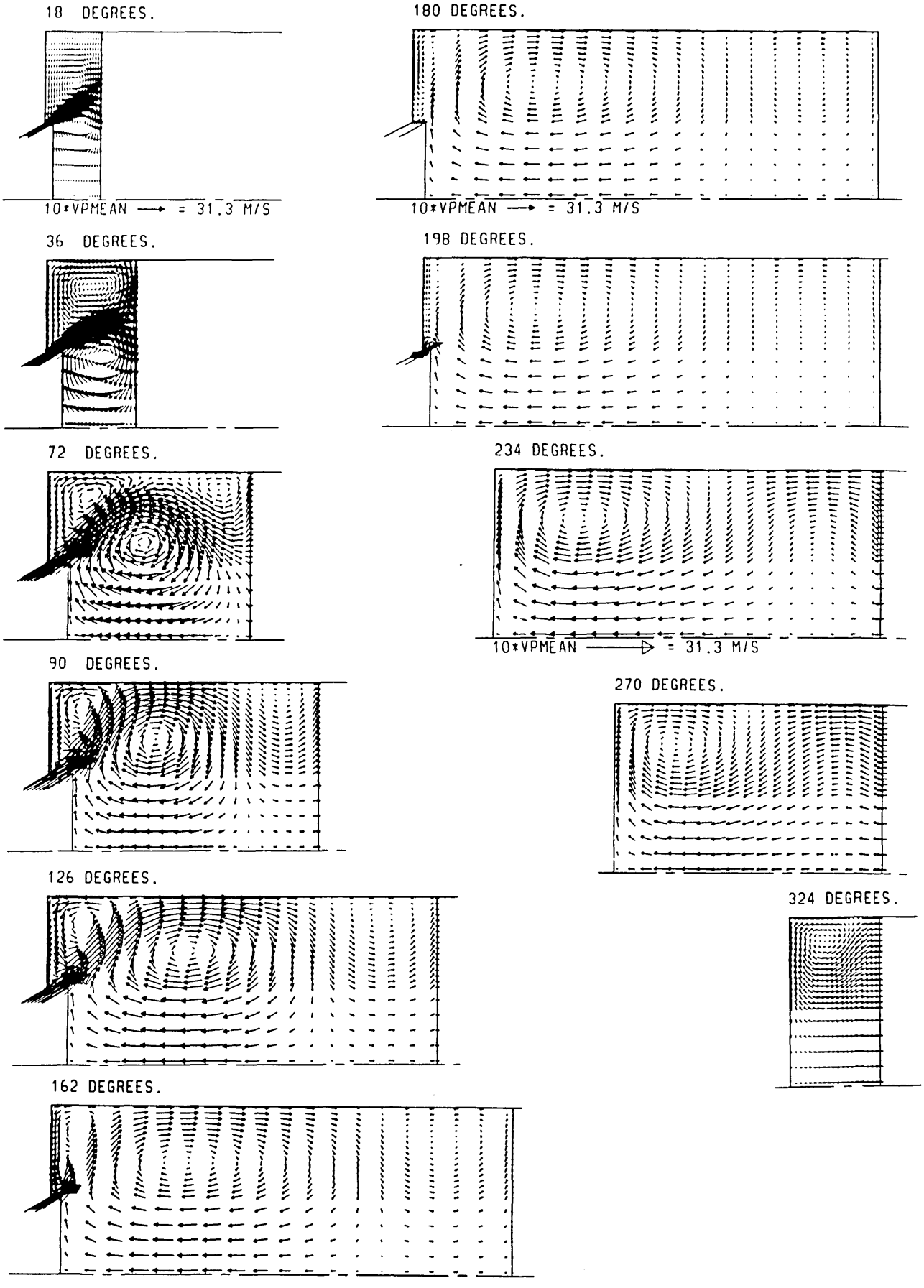


Figure 6.15(a): Predictions of the velocity field for operating condition CR = 10.5 and S = 1000 rpm

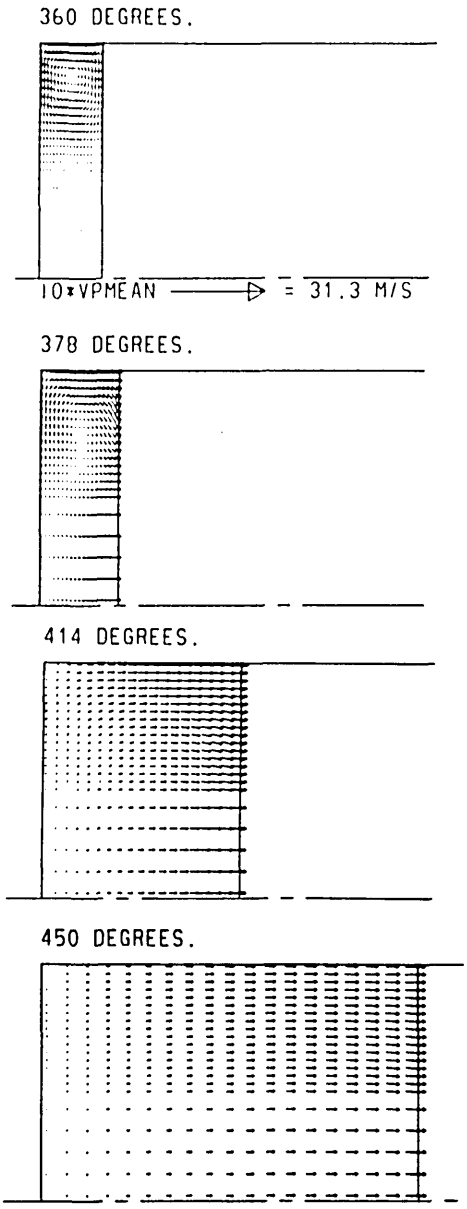


Figure 6.15(a): Continued

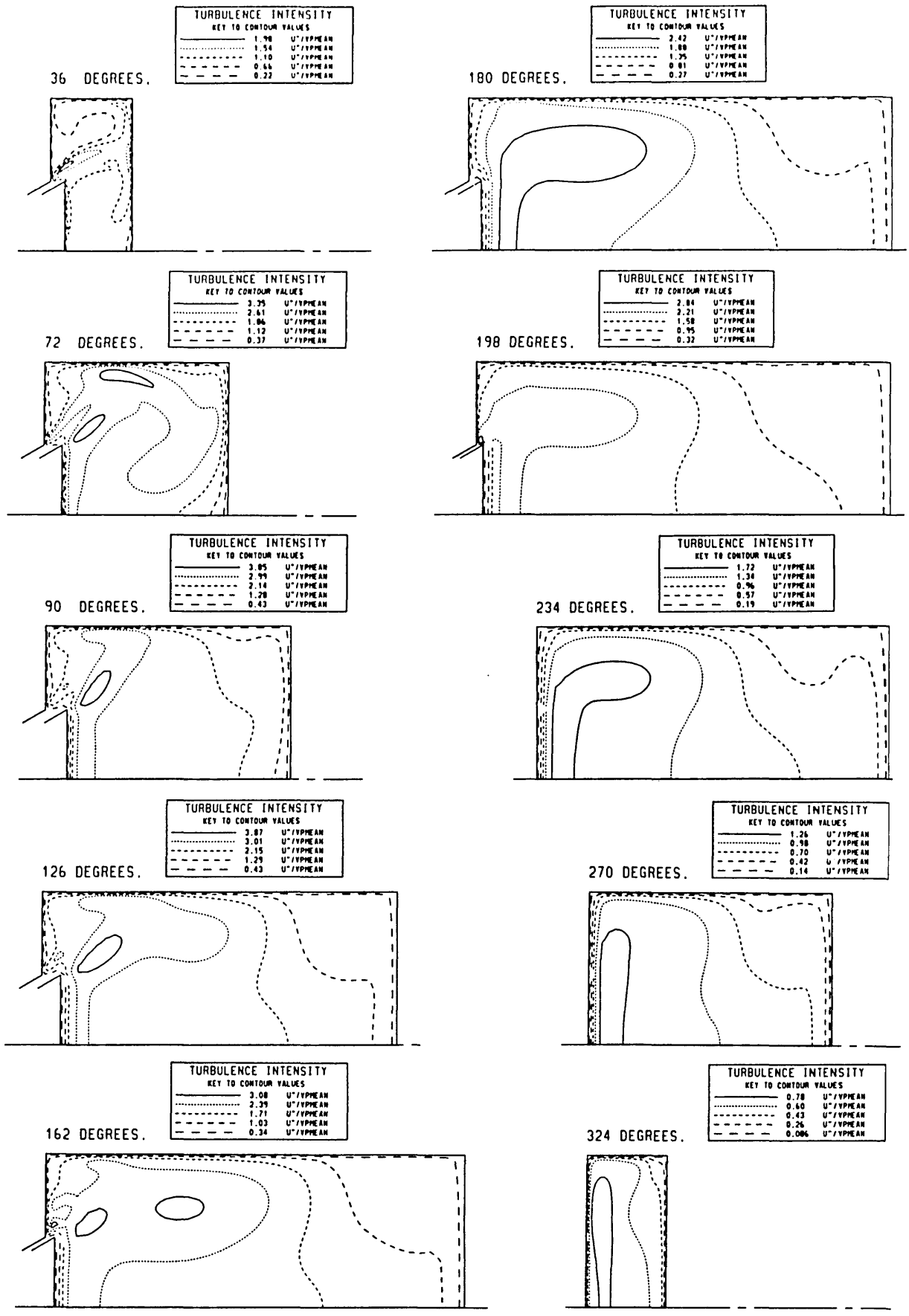


Figure 6.15(b): Predictions of the turbulence intensity distribution for operating condition CR = 10.5 and S = 1000 rpm

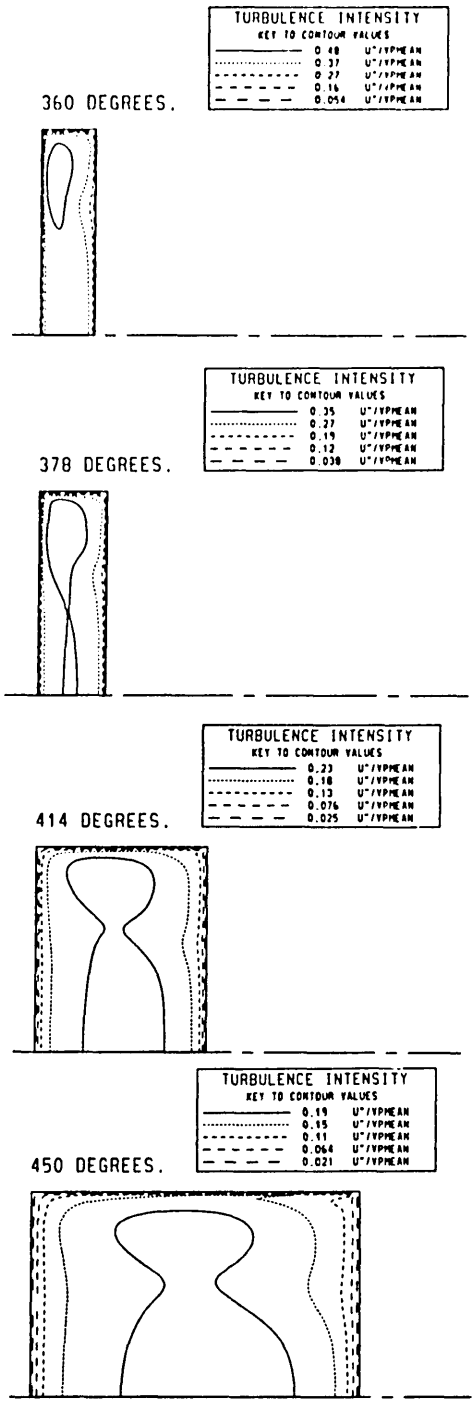


Figure 6.15(b): Continued

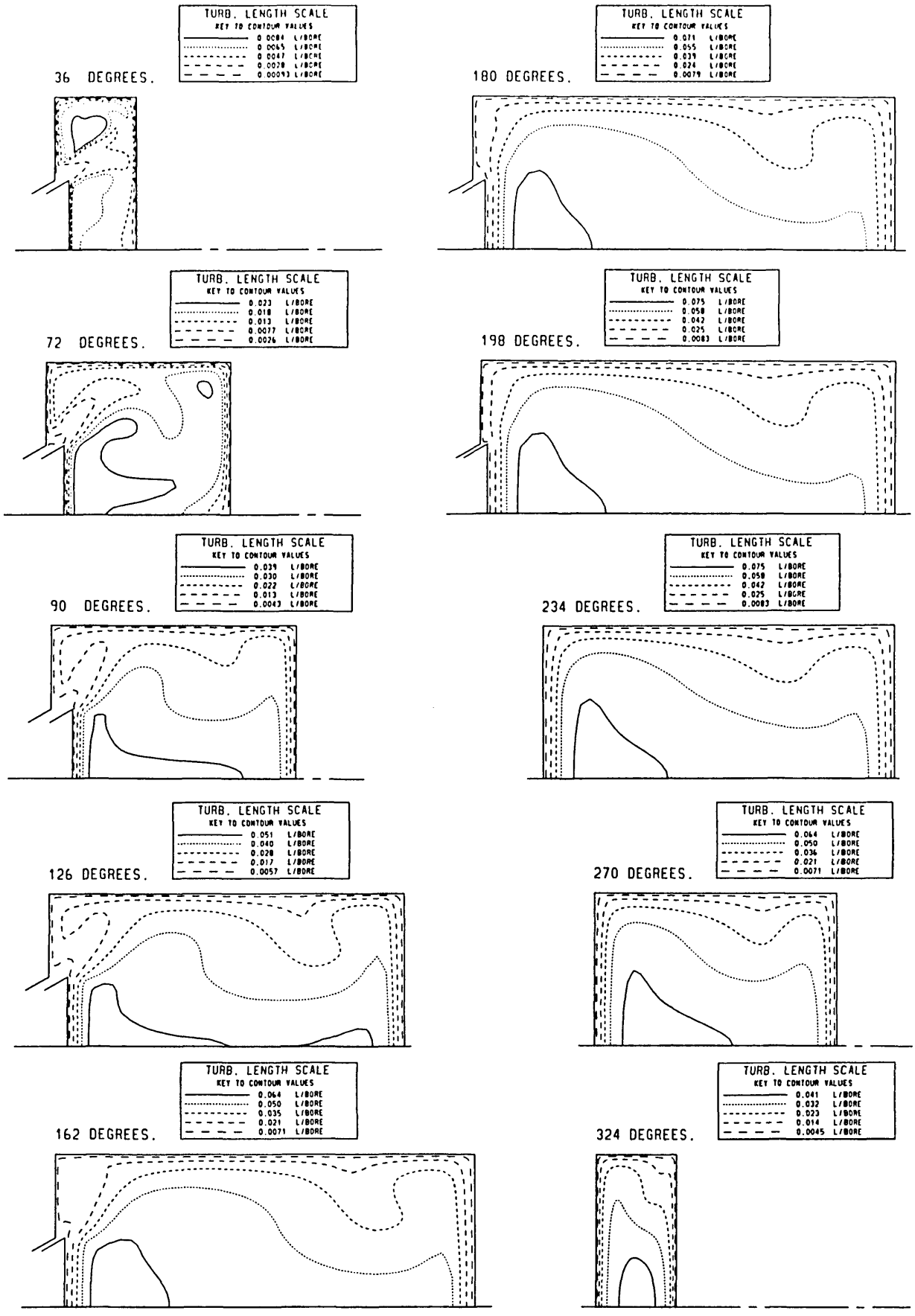


Figure 6.15(c): Predictions of the length scale distribution for operating condition CR = 10.5 and S = 1000 rpm

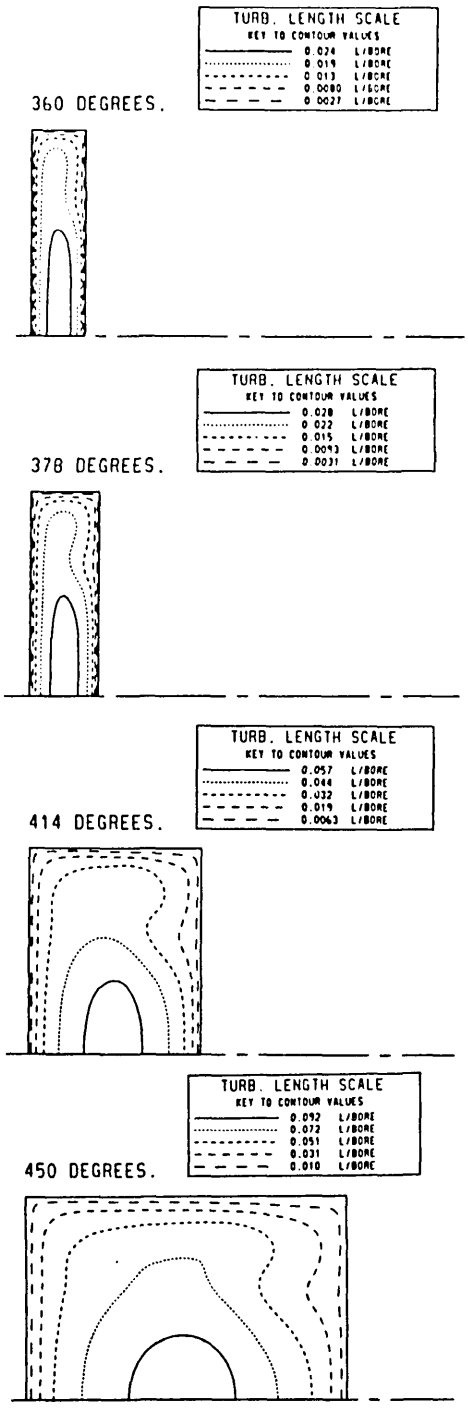


Figure 6.15(c): Continued

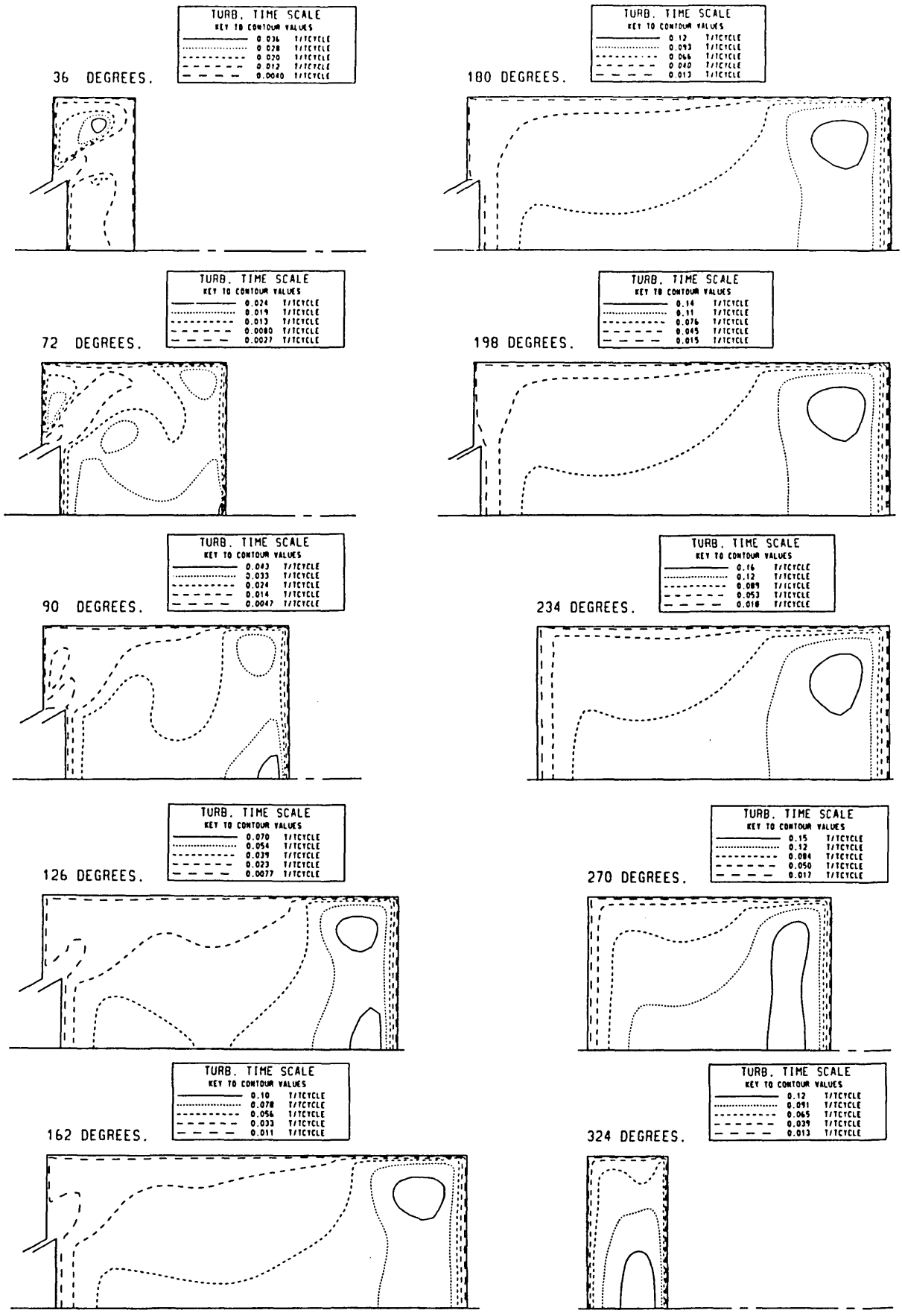


Figure 6.15(d): Predictions of the dissipation time scale distribution for operating condition CR = 10.5 and S = 1000 rpm

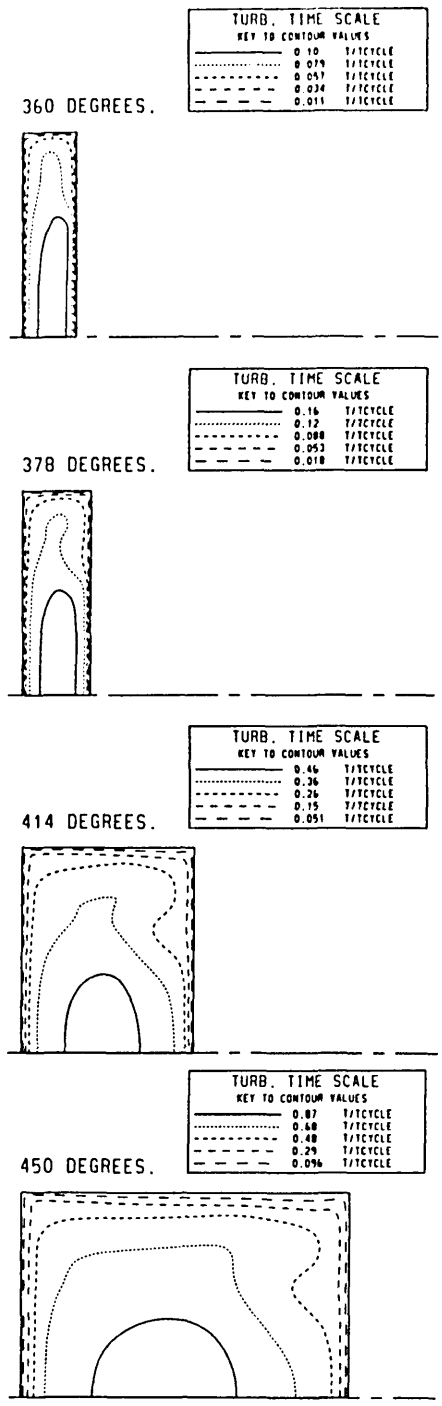


Figure 6.15(d): Continued

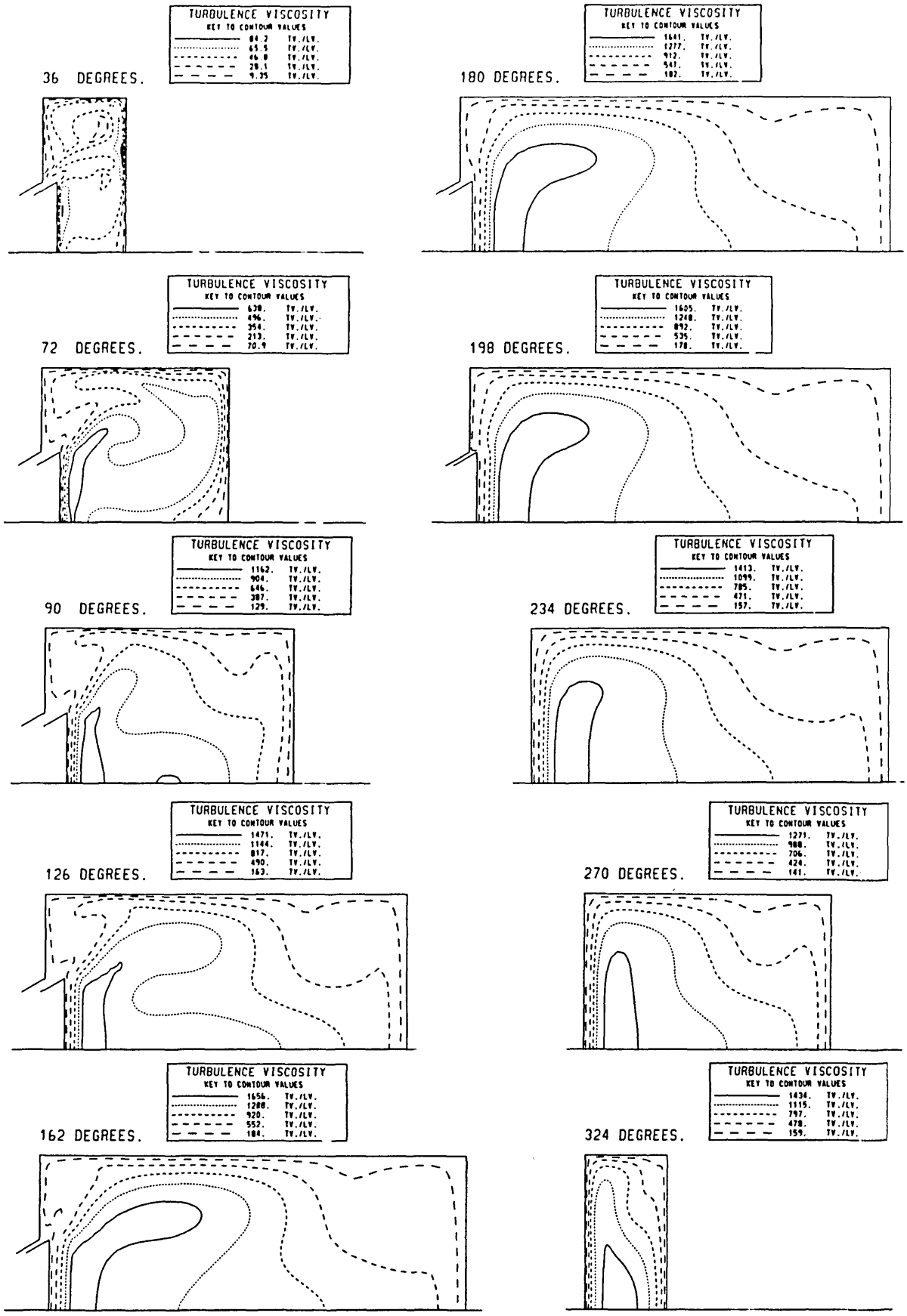


Figure 6.15(e): Predictions of the turbulent viscosity distributions for operating condition CR = 10.5 and S = 1000 rpm

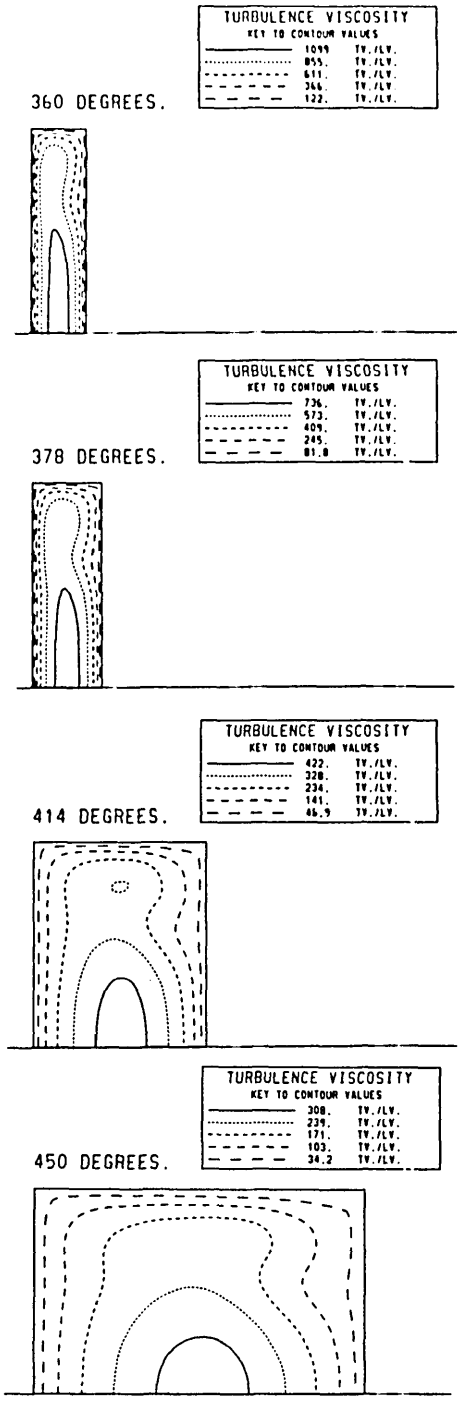
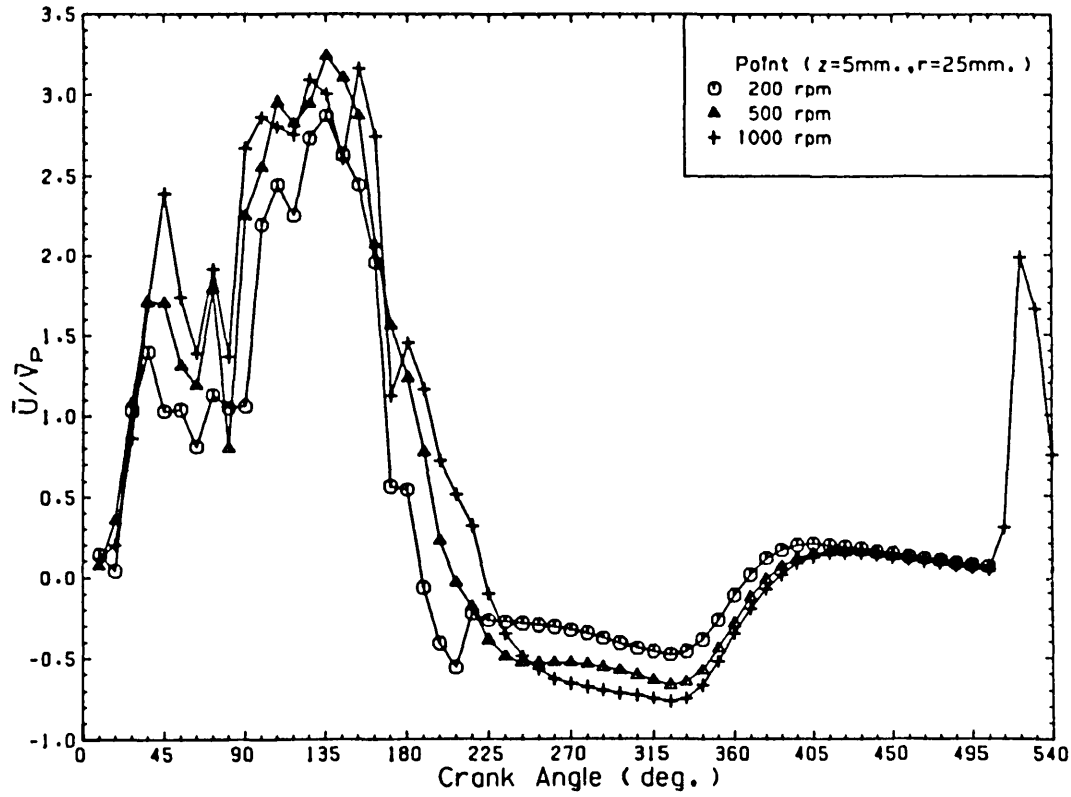


Figure 6.15(e): Continued



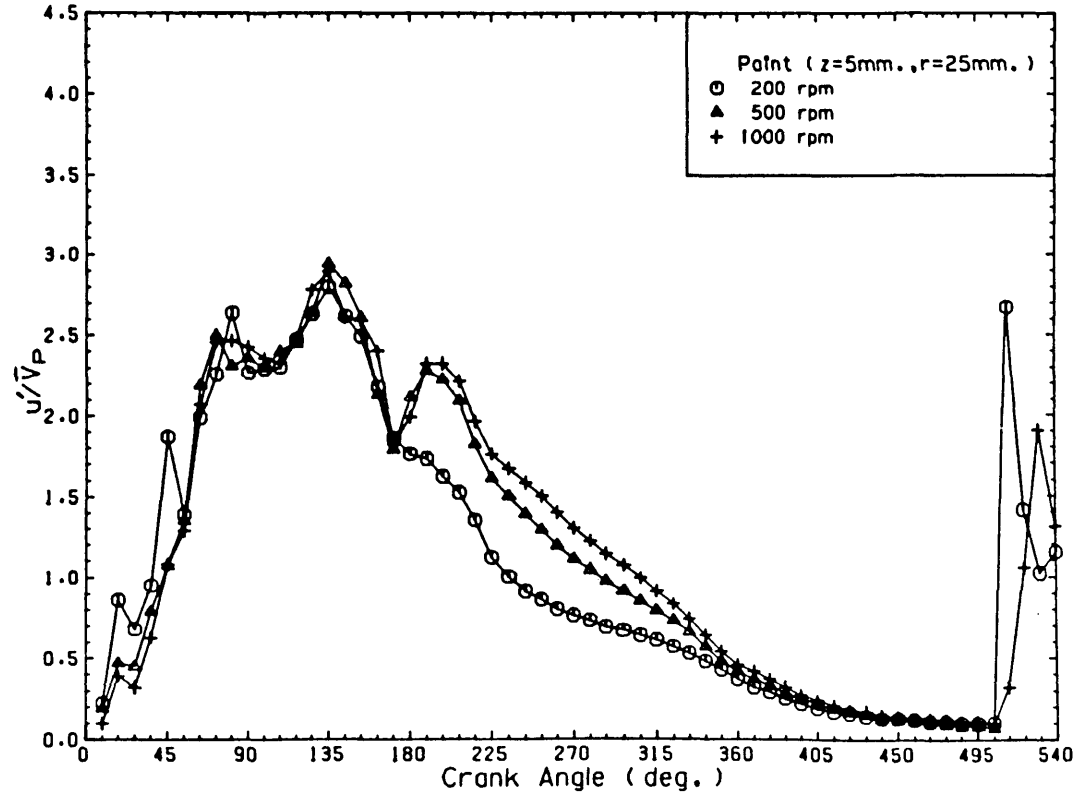
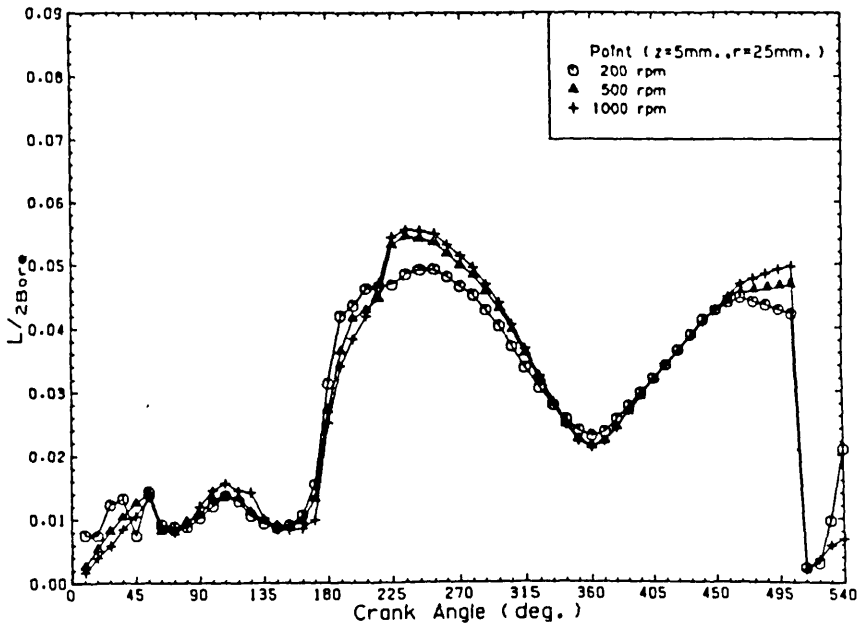
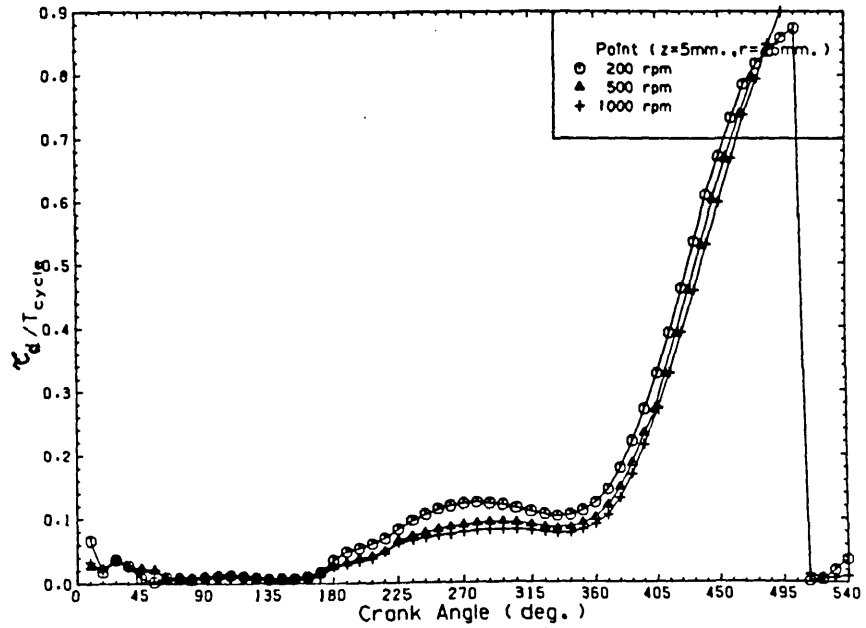


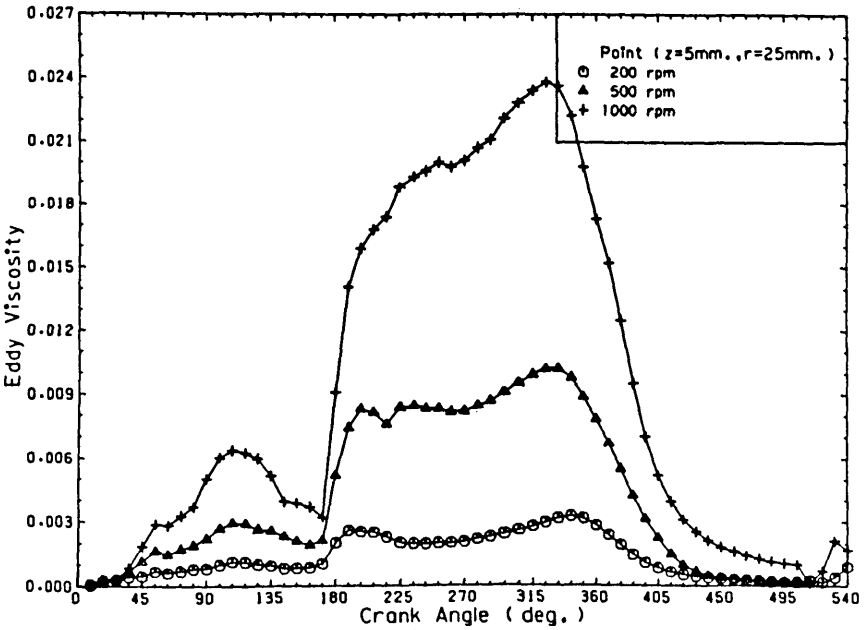
Figure 6.16: Influence of engine speed on the temporal variations of the mean axial velocity and turbulence parameters at a monitoring location



(c)

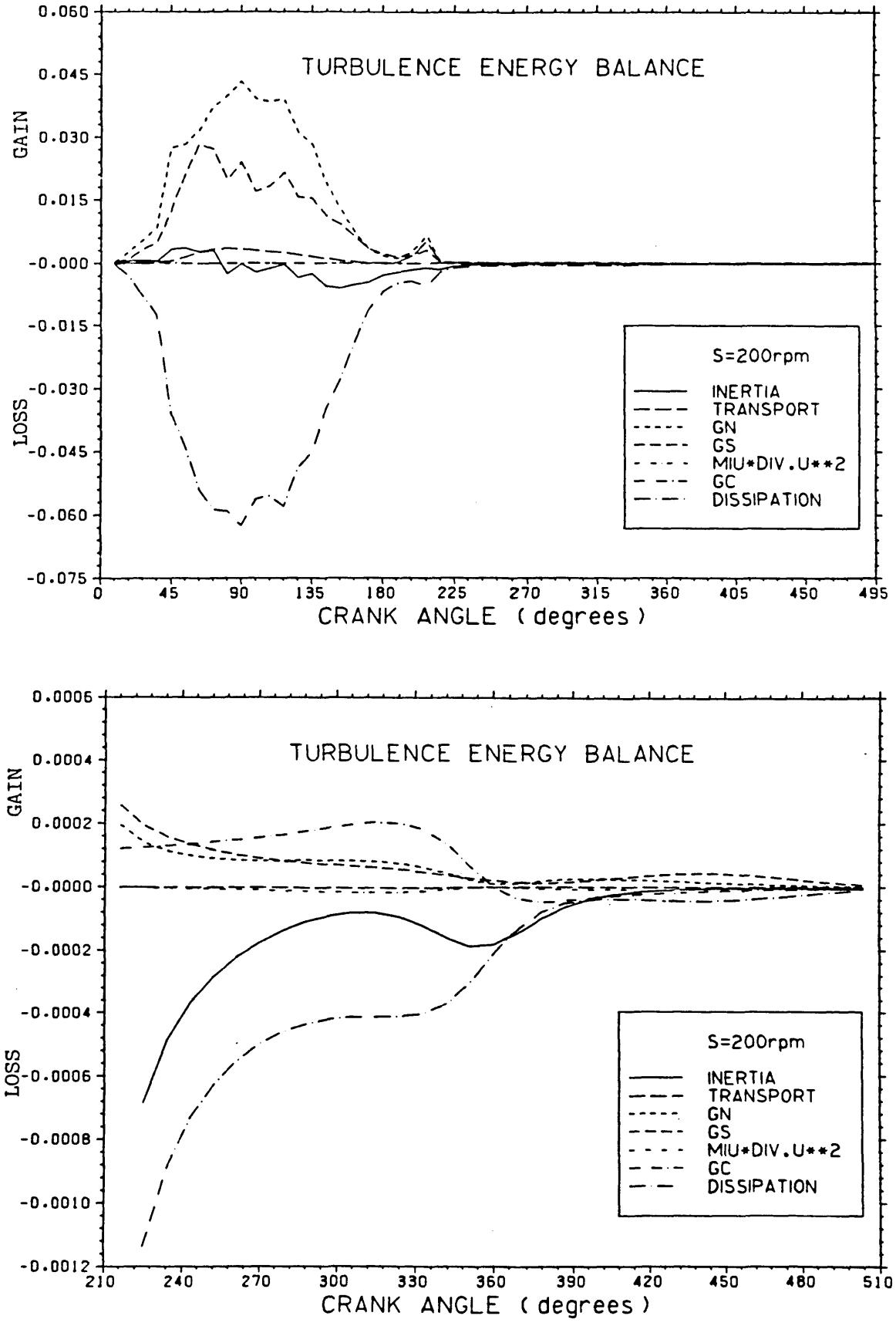


(d)



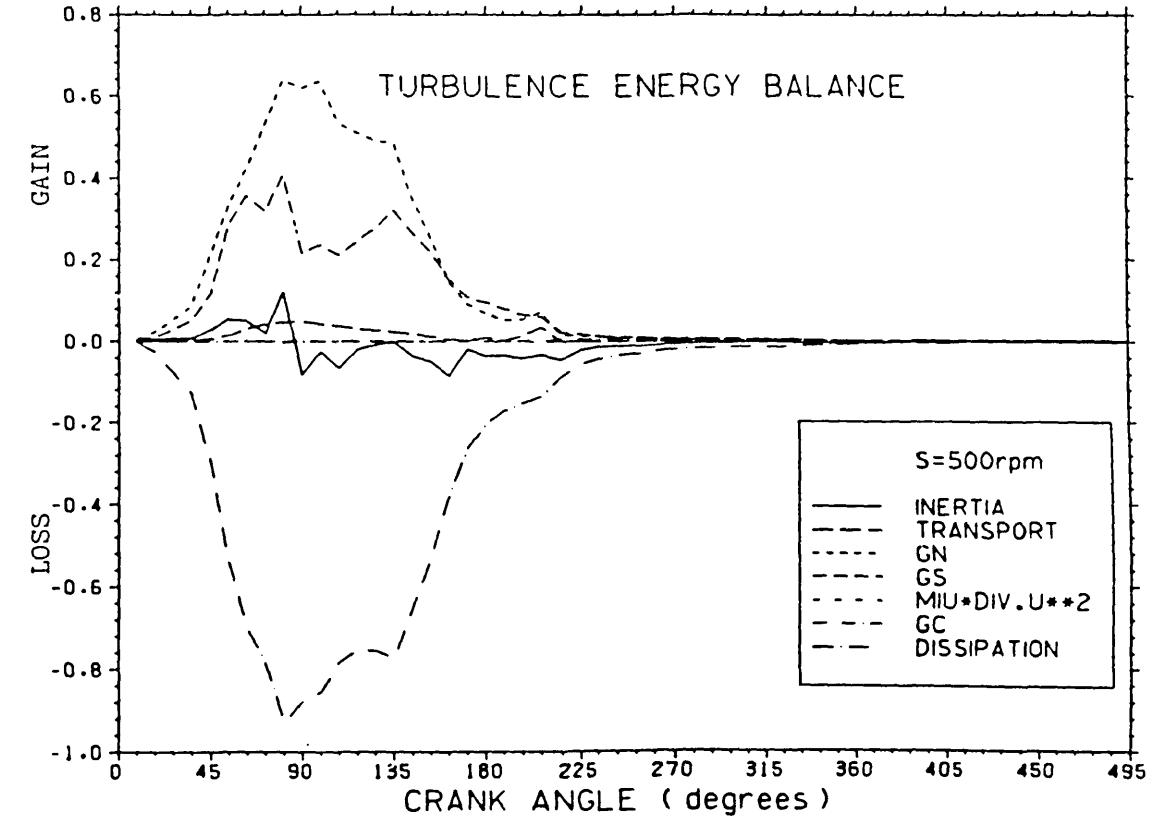
(e)

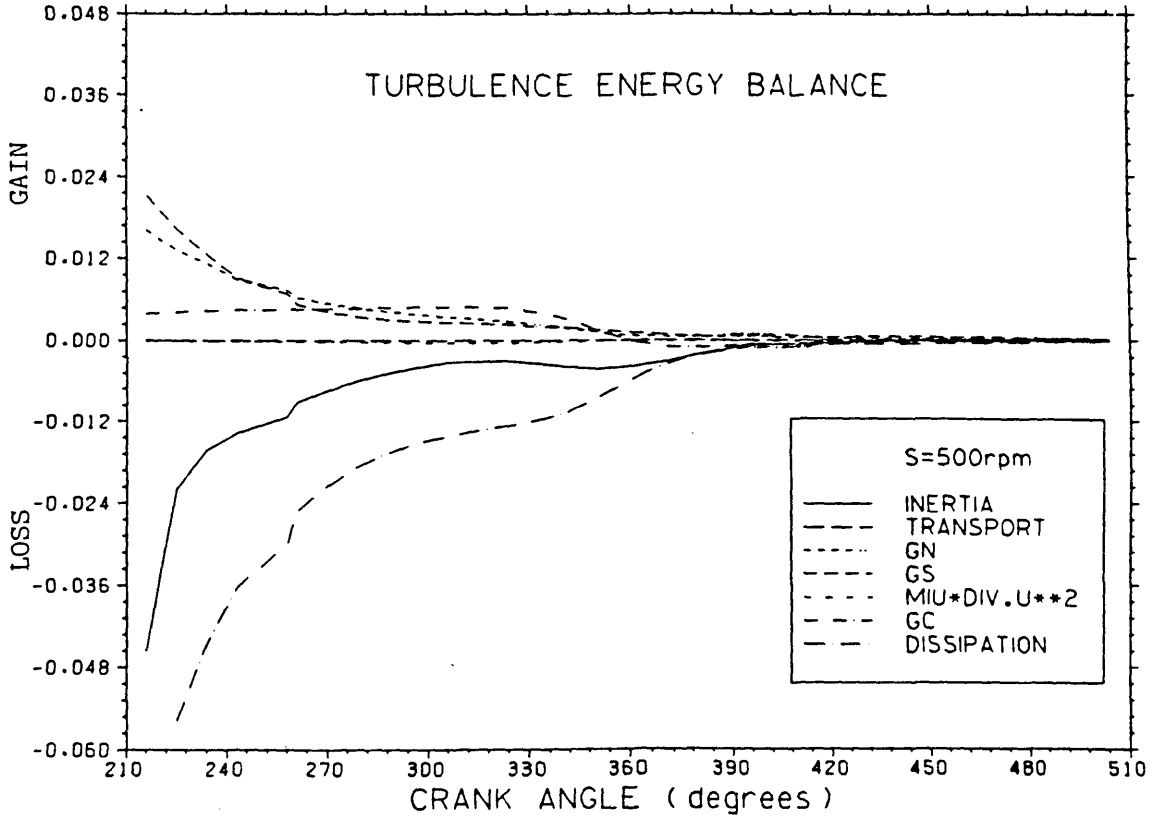
Figure 6.16: Continued



(a)

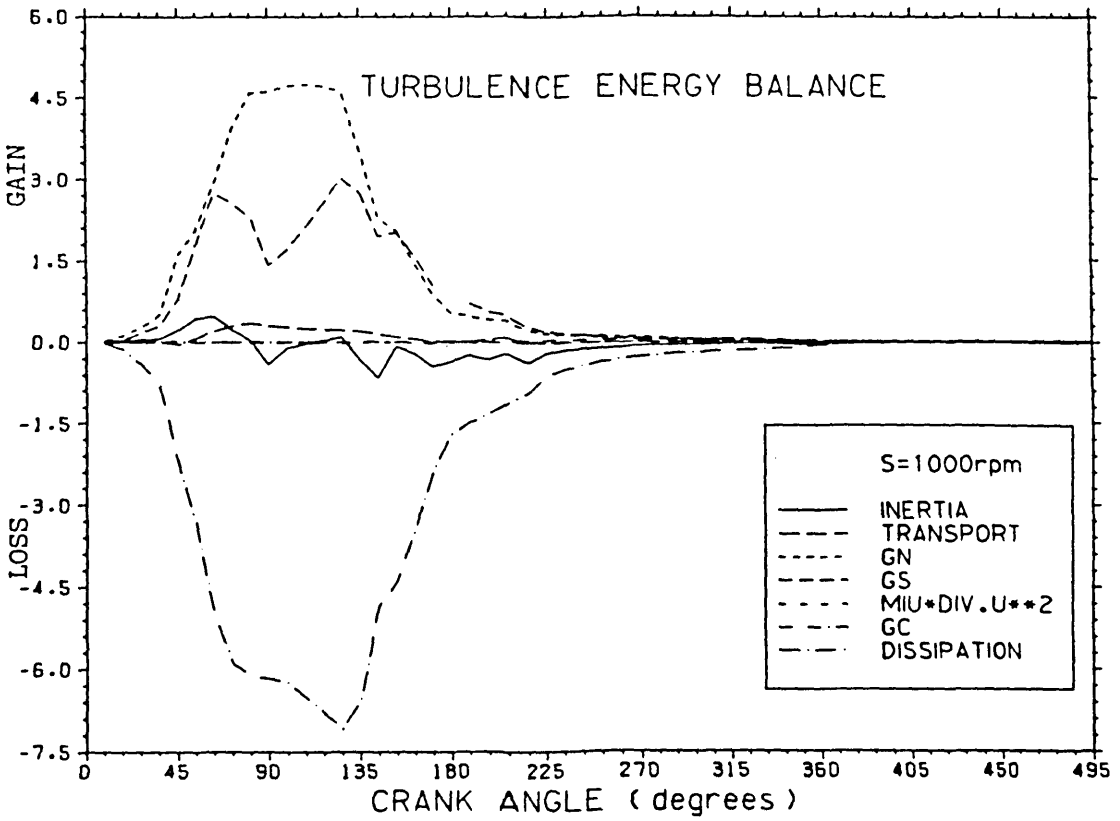
Figure 6.17: The influence of engine speed on the volume-integral balances of the k-transport equation; (a) S = 200 rpm, (b) S = 500 rpm and (c) S = 1000 rpm

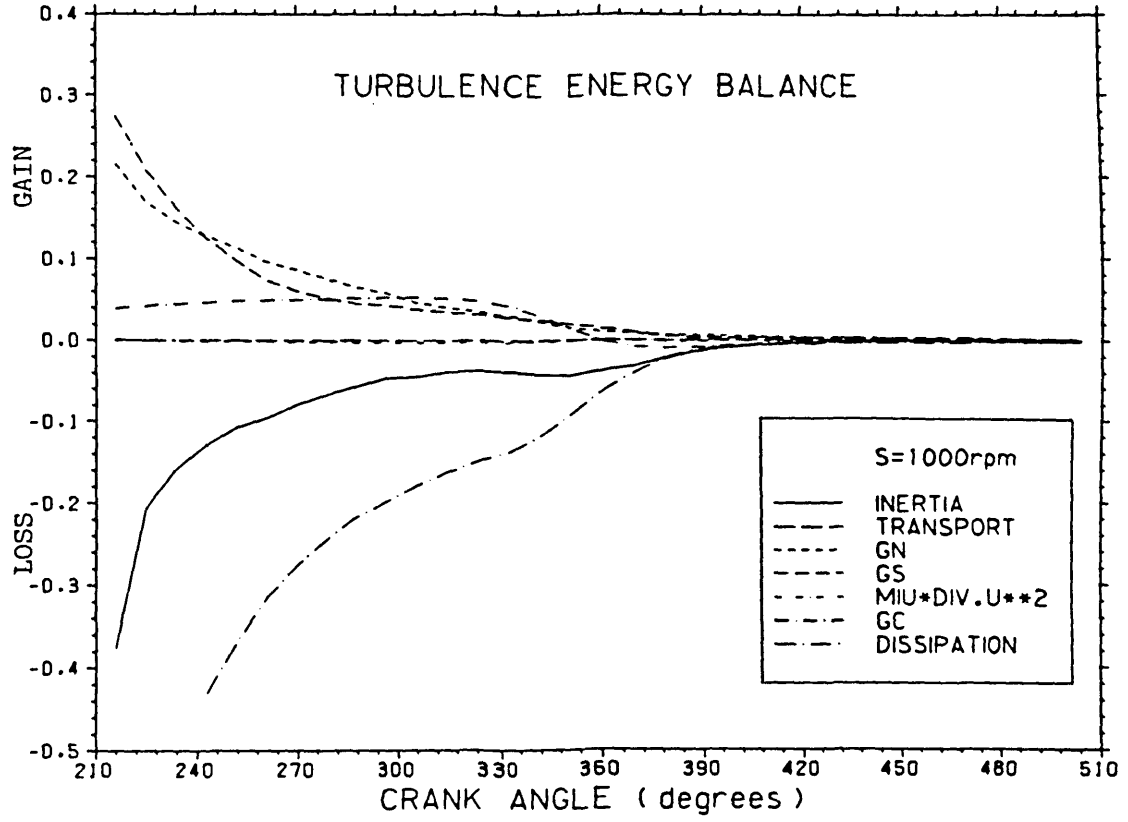




(b)

Figure 6.17: Continued





(c)

Figure 6.17: Continued